Oxidative Medicine and Cellular Longevity

Oxidative Stress and Senescence in Fibrotic Diseases

Lead Guest Editor: Yingqing Chen
Guest Editors: Denan Jin and Xun Cui

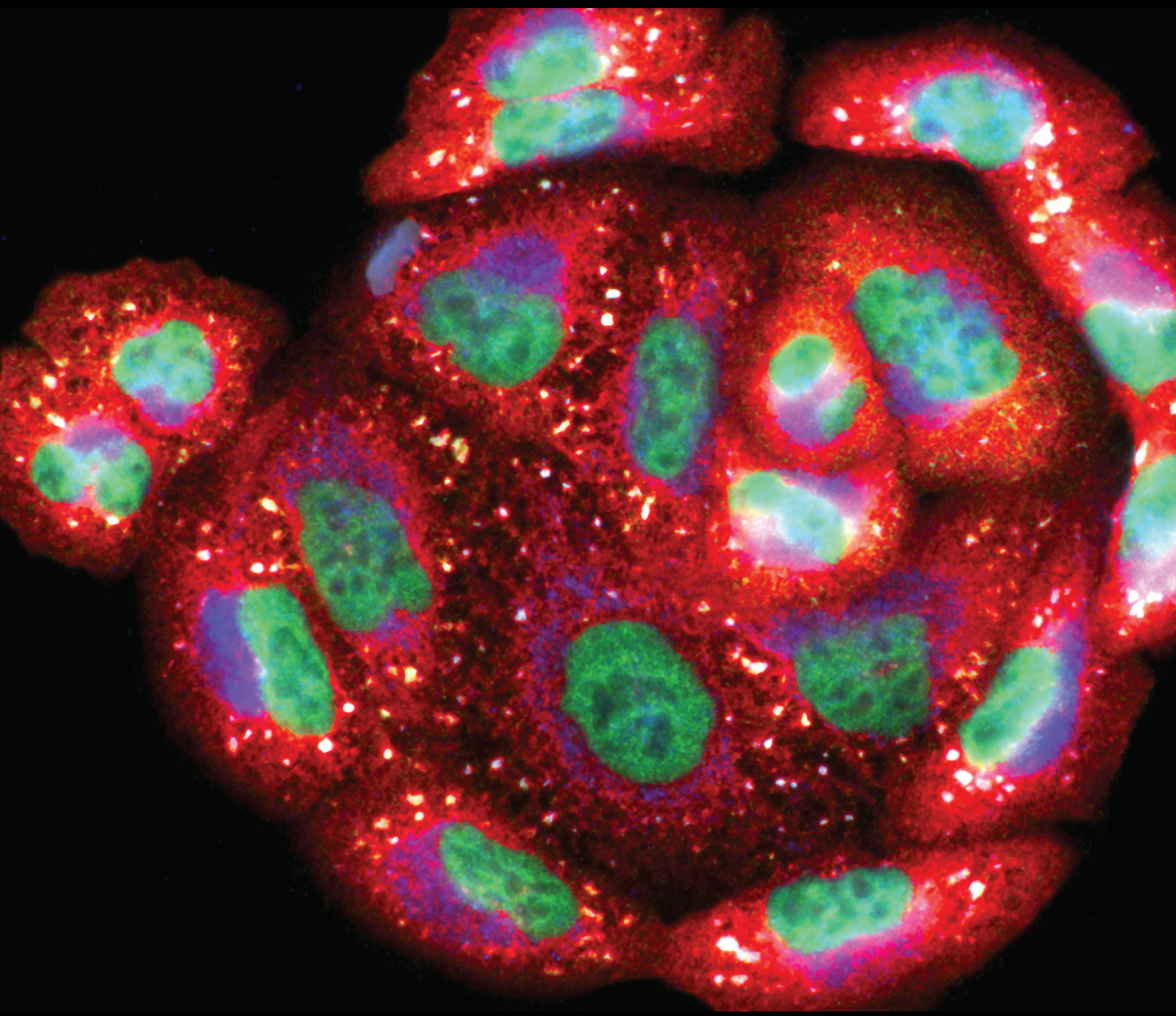

Oxidative Stress and Senescence in Fibrotic Diseases

Oxidative Medicine and Cellular Longevity

Oxidative Stress and Senescence in Fibrotic Diseases

Lead Guest Editor: Yingqing Chen
Guest Editors: Denan Jin and Xun Cui

Chief Editor

Jeannette Vasquez-Vivar, USA

Associate Editors

Amjad Islam Aqib, Pakistan
Angel Catalá, Argentina
Cinzia Domenicotti, Italy
Janusz Gebicki, Australia
Aldrin V. Gomes, USA
Vladimir Jakovljevic, Serbia
Thomas Kietzmann, Finland
Juan C. Mayo, Spain
Ryuichi Morishita, Japan
Claudia Penna, Italy
Sachchida Nand Rai, India
Paola Rizzo, Italy
Mithun Sinha, USA
Daniele Vergara, Italy
Victor M. Victor, Spain

Academic Editors

Ammar AL-Farga, Saudi Arabia
Mohd Adnan, Saudi Arabia
Ivanov Alexander, Russia
Fabio Altieri, Italy
Daniel Dias Rufino Arcanjo, Brazil
Peter Backx, Canada
Amira Badr, Egypt
Damian Bailey, United Kingdom
Rengasamy Balakrishnan, Republic of Korea
Jiaolin Bao, China
Ji C. Bihl, USA
Hareram Birla, India
Abdelhakim Bouyahya, Morocco
Ralf Braun, Austria
Laura Bravo, Spain
Matt Brody, USA
Amadou Camara, USA
Marcio Carocho, Portugal
Peter Celec, Slovakia
Giselle Cerchiaro, Brazil
Arpita Chatterjee, USA
Shao-Yu Chen, USA
Yujie Chen, China
Deepak Chhangani, USA
Ferdinando Chiaradonna, Italy
Zhao Zhong Chong, USA
Fabio Ciccarone, Italy
Alin Ciobica, Romania
Ana Cipak Gasparovic, Croatia
Giuseppe Cirillo, Italy
Maria R. Ciriolo, Italy
Massimo Collino, Italy
Manuela Corte-Real, Portugal
Manuela Curcio, Italy
Domenico D'Arca, Italy
Francesca Danesi, Italy
Claudio De Lucia, USA
Damião De Sousa, Brazil
Enrico Desideri , Italy
Francesca Diomede, Italy
Raul Dominguez-Perles, Spain
Joël R. Drevet, France
Grégory Durand, France
Alessandra Durazzo, Italy
Javier Egea, Spain
Pablo A. Evelson, Argentina
Mohd Farhan, USA
Ioannis G. Fatouros, Greece
Gianna Ferretti, Italy
Swaran J. S. Flora, India
Maurizio Forte, Italy
Teresa I. Fortoul, Mexico
Anna Fracassi , USA
Rodrigo Franco, USA
Juan Gambini, Spain
Gerardo García-Rivas, Mexico
Husam Ghanim, USA
Jayeeta Ghose, USA
Rajeshwary Ghosh, USA
Lucia Gimeno-Mallench , Spain
Anna M. Giudetti, Italy
Daniela Giustarini, Italy
José Rodrigo Godoy, USA
Saeid Golbidi, Canada
Guohua Gong, China
Tilman Grune, Germany
Solomon Habtemariam, United Kingdom
Eva-Maria Hanschmann, Germany
Md Saquib Hasnain, India
Md Hassan, India

Contents

miR-154-5p Affects the TGFβ1/Smad3 Pathway on the Fibrosis of Diabetic Kidney Disease via Binding E3 Ubiquitin Ligase Smurf1
Che Bian, Zhilin Luan, Haibo Zhang, Ruijing Zhang, Jing Gao, Yuxia Wang, Jia Li, and Huiwen Ren
Research Article (17 pages), Article ID 7502632, Volume 2022 (2022)

Discoidin Domain-Containing Receptor 2 Is Present in Human Atherosclerotic Plaques and Involved in the Expression and Activity of MMP-2
Qi Yu, Ruihan Liu, Ying Chen, Ahmed Bilal Waqar, Fuqiang Liu, Juan Yang, Ting Lian, Guangwei Zhang, Hua Guan, Yuanyuan Cui, and Cangbao Xu
Research Article (10 pages), Article ID 1010496, Volume 2021 (2021)

Intraperitoneal Lavage with *Crocus sativus* Prevents Postoperative-Induced Peritoneal Adhesion in a Rat Model: Evidence from Animal and Cellular Studies
Pouria Rahmanian-Devin, Hassan Rakhshandeh, Vafa Baradaran Rahimi, Zahra Sanei-Far, Maede Hasanpour, Arghavan Memarzia, Mehrdad Iranshahi, and Vahid Reza Askari
Research Article (22 pages), Article ID 5945101, Volume 2021 (2021)

Hindawi
Oxidative Medicine and Cellular Longevity
Volume 2022, Article ID 5905374, 19 pages
https://doi.org/10.1155/2022/5905374

Research Article

Cholecystokinin Octapeptide Promotes ANP Secretion through Activation of NOX4–PGC-1α–PPARα/PPARγ Signaling in Isolated Beating Rat Atria

Zhuo-na Han,[1] Xiao-xue Lin,[1] Yue-ying Wang,[1] Ran Ding,[1] Lan Hong,[1] and Xun Cui[1,2]

[1]*Department of Physiology, School of Medical Sciences, Yanbian University, Yanji 133-002, China*
[2]*Cellular Function Research Center, Yanbian University, Yanji 133-002, China*

Correspondence should be addressed to Lan Hong; honglan@ybu.edu.cn and Xun Cui; cuixun@ybu.edu.cn

Received 7 January 2022; Revised 15 May 2022; Accepted 19 May 2022; Published 20 June 2022

Academic Editor: Abdur Rauf

Atrial natriuretic peptide (ANP), a canonical cardiac hormone, is mainly secreted from atrial myocytes and is involved in the regulation of body fluid, blood pressure homeostasis, and antioxidants. Cholecystokinin (CCK) is also found in cardiomyocytes as a novel cardiac hormone and induces multiple cardiovascular regulations. However, the direct role of CCK on the atrial mechanical dynamics and ANP secretion is unclear. The current study was to investigate the effect of CCK octapeptide (CCK-8) on the regulation of atrial dynamics and ANP secretion. Experiments were performed in isolated perfused beating rat atria. ANP was measured using radioimmunoassay. The levels of hydrogen peroxide (H_2O_2) and arachidonic acid (AA) were determined using ELISA Kits. The levels of relative proteins and mRNA were detected by Western blot and RT-qPCR. The results showed that sulfated CCK-8 (CCK-8s) rather than desulfated CCK-8 increased the levels of phosphorylated cytosolic phospholipase A2 and AA release through activation of CCK receptors. This led to the upregulation of NADPH oxidase 4 (NOX4) expression levels and H_2O_2 production and played a negative inotropic effect on atrial mechanical dynamics via activation of ATP-sensitive potassium channels and large-conductance calcium-activated potassium channels. In addition, CCK-8s-induced NOX4 subsequently upregulated peroxisome proliferator-activated receptor γ (PPARγ) coactivator-1α (PGC-1α) expression levels through activation of p38 mitogen-activated protein kinase as well as the serine/threonine kinase signaling, ultimately promoting the secretion of ANP via activation of PPARα and PPARγ. In the presence of the ANP receptor inhibitor, the CCK-8-induced increase of AA release, H_2O_2 production, and the upregulation of NOX4 and CAT expressions was augmented but the SOD expression induced by CCK-8s was repealed. These findings indicate that CCK-8s promotes the secretion of ANP through activation of NOX4–PGC-1α–PPARα/PPARγ signaling, in which ANP is involved in resistance for NOX4 expression and ROS production and regulation of SOD expression.

1. Introduction

Atrial natriuretic peptide (ANP), as a cardiac hormone, is synthesized and secreted mainly from atrial myocytes in response to stretch and other stimuli; it is primarily involved in the regulation of body fluid volume and blood pressure [1–3]. In addition, ANP has anti-ischemic [4], anti-inflammatory [5], antihypertrophic [6], and anticancer [7] properties. Although very little is known about the relationship between ANP and reactive oxygen species (ROS) production under physiological conditions or during the development of cardiovascular disease, ANP is associated with important antioxidant defense in cardiomyocytes and vascular cells [5].

Cholecystokinin (CCK) is a classical gut hormone and a potent stimulator of gallbladder contraction that was found in extracts of small intestinal mucosa in the 1920s [8, 9]. Subsequently, CCK has also been found in neurons [10], immune cells [11], kidney cells, and lung cells [12]. Pro-CCK is processed into several molecular forms such as CCK-58, CCK-33, CCK-22, CCK-8, and CCK-4; however, sulfated carboxyl-terminal CCK octapeptide (CCK-8) is the major biological active fragment of CCK, which retains most

of the bioactivities of CCK. Two types of receptors for CCK (CCK_1 receptor (CCK_1R) and CCK_2 receptor (CCK_2R)) have been classified as belonging to the G protein-coupled receptor superfamily (GPCRs) and its distribution is tissue-dependent [12–14]. Recently, it has been demonstrated that pro-CCK, CCK, and its receptors are expressed in mammalian cardiomyocytes [15, 16]. Studies have shown that CCK has physiological roles in regulating blood pressure [17] and heart rate [15] and can enhance cardiac contractility [18]. In addition, CCK can alleviate fibrosis in the noninfarcted regions and delay the left ventricular remodeling and the progress of heart failure in left coronary artery ligation induced myocardial infarction of rats [19]. Nevertheless, the development of post-infarction heart failure is associated with the upregulation of CCK levels in relation to cardiac functional parameters and brain natriuretic peptide levels [20]. Furthermore, mRNA and protein levels of CCK are increased in the hypertrophic myocardial tissue of rats, which was positively correlated with changes in the left ventricular wall thickness [12]. In clinical studies of heart failure patients, an increase in plasma CCK is associated with mortality in elderly females [21]. Thus, CCK signaling induces multiple effects on cardiovascular physiology and pathophysiology. Still, the direct roles of CCK on the regulation of atrial mechanical dynamics and ANP secretion are not yet identified.

Nicotinamide adenine dinucleotide phosphate oxidases (NOXs), a major enzymatic source of ROS in the cardiovascular system, are activated in specific cardiovascular diseases [22]. Previously, we have found that NOX4, controlled by phospholipase A2 (PLA2), is involved in the regulation of ANP secretion in isolated beating rat atria under hypoxic conditions [23]. Moreover, it has been confirmed that the insensitivity of the CCK_1R inositol phosphate signaling to pertussis toxin (PTX) indicates that it couples through the Gq family of the G proteins, thereby linking with the PLA2–arachidonic acid (AA) pathway to mediate calcium oscillation and amylase secretion [24, 25]. In contrast, CCK_2R is coupled to two pathways through PTX-sensitive and PTX-insensitive G proteins, resulting in the regulation of AA release by PTX-sensitive G proteins [24, 26] and mitogen-activated protein kinase (MAPK) signaling pathways [24, 27]. Owing to the effect of PLA2–AA signaling on NOX4 activity and its role in the regulation of atrial ANP secretion [23, 28], we hypothesize that CCK regulates ANP secretion through activation of NOX4 via PLA2–AA signaling. This study is to verify the hypothesis using CCK-8 in isolated perfused beating rat atria. This study shows that sulfated CCK-8 (CCK-8s) rather than desulfated CCK-8 promotes ANP secretion through activation of NOX4–peroxisome proliferator-activated receptor γ (PPARγ) coactivator-1α (PGC-1α)–PPARα/PPARγ signaling, in which CCK-8s-induced ANP is involved in the resistance for NOX4 expression and ROS production and regulation of SOD expression.

2. Materials and Methods

2.1. Preparation of a Perfused Beating Rat Atrium Model In Vitro. All animal experiments in this study were reviewed and approved by the Institutional Animal Care and Use Committee of Yanbian University and were in accordance with the National Institutes of Health Laboratory Animal Care Guidelines. Specific pathogen-free (SPF) Sprague-Dawley (SD) rats (250~300 g, 18 weeks, male) were obtained from the Laboratory Animal Center of Yanbian University (laboratory animal use license number: SYXK (Ji) 2020-0009) for preparation for the beating rat atrial perfusion model. The environmental temperature for the rats was about 18°C~26°C, the relative humidity was 40%~70%, the light cycle was 12 h light/dark, and water was available ad libitum alongside a standard diet. Sterile normal saline was used to prepare the pentobarbital sodium solution, and SD rats were intraperitoneally anesthetized at a dose of 90 mg/kg. Immediate thoracotomy was performed, and the left atrium of the rat was harvested and fixed on a self-made beating rat atrial perfusion device. Each rat left atrium was subjected to atrial electrical stimulation, and a peristaltic pump was used to infuse HEPES buffer and the reagents required for the experiment into the atria at a constant rate of 1.0 mL/min. A continuous oxygen supply was maintained along with an atrial temperature of 36°C. HEPES buffer contained (in mM) 118.0 NaCl, 4.7 KCl, 2.5 $CaCl_2$, 1.2 $MgCl_2$, 25.0 $NaHCO_3$, 10.0 glucose, 10.0 HEPES (pH 7.4 with NaOH), and 0.1% BSA.

2.2. Experimental Protocols and Treatment Reagents

2.2.1. Experimental Grouping and Treatment Reagents. Rats were randomized into 18 different groups: (1) control; (2) CCK-8s (sulfated cholecystokinin octapeptide, 100.0 pM; AS-200741; Eurogentec, Germany); (3) CCK-8d (desulfated cholecystokinin octapeptide, 100.0 pM; HY-P0196A; MedChemExpress, USA); (4) Loxiglumid (an antagonist of CCK_1R, 0.5 mM; HY-B2154; MedChemExpress, USA) + CCK-8s (100.0 pM); (5) YM022 (an antagonist of CCK_2R, 70.0 pM; HY-103355; MedChemExpress, USA) + CCK-8s (100.0 pM); (6) U-73122 (an inhibitor of phospholipase C (PLC), 10.0 μM; HY-13419; MedChemExpress, USA) + CCK-8s (100.0 pM); (7) CAY10650 (an inhibitor of cytosolic phospholipase A2 (cPLA2), 120.0 nM; HY-10801; MedChemExpress, USA) + CCK-8s (100.0 pM); (8) GLX351322 (an inhibitor of NADPH oxidase 4 (NOX4), 25.0 μM; HY-100.0111; MedChemExpress, USA) + CCK-8s (100.0 pM); (9) GLX351322 (25.0 μM); (10) Glibenclamide (an inhibitor of ATP-sensitive potassium (K_{ATP}) channel, 0.1 mM; PHR1287; Sigma-Aldrich, USA) + CCK-8s (100.0 pM); (11) GAL-021 (a blocker of large-conductance calcium-activated potassium (BK_{Ca}), 30.0 μM; HY-101422; MedChemExpress, USA) + CCK-8s (100.0 pM); (12) SB239063 (an antagonist of p38 MAPK, 15.0 μM; HY-11068; MedChemExpress, USA) + CCK-8s (100.0 pM); (13) LY294002 (an inhibitor of serine/threonine kinase (Akt), 10.0 μM; HY-10108; MedChemExpress, USA) + CCK-8s (100.0 pM); (14) SR-18292 (an antagonist of peroxisome proliferator-activated receptor γ (PPARγ) coactivator-1α (PGC-1α), 50.0 μM; HY-101491; MedChemExpress, USA) + CCK-8s (100.0 pM); (15) GW6471 (an antagonist of PPARα, 10.0 μM; HY-15372; MedChemExpress, USA) + CCK-8s (100.0 pM); (16) GW9662 (an inhibitor of PPARγ,

0.1 μM; HY-16578; MedChemExpress, USA) + CCK-8s (100.0 pM); (17) A71915 (an antagonist of ANP, 0.3 μM; SML2908; Sigma-Aldrich, USA) + CCK-8s (100.0 pM); (18) A71915 (0.3 μM).

2.2.2. Experimental Protocols. Each left atrium was first stably perfused for 60 min, followed by six cycles of reperfusion according to the experimental group, each cycle for 12 min, as shown in Table 1. To evaluate the effects of CCK-8 on atrial pulse pressure and ANP secretion, two cycles of control period were followed by infusion of CCK-8s or CCK-8d for four cycles. In another series of experiments, one cycle of the control period was followed by one cycle of treatment reagents and then CCK-8s for four cycles in the continuous presence of the treatment reagents. To test the effects of GLX and A71 on the atrial pulse pressure and ANP secretion, the control period was followed by five cycles of GLX or A71. All atria were harvested immediately after the end of perfusion and cryopreserved at -80°C for subsequent experiments.

2.3. Determination of ANP and Pulse Pressure. As previously described [23], ANP levels of perfusates were detected using an Iodine [^{125}I] Atrial Natriuretic Factor Radioimmunoassay Kit (North Institute of Biological Technology, Beijing, China). Changes in atrial pulse pressure were recorded using a multichannel physiological signal acquisition system (RM6240BD, 1.5 Hz, 0.3 ms, 35.0 V; Chengdu, China) via a baroreceptor (Statham P23Db; Oxnard, CA, USA).

2.4. ELISA. The levels of hydrogen peroxide (H_2O_2) and AA in equal volumes of rat left atrial lysis solutions were determined using the Rat H_2O_2 ELISA Kit and Rat AA ELISA Kit; these kits were purchased from SinoBestBio (Shanghai, China)

2.5. Western Blot Analysis and Antibodies. Left atria were lysed and homogenized adequately using RIPA buffer (high) (R0010, Solarbio Science & Technology; Beijing, China) in an ice bath. Protein quantification was then performed using an Enhanced BCA Protein Assay Kit (P0009, Beyotime; Shanghai, China). The samples were subjected to protein denaturation with 5× sodium dodecyl sulfate-polyacrylamide gel electrophoresis (SDS-PAGE) loading buffer (ComWin Biotech; Beijing, China). Denatured samples were electrophoresed in 8% or 15% SDS-PAGE gels at room temperature. After electrophoresis, the separated proteins were transferred from the gel to a polyvinylidene fluoride (PVDF) membrane using the wet transfer method and transferred for 60 min or 90 min at 4°C. The blotted membranes were blocked with 5% nonfat dry milk in PBS for 2 h at room temperature, followed by incubation with primary antibodies overnight at 4°C. The next day, after incubation with secondary antibodies for 2 h, the membranes were washed for 30 min and developed using a sensitive ECL chemiluminescence detection kit (PK10002, Proteintech; Wuhan, China). The bands were analyzed grayscale using ImageJ (National Institutes of Health; Bethesda, USA) software, and the results of the analysis were normalized.

The following antibodies were used in this experiment: an antibody of CCK_1R (DF4914), an antibody of CCK_2R (DF2793), an antibody of phospho-cPLA2 (Ser505) (AF3329), an antibody of cPLA2 (AF6329), an antibody of NOX4 (DF6924), an antibody of PGC-1α (AF5395), an antibody of phospho-PPARα (Ser12) (AF8392), an antibody of PPARα (AF5301), an antibody of phospho-PPARγ (Ser112) (AF3284), an antibody of PPARγ (AF6284), an antibody of superoxide dismutase (SOD) (AF5144), an antibody of catalase (CAT) (DF7545), an antibody of glutathione peroxidase (GPX) (DF6701), an antibody of phospho-pan-AKT1/2/3 (Ser473) (AF0016), and an antibody of pan-AKT1/2/3 (AF6261) were all purchased from Affinity Biosciences (Jiangsu, China). An antibody of phospho-p38 MAPK (Thr180/Tyr182) polyclonal (28796-1-AP), an antibody of p38 MAPK polyclonal (14064-1-AP), and HRP goat anti-rabbit IgG were all bought from Proteintech (Wuhan, China). Natriuretic peptide A (NPPA) rabbit pAb (A14755) and β-actin rabbit mAb (High Dilution) (AC026) were from ABclonal Technology (Wuhan, China).

Table 1: Experimental protocols.

Time (min)	0	12	24	36	48	60	72
1 group				Cont			
2 group		Cont			CCK-8s		
3 group		Cont			CCK-8d		
4 group	Cont	Lo			Lo+CCK-8s		
5 group	Cont	YM			YM+ CCK-8s		
6 group	Cont	U			U+CCK-8s		
7 group	Cont	CAY			CAY+CCK-8s		
8 group	Cont	GLX			GLX+CCK-8s		
9 group	Cont			GLX			
10 group	Cont	Gli			Gli+CCK-8s		
11 group	Cont	GAL			GAL+CCK-8s		
12 group	Cont	SB			SB+CCK-8s		
13 group	Cont	LY			LY+CCK-8s		
14 group	Cont	SR			SR+CCK-8s		
15 group	Cont	GW64			GW64+CCK-8s		
16 group	Cont	GW96			GW96+CCK-8s		
17 group	Cont	A71			A71+CCK-8s		
18 group	Cont			A71			

Note: control (Cont); sulfated CCK-8 (CCK-8s); desulfated CCK-8 (CCK-8d); Loxiglumid (Lo); YM022 (YM); U-73122 (U); CAY10650 (CAY); GLX351322 (GLX); Glibenclamide (Gli); GAL-021 (GAL); SB239063 (SB); LY294002 (LY); SR-18292 (SR); GW6471 (GW64); GW9662 (GW96); A71915 (A71).

2.6. RT-qPCR. In brief, total RNA was extracted from left atrial tissues using an RNApure Total RNA Kit (RN03, Aidlab; Beijing, China). The first strand of cDNA was then synthesized by high-performance reverse transcription using a SweScript RT I First Strand cDNA Synthesis Kit (G3330, Servicebio; Wuhan, China). Finally, the real-time quantitative polymerase chain reaction (RT-qPCR) was performed with 2× SYBR Green qPCR Master Mix (High ROX) (G3322, Servicebio; Wuhan, China). Results were calculated using the $2^{-\Delta\Delta CT}$ relative quantification method and were normalized. Primer sequences are shown in Table 2.

2.7. Statistical Analysis. Statistical analysis was performed by one-way ANOVA and two-way ANOVA with Tukey's multiple comparison test using GraphPad Prism 9.0 (GraphPad

Table 2: Primer sequences.

Gene	Primer sequence
NPPA	S: 5′-TTCCTCTTCCTGGCCTTTTG-3′ A: 5′-TCTAGCAGGTTCTTGAAATCCATC-3′
PPARα	S: 5′-TCCACAAGTGCCTGTCCGTC-3′ A: 5′-CTTCAGGTAGGCTTCGTGGATT-3′
PPARγ	S: 5′-TTTCAAGGGTGCCAGTTTCG-3′ A: 5′-GGAGGCCAGCATGGTGTAGAT-3′
β-Actin	S: 5′-TGCTATGTTGCCCTAGACTTCG-3′ A: 5′-GTTGGCATAGAGGTCTTTACGG-3′

Note: S: sense primer; A: antisense primer.

Software; San Diego, USA). All data were normally distributed (Kolmogorov-Smirnov test) and given as mean ± standard error of the mean (SEM). $P < 0.05$ was considered statistically significant.

3. Results

3.1. Effects of CCK-8 on the ANP Secretion and Atrial Dynamics. To determine the effects of CCK-8 on atrial dynamics and ANP secretion, CCK-8s and CCK-8d were used in the experiments. In isolated beating rat atria, the infusion of CCK-8s significantly increased ANP secretion and inhibition of atrial pulse pressure ($P < 0.001$ vs. control period; Figures 1(a) and 1(b)) in a time-dependent manner. Meanwhile, CCK-8d obviously inhibited the atrial pulse pressure ($P < 0.001$ vs. control period; Figure 1(d)) but did not affect the ANP secretion (Figure 1(c)). In the presence of CCK_1R and CCK_2R antagonists, Loxiglumid and YM022, the CCK-8s-induced increase of ANP secretion was abolished completely ($P < 0.001$ vs. CCK-8s alone period; Figures 1(e) and 1(g)). The CCK-8s-induced inhibition of atrial pulse pressure was almost completely blocked by Loxiglumid ($P < 0.001$ vs. CCK-8s alone period; Figure 1(f)) and notably attenuated by YM022 ($P < 0.001$ vs. CCK-8s alone period; Figure 1(h)). In addition, the expressions of CCK_1R and CCK_2R were significantly upregulated in atrial tissue after infusion of CCK-8s rather than CCK-8d ($P < 0.001$ vs. control group; Figures 1(i)–1(k)). The results indicated that sulfated rather than desulfated CCK-8 was able to promote ANP secretion through CCK receptors and has a negative inotropic effect on the mechanical dynamics of isolated perfused beating rat atria.

3.2. Effects of PLC and cPLA2 on CCK-8s-Induced ANP Secretion. CCK receptors couple Gq proteins to PLC and PLA2, subsequently leading to downstream signaling [24–27]. Therefore, to investigate the mechanism by which CCK-8s promotes ANP secretion, the effects of CCK-8s on the levels of p-cPLA2 and its role in ANP secretion were observed. As shown in Figure 2, the levels of p-cPLA2 were markedly increased in atrial tissue after infusion of CCK-8s ($P < 0.01$ vs. control group; Figures 2(a)–2(c)), which were blocked by pretreatment with antagonists of CCK receptors ($P < 0.01$ vs. CCK-8s group; Figures 2(a) and 2(b)) and U73122, an inhibitor of PLC ($P < 0.01$ vs. CCK-8s group; Figures 2(a) and 2(c)). In addition, infusion of the CCK-8s increased ANP secretion which was also prevented by pretreatment with U73122 ($P < 0.001$ vs. CCK-8s alone period; Figure 2(d)) and CAY10650, an inhibitor of cPLA2 ($P < 0.001$ vs. CCK-8s alone period; Figure 2(f)), while CCK-8s-induced inhibition of pulse pressure was not affected by U73122 and CAY10650 (Figures 2(e) and 2(g)). The data suggested that PLC and cPLA2 mediate the process of CCK-8s-induced increase of atrial ANP secretion.

3.3. Effects of CCK-8s on NOX4 Expression and Its Role in ANP Secretion. According to the role of CCK-8s on the levels of p-cPLA2 and the effect of cPLA2 on AA release and NOX4 activation [29], the levels of AA, NOX4 expression, and H_2O_2 production induced by CCK-8s were observed. Results revealed that the levels of AA were remarkably increased in atrial tissue after infusion of CCK-8s ($P < 0.001$ vs. control group; Figure 3(a)), which were blocked by pretreatment with antagonists of CCK receptors and U73122 ($P < 0.001$ and $P < 0.01$ vs. CCK-8s group; Figure 3(a)). In addition, the expression of NOX4 was dramatically upregulated in CCK-8s-infused atrial tissue ($P < 0.001$ vs. control group; Figures 3(b)–3(d)); this effect was blocked by antagonists of CCK receptors and CAY10650 pretreatment ($P < 0.001$ vs. CCK-8s group; Figures 3(b)–3(d)). The levels of H_2O_2 were also markedly increased in atrial tissue after infusion of CCK-8s ($P < 0.001$ vs. control group; Figure 3(e)), which were abolished by pretreatment with antagonists of CCK receptors ($P < 0.001$ vs. CCK-8s group; Figure 3(e)). Furthermore, in the presence of GLX351322, an inhibitor of NOX4, CCK-8s-induced increase of ANP secretion was not observed ($P < 0.001$ vs. CCK-8s alone period; Figure 3(f)), and the inhibition of atrial pulse pressure was also removed ($P < 0.001$ vs. control period and CCK-8s alone period; $P > 0.05$ vs. GLX351322 alone period; Figure 3(g)). In the presence of Glibenclamide, an inhibitor of K_{ATP}, the effects of CCK-8s on atrial ANP secretion and mechanical dynamics were removed ($P < 0.001$ vs. CCK-8s alone period, respectively; Figures 3(h) and 3(i)), and a blocker of BK_{Ca}, GAL-021, mimicked the role of Glibenclamide ($P < 0.001$ vs. CCK-8s alone period, respectively; Figures 3(j) and 3(k)). These results suggested that CCK-8s upregulated the expression of NOX4 via cPLA2–AA signaling, thereby increasing the secretion of ANP and exerting a negative inotropic effect on atrial mechanical dynamics, in which K_{ATP} and BK_{Ca} were involved.

3.4. Effects of CCK-8s-Induced NOX4 on p38 MAPK and Akt Expressions. In accordance with the relationship between the activation of the NOX4-dependent p38 MAPK axis and cell oxidative damage [30], the effects of CCK-8s-induced NOX4 on the p38 MAPK and Akt protein expression in atrial tissue after infusion of CCK-8s were observed. The data showed that CCK-8s notably increased the levels of phosphorylated p38 (p-p38) MAPK, ($P < 0.05$ vs. control group; Figures 4(a) and 4(b)) and phosphorylated Akt (p-Akt) ($P < 0.01$ vs. control group; Figures 4(a) and 4(c)), which

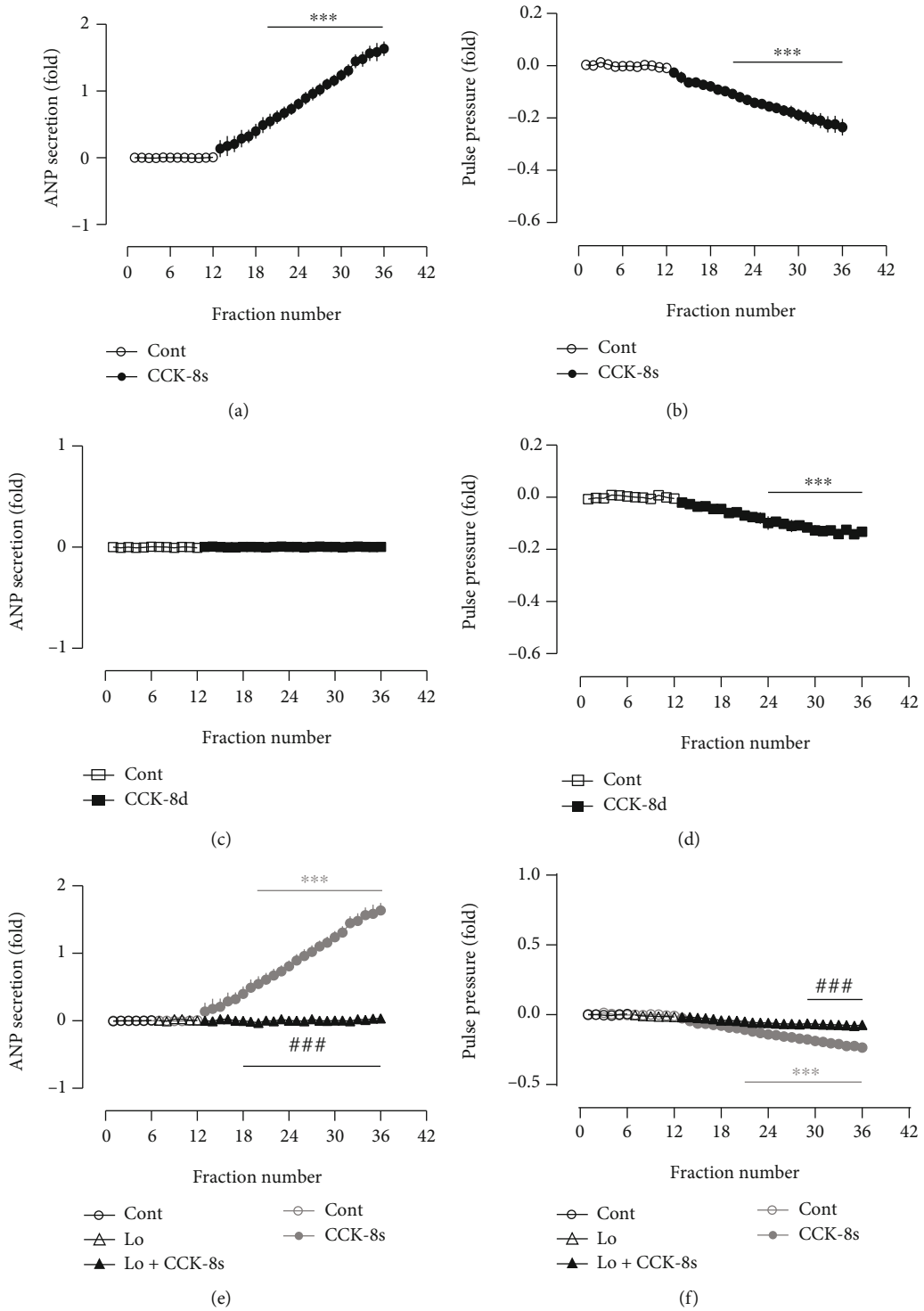

Figure 1: Continued.

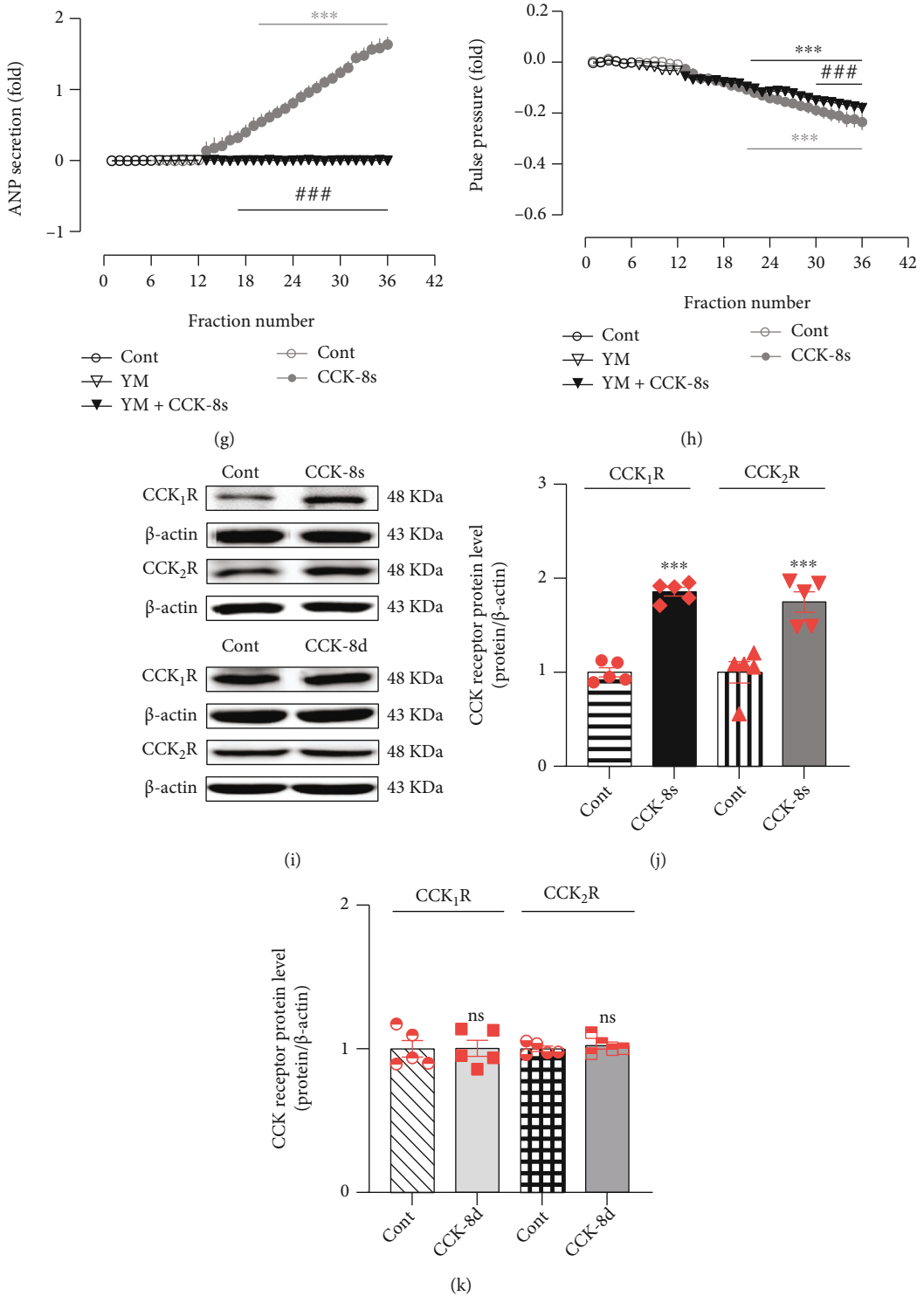

Figure 1: CCK-8 role in ANP secretion and dynamics and its effects on CCK receptor expressions in isolated beating rat atria. (a, c, e, g) Atrial ANP secretion by radioimmunoassay. (b, d, f, h) Atrial pulse pressure by RM6240BD. (i) The protein expression levels of CCK_1R and CCK_2R were detected by Western blot. (j, k) The statistics histograms of Western blot were expressed as band density normalized versus β-actin. Cont: control; CCK-8s: sulfated CCK-8; CCK-8d: desulfated CCK-8; Lo: Loxiglumid, an antagonist of CCK_1 receptor; YM: YM022, an antagonist of CCK_2 receptor. Data were expressed as mean ± SEM. (a–h) $n = 6$; (i–k) $n = 5$. $^{***}P < 0.001$ vs. control period or group; $^{###}P < 0.001$ vs. CCK-8s period or group; ns: no significant.

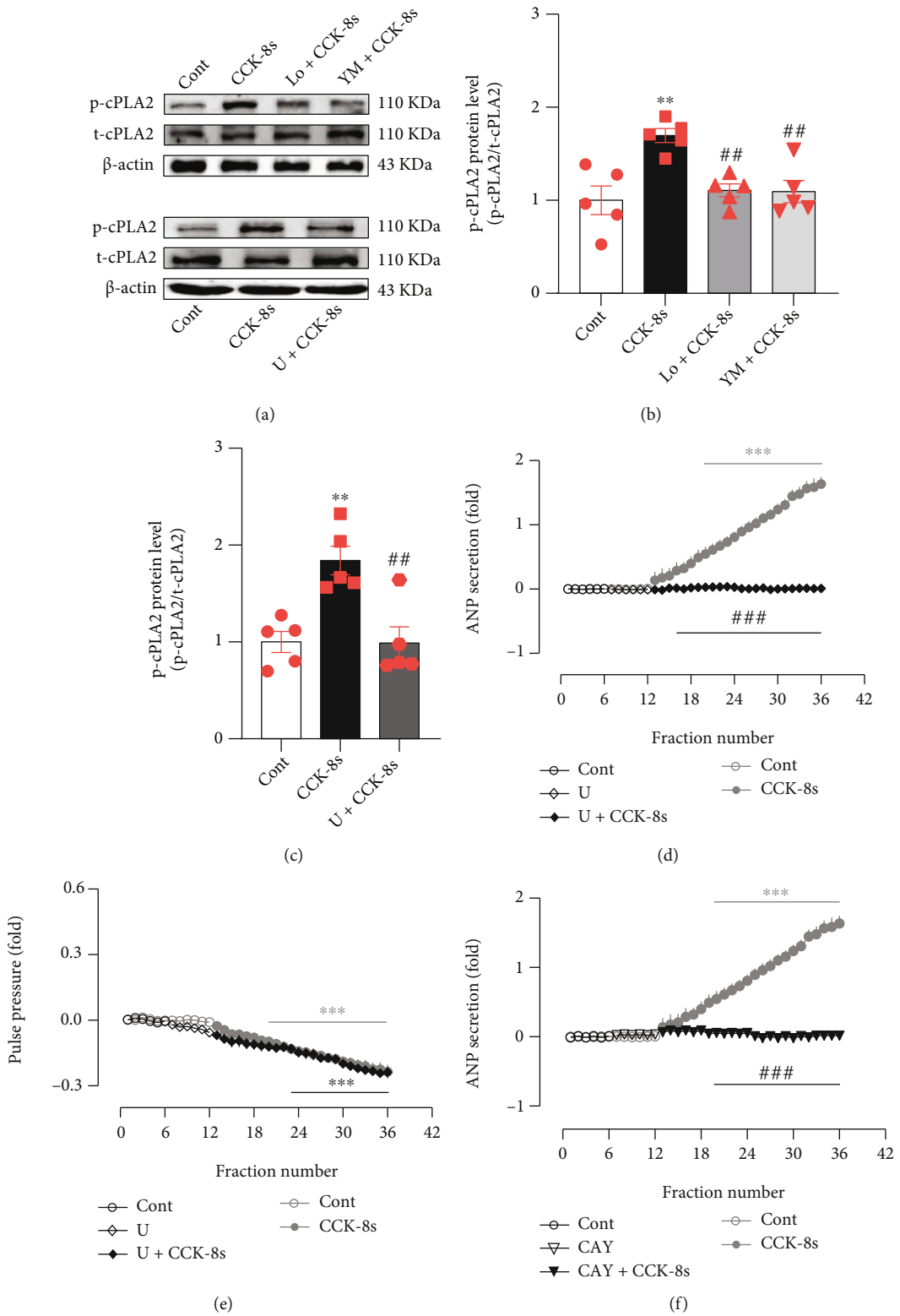

Figure 2: Continued.

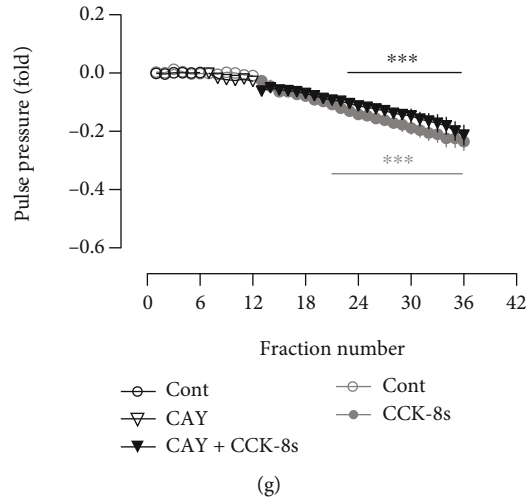

Figure 2: Effects of CCK-8s and PLC on cPLA2 expression and its role in ANP secretion and dynamics in isolated beating rat atria. (a) The protein expression levels of p-cPLA2 were detected by Western blot. (b, c) The statistics histograms of Western blot were expressed as band density normalized versus t-cPLA2. (d, f) Atrial ANP secretion by radioimmunoassay. (e, g) Atrial pulse pressure by RM6240BD. Cont: control; CCK-8s: sulfated CCK-8; Lo: Loxiglumid, an antagonist of CCK_1 receptor; YM: YM022, an antagonist of CCK_2 receptor; U: U-73122, an inhibitor of PLC; CAY: CAY10650, an inhibitor of cPLA2. Data were expressed as mean ± SEM. (a–c) $n = 5$; (d–g) $n = 6$. $^{**}P < 0.01$ and $^{***}P < 0.001$ vs. control period or group; $^{\#\#}P < 0.01$ and $^{\#\#\#}P < 0.001$ vs. CCK-8s period or group.

were eliminated by GLX351322 ($P < 0.05$ and $P < 0.01$ vs. CCK-8s group; Figures 4(a)–4(c)). Moreover, the CCK-8s-induced ANP secretion was blocked by inhibitors of p38 MAPK and Akt, SB239063, and LY294002 ($P < 0.001$ vs. CCK-8s alone period; Figures 4(d) and 4(f)), while the inhibition of atrial pulse pressure induced by CCK-8s was not notably changed by SB239063 and LY294002 (Figures 4(e) and 4(g)). These results demonstrated that p38 MAPK and Akt controlled by NOX4 were involved in the regulation of CCK-8s-induced ANP secretion.

3.5. Effects of CCK-8s on the Expressions of PGC-1α and PPARα as well as PPARγ. To investigate the downstream mechanism that p38 MAPK and Akt regulate the CCK-8s-induced increase of ANP secretion, effects of CCK-8s on the expressions of PGC-1α and PPARα as well as PPARγ were determined. CCK-8s notably upregulated the expression of PGC-1α ($P < 0.001$ vs. control group; Figures 5(a)–5(c)), which was abolished by SB239063 and LY294002 ($P < 0.001$ and $P < 0.01$ vs. CCK-8s group respectively; Figures 5(a)–5(c)). In the presence of SR18292, an antagonist of PGC-1α, the CCK-8s-induced increase of ANP secretion was not observed ($P < 0.001$ vs. CCK-8s alone period; Figure 5(d)), while the inhibition of pulse pressure induced by CCK-8s was augmented ($P < 0.001$ vs. CCK-8s alone period; Figure 5(e)).

In addition, CCK-8s noticeably increased the mRNA levels of PPARα and PPARγ ($P < 0.001$ vs. control group; Figures 6(a) and 6(b)), concomitant with upregulation of p-PPARα and p-PPARγ protein expression levels ($P < 0.001$ vs. control group; Figures 6(c)–6(e)). The CCK-8s-induced increases of PPARα and PPARγ mRNA were notably inhibited by SR18292 ($P < 0.001$ vs. CCK-8s group; Figures 6(a) and 6(b)), and the protein expression levels of PPARα and PPARγ were also abolished by SR18292 ($P < 0.001$ vs. CCK-8s group; Figures 6(c)–6(e)). CCK-8s also enhanced the NPPA mRNA levels ($P < 0.001$ vs. control group; Figure 6(f)), which were abrogated by inhibitors of CCK receptors ($P < 0.001$ vs. CCK-8s group; Figure 6(f)). Moreover, inhibitors of PPARα and PPARγ, GW6471 and GW9662, not only markedly inhibited the effect of CCK-8s-enhanced mRNA levels of the NPPA ($P < 0.001$ vs. control group; $P < 0.001$ vs. CCK-8s group; Figure 6(f)), but also abolished the role of CCK-8s on ANP secretion ($P < 0.001$ vs. CCK-8s alone period; Figures 6(g) and 6(h)). However, the inhibition of atrial pulse pressure induced by CCK-8s was not affected by GW6471 and GW9662 (Figures 6(i) and 6(j)). These results demonstrated that PGC-1α regulated PPARα and PPARγ were involved in the regulation of CCK-8s-induced increase of ANP secretion.

3.6. Effects of Endogenous ANP on NOX4, SOD, and CAT Expressions under CCK-8s Action. To define the effects of endogens ANP on NOX4, SOD, and CAT protein expressions under CCK-8s action, another series of experiments were performed with an ANP receptor antagonist. Results showed that CCK-8s significantly increased SOD and CAT rather than GPX protein expression levels ($P < 0.01$ and $P < 0.001$ vs. control group; Figures 7(a)–7(d)); these effects were blocked by inhibitors of CCK receptors and PPARα as well as PPARγ ($P < 0.001$ vs. CCK-8s group; Figures 7(a)–7(c) and 7(e)–7(g)). In the presence of an antagonist of the ANP receptor, A71915, the CCK-8s-induced increase of AA release and H_2O_2 levels were further augmented ($P < 0.05$ and $P < 0.001$ vs. CCK-8s group; Figures 8(a) and 8(b)). In addition, A71915 further enhanced the effects of CCK-8s-induced increase of NOX4 and CAT protein expression levels ($P < 0.05$ vs. CCK-8s group; Figures 8(c)–8(e)), but the CCK-8s-induced increase of SOD protein expression was abolished by A71915 ($P < 0.05$

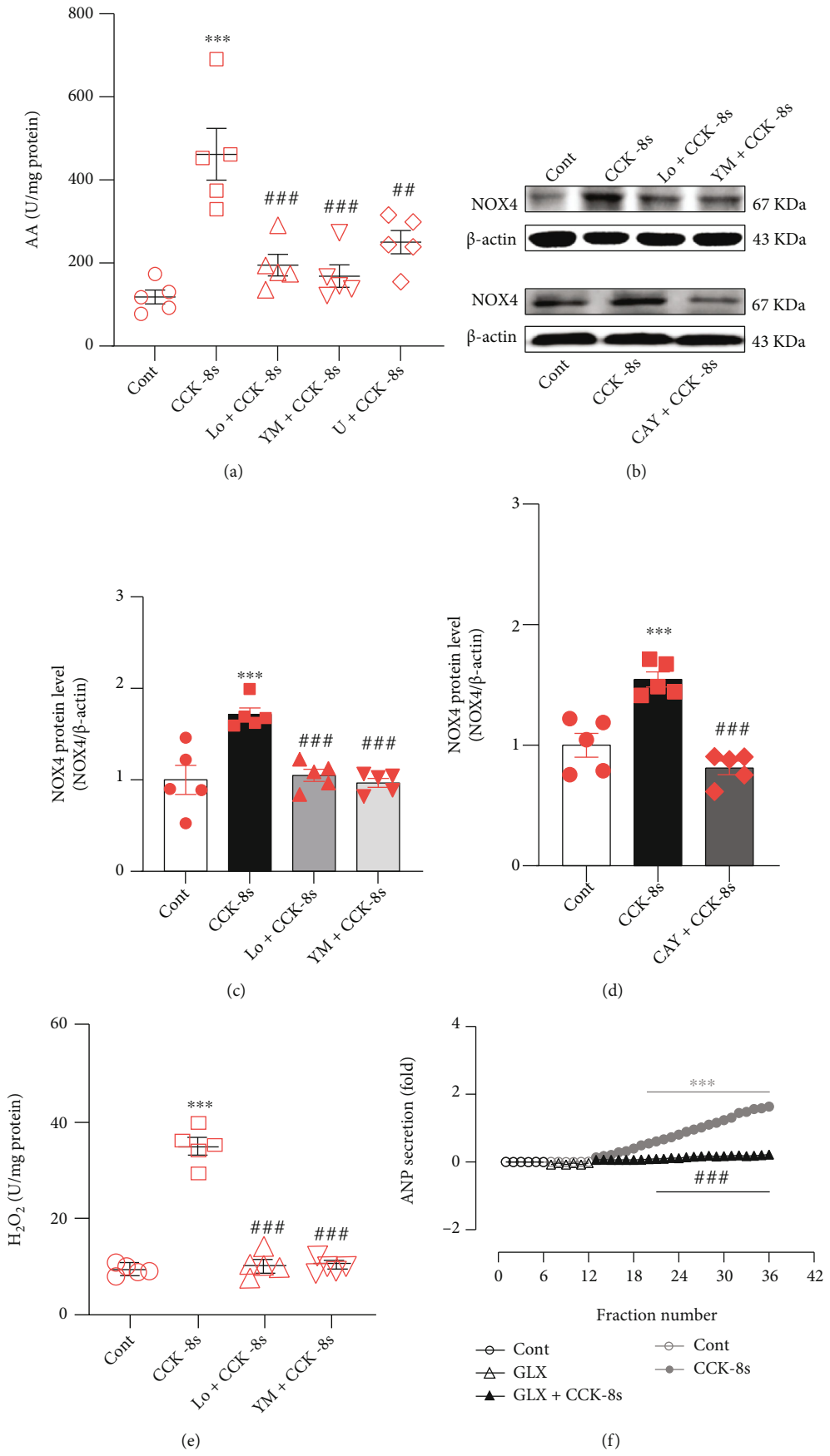

Figure 3: Continued.

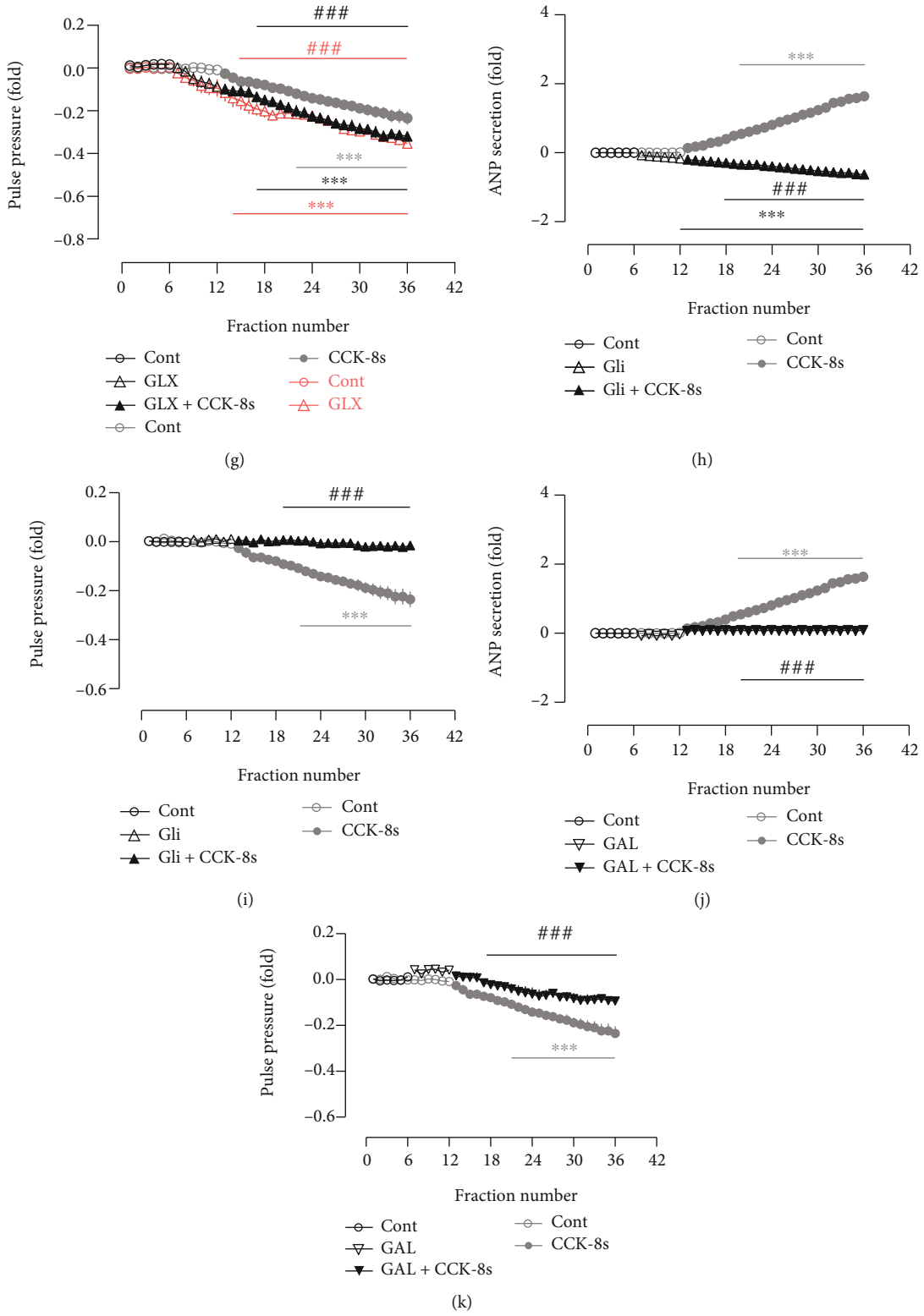

Figure 3: Effects of CCK-8s on NOX4 expression and its role in ANP secretion and dynamics in isolated beating rat atria. (a) The level of AA was tested by the ELISA method. (b) The protein expression levels of NOX4 were detected by Western blot. (c, d) The statistics histograms of Western blot were expressed as band density normalized versus β-actin. (e) The level of H_2O_2 was tested by ELISA. (f, h, j) Atrial ANP secretion by radioimmunoassay. (g, i, k) Atrial pulse pressure by RM6240BD. Cont: control; CCK-8s: sulfated CCK-8; Lo: Loxiglumid, an antagonist of CCK_1 receptor; YM: YM022, an antagonist of CCK_2 receptor; U: U-73122, an inhibitor of PLC; CAY: CAY10650, an inhibitor of cPLA2; GLX: GLX351322, an inhibitor of NOX4; Gli: Glibenclamide, an inhibitor of K_{ATP}; GAL: GAL-021, a blocker of BK_{Ca}. Data were expressed as mean ± SEM. (a–e) $n = 5$; (f–k) $n = 6$. $^{***}P < 0.001$ vs. control period or group; $^{\#\#}P < 0.01$ and $^{\#\#\#}P < 0.001$ vs. CCK-8s period or group.

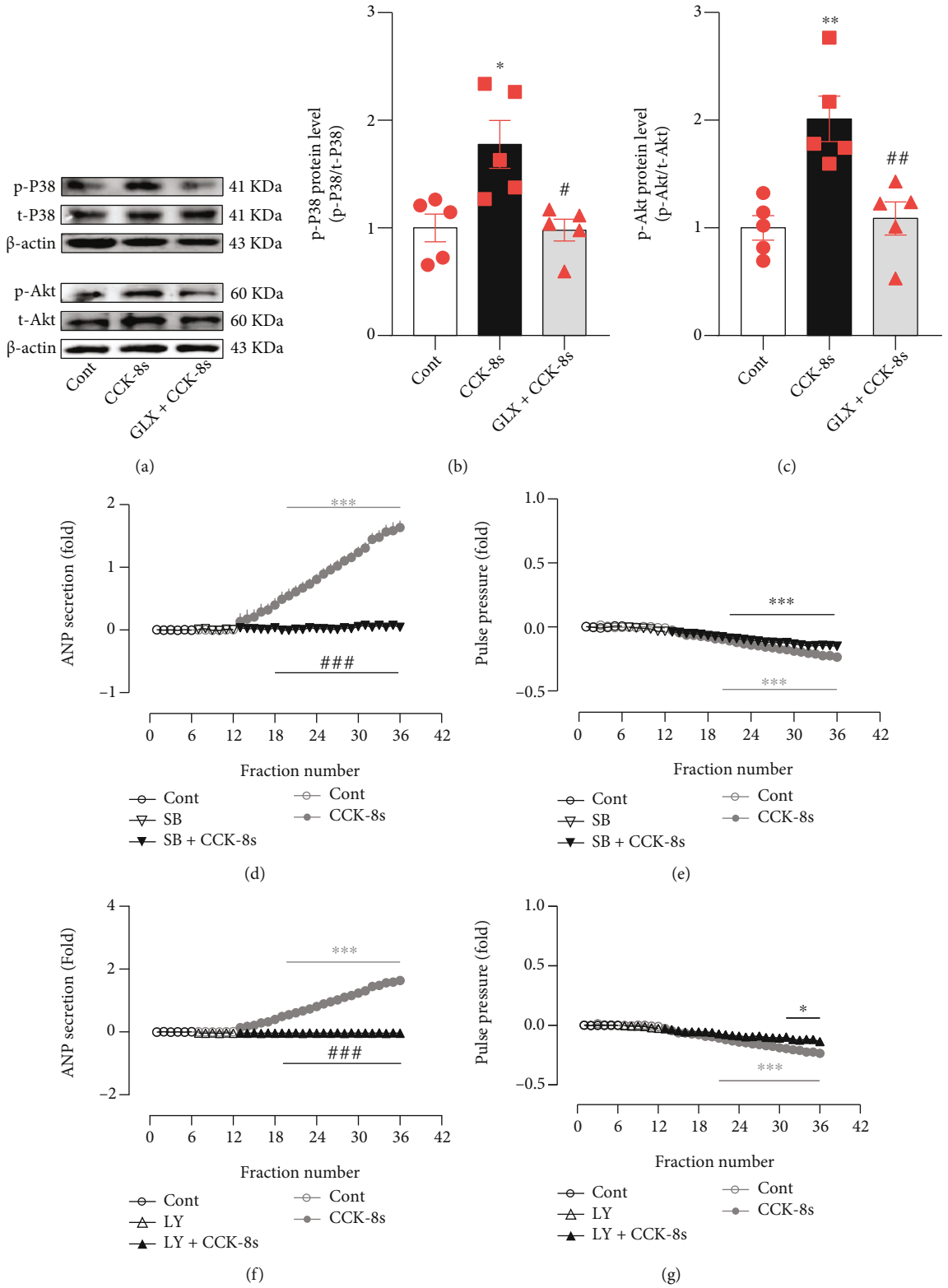

Figure 4: Effects of p38 MAPK and Akt on ANP secretion and dynamics induced by CCK-8s in isolated beating rat atria. (a) The protein expression levels of p-p38 MAPK and p-Akt were detected by Western blot. (b) The statistics histograms of Western blot were expressed as band density normalized versus t-p38. (c) The statistics histograms of Western blot were expressed as band density normalized versus t-Akt. (d, f) Atrial ANP secretion by radioimmunoassay. (e, g) Atrial pulse pressure by RM6240BD. Cont: control; CCK-8s: sulfated CCK-8; GLX: GLX351322, an inhibitor of NOX4; SB: SB239063, an antagonist of p38 MAPK; LY: LY294002, an inhibitor of Akt. Data were expressed as mean ± SEM. (a–c) $n = 5$; (d–g) $n = 6$. $^{*}P < 0.05$, $^{**}P < 0.01$, and $^{***}P < 0.001$ vs. control period or group; $^{\#}P < 0.05$, $^{\#\#}P < 0.01$, and $^{\#\#\#}P < 0.001$ vs. CCK-8s period or group.

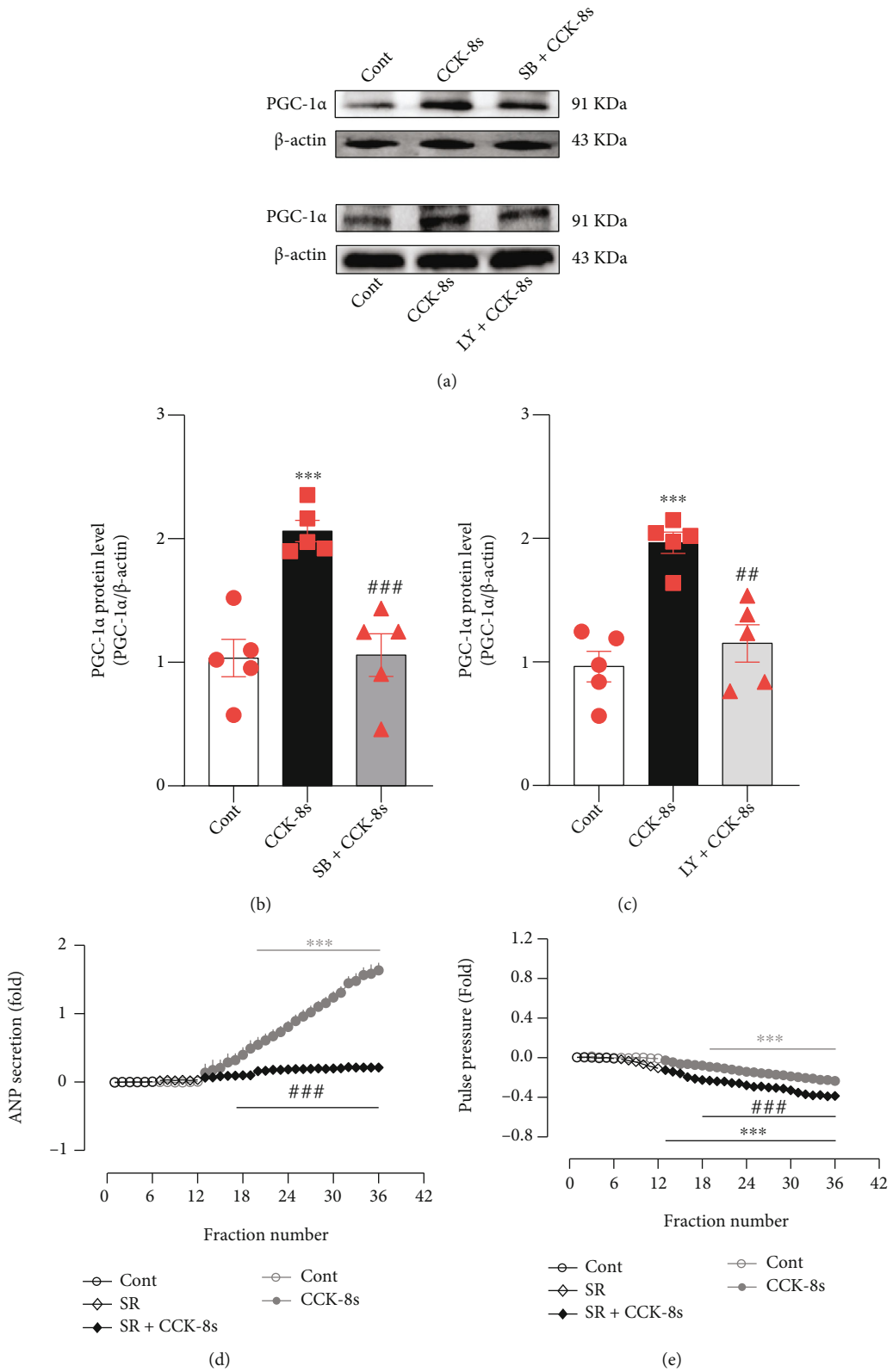

Figure 5: Effects of CCK-8s on PGC-1α expression and its role on ANP secretion and dynamics in isolated beating rat atria. (a) The protein expression levels of PGC-1α were detected by Western blot. (b, c) The statistics histograms of Western blot were expressed as band density normalized versus β-actin. (d) Atrial ANP secretion by radioimmunoassay. (e) Atrial pulse pressure by RM6240BD. Cont: control; CCK-8s: sulfated CCK-8; SB: SB239063, an antagonist of p38 MAPK; LY: LY294002, an inhibitor of Akt; SR: SR-18292, an antagonist of PGC-1α. Data were expressed as mean ± SEM. (a–c) $n = 5$; (d, e) $n = 6$. $^{***}P < 0.001$ vs. control period or group; $^{\#\#}P < 0.01$ and $^{\#\#\#}P < 0.001$ vs. CCK-8s period or group.

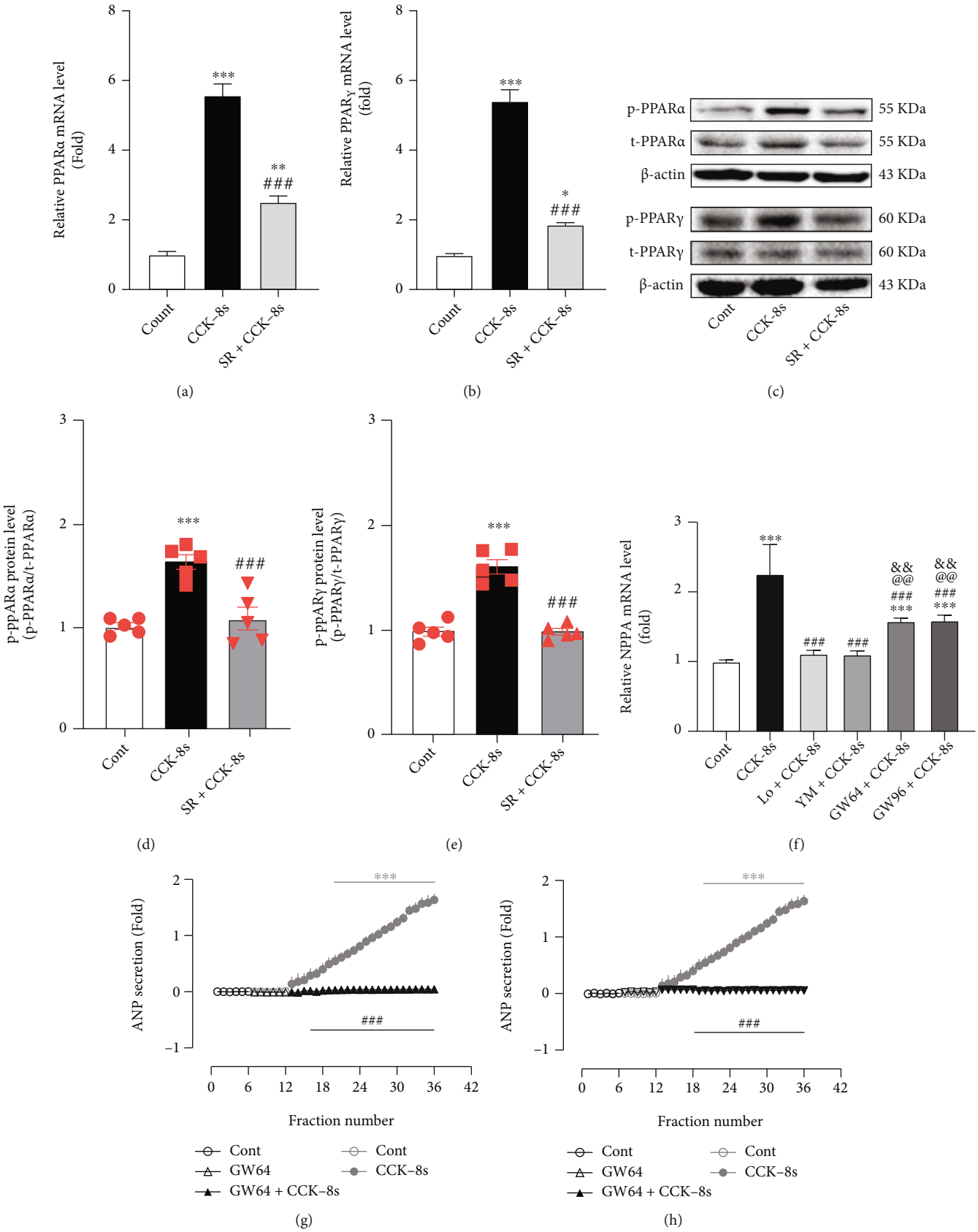

Figure 6: Continued.

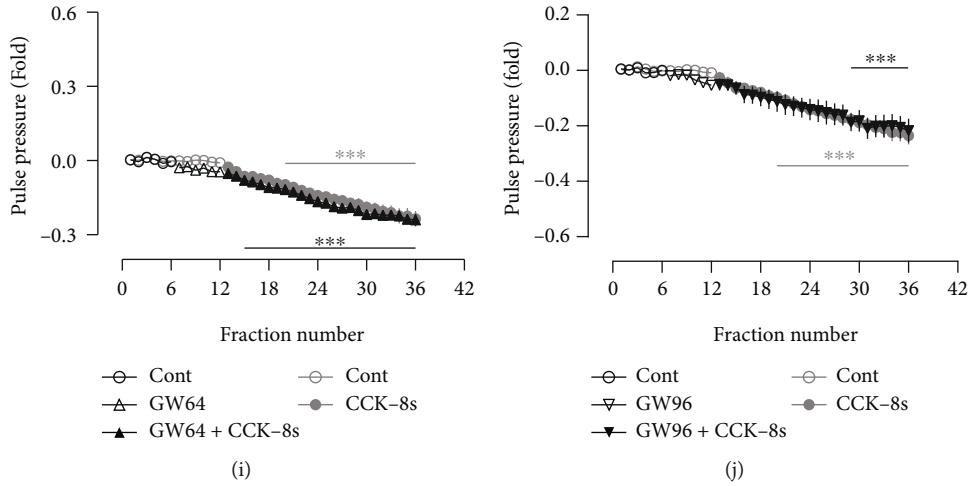

Figure 6: Effects of CCK-8s on PPARα as well as PPARγ expression and its role in ANP secretion and dynamics in isolated beating rat atria. (a, b, f) The mRNA levels of PPARα, PPARγ, and NPPA were tested by RT-qPCR. (c) The protein expression levels of p-PPARα and p-PPARγ were detected by Western blot. (d) The statistics histograms of Western blot were expressed as band density normalized versus t-PPARα. (e) The statistics histograms of Western blot were expressed as band density normalized versus t-PPARγ. (g, h) Atrial ANP secretion by radioimmunoassay. (i, j) Atrial pulse pressure by RM6240BD. Cont: control; CCK-8s: sulfated CCK-8; SR: SR-18292, an antagonist of PGC-1α; Lo: Loxiglumid, an antagonist of CCK_1 receptor; YM: YM022, an antagonist of CCK_2 receptor; GW64: GW6471, an antagonist of PPARα; GW96: GW9662, an inhibitor of PPARγ. Data were expressed as mean ± SEM. (a–f) $n = 5$; (g–j) $n = 6$. $^{*}P < 0.05$, $^{**}P < 0.01$, and $^{***}P < 0.001$ vs. control period or group; $^{\#\#\#}P < 0.001$ vs. CCK-8s period or group; $^{@@}P < 0.01$ vs. Lo+CCK-8s group; $^{\&\&}P < 0.01$ vs. YM+CCK-8s group.

vs. CCK-8s group; Figures 8(c) and 8(f)). Data showed that CCK-8s upregulated the expression of SOD and CAT through activation of PPARα as well as PPARγ. Moreover, endogenous ANP was involved in the inhibition of NOX4 expression and H_2O_2 production and the regulation of SOD activity under the action of CCK-8s.

4. Discussion

NOX4 is one of the enzymatic sources of ROS generation in the cardiovascular system expressed in the heart [22]. In addition, the role of PLA2 and AA on the activation of NOXs has been demonstrated [28]. In our previous study, we have demonstrated that activated cPLA2 induced by endothelin-1 was involved in the regulation of hypoxia-induced ANP secretion through activation of NOX4 and H_2O_2 production in isolated beating rats' atria [23]. The increased NOX4 activity in response to a high pacing frequency also promoted ANP secretion in rat atria [31]. These results suggest that NOX4 is one of the regulatory factors for the secretion of ANP in the atria.

In the current study, CCK-8s rather than CCK-8d significantly upregulated the expression of CCK_1 and CCK_2 receptors and increased the levels of p-cPLA2, AA release, NOX4 relative protein levels, and H_2O_2 production, concomitant with an increase of ANP secretion and inhibition of mechanical dynamics in isolated beating rat atria. The CCK-8s-induced increases of p-cPLA2 expression and AA release were blocked by inhibitors of CCK receptors and PLC, respectively. Similarly, the CCK-8s-induced upregulation of NOX4 expression and H_2O_2 production was abolished by antagonists of CCK receptors, and an inhibitor of cPLA2 also nullified the effect of CCK-8s on NOX4 expression. Furthermore, CCK-8s-induced promotion of ANP secretion was blocked by antagonists of CCK receptors, PLC and cPLA2, respectively, without changes in the inhibition of atrial mechanical dynamics induced by CCK-8s. Nevertheless, CCK-8s-induced inhibition of atrial dynamics was abolished by inhibitors of NOX4, K_{ATP}, and BK_{Ca}, which was accompanied by blockage of CCK-8s-induced ANP secretion. These results demonstrated that CCK-8s (but not CCK-8d) triggered NOX4 activation and increased H_2O_2 production through CCK receptor-mediated activation of cPLA2, leading to an increase in ANP secretion and a negative inotropic action, in which K_{ATP} and BK_{Ca} were involved. The results of the current study are similar to those of the previous studies mentioned above and support previous reports that K_{ATP} and BK_{Ca} are regulated by H_2O_2[32–34].

The PGC-1α is a member of the PGC-1 family that regulates adaptive thermogenesis and mitochondrial function [35]. PGC-1α can be directly activated by p38 MAPK [36] and participates in the elimination of ROS in the heart [37, 38]. PPARα and PPARγ, as downstream signal molecules of PGC-1α, inhibit NOX and ROS generation by enhancing the activity of SOD as well as CAT, thereby resisting oxidative stress damage [39, 40]. In addition, the promoter region of the human ANP gene located on the short arm of chromosome 1 contains binding sites for many transcription factors, including PPARα and PPARγ [41]. Furthermore, it has been demonstrated that PPARγ is involved in the regulation of ANP secretion in beating rat atria under normoxic or hypoxic conditions [42–44]. These results suggest that the changes in PPARα and PPARγ activity are closely related to the secretion of ANP.

In the current study, CCK-8s obviously increased the levels of p-p38 MAPK and p-Akt simultaneously with

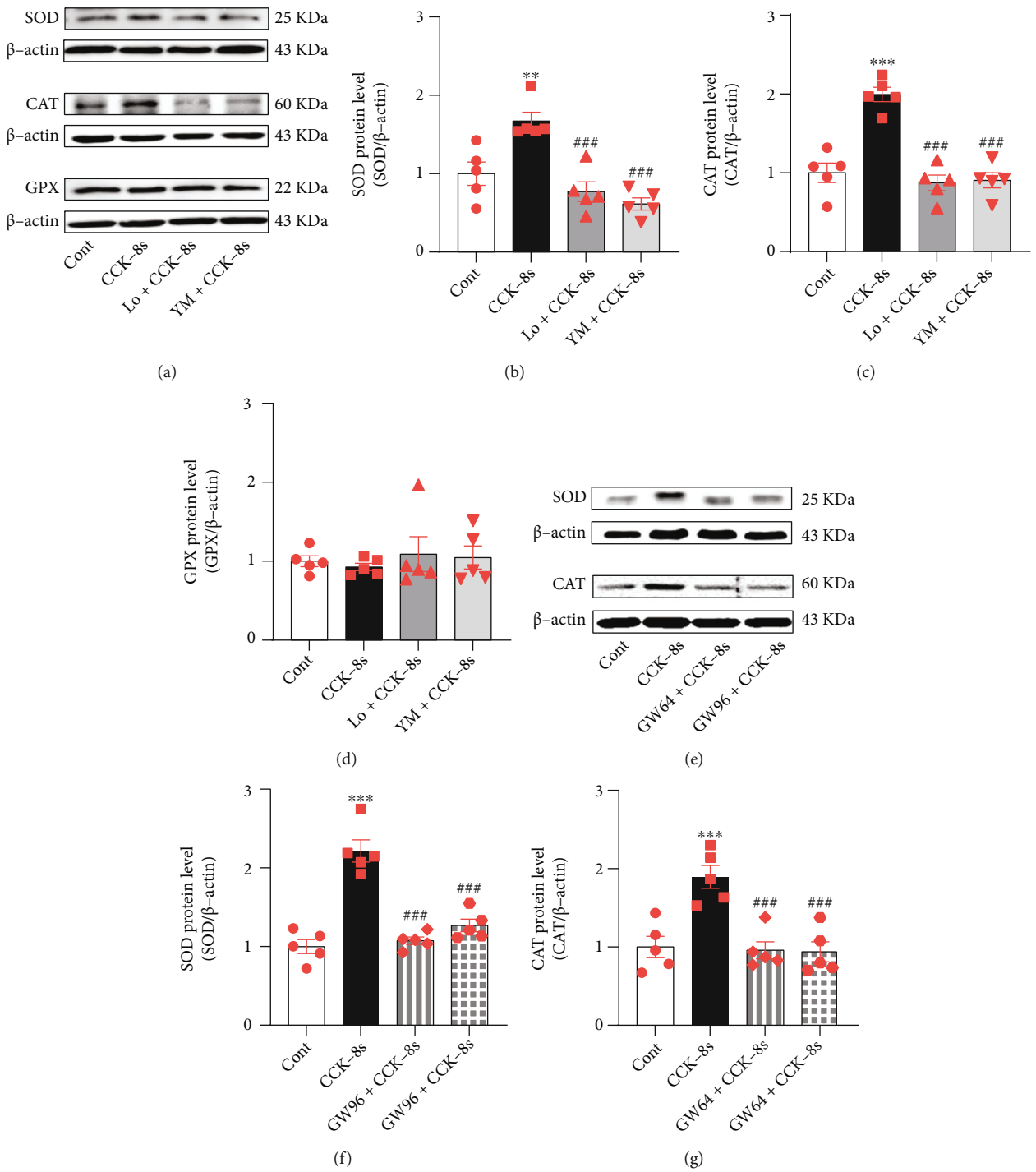

Figure 7: Effects of PPARα and PPARγ on CCK-8s-induced SOD and CAT expressions in isolated beating rat atria. (a) The protein expression levels of SOD, CAT, and GPX were detected by Western blot. (b–d) The statistics histograms of Western blot were expressed as band density normalized versus β-actin. (e–g) The bands of SOD and CAT and their statistics histograms. Cont: control; CCK-8s: sulfated CCK-8; Lo: Loxiglumid, an antagonist of CCK_1 receptor; YM: YM022, an antagonist of CCK_2 receptor; GW64: GW6471, an antagonist of PPARα; GW96: GW9662, an inhibitor of PPARγ. Data were expressed as mean ± SEM. (a–g) $n = 5$. $^{**}P < 0.01$ and $^{***}P < 0.001$ vs. control group; $^{\#\#\#}P < 0.001$ vs. CCK-8s group.

the upregulation of PGC-1α expression. The CCK-8s-induced increase of p-p38 MAPK and p-Akt levels was blocked by an inhibitor of NOX4, and the CCK-8s-induced upregulation of PGC-1α expression was repealed by inhibitors of p38 MAPK and Akt, respectively. In addition, CCK-8s also markedly increased PPARα as well as PPARγ mRNA levels and their phosphorylated protein expressions, concomitant with the promotion of ANP secretion. An inhibitor of PGC-1α abolished the CCK-8s-induced increase of phosphorylated PPARα as well as

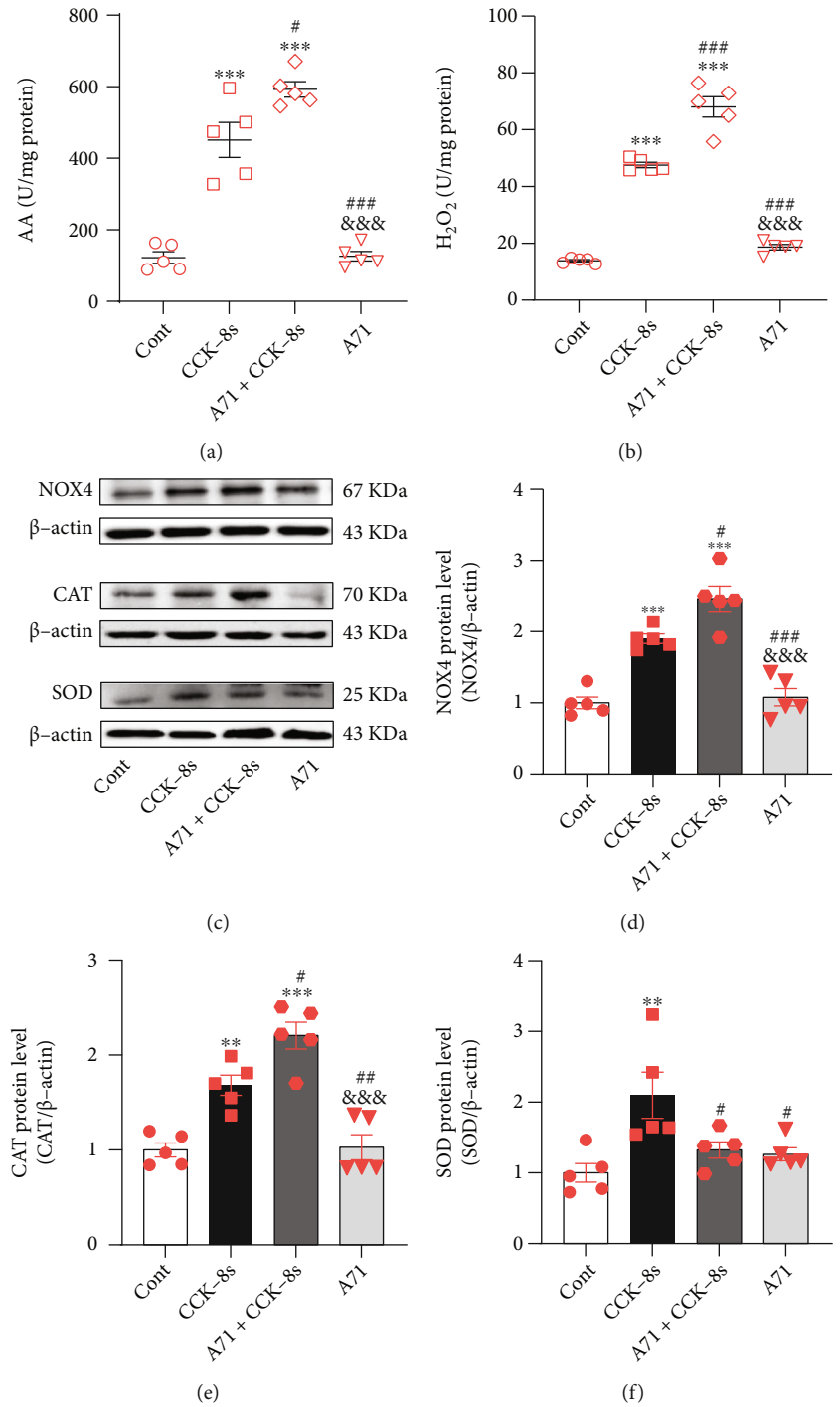

Figure 8: Effects of endogenous ANP on SOD, CAT, and NOX4 expressions under CCK-8s action in isolated beating rat atria. (a, b) The levels of AA and H_2O_2 were tested by ELISA method. (c) The protein expression levels of NOX4, CAT, and SOD were detected by Western blot. (d–f) The statistics histograms of Western blot were expressed as band density normalized versus β-actin. Cont: control; CCK-8s: sulfated CCK-8; A71: A71915, an antagonist of ANP receptor. Data were expressed as mean ± SEM. (a–f) $n = 5$. $^{**}P < 0.01$ and $^{***}P < 0.001$ vs. control group; $^{\#}P < 0.05$, $^{\#\#}P < 0.01$, and $^{\#\#\#}P < 0.001$ vs. CCK-8s group; $^{\&\&\&}P < 0.001$ vs. A71+CCK-8s group.

phosphorylated PPARγ levels by attenuation of PPARα as well as PPARγ mRNA levels; it also abrogated the CCK-8s-induced promotion of ANP secretion. Similarly, inhibitors of PPARα as well as PPARγ attenuated the CCK-8s-induced upregulation of NPPA mRNA levels and repealed the promotion of ANP secretion induced by CCK-8s. The current study data indicate that CCK-8s-induced NOX4 upregulates PGC-1α expression through phosphorylation of p38 MAPK and Akt, leading to the activation of PPARα as well as PPARγ, thereby promoting the secretion of ANP. The data is similar to those of the previous studies mentioned above.

SOD, CAT, and GPX are important antioxidant defenses that protect biological systems from ROS toxicity. The superoxide anion produced by NOXs can be converted to H_2O_2 and O_2 by the action of SOD, and the H_2O_2 is ultimately detoxified into the water by the action of several enzymes, including CAT and GPX [45]. In the current study, CCK-8s significantly increased NOX4 expression and H_2O_2 production concomitant with the upregulation of SOD and CAT rather than GPX expression; this was abolished by inhibitors of CCK receptors. The CCK-8s-induced SOD and CAT expressions were also abolished by antagonists of PPARα and PPARγ. Based on the effect of CCK-8s on PPARα and PPARγ activities, it is suggested that the CCK-8s-induced upregulation of SOD and CAT expressions was related to the PPAR activation. In addition, in the presence of an inhibitor of the ANP receptor, the CCK-8-induced increase of AA release, H_2O_2 production, and the upregulation of NOX4 as well as CAT expression was dramatically augmented. These results hint that CCK-8s-induced ANP is involved, at least in part, in the inhibition of AA release, NOX4 expression, and H_2O_2 production. As for the augmentation of CAT expression induced by CCK-8s under the presence of an inhibitor of the ANP receptor, we considered that is related to further increase of H_2O_2 production, as the CAT can detoxify H_2O_2 into water depending on the concentration of H_2O_2 [45]. Moreover, the inhibitor of the ANP receptor repealed the CCK-8s-induced expression of SOD. This means that endogenous ANP has participated in the regulation of SOD expression. Results of the current study support previous studies that ANP stimulates antioxidant defense in the cardiovascular system [5] and protects endplate chondrocytes against H_2O_2-induced oxidative stress damage by increasing SOD levels and inhibiting apoptotic factors [46].

In summary, CCK-8s promoted ANP secretion through the activation of NOX4–PGC-1α–PPARα/PPARγ signaling and played a negative inotropic effect through the activation of K_{ATP} and BK_{Ca}. The CCK-8s-induced endogenous ANP was involved in resistance for NOX4 expression and ROS production and regulation of SOD activity. This suggests that the CCK–ANP signaling is implicated in cardiac physiology and pathophysiology.

Data Availability

The data supporting the findings of this study are available from the corresponding author upon reasonable request.

Conflicts of Interest

The authors declare that there is no conflict of interest in this article.

Authors' Contributions

Zhuo-na Han and Xiao-xue Lin contributed equally to this work.

Acknowledgments

We sincerely thank all the participants in this study. This study was supported by the National Natural Science Foundation of China (No. 81960099).

References

[1] J. P. Goetze, B. G. Bruneau, H. R. Ramos, T. Ogawa, M. K. de Bold, and A. J. de Bold, "Cardiac natriuretic peptides," *Nature Reviews Cardiology.*, vol. 17, no. 11, pp. 698–717, 2020.

[2] D. V. Ilatovskaya, V. Levchenko, K. Winsor et al., "Effects of elevation of ANP and its deficiency on cardiorenal function," *Insight*, vol. 7, no. 9, article e148682, 2022.

[3] V. Cannone and J. C. Burnett Jr., "Natriuretic peptides and blood pressure homeostasis: implications for MANP, a novel guanylyl cyclase a receptor activator for hypertension," *Frontiers in Physiology*, vol. 12, article 815796, 2022.

[4] S. P. D'Souza, M. Davis, and G. F. Baxter, "Autocrine and paracrine actions of natriuretic peptides in the heart," *Pharmacology & Therapeutics*, vol. 101, no. 2, pp. 113–129, 2004.

[5] P. De Vito, S. Incerpi, J. Z. Pedersen, and P. Luly, "Atrial natriuretic peptide and oxidative stress," *Peptides*, vol. 31, no. 7, pp. 1412–1419, 2010.

[6] A. Laskowski, O. L. Woodman, A. H. Cao et al., "Antioxidant actions contribute to the antihypertrophic effects of atrial natriuretic peptide in neonatal rat cardiomyocytes," *Cardiovascular Research*, vol. 72, no. 1, pp. 112–123, 2006.

[7] A. Serafino and P. Pierimarchi, "Atrial natriuretic peptide: a magic bullet for cancer therapy targeting Wnt signaling and cellular pH regulators," *Current Medicinal Chemistry*, vol. 21, no. 21, pp. 2401–2409, 2014.

[8] J. F. Rehfeld, "Cholecystokinin and the hormone concept," *Endocrine Connections*, vol. 10, no. 3, pp. R139–R150, 2021.

[9] J. F. Rehfeld, "Cholecystokinin—from local gut hormone to ubiquitous messenger," *Front Endocrinol (Lausanne).*, vol. 8, p. 47, 2017.

[10] D. R. Nässel and S. F. Wu, "Cholecystokinin/sulfakinin peptide signaling: conserved roles at the intersection between feeding, mating and aggression," *Cellular and Molecular Life Sciences*, vol. 79, no. 3, p. 188, 2022.

[11] R. S. Saia, G. Bertozi, F. L. Mestriner, J. Antunes-Rodrigues, F. Queiróz Cunha, and E. C. Cárnio, "Cardiovascular and inflammatory response to cholecystokinin during endotoxemic shock," *Shock*, vol. 39, no. 1, pp. 104–113, 2013.

[12] Z. Han, S. Bi, Y. Xu et al., "Cholecystokinin expression in the development of myocardial hypertrophy," *Scanning*, vol. 2021, Article ID 8231559, 10 pages, 2021.

[13] G. J. Dockray, "Cholecystokinin," *Current Opinion in Endocrinology, Diabetes, and Obesity*, vol. 19, no. 1, pp. 8–12, 2012.

[14] S. Shrivastava, M. Jafurulla, S. Tiwari, and A. Chattopadhyay, "Identification of sphingolipid-binding motif in G protein-coupled receptors," *Advances in Experimental Medicine and Biology*, vol. 1112, pp. 141–149, 2018.

[15] J. P. Goetze, A. H. Johnsen, C. Kistorp, F. Gustafsson, C. B. Johnbeck, and J. F. Rehfeld, "Cardiomyocyte expression and cell-specific processing of procholecystokinin∗," *The Journal of Biological Chemistry*, vol. 290, no. 11, pp. 6837–6843, 2015.

[16] C. Wang, H. Yu, L. Wei et al., "Protective effect of cholecystokinin octapeptide on angiotensin II-induced apoptosis in H9c2

cardiomyoblast cells," *Journal of Cellular Biochemistry*, vol. 121, no. 7, pp. 3560–3569, 2020.

[17] M. Ruiz-Gayo, M. C. González, and S. Fernández-Alfonso, "Vasodilatory effects of cholecystokinin: new role for an old peptide?," *Regulatory Peptides*, vol. 137, no. 3, pp. 179–184, 2006.

[18] X. Y. Zhao, Y. L. Ling, Y. G. Li, A. H. Meng, and H. Y. Xing, "Cholecystokinin octapeptide improves cardiac function by activating cholecystokinin octapeptide receptor in endotoxic shock rats," *World Journal of Gastroenterology*, vol. 11, no. 22, pp. 3405–3410, 2005.

[19] C. Wang, C. Zhang, D. Wu et al., "Cholecystokinin octapeptide reduces myocardial fibrosis and improves cardiac remodeling in post myocardial infarction rats," *The International Journal of Biochemistry & Cell Biology*, vol. 125, article 105793, 2020.

[20] X. Dong, C. Wang, J. Zhang et al., "Cholecystokinin expression in the development of postinfarction heart failure," *Cellular Physiology and Biochemistry*, vol. 43, no. 6, pp. 2479–2488, 2017.

[21] J. P. Goetze, J. F. Rehfeld, and U. Alehagen, "Cholecystokinin in plasma predicts cardiovascular mortality in elderly females," *International Journal of Cardiology*, vol. 209, pp. 37–41, 2016.

[22] Y. Zhang, P. Murugesan, K. Huang, and H. Cai, "NADPH oxidases and oxidase crosstalk in cardiovascular diseases: novel therapeutic targets," *Nature Reviews. Cardiology*, vol. 17, no. 3, pp. 170–194, 2020.

[23] C. Z. Wu, X. Li, L. Hong et al., "NOX4/Src regulates ANP secretion through activating ERK1/2 and Akt/GATA4 signaling in beating rat hypoxic atria," *Korean J Physiol Pharmacol.*, vol. 25, no. 2, pp. 159–166, 2021.

[24] Q. Zeng, L. Ou, W. Wang, and D. Y. Guo, "Gastrin, cholecystokinin, signaling, and biological activities in cellular processes," *Front Endocrinol (Lausanne).*, vol. 11, p. 112, 2020.

[25] H. Yoshida, Y. Tsunoda, and C. Owyang, "Cholecystokinin peptides stimulate pancreatic secretion by multiple signal transduction pathways," *The American Journal of Physiology*, vol. 273, pp. G735–G747, 1997.

[26] B. Pommier, S. Da Nascimento, S. Dumont et al., "The cholecystokininB receptor is coupled to two effector pathways through pertussis toxin-sensitive and -insensitive G proteins," *Journal of Neurochemistry*, vol. 73, no. 1, pp. 281–288, 1999.

[27] E. Rozengurt and J. H. Walsh, "Gastrin, CCK, signaling, and cancer," *Annual Review of Physiology*, vol. 63, no. 1, pp. 49–76, 2001.

[28] L. C. Mangum, A. Borazjani, J. V. Stokes et al., "Organochlorine insecticides induce NADPH oxidase-dependent reactive oxygen species in human monocytic cells via phospholipase A2/arachidonic acid," *Chemical Research in Toxicology*, vol. 28, no. 4, pp. 570–584, 2015.

[29] J. T. Colston, S. D. de la Rosa, J. R. Strader, M. A. Anderson, and G. L. Freeman, "H_2O_2 activates Nox4 through PLA2-dependent arachidonic acid production in adult cardiac fibroblasts," *FEBS Letters*, vol. 579, no. 11, pp. 2533–2540, 2005.

[30] T. Zhou, S. Li, L. Yang, and D. Xiang, "MicroRNA-363-3p reduces endothelial cell inflammatory responses in coronary heart disease via inactivation of the NOX4-dependent p38 MAPK axis," *Aging (Albany NY)*, vol. 13, no. 8, pp. 11061–11082, 2021.

[31] S. Gao, K. Yuan, A. Shah, J. S. Kim, W. H. Park, and S. H. Kim, "Suppression of high pacing-induced ANP secretion by antioxidants in isolated rat atria," *Peptides*, vol. 32, no. 12, pp. 2467–2473, 2011.

[32] X. Zhou, B. Teng, S. Tilley, and S. J. Mustafa, "A1 adenosine receptor negatively modulates coronary reactive hyperemia via counteracting A2A-mediated H_2O_2 production and K_{ATP} opening in isolated mouse hearts," *American Journal of Physiology. Heart and Circulatory Physiology*, vol. 305, no. 11, pp. H1668–H1679, 2013.

[33] X. Q. Hu and L. Zhang, "Function and regulation of large conductance Ca^{2+}-activated K^+ channel in vascular smooth muscle cells," *Drug Discovery Today*, vol. 17, no. 17-18, pp. 974–987, 2012.

[34] D. M. Zhang and Y. F. Lin, "Functional modulation of sarcolemmal KATPchannels by atrial natriuretic peptide-elicited intracellular signaling in adult rabbit ventricular cardiomyocytes," *American Journal of Physiology. Cell Physiology*, vol. 319, no. 1, pp. C194–C207, 2020.

[35] E. Doukbi, A. Soghomonian, C. Sengenès et al., "Browning epicardial adipose tissue: friend or foe?," *Cell*, vol. 11, no. 6, p. 991, 2022.

[36] M. Scharf, S. Neef, R. Freund et al., "Mitogen-activated protein kinase-activated protein kinases 2 and 3 regulate SERCA2a expression and fiber type composition to modulate skeletal muscle and cardiomyocyte function," *Molecular and Cellular Biology*, vol. 33, no. 13, pp. 2586–2602, 2013.

[37] Z. Lu, X. Xu, X. Hu et al., "PGC-1α regulates expression of myocardial mitochondrial antioxidants and myocardial oxidative stress after chronic systolic overload," *Antioxidants & Redox Signaling*, vol. 13, no. 7, pp. 1011–1022, 2010.

[38] C. J. McLeod, I. Pagel, and M. N. Sack, "The mitochondrial biogenesis regulatory program in cardiac adaptation to ischemia–a putative target for therapeutic intervention," *Trends in Cardiovascular Medicine*, vol. 15, no. 3, pp. 118–123, 2005.

[39] L. Ibarra-Lara, E. Hong, E. Soria-Castro et al., "Clofibrate PPARα activation reduces oxidative stress and improves ultrastructure and ventricular hemodynamics in no-flow myocardial ischemia," *Journal of Cardiovascular Pharmacology*, vol. 60, no. 4, pp. 323–334, 2012.

[40] T. Chen, X. Jin, B. H. Crawford et al., "Cardioprotection from oxidative stress in the newborn heart by activation of PPARγ is mediated by catalase," *Free Radical Biology & Medicine*, vol. 53, no. 2, pp. 208–215, 2012.

[41] L. Mezzasoma, M. J. Peirce, A. Minelli, and I. Bellezza, "Natriuretic peptides: the case of prostate cancer," *Molecules*, vol. 22, no. 10, p. 1680, 2017.

[42] Y. Zhang, X. Li, L. P. Liu et al., "Peroxisome proliferator-activated receptor γ is essential for secretion of ANP induced by prostaglandin D2in the beating rat atrium," *The Korean Journal of Physiology & Pharmacology*, vol. 21, no. 3, pp. 293–300, 2017.

[43] X. Li, Y. Zhang, B. Zhang et al., "HIF-1α-l-PGDS-PPARγ regulates hypoxia-induced ANP secretion in beating rat atria," *Prostaglandins & Other Lipid Mediators*, vol. 134, pp. 38–46, 2018.

[44] X. Li, Z. N. Han, Y. Liu, L. Hong, B. R. Cui, and X. Cui, "Endogenous ET-1 promotes ANP secretion through activation of COX2-L-PGDS-PPARγ signaling in hypoxic beating rat atria," *Peptides*, vol. 122, article 170150, 2019.

[45] E. Dubois-Deruy, V. Peugnet, A. Turkieh, and F. Pinet, "Oxidative stress in cardiovascular diseases," *Antioxidants (Basel)*, vol. 21, 2017.

[46] F. He, J. Gai, J. Wang, L. Tang, Y. Liu, and Q. Feng, "Atrial natriuretic peptide protects vertebral endplate chondrocytes against H_2O_2-induced apoptosis and oxidative stress through activation of the Nrf2/HO-1 signaling pathway," *Molecular Medicine Reports*, vol. 24, no. 5, p. 754, 2021.

Hindawi
Oxidative Medicine and Cellular Longevity
Volume 2022, Article ID 5080190, 7 pages
https://doi.org/10.1155/2022/5080190

Research Article

Association of Probiotics with Atopic Dermatitis among Infant: A Meta-analysis of Randomized Controlled Trials

Hua Pan and Jingqiu Su

Department of Dermatology, The Fourth Affiliated Hospital of China Medical University, 110004, China

Correspondence should be addressed to Jingqiu Su; jqsu@cmu.edu.cn

Received 7 January 2022; Revised 12 March 2022; Accepted 23 March 2022; Published 23 May 2022

Academic Editor: Yingqing Chen

Background. Previous studies have explored the relationship between probiotics and risk of atopic dermatitis among infant; however, the results are still inconclusive. We aimed to assess the abovementioned association. *Methods*. PubMed, Web of Science, Embase, and China National Knowledge Infrastructure were retrieved for association between probiotics and atopic dermatitis with randomized controlled trials (RCTs) until Nov 20, 2021. The effect size was pooled by using random or fixed effect models according to the heterogeneity. Stata 12.0 was used for meta-analysis, sensitivity analysis, and bias analysis. *Results*. At the end of the screening article, 2575 infants were extracted from 8 trials and finally met the qualification criteria. In comparison to placebo, probiotics dramatically reduced incidence of childhood atopic dermatitis (RR = 0.86, 95% CI = 0.78 -0.95). However, probiotics did not exhibit benefit over placebo in preventing the development of either IgE-associated infant AD (RR = 0.98, 95% CI = 0.79-1.22) or sensitive constitution (RR = 0.93, 95% CI = 0.81-1.08). From the results of sensitivity and publication bias, we found that these results were robust with little publication bias. *Conclusion*. During the late stages of pregnancy, women taking probiotics could lower the risk of infantile atopic dermatitis, but not for IgE-associated infant AD or sensitive constitution. The results could provide evidence for the fibrosis. Future studies are needed to confirm the results.

1. Introduction

Atopic dermatitis (AD) is one of the most common skin diseases in children. It could be divided into different stages: infant period, childhood period, and youth adult period. About 60% of patients with AD develop before the age of 1, and 85% develop AD before the age of five [1]. Nearly a quarter of children with the disease can be delayed into young adulthood [2]. In the past few decades, the incidence of the disease in the worldwide has increased significantly and is now 10-20 percent among infants and children [3]. Mancini et al. proposed in 2013 that the direct national expenditure on AD treatment in the United States was as high as 3.8 billion dollars, which costs $167 to $580 per person per year [4].

AD is related to genetic allergic diathesis, often accompanied by allergic rhinitis and asthma, and the three diseases are allergic progression, while atopic dermatitis is often the first symptom [5]. AD patients also have the following characteristics: easy to xenoprotein allergy, serum immunoglobulin-E (IgE) increased, and blood eosinophils increased [6]. The main treatment currently involves topical sugars corticosteroids, antihistamines, and even antibiotics, while long-term use of drugs can lead to side effects [7]. In addition, AD symptoms may recur rapidly after the stop of treatment. Therefore, prevention methods are needed in the face of recurrent AD. In addition, the association between AD and fibrosis has been studied for several years; however, the results between studies are controversial.

Previous studies revealed that gastrointestinal flora plays an important role in infant atopic dermatitis [8]. It is showed that the contents of bifidobacteria and lactobacillus decreased in the intestinal tract of AD patients, while the contents of clostridium increased [9]. All these evidences have indicated that probiotics may have a positive effect on the prevention and treatment of AD.

Since some researches have explored the effect of probiotics on AD, but there is little comprehensive analysis for the

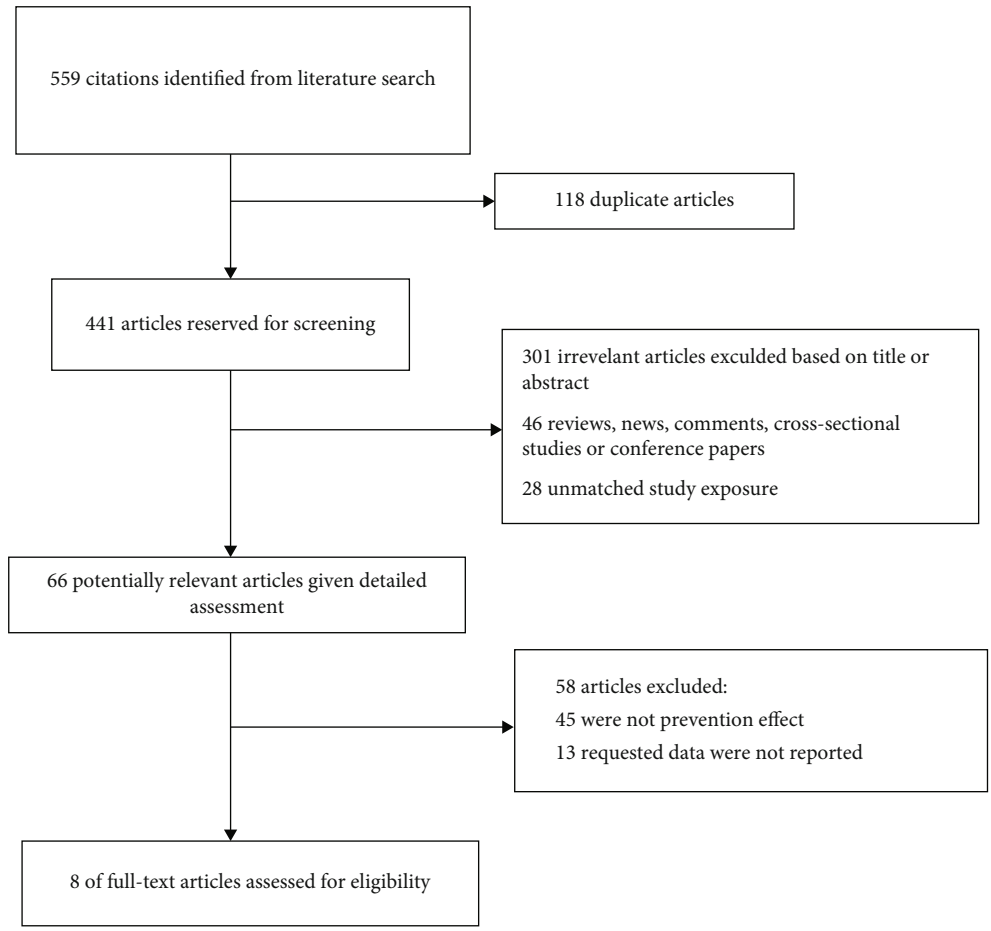

Figure 1: Flow chart for selection of eligible studies.

topic. Therefore, we conducted this research to overall analyze the effect of probiotics on AD.

2. Methods

2.1. Literature Search Strategy. We searched the randomized controlled trials from PubMed, Web of Science, Embase, and China National Knowledge Infrastructure up to Nov 20, 2021, using the following keywords: (1) probiotics, (2) atopic dermatitis, and (3) clinical effect. The search strategy involves medical subject headings (mesh) and text words combined by the Boolean operator "and."

We will conduct a comprehensive search in multiple databases, regardless of the language or publication status. In order to maximize the specificity and sensitivity of the search, the author should also refer to the list of retrieved references to find other relevant studies not found through the search strategy. The literature search was conducted in accordance with PRISMA.

2.2. Study Selection. We conducted a comprehensive review of potentially relevant articles to ensure that they met all inclusion criteria: (1) study design was double-blind, randomized, placebo-controlled trials; (2) the intervention was probiotics or placebo; (3) mother during gestation and/or one year after birth received probiotics or placebo; (4) the outcome was AD or IgE related AD or sensitive constitution; (5) the full text is available for reference.

Studies were excluded according to the following predetermined exclusion criteria: (1) studies on other subjects; (2) comparison of other interventions; (3) lack of research on available data; (4) the outcome was the treatment effect, not the prevention effect; and (5) comments, abstracts, and reproduction of publications.

For studies with duplicate data from a single database, we selected the study with the most complete information on results or the largest sample size.

2.3. Data Collection and Quality Assessment. Two reviewers extracted detailed information including the titles, abstracts, and full-text articles of potentially qualified studies and resolved their differences through discussion. The following data parameters were extracted: name of main author, publication year, number of participants in each group, characteristics of drug intervention during follow-up in each group, and infants' age in the follow-up time. The Jadad questionnaire was used to evaluate the effectiveness of qualified randomized controlled trials. Egger's test and funnel plot program were used to assess the risk of bias in the study.

Table 1: Characteristics of eligible studies.

Author	Year	Outcome	Number of population (trial/control)	Events (trial/control)	Types of probiotics	Intervention	Jadad score
Kalliomäki et al.	2007	AD, sensitive constitution	53/62	23/41	ATCC53103	Mother 2 ~ 4 weeks before prenatal start to take; postpartum use up to 6 months (not breast milk) feeders, to give to babies	6
Kuitunen et al.	2009	AD, related AD	445/446	175/193	ATCC53103 + DSM 7061 + DSM13692 + DSM7076	Starting two to four weeks before birth, babies are taken from birth until 6 months of age	7
Jensen et al.	2012	AD, related AD, sensitive constitution	62/56	19/9	LAVRI-A1	Babies are taken from birth until 6 months of age	7
West et al.	2013	AD, related AD, sensitive constitution	59/62	16/19	LF19	Babies take it from 4 months to 13 months	5
Wickens et al.	2013	AD, sensitive constitution	309/156	123/156	HN001 + HN019	Mothers take it from the 35th week until postpartum for 6 months; babies take it from birth to 2 years old	7
Loo et al.	2014	AD, sensitive constitution	124/121	31/38	BL999 + LPR	Babies are taken from birth until 6 months of age	5
Allen et al.	2014	AD	214/222	73/72	CUL61 + CUL08 + CUL34 + CUL20	Mothers take it from the 36th week until birth; babies take it from birth to 6 months	5
Cabana et al.	2017	AD	92/92	26/28	LPR	Babies are taken from birth until 6 months of age	5

2.4. Statistical Analysis. The effect size was pooled by using random or fixed effect models according to the heterogeneity. Heterogeneity of effect size across studies was tested by I^2 statistics ($I^2 > 50\%$ is considered significant). The random effect model was used for analysis if $P < 0.05$ or $I^2 > 50\%$, or else fixed effect model was used to conduct the analysis. Visual examination of the funnel plot was used to assess publication bias. Sensitivity analysis was explored by deleting one study in turn to observe the impact of individual results on the overall analysis. The study was conducted by using STATA version 12.0. All P values are two tailed, and we set $P < 0.05$ as the threshold for significance.

3. Results

3.1. Search Process. The initial search yielded 559 articles from four databases, including PubMed, Embase, Web of Science, and CNKI. After the first screening, 441 records were retained. By screening titles and abstracts, an additional 375 records were excluded because they were review articles, letters, case reports, comments, or editorials, remaining 66 articles. A total of 58 articles were further excluded for various reasons, including different research designs or insufficient available data. Finally, 8 studies met the inclusion criteria and were included in this meta-analysis [10–17], with a total of 2575 infants. The process followed PRISMA guidelines, including the reasons for excluding the study, as shown in Figure 1.

3.2. Characteristics of Included Studies. Table 1 lists the main characteristics of the eight studies. These studies included 2575 patients (1358 patients in the experimental group and 1217 patients in the control group). The sample size ranged from 115 to 891.

3.3. Results of Meta-analysis

3.3.1. Association between Probiotics and AD. All the eight studies revealed the association between probiotics and AD; the overall results showed that the incidence of AD in the experimental group was lower than that of the control

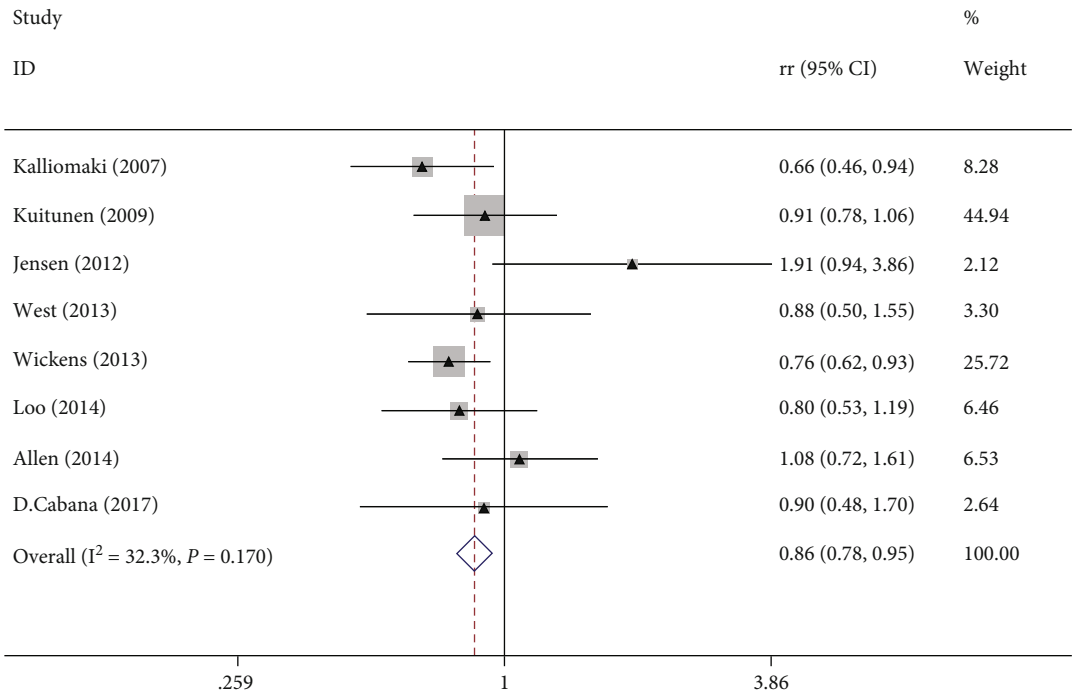

Figure 2: Association between probiotics and AD.

group (RR = 0.86, 95% confidence interval (0.78, 0.95), P = 0.170, I^2 = 32.3% fixed effect model) (Figure 2).

3.3.2. Association between Probiotics and Related AD. Three studies revealed the association between probiotics and related AD; the overall results showed that the difference of incidence of related AD in the experimental group was not statistically significant from that of the control group (RR = 0.98, 95% CI (0.79, 1.22), P = 0.353, I^2 = 4% fixed effect model) (Figure 3).

3.3.3. Association between Probiotics and Sensitive Constitution. Five studies revealed the association between probiotics and sensitive constitution; the overall results showed that the difference of incidence of sensitive constitution in the experimental group was not statistically significant from that of the control group (RR = 0.93, 95% CI (0.81, 1.08), P = 0.619, I^2 = 0% fixed effect model) (Figure 4).

3.3.4. Results of Quality Assessment. Jadad assessment tool was used to assess the quality in the study. All 6 literatures were analyzed from three aspects of "random grouping sequence generation method," "allocation hiding," and "blind method," and all 8 articles were of high quality (Table 1).

3.4. Results of Sensitivity Analysis and Publication Bias. Sensitivity analysis was used to explore the potential sources of heterogeneity (Figure S1-S3). Excluding a single study in turn did not alter the combined RR significantly. Visual inspection of funnel plots did not identify substantial asymmetry (Figure S4-S6). No evidence of publication bias was found by Begg's and Egger's test.

4. Discussion

In this study, we found that the incidence of AD in the control group was higher than that of the probiotics group. However, the difference of incidence of related AD and sensitive constitution in the experimental group was not statistically significant from that of the control group. The results of our study may have important clinical practice, which indicated that probiotics may play a role in the prevention of AD, though it was not in the related AD and sensitive constitution.

AD is a chronic inflammatory skin condition associated with inherited allergic predisposition skin disease; the performance is pruritus, pleomorphic skin lesions, and exudate tendency, often concurrent asthma and allergic rhinitis. Studies have found that the allergic constitution of children in the intestines of E. coli number significantly more than the children allergic constitution, and allergic constitution of infants and young children, the intestinal microbial flora changes prior to the clinical manifestations of allergic disease speculated that the intestinal engraftment has proper number of bacteria and may be related to lower the risk of allergic diseases; improving the intestinal microecological environment in infants may help prevent allergic diseases in infants [18]. In addition, other results showed that after 1 year of age, children with eczema had more diversity of intestinal flora than normal children [19, 20]. The contents of bifidobacteria and lactobacillus were reduced in the intestines of AD patients. Pike et al. also found that intestinal permeability was increased in AD patients [21], which may be related to changes in intestinal flora. And the elevation of intestinal permeability may be related to the occurrence of food allergy. These theoretical evidences may suggest that

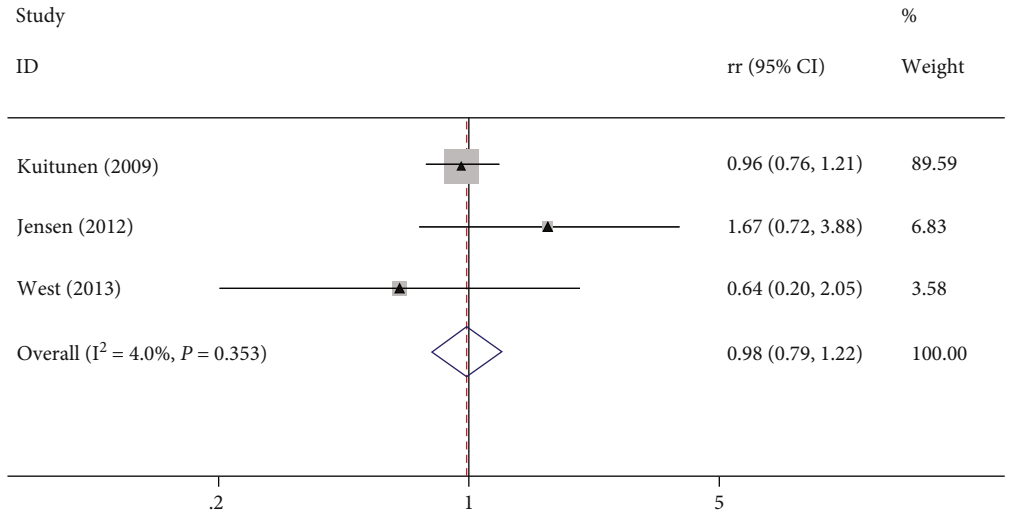

Figure 3: Association between probiotics and related AD.

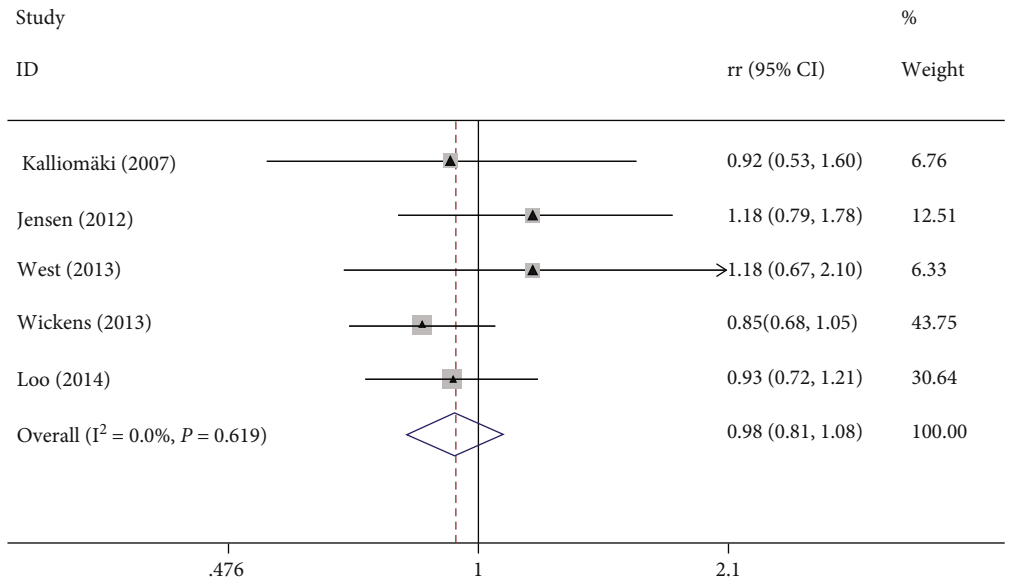

Figure 4: Association between probiotics and sensitive constitution.

exogenous supplementation of intestinal probiotics may be beneficial to the prevention and treatment of AD by changing the composition of intestinal flora.

The prevention mechanisms of probiotics on AD are still unknown. Probiotics can stimulate the production of intestinal IgA and reduce the adhesion of pathogenic bacteria and form a tight intercellular connection with intestinal epithelial cells to reduce intestinal permeability [22]. The toll-like receptor plays a role in inducing defensin, inhibiting the invasion of pathogenic bacteria and reducing local inflammation [23]. Exposure to specific skin pathogens can enhance the expression of thymic stromal lymphopoietin, which can induce the differentiation of primitive T cells into Th2 cells and Th17 cells, mediating allergic inflammation of the skin. Probiotics can act on DC cells and induce the production of regulatory T cells in mesenteric lymph nodes to migrate to inflammatory sites and produce IL-10 and TGF-β, thereby inhibiting Th2 and Th17 cell-mediated allergic reactions and the production of inflammatory factors and correcting the immune response to Th2 [24]. In our study, no significant difference was found in the incidence of IgE-related AD and the proportion of sensitive constitution between the probiotics group and the placebo group, suggesting that the probiotics' prevention effect on AD may not be mediated by IgE.

A few potential limitations of the present meta-analysis should also be acknowledged. First, baseline data are inconsistent in some literatures. Second, single language, different types, dosages, dosage forms, and study regions of probiotics may lead to biased results. Third, only eight studies were

included in the meta-analysis, and the results should be further confirmed by more studies conducted in different populations.

5. Conclusion

In conclusion, our meta-analysis shows that probiotics may have a protective effect on the prevention of AD; the results of our study provide practical and valuable insights for the prevention of AD. Additional studies are needed to establish causality and elucidate the underlying mechanisms.

Data Availability

The datasets used and analyzed during the current study are available from the corresponding author upon reasonable request.

Conflicts of Interest

The authors declare that they have no conflicts of interest.

Supplementary Materials

Figure S1: sensitivity analyses for studies of probiotics and AD. Figure S2: sensitivity analyses for studies of probiotics and related AD. Figure S3: sensitivity analyses for studies of probiotics and sensitive constitution. Figure S4: funnel plot for studies of probiotics and AD. Figure S5: funnel plot for studies of probiotics and related AD. Figure S6: funnel plot for studies of probiotics and sensitive constitution. *(Supplementary Materials)*

References

[1] T. Bieber, "Atopic dermatitis," *The New England Journal of Medicine*, vol. 358, no. 14, pp. 1483–1494, 2008.

[2] H. C. Williams, "Atopic dermatitis," *The New England journal of Medicine*, vol. 352, no. 22, pp. 2314–2324, 2005.

[3] R. Huang, H. Ning, M. Shen, J. Li, J. Zhang, and X. Chen, "Probiotics for the treatment of atopic dermatitis in children: a systematic review and meta-analysis of randomized controlled trials," *Frontiers in Cellular and Infection Microbiology*, vol. 7, p. 392, 2017.

[4] A. J. Mancini, K. Kaulback, and S. L. Chamlin, "The socioeconomic impact of atopic dermatitis in the United States: a systematic review," *Pediatric Dermatology*, vol. 25, no. 1, pp. 1–6, 2008.

[5] E. K. Ha, J. H. Kim, J. H. Kwak et al., "Association of clinical and social factors with risk of fracture in children with atopic dermatitis," *Pediatric Allergy and Immunology*, vol. 33, no. 2, p. e13712, 2021.

[6] S. Ren, Y. Gao, L. Wang et al., "Sacran polysaccharide improves atopic dermatitis through inhibiting Th2 type immune response," *Life Sciences*, vol. 288, p. 120205, 2022.

[7] M. Costley and B. Murphy, "Severe atopic dermatitis treated successfully with dupilumab throughout pregnancy," *Clinical and Experimental Dermatology*, vol. 47, no. 5, pp. 960-961, 2022.

[8] N. Sudo, S. Sawamura, K. Tanaka, Y. Aiba, C. Kubo, and Y. Koga, "The requirement of intestinal bacterial flora for the development of an IgE production system fully susceptible to oral tolerance induction," *Journal of Immunology*, vol. 159, pp. 1739–1745, 1997.

[9] U. Wollina, "Microbiome in atopic dermatitis," *Clinical, Cosmetic and Investigational Dermatology*, vol. Volume 10, pp. 51–56, 2017.

[10] M. Kalliomäki, S. Salminen, T. Poussa, and E. Isolauri, "Probiotics during the first 7 years of life: a cumulative risk reduction of eczema in a randomized, placebo-controlled trial," *The Journal of Allergy and Clinical Immunology*, vol. 119, no. 4, pp. 1019–1021, 2007.

[11] M. Kuitunen, K. Kukkonen, K. Juntunen-Backman et al., "Probiotics prevent IgE-associated allergy until age 5 years in cesarean- delivered children but not in the total cohort," *The Journal of Allergy and Clinical Immunology*, vol. 123, no. 2, pp. 335–341, 2009.

[12] M. P. Jensen, S. Meldrum, A. L. Taylor, J. A. Dunstan, and S. L. Prescott, "Early probiotic supplementation for allergy prevention: long-term outcomes," *The Journal of Allergy and Clinical Immunology*, vol. 130, no. 5, pp. 1209–1211, 2012, e5.

[13] C. E. West, M. L. Hammarström, and O. Hernell, "Probiotics in primary prevention of allergic disease–follow-up at 8-9 years of age," *Allergy*, vol. 68, no. 8, pp. 1015–1020, 2013.

[14] K. Wickens, T. V. Stanley, E. A. Mitchell et al., "Early supplementation with Lactobacillus rhamnosus HN001 reduces eczema prevalence to 6 years: does it also reduce atopic sensitization?," *Clinical and Experimental Allergy*, vol. 43, no. 9, pp. 1048–1057, 2013.

[15] E. X. Loo, G. V. Llanora, Q. Lu, M. M. Aw, B. W. Lee, and L. P. Shek, "Supplementation with probiotics in the first 6 months of life did not protect against eczema and allergy in at-risk Asian infants: a 5-year follow-up," *International Archives of Allergy and Immunology*, vol. 163, no. 1, pp. 25–28, 2014.

[16] S. J. Allen, S. Jordan, M. Storey et al., "Probiotics in the prevention of eczema: a randomised controlled trial," *Archives of Disease in Childhood*, vol. 99, no. 11, pp. 1014–1019, 2014.

[17] M. D. Cabana, M. McKean, A. B. Caughey et al., "Early probiotic supplementation for eczema and asthma prevention: a randomized controlled trial," *Pediatrics*, vol. 140, no. 3, 2017.

[18] B. Björkstén, "Environment and infant immunity," *The Proceedings of the Nutrition Society*, vol. 58, no. 3, pp. 729–732, 1999.

[19] L. Nylund, R. Satokari, S. Salminen, and W. M. de Vos, "Intestinal microbiota during early life - impact on health and disease," *The Proceedings of the Nutrition Society*, vol. 73, no. 4, pp. 457–469, 2014.

[20] L. Nylund, R. Satokari, J. Nikkilä et al., "Microarray analysis reveals marked intestinal microbiota aberrancy in infants having eczema compared to healthy children in at-risk for atopic disease," *BMC Microbiology*, vol. 13, no. 1, p. 12, 2013.

[21] M. G. Pike, R. J. Heddle, P. Boulton, M. W. Turner, and D. J. Atherton, "Increased intestinal permeability in atopic eczema," *The Journal of Investigative Dermatology*, vol. 86, no. 2, pp. 101–104, 1986.

[22] G. R. Gibson, R. Hutkins, M. E. Sanders et al., "Expert consensus document: the International Scientific Association for Probiotics and Prebiotics (ISAPP) consensus statement on the definition and scope of prebiotics," *Nature Reviews Gastroenterology & Hepatology*, vol. 14, no. 8, pp. 491–502, 2017.

[23] R. Fölster-Holst, F. Müller, N. Schnopp et al., "Prospective, randomized controlled trial on Lactobacillus rhamnosus in infants with moderate to severe atopic dermatitis," *The British Journal of Dermatology*, vol. 155, no. 6, pp. 1256–1261, 2006.

[24] R. L. Jan, K. C. Yeh, M. H. Hsieh et al., "Lactobacillus gasseri suppresses Th17 pro-inflammatory response and attenuates allergen-induced airway inflammation in a mouse model of allergic asthma," *The British Journal of Nutrition*, vol. 108, no. 1, pp. 130–139, 2012.

Hindawi
Oxidative Medicine and Cellular Longevity
Volume 2022, Article ID 9014155, 20 pages
https://doi.org/10.1155/2022/9014155

Research Article

Molecular Correlates of Early Onset of Diabetic Cardiomyopathy: Possible Therapeutic Targets

Dongjuan Wang,[1] **Kun Liu**,[2] **Jinyan Zhong**,[1] **Xin Li**,[3] **Jie Zhang**,[3] **Gongxin Wang**,[4] **Ni Li**,[2] **Tianwen Li**,[5] **Harvey Davis**,[6] **Ibrahim El-gaby**,[2] **Guoliang Hao**,[2,4] **Honghua Ye**,[1] **and Dan Li**[2]

[1]*Department of Cardiology, HwaMei Hospital, University of Chinese Academy of Sciences, Ningbo, Zhejiang 315000, China*
[2]*Burdon Sanderson Cardiac Science Centre and BHF Centre of Research Excellence, Department of Physiology, Anatomy and Genetics, University of Oxford, Oxford OX1 3PT, UK*
[3]*Department of Endocrinology, HwaMei Hospital, University of Chinese Academy of Sciences, Ningbo, Zhejiang 315000, China*
[4]*Henan SCOPE Research Institute of Electrophysiology Co. Ltd., Kaifeng 475000, China*
[5]*Ningbo Institute of Life and Health Industry, University of Chinese Academy of Sciences, Ningbo, Zhejiang 315000, China*
[6]*Department of Neuroscience, Physiology and Pharmacology, University College London, London WC1E 6BT, UK*

Correspondence should be addressed to Honghua Ye; lindayenbzjch@163.com and Dan Li; dan.li@dpag.ox.ac.uk

Received 6 January 2022; Accepted 24 March 2022; Published 14 April 2022

Academic Editor: Xun Cui

Diabetes mellitus (DM) is associated with mitochondrial dysfunction and oxidative stress that can lead to diabetic cardiomyopathy (DCM), which can often remain undetected until late stages of the disease. However, myocardial injury occurs before the onset of measurable cardiac dysfunction, although its molecular correlates are poorly understood. In this study, we made a DM rat induced by a high-fat diet combined with low and high doses of streptozotocin (STZ) to emulate pre and early DCM. RNA-sequencing analysis of ventricular tissue revealed a differential transcriptome profile and abnormal activation of pathways involved in fatty acid metabolism, oxidative phosphorylation, cardiac structure and function, insulin resistance, calcium signalling, apoptosis, and TNF signalling. Moreover, using high glucose-treated human induced pluripotent stem cell-derived cardiomyocytes (iPSC-CM), we recapitulated the cardiac cellular phenotype of DM and identified several molecular correlates that may promote the development of DCM. In conclusion, we have developed an experimental framework to target pathways underlying the progression of DCM.

1. Introduction

Diabetes mellitus (DM) is a metabolic disorder that leads to chronic impairment of the cardiovascular system, kidneys, peripheral nervous system, and retina [1]. Accumulating evidence has demonstrated that DM (particularly type 2 diabetes, T2DM) adversely affects patient long-term survival [2]. In particular, T2DM is associated with a higher risk of cardiovascular disease-related death [3] that is coupled to diabetic cardiomyopathy (DCM), which is independent of hypertension, coronary artery disease, or valvular heart disease [4]. DCM is usually clinically asymptomatic can often remain undetected until late stages of the disease, although cardiac functional abnormalities is clearly present during the early stages of the disease.

Mitochondria supply most of the energy that is essential for the heartbeat and control basic cellular functions, including Ca^{2+} signalling homeostasis, ROS generation, and apoptotic cell death regulation [5]. In T2DM, both basic science and clinical studies suggest that cardiac impairment occurs as a result of dysregulated glucose and lipid metabolism, which leads to increased oxidative stress and the

activation of multiple signal pathways resulting in myocardial injury [6]. High levels of reactive oxygen species (ROS) uncouple the mitochondria electron transport chain (ETC), thereby reducing mitochondrial ATP production. This eventually triggers mitochondrial permeability transition pore (mPTP) opening and cardiomyocyte death [7]. Although measures of cardiac performance can be used to assess subclinical cardiac abnormalities, myocardial injury occurs early and before the onset of measurable cardiac dysfunction. The extent to which diabetes status may confer the risk of myocardial injury remains unclear.

The present study was designed to characterize the underlying molecular correlates associated with cardiac abnormalities in a rat model of DM. We used whole transcriptome analysis with total RNA sequencing (RNA-Seq) to capture the effect of changes in gene expression caused by DM. To test whether these targets could be recapitulated in an analogue model of cardiac DM, we used high glucose-treated human induced pluripotent stem cell- (hiPSC-) derived cardiomyocytes to explore potential therapeutic target genes that may promote the development of DCM.

2. Materials and Methods

2.1. Rat DM Model Experiments

2.1.1. Animal Preparation. Male Sprague–Dawley rats (250–300 g) were randomly assigned to 3 groups: control group (Con, $n = 10$), low dose group (Low, $n = 15$), and high dose group (High, $n = 15$). The control group was fed with a normal chow diet consisting of 12% fat, 66% carbohydrates, and 22% protein, and the other two groups were fed with a high-fat diet consisting of 60% fat, 5% carbohydrates, and 34% protein, according to the protocol of Mansor et al. [8]. After 2 weeks, the low and high groups received a single intraperitoneal injection of STZ (Sigma, Low: 35 mg/kg; High: 50 mg/kg) [9]. Fasting blood glucose levels were tested once a week. All experiments were conducted under the National Institutes of Health Guidelines on the Use of Laboratory Animal and were approved by the University of Chinese Academy of Sciences on Animal Care.

Nine weeks after STZ injection, rats fasted overnight and blood glucose, insulin, triglyceride (TG), total cholesterol (TC), low-density lipoprotein cholesterol (LDL-C), lactate dehydrogenase (LDH), and free fatty acid (FFA) were measured. An oral glucose tolerance test (OGTT) was performed as described previously [8]. The homeostasis model assessment estimated insulin resistance (HOMA-IR) was calculated as (fasting serum glucose × fasting serum insulin/22.5 [10]. The cardiac weight index was used to evaluate the hypertrophic response, which was calculated as the heart weight (HW, g)/body weight (BW, g) as previously described [11].

2.1.2. Real-Time RT-PCR. Hearts from each group were isolated, and total mRNA was extracted with Trizol reagent (Invitrogen, USA). PrimeScript RT Master Mix kit (Takara Biotechnoly (Dalian) Co., China) was used to conduct reverse transcription, then, Fast SYBR Green Master Mix (Applied Biosystems, USA) was used to perform real-time RT-PCR (Applied Biosystems, USA). RT-PCR was carried out in a total volume of 20 μl reaction mixture according to the manufacture's protocol. Amplifications were carried out as follows: 95°C for 3 min, 40 cycles of 95°C for 15 s, and 60°C for 45 s. Primers used are listed in Supplementary Table 1. Gene expression was normalized to GAPDH that was used as an internal control. Fold changes in gene expression were measured using the $2^{-\Delta\Delta CT}$ method.

2.1.3. RNA-Seq and Bioinformatics. RNA-Seq was based on previous rat studies [12, 13]. Here, total RNA was extracted from freshly isolated rat left ventricular tissue (4 samples per group) by using the RNeasy Kit from QIAGEN (Qiagen, Hilden, Germany) with DNase I treatment used according to the manufacturer's protocol. RNA quality and concentration were tested with Bioanalyzer 2100 (Agilent, CA, USA). All samples fulfilled the criteria of RNA integrity number > 7 and concentration > 50 ng/μl. Sequencing libraries were constructed in Beijing Genomics Institute (Beijing, China) using a modified protocol similar to the TrueSeq Stranded Total RNA with RiboZero Kit (Illumina Inc.). RNA sequence was performed on BGISEQ-500 platform.

SOAPnuke (v1.5.2) was used to filter reads and generate FASTQ format. Clean reads were aligned to the reference rat genome using the Bowtie2 (v2.2.5) with default parameters and calculated gene expression level with RSEM (v1.2.12). The differentially expressed genes (DEGs) were identified with more than double fold change, and the corrected P value is less than or equal to 0.05. In gene ontology (GO) analysis and pathway analysis, DEGs were classified according to official classification with the GO or Kyoto Encyclopedia of Genes and Genomes (KEGG) annotation results, and Phyper (a function of R) was performed on GO and pathway functional enrichment. The false discovery rate (FDR) was calculated for each P value with FDR ≤ 0.05 defined as significantly enriched. Protein-protein interaction results obtained from STRING database (v11.5) with default settings. Cytoscape software (v3.8.2) was applied to visualize the protein interaction relationship network and analyze hub genes.

2.1.4. Histological Analysis. Hematoxylin–eosin (HE) staining and Masson's trichrome staining were conducted as previously described [14, 15]. Briefly, the excised heart tissues were embedded in paraffin, cut into 5 μm thick serial sections, and then stained with HE or Masson's trichrome. Masson's trichrome was used to analyze the collagen fraction in the myocardium with cardiomyocytes stained red and collagen fibers stained blue. The percentage of the total area covered by collagen was analyzed with Image-Pro Plus software version 6.0, which calculated as follows: collagen area/view area × 100.

2.1.5. DHE Staining. Dihydroethidine (DHE) staining was used to measure the intracellular ROS according to the oxidative fluorescent microtopography, as described recently [16]. Frozen left ventricular cardiac sections from rats were stained with 10 μmol/L DHE in a dark and humidified chamber for 30 minutes at 37°C. Omission of DHE was used

as a negative control. DHE staining was visualized under a confocal microscope (Olympus FV 1000, Tokyo, Japan), and images were analyzed with Image-Pro Plus software version 6.0. The mean fluorescence intensity of each section was calculated, and the total section emission signals per field were averaged for data analysis.

2.1.6. Caspase-3 Expression. Caspase-3 expression in heart was measured in the heart via immunofluorescence staining. Briefly, the isolated heart tissues were embedded in a paraffin and cut into 5 μm thick serial sections. After dehydrating, heat-induced antigen retrieval was performed by boiling the sections in citrate buffer, pH 6.0, in a microwave oven. To block endogenous peroxidase activity, sections were incubated in a solution of 3% H_2O_2 for 20 min at room temperature. Then, caspase-3 antibody (1:200; Tocris Bioscience) was incubated overnight at 4°C, followed by detection with corresponding fluorescent secondary antibodies (Santa Cruz Biotechnology, CA) for 1 h at 37°C. Nuclei were counterstained with DAPI. Samples were examined by a confocal microscope (Olympus FV 1000).

2.1.7. TUNEL Assay. Terminal deoxy-nucleotidyl transferase-mediated dUTP nick end-labeling (TUNEL, in green) assay was conducted to detect myocardial apoptosis using an In Situ Cell Death Detection Kit (Roche, Germany) according to the manufacturer's instructions. The index of apoptosis was expressed as the proportion of TUNEL positive nuclei to the total number of nuclei (DAPI, in blue) in percentage.

2.1.8. Optical Mapping of Ex Vivo Cardiac Preparations. The rats were euthanized (isoflurane; 1 ml/kg) and heparinized (120 IU). Hearts were excised and retrogradely perfused via the aorta with KH solution (in mmol/L: 119 NaCl, 4 KCl, 1.8 $CaCl_2$, 1 $MgCl_2$, 1.2 NaH_2PO_4, 25 $NaHCO_3$, and 10 glucose; 95% O2/5% CO_2) at 10 mL/min and 37°C. Dye loading was transfused by preperfusion with pluronic F127 (20% *w*/*v* in DMSO). Rhod2-AM (1 mg/ml) was perfused for 25 minutes at 37°C to perform Ca^{2+} measurements. The heart was illuminated by 530 ± 25 nm LED (MappingLab). The fluorescence light was bandpass filtered (wavelengths 511–551 nm) to minimize stray excitation light reaching the dyes. The emitted fluorescence signal was filtered with a 590 nm bandpass filter (bandwidth 35 nm), then imaged by a CMOS camera (OMS-PCIE-2002, MappingLab). Digital images (150 × 150 pixels) were gathered at a sampling rate of 0.8 kHz from a 2.2 × 2.2 mm field of view.

Optical mapping data were analyzed using a commercially available software (OMapScope5.7.8, MappingLab). Optical signals were spatially aligned and processed using a Gaussian spatial filter (3 × 3 pixels). Local activation time was assigned based on the maximum departure velocity of the Vm upstroke. Time to peak was defined as the time from initiation of Ca^{2+} to peak fluorescence. CTD90 was calculated.

2.2. Human Induced Pluripotent Stem Cell-Derived Cardiomyocyte Experiment

2.2.1. hiPSC-CM Differentiation and Maturation. Healthy hiPSC lines SFC-854 and OX1-19 were cultured in mTeSR medium on Matrigel-coated plates and were dissociated using ReLeSR at 90-100% confluency. After 3 passages, the cells were then transferred onto Matrigel–coated 12 well plates for differentiation. The hiPSC-CM differentiation was carried out according to the procedure described in a previous report [17]. In brief, cells were cultured and expanded to 90% cell confluence and then treated for 2 days with 6 μmol/L CHIR99201 in differentiation medium (RPMI medium supplemented with 1% B-27 supplement minus insulin). On day 3, cells were treated with 2.5 mmol/L Wnt-C59 to inhibit the Wnt signalling pathway. The purification medium was applied on day 11 and 13 by changing of the medium to no-glucose RPMI with 1% B27 minus insulin and 5 mmol/L sodium lactate. hiPSC-CM maturation was initiated from day 16 to day 20 with maturation medium (MM): DMEM containing 5 mmol/L glucose supplemented with 0.4 mmol/L oleic acid conjugated to BSA, 50 nmol/L insulin, 10% fetal calf serum inactive, 1% glutamine, and 1% penicillin–streptomycin (P/S). To achieve a high glucose environment, hiPSC-CM was treated with 5.5, 11, and 25 mmol/L glucose for 2 days.

2.2.2. Cell Area and Nuclear Area Measurement. Cell size and nuclear size were measured using ImageJ (v1.53n, NIH, US). iPSCs-CMs were dissociated and replated in fluorodish, cultured in maturation medium for 2 days, and incubated with 5.5, 11, and 25 mmol/L glucose for 48 hours. Cells were fixed with 4% formaldehyde, permeabilized with 0.1% Triton, blocked with 6% donkey serum, and then stained with antibodies against the cytoskeleton protein troponin-T (ab45932) and α-actinin (sigmaA7811), and Hoechst for nucleus. Immunofluorescence images of the same scale were taken using a Leica confocal microscope (Leica TCS SP5) with a 60× oil immersion objective, which were then loaded in ImageJ for area measurement. For each image, all cells were manually selected with the freehand selection tool of ImageJ for the measurement of cell size, and nuclei were automatically selected by thresholding the images of the channel of nuclei.

2.2.3. Glucose Uptake. hiPSC-CMs were seeded on 96-well plates (3.5×10^4 cells/well), then, cells were treated with 5.5, 11, or 25 mmol/L glucose for 2 days. Glucose uptake of 2-deoxyglucose (2DG) was measured in hiPSC-CMs using a glucose uptake Glo™ assay kit (Promega, J1342), and luminescence intensity (Relative light unit, RLU) was measured following the manufacturer's instruction.

2.2.4. Production of Reactive Oxygen Species (ROS). hiPSC-CMs were seeded in 96-well plates (3.5×10^4 cells/well) and treated with 5.5, 11, or 25 mmol/L glucose for 2 days. ROS in live hiPSC-CMs were quantitatively assessed using a cellular ROS assay kit (ab113851, Abcam) according to the manufacturers' instructions.

2.2.5. ATP Assay of Cell Viability. The amount of ATP in cells correlated with cell viability was determined by CellTiter-Glo 2.0 Cell Viability Assay (Promega, USA, G9242) according to the manufacturer's protocol. hiPSC-

CMs were seeded on 96-well plates (3.5×10^4 cells/well), incubated with 5.5, 11, or 25 mmol/L glucose for 2 days.

2.2.6. Intracellular Free Calcium Concentration Measurement. Intracellular free calcium concentration ($[Ca^{2+}]_i$) using Fura-2-acetoxymethyl ester (Fura-2/AM) was performed as described earlier with slight modification [18]. Briefly, cultured hiPSC-CMs were incubated in 5 μmol/L Fura-2/AM for 30 min at 37°C. Loaded hiPSC-CMs were imaged with a QICLICK digital CCD camera (Photometrics) connected to an OptoLED fluorescence imaging system housed on an inverted Nikon microscope equipped with a 40× oil immersion objective. The evoked $[Ca^{2+}]_i$ transient was evaluated by 30-second exposure to 1 Hz field stimulation or FCCP (carbonylcyanide-p-trifluoromethoxyphenylhydrazone, 3 μmol/L). The ratio of the fluorescence intensity (R) emitted at 510 nm obtained by alternately exciting at 340 and 380 nm at each time interval is used to estimate the changes in intracellular free Ca^{2+} concentration.

2.2.7. Detection of Mitochondrial Calcium. To measure mitochondrial Ca^{2+} ($[Ca^{2+}]_m$), hiPSC-CMs were loaded with 5 μmol/LRhod-2/AM for 25 min at 37°C. Rhod-2 has a net positive charge, which promotes preferential sequestration in the mitochondria due to potential-driven uptake. FCCP-induced $[Ca^{2+}]_m$ release was assessed by the decline in Rhod-2/AM fluorescence intensity.

2.2.8. Mitochondrial Membrane Potential Measurement. Mitochondrial membrane potential (MMP) change was assessed in hiPSC-CMs using the lipophilic cationic probe 5,5′,6,6′-tetrachloro-1,1′,3,3′-tetraethylbenzimidazol-carbocyanine iodide (JC-1,thermofisher, T3168) following the manufacturer's protocol. hiPSC-CMs were cultured at a density of 3.5×10^5 cells/FluoroDish for 2 days and then treated with 5.5, 11, or 25 mmol/L glucose for a further 2 days. Cells were incubated with 2 μmol/L JC-1 dye for 30 min at 37°C. The green and red fluorescences were measured using an Airyscan confocal microscope (ZEISS 880). The ratio of red to green mean fluorescence intensity was quantified using ImageJ.

2.3. Statistical Analysis. Statistical analyses were performed using Prism version 9 software (GraphPad Software, La Jolla, CA). Unpaired *t*-test or one-way analysis of variance was used to determine differences between the control and two treatment groups. The values are presented as the means ± SE. Statistically significant difference was set at $P < 0.05$.

3. Results

3.1. Assessment of Cardiac Parameters and Glucose Handling across Experimental Groups. After 9 weeks of STZ treatment, the heart rate did not differ among groups (Figure 1(a)). Rats from the high STZ group exhibited significant higher serum levels of glucose, insulin, HOMA-IR, TC, TG, and FFA compared with control. In addition, glucose, insulin, HOMA-IR, TG, and FFA in the high STZ group displayed a significant difference relative to the low group, and the glucose level in the low STZ was enhanced when compared to the control (Figures 1(b)–1(f) and 1(i)). Furthermore, LDL-C and LDH levels did not differ among groups (Figures 1(g) and 1(h)). All rats received OGTT. Figure 1(j) displays the serum glucose concentrations after an oral glucose challenge in these animals. It is apparent that serum glucose concentration in response to oral glucose was higher in the low and high STZ groups, which demonstrated that the diabetic model was successfully established.

3.2. Cardiac Remodelling in Different Experimental Groups. To determine the degree of cardiac remodelling in diabetic rats, cardiac weight index and myocardial collagen deposition were measured. As shown in Figure 2(a), heart weight was normalized to body weight and did not differ between the control and low STZ groups, while in the high STZ group the cardiac weight index was significantly enhanced relative to control. Increased ANP and BNP gene expression by qRT-PCR was observed in STZ groups when compared with controls (Figures 2(b) and 2(c)). HE staining (Figure 2(d)) revealed an approximately normal microstructure of cardiomyocytes in the control. In the high STZ group, cardiomyocytes showed interstitial edema and lymphocytic infiltration (marked with red arrow). These abnormal structures were less frequent in the low STZ group. Masson's trichrome staining demonstrated that interstitial collagen deposition was significantly increased in the high group as compared with the control group, but the low STZ group did not display increased collagen deposition in the myocardium (Figures 2(e) and 2(f)).

3.3. RNA-Seq Analysis Revealed a Differential Transcriptome in DM Rats. Previous studies have identified multiple intracellular pathways involved in the pathogenesis of diabetic cardiomyopathy [19], but the molecular cues underlying cardiac damage in DM remain elusive, especially in different diabetes status. To further investigate the molecular mechanisms behind the progression of diabetic damage, we performed genome-wide RNA-Seq by comparing control, low, and high STZ treated rats. We observed that 116 genes out of 37,246 total genes (87 upregulated and 29 downregulated) were differentially expressed in control vs. low STZ; 253 genes (91 upregulated and 162 downregulated) were differentially expressed in low vs. high STZ; 1189 genes (582 upregulated, and 607 downregulated) were differentially expressed in control vs. high (Figures 3(a) and 3(b)). Among these, there are 2 common differentially expressed genes (DEGs) from 3 comparison groups: *Hist2h2aa2*, histone cluster 2 H2A family member A2, which is the core component of the nucleosome, enables protein heterodimerization activity; *Decr1*, is an enzyme that participates in fatty acid β-oxidation and metabolism of polyunsaturated fatty enoyl-CoA esters[3]. These two common genes can be candidates to be further analyzed and validated as diagnostic markers to track the process of diabetic cardiomyopathy (Figure 4(b)). According to Log2-fold change between control and high STZ groups, the top 50 upregulated and 50 downregulated genes were selected, and the clean reads value of these genes in the 3 groups are displayed as a

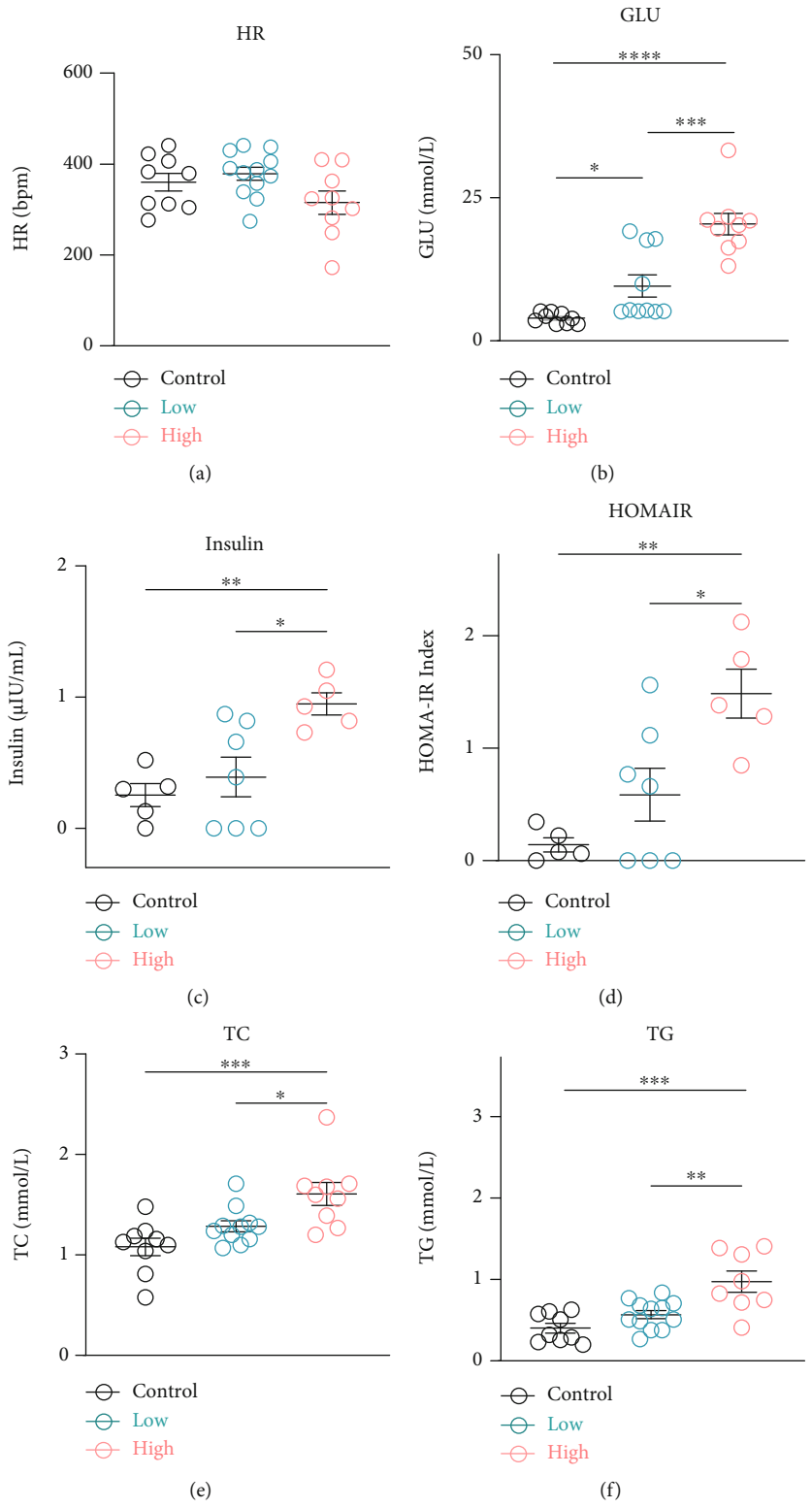

Figure 1: Continued.

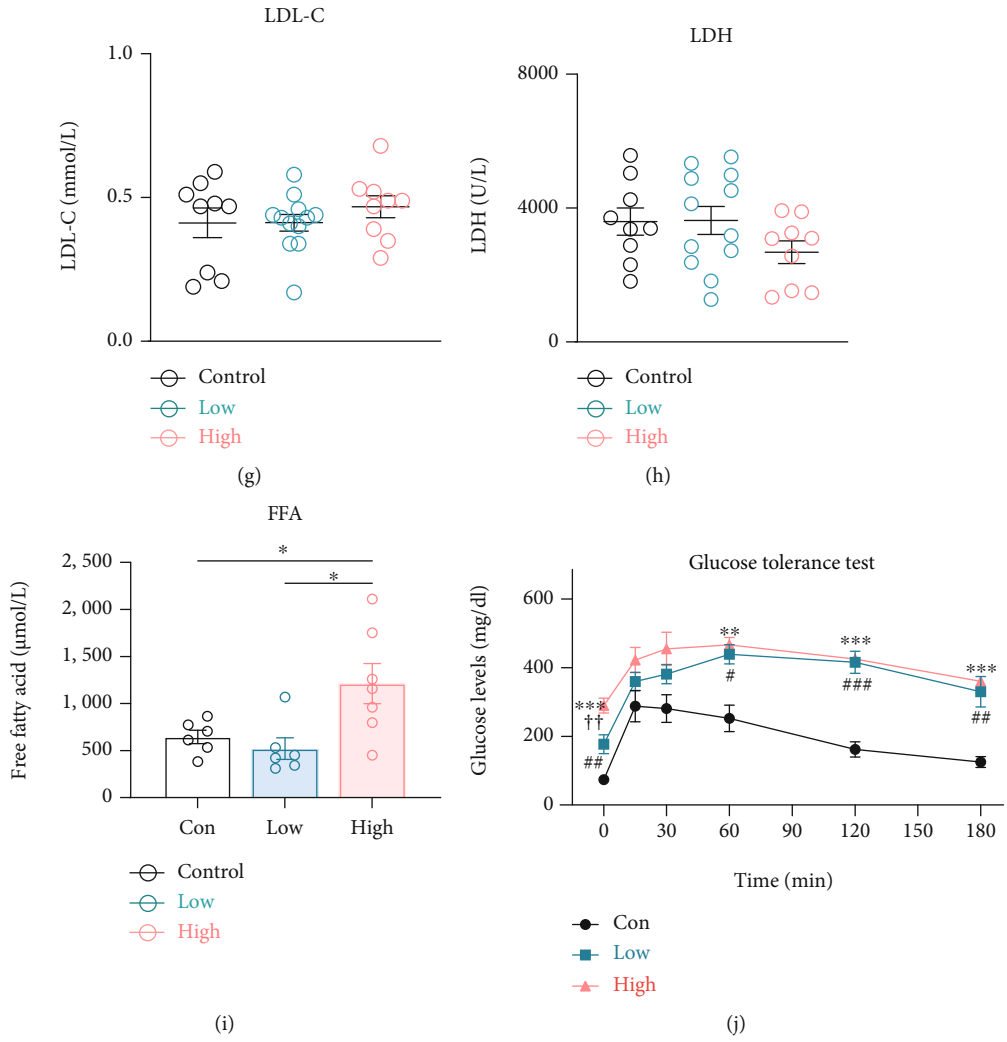

Figure 1: Basic parameters of rats in different experimental groups. (a) HR in the three groups. Serum levels of GLU (b), insulin (c), TC (e), TG (f), LDL-C (g), LDH (h), and FFA (i) in the three groups. (d) Assessment of insulin resistance in the three groups. (j) Mean plasma glucose concentration in response to an oral glucose challenge. Data are expressed as mean ± SE. $^{*}P < 0.05$, $^{**}P < 0.01$, $^{***}P < 0.001$, $^{****}P < 0.0001$. For (j): $^{**}P < 0.01$, $^{***}P < 0.001$, high STZ treated group compared with control; $^{\#}P < 0.05$, $^{\#\#}P < 0.01$, $^{\#\#\#}P < 0.001$, low STZ group compared with control; $^{\dagger\dagger}P < 0.01$, low STZ compare with high STZ treated group. Con: control group; Low: low STZ group; High: high STZ group; HR: heart rate; GLU: glucose; TC: total cholesterol; TG: triglyceride; LDL-C: low-density lipoprotein cholesterol; LDH: lactate dehydrogenase; FFA: free fatty acid. $n = 9 - 12$ per group.

heatmap (Figure 3(c)), demonstrating the differential gene expression pattern between the 3 groups.

Based on the GO enrichment, the top 10 GO terms in biological processes which the DEGs were enriched according to the gene count are presented in Figure 3(d). GO analysis revealed that genes were enriched in "fatty acid beta-oxidation," "fatty acid metabolism," "lipid metabolic process," and "skeletal muscle cell differentiation" from Con vs. Low; "protein folding," "negative regulation of transcription by RNA polymerase II," "negative regulation of apoptotic process," and "cellular response to oxygen levels" by comparing low and high STZ; and "mitochondrial respiratory chain complex I assembly," "oxidation-reduction process," "fatty acid metabolic process," and "fatty acid beta-oxidation" from control vs. high STZ. According to the KEGG pathway classification, we also selected key genes which related to fatty acid metabolism, oxidative phosphorylation, cardiac structure and function related, insulin resistance, calcium signalling, apoptosis, and TNF pathway (Figure S1) are significant changed between the control and high STZ groups. There is also a corresponding trend in the low STZ group. These results indicate a differential transcriptomic profile expressed in different stages of diabetic cardiomyopathy.

Dysregulation in a protein subnetwork may yield dysfunctional multiple protein subnetworks. We performed the protein-protein interaction (PPI) analysis to identify the functional subnetworks of the genes of interest for KEGG pathways using the web-based visualisation resource STRING. Nodes encircled in pink, red, blue, yellow, green, and brown indicate significant genes in pathways involved oxidative phosphorylation, cardiac muscle contraction,

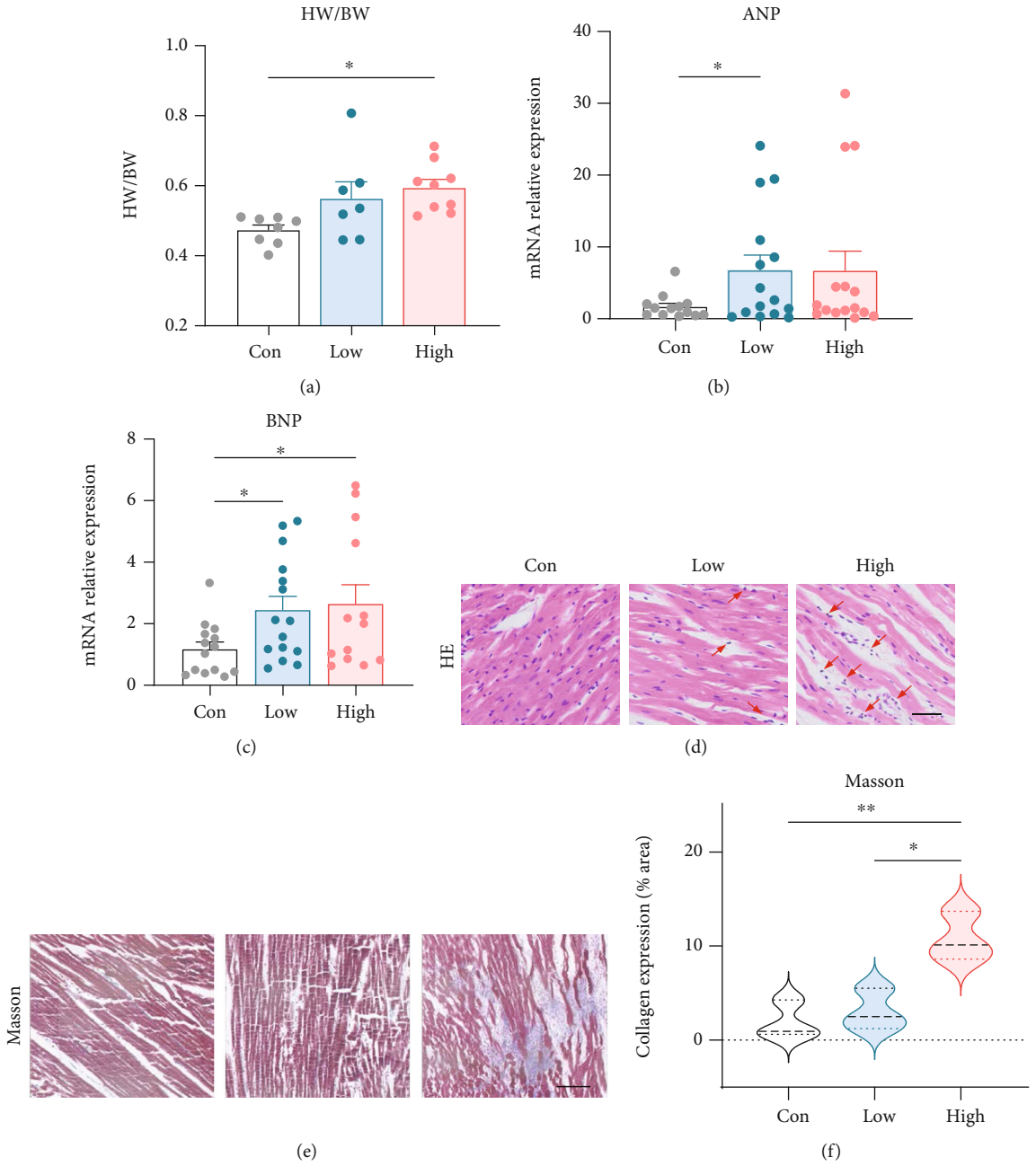

Figure 2: Cardiac remodeling in different experimental groups. (a) Heart weight normalized to body weight. qRT-PCR assay for *ANP* (b) and *BNP* (c) mRNA expression in myocardial tissue. Representative images of HE staining ((d), arrows indicated lymphocytic infiltration; scale bar, 12.5 μm) and Masson's trichrome staining ((e): red, cardiomyocytes; blue, collagen fibers; scale bar, 50 μm). (f) Quantitative analyses of the positive staining of collagen expression (results are from 3-4 images per group). $^{*}P < 0.05$, $^{**}P < 0.01$. Con: control group; Low: low STZ group; High: high STZ group; HW: heart weight; BW: body weight.

calcium signalling, fatty acid metabolism, insulin resistance, apoptosis, and TNF pathway, respectively (Figure 4(a)). All genes in this network were quantified and ranked by the clustering coefficient measurement with cytoscape software, in which the TOP 20 nodes were identified as hub genes (indicated in bigger icons) and listed at supplement table 2.

To validate the identified genes from control and STZ treated rats, myocardial tissues were extracted to measure mRNA levels. Two common DEGs from 3 comparison groups (*Hist2h2aa2* and *Decr1)* and 7 hub genes from listed supplement table 2 (*Ndufv2*, *Ndufa5*, *Cox7c*, *Calm2*, *Ddit3*, *Scp2*, and *Prkag1*, based on $\log_2$FC and *Q* values in RNA-Seq analysis) were selected. Only *Decr1*, *Calm2*, and *Ddit3* were expressed statistical significance when compare with control group (Figure 4(b)).

3.4. Measurements of Cardiac Oxidative Stress and Apoptosis in Different Experimental Groups. Based on the results from RNA-Seq, we verified whether oxidative stress and apoptosis are altered in different stages of DCM rat models. ROS

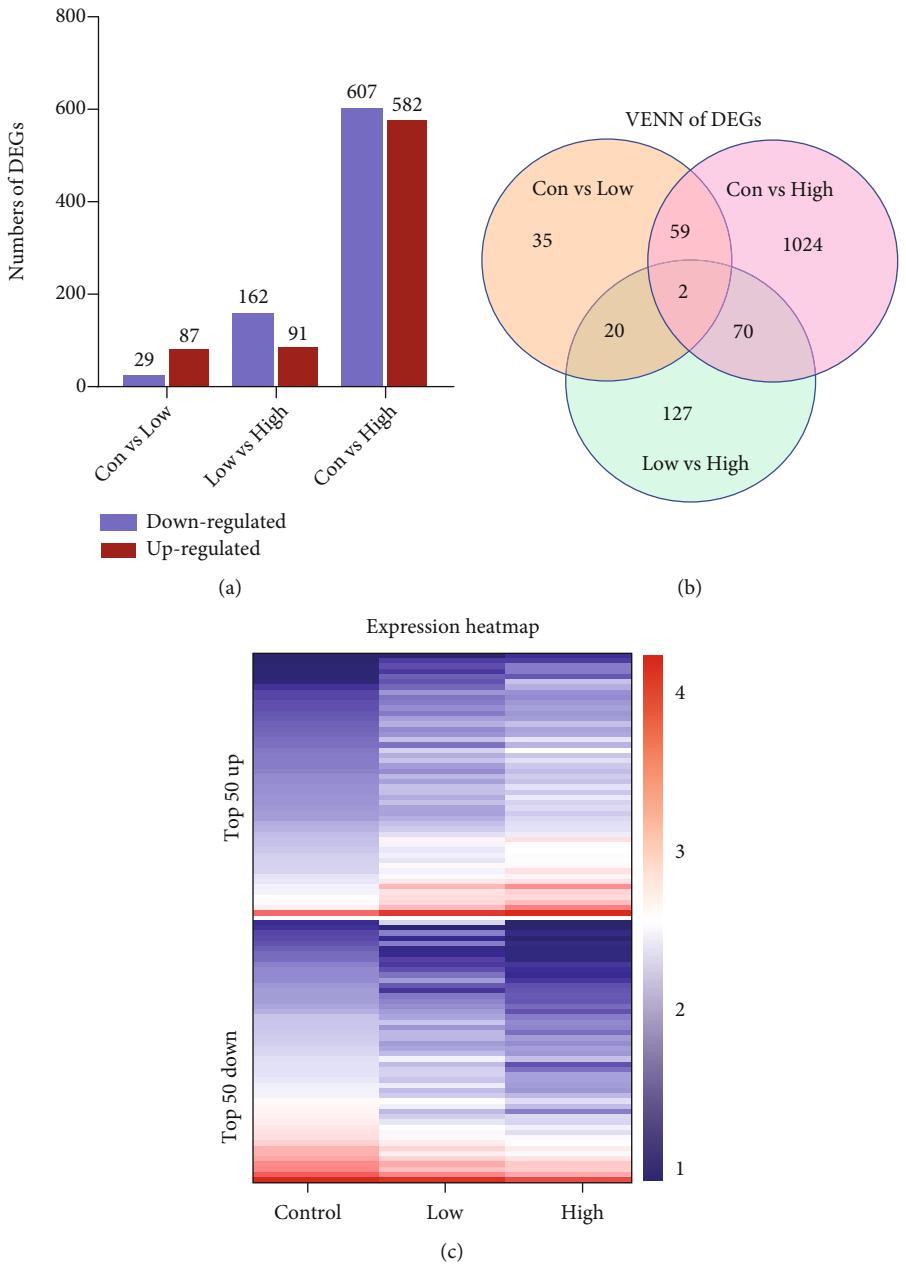

Figure 3: Continued.

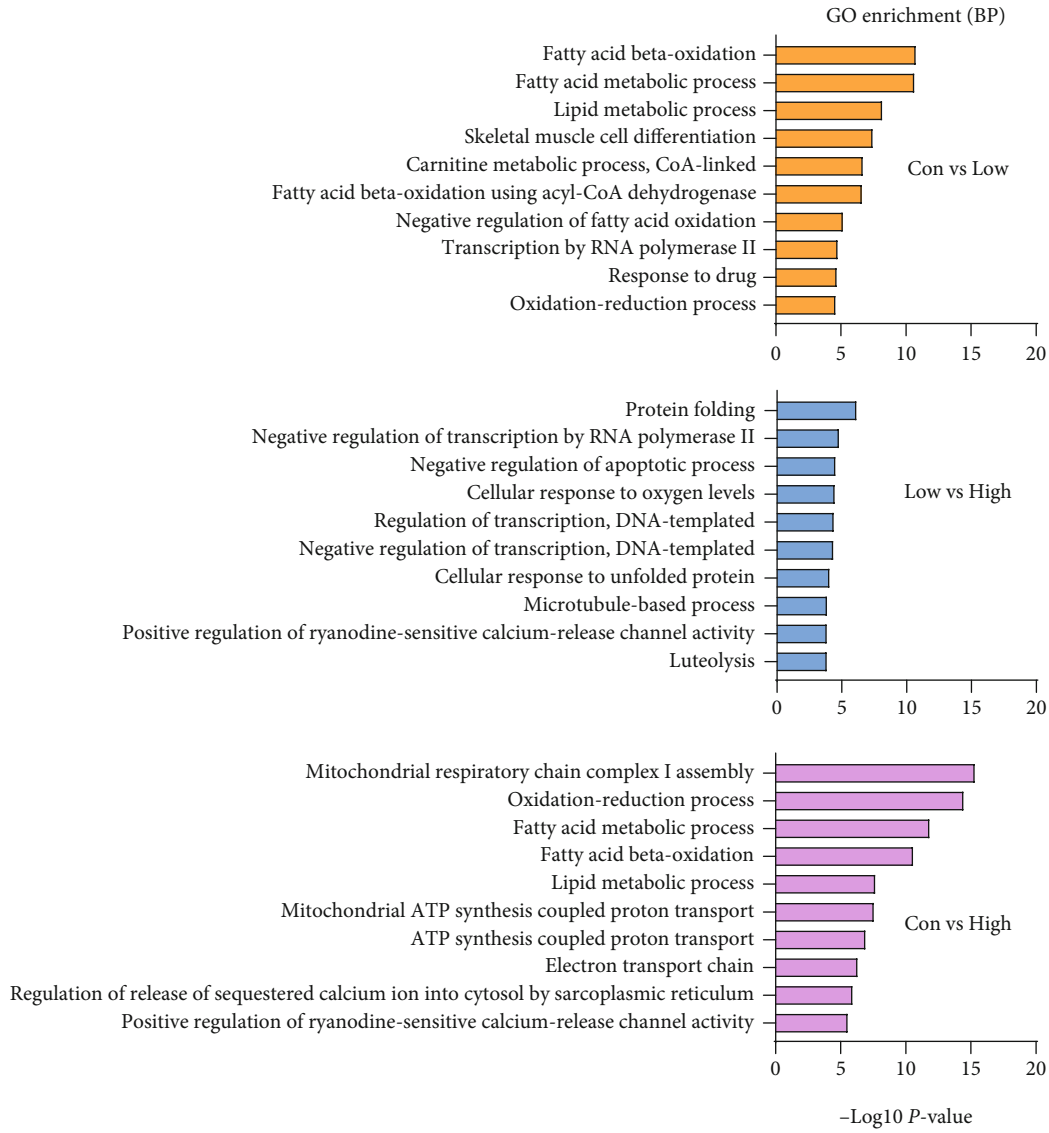

(d)

Figure 3: RNA-Seq analysis revealed differentially expressed genes (DEGs) in the left ventricle from control, low, and high doses of streptozotocin-injected high-fat diet rats. (a) The bar graph shows the number of up and downregulated DEGs in Con vs. high is great than Con vs. low and low vs. high comparison. (b) Venn diagram showing separate and overlapping expression of DEGs when the control, low, and high groups are compared with each other. Each circle represents a group of gene sets, and the areas superimposed by different circles represent the intersection of these gene sets. (c) Heatmap expression of the top 50 upregulated and 50 downregulated DEGs which selected from Con vs. high, and the reads value of these genes in the 3 groups are displayed. (d) The 10 most significantly ($P < 0.05$) enriched GO terms in the biological process branch are presented in three groups of comparisons. Con: control group; Low: low STZ treated group; High: high STZ treated group.

accumulation is known to play a major role in diabetic complications including diabetic cardiovascular disease. DHE staining showed that ROS production from the left ventricle trended upward in both low and high STZ groups and was significantly enhanced in the low and high STZ treated groups (Figure 5(a)).

To investigate cardiac apoptosis in diabetic hearts, caspase-3 immunofluorescence staining and TUNEL assay were performed. As shown in Figures 5(b) and 5(c), the high-dose group had a significant higher rate of myocardial apoptosis on caspase-3, but this did not reach a significant difference on TUNEL when compared with control. There was no significant difference between the control and low STZ groups.

3.5. Optical Mapping of Intracellular Calcium in Different Experimental Groups. From the RNA-seq analysis, we detected calcium signalling pathway genes, especially *Calm2* and *Atp2A2* that were significantly altered in the STZ treated group. To investigate whether the intracellular calcium transient was impaired in the pre and early stage of DCM rats, we performed optical fluorescence mapping using

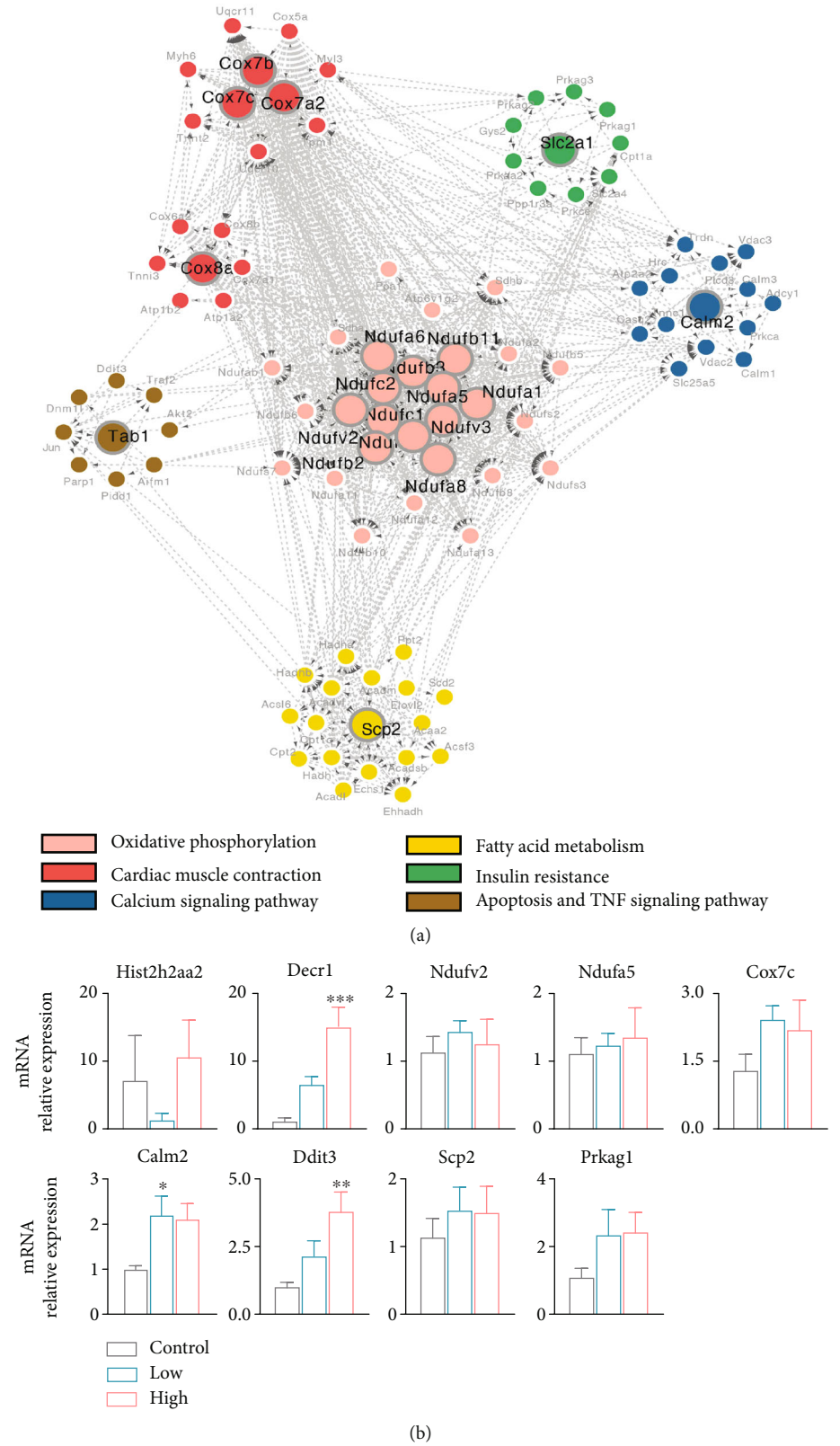

Figure 4: (a) Analysis of hub genes from protein-protein interaction (PPI) network for the candidate pathways. Nodes encircled in pink, red, blue, yellow, green, and brown indicate significant genes in pathways involved oxidative phosphorylation, cardiac muscle contraction, calcium signalling, fatty acid metabolism, insulin resistance, apoptosis, and TNF pathway, respectively. (b) Validation of key genes in ventricular tissue of rats in control, low and high STZ treatment groups using RT-PCR. $^{*}P < 0.05$, $^{**}P < 0.01$, $^{***}P < 0.001$. Compared with control. $n = 6 - 7$ per group.

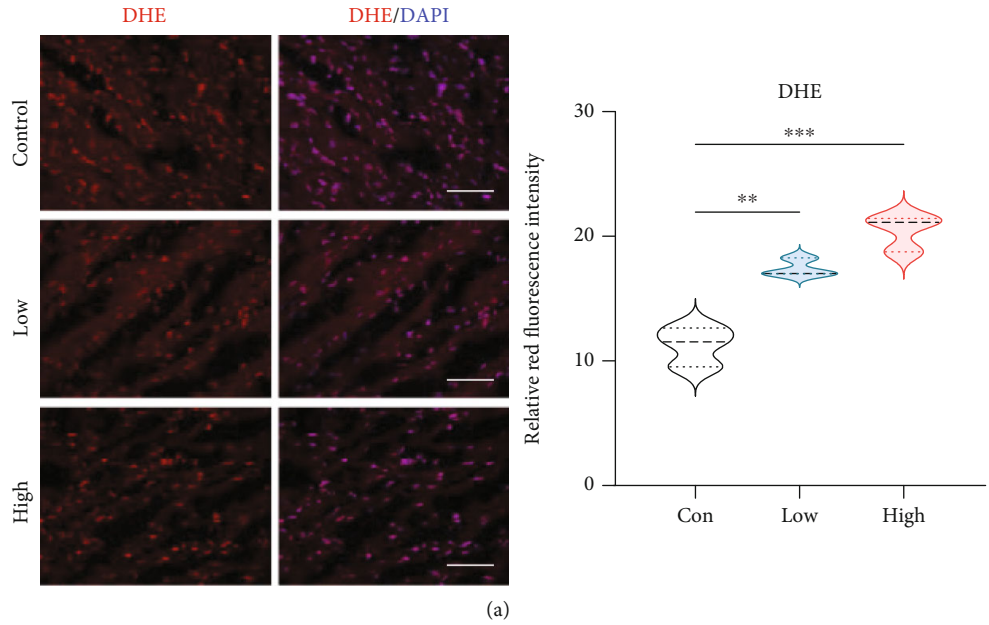

(a)

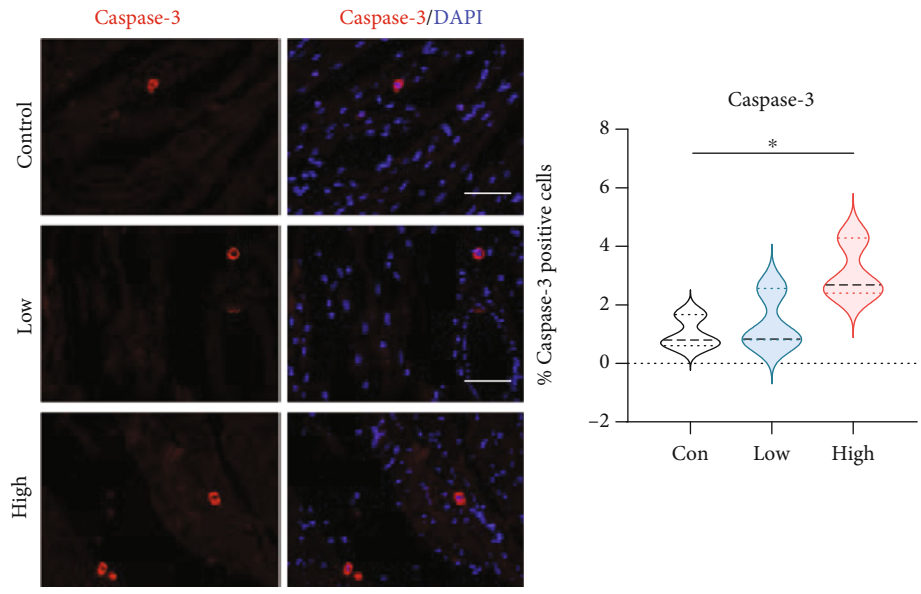

(b)

Figure 5: Continued.

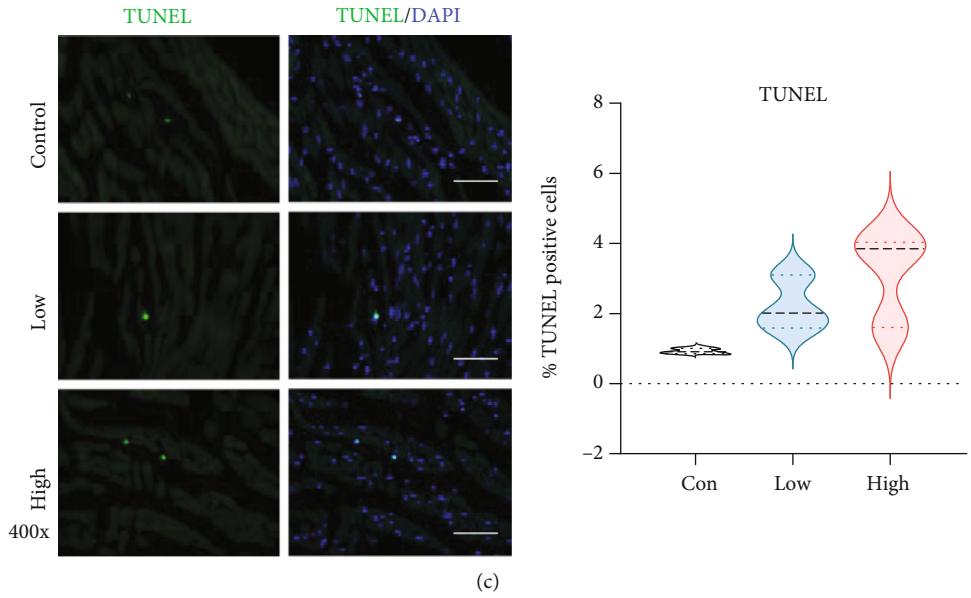

Figure 5: Cardiac oxidative stress and apoptosis in different experimental groups. (a) Representative images of DHE staining for myocardial tissues (red, DHE; blue, DAPI) and the average fluorescence intensity were summarized. (b) Representative images of immunofluorescence for apoptotic cells (red, caspase-3; blue, DAPI). The apoptotic index was quantified by Image-Pro Plus software. (c) Representative images of immunofluorescence for apoptotic cells (green, TUNEL; blue, DAPI). The apoptotic index was quantified by Image-Pro Plus software. Results are from 3-4 images per group. Data are expressed as mean ± SE. $^{*}P < 0.05$, $^{**}P < 0.01$, $^{***}P < 0.001$. Con: control group; Low: low STZ treated group; High: high STZ treated group. Scale bar, 12.5 μm.

Rhod-2AM on sinus-paced Langendorff-perfused hearts (Figure 6(a)). The mapping of intracellular calcium transients at the anterior ventricular wall demonstrated that the conduction time (Figures 6(c) and 6(e)) and amplitude (Figure 6(f)) of the intracellular calcium transient did not significantly change with the intrinsic heart rate. However, there was a significant prolongation in the 90% calcium transient duration (CTD90, Figures 6(d) and 6(g)), especially in the high-dose group during high frequency (5 Hz) stimulation. The reduction of *Atp2A2* (ATPase Sarcoplasmic/Endoplasmic Reticulum Ca^{2+} Transporting 2) gene expression in high STZ group, which is responsible for calcium uptake into the sarcoplasmic reticulum (SR), may contribute to prolonging the CTD90.

3.6. Physiological Phenotyping of High Glucose-Treated Human iPSC-Derived Cardiomyocytes

3.6.1. Cell Size, Glucose Uptake, ROS, and ATP Production in High Glucose-Treated iPSC-CM. Exposure to high levels of glucose increased both cell area and nuclear area (Figures 7(a) and 7(b)). iPSC-CMs of the 25 mmol/L glucose group presented a significant nuclear enlargement compared to 5.5 mmol/L control group, while the increase of nuclear size of the 11 mmol/L group was insignificant. Cell size also showed a tendency to increase with the elevation of glucose level, although the difference is less remarkable than nuclear change. Cellular and nuclear hypertrophies suggest activated cellular metabolic biosynthesis under the effect of high glucose. The glucose uptake (Figure 7(c)) and ATP production (Figure 7(e)) displayed significant suppressed; ROS production (Figure 7(d)) enhanced in the 25 mmol/L glucose group compared to 5.5 mmol/L control group. The glucose uptake was also reduced in the 11 mmol/L glucose group, but did not detect changes in ROS and ATP.

3.6.2. $[Ca^{2+}]_i$ Measurement in hiPSC-CMs. To explore if the high glucose environment could alter calcium handling in hiPSC-CMs, we first measured intracellular free calcium concentration ($[Ca^{2+}]_i$) using ratiometric recordings with Fura-2/AM. A trace for the calcium transient in response to 1 Hz field stimulation is shown in Figure 8(a). Baseline ratio was elevated in the 25 mmol/L glucose group, while no change was found from 11 mmol/L compared with control 5.5 mmol/L cells (Figure 8(b)). Stimulation evoked increases in $[Ca^{2+}]_i$ were significantly enhanced in both 11 and 25 mmol/L glucose groups when compared with 5.5 mmol/L control (Figure 8(c)), and the difference between the 11 and 25 mmol/L glucose groups was also remarkable. These results suggest that high glucose exposure impaired calcium handling in hiPSC-CMs.

Evoked $[Ca^{2+}]_i$ responses are influenced by multiple factors. To check if the sarco(endo)plasmic reticulum calcium transport ATPase (SERCA) pump, which is modulated by the protein products of the *Atp2a2* gene, a SERCA pump inhibitor thapsigargin was introduced into the cells (Figure 8(b)). 1 μmol/L thapsigargin showed rapidly increased $[Ca^{2+}]_i$. This enhancement tended to reduce with the elevation of glucose level on both peak and plateau measurements, although the difference is less remarkable at the peak, indicating that impairment of SERCA pump may be involved in the mechanism of enhanced calcium handling in high glucose treated hiPSC-CMs.

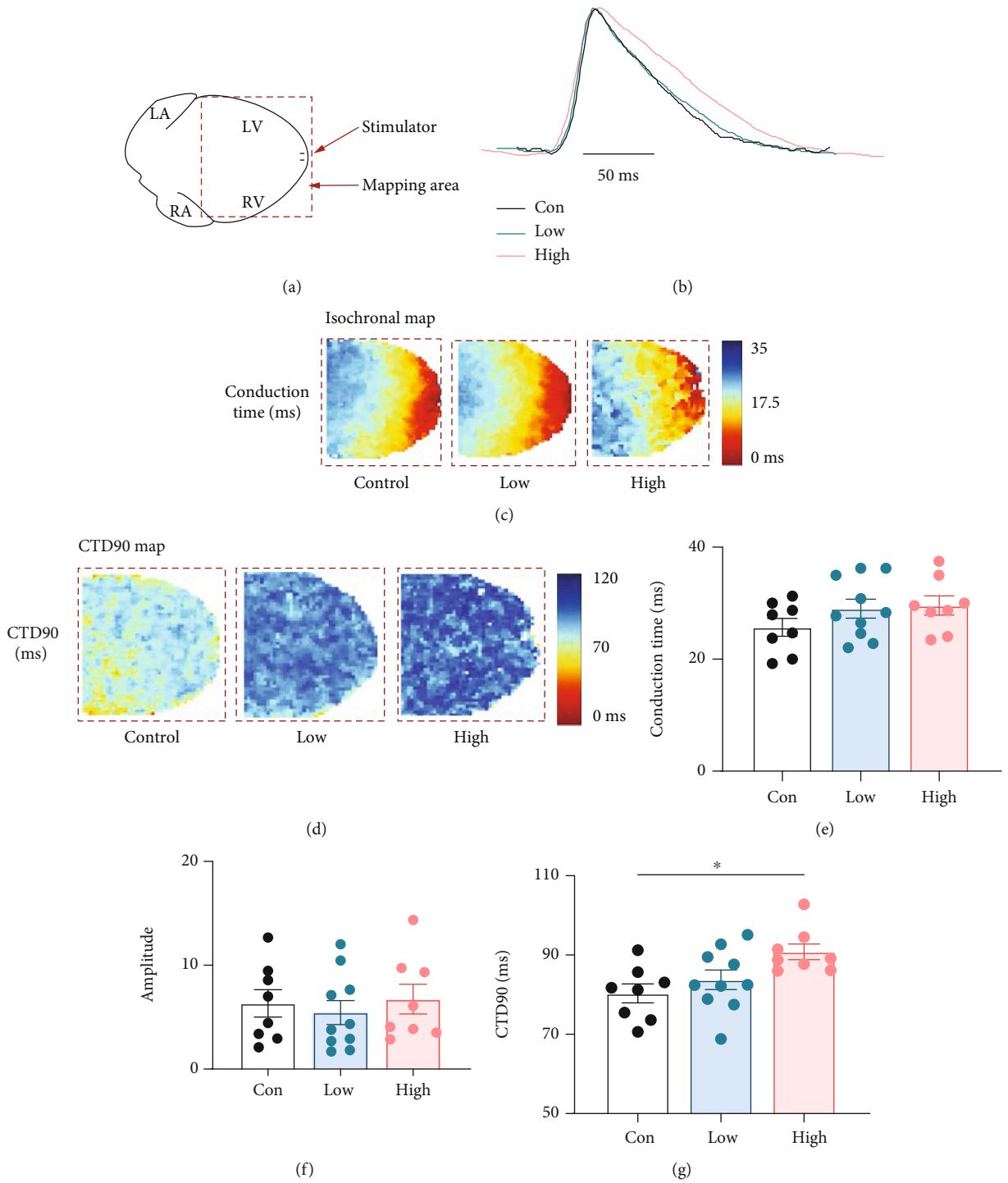

Figure 6: Calcium Rhod-2 optical mapping in isolated perfused hearts in different experimental groups. (a) Optical mapping configuration. (b) Comparison of typical calcium transients averaged over defined regions of interest. (c) Map of calcium transient conduction during 1 Hz stimulation. (d) Map of calcium transient duration at 90% recovery (CTD90) during 1 Hz stimulation. Bar charts display the average value of the calcium transient conduction time (e), amplitude (f), and CTD90 (g) changes of the control, low, and high STZ groups. Data are expressed as mean ± SE. $^*P < 0.05$. Control: control group; Low: low STZ treated group; High: high STZ treated group.

3.6.3. Mitochondrial [Ca^{2+}] and Mitochondrial Membrane Potential (MMP) Level in hiPSC-CMs. We applied the proton uncoupler FCCP (3 μmol/L) to depolarize the inner mitochondrial membrane, using Fura2-AM, to monitor the release of stored mitochondrial Ca^{2+} (Figures 8(c) and 8(d)) or directly measure mitochondrial Ca^{2+} content using the Rhod-2/AM (5 μmol/L) which can selectively accumulate within mitochondria (Figures 8(c) and 8(e)). The peak of the $[Ca^{2+}]_i$ transient increased in the hiPSC-CMs with 11 or 25 mmol/L glucose group when compared with

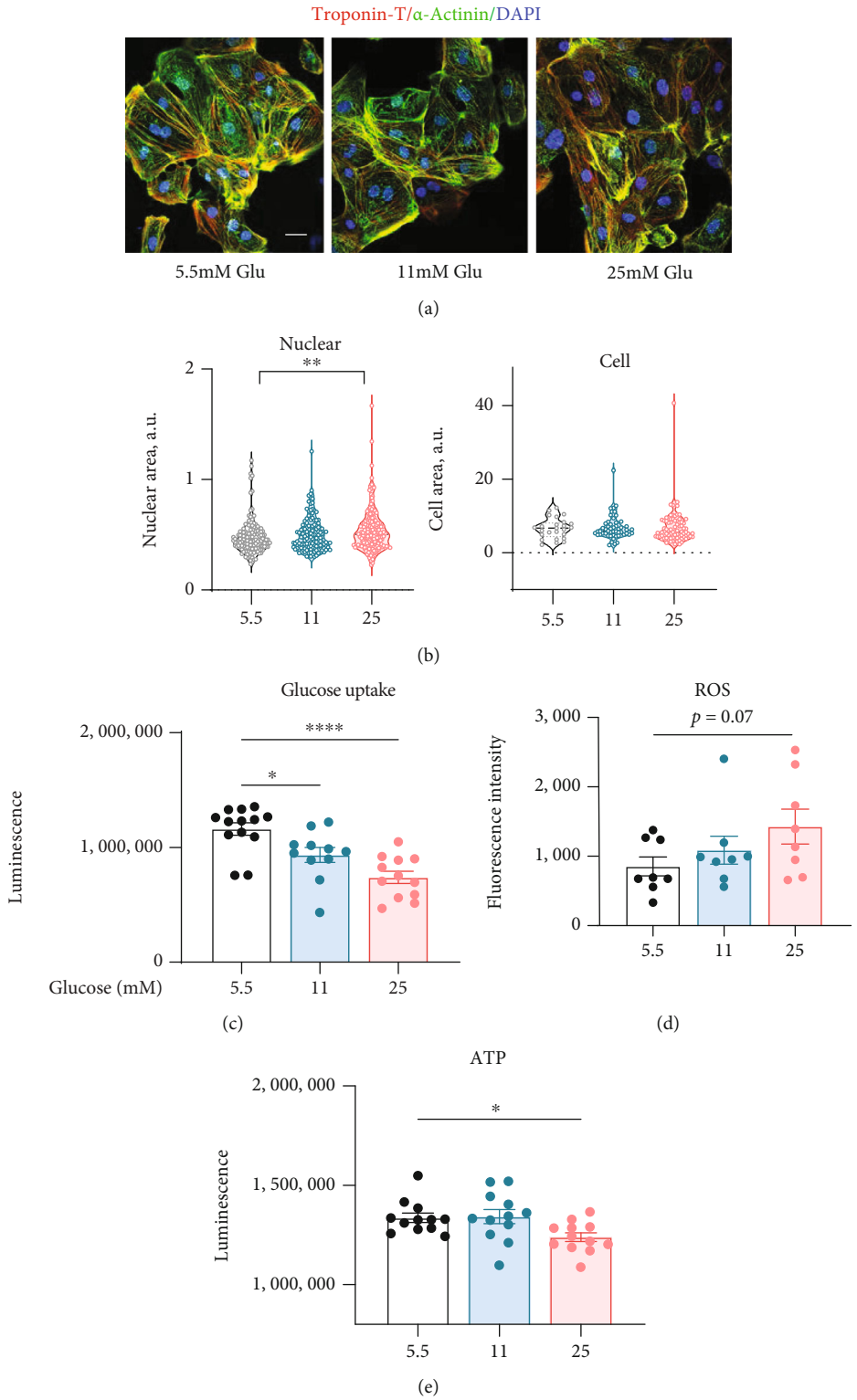

Figure 7: (a) iPSC-CMs stained positive for cardiac troponin T (cTnT, red), α-actinin (green), and DAPI (blue). Scale bar, 25 μm. (b) Statistical comparison of nuclear area and cell area among different glucose treatment groups. Comparison of glucose uptake (c), reactive oxygen species (ROS, (d)), and ATP production (e) among different glucose treatment groups. Data are expressed as mean ± SE. $^{*}P < 0.05$, $^{**}P < 0.01$, $^{****}P < 0.0001$.

5.5 mmol/L (control) group, but there was no significant difference between high glucose groups (Figure 8(d)). For $[Ca^{2+}]_m$ (Figure 8(e)), FCCP significantly reduced the mitochondrial Ca^{2+} signal in the 25 mmol/L glucose group when compared with the control, but there was minimal difference between 11 mmol/L and control groups. Interestingly, there

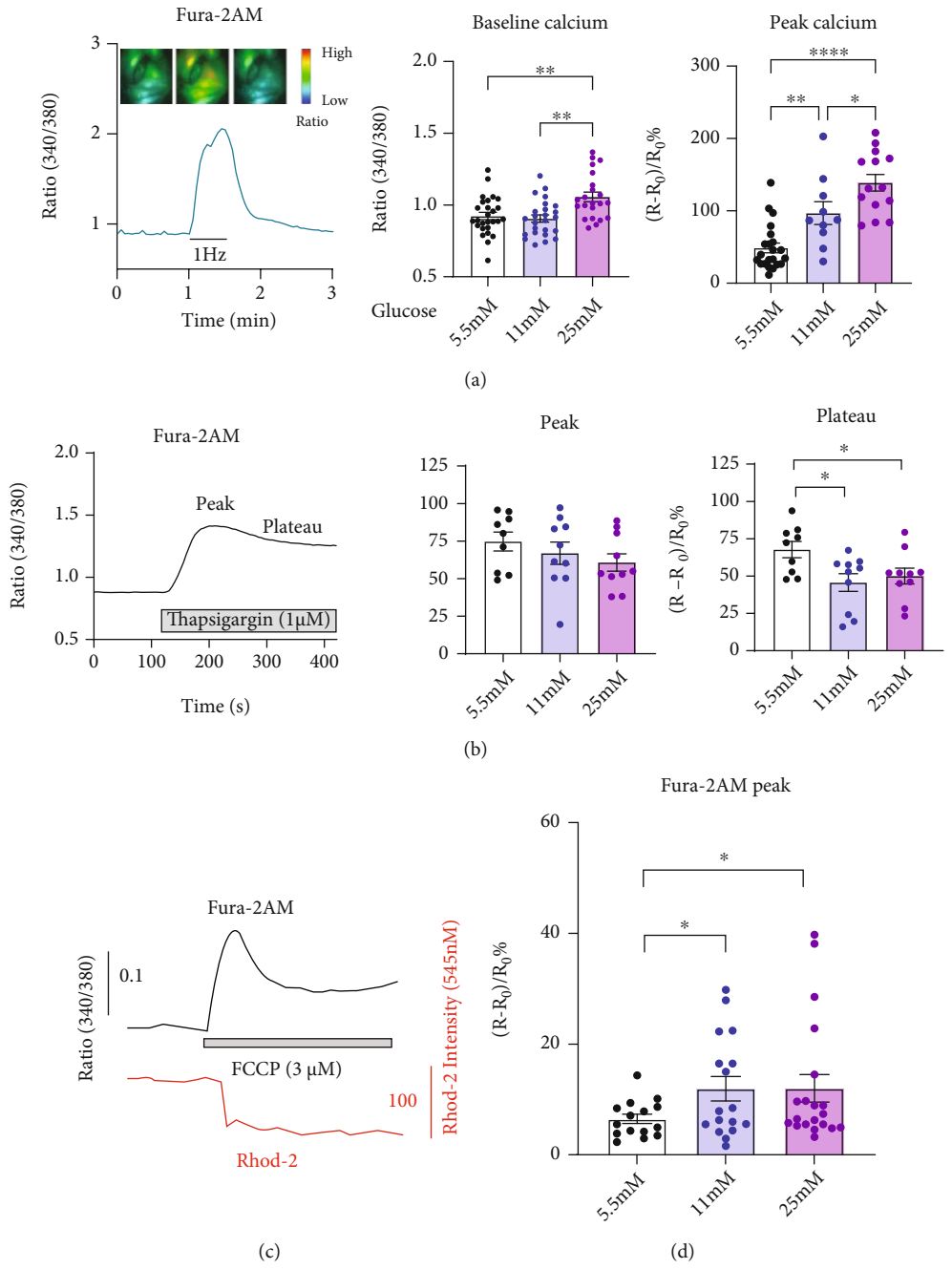

Figure 8: Continued.

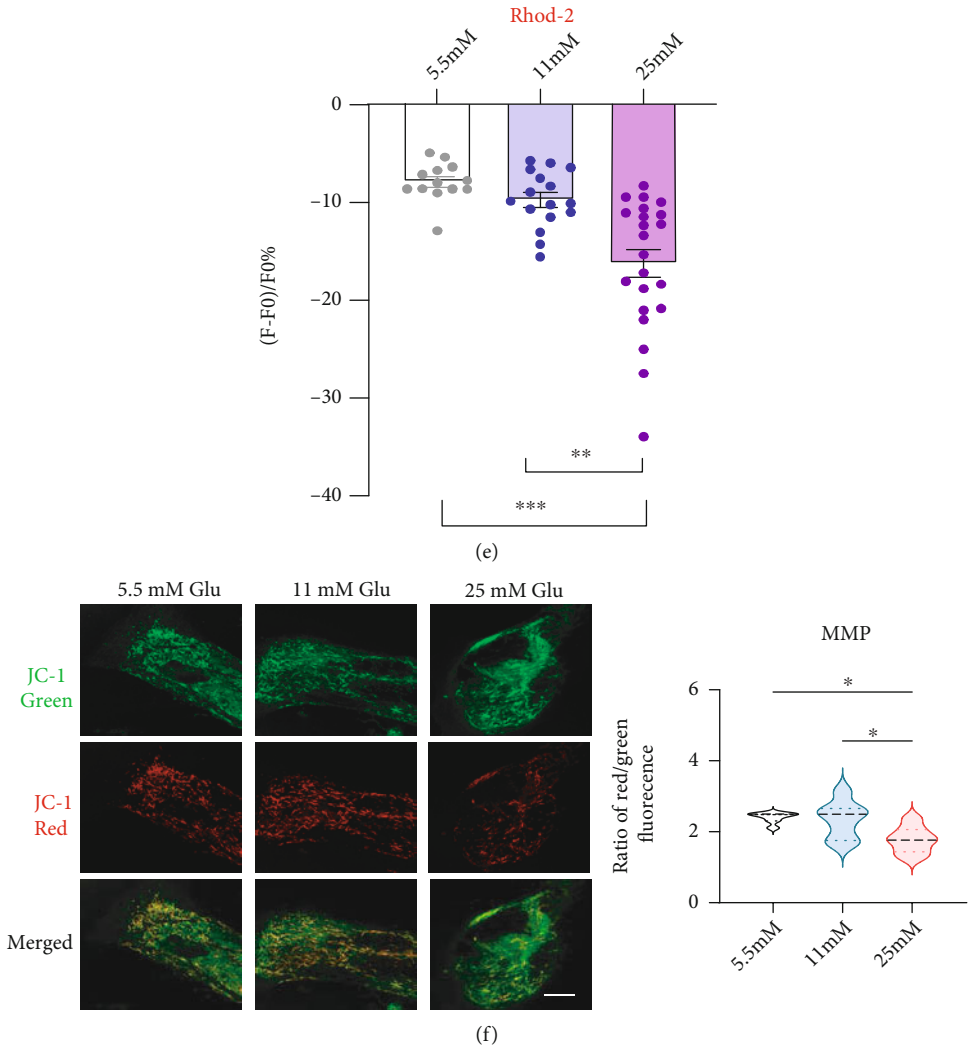

Figure 8: Functional phenotyping of high glucose-treated human iPSC-derived cardiomyocytes. (a) Fluorescence ratio profile showing the intracellular free calcium transients ($[Ca^{2+}]_i$) response to 1 Hz field stimulation using Fura-2AM in hiPSC-CMs (left). Measurement of baseline (middle) and peak (right) $[Ca^{2+}]_i$ in hiPSC-CMs with 5.5 mmol/L (control), 11 or 25 mmol/L glucose treatment. (b) $[Ca^{2+}]_i$ changes in hiPSC-CMs by inhibition of the sarcoplasmic reticulum Ca^{2+} pump with thapsigargin among the group. Peak and plateau were expressed as % of ratio changes. (c) Measurement of $[Ca^{2+}]_i$ with Fura-2AM (top, black line) and mitochondrial Ca^{2+} ($[Ca^{2+}]_m$) using Rhod-2/AM (bottom, red line) after mitochondrial Ca^{2+} store depletion with FCCP in hiPSC-CMs. (d) The peak evoked $[Ca^{2+}]_i$ after FCCP treatment among the groups. (e) The reduction of $[Ca^{2+}]_m$ changes after FCCP treatment among the groups of hiPSC-CMs. (f) Analysis of mitochondrial membrane potential (MMP) changes using the cationic JC-1 dye as a fluorescent probe in hiPSC-CMs. The changes were expressed as the ratio of red/green fluorescence intensity (results are analyzed from 6-8 images per group; scale bar, 10 μm). Data are expressed as mean ± SE. $^*P < 0.05$, $^{**}P < 0.01$. $^{***}P < 0.001$.

was a significant reduction in 25 mmol/L in comparison with the 11 mmol/L group. Altogether, these data indicate that mitochondria play an important role in the modulation of Ca^{2+} signalling resulting from a high glucose environment.

To exclude a hyperosmolar effect, we cultured iPSC-CMs in 5.5 mmol/L glucose plus 19.5 mmol/L mannitol (high mannitol group) to achieve the same osmolarity as 25 mmol/L glucose medium. We found no difference in baseline calcium transient ratios between control (5.5 mmol/L glucose, 0.959 ± 0.008, $n = 15$) and the high mannitol group (0.935 ± 0.016, $n = 9$, Figure S2A). After applied FCCP, there was no significant difference in the peak intracellular calcium transient between the two groups (6.496 ± 0.183% vs. 8.004 ± 0.231%, Figure S2B). These results suggest that hyperosmolarity of our culture conditions does not affect intracellular calcium transients in iPSC-CMs.

We used both fluorescence microscopy and quantitative fluorescence measurements to evaluate the MMP changes in 5.5, 11, or 25 mmol/L glucose-treated hiPSC-CMs (Figure 8(f)). We observed a significant reduction in mitochondrial membrane polarization as indicated by an increase in the MitoProbe JC-1 red:green fluorescence ratio in 25 mmol/L glucose-treated hiPSC-CMs, however, we did not observe any changes in the 11 mmol/L glucose group, suggesting that high glucose affects the MMP. We also performed transmission electron microscopy (TEM) to examine

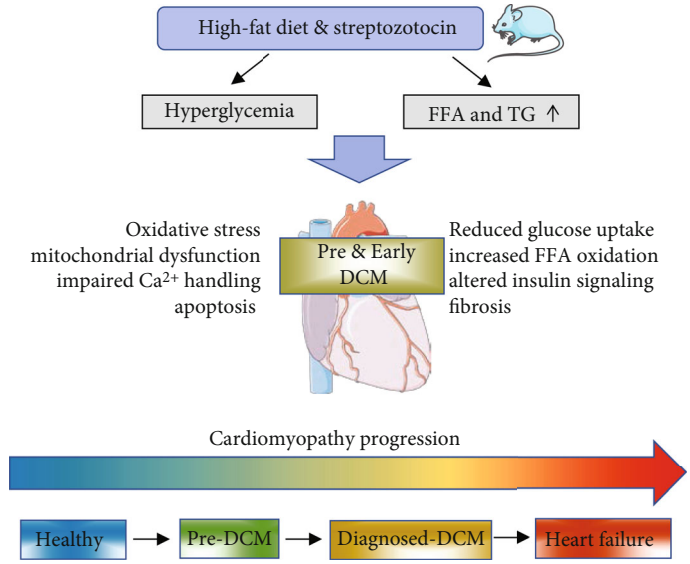

Figure 9: Summary diagram illustrating the potential mechanism of pre and early state of diabetic cardiomyopathy during cardiomyopathy progression in a diabetic rat model induced by high-fat diet combined with Streptozotocin injection.

whether there were differences in the ultrastructural features between 5.5 and 25 mmol/L glucose-treated hiPSC-CM. Myofibrils were well organized into sarcomeres with clearly aligned Z-lines in both groups, whereas mitochondria and endoplasmic reticulum (ER) had no morphological changes (Figure S3).

4. Discussion

In this study, we have successfully established different stages of DM in a rat model by feeding a high-fat diet combined with different doses of STZ to emulate pre- and early DCM status. We provide several lines of evidence demonstrating functional and structural alterations in the myocardium because of metabolic and cellular abnormalities in the different stages of DM. We showed that Ca^{2+} signalling homeostasis, ROS generation, and apoptotic cell death regulation are dysregulated in the early stage of DCM. We used RNA-Seq to explore a differential transcriptomic profile and captured the effect of changes in gene expression and important signalling pathways at different stages of DM. Moreover, we clarified further underlying molecule correlates by using high glucose-treated iPSC-CM that mimic a diabetogenic environment.

T2DM is characterized by a metabolic disorder that elevates blood glucose concentration. It is well known that chronic hyperglycemia has been associated with many aspects of health in T2DM patients, including severe cardiovascular outcomes. The typical clinical features of cardiac dysfunction associated with T2DM include reduced ventricular compliance and diastolic function, decreased exercise capacity, as well as increased incidence of cardiac arrhythmias [20]. T2DM patients are identified as a high-risk subgroup for developing HF. In addition, impaired glucose tolerance (IGT) has been shown to contribute to poor prognosis and is an independent factor in patients with HF [21]. Although diabetic cardiac dysfunction has been recognized for many years through a broad range of investigations, effective strategies for cardiac prevention and treatment remain elusive.

Accumulating evidence demonstrated that high blood glucose levels are strongly associated with a greater risk of cardiac abnormality among T2DM. Patients with poor glycemic control have an increased incidence of cardiovascular disease and experience worse clinical outcomes [19]. Reaven et al. reported that participants with T2DM who had intensive glucose control had a lower risk of cardiovascular events, while there was no evidence of a mortality benefit with intensive glucose control [22]. Furthermore, some studies confirmed that there were no substantially beneficial effects of intensive glycemic control on major cardiovascular outcomes and all-cause mortality in T2DM patients [23]. These findings suggest that the contribution of intensive glucose control in the reduction of major cardiovascular outcomes remains an open question.

The onset of cardiac injury occurs early and before the onset of measurable cardiac dysfunction. More importantly, effective approaches that can reverse cardiac injury are limited. The effects of different blood glucose levels on cardiac injury, and mechanisms underlying such effects are not fully elucidated. Early detection of the effects of T2DM on the heart would enable the optimal implementation of effective therapies that prevent HF development. Therefore, the purpose of the present study was to characterize the underlying cardiac molecular mechanisms and cardiac abnormalities in T2DM rats with different diabetes status, which may provide evidence for optimal timing and strategies of prevention and treatment.

In this study, we developed T2DM animal model by high-fat diet combined with STZ injection, as previously described [9]. The low dose group received a single intraperitoneal injection of STZ at 35 mg/kg, while the high-dose

group received a single intraperitoneal injection of STZ at 50 mg/kg. Various investigators have used protocols ranging from a single dose of STZ at 50 to 150 mg/kg [24, 25]. We adopted a relatively low-dose strategy, because this strategy minimizes the nonspecific toxic effects of high-dose STZ [14]. After 9 weeks, our results from the present study showed that rats from the high-dose group exhibited significant higher levels of fasting glucose, insulin, TC, TG, FFA, and HOMA-IR compared with the low dose group, while the insulin, TC, TG, FFA, and HOMA-IR levels did not differ between the low dose group and the control group. Furthermore, the rats from the low dose group received OGTT, which confirmed the success of T2DM establishment. It has been reported that hyperglycemia is associated with an altered myocardial substrate, which has been hypothesized to lead to cardiac injury [26].

Interstitial fibrosis is important mechanism underlying the pathogenesis of cardiac injury, which could aggravate myocardial stiffness. The degree of cardiac remodelling in the two T2DM rat models was assessed. In the high STZ treated group, the cardiac weight index and myocardial collagen deposition were significantly increased when compared with controls. In addition, by RNA-Seq, we also detected cardiac structure modulated genes such as *Myh6*, *Tnnt2*, *Tpm1*, *Myl3*, *Tnni3*, *Ttn*, and *Tnnc1* were reduced, *Tab1* (TGF-beta activated kinase 1 and MAP3K7-binding protein 1) which participates fibrotic response was enhanced in the high STZ dose group (Figure S1). However, these indicators did not find any statistical differences in the low STZ treated group. Combining the results of basic parameters, we confirmed that our high and low doses of STZ treated T2DM models belong to pre and early stage of DCM. We also found the *ANP* and *BNP* mRNA expression of the ventricular tissues enhanced in STZ-treated groups relative to control (Figures 2(b) and 2(c)). Several lines of evidence have indicated that BNP elevation represents the earliest change of cardiac injury, preceding the appearance of cardiac remodelling [27]. This is consistent with our findings and further confirmed cardiac hypertrophy in our T2DM model.

Oxidative stress is one of the major components triggering cardiac changes in DM. The increase in ROS production may subsequently induce apoptosis, inflammation, and other pathologic changes [28, 29]. The present study showed that ROS production was enhanced in both low and high-dose group and was much higher in the high-dose group (Figure 5(a)). The high-dose STZ group had a higher rate of myocardial apoptosis with caspase-3 activity (Figure 5(b)). Moreover, our RNA-Seq results confirmed that the fatty acid metabolism, oxidative phosphorylation, apoptosis, and TNF pathway-related genes were altered in the high-dose group. These results indicate that the accumulation of ROS occurs from the pre to the early onset of DCM. Our work agrees with the previous report that excess generation of ROS is considered a central mechanism for T2DM-related cardiac apoptosis and remodelling during both the early and late stages of diabetic cardiomyopathy [30]. We also detected two glucose transporters, *Slc2a4* (Glut4) and *Slc2A1* (Glut1) genes decreased in the high-dose STZ group (Figure S1). This induced impairment of glucose metabolism, while increased fatty acid metabolism led to mitochondrial dysfunction, which together increase ROS production [31]. We validated some key genes by real-time PCR and found *Decr1* (an enzyme which participates in fatty acid β-oxidation), *Calm2* (associated with cardiac arrhythmias), and *Ddit3* (a proapoptotic transcription factor) expressed a statistically significant increase when compare with the control group. These genes might be therapeutic targets for the treatment of diabetic cardiomyopathy in the future.

The prevalence and severity of T2DM-induced cardiac injury warrant a deeper investigation of the mechanisms and implicating factors. In recent years, the emergence of iPSC has allowed for the generation of iPSC-CMs, human-derived cells that can be applied to the in vitro study [32]. In the present study, iPSC-CMs were cultured in physiological (5.5 mmol/L glucose) or high glucose environment (11 and 25 mmol/L glucose) conditions. We demonstrated cellular and nuclear hypertrophy in the 25 mmol/L glucose-treated iPSC-CM, and the glucose uptake, ROS, and ATP production were also significantly altered. These findings were consistent with our DM rat model results. In addition, mitochondrial membrane potential was significantly decreased in the 25 mmol/L group, which indicated impaired electron transport and oxidative phosphorylation. Evoked $[Ca^{2+}]_i$ responses are influenced by multiple factors, including Ca^{2+} entry, extrusion across the plasma membrane, Ca^{2+} uptake and release from internal stores, and endogenous and exogenous Ca^{2+} buffering [33, 34]. The present study suggests a central role for mitochondria in impaired calcium transients, alongside reduced SERCA pump activity resulting in slowing of SR Ca^{2+} reuptake, which could contribute to high cytosolic calcium, as well as prolonged intracellular calcium transient duration (CTD90) measured by optical mapping in the high STZ treated DM rats. Calcium transportation is a fundamental biological process that has critical effects on cellular metabolism, signalling, and survival [35].

In conclusion, cardiac remodelling, fibrosis, increased stiffness, and cardiomyocyte loss are all consequences of dysregulated glucose and lipid metabolism that triggers oxidative stress as well as mitochondrial dysfunction during the development of DCM (Figure 9). In this study, we have profiled the different stages of T2DM in a rat model by feeding high-fat diet combined with difference doses of STZ to emulate pre and early DCM status. Moreover, high glucose-treated iPSC-CM mimics a diabetogenic environment. This experimental framework may be utilised to investigate pathways underlying the progression of DCM.

Data Availability

The data used to support the findings of this study are available from the corresponding authors upon reasonable request.

Conflicts of Interest

The authors declare that they have no conflict of interest to disclose.

Authors' Contributions

Dongjuan Wang and Kun Liu contributed equally to this work.

Acknowledgments

We are very grateful to Professor David Paterson for his careful reading and thoughtful comments on the manuscript. We also thank Lisa Heather for the suggestion of establishing animal models, Ujang Purnama for technical assistance, and Errin Johnson (Dunn School EM Facility, Oxford) for performing the EM work. This research was supported by HwaMei Hospital, University of the Chinese Academy of Sciences University of Oxford International Research Collaboration Fund (AVR02500); National Nature Science Foundation of China (no. 81900340); Zhejiang Provincial Natural Science Foundation, China (LQ19H020001); Ningbo Natural Science Foundation, China (2019A610342); and Ningbo Health Branding Subject Fund (PPXK2018-01).

Supplementary Materials

Supplementary table 1: list of primer sequences used for RT-PCR analysis. Supplementary table 2: hub genes from PPI network for the candidate pathways. Figure S1: bar graph to compare the TPM (transcript per million) values of key genes from RNA-Seq analysis according to the KEGG pathway classification. List of DEGs selected from the comparison of control vs. high STZ treated group, which related to fatty acid metabolism (a), oxidative phosphorylation (b), calcium signalling (c), cardiac structure and function related (d), insulin resistance (e), and apoptosis and TNF pathway (f). Figure S2: intracellular free calcium concentration on the baseline (a) and after treatment with 3 μmol/L FCCP (b) in hiPSC-CMs exposed to 5.5 mmol/L glucose or high mannitol (5.5 mmol/L glucose with 19.5 mmol/L mannitol) media. Figure S3: transmission electron microscopy (TEM) of human induced pluripotent stem cell-derived cardiomyocytes (iPSC-CMs) treated in 5.5 (a) and 25 mmol/L glucose (b) culture media. ER: endoplasmic reticulum. Scale bar: 2 μm. *(Supplementary Materials)*

References

[1] S. Demir, P. P. Nawroth, S. Herzig, and B. Ekim Üstünel, "Emerging targets in type 2 diabetes and diabetic complications," *Adv Sci (Weinh)*, vol. 8, no. 18, article e2100275, 2021.

[2] A. D. Shah, C. Langenberg, E. Rapsomaniki et al., "Type 2 diabetes and incidence of cardiovascular diseases: a cohort study in 1∗9 million people," *The Lancet Diabetes and Endocrinology*, vol. 3, no. 2, pp. 105–113, 2015.

[3] M. Dauriz, A. Mantovani, S. Bonapace et al., "Prognostic impact of diabetes on long-term survival outcomes in patients with heart failure: a meta-analysis," *Diabetes Care*, vol. 40, no. 11, pp. 1597–1605, 2017.

[4] Y. Tan, Z. Zhang, C. Zheng, K. A. Wintergerst, B. B. Keller, and L. Cai, "Mechanisms of diabetic cardiomyopathy and potential therapeutic strategies: preclinical and clinical evidence," *Nature Reviews. Cardiology*, vol. 17, no. 9, pp. 585–607, 2020.

[5] M. Federico, S. De la Fuente, J. Palomeque, and S. S. Sheu, "The role of mitochondria in metabolic disease: a special emphasis on heart dysfunction," *The Journal of Physiology*, vol. 599, no. 14, pp. 3477–3493, 2021.

[6] A. Faria and S. J. Persaud, "Cardiac oxidative stress in diabetes: Mechanisms and therapeutic potential," *Pharmacology & Therapeutics*, vol. 172, pp. 50–62, 2017.

[7] K. Schwarz, N. Siddiqi, S. Singh, C. J. Neil, D. K. Dawson, and M. P. Frenneaux, "The breathing heart – Mitochondrial respiratory chain dysfunction in cardiac disease," *International Journal of Cardiology*, vol. 171, no. 2, pp. 134–143, 2014.

[8] L. S. Mansor, E. R. Gonzalez, M. A. Cole et al., "Cardiac metabolism in a new rat model of type 2 diabetes using high-fat diet with low dose streptozotocin," *Cardiovascular Diabetology*, vol. 12, no. 1, p. ???, 2013.

[9] M. J. Reed, K. Meszaros, L. J. Entes et al., "A new rat model of type 2 diabetes: The fat-fed, streptozotocin-treated rat," *Metabolism*, vol. 49, no. 11, pp. 1390–1394, 2000.

[10] I. Osegbe, H. Okpara, and E. Azinge, "Relationship between serum leptin and insulin resistance among obese Nigerian women," *Annals of African Medicine*, vol. 15, no. 1, pp. 14–19, 2016.

[11] V. Addepalli and S. V. Suryavanshi, "Catechin attenuates diabetic autonomic neuropathy in streptozotocin induced diabetic rats," *Biomedicine & Pharmacotherapy*, vol. 108, pp. 1517–1523, 2018.

[12] H. Davis, E. N. Bardsley, and D. J. Paterson, "Transcriptional profiling of stellate ganglia from normotensive and spontaneously hypertensive rat strains," *Sci Data*, vol. 5, no. 1, article 180123, 2018.

[13] E. N. Bardsley, O. C. Neely, and D. J. Paterson, "Angiotensin peptide synthesis and cyclic nucleotide modulation in sympathetic stellate ganglia," *Journal of Molecular and Cellular Cardiology*, vol. 138, pp. 234–243, 2020.

[14] D. Wang, L. Jiang, B. Feng, N. He, Y. Zhang, and H. Ye, "Protective effects of glucagon-like peptide-1 on cardiac remodeling by inhibiting oxidative stress through mammalian target of rapamycin complex 1/p70 ribosomal protein S6 kinase pathway in diabetes mellitus," *J Diabetes Investig*, vol. 11, no. 1, pp. 39–51, 2020.

[15] D. Zhang, Y. Cui, B. Li, X. Luo, B. Li, and Y. Tang, "miR-155 regulates high glucose-induced cardiac fibrosis via the TGF-β signaling pathway," *Molecular BioSystems*, vol. 13, no. 1, pp. 215–224, 2017.

[16] L. Zuo, D. J. Youtz, and L. E. Wold, "Particulate matter exposure exacerbates high glucose-induced cardiomyocyte dysfunction through ROS generation," *PLoS One*, vol. 6, no. 8, article e23116, 2011.

[17] M. D. L. Sousa Fialho, U. Purnama, K. Dennis et al., "Activation of HIF1α rescues the hypoxic response and reverses metabolic dysfunction in the diabetic heart," *Diabetes*, vol. 70, no. 11, pp. 2518–2531, 2021.

[18] D. Li, C. J. Lu, G. Hao et al., "Efficacy of B-type natriuretic peptide is coupled to phosphodiesterase 2A in cardiac sympathetic neurons," *Hypertension*, vol. 66, no. 1, pp. 190–198, 2015.

[19] M. Leung, V. W. Wong, M. Hudson, and D. Y. Leung, "Impact of improved glycemic control on cardiac function in type 2 diabetes mellitus," *Circulation. Cardiovascular Imaging*, vol. 9, no. 3, article e003643, 2016.

[20] T. H. Marwick, R. Ritchie, J. E. Shaw, and D. Kaye, "Implications of Underlying Mechanisms for the Recognition and Management of Diabetic Cardiomyopathy," *Journal of the American College of Cardiology*, vol. 71, no. 3, pp. 339–351, 2018.

[21] Y. Matsue, M. Suzuki, R. Nakamura et al., "Prevalence and prognostic implications of pre-diabetic state in patients with heart failure," *Circulation Journal*, vol. 75, no. 12, pp. 2833–2839, 2011.

[22] P. D. Reaven, N. V. Emanuele, W. L. Wiitala et al., "Intensive glucose control in patients with type 2 diabetes — 15-Year follow-up," *The New England Journal of Medicine*, vol. 380, no. 23, pp. 2215–2224, 2019.

[23] J. Tian, T. Ohkuma, M. Cooper et al., "Effects of intensive glycemic control on clinical outcomes among patients with type 2 diabetes with different levels of cardiovascular risk and hemoglobin A1c in the ADVANCE trial," *Diabetes Care*, vol. 43, no. 6, pp. 1293–1299, 2020.

[24] Y. Tang, X. Lei, W. Jian, J. Yan, Z. Wu, and T. Zhao, "Optimization of streptozotocin dosing for establishing tumor-bearing diabetic mouse models," *Nan Fang Yi Ke Da Xue Xue Bao*, vol. 34, no. 6, pp. 827–831, 2014.

[25] J. Y. Lee, H. Y. Choi, C. S. Park et al., "GS-KG9 ameliorates diabetic neuropathic pain induced by streptozotocin in rats," *Journal of Ginseng Research*, vol. 43, no. 1, pp. 58–67, 2019.

[26] J. Buchanan, P. K. Mazumder, P. Hu et al., "Reduced cardiac efficiency and altered substrate metabolism precedes the onset of hyperglycemia and contractile dysfunction in two mouse models of insulin resistance and obesity," *Endocrinology*, vol. 146, no. 12, pp. 5341–5349, 2005.

[27] T. Walther, S. Heringer-Walther, R. Tschope, A. Reinecke, H. P. Schultheiss, and C. Tschope, "Opposite regulation of brain and C-type natriuretic peptides in the streptozotocin-diabetic cardiopathy," *Journal of Molecular Endocrinology*, vol. 24, no. 3, pp. 391–395, 2000.

[28] M. Khullar, A. A. R. S. Al-Shudiefat, A. Ludke, G. Binepal, and P. K. Singal, "Oxidative stress: a key contributor to diabetic cardiomyopathyThis review is one of a selection of papers published in a Special Issue on Oxidative Stress in Health and Disease," *Canadian Journal of Physiology and Pharmacology*, vol. 88, no. 3, pp. 233–240, 2010.

[29] K. Huynh, B. C. Bernardo, J. R. McMullen, and R. H. Ritchie, "Diabetic cardiomyopathy: Mechanisms and new treatment strategies targeting antioxidant signaling pathways," *Pharmacology & Therapeutics*, vol. 142, no. 3, pp. 375–415, 2014.

[30] A. J. Wilson, E. K. Gill, R. A. Abudalo, K. S. Edgar, C. J. Watson, and D. J. Grieve, "Reactive oxygen species signalling in the diabetic heart: emerging prospect for therapeutic targeting," *Heart*, vol. 104, no. 4, pp. 293–299, 2018.

[31] J. N. Peoples, A. Saraf, N. Ghazal, T. T. Pham, and J. Q. Kwong, "Mitochondrial dysfunction and oxidative stress in heart disease," *Experimental & Molecular Medicine*, vol. 51, no. 12, pp. 1–13, 2019.

[32] D. A. M. Feyen, W. L. McKeithan, A. A. N. Bruyneel et al., "Metabolic Maturation Media Improve Physiological Function of Human iPSC- Derived Cardiomyocytes," *Cell Reports*, vol. 32, no. 3, article 107925, 2020.

[33] D. Li, C. W. Lee, K. Buckler, A. Parekh, N. Herring, and D. J. Paterson, "Abnormal intracellular calcium homeostasis in sympathetic neurons from young prehypertensive rats," *Hypertension*, vol. 59, no. 3, pp. 642–649, 2012.

[34] J. Shanks, N. Herring, E. Johnson, K. Liu, D. Li, and D. J. Paterson, "Overexpression of sarcoendoplasmic reticulum calcium ATPase 2a promotes cardiac sympathetic neurotransmission via abnormal endoplasmic reticulum and mitochondria Ca2+Regulation," *Hypertension*, vol. 69, no. 4, pp. 625–632, 2017.

[35] J. F. Garbincius and J. W. Elrod, "Mitochondrial calcium exchange in physiology and disease," *Physiological Reviews*, vol. 102, no. 2, pp. 893–992, 2022.

Hindawi
Oxidative Medicine and Cellular Longevity
Volume 2022, Article ID 5696686, 16 pages
https://doi.org/10.1155/2022/5696686

Research Article

Cigarette Smoke Exposure Increases Glucose-6-phosphate Dehydrogenase, Autophagy, Fibrosis, and Senescence in Kidney Cells *In Vitro* and *In Vivo*

Wen-Chih Liu,[1,2] Hsiao-Chi Chuang,[3,4] Chu-Lin Chou,[5,6,7,8] Yu-Hsuan Lee,[9] Yu-Jhe Chiu,[10] Yung-Li Wang,[10] and Hui-Wen Chiu[7,10,11]

[1]*Division of Nephrology, Department of Internal Medicine, Taipei Hospital, Ministry of Health and Welfare, New Taipei City, Taiwan*
[2]*Department of Biology and Anatomy, National Defense Medical Center, Taipei, Taiwan*
[3]*School of Respiratory Therapy, College of Medicine, Taipei Medical University, Taipei, Taiwan*
[4]*Division of Pulmonary Medicine, Department of Internal Medicine, Shuang Ho Hospital, Taipei Medical University, New Taipei City, Taiwan*
[5]*Division of Nephrology, Department of Internal Medicine, Shuang Ho Hospital, Taipei Medical University, New Taipei City, Taiwan*
[6]*Division of Nephrology, Department of Internal Medicine, School of Medicine, College of Medicine, Taipei Medical University, Taipei, Taiwan*
[7]*TMU Research Center of Urology and Kidney, Taipei Medical University, Taipei, Taiwan*
[8]*Division of Nephrology, Department of Internal Medicine, Hsin Kuo Min Hospital, Taipei Medical University, Taoyuan City, Taiwan*
[9]*Department of Cosmeceutics, China Medical University, Taichung, Taiwan*
[10]*Graduate Institute of Clinical Medicine, College of Medicine, Taipei Medical University, Taipei, Taiwan*
[11]*Department of Medical Research, Shuang Ho Hospital, Taipei Medical University, New Taipei City, Taiwan*

Correspondence should be addressed to Hui-Wen Chiu; leu3@tmu.edu.tw

Received 4 January 2022; Revised 25 February 2022; Accepted 2 March 2022; Published 27 March 2022

Academic Editor: Xun Cui

Cigarette smoke (CS) is a risk factor for chronic obstructive pulmonary disease. We attempted to investigate fully the possible effects of CS on kidney cells. We found that the viability of a human kidney proximal tubular epithelial cell line (HK-2 cells) was decreased after treatment with CS extract (CSE). In particular, the effects of CSE at low concentrations did not change the expression of apoptosis and necrosis. Furthermore, CSE increased autophagy- and fibrosis-related proteins in HK-2 cells. Senescence-related proteins and the senescence-associated secretory phenotype (SASP) increased after HK-2 cells were treated with CSE. In addition, both RNA sequencing and gene set enrichment analysis data revealed that glucose-6-phosphate dehydrogenase (G6PD) in the reactive oxygen species (ROS) pathway is responsible for the changes in CSE-treated HK-2 cells. CSE increased G6PD expression and its activity. Moreover, the inhibition of G6PD activity increased senescence in HK-2 cells. The inhibition of autophagy reinforced senescence in the CSE-treated cells. In a mouse model of CS exposure, CS caused kidney damage, including tubular injury and glomerulosclerosis. CS increased fibrosis, autophagy, and G6PD expression in kidney tissue sections. In conclusion, CS induced G6PD expression, autophagy, fibrosis, and senescence in kidney cells. G6PD has a protective role in CS-induced nephrotoxicity.

1. Introduction

One of the main causes of death, chronic obstructive pulmonary disease (COPD), occurs in the United States [1] and worldwide [2]. Clinically, cigarette smoking (CS) is a risk factor leading to the progress of COPD [3]. Fibroblasts in the lung play a vital role in repair, regeneration, and lung homeostasis [4]. Recent studies have indicated that lung fibroblasts of patients with COPD display a decreased growth rate [5]. CS reduces the proliferation of lung fibroblasts and upregulates pathways related to cellular senescence [5] and the p53 [6], p16, and p21 retinoblastoma protein pathways [7]. Moreover, CS also induces senescence-associated secretory phenotype- (SASP-) related inflammation in human epidermal keratinocytes and skin [8]. Apoptosis resulting from smoke extract-induced COPD has been observed in *in vitro* and *in vivo* studies [9]. Furthermore, CS, nicotine, and cotinine affect red blood cell hemolysis [10]. Glucose-6-phosphate dehydrogenase (G6PD) deficiency causes substantial oxidant damage to the erythrocyte membrane [11]. A previous study reported that CS [12] and nicotine [13] increase oxidant stress to red blood cells in healthy donor volunteers. In addition, CS also induces oxidative stress as a result of reactive oxygen species (ROS) in the brain [14]. In other cases, ROS have been shown to activate transforming growth factor β (TGF-β) in the modulation of profibrotic effects [15]. ROS accumulation or antioxidant depletion occurs could destroy to cellular elements, containing DNA, RNA, proteins, lipids, and carbohydrates [16]. Early reports have shown that heat shock protein 27 (Hsp27) is a neuroprotective biomarker in ischemic stroke [17]. On the other hand, intraperitoneal injection of recombinant soluble Klotho protein improves the premature aging-related phenotype in mice with the homozygous mutated allele [18]. Klotho reduces kidney senescence and fibrosis [19] by targeting mitochondrial dysfunction in renal tubular cells [20]. CS extract (CSE) reduces the expression and secretion of Klotho in alveolar macrophages and airway epithelial cells in COPD patients [21].

CSE not only induces oxidative stress but also fibrosis-related gene expresses in orbital fibroblasts in Graves' ophthalmopathy patients [22]. Autophagy is an important and conserved "self-cleansing" pathway [23], and other studies have shown that fibrosis is often companied by autophagy [24, 25]. In the kidney, autophagy can protect the proximal tubule from damage [26] to overcome many types of kidney injury [27], aging [28], and disease [29]. Autophagy is an essential cellular process that promotes cell survival by removing protein aggregates during kidney injury [30]. However, autophagy also promotes cell death or enhances apoptosis [31]. Therefore, autophagy has two contrasting outcomes in response to stress [32]. Studies have shown that CS causes autophagy [33] and accelerates lung aging via autophagy [34]. CSE-induced autophagy regulates many cellular processes such as FOXO transcription factors in human lung adenocarcinoma cells (A549) [35] and Galectin-3 in endothelial progenitor cells [36]. In addition, SIRT1 is downregulated by autophagy in senescence and aging [37]. On the other hand, Hsp27 phosphorylation plays a crucial role in the activation of G6PD to reduce cerebral ischemia/reperfusion injury in male Wistar rats [38]. G6PD is a major source of NADPH, which drives many essential cellular processes including antioxidant pathways [39] such as the suppression of oxidative stress in cerebral ischemic male Sprague-Dawley rats [40].

Many diverse diseases may lead to chronic kidney disease (CKD) via irreversibly impaired formation or dysfunctions of the kidney, such as fibrosis [41]. Recently, a meta-analysis suggested that CS is an independent risk factor in the general adult population with CKD [42]. The database of the Korean genome and epidemiology study also revealed that the healthy middle-aged adults who smoke have a high risk of CKD [43]. COPD patients have shown renal function worsening [44]. Additionally, tobacco CS promotes kidney injuries related to biochemical changes in male adult Wistar rats [45]. In this study, we examined the effect of CS on kidney cells *in vitro* and *in vivo*. Furthermore, gene set enrichment analysis (GSEA) was performed after HK-2 cells were treated with CSE. We also observed autophagy, fibrosis, senescence, and ROS generation after CS treatment.

2. Material and Methods

2.1. Cell Line. HK-2 cells, the proximal tubular epithelial cell line from human kidney, were obtained from the American Type Culture Collection (ATCC, Manassas, VA). The cells were kept in keratinocyte-serum-free medium (K-SFM) with bovine pituitary extract (BPE) and human recombinant EGF (Invitrogen, CA), and the cells were incubated at 37°C and 5% CO_2. The culture medium was refreshed two or three times per week. The $ATG5^{KD}$ HK-2 cells were incubated and maintained in the K-SFM medium with rEGF and BPE at 37°C with 5% CO_2 and cultured every two or three days. Lentivirus with control shRNA and ATG5 siRNA were purchased from the National RNAi Core Facility at Academia Sinica in Taiwan [46].

2.2. Preparation of Cigarette Smoke Extract. CSE solutions were prepared using a modification of standardized methods [47]. Three cigarette types (Longlife, Taipei, Taiwan; 11 mg of tar and 0.9 mg of nicotine) were subsequently collected by a liquid impinger device and then mixed with 15 ml of K-SFM. One of the cigarettes was dissolved in 5 ml of K-SFM, which was designated as 100% CSE solution.

2.3. Cell Viability Assay. Cell proliferation was accessed with sulforhodamine B (SRB, Sigma-Aldrich, St. Louis, MO). HK-2 cells (5×10^3/well) were plated in 96-well plates and cultured with or without CSE solutions in a 37°C and 5% CO_2 incubator overnight. After 24 h of incubation at 37°C and 5% CO_2, the plates were moved out, washed with PBS twice, and then fixed with iced 10% trichloroacetic acid (TCA, Sigma) at 4°C for 1 h. Each well was washed 2 times with distillation-distillation H_2O, and then, 0.1% SRB/1% acetic acid was incubated for 1 h. The wells were rinsed 2 times with 1% acetic acid and dried in an oven at 60°C for 20 min. In the end, the dye form SRB-positive cells were redissolved in 20 mM Tris buffer (Sigma) for 30 min. The

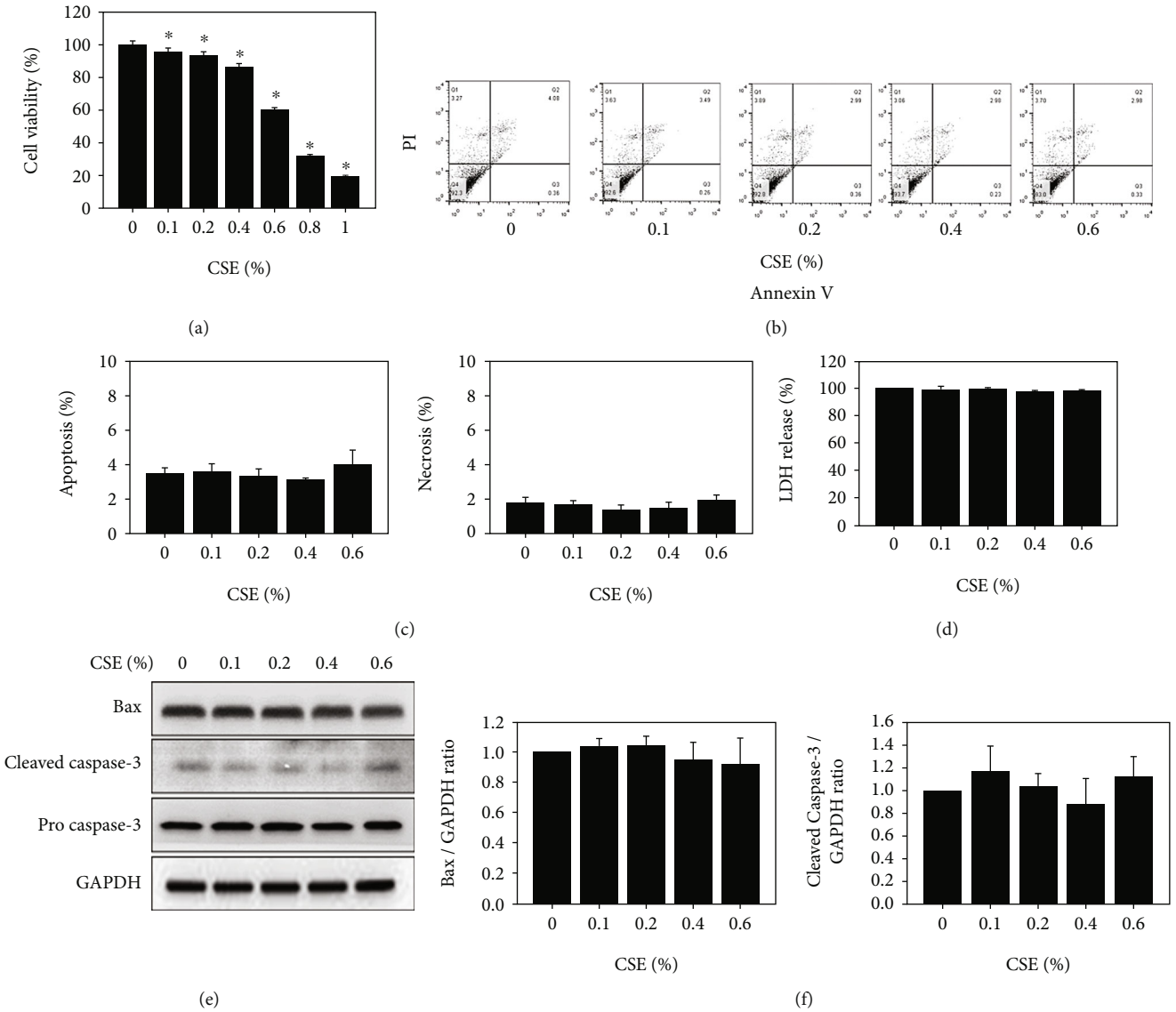

Figure 1: Cell viability, cell death, and apoptosis-related protein expression after treatment with CSE in HK-2 cells. (a) Cell proliferation was measured after cells were treated with CSE at concentrations of 0.1, 0.2, 0.4, 0.6, 0.8, and 1% for 24 h. $^{*}p < 0.05$ compared to the control group. (b) The apoptosis assay of HK-2 cells was performed by flow cytometry after treatment with CSE at concentrations of 0.1, 0.2, 0.4, and 0.6% for 24 h. (c) The apoptosis and necrosis indices of HK-2 cells were measured and diagramed after treatment with CSE at concentrations of 0.1, 0.2, 0.4, and 0.6% for 24 h. (d) The LDH assay was performed after treatment with CSE at concentrations of 0.1, 0.2, 0.4, 0.6, 0.8, and 1% for 24 h in HK-2 cells. (e) The expression levels of the apoptosis-related proteins Bax and caspase 3 after treatment with CSE at concentrations of 0.1, 0.2, 0.4, and 0.6% for 24 h in HK-2 cells. (f) Bax and cleaved caspase 3 were measured and diagramed for CSE-treated cells at concentrations of 0.1, 0.2, 0.4, and 0.6% for 24 h.

absorbance was detected at a wavelength of 562 nm in an ELISA reader.

2.4. Flow Cytometry Analysis of Apoptosis and Necrosis. HK-2 cells were treated with CSE solutions at different doses for different times. The cells were washed with PBS and collected with Accutase (Innovative Cell Technologies, San Diego, CA). Apoptosis and necrosis were measured with a FITC Annexin V/PI apoptosis detection kit according to the manufacturer's protocol (BioLegend, San Diego, CA). The signal was detected with a flow cytometer (BD, Biosciences).

2.5. Lactate Dehydrogenase Assay. HK-2 cells were collected and washed in an assay medium. Cells were plated in a 96-well plate and incubated for 24 h after CSE treatment. The plate was centrifuged at 250 g for 10 min and transferred 100 μl/well supernatant into corresponding wells. Cells were added to a 100 μl reaction mixture and incubated for up to 30 min at room temperature. The plate was detected the absorbance at 495 nm in an ELISA reader.

2.6. Western Blot Analysis. All collected proteins were added to sodium dodecyl sulfate (SDS) sample buffer (62.5 mM Tris (pH 6.7), 1.25% SDS, 12.5% glycerol, and 2.5% β-

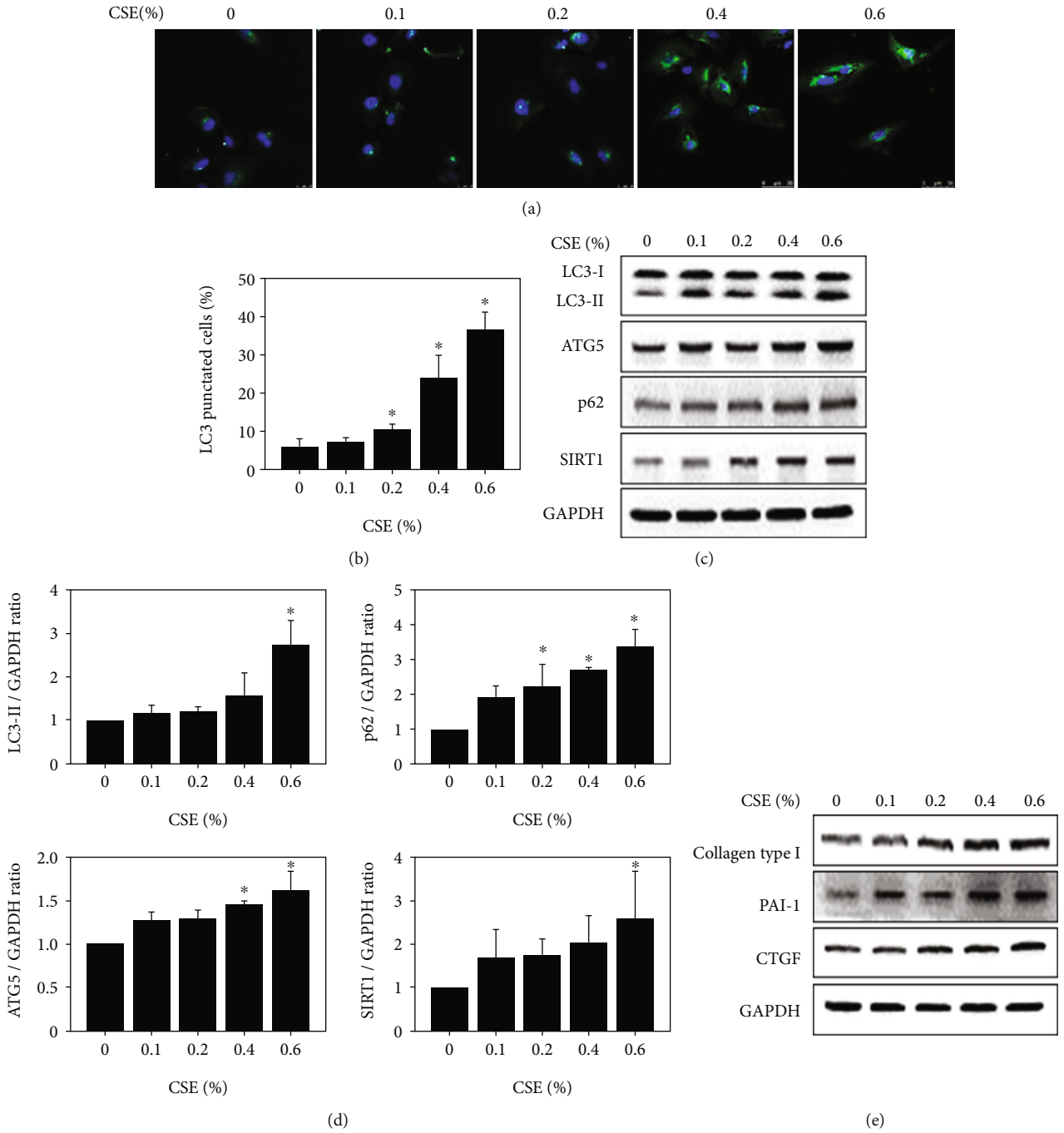

Figure 2: Continued.

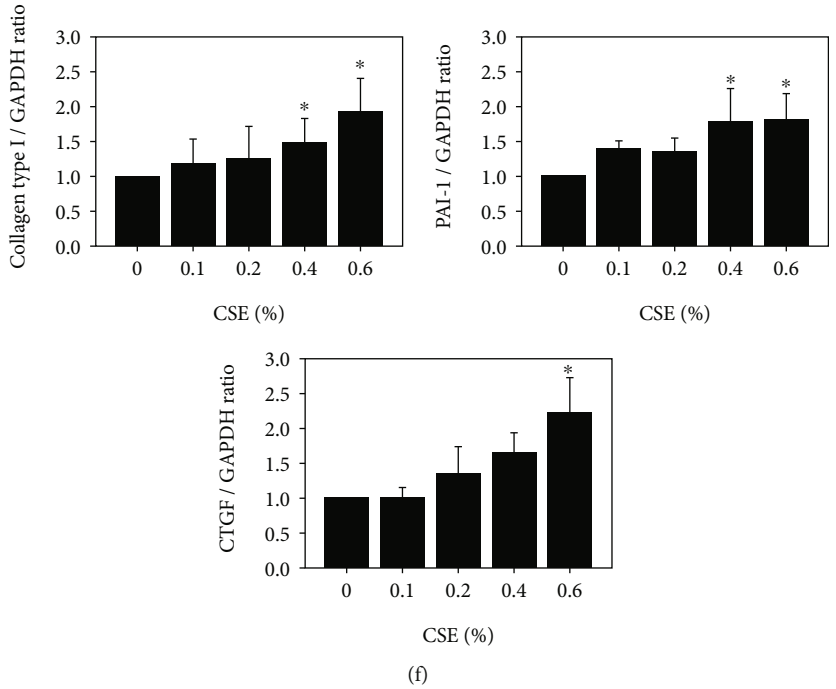

(f)

Figure 2: Autophagosome-related protein, SIRT1, and fibrosis-related protein expression after HK-2 cells were treated with CSE. (a) The expression levels of LC3 (green color) were measured in HK-2 cells after treatment with CSE at concentrations of 0.1, 0.2, 0.4, and 0.6% for 24 h. 4′,6-Diamidino-2-phenylindole (DAPI) (blue color) was used to stain nuclei. Scale bar: 50 μm. (b) Images of LC3-punctuated cells treated with CSE were graphed and statistically analyzed at concentrations of 0.1, 0.2, 0.4, and 0.6% for 24 h. $^*p < 0.05$ compared to the control group. (c) Western blot showing the expression of SIRT1 and the autophagy-related proteins p62, ATG5, and LC3 after CSE treatment at concentrations of 0.1, 0.2, 0.4, and 0.6% for 24 h. (d) Protein expression of LC3-II, p62, ATG5, and SIRT1 was measured and diagramed for CSE-treated cells at concentrations of 0.1, 0.2, 0.4, and 0.6% for 24 h. $^*p < 0.05$ compared to the control group. (e) The expression levels of the fibrosis-related proteins collagen type 1, PAI-1, and CTGF after treatment with CSE at concentrations of 0.1, 0.2, 0.4, and 0.6% for 24 h. (f) Collagen type 1, PAI-1, and CTGF were measured and diagramed in HK-2 cells after treatment with CSE at concentrations of 0.1, 0.2, 0.4, and 0.6% for 24 h. $^*p < 0.05$ compared to the control group.

mercaptoethanol). Proteins and the prestained protein marker (10–315 kDa) (TD-PM10315, BIOTOOLS Co., Ltd., Taipei, Taiwan) were loaded into an SDS-PAGE gel. A PVDF membrane containing transferred proteins was incubated with 5% nonfat milk with primary antibodies anti-microtubule-associated protein 1A/1B-light chain 3 (LC3) (Cell Signaling, Beverly, MA), collagen 1 (Proteintech, Rosemont IL), autophagy-related 5 (ATG5) (Proteintech), CTGF (Proteintech), PAI-1 (Cell Signaling), SIRT1 (ABclonal Inc., Woburn, MA), caspase-3 (ABclonal Inc.), Hsp27 (ABclonal Inc.), BAX (ABclonal Inc.), Klotho (Proteintech), p53 (Proteintech), p21(Proteintech), p16 (Proteintech), G6PD (Proteintech), and GAPDH (Proteintech). After the hybridization process with the abovementioned antibodies on the PVDF membrane, the membrane was rinsed with TBS-T for 15 min three times. Subsequently, the PVDF membrane was further treated with anti-mouse (Jackson) or anti-rabbit (Jackson) secondary antibody for 2 h and rinsed with TBS-T for 15 min over three times. The protein bands of the PVDF membrane were visible by performing an enhanced chemiluminescence system (Amersham, Little Chalfont, United Kingdom).

2.7. RNA Sequencing and Analysis. RNA sequencing used to characterize and analyze the transcriptome (RNA sequencing, Tools, Taiwan). Briefly, the purity and quantification of RNA were detected with SimpliNano™–Biochrom Spectrophotometers (Biochrom, MA, USA). The levels of RNA degradation and integrity were detected by a BiOptic Qsep100 DNA/RNA Analyzer (BiOptic Inc., Taiwan). The sequencing library was established with the KAPA mRNA HyperPrep Kit (KAPA Biosystems, Roche, Basel, Switzerland). mRNA was extracted from total RNA with magnetic oligo-dT beads and incubated at a high temperature in KAPA buffer that contained magnesium. cDNA was generated with random hexamer priming. cDNA fragments with a length of 300~400 bp were selected, and library fragments were extracted with the KAPA Pure Beads system (KAPA Biosystems, Roche, Basel, Switzerland). The library was increased with KAPA HiFi HotStart ReadyMix (KAPA Biosystems, Roche, Basel, Switzerland). Finally, the library was extracted with the KAPA Pure Beads system and qualified with the Qsep100 DNA/RNA Analyzer (BiOptic Inc). The library data were detected with high-throughput sequencing (Illumina NovaSeq 6000 platform), which was transformed into raw sequenced reads with CASAVA base calling and then stored in FASTQ format. The FASTQ files were used with FastQC and MultiQC [48]. The raw paired-end reads were filtered with Trimmomatic (v0.38) [49]. The obtained high-quality data were aligned to the reference genome

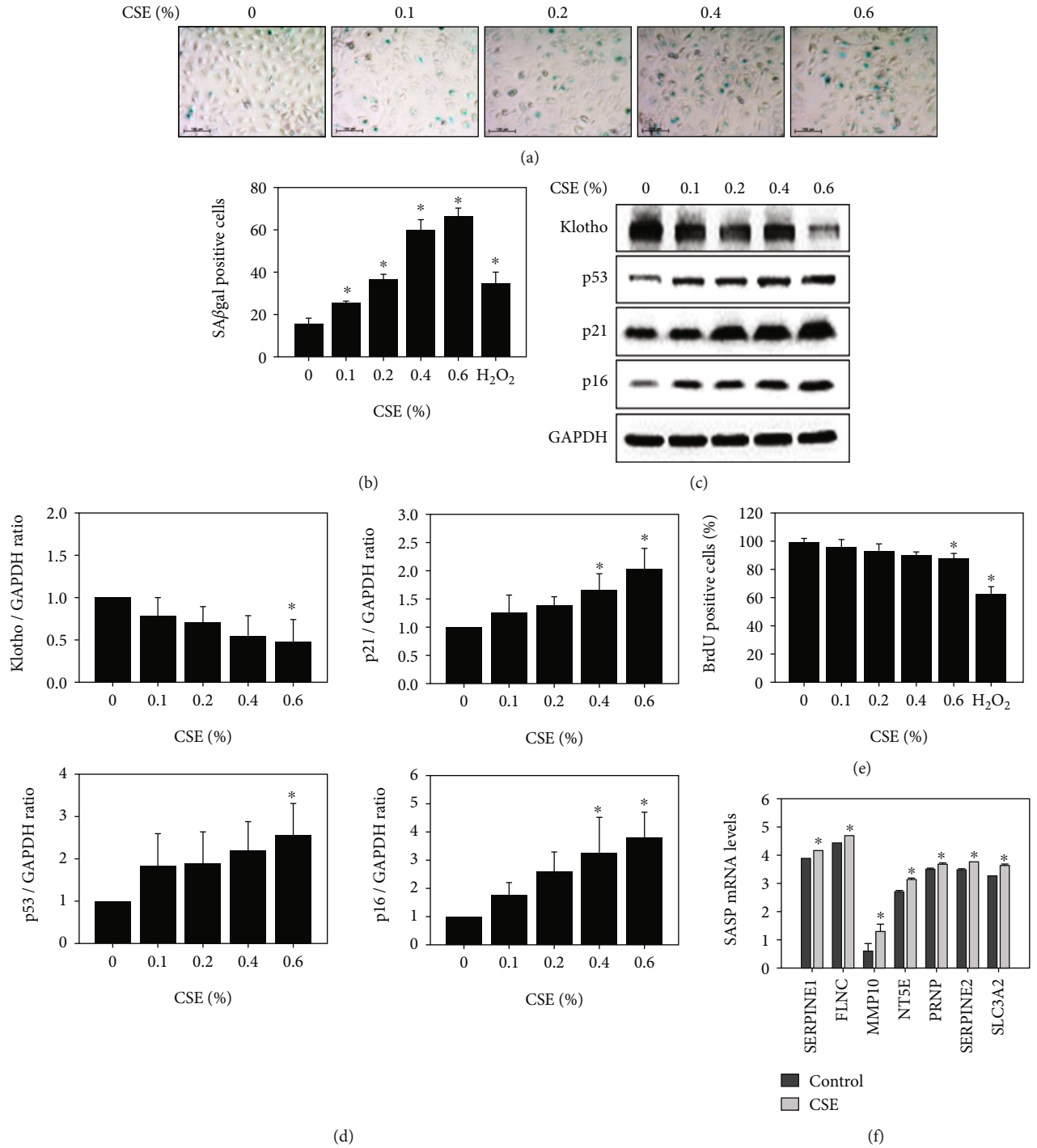

Figure 3: Senescence, senescence-related proteins, and senescence-associated secretory phenotype-related inflammation in HK-2 cells after treatment with CSE. (a) The expression of SAβgal (turquoise color) was detected after treatment with CSE at concentrations of 0.1, 0.2, 0.4, and 0.6% for 24 h. (b) The results of SAβgal-positive cells were graphed and statistically analyzed after treatment with CSE at concentrations of 0.1, 0.2, 0.4, and 0.6% for 24 h. $^*p < 0.05$ compared to the control group. (c) The expression of senescence-related proteins Klotho, p53, p21, and p16 in CSE-treated cells at concentrations of 0.1, 0.2, 0.4, and 0.6% for 24 h. (d) Klotho, p53, p21, and p16 were graphed and analyzed after cells were treated with CSE at concentrations of 0.1, 0.2, 0.4, and 0.6% for 24 h. $^*p < 0.05$ compared to the control group. (e) The results of BrdU-positive cells were graphed and statistically analyzed after treatment with CSE at concentrations of 0.1, 0.2, 0.4, and 0.6% for 24 h. $^*p < 0.05$ compared to the control group. H_2O_2 served as a positive control. (f) SASP was graphed and statistically analyzed from RNA sequencing data of CSE-treated HK-2 cells following 24 h. $^*p < 0.05$ compared to the control group.

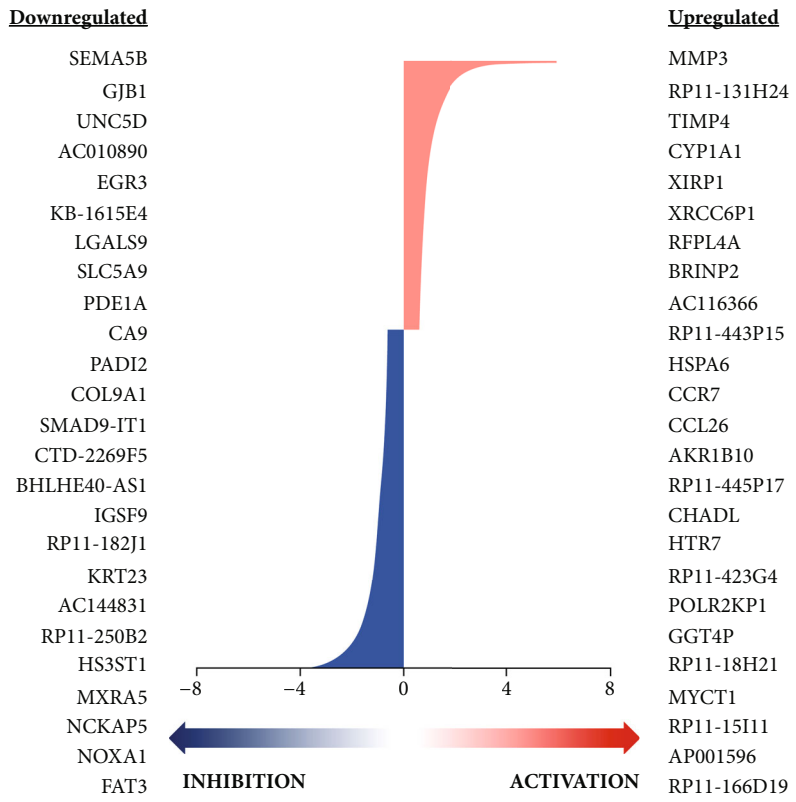

(a)

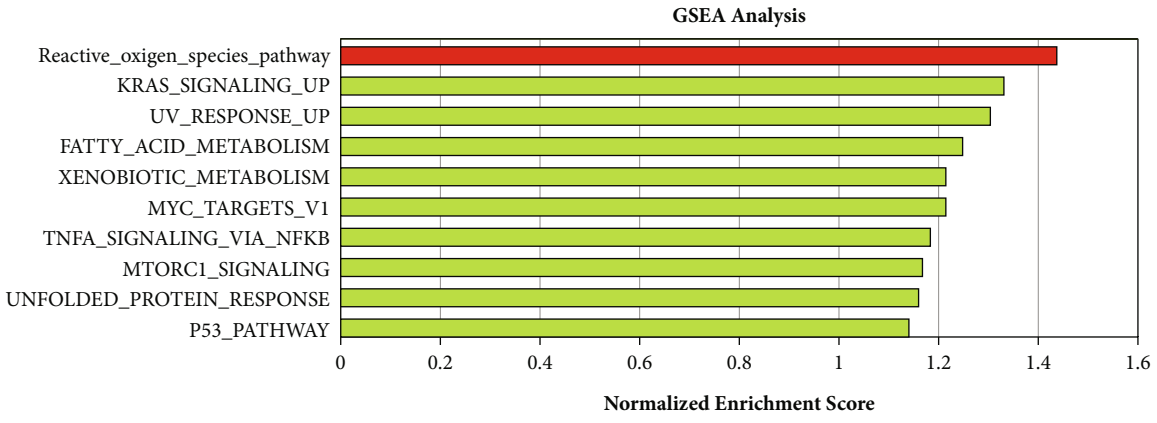

(b)

Figure 4: Continued.

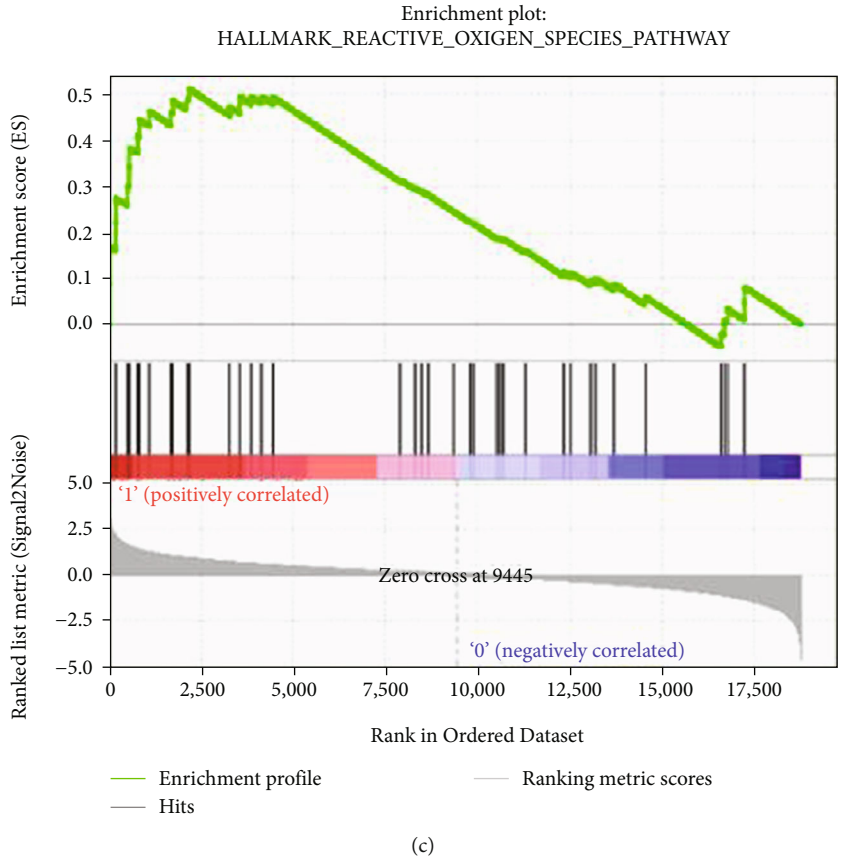

(c)

Figure 4: RNA sequencing and gene set enrichment analysis of CSE-treated HK-2 cells. (a) RNA was extracted from HK-2 cells and sequenced after treatment with or without CSE at a concentration of 0.6%. Upregulation and downregulation of mRNA are presented as the fold change $-0.58 < FC > 0.58$. (b) GSEA was used to analyze the pathways of HK-2 cells after treatment with CSE and showed a normalized enrichment score. (c) The Hallmark reactive oxygen species gene set database of the enrichment plot was used as the gene set collection for analysis.

(e.g., H. sapiens, GRCh38) with HISAT2 software (v2.1.0) [50, 51]. featureCounts (v1.6.0) was used to count the read numbers mapped to individual genes [52]. The RNA series dataset was uploaded to the Gene Expression Omnibus (Accession: GSE182541). GSEA was analyzed with 1000 permutations to identify enriched biological functions and activated pathways from the molecular signature database [53] (MSigDB) (https://www.gsea-msigdb.org/gsea/msigdb).

2.8. Quantitative Polymerase Chain Reaction (Q-PCR). Total RNA of the kidney will be extracted using the TRIzol reagent (Invitrogen). Purity and quantification of RNA will be detected. Complementary DNA (cDNA) will be synthesized using the Easy Fast RT Kit (TOOLS, Taiwan). Q-PCR will be detected using SYBR Green (TOOLS, Taiwan). Glyceraldehyde 3-phosphate dehydrogenase (GAPDH) will be used as an internal control. The $2^{-\Delta\Delta Ct}$ method will be used to calculate the expression changes. All primers are listed as follows: G6PD, Hsp27, and GAPDH.

2.9. Senescence β-Galactosidase Staining. The cells were treated with CSE for 24 h, washed, fixed, and cultured in a 37°C/5% CO_2 incubator with X-gal chromogenic substrate at pH 5.5 overnight by following the protocol for SA-β-gal staining (BioVision, Milpitas, CA). The images for β-galactosidase were collected using a digital microscope. The positive cell intensity was counted in 3 fields of view (>50 cells/field). Polydatin (MCE, Monmouth Junction, NJ) is an inhibitor of G6PD activity [54].

2.10. Enzyme-Linked Immunosorbent Assay. The amount of the NADPH-producing enzyme G6PD was measured using ELISA kits specific for human G6PD according to the manufacturer's protocol (Cayman Chemical, Ann Arbor, MI). The fluorescent product was measured under an excitation wavelength of 530/540 and an emission wavelength of 585-595 nm.

2.11. BrdU Cell Proliferation Assay. HK-2 cells were plated in a 96-well plate and incubated. BrdU was measured using BrdU Cell Proliferation Assay Kit (BioVision). Briefly, cells were added 1x 5-bromo-2-deoxyuridine (BrdU) solution and incubated plate at 37°C. Cells were fixed and denatured. Cells were hybrid with BrdU detection antibody solution. Finally, cells were added 3,3′,5,5′-tetramethylbenzidine (TMB) substrate and measured the absorbance at 650 nm.

2.12. Cigarette Smoke Exposure of Mouse Model. Eight-week-old male C57BL/6JNarl mice were purchased from the National Laboratory Animal Center (Taipei, Taiwan). The animal protocol was approved by the Animal and Ethics Review Committee of the Laboratory Animal Center at Taipei Medical University, Taiwan (IACUC: LAC-2017-0231). Mice were maintained under a light/dark cycle of 12 h/12 h, and the room temperature was kept at 22 ± 2°C with relative humidity of 55 ± 10%. The mouse model ($n = 5$ per group) was established by exposure to CS for 4 months. Details of the CS exposure system were reported in a previous study [55]. Briefly, the system consisted of a CS generator in a whole-body exposure chamber (TECNIPLAST, VA, Italy) with a particulate matter monitor. A side stream was placed into the whole-body exposure chamber at a flow rate of 15 l/min. Sixteen commercial cigarettes (Longlife) were combusted for 8 h/day and 5 days/week for 4 months. The mass concentration of particulate matter of <2.5 μm in aerodynamic diameter was monitored using a DustTrak monitor (TSI, Shoreview, MN). The mice were sacrificed by CO_2, and the kidneys were excised and fixed with 10% neutral formalin.

2.13. Histological Analysis. The kidney tissues were embedded, dehydrated, sectioned into 2 μm thick slices slicing a microtome, and then stained with hematoxylin and eosin (H&E) (Sigma) for histological analysis. The glomerulosclerosis and tubular injury scores were measured. Details of the glomerulosclerosis and tubular injury scores are provided in a previously reported study [56].

2.14. Immunohistochemical (IHC) Staining Analysis. Kidney sections were maintained in an oven at 60°C. The kidney sections were sequentially washed with xylene (Sigma), 100% ethanol (Sigma), 95% ethanol, and 75% ethanol. Finally, the kidney sections soaked in MQ water and boiled with sodium citrate buffer (0.01 M, pH 6.0, 1% Tween 20). The sections then washed with PBS, soaked in 3% H_2O_2/methanol, and finally with PBS. UltraVision protein block buffer was applied to analyze the kidney after treatment with G6PD (Proteintech), LC3 (MBL) or β-gal (Invitrogen) antibody in 3% BSA overnight at 4°C. The sections were washed with PBS, treated with Trekkie Universal Link for 20 min, and then mixed with poly-HRP reagent for 20 min. The DAB coloring agent was used to stain the sections, followed by placement in MQ water to terminate the reaction. For the next step, hematoxylin was also used as a contrast dye for the second staining assay. In the end, the mounting buffer was added to the kidney sections, which were covered with a cover slip. Masson's trichrome staining was used according to the protocol (TRM-2-IFU, ScyTek). After the sections solidified with mounting buffer, the slices were recorded with Motic Digital Slide Assistant (Motic VM3.0, New York, NY).

2.15. Statistical Analysis. The results were analyzed by SPSS (SPSS Software, CA, San Diego) and plotted as the mean ± standard deviation. The statistical significance between groups was determined by Student's t-test. Comparisons of three or more groups were calculated by ANOVA. Significance was confirmed at $p < 0.05$.

Table 1: The top 20 genes of Hallmark reactive oxygen species gene set.

Gene	FC	p value
G6PD	0.979605	$6.56E-76$
GCLM	0.960879	$3.98E-50$
SOD1	0.952822	$2.29E-67$
TXN	0.843715	$4.23E-36$
HHEX	0.820415	$3.26E-08$
GSR	0.743549	$9.59E-52$
PRNP	0.613288	$3.58E-33$
PRDX1	0.609423	$1.24E-39$
HMOX2	0.551601	$1.50E-15$
GCLC	0.545956	$8.41E-12$
PRDX6	0.418619	$3.87E-18$
SCAF4	0.396722	$6.68E-10$
GLRX	0.39422	$2.50E-05$
ATOX1	0.370471	0.001248
GLRX2	0.343887	$8.97E-06$
GPX3	0.324067	$4.18E-07$
SBNO2	0.095644	0.149361
ERCC2	0.071641	0.329135
TXNRD2	0.053783	0.564995
NDUFA6	0.045766	0.533123

3. Results

3.1. Cell Viability, Cell Death, and Apoptosis-Related Protein Expression in CSE-Treated HK-2 Cells. The viability of CSE-treated HK-2 cells was significantly decreased in a concentration-dependent manner, as shown in Figure 1(a). After HK-2 cells were treated with CSE at low concentrations of 0.1%, 0.2%, 0.4%, and 0.6%, the cell viability decreased to 94.6%, 92.8%, 81.3%, and 67.9%, respectively. Flow cytometry analysis revealed that the CSE-treated cells at low concentrations of 0.1%, 0.2%, 0.4%, and 0.6% had no significant differences in either index of apoptosis or necrosis (Figures 1(b) and 1(c)). In addition, LDH assay revealed that the necrosis index did not have any significant differences (Figure 1(d)). Moreover, western blotting analysis showed that low concentrations of CSE did not increase Bax and cleaved caspase 3 protein expression (Figures 1(e) and 1(f)).

3.2. Expression of Autophagosome-Related and Fibrosis-Related Proteins in HK-2 Cells after Treatment with CSE. The expression levels of LC3 determined by immunofluorescence were concentration-dependent (Figure 2(a)). Statistical analysis also showed that LC3 levels were CSE concentration-dependent in HK-2 cells (Figure 2(b)). Approximately 35 ± 2.5% of HK-2 cells expressed LC3

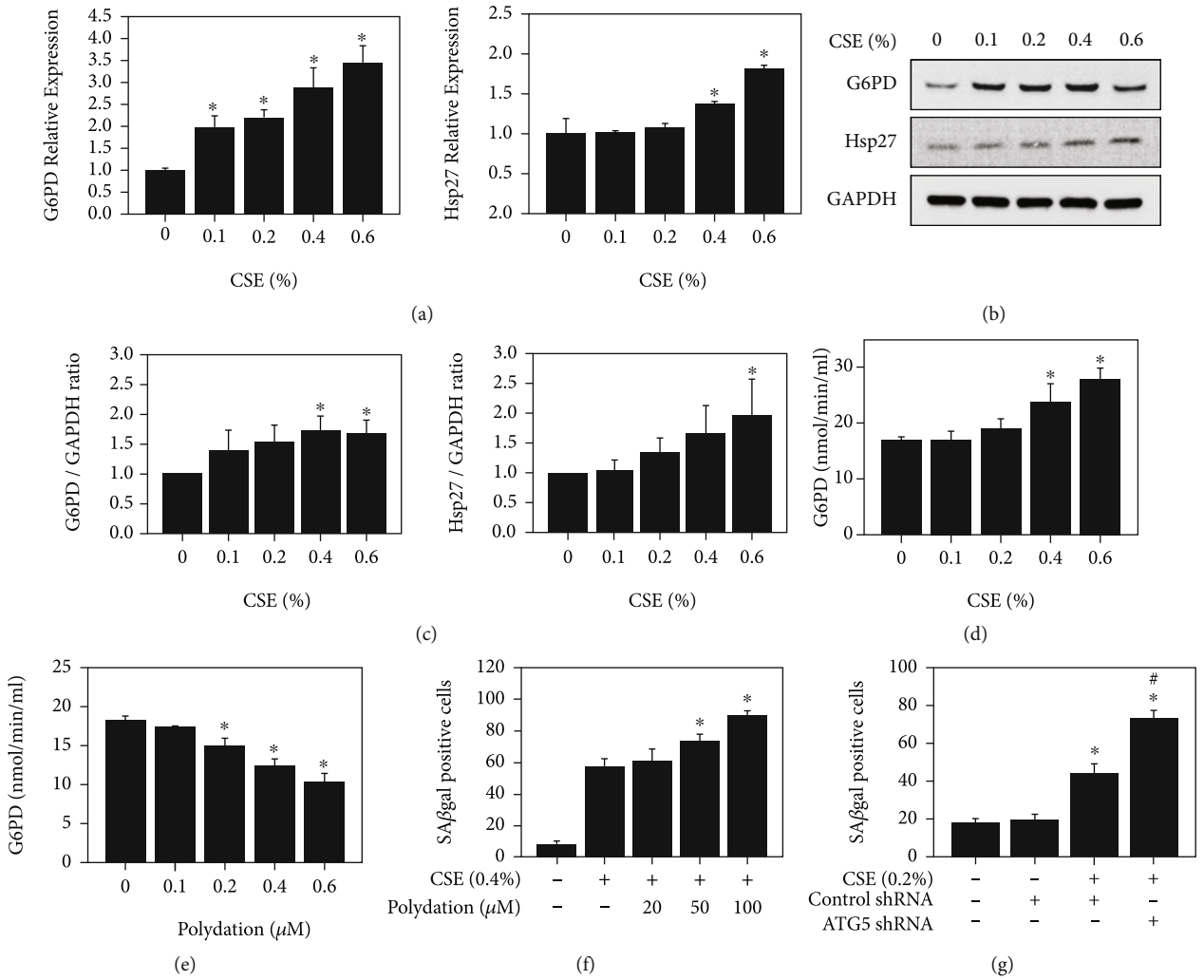

Figure 5: The expression profile of heat shock protein 27 and glucose-6-phosphate dehydrogenase, activity of glucose-6-phosphate dehydrogenase, and senescence-associated β-galactosidase assay with polydatin or ATG shRNA in HK-2 cells after treatment with CSE. (a) Relative expression in Hsp27 and G6PD mRNA was measured in CSE-treated cells at concentrations of 0.1, 0.2, 0.4, and 0.6% for 24 h. $^*p < 0.05$ compared to the control group. (b) The expression of Hsp27 and G6PD in HK-2 cells after treatment with CSE at concentrations of 0.1, 0.2, 0.4, and 0.6% for 24 h. $^*p < 0.05$ compared to the control group. (c) Hsp27 and G6PD expressions were graphed and analyzed for CSE-treated cells at concentrations of 0.1, 0.2, 0.4, and 0.6% for 24 h. $^*p < 0.05$ compared to the control group. (d) The activation of G6PD was detected after CSE treatment at concentrations of 0.1, 0.2, 0.4, and 0.6% for 24 h. $^*p < 0.05$ compared to the control group. (e) The expression of G6PD activation was detected after polydatin treatment at concentrations of 10, 20, 50, and 100 μM for 24 h. $^*p < 0.05$ compared to the control group. (f) SAβgal expression was detected in cells after treatment with CSE at concentrations of 0.6% and polydatin at concentrations of 10, 20, 50, and 100 μM for 24 h. $*p < 0.05$, CSE compared to CSE+polydatin. (g) The expression of SAβgal was measured after treatment with CSE, control shRNA, and ATG5 shRNA at concentrations of 100 μM for 24 h. $^*p < 0.05$ compared to the control group. $^\#p < 0.05$, CSE+control shRNA compared to CSE+ATG5 shRNA.

signals after treatment with 0.6% CSE. Furthermore, CSE-treated HK-2 cells revealed higher expression of the autophagy-related proteins LC3, p62, ATG5, and SIRT1, as determined by western blotting (Figure 2(c)). The expression levels of LC3, p62, ATG5, and SIRT1 were also concentration-dependent in HK-2 cells after CSE treatment (Figure 2(d)). On the other hand, HK-2 cells exposed to CSE exhibited higher expression of the fibrosis-related proteins collagen type 1, PAI-1, and CTGF, as determined by western blotting (Figure 2(e)). Statistical analysis also revealed that the levels of collagen type 1, PAI-1, and CTGF after treatment with CSE in HK-2 cells were also concentration-dependent (Figure 2(f)).

3.3. Senescence, Senescence-Related Proteins, and Senescence-Associated Secretory Phenotype-Related Inflammation in HK-2 Cells after CSE Treatment. Senescence-positive cells were observed in concentration-dependent manner as determined by the SAβgal assay as shown in Figure 3(a). Analysis of SAβgal-positive CSE-treated HK-2 cells also demonstrated concentration dependence (Figure 3(b)). CSE-treated HK-2 cells displayed higher expression of the

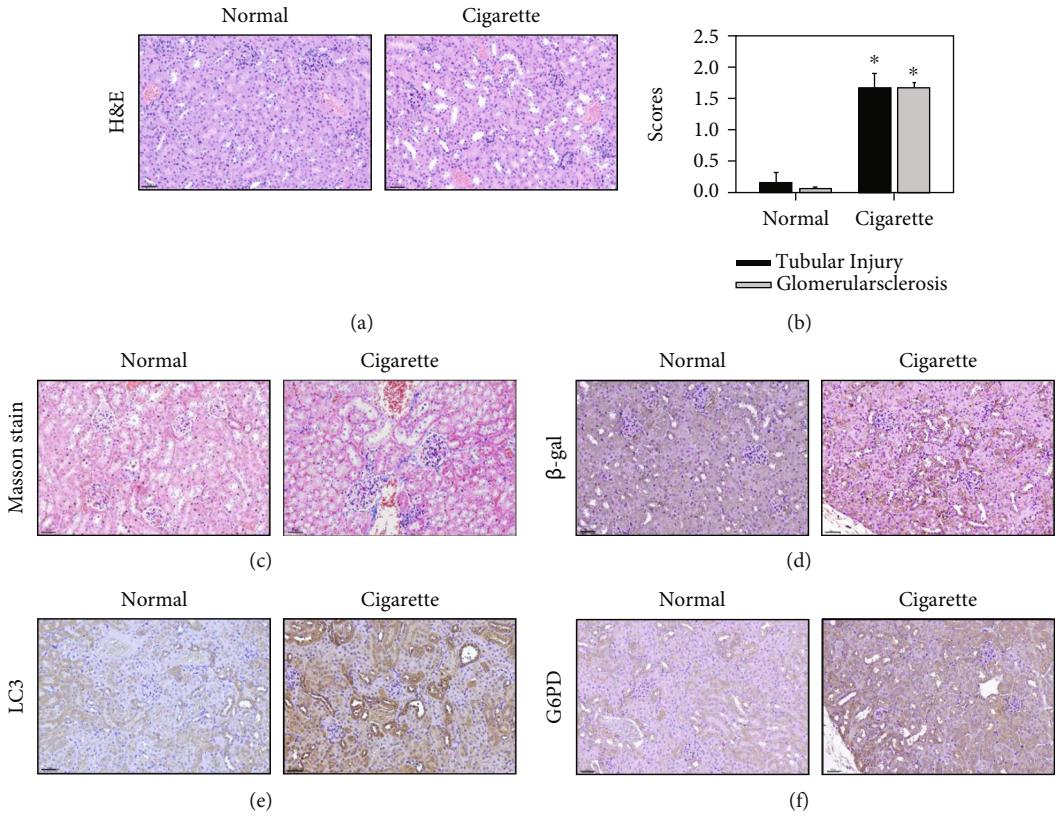

Figure 6: Hematoxylin and eosin staining in kidney samples. Tubular injury, glomerulosclerosis score, and Masson staining after treatment of mice with CS. (a) C57BL/6 mice were treated with CSE and harvested for 4 months. H&E staining was examined in kidney samples. The cell nuclei were stained blue by hematoxylin. Both the extracellular matrix and cytoplasm were stained by eosin (pink). Scale bar: 50 μm. (b) Tubular injury and glomerulosclerosis were analyzed in kidneys ($N = 5$). The data are presented as the means ± SD. Twenty fields of view per kidney. $^{*}p < 0.05$ and $^{***}p < 0.001$ compared to the normal group samples. (c) Kidneys were stained with Masson's trichrome. Scale bar = 50 μm. Immunohistochemistry for senescence-associated β-galactosidase, autophagy-related proteins, glucose-6-phosphate dehydrogenase, and kidney samples of after treatment of mice with CSE. (d) C57BL/6 mice were treated with CSE and then harvested after 4 months. IHC staining of SAβgal was examined in kidney samples. (e) IHC staining of LC3 was examined in kidney samples. (f) IHC staining of G6PD was examined in kidney samples. Scale bar: 50 μm.

senescence-related proteins p53, p21, and p16 as determined by western blotting (Figure 3(c)). A previous study showed that Klotho reduced kidney senescence and fibrosis [19]. Klotho exhibited lower expression after treatment with CSE (Figure 3(c)). p53, p21, p16, and Klotho levels in HK-2 cells treated with CSE were also concentration-dependent (Figure 3(d)). Senescent cells have inhibited cellular proliferation [57], which can be detected by BrdU. BrdU-positive HK-2 cells treated with CSE were also observed to be concentration-dependent (Figure 3(e)). Furthermore, SLC3A2, SERPINE2, PRNP, NT5E, MMP10, FLNC, and SERPINE1 showed higher expression after treatment with CSE in HK-2 cells, as determined by RNA sequencing (Figure 3(f)).

3.4. RNA Sequencing, Gene Set Enrichment Analysis, and Interpretative Phenomenological Analysis in CSE-Treated HK-2 Cells. The RNA sequencing data after treatment of HK-2 cells with CSE are shown in Figure 4(a). The most upregulated gene was MMP3 in CSE-treated cells, while the most downregulated gene was SEMA5B. In addition, the data were further analyzed by GSEA (Figure 4(b)). The results showed higher expression of the ROS pathway in HK-2 cells after treatment with CSE (Figure 4(b)). The enrichment plot showed higher enrichment of the ROS pathway after cells were exposed to CSE (Figure 4(c)). Moreover, ROS-related gene expression is shown in Table 1. The most upregulated gene was G6PD in HK-2 cells after CSE treatment as shown in Table 1.

3.5. Expression Profile of Heat Shock Protein 27, Glucose-6-phosphate Dehydrogenase, and Senescence-Associated β-Galactosidase Assay Regulation with Autophagy in CSE-Treated HK-2 Cells. Hsp27 and G6PD were observed to be concentration-dependently increased, as determined by real-time polymerase chain reaction (Q-PCR) assay (Figure 5(a)) and western blotting (Figure 5(b)). The expression of Hsp27 and G6PD in HK-2 cells after treatment with CSE was also concentration-dependent (Figure 5(c)). The G6PD activity after HK-2 cell treatment with CSE was also concentration-dependent (Figure 5(d)). G6PD activity was higher in HK-2 cells after CSE treatment at concentrations of 0.6% and decreased after polydatin treatment at concentrations of 10, 20, 50, and 100 μM (Figure 5(e)).

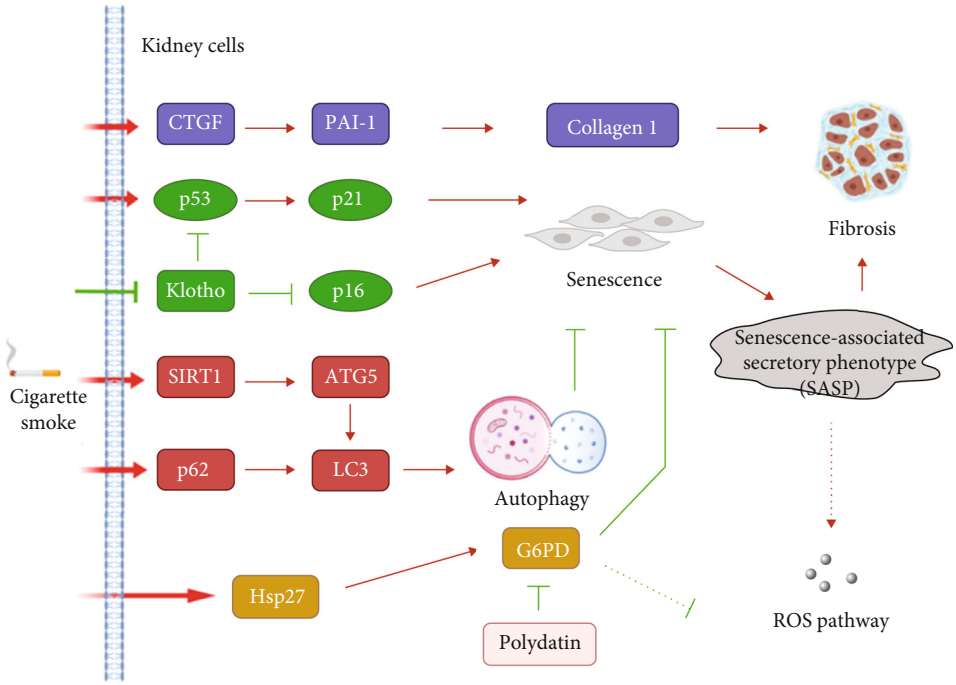

Figure 7: Schematic of the putative mechanism illustrating the CSE-induced G6PD, autophagy-related, fibrosis-related, and senescence-related protein expressions in kidney cells. Kidney cells were induced by CSE via several related pathways that increase the expression of the fibrosis-related proteins, autophagy-related proteins, and senescence-related proteins in kidney cells. CSE regulates senescence and fibrosis via inhibition of Hsp27, G6PD, Klotho, and autophagy.

Furthermore, the statistical expression of SAβgal-positive cells was increased in CSE-treated HK-2 cells, and the expression increased at concentrations of 20, 50, and 100 μM after treatment with polydatin (Figure 5(f)). In addition, the number of SAβgal-positive cells treated with both ATG5 shRNA and control shRNA was increased after CSE exposure compared with that in the control groups (Figure 5(g)). Moreover, ATG5 shRNA enhanced the number of CSE-induced SAβgal-positive cells.

3.6. Tubular Injury and Glomerulosclerosis Score Analysis of Senescence, Senescence-Associated β-Galactosidase, Autophagy Protein LC3, and Glucose-6-phosphate Dehydrogenase after treatment of Mice with CS. A mouse model was established by exposure of mice to CS for 4 months. H&E staining displayed varying degrees of tubular injury and glomerulosclerosis when comparing the CS-treated group to the normal group (Figure 6(a)). The tubular injury and glomerulosclerosis scores were significantly increased after treatment of mice with CS (Figure 6(b)). The kidney sample also revealed varying degrees of fibrosis staining with Masson's trichrome (purple) (Figure 6(c)). IHC staining showed higher expression of SAβgal, LC3 and G6PD than that of the normal group at 4 months (Figures 6(d)–6(f)).

4. Discussion

A previous study showed that CS altered cell viability in gingival mesenchymal cells at a concentration of 250 μg/ml [58]. The cell viability of mouse embryonic fibroblasts and NIH3T3 cells decreased below 50% after exposure to 400 μl of 4% CSE solution [59]. In addition, the cell viability of human lung bronchial epithelial cells (BEAS-2B) decreased to 50% after treatment with 10-20% CSE [60]. Our results showed that cell viability decreased by over 50% in HK-2 kidney cells after treatment with CSE (0.8% and 1%) (Figure 1(a)). Early reports indicated that apoptosis was significantly induced in BEAS-2B cells by CSE [61]. However, our results showed that low concentrations CSE (0.1%-0.6%) did not induce apoptosis in HK-2 cells (Figures 1(b)–1(e)). A previous study showed that the CSE-induced autophagy in A549 cells is associated with many cellular processes [35]. Our results indicated that CSE-treated HK-2 cells not only induced autophagy but also induced SIRT1 after CSE (0-0.6%) exposure (Figures 2(a)–2(d)). Hence, our results indicated that autophagy was regulated by SIRT1, which has been reported in other studies [62–64].

CSE is a risk factor for the development of lung fibrosis [65]. Renal fibrosis is involved in various kidney diseases [66]. Previous studies have demonstrated that through the autocrine and paracrine stimulation of cells by TGF-β1, CTGF is released and synthesized, which plays a role in fibrogenesis [67]. Furthermore, PAI-1 is the major physiologic inhibitor of the plasmin-based pericellular cascade and a causative factor in the fibroproliferative disorders [68]. The upregulation of CTGF and PAI-1 caused extracellular matrix (ECM) accumulation [69, 70]. In the current study, CSE exhibited higher expression of the fibrosis-related proteins including collagen type 1, PAI-1, and CTGF in HK-2 cells (Figures 2(e) and 2(f)). In *in vivo* study, the

significant accumulation of collagen fibers in the kidney tissues of the CS group (Figure 6(c)). These results indicated that CS may cause kidney fibrosis. Previous research has shown that CS induces SASP-related inflammation in human epidermal keratinocytes and skin [8]. The expression of fibrosis-related genes is induced in orbital fibroblasts from patients with Graves' ophthalmopathy [22]. In addition, previous study revealed that CS reduced the proliferation of lung fibroblasts by upregulating signaling pathways such as cell senescence, p53, and p16-retinoblastoma [5]. The p53 [6], p16, and p21 pathways [7] were related to cellular senescence, including fibrosis accompanied by senescence, senescence-related proteins, and SASP-related inflammation (Figures 3(a)–3(f) and Figure 6(d)). Early reports showed that CSE reduces the expression and secretion of Klotho in alveolar macrophages and airway epithelial cells in COPD patients [21]. The present study demonstrated that Klotho significantly decreased in human kidney cells after the CSE (0%-0.6%) treatment (Figure 3(c)).

Recently, a meta-analysis suggested that CS is an independent risk factor for the general adult population with CKD [42] and healthy middle-aged adults [43]. In addition, GSEA revealed that three pathways were involved in CS-treated BEAS-2B cells, namely, cell matrix adhesion and the TGF-β receptor signaling pathway, RNA catabolic processes, and the regulation of cell cycle phase transition, as well as calcium-mediated signaling and regulation of cell-cell adhesion [71]. Deficiency of G6PD in the erythrocyte membrane causes substantial oxidant damage [11]. G6PD is a major source of NADPH that is involved in antioxidant pathways [39]. Furthermore, GSEA showed that the ROS pathway is the primary regulator in HK-2 cells after treatment with CSE. In particular, the expression of G6PD increased in the ROS-related gene expression pathway after treatment with CSE (Figures 4(a)–4(c) and Table 1). G6PD and Hsp27 were highly expressed in CSE-treated HK-2 cells (Figures 5(a)–5(c)). On the other hand, Hsp27 phosphorylation plays an important role in the activation of G6PD [38], and the phosphorylation of G6PD results in a reduction of NADPH, subsequently causing oxidative stress which may lead to metabolic syndromes [72, 73]. Polydatin is a new inhibitor of G6PD that can block the pentose phosphate pathway [54]. Our results showed that polydatin decreased the activity of G6PD in a dose-dependent manner (Figure 5(e) and Table 1). The expression of senescence-related factors was increased after treatment with polydatin in HK-2 cells (Figure 5(f)). These data showed that G6PD plays an important role in the protection of kidney cells. A previous study indicated that CS accelerated lung aging [34] and kidney injury [74] via autophagy. Our results showed that CSE induced autophagy (Figures 2(a)–2(d)). Here, we used ATG5 shRNA to increase senescence expression in HK-2 cells (Figure 5(g)) and found that CSE-induced autophagy may inhibit senescence and has a protective role in kidney cells.

5. Conclusions

We found that CSE induced autophagy, fibrosis, senescence, and SASP in kidney cells (Figure 7). In contrast, Klotho expression was decreased in kidney cells after CSE treatment. Furthermore, RNA sequencing and GSEA revealed that G6PD played an important role in ROS pathway regulation in kidney cells after CSE exposure. G6PD expression and G6PD activity increased in CSE-treated kidney cells. In addition, G6PD inhibited senescence in kidney cells. In an animal model after CS exposure for 4 months, CS caused tubular injury and glomerulosclerosis and induced fibrosis, autophagy, and G6PD. In conclusion, CS induced G6PD, autophagy, fibrosis, and senescence and decreased Klotho in kidney cells. These findings offer more precise molecular mechanism of CS and the chance to find potential preventive or therapeutic strategies for CS-related renal injury. In the current study, we focus on *in vitro* study and an animal model. In the future, we hope to utilize clinical data and samples for validation of the research that we currently perform on in vitro and animal models.

Abbreviations

CS: Cigarette smoke
COPD: Chronic obstructive pulmonary disease
SASP: Senescence-associated secretory phenotype
Hsp27: Heat shock protein 27
G6PD: Glucose-6-phosphate dehydrogenase
CKD: Chronic kidney disease
ROS: Reactive oxygen species
DAPI: 4′,6-Diamidino-2-phenylindole
GSEA: Gene set enrichment analysis
SAβgal: Senescence-associated β-galactosidase
IHC: Immunohistochemistry.

Data Availability

The data used to support the findings of this study are available from the corresponding author upon reasonable request.

Disclosure

Experiments and data analysis were performed in part through the use of the Medical Research Core Facilities Center, Office of Research & Development at China Medical University, Taichung, Taiwan.

Conflicts of Interest

The authors declare that they have no competing interests.

Authors' Contributions

Wen-Chih Liu contributed to the conceptualization, data curation, investigation, and writing of original draft. Hsiao-Chi Chuang contributed to the formal analysis and review. Chu-Lin Chou contributed to the methodology, formal analysis, supervision, and project administration, Yu-Hsuan Lee contributed to the writing— review and editing, Yu-Jhe Chiu contributed to the formal analysis and review. Yung-Li Wang contributed to the formal analysis and writing—review and editing. Hui-Wen Chiu contributed to the

validation, formal analysis, and writing—review and editing. Wen-Chih Liu and Yung-Li Wang contributed equally to this work.

Acknowledgments

Figure 7 was created with http://BioRender.com. This study was supported by the Ministry of Science and Technology, Taiwan (MOST 108-2314-B-039-061-MY3, MOST 109-2314-B-038-078-MY3, MOST 110-2314-B-038-140 and MOST 110-2314-B-039-018), Taipei Hospital, Ministry of Health and Welfare, Taiwan (Grant no. 202104), and China Medical University, Taichung, Taiwan (CMU110-MF-21).

References

[1] R. A. Pauwels, A. S. Buist, P. M. Calverley, C. R. Jenkins, S. S. Hurd, and G. S. Committee, "Global strategy for the diagnosis, management, and prevention of chronic obstructive pulmonary Disease," *American Journal of Respiratory and Critical Care Medicine*, vol. 163, no. 5, pp. 1256–1276, 2001.

[2] K. F. Rabe, S. Hurd, A. Anzueto et al., "Global strategy for the diagnosis, management, and prevention of chronic obstructive pulmonary disease: GOLD executive summary," *American Journal of Respiratory and Critical Care Medicine*, vol. 176, no. 6, pp. 532–555, 2007.

[3] L. Shahab, M. J. Jarvis, J. Britton, and R. West, "Prevalence, diagnosis and relation to tobacco dependence of chronic obstructive pulmonary disease in a nationally representative population sample," *Thorax*, vol. 61, no. 12, pp. 1043–1047, 2006.

[4] M. G. Ushakumary, M. Riccetti, and A. K. T. Perl, "Resident interstitial lung fibroblasts and their role in alveolar stem cell niche development, homeostasis, injury, and regeneration," *Stem Cells Translational Medicine*, vol. 10, no. 7, pp. 1021–1032, 2021.

[5] T. Nyunoya, M. M. Monick, A. Klingelhutz, T. O. Yarovinsky, J. R. Cagley, and G. W. Hunninghake, "Cigarette smoke induces cellular senescence," *American Journal of Respiratory Cell and Molecular Biology*, vol. 35, no. 6, pp. 681–688, 2006.

[6] M. Mijit, V. Caracciolo, A. Melillo, F. Amicarelli, and A. Giordano, "Role of p53 in the regulation of cellular senescence," *Biomolecules*, vol. 10, no. 3, p. 420, 2020.

[7] A. Caliò, A. Zamò, M. Ponzoni et al., "Cellular senescence markers p16INK4a and p21CIP1/WAF are predictors of Hodgkin lymphoma outcome," *Clinical Cancer Research*, vol. 21, no. 22, pp. 5164–5172, 2015.

[8] J. C. Bierman, T. Laughlin, M. Tamura et al., "Niacinamide mitigates SASP-related inflammation induced by environmental stressors in human epidermal keratinocytes and skin," *International Journal of Cosmetic Science*, vol. 42, no. 5, pp. 501–511, 2020.

[9] X. Sun, X. Feng, D. Zheng et al., "Ergosterol attenuates cigarette smoke extract-induced COPD by modulating inflammation, oxidative stress and apoptosisin vitroandin vivo," *Clinical Science*, vol. 133, no. 13, pp. 1523–1536, 2019.

[10] S. Asgary, G. Naderi, and A. Ghannady, "Effects of cigarette smoke, nicotine and cotinine on red blood cell hemolysis and their -SH capacity," *Experimental and Clinical Cardiology*, vol. 10, no. 2, pp. 116–119, 2005.

[11] R. M. Johnson, Y. Ravindranath, M. S. ElAlfy, and G. Goyette Jr., "Oxidant damage to erythrocyte membrane in glucose-6-phosphate dehydrogenase deficiency: correlation with in vivo reduced glutathione concentration and membrane protein oxidation," *Blood*, vol. 83, no. 4, pp. 1117–1123, 1994.

[12] R. A. DeSimone, J. A. Hayden, C. A. Mazur et al., "Red blood cells donated by smokers: a pilot investigation of recipient transfusion outcomes," *Transfusion*, vol. 59, no. 8, pp. 2537–2543, 2019.

[13] D. Stefanoni, X. Fu, J. A. Reisz et al., "Nicotine exposure increases markers of oxidant stress in stored red blood cells from healthy donor volunteers," *Transfusion*, vol. 60, no. 6, pp. 1160–1174, 2020.

[14] T. Ramesh, C. Sureka, S. Bhuvana, and V. H. Begum, "Oxidative stress in the brain of cigarette smoke-induced noxiousness: neuroprotective role of Sesbania grandiflora," *Metabolic Brain Disease*, vol. 30, no. 2, pp. 573–582, 2015.

[15] R. M. Liu and L. P. Desai, "Reciprocal regulation of TGF-β and reactive oxygen species: a perverse cycle for fibrosis," *Redox Biology*, vol. 6, pp. 565–577, 2015.

[16] E. Birben, U. M. Sahiner, C. Sackesen, S. Erzurum, and O. Kalayci, "Oxidative stress and antioxidant defense," *World Allergy Organization Journal*, vol. 5, no. 1, pp. 9–19, 2012.

[17] M. Behdarvandy, M. Karimian, M. A. Atlasi, and A. Azami Tameh, "Heat shock protein 27 as a neuroprotective biomarker and a suitable target for stem cell therapy and pharmacotherapy in ischemic stroke," *Cell Biology International*, vol. 44, no. 2, pp. 356–367, 2020.

[18] T. H. Chen, O. M. Kuro, C. H. Chen et al., "The secreted Klotho protein restores phosphate retention and suppresses accelerated aging in Klotho mutant mice," *European Journal of Pharmacology*, vol. 698, no. 1-3, pp. 67–73, 2013.

[19] J. Maique, B. Flores, M. Shi et al., "High phosphate induces and klotho attenuates kidney epithelial senescence and fibrosis," *Frontiers in Pharmacology*, vol. 11, p. 1273, 2020.

[20] J. Miao, J. Huang, C. Luo et al., "Klotho retards renal fibrosis through targeting mitochondrial dysfunction and cellular senescence in renal tubular cells," *Physiological Reports*, vol. 9, no. 2, article e14696, 2021.

[21] J. Qiu, Y. N. Zhang, X. Zheng, P. Zhang, G. Ma, and H. Tan, "Notch promotes DNMT-mediated hypermethylation of Klotho leads to COPD-related inflammation," *Experimental Lung Research*, vol. 44, no. 7, pp. 368–377, 2018.

[22] H. C. Kau, S. B. Wu, C. C. Tsai, C. J. Liu, and Y. H. Wei, "Cigarette Smoke Extract-Induced Oxidative Stress and Fibrosis-Related Genes Expression in Orbital Fibroblasts from Patients with Graves' Ophthalmopathy," *Oxidative Medicine and Cellular Longevity*, vol. 2016, Article ID 4676289, 2016.

[23] Z. Yang and D. J. Klionsky, "Eaten alive: a history of macroautophagy," *Nature Cell Biology*, vol. 12, no. 9, pp. 814–822, 2010.

[24] S. Park, S. Kim, M. J. Kim et al., "GOLGA2 loss causes fibrosis with autophagy in the mouse lung and liver," *Biochemical and Biophysical Research Communications*, vol. 495, no. 1, pp. 594–600, 2018.

[25] K. Kawaoka, S. Doi, A. Nakashima et al., "Valproic acid attenuates renal fibrosis through the induction of autophagy," *Clinical and Experimental Nephrology*, vol. 21, no. 5, pp. 771–780, 2017.

[26] T. Kimura, Y. Takabatake, A. Takahashi et al., "Autophagy protects the proximal tubule from degeneration and acute

ischemic injury," *Journal of the American Society of Nephrology*, vol. 22, no. 5, pp. 902–913, 2011.

[27] A. Takahashi, T. Kimura, Y. Takabatake et al., "Autophagy guards against cisplatin-induced acute kidney injury," *The American Journal of Pathology*, vol. 180, no. 2, pp. 517–525, 2012.

[28] S. Liu, B. Hartleben, O. Kretz et al., "Autophagy plays a critical role in kidney tubule maintenance, aging and ischemia-reperfusion injury," *Autophagy*, vol. 8, no. 5, pp. 826–837, 2012.

[29] F. Belibi, I. Zafar, K. Ravichandran et al., "Hypoxia-inducible factor-1α (HIF-1α) and autophagy in polycystic kidney disease (PKD)," *American Journal of Physiology. Renal Physiology*, vol. 300, no. 5, pp. F1235–F1243, 2011.

[30] F. Riediger, I. Quack, F. Qadri et al., "Prorenin receptor is essential for podocyte autophagy and survival," *Journal of the American Society of Nephrology*, vol. 22, no. 12, pp. 2193–2202, 2011.

[31] C. T. Chien, S. K. Shyue, and M. K. Lai, "Bcl-xL augmentation potentially reduces ischemia/reperfusion induced proximal and distal tubular apoptosis and autophagy," *Transplantation*, vol. 84, no. 9, pp. 1183–1190, 2007.

[32] L. E. Fuess, C. J. Pinzon, E. Weil, R. D. Grinshpon, and L. D. Mydlarz, "Life or death: disease-tolerant coral species activate autophagy following immune challenge," *Proceedings of the Biological Sciences*, vol. 284, no. 1856, article 20170771, 2017.

[33] H. P. Kim, X. Wang, Z. H. Chen et al., "Autophagic proteins regulate cigarette smoke-induced apoptosis: protective role of heme oxygenase-1," *Autophagy*, vol. 4, no. 7, pp. 887–895, 2008.

[34] N. Vij, P. Chandramani-Shivalingappa, C. Van Westphal, R. Hole, and M. Bodas, "Cigarette smoke-induced autophagy impairment accelerates lung aging, COPD-emphysema exacerbations and pathogenesis," *American Journal of Physiology. Cell Physiology*, vol. 314, no. 1, pp. C73–C87, 2018.

[35] P. Bagam, G. Kaur, D. P. Singh, and S. Batra, "In vitro study of the role of FOXO transcription factors in regulating cigarette smoke extract-induced autophagy," *Cell Biology and Toxicology*, vol. 37, no. 4, pp. 531–553, 2021.

[36] C. Pei, X. Wang, Y. Lin, L. Fang, and S. Meng, "Inhibition of galectin-3 alleviates cigarette smoke extract-induced autophagy and dysfunction in endothelial progenitor cells," *Oxidative Medicine and Cellular Longevity*, vol. 2019, Article ID 7252943, 2019.

[37] C. Xu, L. Wang, P. Fozouni et al., "SIRT1 is downregulated by autophagy in senescence and ageing," *Nature Cell Biology*, vol. 22, no. 10, pp. 1170–1179, 2020.

[38] K. Matsuo, K. Hosoda, J. Tanaka et al., "Abstract WP342: activate the pentose phosphate pathway to reduce the cerebral ischemia/reperfusion injury: the impact of heat shock protein 27 phosphorylation," *Stroke*, vol. 50, article AWP342, Suppl_1, 2019.

[39] R. C. Stanton, "Glucose-6-phosphate dehydrogenase, NADPH, and cell survival," *IUBMB Life*, vol. 64, no. 5, pp. 362–369, 2012.

[40] Y. Wei, R. Wang, and J. Teng, "Inhibition of calcium/calmodulin-dependent protein kinase IIα suppresses oxidative stress in cerebral ischemic rats through targeting glucose 6-phosphate dehydrogenase," *Neurochemical Research*, vol. 44, no. 7, pp. 1613–1620, 2019.

[41] A. S. Levey and M. T. James, "Acute kidney injury," *Annals of Internal Medicine*, vol. 167, no. 9, pp. ITC66–ITC80, 2017.

[42] J. Xia, L. Wang, Z. Ma et al., "Cigarette smoking and chronic kidney disease in the general population: a systematic review and meta-analysis of prospective cohort studies," *Nephrology, Dialysis, Transplantation*, vol. 32, no. 3, pp. 475–487, 2017.

[43] W. Jo, S. Lee, Y. S. Joo et al., "Association of smoking with incident CKD risk in the general population: a community-based cohort study," *PLoS One*, vol. 15, no. 8, article e0238111, 2020.

[44] C. Pelaia, D. Pastori, G. Armentaro et al., "Predictors of renal function worsening in patients with chronic obstructive pulmonary disease (COPD): a multicenter observational study," *Nutrients*, vol. 13, no. 8, p. 2811, 2021.

[45] S. Bandiera, R. R. Pulcinelli, F. Huf et al., "Hepatic and renal damage by alcohol and cigarette smoking in rats," *Toxicology Research*, vol. 37, no. 2, pp. 209–219, 2021.

[46] Y. L. Wang, Y. H. Lee, Y. H. Hsu et al., "The kidney-related effects of polystyrene microplastics on human kidney proximal tubular epithelial cells HK-2 and male C57BL/6 mice," *Environmental Health Perspectives*, vol. 129, no. 5, p. 57003, 2021.

[47] C. Wright, "Standardized methods for the regulation of cigarette-smoke constituents," *TrAC Trends in Analytical Chemistry*, vol. 66, pp. 118–127, 2015.

[48] P. Ewels, M. Magnusson, S. Lundin, and M. Kaller, "MultiQC: summarize analysis results for multiple tools and samples in a single report," *Bioinformatics*, vol. 32, no. 19, pp. 3047-3048, 2016.

[49] A. M. Bolger, M. Lohse, and B. Usadel, "Trimmomatic: a flexible trimmer for Illumina sequence data," *Bioinformatics*, vol. 30, no. 15, pp. 2114–2120, 2014.

[50] D. Kim, B. Langmead, and S. L. Salzberg, "HISAT: a fast spliced aligner with low memory requirements," *Nature Methods*, vol. 12, no. 4, pp. 357–360, 2015.

[51] S. M. E. Sahraeian, M. Mohiyuddin, R. Sebra et al., "Gaining comprehensive biological insight into the transcriptome by performing a broad-spectrum RNA-seq analysis," *Nature Communications*, vol. 8, no. 1, p. 59, 2017.

[52] Y. Liao, G. K. Smyth, and W. Shi, "featureCounts: an efficient general purpose program for assigning sequence reads to genomic features," *Bioinformatics*, vol. 30, no. 7, pp. 923–930, 2014.

[53] A. Subramanian, P. Tamayo, V. K. Mootha et al., "Gene set enrichment analysis: a knowledge-based approach for interpreting genome-wide expression profiles," *Proceedings of the National Academy of Sciences of the United States of America*, vol. 102, no. 43, pp. 15545–15550, 2005.

[54] L. Mele, F. Paino, F. Papaccio et al., "A new inhibitor of glucose-6-phosphate dehydrogenase blocks pentose phosphate pathway and suppresses malignant proliferation and metastasis in vivo," *Cell Death & Disease*, vol. 9, no. 5, p. 572, 2018.

[55] X. Y. Chen, Y. Y. Chen, W. Lin et al., "Effects of human umbilical cord-derived mesenchymal stem cells on the acute cigarette smoke-induced pulmonary inflammation model," *Frontiers in Physiology*, vol. 11, p. 962, 2020.

[56] Y. H. Hsu, H. C. Chuang, Y. H. Lee et al., "Induction of fibrosis and autophagy in kidney cells by vinyl chloride," *Cell*, vol. 8, no. 6, p. 601, 2019.

[57] R. K. Thapa, H. T. Nguyen, J. H. Jeong et al., "Progressive slowdown/prevention of cellular senescence by CD9-targeted delivery of rapamycin using lactose-wrapped calcium carbonate nanoparticles," *Scientific Reports*, vol. 7, no. 1, p. 43299, 2017.

[58] D. Silva, M. Caceres, R. Arancibia, C. Martinez, J. Martinez, and P. C. Smith, "Effects of cigarette smoke and nicotine on cell viability, migration and myofibroblastic differentiation," *Journal of Periodontal Research*, vol. 47, no. 5, pp. 599–607, 2012.

[59] J. S. Bourgeois, J. Jacob, A. Garewal, R. Ndahayo, and J. Paxson, "The bioavailability of soluble cigarette smoke extract is reduced through interactions with cells and affects the cellular response to CSE exposure," *PLoS One*, vol. 11, no. 9, article e0163182, 2016.

[60] A. A. Dera, M. Al Fayi, H. Otifi, M. Alshyarba, M. Alfhili, and P. Rajagopalan, "Thymoquinone (Tq) protects necroptosis induced by autophagy/mitophagy- dependent oxidative stress in human bronchial epithelial cells exposed to cigarette smoke extract (CSE)," *Journal of Food Biochemistry*, vol. 44, no. 9, article e13366, 2020.

[61] E. S. Son, S. H. Kim, S. W. Ryter et al., "Quercetogetin protects against cigarette smoke extract-induced apoptosis in epithelial cells by inhibiting mitophagy," *Toxicology In Vitro*, vol. 48, pp. 170–178, 2018.

[62] G. Luo, Z. Jian, Y. Zhu et al., "Sirt1 promotes autophagy and inhibits apoptosis to protect cardiomyocytes from hypoxic stress," *International Journal of Molecular Medicine*, vol. 43, no. 5, pp. 2033–2043, 2019.

[63] A. Sathyanarayan, M. T. Mashek, and D. G. Mashek, "ATGL promotes autophagy/lipophagy via SIRT1 to control hepatic lipid droplet catabolism," *Cell Reports*, vol. 19, no. 1, pp. 1–9, 2017.

[64] D. Liang, Y. Zhuo, Z. Guo et al., "SIRT1/PGC-1 pathway activation triggers autophagy/mitophagy and attenuates oxidative damage in intestinal epithelial cells," *Biochimie*, vol. 170, pp. 10–20, 2020.

[65] R. Sangani, A. Ghio, S. Culp, Z. Patel, and S. Sharma, "Combined pulmonary fibrosis emphysema: role of cigarette smoking and pulmonary hypertension in a rural cohort," *International Journal of Chronic Obstructive Pulmonary Disease*, vol. Volume 16, pp. 1873–1885, 2021.

[66] P. Devarajan, "Update on mechanisms of ischemic acute kidney injury," *J Am Soc Nephrol*, vol. 17, no. 6, pp. 1503–1520, 2006.

[67] A. Leask and D. J. Abraham, "TGF-beta signaling and the fibrotic response," *The FASEB Journal*, vol. 18, no. 7, pp. 816–827, 2004.

[68] R. Samarakoon, J. M. Overstreet, and P. J. Higgins, "TGF-β signaling in tissue fibrosis: redox controls, target genes and therapeutic opportunities," *Cellular Signalling*, vol. 25, no. 1, pp. 264–268, 2013.

[69] J. R. Montford and S. B. Furgeson, "A new CTGF target in renal fibrosis," *Kidney International*, vol. 92, no. 4, pp. 784–786, 2017.

[70] J. S. Park, I. A. Jung, H. S. Choi et al., "Anti-fibrotic effect of 6-bromo-indirubin 3′-oxime (6-BIO) via regulation of activator protein-1 (AP-1) and specificity protein-1 (SP-1) transcription factors in kidney cells," *Biomedicine & Pharmacotherapy*, vol. 145, no. 5, article 112402, 2022.

[71] J. Wang, T. Chen, X. Yu et al., "Identification and validation of smoking-related genes in lung adenocarcinoma using an in vitro carcinogenesis model and bioinformatics analysis," *Journal of Translational Medicine*, vol. 18, no. 1, p. 313, 2020.

[72] G. Mahnaz, Q. Farshad, F. Mohammad Hosein, M. Fariba, Y. Namdar, and J. Tanuj, "Inflammation, oxidative stress, insulin resistance, and hypertension as mediators for adverse effects of obesity on the brain: a review," *Biomedicine*, vol. 11, no. 4, pp. 13–22, 2021.

[73] Y. Xu, B. W. Osborne, and R. C. Stanton, "Diabetes causes inhibition of glucose-6-phosphate dehydrogenase via activation of PKA, which contributes to oxidative stress in rat kidney cortex," *American Journal of Physiology. Renal Physiology*, vol. 289, no. 5, pp. F1040–F1047, 2005.

[74] M. A. Pabon, E. Patino, D. Bhatia et al., "Beclin-1 regulates cigarette smoke-induced kidney injury in a murine model of chronic obstructive pulmonary disease," *JCI Insight*, vol. 3, no. 18, article e99592, 2018.

Hindawi
Oxidative Medicine and Cellular Longevity
Volume 2022, Article ID 8200189, 16 pages
https://doi.org/10.1155/2022/8200189

Research Article

GSPE Protects against Bleomycin-Induced Pulmonary Fibrosis in Mice via Ameliorating Epithelial Apoptosis through Inhibition of Oxidative Stress

Ok Joo Sul,[1] **Jin Hyoung Kim**,[2] **Taehoon Lee**,[2] **Kwang Won Seo**,[2] **Hee Jeong Cha**,[3] **Byungsuk Kwon**,[4] **Jong-Joon Ahn**,[2] **You Sook Cho**,[5] **Yeon-Mok Oh**,[6] **Yangjin Jegal**,[2] **and Seung Won Ra**[2]

[1]*Biomedical Research Center, Ulsan University Hospital, School of Medicine, University of Ulsan, Ulsan 44033, Republic of Korea*
[2]*Department of Pulmonary and Critical Care Medicine, Ulsan University Hospital, University of Ulsan College of Medicine, Ulsan 44033, Republic of Korea*
[3]*Department of Pathology, Ulsan University Hospital, University of Ulsan College of Medicine, Ulsan 44033, Republic of Korea*
[4]*School of Biological Science, University of Ulsan, Ulsan 44610, Republic of Korea*
[5]*Department Allergy and Clinical Immunology, Asan Medical Center, University of Ulsan College of Medicine, Seoul 05505, Republic of Korea*
[6]*Department of Pulmonary and Critical Care Medicine, Asan Medical Center, University of Ulsan College of Medicine, Seoul 05505, Republic of Korea*

Correspondence should be addressed to Yangjin Jegal; yjjegal@gmail.com and Seung Won Ra; docra@docra.pe.kr

Received 7 January 2022; Accepted 2 March 2022; Published 20 March 2022

Academic Editor: Yingqing Chen

Idiopathic pulmonary fibrosis (IPF) is a chronic, progressive interstitial lung disease of unknown cause which leads to alveolar epithelial cell apoptosis followed by basement membrane disruption and accumulation of extracellular matrix, destroying the lung architecture. Oxidative stress is involved in the development of alveolar injury, inflammation, and fibrosis. Oxidative stress-mediated alveolar epithelial cell (AEC) apoptosis is suggested to be a key process in the pathogenesis of IPF. Therefore, the present study investigated whether grape seed proanthocyanidin extract (GSPE) could inhibit the development of pulmonary fibrosis via ameliorating epithelial apoptosis through the inhibition of oxidative stress. We found that GSPE significantly ameliorated the histological changes and the level of collagen deposition in bleomycin (BLM)-induced lungs. Moreover, GSPE attenuated lung inflammation by reducing the total number of cells in bronchoalveolar lavage (BAL) fluid and decreasing the expression of IL-6. We observed that the levels of H_2O_2 leading to oxidative stress were increased following BLM instillation, which significantly decreased with GSPE treatment both *in vivo* and *in vitro*. These findings showed that GSPE attenuated BLM-induced epithelial apoptosis in the mouse lung and A549 alveolar epithelial cell through the inhibition of oxidative stress. Furthermore, GSPE could attenuate mitochondrial-associated cell apoptosis via decreasing the Bax/Bcl-2 ratio. The present study demonstrates that GSPE could ameliorate bleomycin-induced pulmonary fibrosis in mice via inhibition of epithelial apoptosis through the inhibition of oxidative stress.

1. Introduction

Idiopathic pulmonary fibrosis (IPF) is a chronic, progressive interstitial lung disease of unknown cause and is characterized by scarring of interstitial lung tissue and decline in lung function, leading eventually to respiratory failure. The prevalence of IPF is estimated at 13 to 20 cases per 100,000 people per year with a median survival of 3 to 5 years after diagnosis. The prognosis of IPF is significantly worse than in many interstitial lung diseases, and no curable treatments for IPF exist.

Studies have reported the association between genetic, infectious, and environmental factors, such as smoking and pollutants, gastroesophageal reflux disease and aging, and the development of IPF. The mechanism by which these factors influence the pathogenesis of IPF is not fully known. Previously, it has been proposed that IPF is an inflammatory response that eventually leads to chronic lung injury with fibrosis. However, it has recently been suggested that progressive fibrosis involves damage to alveolar epithelial cells (AECs), activation of fibroblasts followed by abnormal wound recovery that leads to fibrosis. Alveolar epithelial damage is the characteristic feature of IPF, in which AEC injury is a significant initial event [1–3].

The production of reactive oxygen species (ROS) is increased under conditions such as exposure to air pollutants and cigarette smoke. ROS is generated by activated macrophages and neutrophils during acute inflammatory reactions and plays an important role as an antibacterial and anticancer. However, continuous ROS exposure may lead to cell damage through the oxidation of DNA, RNA, carbohydrates, proteins, and lipids. There have been many studies showing that an imbalance between oxidants and antioxidants participates in the pathophysiology of IPF and that ROS causes damage to AECs, resulting ultimately in apoptosis. Daniil et al. showed that serum oxidative stress was significantly increased in patients with IPF compared with healthy controls [4], and there are significant correlations between the levels of systemic oxidative stress and disease severity in IPF and the levels of dyspnea.

N-Acetylcysteine, an antioxidant drug, was reported to decrease inflammation and collagen deposition in a mouse model of bleomycin- (BLM-) induced lung fibrosis [5]. However, beneficial effects of NAC on IPF patients have not been demonstrated [6]. The different doses of NAC, the length of time following treatment, or samples from different ethnic origins can be the causes of different results. Oldham et al. recently reported that the efficacy of NAC on IPF patients may be associated with genotype characteristics, suggesting that NAC had a beneficial effect in a subgroup of IPF patients [7].

Grape seed proanthocyanidin extract (GSPE), a flavonoid compound extracted from grape seeds, consists of catechin and epicatechin that form oligomers or polymers. GSPE has various pharmacological properties such as anticarcinogenic [8], antiallergic [9], anti-inflammatory [10], antihypertensive [11], and antiviral activities [12]. Furthermore, GSPE is revealed to be a more effective antioxidant than ascorbic acid and α-tocopherol *in vitro* and *in vivo* [13]. Recent studies on GSPE have also reported that GSPE prevents amiodarone-induced lung toxicity [14].

BLM is a chemotherapeutic antibiotic that is used as an anticancer agent but is identified as a profibrotic agent due to it inducing pulmonary fibrosis as a side effect. The model of BLM-induced lung fibrosis is extensively used as an animal model for studying the mechanisms of IPF, as it is easy to perform and is reproducible. BLM causes pulmonary injury, inflammation, and subsequent fibrosis, and ROS generated in response to BLM is involved in the mechanism driving fibrosis in this model [15].

We investigated whether GSPE attenuates BLM-induced ROS production and inflammation levels, resulting in alleviation of epithelial cell apoptosis and eventually fibrosis.

2. Materials and Methods

2.1. Animal Experiments. Specific pathogen-free (SPF) 8-week-old female C57BL/6 mice, weighing between 18 and 20 g, were purchased from Orient Bio Inc. (Daejeon, Korea). The mice were housed in SPF animal facility and used after 1 week of acclimatization. Experiments were approved by the Institutional Animal Care and Use Committee (IACUC) of Ulsan University.

After one week of acclimation, the mice were randomly divided into five groups ($n = 6$ per group) as follows: after 24 h of inoculation, mice were exposed for 6 days as follows: Experiment #1, (1) PBS (IT)+PBS (IP) group: mice treated with normal saline; (2) BLM (IT)+PBS (IP) group: mice injected with 2 mg/kg of BLM (IT) and PBS (IP); (3) PBS (IT)+GSPE(IP) group: mice injected with PBS (IT) and 90 mg/kg of GSPE; (4–6) BLM (IT)+GSPE (IP, 30, 60, and 90 mg/kg) group: mice treated with 2 mg/kg of BLM and 30, 60, and 90 mg/kg of GSPE; Experiment #2, (1) PBS (IT)+PBS (PO) group: mice treated with normal saline; (2) BLM (IT)+PBS (PO) group: mice injected with 2 mg/kg of BLM and PBS (PO); (3) PBS (IT)+GSPE (PO) group: mice injected with PBS (IT) and 100 mg/kg of GSPE; (4–6) BLM (IT)+GSPE (PO, 50, 100, and 150 mg/kg) group: mice treated with 2 mg/kg of BLM and 50, 100, and 150 mg/kg of GSPE.

2.2. Reagents and Antibodies. TNF-α, interleukin-1 β (IL-1β), and IL-6 enzyme-linked immunosorbent assay (ELISA) kits were purchased from BD Biosciences (Cambridge, MA, USA). BLM was purchased from Nippon Kayaku Co. (Ltd., Tokyo, Japan), and GSPE was obtained from SANOFI Co. (Paris, France). Antibody against cPARP (ab32064) was purchased from Abcam (Cambridge, MA, USA). Antibodies against cytokeratin pan (MA5-12231) were obtained from Invitrogen (San Diego, CA, USA). Secondary antibodies tagged with Alexafluor 594 (ab150116) and with Alexafluor 488 (ab150077) were purchased from Abcam. Antibodies against PARP (9532), cleaved caspase-3 (9661), cytochrome c (11940), Bcl-2 (3498), Bax (2772), and Bak (12105) were obtained from Santa Cruz Biotechnology (Santa Cruz, CA, USA). β-Actin (A5441) was purchased from Invitrogen and used as internal controls. Horseradish peroxidase-(HRP-) labeled secondary anti-mouse (7076) and anti-rabbit (7074) antibodies were purchased from Cell Signaling Technology (Danvers, MA, USA). CM-H_2DCFDA and MitoSOX Red were obtained from Invitrogen (San Diego, CA, USA). FITC Annexin V Apoptosis Detection Kit I was purchased from BD Biosciences (San Jose, CA, USA). Hoechst 33342 and MTT (3-(4, 5-dimethylthiazol-2-yl)-2, 5-diphenyltetrazolium bromide) were obtained from Sigma Chemical (St. Louis, MO, USA). M-MLV reverse transcriptase was obtained from Promega (Madison, WI, USA). SYBR Green Real-Time PCR Master Mix was obtained from

Enzynomics (Daejeon, South Korea). QIAzol reagent was purchased from Qiagen (Hilden, Germany).

2.3. Induction of Lung Injury by BLM. Mice were administered a single dose of 2 mg/kg BLM (Nippon Kayaku Co., Ltd., Tokyo) or saline intratracheally. Intraperitoneal (IP) or per oral (PO) administration of GSPE was performed daily starting at day -4 before BLM (day 0) and lasting 5 times weekly for 3 weeks. All mice were sacrificed 21 days after BLM administration.

2.4. Histological Analysis and Ashcroft Scoring. Lung tissues were fixed in 4% paraformaldehyde and dehydrated with graded ethanol. After embedding in paraffin, the sections (4 μm) were prepared and stained with hematoxylin and eosin (H&E) and Masson's trichrome (MT). Lung fibrosis was calculated by semiquantitative analysis of H&E and MT staining using the Ashcroft scoring system as previously described [16]. To quantify the severity of interstitial fibrosis in lung histopathology, each successive field was given a score ranging from 0 (normal lung) to 8 (total fibrous obliteration of the field).

2.5. Hydroxyproline Assay. The procedure for quantitation of lung hydroxyproline was performed as previously described [17]. Briefly, whole lung tissue was washed in PBS and hydrolyzed for 18 h in 6 N HCl at 110°C. The pH was adjusted to 6.0 with NaOH titration. The samples were centrifuged, and the pellets were oxidized with chloramine T for 30 minutes. p-Dimethylaminobenzaldehyde was added to each sample, and the samples were incubated at 65°C for 15 minutes. The absorbance was measured at 560 nm on a spectrophotometer. Lung hyroxyproline was quantitated with a standard curve of purified hydroxyproline (Sigma, St. Louis, MO), and the values were corrected for total lung wet weight.

2.6. Bronchoalveolar Lavage and Cell Count. On day 7 after BLM administration, bronchoalveolar lavage fluid (BALF) was collected by washing of the lung with an initial 800 μl of sterile PBS, followed by eight 500 μl PBS washes. The fluid was centrifuged, and the supernatant of the first BAL was used for the determination of cytokines. The cell pellet was resuspended in 1 ml of PBS, and the cell number was counted using a hemocytometer.

2.7. Immunohistochemical Analysis. From paraffin-embedded lung tissues, 4 μm thick sections were prepared and mounted on glass slides. The sections are deparaffinized with xylene three times each for 15 min and then rehydrated with decreasing alcohol concentrations (100-70%) for 5 min. The protease-induced antigen retrieval was performed, and blocking buffer was added. Next, the slides were incubated overnight at 4°C with anti-PARP p85 fragment polyclonal antibody (Cell Signaling Technology, Danvers, MA, USA), followed by incubation with FITC-conjugated Goat Anti-rabbit IgG secondary antibody (Santa Cruz Biotechnology, Dallas, Texas, USA), and incubated with anti-pan cytokeratin monoclonal antibody PE (Santa Cruz Biotechnology, Dallas, Texas, USA).

2.8. RNA Isolation, Purification, and Quantitative Real-Time PCR. Total RNA was extracted from lung tissue samples and cultured A549 cells using TRIZOL reagent. Then, cDNA was synthesized from 1 μg of total RNA using oligo (dT) primers and M-MLV reverse transcriptase. Quantitative PCR was performed using SYBR Green qPCR Master Mix and the appropriate primers on an ABI 7500 Fast Real-Time PCR System (Applied Biosystems, Carlsbad, CA, USA). The housekeeping gene 18S rRNA (RPS) was amplified in parallel with the genes of interest. The following primers were used: Relative expression standardized to RPS was calculated using the comparative cycle threshold method ($2^{-\Delta\Delta Ct}$). The primer sequences used were as follows: 5′-GTGCTCGGCTT CCCGTGCAAC-3′ and 5′-CTCGAA GAGCATGAAGT TGGGC-3′ (GPX); 5′-CTGCCAAGTGATTGGTGCTTC TG-3′ and 5′-AATGGTGCGCTTCGG GTCTGAT-3′ (PRDX); 5′-CAAATGCATGCCGACCTTCCAG-3′ and 5′ -GCTGGTTACACTTTTCAGAGCATG-3′ (TRX); 5′-CAAGGAAGCACATGACCGAGCA-3′ and 5′-CTTGTT GCGGTCCATTTCCTC-3′ (RPS).

2.9. Measurement of Cytokines. For cytokine measurements, whole lung tissue was homogenized in 10 volumes (w/v) of ice-cold PBS containing protease inhibitors. Homogenates were centrifuged at 12,000 × g at 4°C for 5 min, and the supernatants were collected for analysis. The levels of TNF-α, IL-1β, and IL-6 were measured by ELISAs according to the manufacturer's instructions (R&D Systems).

2.10. Cell Culture. Human alveolar epithelial A549 cells (KCLB, Seoul, Korea) were grown in RPMI 1640 medium (Welgene, Daegu, Korea) supplemented with 10% FBS and 1% penicillin-streptomycin solution at 37°C in a humidified atmosphere with 5% CO_2. A549 cells were pretreated with GSPE (1 μg/ml) for 4 h and then stimulated with BLM (1 μg/ml) for an additional 40 h.

2.11. Western Blot Analysis. Lung tissue samples were homogenized in extraction buffer (50 mM Tris-HCl, pH 8.0, 150 mM NaCl, 1 mM EDTA, 0.5% Nonidet P-40, 0.01% protease inhibitor mixture). After centrifugation for 20 min at 100,000 × g, the supernatants were recovered. A549 cells were harvested and treated with the extraction buffer after washing with PBS. Typically, 20 μg of protein per lane was loaded on SDS-PAGE and transferred onto the nitrocellulose membrane. The membranes were blocked for 1 h with 5% skim milk in Tris-buffered saline containing 0.05% Tween 20 (TBST) and were incubated overnight at 4°C with primary antibodies against PARP, cleaved PARP, cleaved caspase-3, cytochrome c, Bax, Bak, Bcl-2, and β-actin. After washing with TBST, the membrane was incubated for 1 h with HRP-conjugated secondary antibodies and developed using chemiluminescence HRP substrates.

2.12. Measurement of Reactive Oxygen Species (ROS). Whole lung tissue was homogenized in ice-cold PBS containing protease inhibitors. Homogenates were centrifuged, and the resulting supernatants were used for the assay. H_2O_2 levels in homogenates were measured using a hydrogen

peroxide assay kit (Cell BioLabs, San Diego, CA) according to the manufacturer's protocol. Briefly, 25 μl of sample or diluted H_2O_2 standards was added to 96-well plates, mixed with 25 μl of working solution, and incubated for 30 min at room temperature. Absorbance was monitored at 540 nm, and H_2O_2 concentrations were determined using the standard curve.

To measure intracellular ROS, A549 cells were pretreated with GSPE (1 μg/ml) for 4 h and then stimulated with BLM (1 μg/ml) for an additional 24 h. Then, the cells were rinsed briefly in PBS and incubated with culture medium containing 5 μM CM-H_2DCFDA at 37°C for 30 min in the dark. Fluorescence was detected by flow cytometry (FACSCanto II), and the data were analyzed by FlowJo V10 software (Tree Star Inc., San Carlos, CA).

To perform mitochondrial ROS (mtROS) measurements, A549 cells were pretreated with GSPE (1 μg/ml) for 4 h and then stimulated with BLM (1 μg/ml) for an additional 24 h. After treatment, the cells were stained with MitoSOX Red (5 μM) for 30 min and then washed three times with PBS. mtROS was assessed by using flow cytometry, and the data were analyzed by FlowJo V10.

2.13. Cell Viability Assay. Cell viability was determined by MTT assay. A549 cells were seeded in a 96-well plate at 3 $\times 10^4$ cells per well and were allowed to grow to 80% confluency. The cells were then pretreated with GSPE at various concentrations (0, 0.5, 1, 5, 10, and 20 μg/ml) for 4 h and stimulated with or without BLM at different concentrations (0, 0.5, 1, 10, 20, and 40 μg/ml). Next, the cells were incubated with 0.5 mg/ml of thiazolyl blue tetrazolium bromide for 3 h. The MTT was removed, and 100 μlL of dimethylformamide (DMSO) was added. Then, the optical densities of the samples were read at 540 nm on a spectrophotometer.

2.14. Apoptosis Assay. The A549 cells were harvested, washed twice with cold PBS, and resuspended in 100 μl annexin binding buffer. The cells were then stained for 15 min at RT in the dark with 5 μl FITC-conjugated annexin V and 5 μl propidium iodide (PI) using the FITC-Annexin V Apoptosis Detection Kit (BD Bioscience, Heidelberg, Germany), according to the manufacturer's instructions, and analyzed by flow cytometry.

2.15. Statistics. Values are expressed as means ± SEM. Each series of experiments was repeated at least three times. Since the sample means are normally distributed, the one-way ANOVA was used for more than two groups' comparison, followed by Bonferroni posttests. The *t*-test method was used for a two-group comparison. The statistical analysis was performed using GraphPad Prism 5 (GraphPad Prism Software Inc., CA, USA) and SPSS 24.0 (SPSS, Inc., IL, USA). A p value < 0.05 was considered statistically significant.

3. Results

3.1. GSPE Attenuated BLM-Induced Lung Fibrosis. To investigate the effect of GSPE on the pathogenesis of lung fibrosis, we established a BLM-induced lung fibrosis mouse model (Figure 1(a)). Mice were treated with GSPE (IP or PO) or saline from -4 days for 25 days before intratracheal administration of BLM to induce lung fibrosis on 0 days. For histopathological analysis, lung sections were stained with hematoxylin and eosin (H&E) and Masson's trichrome (MT). Interestingly, we observed that peribronchial interstitial infiltration with inflammatory cells and alveolar edema was increased in the BLM-treated group (Figures 1(a) and 1(b)). However, treatment with GSPE attenuated these BLM-induced lung lesions (Figure 1(b), left), as shown by the H&E-stained lung sections. Furthermore, histological sections stained with Masson's trichrome showed that increased interstitial collagen was present in the BLM-treated group in Figure 1(d). However, administration of GSPE alleviated the interstitial collagen in the lung induced by BLM (Figure 1(b), right). In addition, the fibrosis scores of lung fibrosis in the BLM-treated group were significantly higher than those in PBS- and GSPE-treated control groups. In contrast, the Ashcroft scores of lung fibrosis were lower in both the BLM+IP GSPE and BLM+PO GSPE groups in a dose-dependent manner compared with the BLM+PBS group (Figure 1(c).

To assess whether GSPE reduced the level of collagen deposition in BLM-induced lung, we next measured the lung hydroxyproline content, a fibrotic marker of deposited collagen on day 21. Consistent with the histopathological results of Masson's trichrome staining, we found that the lung hydroxyproline content was considerably elevated in the BLM group compared with the PBS-treated control mice. However, the BLM+IP GSPE group exhibited a marked reduction of hydroxyproline content compared with the BLM+PBS group (55.3, 51.9, and 50.4 vs. 62.9 μg/ml). (Figure 1(d)). In addition, to determine the effects of GSPE on the expression of fibrogenic cytokines, we measured the expression of TGF-β in the lungs at days 7 and 21 after BLM instillation. We observed that the protein levels of TGF-β increased at day 21 but that GSPE treatment substantially reduced the fibrogenic cytokine at 21 days (Figure 1(e)). Taken together, these results indicate that GSPE significantly improves lung fibrosis-triggered BLM.

3.2. GSPE Attenuates BLM-Induced Lung Inflammation. To evaluate the effect of GSPE on initial lung inflammation induced by BLM, we determined the total number of cells in BALF at day 7 of BLM instillation. Consistent with the H&E staining results, the total number of cells in the BLM-treated group was significantly higher than in the PBS-treated control group. However, treatment of BLM-induced mice with 90 mg/kg GSPE dramatically decreased total cell numbers when compared to the BLM+PBS group (Figure 2(a)). As expected, the administration of BLM increased the levels of TNF-α and IL-1β on days 3 and 7 and IL-6 on days 3, 7, and 21. We next measured whether GSPE reduces the BLM-induced increases in proinflammatory cytokines in the lung tissue. Interestingly, GSPE significantly attenuated the expression of IL-6 on days 3 and 7 (Figure 1(e)) but had no difference in the levels of TNF-α and IL-1ß. These data showed that GSPE attenuated lung inflammation via reducing the numbers of total cells,

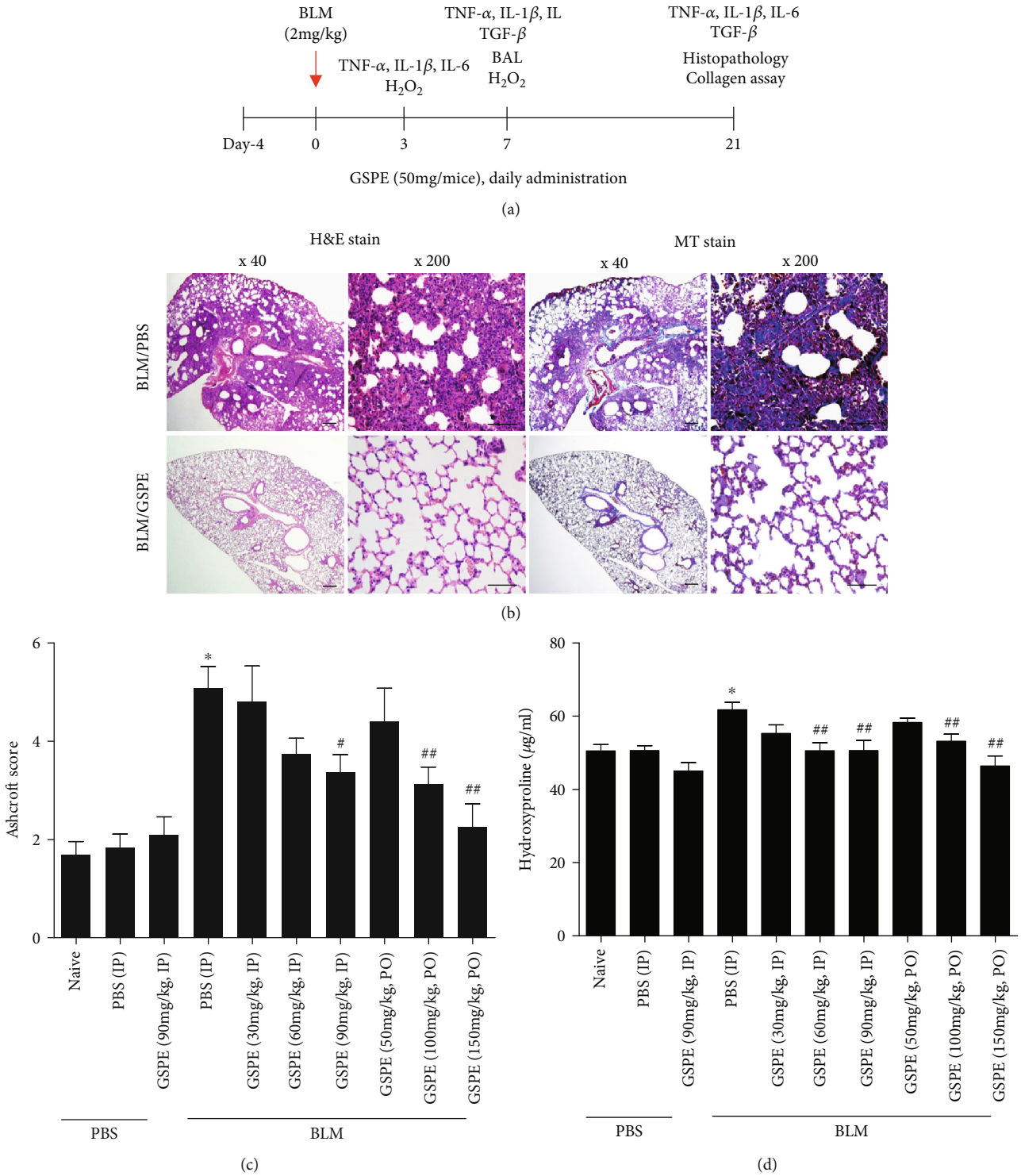

Figure 1: Continued.

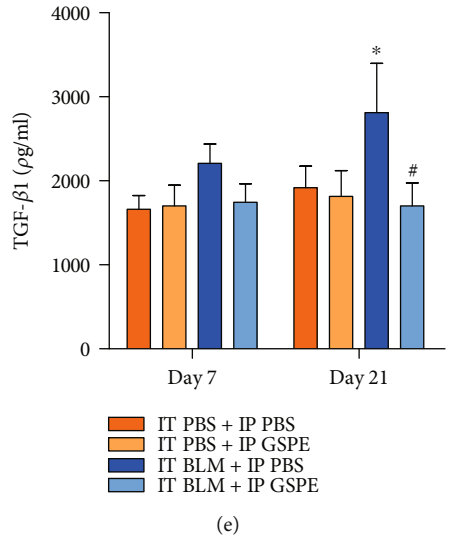

(e)

Figure 1: Grape seed proanthocyanidin extract (GSPE) attenuated bleomycin- (BLM-) induced lung fibrosis. (a) Experimental protocol for bleomycin-induced pulmonary fibrosis and timetable for drug administration or sampling. Intraperitoneal (IP) or peroral (PO) administration of GSPE started from day 4 to day 21. Administration of intratracheal (IT) BLM on day 0. Sampling for cytokines, H_2O_2 and collagen bioassay, immunohistochemistry (IHC), and bronchoalveolar lavage (BAL) at different time points. (b) Representative photomicrographs of lung pathology in the BLM+PBS group and BLM+GSPE group at 21 days post-BLM. Left shows that lung sections are stained with hematoxylin–eosin. A marked peribronchial interstitial infiltration of inflammatory cells and alveolar edema are present in PBS-treated animals. Treatment with GSPE attenuated these pulmonary lesions. Right shows lung sections stained with Masson trichrome at 21 days post-BLM. BLM caused a significant increase in the interstitial collagen of the lung. The interstitial collagen in the lung was diminished by treatment with GSPE. Original magnifications, ×40 and ×200. Scale bars, 200 μm and 100 μm. (c) Ashcroft scores in experimental groups. Treatment with GSPE reduced the Ashcroft score in a dose-dependent manner. (d) Hydroxyproline levels in experimental groups. Treatment with GSPE reduced lung content of hydroxyproline in a dose-dependent manner. (e) Expression of fibrogenic cytokine, TGF-β1. Intratracheal (IT) administration of BLM-induced increased levels of TGF-β1 on day 21. Compared with the BLM+PBS treatment group, the level of TGF-β1 was significantly lower in the BLM+GSPE treatment group on day 21. Data are expressed as the mean ± SEM ($n = 4$–6 per group) and are representative of three to five independent experiments. $^{\#}p < 0.01$ versus the IT PBS+IP PBS group. $^{*}p < 0.05$ and $^{**}p < 0.01$ versus the IT BLM (bleomycin)+IP PBS group.

macrophages, neutrophils, and lymphocytes and decreasing the expression of IL-6 (Figure 2(b)).

3.3. GSPE Attenuates BLM-Induced Oxidative Damage In Vivo and In Vitro. Previous studies have shown that oxidative stress plays a major role in BLM-induced lung fibrosis. To evaluate whether GSPE inhibited BLM-induced oxidative damage *in vivo*, we measured ROS generation at day 3 of BLM instillation. The levels of H_2O_2 were increased by BLM on day 3 compared to those of the PBS-treated controls. However, the BLM+GSPE group ameliorated the levels of H_2O_2 compared to the BLM+vehicle group, suggesting that GSPE considerably prevented BLM-induced oxidative stress (Figure 3(a)). Next, to evaluate whether GSPE inhibited BLM-induced oxidative stress *in vitro*, we measured ROS generation at day 3 of BLM instillation in A549 cells. The cells were pretreated with GSPE (1 μg/ml) for 4 h and then stimulated with BLM (1 μg/ml) for an additional 24 h. The production of mitochondrial ROS was detected by staining with MitoSOX using flow cytometry (Figure 3(b)), and intracellular ROS levels were detected by staining with DCF-DA using confocal microscopy (Figure 3(c)) and flow cytometry (Figure 3(d)). GSPE significantly decreased mitochondrial ROS and intracellular ROS production induced after BLM treatment. Impaired expression of these antioxidants can lead to an overload of ROS. In IPF, changes in the antioxidant defense system are associated with increased oxidant production. Therefore, since ROS levels increasing in response to BLM may be a result of the inhibited expression of antioxidant enzymes, we measured the mRNA level of several antioxidant enzymes. Interestingly, BLM decreased the protein expressions of Peroxiredoxin 2 (PRX2), glutathione peroxidase (GPX), and thioredoxin (TRX) in lung tissues. However, GSPE treatment restored the expressions of these genes reduced by BLM, indicating that these genes contributed to the decreased oxidant burden (Figure 3(c)).

3.4. GSPE Attenuates BLM-Induced Apoptosis in the Lung and AECs. Alveolar epithelium, which represents 99% of the surface area of the lung, is composed of type I and type II AECs. Apoptosis in the alveolar epithelium (AECs) is essential in the pathogenesis of lung fibrosis [18]. Therefore, we investigated whether GSPE has an antiapoptotic effect on lung epithelial cells. First, we analyzed cleaved PARP-1 (cPARP-1) as a marker for detecting apoptotic cells in lung tissues using immunohistochemical staining. Colocalization between cytokeratin and cPARP-1 confirms the apoptotic status of epithelial cells. Interestingly, double staining for cytokeratin (red) and cleaved PARP (green) showed that epithelial apoptosis was not found in the PBS-treated control group but increased in the BLM+vehicle group at day 7 of

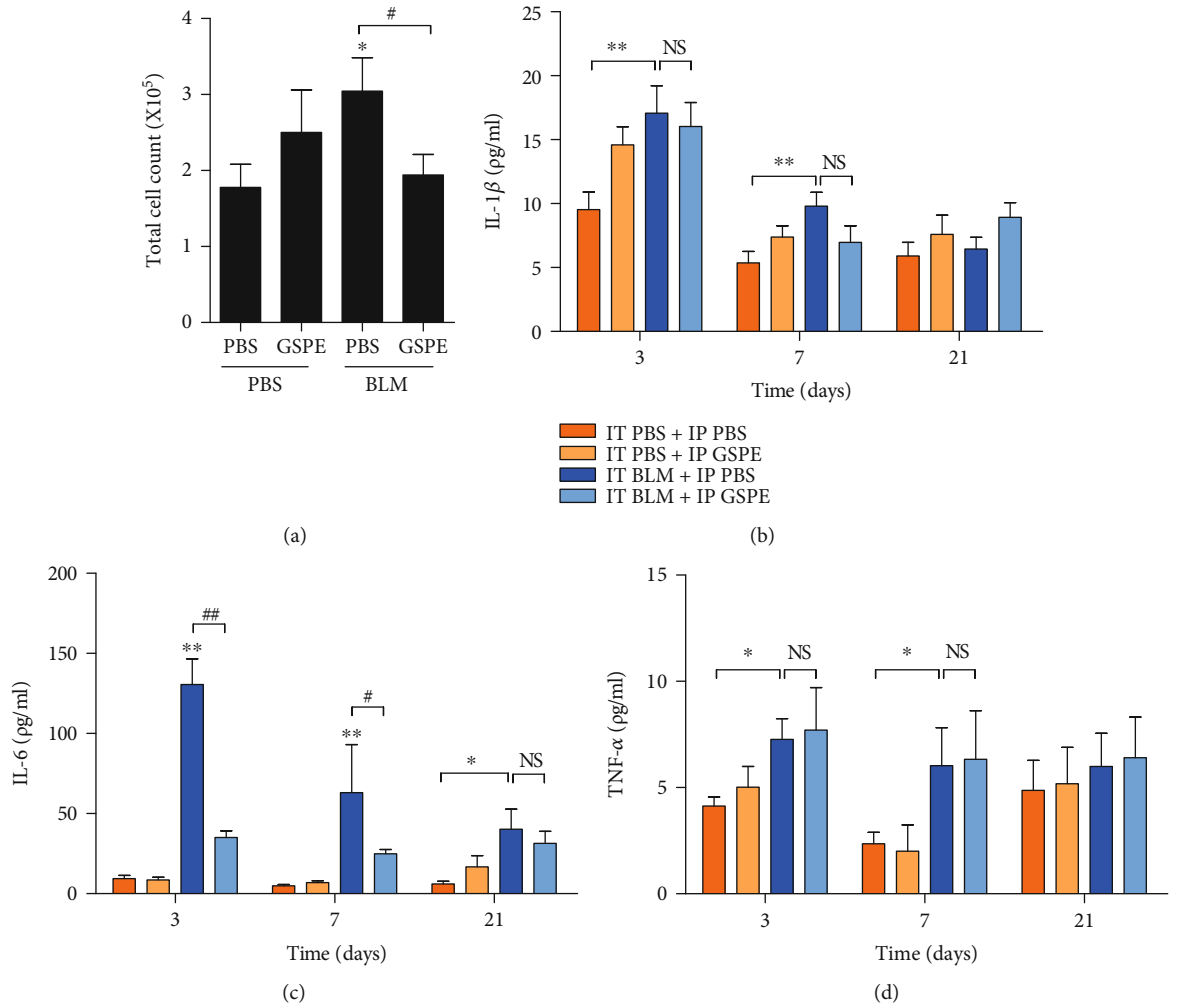

Figure 2: Grape seed proanthocyanidin extract (GSPE) attenuates bleomycin- (BLM-) induced lung inflammation. (a) Total numbers of cells in bronchoalveolar lavage (BAL) fluid were determined at day 7 of BLM instillation to assess the protective effects of GSPE on BLM-induced lung inflammation. Intratracheal (IT) administration of BLM increased total cell counts in BALF on day 7. Compared with the BLM+PBS group, total cell counts in BALF were significantly lower in the BLM+GSPE group on day 7. (b–d) The levels of TNF-α, IL-1ß, and IL-6 were measured by ELISA in whole lung tissue homogenates. IT administration of BLM induced increased levels of TNF-α and IL-1ß on days 3 and 7 and IL-6 on days 3, 7, and 21. Compared with the BLM+PBS treatment group, the level of IL-6 was significantly lower in the BLM+GSPE treatment group on days 3 and 7. Treatment with GSPE did not reduce the levels of TNF-α and IL-1ß. Data are expressed as the mean ± SEM ($n = 3$–5 per group) and are representative of three independent experiments. $^{**}p < 0.01$ and $^{*}p < 0.05$ versus the IT PBS+IP PBS group. $^{\#\#}p < 0.01$ and $^{\#}p < 0.05$ versus the IT BLM+IP PBS group. NS: not significant.

BLM instillation. However, the cleaved PARP-1 expression increased by BLM administration was significantly decreased by GSPE in the lung (Figure 4(a)). Next, we performed the MTT assay for assessing cell viability in lung epithelial cells. At doses of 0.5, 1, and 5 μg/ml, no significant change in cell viability was observed with GSPE treatment, while at concentrations of 10 to 20 μg/ml, suppression of cell viability was detected. Moreover, the cell viability decreased at concentrations higher than 1 μg/ml after BLM treatment, and at 10 μg/ml, cell viability was decreased to 15% (Figure 4(b)). Additionally, BLM increased an increase of ROS, which leads to oxidative stress and apoptosis in the lung [19]. To identify the effects of GSPE on BLM-induced apoptosis, we performed annexin V-FITC/PI staining. The fraction of annexin V-positive cells decreased dramatically after GSPE treatment compared with that of BLM administration (Figure 4(c)). Next, we performed Hoechst 33342 staining to analyze apoptosis. Positive apoptotic cells show the characteristic fragmented nuclei. As expected, apoptotic cells were reduced in the BLM+GSPE group compared to those in the BLM+vehicle group (Figure 4(d)). These results indicate that GSPE attenuated BLM-induced epithelial apoptosis in the mouse lung and A549 AECs.

3.5. GSPE Inhibits BLM-Induced Epithelial Cell Apoptosis via Downregulating of Bax/Bcl-2 Expression. Previous studies have reported that BLM functions via mitochondria-dependent apoptotic pathway in response to oxidant injury [20–22]. Therefore, we also measured the expression of these proteins associated with mitochondrial apoptosis in BLM-treated cells. Western blotting analysis showed that BLM induced the protein expression of cytochrome c, cleaved

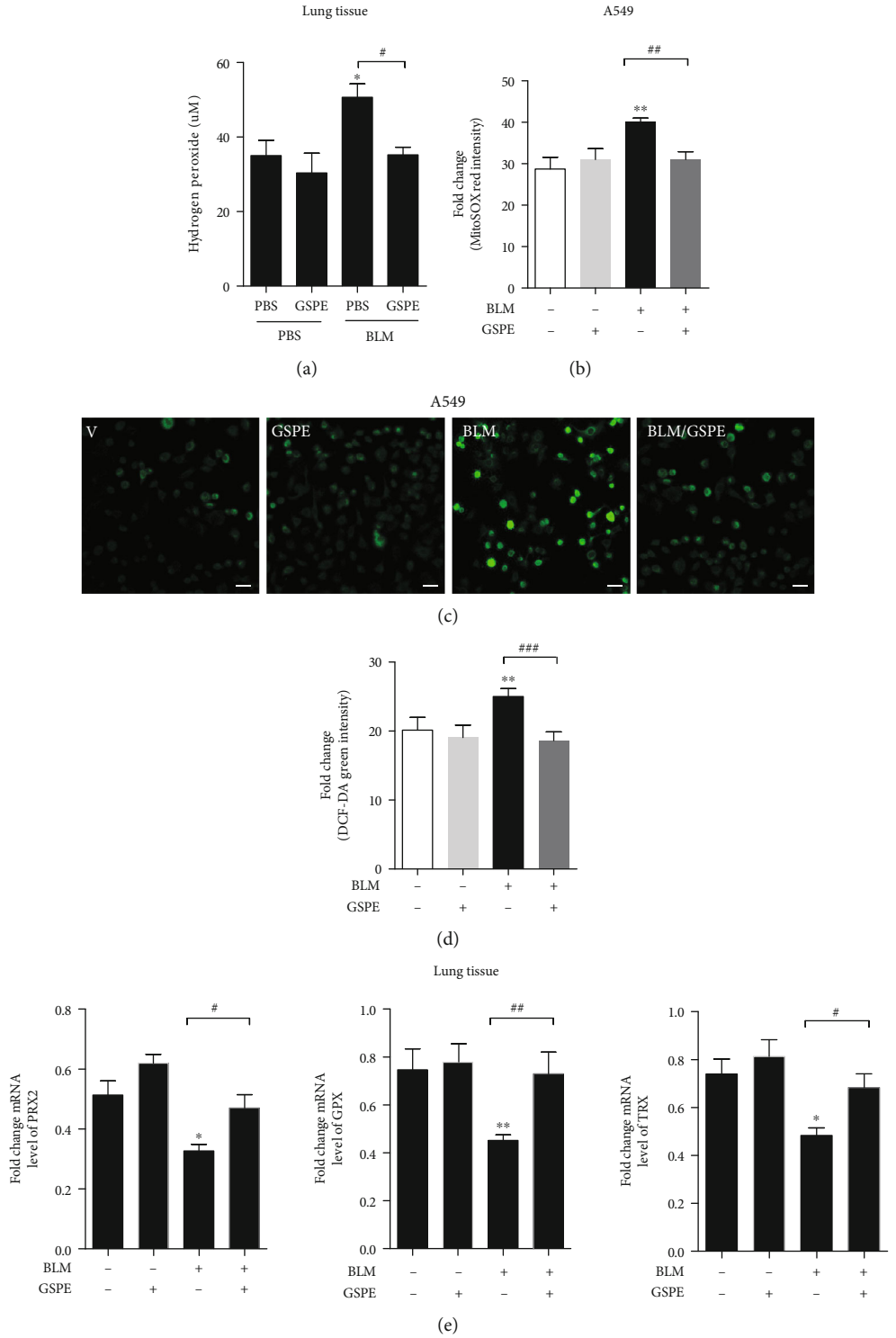

Figure 3: Grape seed proanthocyanidin extract (GSPE) attenuates bleomycin- (BLM-) induced oxidative damage *in vivo* and *in vitro*. (a) The levels of H_2O_2 were measured in whole lung tissue homogenates on day 3. Intratracheal (IT) administration of BLM increased levels of H_2O_2 on day 3. Compared with the BLM+PBS treatment group, the level of H_2O_2 was significantly lower in the BLM+GSPE treatment group on day 3. (b, c) A549 cells were pretreated with GSPE (1 μg/ml) for 4 h and then stimulated with BLM (1 μg/ml) for an additional 24 h. The production of mitochondrial ROS by staining with MitoSOX using flow cytometry was detected. Intracellular ROS were detected by staining with DCF-DA using confocal microscopy (c) and flow cytometry (d). GSPE significantly decreased intracellular ROS and mitochondrial ROS production induced after BLM treatment. (e) mRNA levels of several antioxidant enzymes were measured by qRT-PCR. GSPE treatment restored the mRNA expressions of PRX2, GPX, and TRX reduced by BLM. Scale bar = 20 μm. Data are expressed as the mean ± SEM ($n = 3$–5 per group) and are representative of three independent experiments. $^{*}p < 0.05$ and $^{**}p < 0.01$ versus the PBS+PBS group or nontreated cells.

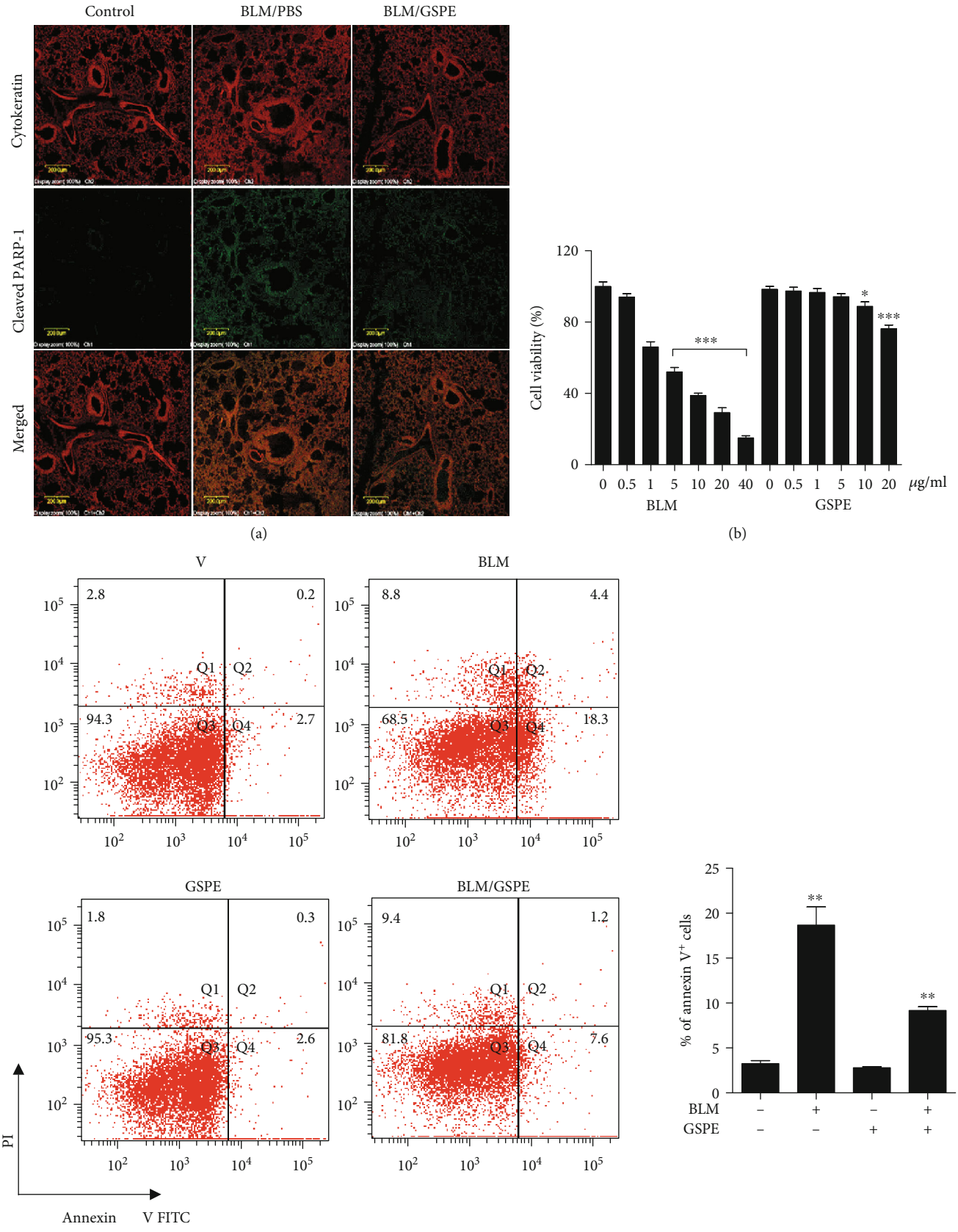

Figure 4: Continued.

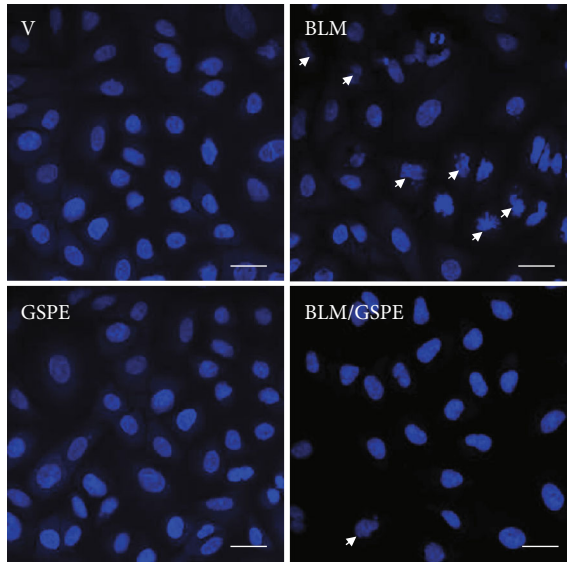

(d)

Figure 4: Grape seed proanthocyanidin extract (GSPE) attenuates bleomycin- (BLM-) induced apoptosis in the lung and alveolar epithelial cells. (a) To investigate the effects of GSPE on BLM-induced alveolar epithelial cell apoptosis on day 7, the slides from paraffin-embedded lung tissues were incubated overnight at 4°C with anti-PARP p85 fragment polyclonal antibody, followed by incubation with FITC-conjugated Goat Anti-rabbit IgG secondary antibody, and incubated with anti-pan cytokeratin monoclonal antibody PE. Double staining for cytokeratin (red) and cleaved PARP (green) showed more epithelial apoptosis in the BLM+PBS group than in the BLM+GSPE group. Scale bar = 10 μm. (b) Lung epithelial A549 cells were treated with GSPE (0–20 μg/ml) for 4 h before the addition of BLM (0–40 μg/ml) for 48 h. Cell viability was measured using the MTT assay. At doses of 0.5, 1, and 5 μg/ml, no difference was observed in cell viability after GSPE treatment. In addition, significant decreases in cell viability were observed at concentrations higher than 1 μg/ml after BLM treatment; at 10 μg/ml, cell viability was decreased to 15%. (c) The cells were then stained for 15 min at RT in the dark with 5 μl FITC-conjugated annexin V and 5 μl propidium iodide (PI). GSPE treatment dramatically reduced the fraction of annexin V-positive cells compared with that of BLM administration. (d) Hoechst 33342 staining was performed to analyze apoptosis. Apoptotic cells (indicated by arrows) were reduced in the BLM+GSPE group than those in the BLM+vehicle group. Scale bar, 20 μm. Data are expressed as the mean ± SEM (n = 3–5 per group) and are representative of three independent experiments. $^{**}p < 0.01$ and $^{***}p < 0.001$ in comparison with nontreated cells.

caspase-3, and cleaved PARP in lung tissues. However, GSPE treatment reversed the expression of apoptotic proteins increased by BLM. BLM exposure causes mitochondrial localization of Bax, resulting in the release of cytochrome c [23]. Bax is associated with mitochondrial-dependent apoptosis. Interestingly, BLM induced an increase of Bax and Bak, which were inhibited by GSPE. Moreover, GSPE restored BLM-mediated Bcl-2 and PARP levels (Figure 5(a)). We found that GSPE treatment could also decrease the Bax/Bcl-2 ratio. Next, we used the A549 type II AEC cell line to investigate BLM-induced apoptosis of lung epithelial cells. Expectedly, we observed that proapoptotic proteins including Bax and Bak were increased after BLM treatment, whereas GSPE restored the expression of these proteins. In addition, antiapoptotic protein, Bcl-2, which was decreased by BLM, yet increased after GSPE. We also found that BLM increased the protein levels of cPARP, cytochrome c, and cleaved caspase 3, whereas GSPE suppressed the increase of these proteins induced after BML treatment. PARP expression induced by BLM was reversed by GSPE (Figure 5(b)). Taken together, our findings suggested that GSPE might protect the BLM-mediated apoptosis induced by oxidative stress via downregulating the Bax/Bcl2 ratio.

4. Discussion

IPF is characterized by a sequence of events starting with alveolar epithelial microinjuries leading to AEC apoptosis and basement membrane disruption followed by the formation of fibroblastic foci and accumulation of extracellular matrix. This results in the subsequent destruction of the lung architecture. The prognosis of IPF is significantly worse than in many interstitial lung diseases, and no effective treatments for IPF exist. Pirfenidone and nintedanib, as well as corticosteroids and other immunosuppressive agents, are used to treat pulmonary fibrosis. However, these clinical drugs have limited efficacy and some side effects. Therefore, new and effective treatments are urgently needed. GSPE, a potent antioxidant, is more effective than ascorbic acid and vitamin E and has anti-inflammatory effects [13, 24]. Considering the antioxidant effects of GSPE and the crucial role of its in pulmonary fibrosis, we hypothesized that GSPE could inhibit the development of pulmonary fibrosis via ameliorating epithelial apoptosis through the inhibition of oxidative stress. To investigate the effect of GSPE on the pathogenesis of lung fibrosis, we first established a BLM-induced lung fibrosis mouse model (Figure 1(a)). H&E, Masson's trichrome staining, and Ashcroft score assessment showed

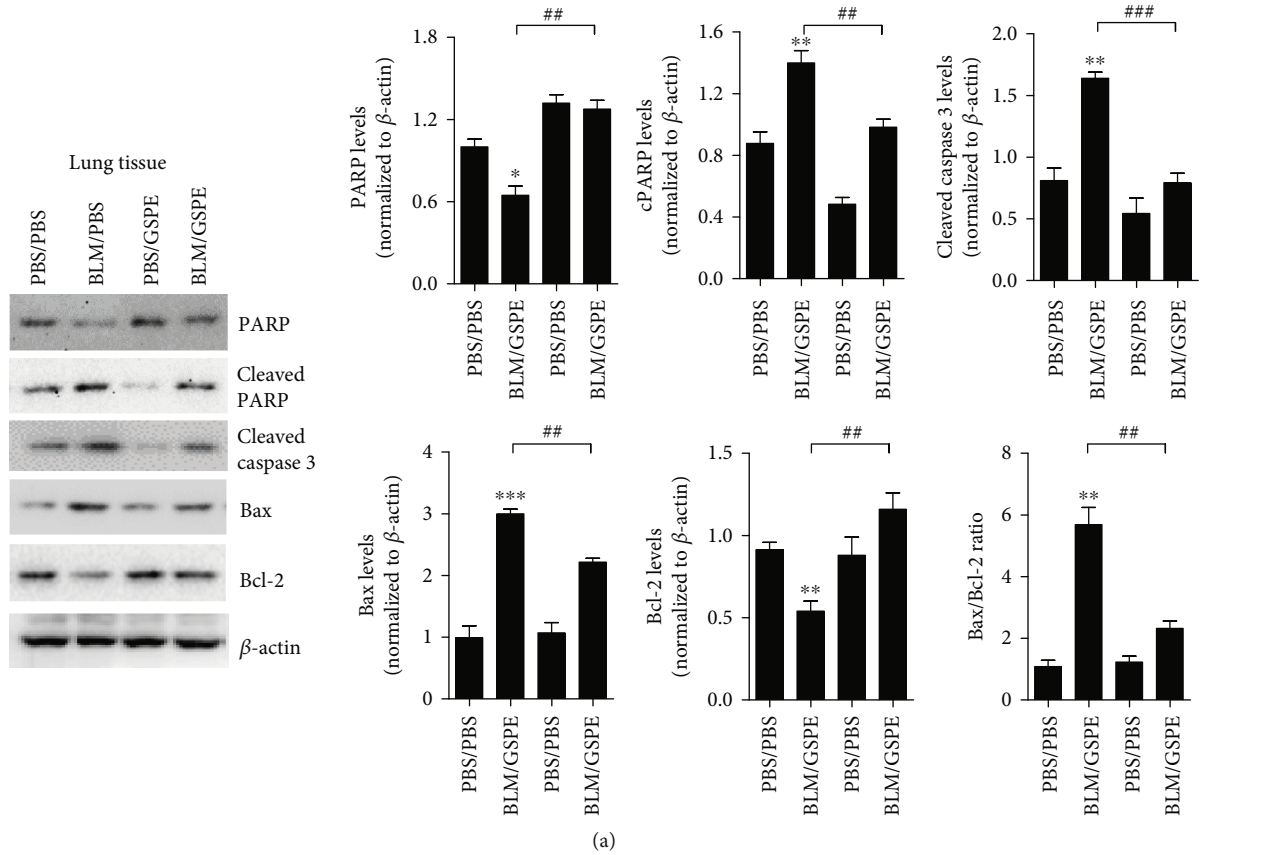

Figure 5: Continued.

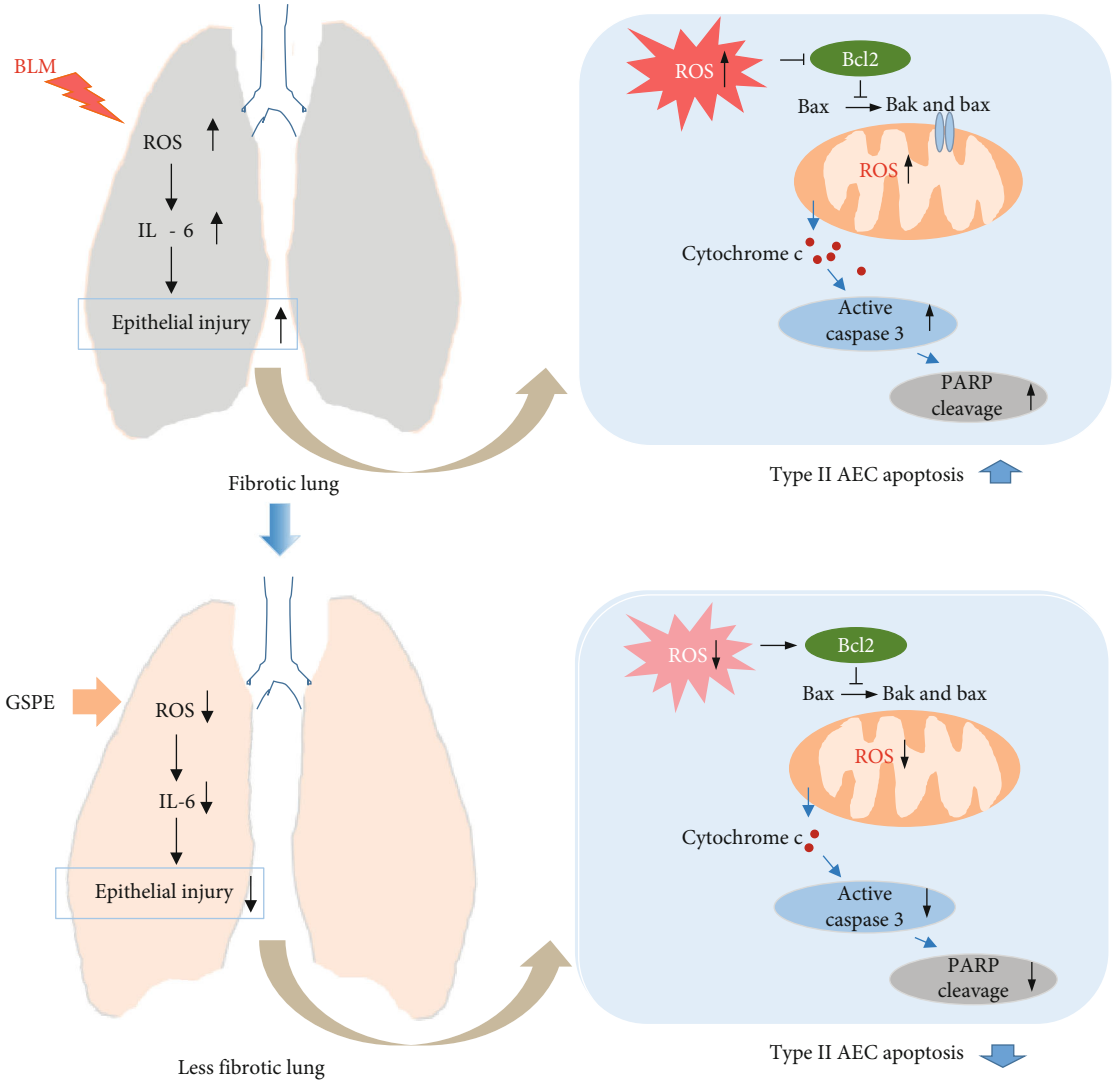

(c)

Figure 5: Grape seed proanthocyanidin extract (GSPE) attenuates bleomycin- (BLM-) induced epithelial cell apoptosis via downregulating of Bax/Bcl-2 expression. (a, b) Expressions of the proteins associated with mitochondrial apoptosis after BLM treatment were detected by western blotting analysis in lung tissues and A549 cells. The protein levels of PARP, cPARP, cleaved caspase 3, Bax, and Bcl-2 in lung tissues and PARP, cPARP, cytochrome c, Bak, cleaved caspase 3, Bax, and Bcl-2 in A549 cells were increased after BLM administration. However, expressions of these proteins were reversed by GSPE treatment and the Bax/Bcl-2 ratio was also decreased. (c) Schematic diagram of proposed pathways. GSPE has protective effects in BLM-induced lung fibrosis by reducing oxidative stress and reducing AEC apoptosis in the lung. Data are expressed as the mean ± SEM ($n = 3$-5 per group) and are representative of three independent experiments. $^{*}p < 0.05$, $^{**}p < 0.01$, and $^{***}p < 0.001$ versus the PBS+PBS group or nontreated cells.

the inhibitory effect of GSPE on BLM-mediated lung fibrosis in mice (Figures 1(b) and 1(c)). GSPE also reduced the level of collagen deposition in BLM-induced lung (Figure 1(d)). These results show that GSPE exerted protective effects via alleviating pathological changes in a BLM-induced lung fibrosis model of mice.

Several studies have reported that oxidative stress was associated with the development of alveolar injury, inflammation, and fibrosis [25]. Oxidative stress might promote a fibrotic microenvironment, where fibroblasts were resistant to the damaging effects of ROS in IPF, but epithelial cells were relatively more sensitive to oxidative stress [26]. Lung myofibroblasts are known to secrete hydrogen peroxide, leading to mediated fibrogenic effects and inducing epithelial apoptosis [27]. Moreover, neutrophils produce matrix-degrading enzymes such as neutrophil elastase and release an excessive amount of ROS that may induce cell and tissue injury. Modulating oxidative stress might be a powerful way to prevent the progression of lung fibrosis. Interestingly, a previous report showed that sivestat, a neutrophil elastase inhibitor, could ameliorate BLM-induced lung fibrosis [28]. Moreover, deficiency of the antioxidant glutathione (GSH) in epithelial lining fluid can increase cell susceptibility to oxidant-mediated injury, which contributes to the initiation and progression of fibrosis [29]. BLM can cause severe lung fibrosis in both animals and humans [30–34]. BLM is

involved in the production of ROS, leading to increased oxidative stress, which results in inflammation and fibrosis [35]. AECs are the main target of oxidative stress-induced lung injury leading to fibrosis [36]. In the present study, we found that BLM instillation increased the levels of ROS leading to oxidative stress in mouse lung tissues. However, GSPE treatment significantly decreased BLM-induced ROS levels. These results indicate that BLM-induced oxidative stress can be ameliorated by treatment with GSPE (Figure 3(a)). *In vitro*, our results showed that intracellular ROS and mitochondrial ROS were significantly increased after BLM treatment, while BLM-induced ROS were alleviated after GSPE treatment (Figure 3(b)). We suggested that these beneficial effects are associated with suppressed production of ROS and inflammation and the prevention of epithelial cell apoptosis in the lungs.

Cytokines and growth factors are involved in both the early inflammatory and late fibrotic phases of lung fibrosis. We examined the effect of GSPE on initial lung inflammation induced by BLM. Administration of BLM induced the levels of TNF-α and IL-1ß on days 3 and 7 and IL-6 on days 3, 7, and 21, while GSPE significantly attenuated the expression of IL-6 on days 3 and 7 but had no difference in the levels of TNF-α and IL-1ß (Figure 2(b)). IL-6 has been implicated in the pathogenesis of many inflammatory disorders of the lung, including IPF, ARDS, and chronic obstructive pulmonary disease [37, 38]. Saito et al. reported that in IL6-deficient mice, BLM-induced inflammatory cell accumulation in the alveolar space, an increase in TGF-β1 and CCL3 expression, and fibrotic changes of the lung after BLM were attenuated [39]. IL-6 is enhanced in mice and humans with pulmonary fibrosis [40, 41]. Several genetic studies revealed the significant association between IL-6 and the development of fibrosis in animals and humans [37, 42]. In lung fibroblasts obtained from patients with IPF, IL-6 seems to promote fibroblast proliferation, which contributes to the development of fibrosis compared with lung fibroblasts obtained from normal patients [43]. In the lung, asbestos-induced oxidative stress increased IL-6 expression, triggering both inflammatory and fibrotic processes, which was significantly suppressed by antioxidants including N-acetylcysteine (NAC) [44]. Additionally, we also observed that GSPE instillation also ameliorated the total number of cells in BALF increased by BLM instillation at day 7 (Figure 2(a)). These data indicated that GSPE exerted protective effects via the downregulation of IL-6 proinflammatory cytokine, as well as by alleviating the number of inflammatory cells in the BAL fluid.

Apoptosis, the process of programmed cell death, plays an important role in normal lung homeostasis and the pathogenesis of various lung diseases including IPF [45]. AEC injury is suggested to be a key process in the pathogenesis of IPF [46, 47]. Repeated injury to the AEC leads to apoptosis, followed by aberrant lung repair and fibroblast activation, resulting in progressive fibrosis. Shulamit et al. reported that initial bleomycin-induced oxidative stress causes a direct apoptosis of lung epithelial cells through caspase activation in a murine lung epithelial (MLE) cell line [19]. In addition, EMT is a pathophysiological process for an epithelial cell to undergo a conversion to a mesenchymal phenotype, which may play a significant role in lung fibrosis. EMT characteristics were detected in bleomycin-treated A549 cells [48]. BLM induced alveolar epithelial cell apoptosis through a mitochondrial-dependent pathway, while other studies showed that Fas/FasL pathway is involved in BLM-induced apoptosis and Fas was also overexpressed in alveolar epithelial cells in lung tissues of human idiopathic pulmonary fibrosis [49–51]. However, Shulamit et al. reported that BLM-induced ROS triggered the initial apoptosis in the fibrotic process and subsequent increase of Fas and FasL level further sensitized cells to Fas-induced apoptosis [19]. Therefore, the Fas/FasL apoptotic pathway appears to take place at a later time and seems essential to clear intra-alveolar granulated tissue [52].

AEC apoptosis is an important early event in BLM-induced lung fibrosis, and in this model, suppression of apoptosis ameliorated lung fibrosis [53, 54]. Thus, new therapies based on the inhibition of apoptosis may prove advantageous for the treatment of patients with IPF. Oxidative stress is known to mediate poly-ADP-ribose polymerase 1 (PARP-1) activation, triggering mitochondrial dysfunction, which leads to caspase-independent cell death [55]. PARP-1 is a major substrate of caspases-3, and its cleavage is a valuable marker of apoptosis [56]. PARP-1 is critical for cellular processes such as DNA repair and transcription. In the present study, double staining for cytokeratin (red) and cleaved PARP (green) showed that in the PBS-treated control group, epithelial apoptosis was not found but increased in the BLM+vehicle group on day 7 after BLM instillation. However, the cleaved PARP-1 expression increased after BLM administration and was significantly decreased by GSPE. Moreover, Figures 4(c) and 4(d) show that GSPE could repress type II AEC apoptosis, as evaluated by morphological alterations of nuclear by Hoechst 33342 staining and by annexin V-positive cells, suggesting that GSPE could attenuate BLM-induced apoptosis via ameliorating epithelial apoptosis.

Caspases are a family of proteolytic enzymes, which play an essential role in AEC apoptosis [57]. It is activated through the intrinsic or extrinsic pathways of apoptotic signaling, ultimately leading to the destruction of the cell. The extrinsic pathway, the death receptor pathway, links death receptors such as Fas and tumor necrosis factor (TNF) receptor 1 and caspase-8 [58], whereas the intrinsic pathway, the mitochondrial pathway, occurs through stimuli such as drugs, infectious agents, and ROS [59, 60]. These stimuli lead to increased expression of proapoptotic proteins including Bax and Bak and reduced expression of antiapoptotic proteins including Bcl-2 and Bcl-xL. With a change in mitochondrial membrane potential, cytochrome c is released from the mitochondria to the cytosol, which induces the formation of the functional apoptosome, resulting in the activation of caspase-9 and a cascade of activation events for the effector caspases-3 [61]. Several studies have shown that BLM induces ROS-induced mitochondrial cell death [20–22]. Moreover, Maeyama et al. found that, in the epithelial cells of IPF patients, the levels of caspase-3 were increased [62]. Consistent with these findings, we also

observed an increase in the protein level of caspase-3 in mouse lung homogenates after BLM instillation, whereas GSPE suppressed BLM-induced caspase-3 levels. Plataki et al. also detected Bax induction and Bcl-2 reduction in epithelial cells from IPF patients [63]. Additionally, Bax protein was increased in epithelial cells, whereas the expression level of Bcl-2 protein showed no difference in a study of BLM-induced pulmonary fibrosis in mice [64]. In this study, we also showed that BLM induced the increase of Bax, which was inhibited by GSPE. Moreover, GSPE restored the expression of Bcl-2 (Figures 5(a) and 5(b)), indicating that GSPE could decrease the Bax/Bcl-2 ratio. Furthermore, we used the A549 type II AEC cell line to investigate BLM-induced apoptosis of lung epithelial cells. Expectedly, the results of western blot indicated that after BLM treatment, the proapoptotic protein Bax was increased, whereas the level of the antiapoptotic protein Bcl-2 was decreased. In contrast, GSPE could reduce these protein levels and decrease the Bax/Bcl-2 ratio. These data suggest that GSPE could attenuate mitochondrial-associated cell apoptosis.

In this study, we showed that BLM administration induced increased protein level of TGF-β1 on day 21. The level of TGF-β1 was significantly lower in the BLM+GSPE treatment group compared with the BLM control group. This result suggested that GSPE could play an antifibrotic role via reducing TGF-β1. However, we could not confirm whether the potential anti-fibrotic effect of GSPE on BLM-induced pulmonary fibrosis animal models was due to the consequence of reduced oxidative stress or inflammation or the effect on fibrosis itself. Therefore, further studies would be needed to determine its contribution to Smad signaling or EMT of lung fibrosis. Besides, more mechanisms of GSPE on pulmonary fibrosis need to be explored so that GSPE can be used in clinical settings as a feasible approach to the treatment of IPF. Nevertheless, this study is the first to report the therapeutic effects of GSPE on BLM-mediated lung fibrosis and to elucidate the possible mechanism of GSPE in BLM-induced lung fibrosis.

In conclusion, we demonstrated that GSPE significantly ameliorated the histological changes and the level of collagen deposition in BLM-induced lungs. GSPE inhibited the BLM-induced IL-6 for early lung fibrosis and TGF-β for late lung fibrosis. In addition, GSPE significantly decreased the levels of ROS, and apoptosis was increased by BLM instillation in lung and epithelial cells. Furthermore, GSPE protected BLM-induced epithelial cell apoptosis via decreasing the Bax/Bcl2 ratio in vitro. Taken together, the findings demonstrate that GSPE can protect against BLM-induced pulmonary fibrosis in mice by inhibiting epithelial apoptosis through the inhibition of oxidative stress (Figure 5(c)), suggesting that GSPE may be useful in the treatment of IPF.

Abbreviations

GSPE: Grape seed proanthocyanidin extract
BLM: Bleomycin
IPF: Idiopathic pulmonary fibrosis
BAL: Bronchoalveolar lavage
AEC: Alveolar epithelial cell
IL-1ß: Interleukin-1ß
IL-6: Interleukin-6
ROS: Reactive oxygen species
TGF-β: Transforming growth factor beta 1
PARP-1: Poly [ADP-ribose] polymerase 1
Bax: BCL2 associated X
Bak: Bcl-2 homologous antagonist killer
Bcl-2: B-cell lymphoma 2.

Data Availability

The data used to support the findings of this study are included in the article.

Conflicts of Interest

The authors have no conflict of interest to declare regarding the publication of this paper.

Authors' Contributions

SW Ra and YJ Jegal conceived and designed the study. OJ Sul performed the study. All authors contributed to the analysis and interpretation of results. SW Ra, YJ Jegal, and OJ Sul wrote the manuscript and critically revised the manuscript, and all authors approved the final version of the manuscript.

Acknowledgments

This work was financially supported by the Ulsan University Hospital Research Grant (UUH-2018; UUH-2018-11) and the Basic Science Research Program (2021R1I1A1A01044304) of the National Research Foundation (NRF) funded by the Korean government.

References

[1] J. J. Coalson, "The ultrastructure of human fibrosing alveolitis," *Virchows Archiv A Pathological Anatomy and Histology*, vol. 395, no. 2, pp. 181–199, 1982.

[2] B. Corrin, M. Jagusch, A. Dewar et al., "Fine structural changes in idiopathic pulmonary haemosiderosis," *The Journal of Pathology*, vol. 153, no. 3, pp. 249–256, 1987.

[3] M. Kasper and G. Haroske, "Alterations in the alveolar epithelium after injury leading to pulmonary fibrosis," *Histology and Histopathology*, vol. 11, no. 2, pp. 463–483, 1996.

[4] Z. D. Daniil, E. Papageorgiou, A. Koutsokera et al., "Serum levels of oxidative stress as a marker of disease severity in idiopathic pulmonary fibrosis," *Pulmonary Pharmacology and Therapeutics*, vol. 21, no. 1, pp. 26–31, 2008.

[5] S. I. Hagiwara, Y. Ishii, and S. Kitamura, "Aerosolized administration of N-acetylcysteine attenuates lung fibrosis induced by bleomycin in mice," *American Journal of Respiratory and Critical Care Medicine*, vol. 162, no. 1, pp. 225–231, 2000.

[6] F. J. Martinez, J. A. de Andrade, K. J. Anstrom, T. E. King Jr, and G. Raghu, "Randomized trial of acetylcysteine in idiopathic pulmonary fibrosis," *The New England Journal of Medicine*, vol. 370, no. 22, pp. 2093–2101, 2014.

[7] J. M. Oldham, S. F. Ma, F. J. Martinez et al., "TOLLIP, MUC5B, and the response to N-acetylcysteine among individuals with idiopathic pulmonary fibrosis," *American Journal of*

Respiratory and Critical Care Medicine, vol. 192, no. 12, pp. 1475–1482, 2015.

[8] L. L. Feng, B. X. Liu, J. Y. Zhong, L. B. Sun, and H. S. Yu, "Effect of grape procyanidins on tumor angiogenesis in liver cancer xenograft models," *Asian Pacific Journal of Cancer Prevention*, vol. 15, no. 2, pp. 737–741, 2014.

[9] H. Akiyama, J. Sakushima, S. Taniuchi et al., "Antiallergic effect of apple polyphenols on the allergic model mouse," *Biological and Pharmaceutical Bulletin*, vol. 23, no. 11, pp. 1370–1373, 2000.

[10] T. Nishizuka, Y. Fujita, Y. Sato et al., "Procyanidins are potent inhibitors of LOX-1: a new player in the French Paradox," *Proceedings of the Japan Academy Series B: Physical and Biological Sciences*, vol. 87, no. 3, pp. 104–113, 2011.

[11] G. Belcaro, A. Ledda, S. Hu, M. R. Cesarone, B. Feragalli, and M. Dugall, "Grape seed procyanidins in pre- and mild hypertension: a registry study," *Evidence-Based Complementary and Alternative Medicine*, vol. 2013, Article ID 313142, 5 pages, 2013.

[12] E. M. Kimmel, M. Jerome, J. Holderness et al., "Oligomeric procyanidins stimulate innate antiviral immunity in dengue virus infected human PBMCs," *Antiviral Research*, vol. 90, no. 1, pp. 80–86, 2011.

[13] D. Bagchi, A. Garg, R. L. Krohn, M. Bagchi, M. X. Tran, and S. J. Stohs, "Oxygen free radical scavenging abilities of vitamins C and E, and a grape seed proanthocyanidin extract in vitro," *Research Communications in Molecular Pathology*, vol. 95, no. 2, pp. 179–189, 1997.

[14] S. D. Ray, D. Patel, V. Wong, and D. Bagchi, "In vivo protection of dna damage associated apoptotic and necrotic cell deaths during acetaminophen-induced nephrotoxicity, amiodarone-induced lung toxicity and doxorubicin-induced cardiotoxicity by a novel IH636 grape seed proanthocyanidin extract," *Research Communications in Molecular Pathology*, vol. 107, no. 1-2, pp. 137–166, 2000.

[15] D. M. Alters and S. D. Kleeberger, "Mouse models of bleomycin-induced pulmonary fibrosis," *Current Protocols in Pharmacology*, vol. 40, 2008.

[16] R. H. Hubner, W. Gitter, N. E. El Mokhtari et al., "Standardized quantification of pulmonary fibrosis in histological samples," *Biotechniques*, vol. 44, no. 4, pp. 507–517, 2008.

[17] C. A. Edwards and W. D. O'Brien, "Modified assay for determination of hydroxyproline in a tissue hydrolyzate," *Clinica Chimica Acta*, vol. 104, no. 2, pp. 161–167, 1980.

[18] B. D. Uhal, "The role of apoptosis in pulmonary fibrosis," *European Respiratory Review*, vol. 17, no. 109, pp. 138–144, 2008.

[19] S. B. Wallach-Dayan, G. Izbicki, P. Y. Cohen, R. Gerstl-Golan, A. Fine, and R. Breuer, "Bleomycin initiates apoptosis of lung epithelial cells by ROS but not by Fas/FasL pathway," *The American Journal of Physiology -Lung Cellular and Molecular Physiology*, vol. 290, no. 4, pp. L790–L796, 2006.

[20] M. M. Alonso, A. Asumendi, J. Villar et al., "New benzo(*b*)thiophenesulphonamide 1,1-dioxide derivatives induce a reactive oxygen species-mediated process of apoptosis in tumour cells," *Oncogene*, vol. 22, no. 24, pp. 3759–3769, 2003.

[21] S. S. Brar, J. N. Meyer, C. D. Bortner, B. van Houten, and W. J. Martin II, "Mitochondrial DNA-depleted A549 cells are resistant to bleomycin," *The American Journal of Physiology-Lung Cellular and Molecular Physiology*, vol. 303, no. 5, pp. L413–L424, 2012.

[22] P. S. Lin, L. Kwock, and N. T. Goodchild, "Copper, superoxide radical, diethyldithiocarbamate, and bleomycin cytotoxicity," *The Lancet*, vol. 313, no. 8119, p. 777, 1979.

[23] J. M. Jürgensmeier, Z. Xie, Q. Deveraux, L. Ellerby, D. Bredesen, and J. C. Reed, "Bax directly induces release of cytochrome c from isolated mitochondria," *Proceedings of the National Academy of Sciences of the United States of America*, vol. 95, no. 9, pp. 4997–5002, 1998.

[24] E. Middleton Jr., C. Kandaswami, and T. C. Theoharides, "The effects of plant flavonoids on mammalian cells: implications for inflammation, heart disease, and cancer," *Pharmacological Reviews*, vol. 52, no. 4, pp. 673–751, 2000.

[25] P. Cameli, A. Carleo, L. Bergantini, C. Landi, A. Prasse, and E. Bargagli, "Oxidant/antioxidant disequilibrium in idiopathic pulmonary fibrosis pathogenesis," *Inflammation*, vol. 43, no. 1, pp. 1–7, 2020.

[26] E. Wang, "Senescent human fibroblasts resist programmed cell death, and failure to suppress bcl2 is involved," *Cancer Research*, vol. 55, no. 11, pp. 2284–2292, 1995.

[27] M. Waghray, Z. Cui, J. C. Horowitz et al., "Hydrogen peroxide is a diffusible paracrine signal for the induction of epithelial cell death by activated myofibroblasts," *The FASEB Journal*, vol. 19, no. 7, pp. 1–16, 2005.

[28] A. Takemasa, Y. Ishii, and T. Fukuda, "A neutrophil elastase inhibitor prevents bleomycin-induced pulmonary fibrosis in mice," *European Respiratory Journal*, vol. 40, no. 6, pp. 1475–1482, 2012.

[29] A. M. Cantin, R. C. Hubbard, and R. G. Crystal, "Glutathione deficiency in the epithelial lining fluid of the lower respiratory tract in idiopathic pulmonary fibrosis," *The American Review of Respiratory Disease*, vol. 139, no. 2, pp. 370–372, 1989.

[30] J. P. Balikian, M. S. Jochelson, K. A. Bauer et al., "Pulmonary complications of chemotherapy regimens containing bleomycin," *AJR. American Journal of Roentgenology*, vol. 139, no. 3, pp. 455–461, 1982.

[31] G. Izbicki, M. J. Segel, T. G. Christensen, M. W. Conner, and R. Breuer, "Time course of bleomycin-induced lung fibrosis," *International Journal of Experimental Pathology*, vol. 83, no. 3, pp. 111–119, 2002.

[32] Y. Chen, F. Jiang, G. Kong et al., "Gasotransmitter CO attenuates bleomycin-induced fibroblast senescence via induction of stress granule formation," *Oxidative Medicine and Cellular Longevity*, vol. 2021, Article ID 9926284, 21 pages, 2021.

[33] Y. Chen, S. Yuan, Y. Cao et al., "Gasotransmitters: potential therapeutic molecules of fibrotic diseases," *Oxidative Medicine and Cellular Longevity*, vol. 2021, Article ID 3206982, 18 pages, 2021.

[34] Q. Wang, X. Shao, E. L. H. Leung, Y. Chen, and X. Yao, "Selectively targeting individual bromodomain: drug discovery and molecular mechanisms," *Pharmacological Research*, vol. 172, article 105804, 2021.

[35] A. Allawzi, H. Elajaili, E. F. Redente, and E. Nozik-Grayck, "Oxidative toxicology of bleomycin: role of the extracellular redox environment," *Current Opinion in Toxicology*, vol. 13, pp. 68–73, 2019.

[36] S. Sleijfer, "Bleomycin-induced pneumonitis," *Chest Journal*, vol. 120, no. 2, pp. 617–624, 2001.

[37] P. Pantelidis, G. C. Fanning, A. U. Wells, K. I. Welsh, and R. M. Du Bois, "Analysis of tumor necrosis factor-α, lymphotoxin-α, tumor necrosis factor receptor II, and interleukin-6 polymorphisms in patients with idiopathic pulmonary

fibrosis," *American Journal of Respiratory and Critical Care Medicine*, vol. 163, no. 6, pp. 1432–1436, 2001.

[38] W. Y. Park, R. B. Goodman, K. P. Steinberg et al., "Cytokine balance in the lungs of patients with acute respiratory distress syndrome," *American Journal of Respiratory and Critical Care Medicine*, vol. 164, no. 10, pp. 1896–1903, 2001.

[39] F. Saito, S. Tasaka, K. Inoue et al., "Role of interleukin-6 in bleomycin-induced lung inflammatory changes in mice," *American Journal of Respiratory Cell and Molecular Biology*, vol. 38, no. 5, pp. 566–571, 2008.

[40] M. Pedroza, D. J. Schneider, H. Karmouty-Quintana et al., "Interleukin-6 contributes to inflammation and remodeling in a model of adenosine mediated lung injury," *PLoS One*, vol. 6, article e22667, no. 7, 2011.

[41] Y. Zhou, J. N. Murthy, D. Zeng, L. Belardinelli, and M. R. Blackburn, "Alterations in adenosine metabolism and signaling in patients with chronic obstructive pulmonary disease and idiopathic pulmonary fibrosis," *PLoS One*, vol. 5, no. 2, article e9224, 2010.

[42] Z. Qiu, M. Fujimura, K. Kurashima, S. Nakao, and N. Mukaida, "Enhanced airway inflammation and decreased subepithelial fibrosis in interleukin 6-deficient mice following chronic exposure to aerosolized antigen," *Clinical and Experimental Allergy*, vol. 34, no. 8, pp. 1321–1328, 2004.

[43] Y. P. Moodley, A. K. Scaffidi, N. L. Misso et al., "Fibroblasts isolated from normal lungs and those with idiopathic pulmonary fibrosis differ in interleukin-6/gp130-mediated cell signaling and proliferation," *The American Journal of Pathology*, vol. 163, no. 1, pp. 345–354, 2003.

[44] P. P. Simeonova, W. Toriumi, C. Kommineni et al., "Molecular regulation of IL-6 activation by asbestos in lung epithelial cells: role of reactive oxygen species," *The Journal of Immunology*, vol. 159, no. 8, pp. 3921–3928, 1997.

[45] C. L. Fattman, "Apoptosis in pulmonary fibrosis: too much or not enough?," *Antioxidants & Redox Signaling*, vol. 10, no. 2, pp. 379–386, 2008.

[46] M. Selman and A. Pardo, "Idiopathic pulmonary fibrosis: an epithelial/fibroblastic cross-talk disorder," *Respiratory Research*, vol. 3, no. 1, p. 3, 2002.

[47] K. Kuwano, "Involvement of epithelial cell apoptosis in interstitial lung diseases," *Internal Medicine*, vol. 47, no. 5, pp. 345–353, 2008.

[48] S. Lamouille, J. Xu, and R. Derynck, "Molecular mechanisms of epithelial-mesenchymal transition," *Nature Reviews Molecular Cell Biology*, vol. 15, no. 3, pp. 178–196, 2014.

[49] N. Hagimoto, K. Kuwano, H. Miyazaki et al., "Induction of apoptosis and pulmonary fibrosis in mice in response to ligation of Fas antigen," *American Journal of Respiratory Cell and Molecular Biology*, vol. 17, no. 3, pp. 272–278, 1997.

[50] K. Kuwano, N. Hagimoto, K. Kawasaki et al., "Essential roles of the Fas-Fas ligand pathway in the development of pulmonary fibrosis," *Journal of Clinical Investigation*, vol. 104, no. 1, pp. 13–19, 1999.

[51] K. Kuwano, H. Miyazaki, N. Hagimoto et al., "The involvement of Fas-Fas ligand pathway in fibrosing lung diseases," *American Journal of Respiratory Cell and Molecular Biology*, vol. 20, no. 1, pp. 53–60, 1999.

[52] J. J. Cohen, "Programmed cell death in the immune system," *Advances in Immunology*, vol. 50, pp. 55–85, 1991.

[53] R. Wang, O. Ibarra-Sunga, L. Verlinski, R. Pick, and B. D. Uhal, "Abrogation of bleomycin-induced epithelial apoptosis and lung fibrosis by captopril or by a caspase inhibitor," *The American Journal of Physiology – Lung Cellular and Molecular Physiology*, vol. 279, no. 1, pp. L143–L151, 2000.

[54] K. Kuwano, R. Kunitake, T. Maeyama et al., "Attenuation of bleomycin-induced pneumopathy in mice by a caspase inhibitor," *The American Journal of Physiology – Lung Cellular and Molecular Physiology*, vol. 280, no. 2, pp. L316–L325, 2001.

[55] S. W. Yu, H. Wang, M. F. Poitras et al., "Mediation of poly(-ADP-ribose) polymerase-1-dependent cell death by apoptosis-inducing factor," *Science*, vol. 297, no. 5579, pp. 259–263, 2002.

[56] P. J. Duriez and G. M. Shah, "Cleavage of poly(ADP-ribose) polymerase: a sensitive parameter to study cell death," *Biochemistry and Cell Biology*, vol. 75, no. 4, pp. 337–349, 1997.

[57] G. M. Cohen, "Caspases: the executioners of apoptosis," *Biochemical Journal*, vol. 326, no. 1, pp. 1–16, 1997.

[58] M. Muzio, A. M. Chinnaiyan, F. C. Kischkel et al., "FLICE, a novel FADD-homologous ICE/CED-3-like protease, is recruited to the CD95 (Fas/APO-1) death-inducing signaling complex," *Cell*, vol. 85, no. 6, pp. 817–827, 1996.

[59] K. Kuwano, N. Hagimoto, T. Maeyama et al., "Mitochondria-mediated apoptosis of lung epithelial cells in idiopathic interstitial pneumonias," *Laboratory Investigation*, vol. 82, no. 12, pp. 1695–1706, 2002.

[60] M. P. Luna-Vargas and J. E. Chipuk, "Physiological and pharmacological control of BAK, BAX, and beyond," *Trends in Cell Biology*, vol. 26, no. 12, pp. 906–917, 2016.

[61] P. Li, D. Nijhawan, I. Budihardjo et al., "Cytochrome c and dATP-dependent formation of Apaf-1/caspase-9 complex initiates an apoptotic protease cascade," *Cell*, vol. 91, no. 4, pp. 479–489, 1997.

[62] T. Maeyama, K. Kuwano, M. Kawasaki et al., "Upregulation of Fas-signalling molecules in lung epithelial cells from patients with idiopathic pulmonary fibrosis," *European Respiratory Journal*, vol. 17, no. 2, pp. 180–189, 2001.

[63] M. Plataki, A. V. Koutsopoulos, K. Darivianaki, G. Delides, N. M. Siafakas, and D. Bouros, "Expression of apoptotic and antiapoptotic markers in epithelial cells in idiopathic pulmonary fibrosis," *Chest Journal*, vol. 127, no. 1, pp. 266–274, 2005.

[64] K. Kuwano, N. Hagimoto, T. Tanaka et al., "Expression of apoptosis-regulatory genes in epithelial cells in pulmonary fibrosis in mice," *The Journal of Pathology*, vol. 190, no. 2, pp. 221–229, 2000.

Hindawi
Oxidative Medicine and Cellular Longevity
Volume 2022, Article ID 1348795, 14 pages
https://doi.org/10.1155/2022/1348795

Review Article

Rhodiola rosea: A Therapeutic Candidate on Cardiovascular Diseases

Yingqing Chen[1], **Minli Tang**[1], **Shuo Yuan**[1,2], **Shuang Fu**[1], **Yifei Li**[1], **You Li**[1], **Qi Wang**[1], **Yuying Cao**[3], **Liping Liu**[1] and **Qinggao Zhang**[1]

[1]*Chronic Diseases Research Center, Dalian University College of Medicine, Dalian, Liaoning 116622, China*
[2]*Yanbian University, Yanji, Jilin 133022, China*
[3]*Zhongshan Hospital of Dalian University, Dalian, Liaoning 116001, China*

Correspondence should be addressed to Liping Liu; liuliping@dlu.edu.cn and Qinggao Zhang; zhangqinggao@dlu.edu.cn

Received 13 December 2021; Accepted 17 February 2022; Published 27 February 2022

Academic Editor: Xun Cui

Cardiovascular diseases, also known as circulatory diseases, are diseases of the heart and blood vessels, and its etiology is hyperlipidemia, thick blood, atherosclerosis, and hypertension. Due to its high prevalence, disability, and mortality, it seriously threatens human health. According to reports, the incidence of cardiovascular disease is still on the rise. Rhodiola rosea is a kind of traditional Chinese medicine, which has the effects of antimyocardial ischemia-reperfusion injury, lowering blood fat, antithrombosis, and antiarrhythmia. Rhodiola rosea has various chemical components, and different chemical elements have the same pharmacological effects and medicinal values for various cardiovascular diseases. This article reviews the research on the pharmacological effects of Rhodiola rosea on cardiovascular diseases and provides references for the clinical treatment of cardiovascular diseases.

1. Introduction

Cardiovascular disease (CVD) is the general term for heart and vascular diseases, mainly including ischemic heart disease, cerebrovascular disease, peripheral vascular disease, and rheumatic heart disease. Cardiovascular disease is a global epidemic with 80% of the disease burden in low-income and middle-income countries [1]. The mortality of cardiovascular disease is increasing. In China, the annual number of deaths owing to CVD increased from 2.51 million to 3.97 million between 1990 and 2016; the prevalence rate of CVD overall increased significantly from 1990 to 2016 by 14.7% [2]. In Europe, CVD causes 49% of mortality, which is the most important cause of premature mortality and disability adjusted life years ("DALYS") in Europe. Approximately € 192 billion is the cost of annual health care for CVD in the European Union [3]. CVD has various complex causes and forms of the disease, and it is difficult to treat, which accounts for the first cause of death in the world, about 41%. Hypertension, diabetes, dyslipidemia, obesity, overweight, smoking, and physical inactivity are important influencing factors of CVD [3, 4]. Rhodiola rosea is a perennial herb of the Rhodiola family. According to the Global Biodiversity Information Facility, 136 Rhodiola species are recorded. In China, there are 73 Rhodiola species [5]. As a worldwide plant adaptogen [6], Rhodiola rosea can improve cardiovascular and cerebrovascular system functions. The structure of different chemical components of Rhodiola rosea is different, and its pharmacological effects and medicinal value for various cardiovascular diseases are also other. This article reviews the pharmacological effects of Rhodiola rosea and its active ingredients on cardiovascular diseases in the past ten years.

2. The Main Ingredients of Rhodiola rosea

The main active ingredients of Rhodiola rosea include salidroside (Sal), gallic acid, tyrosol, rosavin, rosaline, etc. The specific composition of the components is shown in Table 1.

Table 1: Components of Rhodiola rosea.

Category	Effective composition	Reference
Ketones	Quercetin, kaempferol, anthocyanin, isoquercitrin, rutin, flavonoid glycoside, cinnamic alcohol glycoside	[7]
Phenyl alkyl glycosides	Tyrosol, salidroside, rosavin, phenol glycosides...	[8] [9–11]
Coumarins	Coumarin, 7-hydroxycoumarin	[10, 11]
Organic acids	Gallic acid, myristic acid, ursolic acid, butyric acid	[12]
Polysaccharides	Arabinose, glucose, mannose, galactose, rhamnose	[10, 11]
Amino acids	Threonine, valine, leucine, isoleucine, lysine, tryptophan, phenylalanine, glycine, histidine, methionine, tyrosine, cysteine, aspartic acid, valine, proline, serine, glutamic acid, arginine	[13]
Vitamins	Vitamin A, vitamin C, vitamin D, vitamin E, vitamin B1	[11]
Inorganic elements	K, Na, Mg, Ba, Al, Ca, Cu, Fe, Zn, Sn, Mo, Mn, Cr, P, Ni, V	[12, 13]
Others	Starch, protein, fat, tannin	[9]

3. Protective Effects of Rhodiola rosea on Myocardial Ischemia-Reperfusion Injury (MIRI)

3.1. Protective Effects on Vascular Endothelial Cells. Vascular endothelial injury begins in the early stage of reperfusion and gradually aggravates. In the early phase of reperfusion, it activates vascular endothelial cells, increases the secretion of adhesion molecules, promotes the adhesion of leukocytes to them, and produces reactive oxygen species (ROS), causing lipid peroxidation, which prevents endothelial cells from secreting vascular relaxing factors and increases the secretion of vasoconstrictive substances, thereby constricting the coronary arteries and coagulating platelets, obstructing coronary blood flow and aggravating myocardial damage.

Studies have shown that salidroside can effectively improve the vasoconstrictor function of vascular endothelium and promote the angiogenesis of ischemic myocardium in rats by affecting the expression of vascular endothelial growth factor (VEGF), promote the angiogenesis of ischemic myocardium in rats, and protect the myocardial ischemia-reperfusion injury. Gao and others used salidroside to intervene in the endothelial cell line of a hypoxia model and tested vascular endothelial cell hypoxia-inducible factor 1α (HIF-1α), endothelin-1 (ET-1), and vascular endothelial cell NO synthase (eNOS) gene expression. It is concluded that salidroside inhibits the gene expression of HIF-1α and ET-1 and promotes the expression of eNOS, as well as the expression of vascular endothelial contractile factors. Salidroside promotes the expression of vascular endothelial relaxing factors and improves vascular endothelial function [14]. Gao et al. [15] investigate the effects of Rhodiola rosea on angiogenesis and expressions of hypoxia-inducible factor 1alpha (HIF-1α), hypoxia-inducible factor 1beta (HIF-1β), and vascular endothelial growth factor (VEGF) in the myocardium of rats with acute myocardial infarction (AMI). They found that Rhodiola rosea may promote angiogenesis in the myocardium of rats with AMI through elevating the expressions of HIF-1α, HIF-1β, and VEGF. Rhodiola rosea increases the expressions of HIF-1α, HIF-1β, and VEGF during ischemia or hypoxia. Leung et al. [16] study the effect of salidroside on aortic function in rats and found that salidroside is effective in preserving the NO bioavailability and thus protects against homocysteine-induced impairment of endothelium-dependent relaxations, mainly through inhibiting the NOX2 expression and ROS production. The relevant mechanism of action is shown in Figure 1.

3.2. Antioxidative Stress Properties. When myocardial ischemia-reperfusion occurs, the myocardium will be ischemic and hypoxic. Oxygen-free radicals (OFR) will be produced in the ischemic part. The body's antioxidant activity will decrease, and the antioxidant capacity will be insufficient, causing oxidative stress. The cardiomyocytes are acidic, and Ca^{2+} enters the cells to balance the pH, causing intracellular calcium overload and promoting the strengthening of the inflammatory response of white blood cells and the lack of high-energy phosphate compounds, which in turn leads to cell damage and even death.

Gupta et al. [17] showed that Rhodiola rosea extracts not only inhibited malondialdehyde (MDA) and lactate dehydrogenase (LDH) in the blood, liver, and muscle of rats but also increased the activities of reducing glutathione (GSH) and superoxide dismutase (SOD) in the blood. Thus, the oxidative capacity of rats during cold (5 degrees C)-hypoxia (428 mmHg)-restraint (C-H-R) exposure (C-H-R) exposure and poststress recovery can be improved, and the membrane permeability can be maintained. As shown in Figure 2, salidroside can significantly reduce the activity of CK and LDH in the serum of rats after MIRI and reduce the levels of tumor necrosis factor-α (TNF-α), interleukin-1β (IL-β), and interleukin-6 (IL-6) in cells [18]. In terms of pathology, the administration of salidroside can attenuate the overall degree of myocardial pathology, the infiltration of inflammatory cells, and the local focal necrosis.

3.3. Interference of Cardiomyocyte Apoptosis. Countless studies have shown the association and or causation between the apoptotic loss of myocytes and the progression of heart diseases, including heart failure, in human and animal models

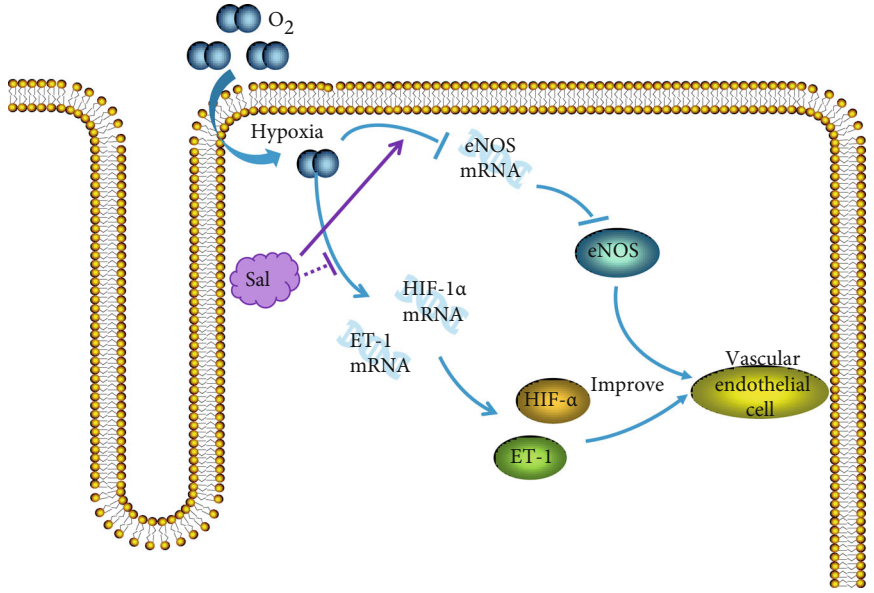

Figure 1: Mechanism of salidroside improving the diastolic and systolic function of vascular endothelium in myocardial ischemia-reperfusion injury model. Salidroside promotes the expression of eNOS by inhibiting HIF-1α and ET-1 produced during tissue hypoxia and improving the vasoconstriction function of vascular endothelium.

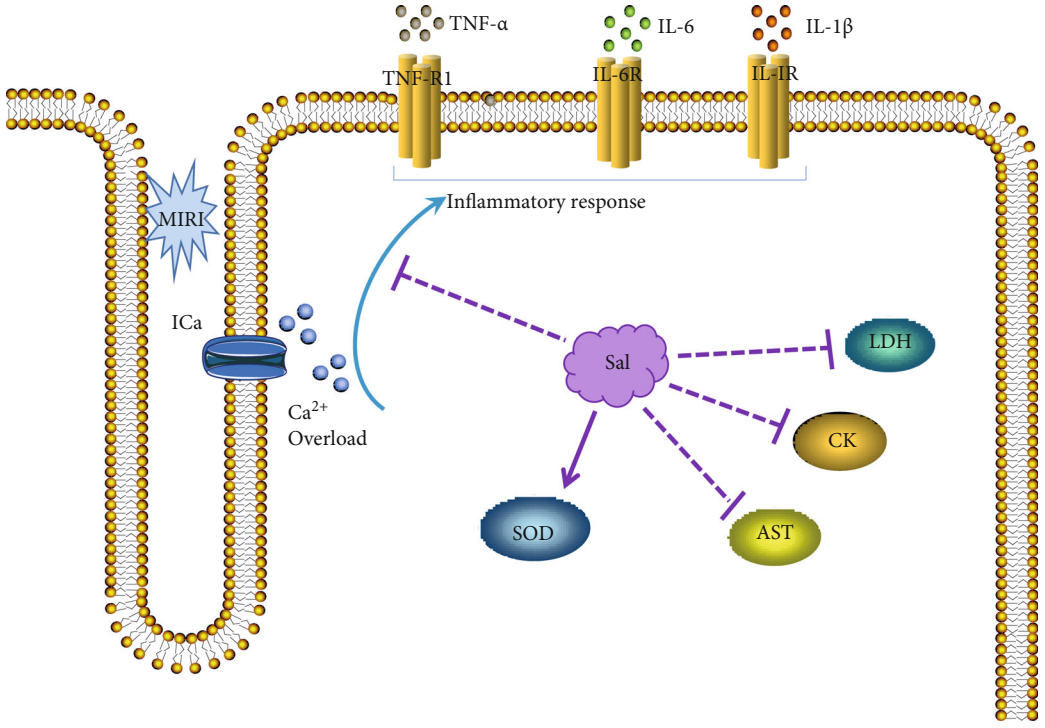

Figure 2: Mechanism of salidroside on antioxidative stress after myocardial ischemia and reperfusion. Salidroside can inhibit LDH, CK, AST, and the infiltration of inflammatory cells, promoting the expression of SOD against oxidative stress.

[19, 20]. Generally, there are three ways to affect cell apoptosis: mitochondrial pathway, endoplasmic reticulum signaling pathway, and death receptor pathway.

Zhong et al. [21] confirmed the protective effect of salidroside on mitochondrial damage from the four aspects, including cardiomyocyte apoptosis rate, mitochondrial membrane potential, degree of mitochondrial division, and cytochrome C (Cyto-C) expression in mitochondria. The expression level of Cyto-C in mitochondria is related to the opening degree of mitochondrial membrane permeable pores. Proteins related to apoptosis include the B-cell lymphoma-2 gene (Bcl-2) family, namely, the antiapoptotic protein Bcl-2 and the proapoptotic protein Bcl-2-associated X (Bax). Besides that, it also includes the death receptor-

mediated apoptosis pathway initiator Fas, the key initiation factor caspase-8, caspase-3, caspase-9, mitochondrial-mediated apoptosis pathway initiator Cyto-C, and so on. Multiple studies have shown that salidroside can inhibit the release of Cyto-C from mitochondria to the cytoplasm by promoting the expression of Bcl-2 protein, inhibiting the expression of Bax protein, and subsequently inhibiting a series of downstream caspase-3 and caspase-9 protein activities and realize the inhibitory effect on cardiomyocyte apoptosis [22–24]. The PI3K-Akt signal transduction pathway is important to protect cardiomyocytes. When PI3K is activated, it will form phosphorylated inositol phospholipid product PIP3 and then activate downstream substances to cause the expression of signal factors such as the Bcl-2 family and glycogen synthase kinase (GSK-3β) [25–28]. Several studies have shown that the phosphorylation of GSK-3β and Akt in cells, after salidroside treatment, is significantly enhanced and which is significantly reduced after the administration of PI3K inhibitors, so it can be proved that salidroside can activate the PI3K/Akt pathway followed by the upregulation of p-Akt and p-GSK-3β, and protects myocardial cells to achieve protection against myocardial ischemia-reperfusion injury [29]. In addition, Sun et al. [30] used the MIRI-treated H9C2 rat cardiomyocyte model to check the influence of tyrosol on the levels of ROS, heat shock protein 70 (Hsp70), extracellular signal-regulated kinase (EPK), c-Jun amino-terminal kinase (JNK), Bcl-2, Bax, and caspase-8. It is known that the cardioprotective effect of tyrosol is related to the reduction of ROS; the inhibition of EPK, JNK, and caspase-8 activation; the increase of Hsp70; and the ratio of Bcl-2/Bax. The relative mechanism is shown in Figure 3.

3.4. Protective Effects on Mitochondrial Damage. Mitochondria is essential for maintaining cardiac homeostasis by providing the major energy required for cardiac excitation-contraction coupling and controlling the intracellular and death pathways [31]. Mitochondrial damage extension suggested as a critical factor for determining myocardial injury under MIRI toward progression to heart failure [32, 33]. MIRI could significantly increase mitochondrial permeability and which resulted in dissipation of electron and proton gradients, dysregulation of mitochondrial calcium homeostasis, and release of superoxide to cause myocardial cell death [34, 35]. One previous study suggested that salidroside could attenuate MIRI-induced myocardial apoptosis via preserving mitochondrial transmembrane potential and enhancing Bcl-2/Bax ratio [21]. Furthermore, Zhuang and his colleagues checked the effect of salidroside on vascular smooth muscle cell (VSMC) proliferation, ROS generation, and mitochondrial dynamics under the challenge of high glucose. They found that salidroside could inhibit VSMC proliferation, dynamin-related protein 1 (Drp1) expression, and mitochondrial ROS level, while upregulate Mitofusin 2 (Mfn2) expression [36]. These results suggested that salidroside might play its therapeutic effect on diabetic cardiomyopathy via maintaining mitochondrial dynamic homeostasis and regulating oxidative stress. In addition, the protective effect of salidroside on diabetic cardiomyopathy is partially associated with the activation of mitochondrial SIRT3, AMPK/Akt, and PGC-1α/TFAM and subsequent improving mitochondrial biogenesis and its function [37]. These findings suggest that salidroside exhibits potential to be a promising drug for preventing and treating ischemic and diabetic myocardial diseases through the prevention of mitochondrial damage and its function (Figure 4).

4. Resisting Myocardial Fibrosis and Heart Failure (HF)

Chen et al. [38] found that Sal might protect against myocardial fibrosis in mice with myocardial infarction (MI) by decreasing the expressions of TNF-α, TGF-β1, IL-1β, and Bax and increasing Bcl-2, VEGF, Akt, and eNOS. In addition, some research also found that Sal significantly upregulated the expression of HO-1 and improved the cardiac dysfunction myocardial hypertrophy and myocardial fibrosis induced by diabetes in mice [39]. The Renin-angiotensin-aldosterone system (RAAS) is involved in the occurrence and development of heart failure and is one of the main factors affecting ventricular remodeling. As shown in Figure 5, Wu et al. [40] found that salidroside might prevent cardiac function and ventricular remodeling in rats with heart failure by inhibiting the activation of the RAAS system in HF. In addition, the ethanol extract of Rhodiola rosea was also reported to increase the expression of peroxisome proliferator-activated receptor (PPAR), to enhance the cardiac output of diabetic heart failure rats, and to increase the myocardial contractility to combat heart failure [41]. Hsiao et al. [42] found that Rhodiola rosea can inhibit the expression of IL-17 and its downstream target genes, thereby reducing the levels of fibrosis and apoptosis and inhibiting ventricular arrhythmia.

4.1. Hypolipidemic Function. The clinical manifestation of hyperlipidemia is high blood lipid levels, often accompanied by various of complications. The leading diagnostic indicators are total cholesterol (TC), triglycerides (TG), low-density lipoprotein cholesterol (LDL-C), and high-density lipoprotein cholesterol (HDL-C) [43]. As shown in Figure 6, Shin et al. [44] used the ethanol extract of Rhodiola rosea angustifolia to gavage a high-fat mouse model, and the results showed that it can significantly reduce the content of TC, TG, and LDL-C and increase the content of HDL-C in the hyperlipidemia model mice. Simultaneously, it can increase the activity of GSH-Px and SOD and reduce the content of malondialdehyde (MDA). It shows that the ethanol extract of Rhodiola rosea angustifolia can reduce blood fat by affecting the absorption, transportation, and the antioxidation of cholesterol. Wang [45] found that Rhodiola rosea extract can effectively reduce the body weight (BW) of rats and improve blood sugar (FBG), blood pressure (BP), and dyslipidemia in rats. The expression of liver peroxisome proliferator-activated receptors (PPAR-α mRNA, PPAR-γ mRNA) in the Rhodiola group was significantly increased because PPAR-γ is closely related to fatty differentiated cells, lipid metabolism, glucose metabolism, and

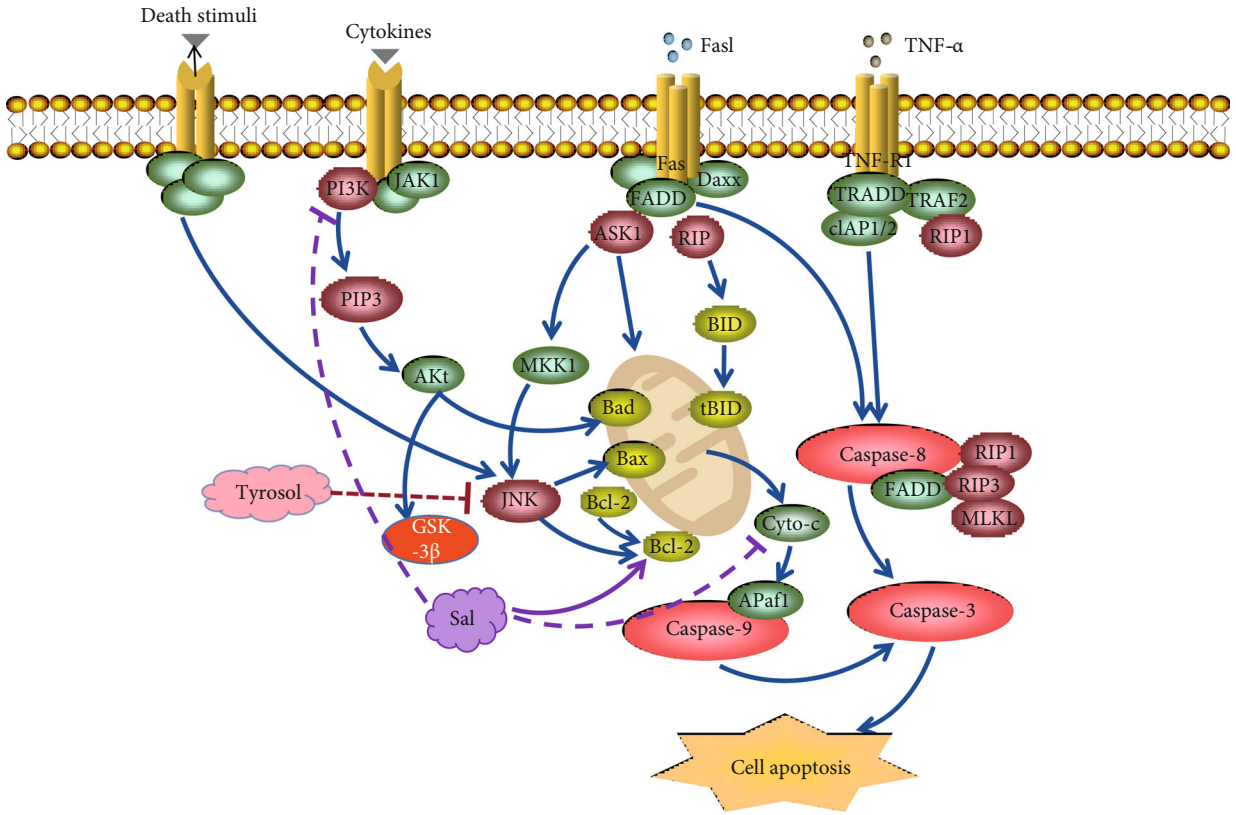

Figure 3: Mechanism of salidroside and tyrosol on cardiomyocyte apoptosis pathway. Salidroside can inhibit the release of Cyto-C from mitochondria to the cytoplasm by promoting the expression of Bcl-2 and Bax and subsequently inhibiting a series of downstream caspase-3 and caspase-9 protein activities from inhibiting cardiomyocyte apoptosis. Moreover, salidroside can activate the PI3K/Akt pathway followed by the upregulation of p-Akt and p-GSK-3β and protects myocardial cells to achieve protection against myocardial ischemia-reperfusion injury.

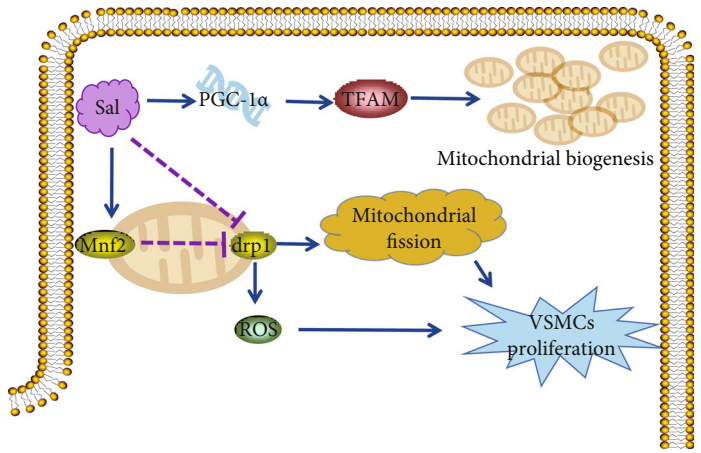

Figure 4: Mechanisms of salidroside on inhibiting VSCM proliferation via promoting mitochondria biogenesis and interfering with mitochondrial fission. Salidroside can promote PGC-1α, TFAM, and Mnf2 and inhibit Drp1 to inhibit VSCM proliferation.

inflammation. Therefore, the effect of Rhodiola rosea extracts on protection against glucose and lipid metabolism disorders may be related to the activation of PPAR-α and PPAR-γ receptors.

4.2. The Protective Effect on Thrombosis. There are mainly three well-known causative factors of thrombosis: (1) Vascular endothelial injury triggers coagulation factors and collagen in the connective tissue and blood to promote

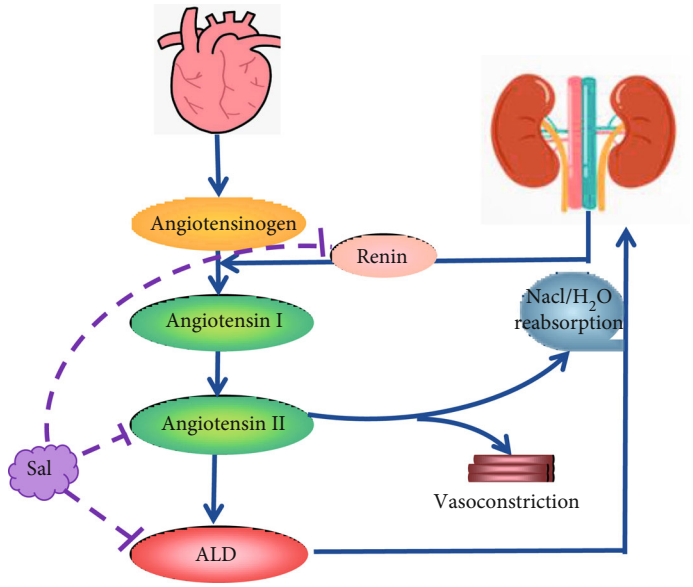

Figure 5: Salidroside participates in the mechanism of resisting heart failure by inhibiting the RAAS system.

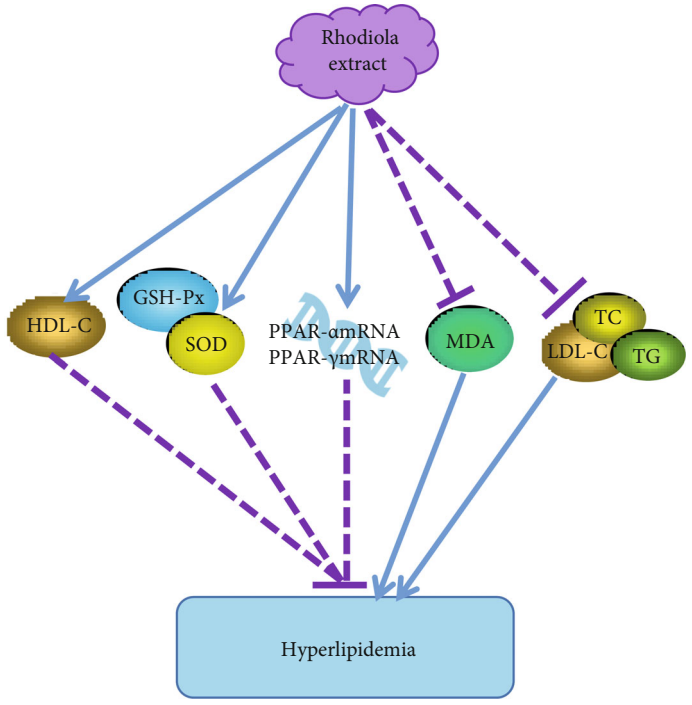

Figure 6: Hypolipidemic mechanism of salidroside. The ethanol extract of Rhodiola rosea angustifolia can reduce blood fat by affecting the absorption, transportation, antioxidation of cholesterol, and the activation of PPAR-α and PPAR-γ receptors.

coagulation, causing platelets to adhere to the thrombus. (2) The blood flow is slow and stagnated due to the change of the vascular state, and the endothelial cells die due to hypoxia. (3) The hypercoagulable state of blood easily forms a thrombus.

Zhang et al. [46] used the in vitro thrombosis method and established a blood stasis rat model to observe the effects of salidroside on coagulation-related indicators such as the length of the in vitro thrombus, dry and wet weight, and blood viscosity. After the treatment of salidroside, thrombus length was significantly shortened; dry weight and wet weight were reduced considerably; hematocrit, high shear viscosity, and the low shear viscosity of the blood were inhibited considerably; and platelet aggregation rate was significantly reduced. It shows that salidroside has a significant inhibitory effect on the formation of in vitro thrombosis, improves blood rheology, and can prolong the clotting time. Liu and Jiang [47] used the Dazhu Rhodiola Rosea Capsule

to treat patients with unstable angina pectoris and reached the same conclusion. However, there was no significant difference in the results in mouse body weight, four items of coagulation, red blood cells, white blood cells, platelet count (PLT), and in mean platelet volume (MPV) detected by Liu ($P > 0.05$). It is suggested that the effect of salidroside and antithrombosis may not be directly related to the coagulation system. He also counted the bleeding time of tail docking and proved that salidroside could prolong bleeding time. Carrageenan is a kind of polysaccharide with a strong inflammatory effect. Subcutaneous or intraperitoneal injection of carrageenan can cause thrombus formation in the tail of mice, which is more intuitive for evaluating antithrombotic drugs. Liu used the intraperitoneal injection of carrageenan to construct thrombosis mouse model and measured the black tail rate and length. He injected salidroside (20 mg/kg) into the mouse intraperitoneally and then measured tail bleeding time, arterial thrombus, and venous thrombosis. These results showed that salidroside has the effect of preventing thrombosis.

As shown in Figure 7, Wei et al. [48] studied human and mouse platelets by treating with salidroside. Salidroside inhibits thrombin or CRP-induced platelet aggregation and adenosine triphosphate release but does not affect the expression of P-selectin and glycoproteins (GP). The platelets treated with salidroside have reduced spreading on fibrinogen and collagen and reduced clot retraction. The phosphorylation of proto-oncogene (c-Src), skin tyrosine kinase (Syk), and phospholipase Cγ2 (PLCγ2) was reduced. In thrombin-stimulated platelets, salidroside inhibits the phosphorylation of AKT (T308/S473) and glycogen synthase kinase 3β (GSK3β). The addition of the GSK3β inhibitor reversed the inhibitory effect of salidroside on platelet aggregation and clot retraction. In short, salidroside inhibits platelet function and thrombosis through the interference of the AKT/GSK3β signaling pathway. It suggests that salidroside may be a new type of therapeutic drug for treating thrombosis and cardiovascular diseases.

4.3. Antiarrhythmic Effect. Arrhythmia is a common cardiovascular disease, which is very harmful and may lead to sudden death. By studying the molecular mechanism and electrophysiological properties of salidroside in inhibiting atrial fibrillation, Liu et al. [49] detected the monophasic action potential, histology, ion channels, and PI3K/AKT/eNOS. Rhodiola rosea can stabilize the ion pumps and calcium channels on the cell membrane, rebuild the atrial potential of rabbits with heart failure, reduce atrial fibrosis, inhibit atrial fibrillation, and eliminate ectopic rhythm. The beneficial electrogenic effects of Rhodiola rosea may be related to voltage-gated potassium channel proteins (Kv1.4, Kv1.5, Kv4.3, KvLQT1) and calcium channel proteins (Cav1.2), and myocardial sarcoplasmic reticulum Ca^{2+}-ATP Enzyme 2a (SERCA2a) is involved in the activation of PI3K/AKT channels. As shown in Figure 8, Hsiao et al. [42] used Rhodiola rosea, and Sal treatment in HF left ventricle in rabbit and found that (1) the levels of WBC and CD4 T cells were decreased; (2) the expression of IL-17 and its downstream target genes, IL-6, TNF-α, IL-1β, IL-8, and CCL20, was reduced; (3) the level of NLRP3 inflammasome was decreased; (4) fibrosis and collagen production were significantly downregulated; (5) p38 MAPK and ERK1/2 phosphorylation were attenuated; (6) the inducibility of VA was decreased; and (7) the levels of Kir2.1, Nav1.5, NCX, PLB, SERCA2a, and RyR were upregulated. RC inhibited the expression of IL-17 and its downstream target genes mediated by activation of several MAPKs, which decreased the levels of fibrosis and apoptosis and suppressed VA. Rhodiola rosea reduces ventricular arrhythmias by inhibiting IL-17 activation and MAPK signaling in the rabbit.

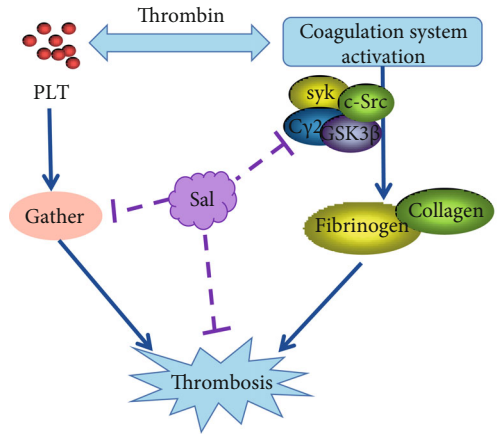

Figure 7: Antithrombotic mechanism of salidroside on AKT/GSK3β signaling pathway. Salidroside can inhibit the expression of syk, c-Src, PLCγ2, GSK3β, and platelet aggregation from inhibiting thrombosis.

4.4. Adjuvant Treatment of Hypertension. Persistent abnormal blood vessel function can lead to worsening hypertension and target organ damage. In spontaneously hypertensive male rats, Lee et al. [50] recorded the systolic blood pressure (SBP) and heart rate of male spontaneously hypertensive rats by the tail-cuff method and measured the plasma β-endorphin content by enzyme-linked immunosorbent assay. They found that the water extract of Rhodiola rosea could induce the release of β-endorphin and reduce the systolic blood pressure of spontaneously hypertensive rats. Rhodiola rosea water extract can induce β-endorphins in spontaneously hypertensive rats to reduce systolic blood pressure (SBP). Long-term salidroside intervention therapy can attenuate blood pressure by dilating resistance blood vessels and volume blood vessels and vascular dysfunction, as well as inhibiting vascular remodeling [51, 52].

Essential hypertension is not only caused by hemodynamic disorders and is also associated with blood lipid metabolism. Yang et al. [53] elaborated on the mechanism of Rhodiola rosea on left ventricular remodeling in hypertensive rats; that is, AngII played an essential role in left ventricular remodeling and participated in the synthesis and release of aldosterone (ALD). ALD can interact with fibroblast cells. The mineralocorticoid receptor in the plasma regulates the synthesis of type I and type III collagen.

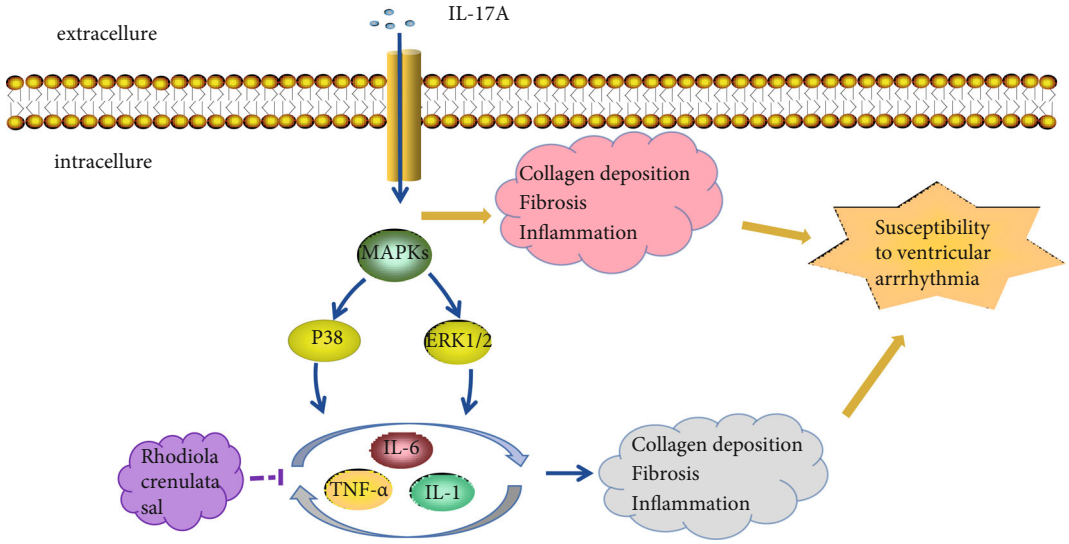

Figure 8: The mechanism for the protective effects of RC in ventricular arrhythmia. RC inhibits cardiac fibrosis by inhibiting the expression of IL-6, TNF-α, IL-1β, and IL-8 from achieving the purpose of interfering arrhythmia.

Rhodiola rosea can inhibit the synthesis of AngII and ALD, thereby promoting left ventricular remodeling.

4.5. Protective Effect on Hyperglycemia. High blood sugar can easily lead to coronary atherosclerosis, leading to cardiovascular diseases such as coronary heart disease. Therefore, improving blood sugar can effectively inhibit cardiovascular illness. As shown in Figure 9, research has found that salidroside can regulate the level of blood glucose and insulin in patients with diabetes and cerebral infarction [54–60]. Salidroside induces the phosphorylation of adenylate-activated kinase (AMPK) and PI3K/AKT and increases GSK3β in hepatocytes in a dose-dependent manner. AMPK activation inhibits the expression of phosphoenolpyruvate carboxy kinase (PEPCK) and glucose-6-phosphatase (G6PD), leading to the phosphorylation of acetyl CoA, reducing lipid accumulation in peripheral tissues, and affecting insulin metabolism in multiple ways. In isolated mitochondria, salidroside can inhibit respiratory chain complex 1, disrupt the oxidation/phosphorylation coupling, and depolarize the mitochondrial membrane potential. Eventually, the body's internal AMP/ATP ratio temporarily increases, thereby significantly reducing blood sugar and serum insulin levels. At this level, it can alleviate insulin resistance and play an antidiabetic effect [59]. The polysaccharides in Rhodiola rosea extract have a two-way regulating effect on blood sugar. It can inhibit the increase of liver glycogen caused by glucose, enhance the decomposition of liver glycogen caused by alloxan and epinephrine, and reduce the hyperglycemia caused by epinephrine. It can also improve hypoglycemia caused by insulin [61]. The hypoglycemic effect of Rhodiola rosea polysaccharide may be due to the reduction of pancreatic tissue damage, improvement of pancreatic tissue morphology, and increased insulin secretion [62, 63]. Besides, many documents show that Rhodiola rosea polysaccharides cannot lower blood sugar after being absorbed through the gastrointestinal tract. However, intramuscular, intraperitoneal, and intravenous injection of Rhodiola rosea polysaccharide can produce significant hypoglycemic effects.

4.6. Antiaging Effect of Rhodiola rosea on Cardiac Diseases. Aging is recognized as an independent risk factor for the development of cardiovascular diseases such as atherosclerosis and heart failure. The fundamental mechanism of aging is the accumulation of senescent cells and which appears to play a crucial role in the process of cardiovascular disease through the secretion of senescence-associated secretory phenotype (SASP) [64]. SASP is a trigger of chronic inflammation, oxidative stress, and decreased nitric oxide resulting in age-associated cardiovascular damage [64, 65]. Recently, growing evidence showed that the epigenetics also exhibited an important role in the chronic inflammation, cellular senescence, and oncogenesis [66–68]. Several studies showed the beneficial effects of Rhodiola rosea on lifespan extension in numerous model organisms, such as fruit flies [69], worms [70], and yeast [71] without interfering with daily food intake and fecundity. One previous study clearly demonstrated that salidroside could slow down the process of human umbilical vein cell senescence by regulating the cell cycle in an atherosclerosis model to clarify the relationship between endothelial cell senescence and atherosclerosis [72]. Sun and his colleagues declared that the possible mechanism is that salidroside might promote the phosphorylation of retinoblastoma protein (Rb) by downregulating the expression of p16, p21, and p66, thus triggering the cell cycle from G0/G1 phase to S phase [72]. In addition, more recent study showed that salidroside could prevent endothelial cell senescence by establishing hyperhomocysteine (HHcy) mouse model through downregulating CD68 and intercellular adhesion molecule 1 (ICAM1) to reduce the activity of senescence-related protein- (SA-) β-gal. Conversely, salidroside can enhance Sirt3 in aorta-derived endothelial cells to

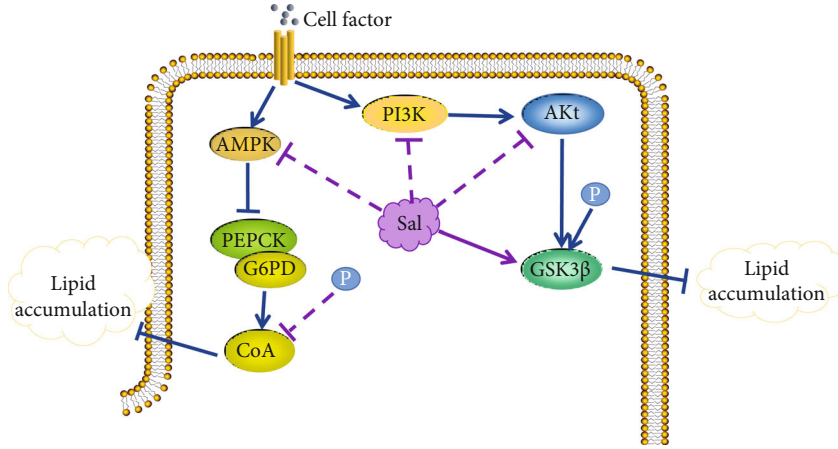

Figure 9: Mechanism of salidroside improving blood glucose. Rosea inhibits PEPCK and G6PD by activating AMPK, leading to reduced phosphorylation of CoA to reduce lipid accumulation, and Sal also reduces lipid accumulation in peripheral tissues by increasing phosphorylation of GSK3β.

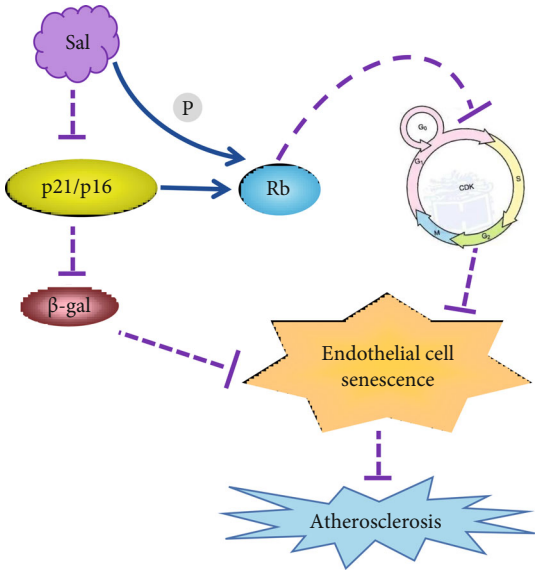

Figure 10: Salidroside protects against atherosclerosis (AS) by attenuating cellular senescence. Salidroside can inhibit the expression of P21 and P16 to promote the cell cycle from G0/G1 phase to S phase and upregulated β-gal, so that inhibits AS.

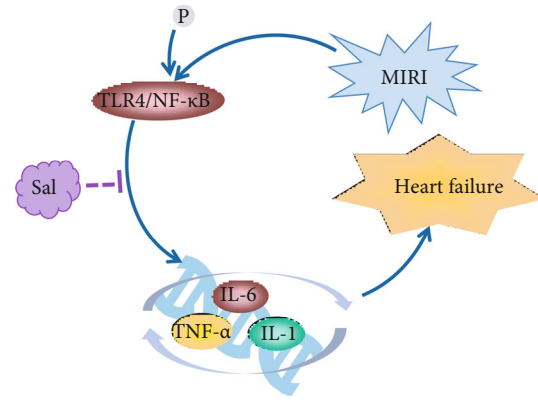

Figure 11: The anti-inflammatory effect of salidroside on preventing cardiovascular disease. Salidroside downregulating the expression of IL-6, IL-1, and TNF-α by inhibiting NF-κB signaling pathway, thus protecting against myocardial infarction and heart failure.

prevent them from premature senescence [73]. Overall, these findings strongly demonstrate that the active component of Rhodiola rosea can protect against cardiac diseases through the amelioration of cellular senescence and which provides a novel therapy for the treatment of diverse cardiomyopathy (Figure 10).

4.7. Anti-inflammatory Effect of Salidroside on Cardiac Diseases. Inflammation plays an important role in both chronic disease and cardiovascular disease, and low-grade inflammation can result in intracellular and mitochondrial oxidative stress that is associated with most cardiovascular disease, representing a cardiovascular risk factor that can be targeted by pharmacological treatment [74, 75]. In the MIRI model, salidroside could attenuated the proinflammatory cytokines including tumor necrosis factor-α (TNF-α), interleukin- (IL-) 1β, and IL-6 in serum by inhibiting TLR4/NF-κB signaling pathway, and that could ameliorate cell apoptosis and the heart failure assessed by histopathological examination and TUNEL assay [24]. In addition, Zhu and his colleagues also investigated the protective effect of salidroside on isoproterenol- (ISO-) induced myocardial ischemia. They found that salidroside could increase SOD activity and decrease NOX4, NF-κB p65, and AP-1 expression in the heart. These results revealed that salidroside might be a potential treatment for ischemic heart disease through attenuating the inflammatory response [18]. Taken together, inflammation is undoubtedly relative to the development of cardiovascular diseases, while salidroside possessed a strong anti-inflammatory effect and which might be a potential for treating chronic cardiac diseases such as MIRI and heart failure (Figure 11).

Table 2: Pharmacological effects of Rhodiola rosea.

Drugs	Dose	Animal	Model/disease	Result	Reference
Sal	300 μM	Endothelial cell strain	Hypoxia model	HIF-1α, EF1mRNA ↓, eNOSmRNA ↑	[14]
Sal	20/40/kg/d	Wistar rat	Acute myocardial infarction model	HIF-1α, HIF-1β, and VEGF ↑	[15]
Sal	100/300 μM	Endothelial cells	Endothelial dysfunction	NOX2, ROS ↓, p-eNOS ↑	[16]
Sal	20/40 mg/kg/d	SD rat	Myocardial ischemia	CK-MB, LDH, TNF-α, IL-6, Nox2, Nox 4, NF-κBP65, P-NF-κBP65, AP1 ↓	[18]
Sal	9.5 mg/kg/2 d	Rabbit	HF	IL-6, TNF-α, IL-1β, IL-8, CCL20, NLRP3, IL-17 ↓, Kir2.1, Nav1.5, NCX, PLB ↑	[42]
Sal	80 mg/kg/d	Male C57 mice	DOX-induced cardiotoxicity	Bax, Bax/Bcl-2, caspase-3 ↓, Bcl-2 ↑	[51]
Sal	600 mg/d	Breast cancer patients	Early left ventricular regional systolic dysfunction	ROS ↓, SR peak ↑	[52]
Sal	0/50/100 mg/kg/d	C57BL/6J mice	Diabetes	PGC-1α ↓, TFAM ↓, SIRT3 ↑	[37]
Sal	6/12/24 mg/kg/d	SD male rat	Heart failure model	LVEDD, LVESD, CL, LVMI, CVF, PVCA, hydroxyproline, RAAS ↓, LVEF, LVFS ↑	[40]
Sal	40 mg/kg/d	Male rats	MIRI model	TNF-α, IL-1β and IL-6, caspase-3, caspase-9 ↓, Bcl-2/Bax ↑	[24]
Sal	0.3/0.5 mM	VSMCs	VSMC proliferation	Drp1 ↓, Mnf2 ↑	[36]
Sal	20 mg/kg/d	Human/mice	Platelet	Platelet aggregation rate ↓, ATP ↓, C-Src, Syk, plcr2 phosphorylation ↓	[48]
Sal	12 mg/kg/d	apoE(-/-) male mice	Atherosclerotic plaque	AMP/ATP ↓	[26]
Sal	50/100/200 mg/kg/d	Wistar male rat	Goto-Kakizaki (GK) rat model of diabetes	Blood glucose, blood pressure, CaL channel ↓	[55]
Sal	40 mg/kg/d	Wistar rat	Goto-Kakizaki (GK) rat model of diabetes	Ach ↑, eNOS ↓	[54]
Sal	270 mg/kg/d	Rabbit	Heart failure model	Atrial fibrosis induction rate ↓, PI3K-AKTmRNA ↑, Kv1.4,1.5,4.3, KvLQT1, Cav1.2 ↑	[49]
Sal	25/50/100 mg/kg/d	Male mice	Type 2 diabetes model	PEPCK, glucose-6-phosphatase ↓, AMPK and PI3K/Akt, GSK3β ↑	[59]
Sal	50 mg/kg/d	C57BL/6J mice	High fat model	Blood glucose, IL-1α, IL-1β, IL-6 ↓, p-Akt, GSK3β ↓	[58]
Sal	500 μM	EA.hy926 cells	Lipid oxidation and AS therapy models	Rb ↓ from G0/G1 phase to S phase	[72]
Sal	50 mg/kg/d	Male BABLc mice	HHcy mouse model	P16 ↓, p21 ↓, ICAM1 ↓, (SA)-β-gal ↓	[73]
Dazhu Rhodiola Rosea Capsules	75 mg/kg/d	STZ-diabetic rats	Type-1 diabetes-like model	β-Endorphin, GLUT 4 ↑, blood glucose, PEPCK ↓	[60]
Rhodiola rosea	100 mg/kg/d	Human cardiomyocyte strain	Oxidative stress injury model	LDH, CK, AST ↓, GSH, MDA, SOD ↑	[17]
Rhodiola-ethanol extract	0.8 g/L	STZ-diabetic rats	Heart failure	PPAR-δ ↑	[41]
Rhodiola-water extract	0.8 g/L	Wistar-Kyoto (WKY) rats	Spontaneously hypertensive rats model	β-Endorphin ↓, CIX1 ↑, SBP ↓	[50]
Tyrosol	0.1/0.25/0.5 mM	Rat	H9c2 rat cardiomyocytes	Caspase-3, cleaved caspase-8, ROS, EPK, JNK ↓, Bcl-2/Bax, Hsp70 ↑	[30]

5. Conclusion

As a worldwide plant adaptogen, Rhodiola rosea is widespread throughout the world. Rhodiola rosea has significant pharmacological effects in the treatment of cardiovascular diseases. As a natural drug, Rhodiola rosea has been applied in clinical practice with little toxicity and side effects. In this paper, many experts and scholars at home and abroad have done a great deal of in-depth research and discussion on the improvement and treatment of cardiovascular diseases by Rhodiola rosea in recent ten years and found that (1) the effective medicinal ingredients of Rhodiola rosea are mainly phenyl alkyl glycosides (salidroside, tyrosol) and polysaccharides. The effective elements of Rhodiola rosea have not been fully explored, and there are still many healing mechanisms that are not clear, which still need to be studied. (2) Rhodiola has the function of multitarget and multipathway in the protection of MIRI; salidroside inhibits the expression of vascular endothelial contractile factor and promotes the expression of vascular endothelial relaxation factor by inhibiting the gene expression of HIF-1α, ET-1, and NOS. Rhodiola rosea inhibited the synthesis of AngII and ALD and promoted left ventricular remodeling. Inhibited the synthesis of AngII and ALD and promoted the left ventricular remodeling. In heart failure, salidroside can inhibit protein phosphorylation in PI3K/AKT/GSK3β pathway and protein expression of collagen-I (Col-I) and profilin-I (profilin-I) in cardiac tissue of heart failure rats, thus reducing the level of cardiac fibrosis and heart failure. (3) There are internal relations among different pathways acted by Rhodiola rosea. For example, Rhodiola can reduce the level of AngII, thereby reducing the level of myocardial fibrosis and heart failure. At the same time, fibrosis and myocardial remodeling can also cause changes in ion channels. (4) The improvement mechanism of Rhodiola on cardiovascular diseases mainly focuses on the PI3K/Akt pathway. In the protection of MIRI, salidroside can activate PI3K/Akt pathway, upregulate the protein expression of P-Akt and P-GSK-3 β, and protect myocardial cells from achieving the protective effect on myocardial ischemia-reperfusion injury. In antiheart failure, salidroside can inhibit the protein phosphorylation level of PI3K/AKT/GSK3β pathway and inhibit the protein expression of Col-I and profilin-I in heart failure rats after acute myocardial infarction (AMI), thus reducing the level of myocardial fibrosis and heart failure. (5) In the antiarrhythmia effect, the beneficial electrophysiological effects of Rhodiola rosea may be related to voltage-gated potassium channel proteins (Kv1.4, Kv1.5, Kv4.3, KvLQT1) and calcium ion channel proteins (Cav1.2); myocardial sarcoplasmic reticulum Ca^{2+} ATPase 2A (SERCA2a) is associated with activation of the PI3K/AKT channel.

In summary as shown in Table 2, Rhodiola rosea and its active ingredients can protect against myocardial ischemia, hypoxia, hypolipidemic, antithrombotic, hemodynamics, vascular function. It can be used to treat common diseases of the cardiovascular system such as coronary heart disease, hypertension, angina pectoris, myocardial infarction, heart failure, and arrhythmia. Although the components of Rhodiola rosea described in articles are not the same, the chemical constituents and effective ingredients contained in the rhizomes of different varieties of Rhodiola rosea are the same. Clinically, Rhodiola rosea has been used in fewer treatments for diseases, and there are still many dark areas in the research of Rhodiola rosea.

Abbreviations

CVD: Cardiovascular disease
DAYS: Disability adjusted life years
Sal: Salidroside
MIRI: Myocardial ischemia-reperfusion injury
ROS: Reactive oxygen species
VEGF: Vascular endothelial growth factor
HIF-1α: Hypoxia-inducible factor 1α
HIF-1β: Hypoxia-inducible factor 1beta
ET-1: Endothelin-1
eNOS: Endothelial cell NO synthase
AMI: Acute myocardial infarction
OFR: Oxygen-free radicals
MDA: Malondialdehyde
LDH: Lactate dehydrogenase
GSH: Glutathione
SOD: Superoxide
C-H-R: Cold (5 degrees C)-hypoxia (428 mmHg)-restraint
TNF-α: Tumor necrosis factor-α
IL-β: Interleukin-1β
IL-6: Interleukin-6
Cyto-C: Cytochrome C
Bcl-2: B-cell lymphoma-2
Bax: Bcl-2-associated X
GSK-3β: Glycogen synthase kinase
Hsp70: Heat shock protein 70
EPK: Extracellular signal-regulated kinase
JNK: c-Jun amino-terminal kinase
HF: Heart failure
RAAS: Renin-angiotensin-aldosterone system
PPAR: Peroxisome proliferator-activated receptor
TC: Total cholesterol
TG: Triglycerides
LDL-C: Low-density lipoprotein cholesterol
HDL-C: High-density lipoprotein cholesterol
MDA: Malondialdehyde
BW: Bodyweight
BP: Blood pressure
FBG: Blood sugar
MPV: Mean platelet volume
PLT: Platelet count
GP: Glycoproteins
Sky: Skin tyrosine kinase
PLCγ2: Phospholipase Cγ2
ALD: Aldosterone
AMPK: Adenylate-activated kinase
PEPCK: Phosphoenolpyruvate carboxy kinase
G6PD: Glucose-6-phosphatase
VSMC: Vascular smooth muscle cells
Drp1: Dynamin-related protein 1
Mfn2: Mitofusin 2
TFAM: Mitochondrial transcription factor A

SASP: Senescence-associated secretory phenotype
Rb: Retinoblastoma protein
HHcy: Hyperhomocysteine
ICAM1: Intercellular adhesion molecule 1
TNF-α: Tumor necrosis factor-α
IL: Interleukin
ISO: Isoproterenol
PGC-1α: Peroxisome proliferator-activated receptor-γ coactivator 1-α.

Data Availability

The data used to support this study are included within the article.

Conflicts of Interest

All authors have disclosed that they do not have any conflicts of interest.

Authors' Contributions

Yingqing Chen, Minli Tang, Shuo Yuan, Shuang Fu, Yifei Li, You Li, Qi Wang, and Yuying Cao contributed to the collection of reference. Yingqing Chen, Minli Tang, and Shuo Yuan contributed to the analysis of reference and writing of the manuscript. Liping Liu and Qinggao Zhang contributed to the topic conception, manuscript revision, and decision to submit for publication. Liping Liu and Qinggao Zhang contributed to the reference analysis (corresponding authors). Yingqing Chen, Minli Tang, and Shuo Yuan contributed equally to this work (co-first authors).

Acknowledgments

This paper was supported by the National Natural Science Foundation of China (82000074), the Scientific Research Funding Project of Liaoning Provincial Department of Education (jyt-dldxjc202005), the Dalian University Doctoral Program (2020QL023), and the Dalian Youth Science and Technology Star Research Project (2020RQ080).

References

[1] M. Dehghan, A. Mente, X. Zhang et al., "Associations of Fats and Carbohydrate Intake with Cardiovascular Disease and Mortality in 18 Countries from Five Continents (PURE): A Prospective Cohort Study," *The Lancet*, vol. 390, no. 10107, pp. 2050–2062, 2017.

[2] C. Wang, C. Wang, M. Liu, Z. Chen, and S. Liu, "Temporal and spatial trends of ischemic heart disease burden in Chinese and subgroup populations from 1990 to 2016: socio-economical data from the 2016 Global Burden of Disease Study," *BMC Cardiovascular Disorders*, vol. 20, no. 1, p. 243, 2020.

[3] S. Francula-Zaninovic and I. Nola, "Management of measurable variable cardiovascular disease' risk factors," *Current Cardiology Reviews*, vol. 14, no. 3, pp. 153–163, 2018.

[4] M. Khoury, C. Manlhiot, D. Gibson et al., "Universal screening for cardiovascular disease risk factors in adolescents to identify high-risk families: a population-based cross-sectional study," *BMC Pediatrics*, vol. 16, no. 1, p. 11, 2016.

[5] H. Tao, X. Wu, J. Cao et al., "Rhodiola species: a comprehensive review of traditional use, phytochemistry, pharmacology, toxicity, and clinical study," *Medicinal Research Reviews*, vol. 39, no. 5, pp. 1779–1850, 2019.

[6] A. Panossian and G. Wikman, "Evidence-based efficacy of adaptogens in fatigue, and molecular mechanisms related to their stress-protective activity," *Current Clinical Pharmacology*, vol. 4, no. 3, pp. 198–219, 2009.

[7] S. Zhang, C. Liu, H. Bi, and C. Wang, "Extraction of flavonoids from Rhodiola sachlinesis A. Bor by UPE and the antioxidant activity of its extract," *Natural Product Research*, vol. 22, no. 2, pp. 178–187, 2008.

[8] Z. Ali, F. Fronczek, and I. Khan, "Phenylalkanoids and monoterpene analogues from the roots of Rhodiola rosea," *Planta Medica*, vol. 74, no. 2, pp. 178–181, 2008.

[9] G. Ma, W. Li, D. Dou et al., "Rhodiolosides A-E, monoterpene glycosides from Rhodiola rosea," *Chemical & Pharmaceutical Bulletin*, vol. 54, no. 8, pp. 1229–1233, 2006.

[10] X. Bai, X. Jia, Y. Lu et al., "Salidroside-mediated autophagic targeting of active Src and caveolin-1 suppresses low-density lipoprotein transcytosis across endothelial cells," *Oxidative Medicine and Cellular Longevity*, vol. 2020, Article ID 9595036, 21 pages, 2020.

[11] A. Tolonen, M. Pakonen, A. Hohtola, and J. Jalonen, "Phenylpropanoid glycosides from Rhodiola rosea," *Chemical & Pharmaceutical Bulletin*, vol. 51, no. 4, pp. 467–470, 2003.

[12] F. Han, Y. Li, X. Mao, R. Xu, and R. Yin, "Characterization of chemical constituents in Rhodiola crenulate by high-performance liquid chromatography coupled with Fourier-transform ion cyclotron resonance mass spectrometer (HPLC-FT-ICR MS)," *Journal of Mass Spectrometry: JMS*, vol. 51, no. 5, pp. 363–368, 2016.

[13] A. Tayade, P. Dhar, J. Kumar, M. Sharma, O. Chaurasia, and R. Srivastava, "Trans-Himalayan Rhodiola imbricata Edgew. root: a novel source of dietary amino acids, fatty acids and minerals," *Journal of Food Science and Technology*, vol. 54, no. 2, pp. 359–367, 2017.

[14] Q. Gao and M. Shao, "Salidroside improve the contractoin and dilatation function of vascular endotheliocyte," *Shaanxi Medical Journal*, vol. 46, no. 2, pp. 304–306, 2017.

[15] X. Gao, H. Shi, T. Sun, and H. Ao, "Effects of Radix et Rhizoma Rhodiolae Kirilowii on expressions of von Willebrand factor, hypoxia-inducible factor 1 and vascular endothelial growth factor in myocardium of rats with acute myocardial infarction," *Journal of Chinese Integrative Medicine*, vol. 7, no. 5, pp. 434–440, 2009.

[16] S. Leung, H. Zhang, C. Lau, Y. Huang, and Z. Lin, "Salidroside improves homocysteine-induced endothelial dysfunction by reducing oxidative stress," *Evidence-Based Complementary and Alternative Medicine : eCAM*, vol. 2013, article 679635, 8 pages, 2013.

[17] V. Gupta, S. Lahiri, S. Sultana, R. Tulsawani, and R. Kumar, "Anti-oxidative effect of Rhodiola imbricata root extract in rats during cold, hypoxia and restraint (C-H-R) exposure and post-stress recovery," *Food and Chemical Toxicology*, vol. 48, no. 4, pp. 1019–1025, 2010.

[18] L. Zhu, T. Wei, X. Chang et al., "Effects of salidroside on myocardial injury in vivo in vitro via regulation of Nox/NF-κB/AP1 pathway," *Inflammation*, vol. 38, no. 4, pp. 1589–1598, 2015.

[19] A. Haunstetter and S. Izumo, "Apoptosis," *Circulation Research*, vol. 82, no. 11, pp. 1111–1129, 1998.

[20] R. Foo, K. Mani, and R. Kitsis, "Death begets failure in the heart," *The Journal of Clinical Investigation*, vol. 115, no. 3, pp. 565–571, 2005.

[21] H. Zhong, H. Xin, L. Wu, and Y. Zhu, "Salidroside attenuates apoptosis in ischemic cardiomyocytes: a mechanism through a mitochondria-dependent pathway," *Journal of Pharmacological Sciences*, vol. 114, no. 4, pp. 399–408, 2010.

[22] M. Kvansakul and M. Hinds, "The Bcl-2 family: structures, interactions and targets for drug discovery," *Apoptosis : An International Journal on Programmed Cell Death*, vol. 20, no. 2, pp. 136–150, 2015.

[23] E. Raemy and J. Martinou, "Involvement of cardiolipin in tBID-induced activation of BAX during apoptosis," *Chemistry and Physics of Lipids*, vol. 179, pp. 70–74, 2014.

[24] L. Zhu, T. Wei, J. Gao et al., "The cardioprotective effect of salidroside against myocardial ischemia reperfusion injury in rats by inhibiting apoptosis and inflammation," *Apoptosis : An International Journal on Programmed Cell Death*, vol. 20, no. 11, pp. 1433–1443, 2015.

[25] W. Zuo, F. Yan, B. Zhang, X. Hu, and D. Mei, "Salidroside improves brain ischemic injury by activating PI3K/Akt pathway and reduces complications induced by delayed tPA treatment," *European Journal of Pharmacology*, vol. 830, pp. 128–138, 2018.

[26] S. Xing, X. Yang, T. Zheng et al., "Salidroside improves endothelial function and alleviates atherosclerosis by activating a mitochondria-related AMPK/PI3K/Akt/eNOS pathway," *Vascular Pharmacology*, vol. 72, pp. 141–152, 2015.

[27] L. Rong, Z. Li, X. Leng et al., "Salidroside induces apoptosis and protective autophagy in human gastric cancer AGS cells through the PI3K/Akt/mTOR pathway," *Biomedicine & Pharmacotherapy*, vol. 122, article 109726, 2020.

[28] B. Zhang, Y. Wang, H. Li et al., "Neuroprotective effects of salidroside through PI3K/Akt pathway activation in Alzheimer's disease models," *Drug Design, Development and Therapy*, vol. 10, pp. 1335–1343, 2016.

[29] W. Zhang, Y. Huai, Z. Miao et al., "Systems pharmacology approach to investigate the molecular mechanisms of herb Rhodiola rosea L. radix," *Drug Development and Industrial Pharmacy*, vol. 45, no. 3, pp. 456–464, 2019.

[30] L. Sun, H. Fan, L. Yang, L. Shi, and Y. Liu, "Tyrosol prevents ischemia/reperfusion-induced cardiac injury in H9c2 cells: involvement of ROS, Hsp70, JNK and ERK, and apoptosis," *Molecules*, vol. 20, no. 3, pp. 3758–3775, 2015.

[31] F. Tahrir, D. Langford, S. Amini, T. Mohseni Ahooyi, and K. Khalili, "Mitochondrial quality control in cardiac cells: mechanisms and role in cardiac cell injury and disease," *Journal of Cellular Physiology*, vol. 234, no. 6, pp. 8122–8133, 2019.

[32] T. Doenst, T. Nguyen, and E. Abel, "Cardiac metabolism in heart failure," *Circulation Research*, vol. 113, no. 6, pp. 709–724, 2013.

[33] B. Niemann, M. Schwarzer, and S. Rohrbach, "Heart and mitochondria: pathophysiology and implications for cardiac surgeons," *The Thoracic and Cardiovascular Surgeon*, vol. 66, no. 1, pp. 11–19, 2018.

[34] P. Kang, C. Chen, P. Lin, W. Chilian, and Y. Chen, "Impairment of pH gradient and membrane potential mediates redox dysfunction in the mitochondria of the post-ischemic heart," *Basic Research in Cardiology*, vol. 112, no. 4, p. 36, 2017.

[35] W. Zhang, C. Chen, J. Wang, L. Liu, Y. He, and Q. Chen, "Mitophagy in cardiomyocytes and in platelets: a major mechanism of cardioprotection against ischemia/reperfusion injury," *Physiology*, vol. 33, no. 2, pp. 86–98, 2018.

[36] X. Zhuang, A. Maimaitijiang, Y. Li, H. Shi, and X. Jiang, "Salidroside inhibits high-glucose induced proliferation of vascular smooth muscle cells via inhibiting mitochondrial fission and oxidative stress," *Experimental and Therapeutic Medicine*, vol. 14, no. 1, pp. 515–524, 2017.

[37] Y. Li, X. Wei, S. Liu, Y. Zhao, S. Jin, and X. Yang, "Salidroside protects cardiac function in mice with diabetic cardiomyopathy via activation of mitochondrial biogenesis and SIRT3," *Phytotherapy Research : PTR*, vol. 35, no. 8, pp. 4579–4591, 2021.

[38] P. Chen, J. Liu, H. Ruan et al., "Protective effects of salidroside on cardiac function in mice with myocardial infarction," *Scientific Reports*, vol. 9, no. 1, p. 18127, 2019.

[39] J. Ni, Y. Li, Y. Xu, and R. Guo, "Salidroside protects against cardiomyocyte apoptosis and ventricular remodeling by AKT/HO-1 signaling pathways in a diabetic cardiomyopathy mouse model," *Phytomedicine : International Journal Of Phytotherapy and Phytopharmacology*, vol. 82, article 153406, 2021.

[40] J. Wu, T. Yin, Q. Zou, and L. Si, "Effects of salidroside on ventricular remodeling and renin angiotensin in chronic heart failure rats effects of aldosterone system," *Chinese Journal of Gerontology*, vol. 19, no. 2, 2016.

[41] Y. Cheng, L. Chen, W. Lee, M. Chen, H. Jung Lin, and J. Cheng, "Increase of myocardial performance by Rhodiola-ethanol extract in diabetic rats," *Journal of Ethnopharmacology*, vol. 144, no. 2, pp. 234–239, 2012.

[42] Y. Hsiao, Y. Tsai, Y. Huang et al., "Rhodiola crenulata reduces ventricular arrhythmia through mitigating the activation of IL-17 and inhibiting the MAPK signaling pathway," *Cardiovascular Drugs and Therapy*, vol. 35, no. 5, pp. 889–900, 2021.

[43] L. Yang, Z. Li, Y. Song et al., "Study on urine metabolic profiling and pathogenesis of hyperlipidemia," *Clinica Chimica Acta*, vol. 495, pp. 365–373, 2019.

[44] H. Shin, J. Han, H. Kim et al., "Anti-atherosclerosis and hyperlipidemia effects of herbal mixture, Artemisia iwayomogi Kitamura and Curcuma longa Linne, in apolipoprotein E-deficient mice," *Journal of Ethnopharmacology*, vol. 153, no. 1, pp. 142–150, 2014.

[45] Z. Wang, G. Ma, J. Wang, and N. Liu, "Effects of Rhodiola rosea extract on liver of rats with metabolic syndrome expression of PPAR -αmRNA and PPAR -γmRNA," *Journal of Hebei TCM and Pharmacology*, vol. 1, no. 1, pp. 365–373, 2001.

[46] B. Zhang, W. Li, R. Guo, and Y. Xu, "Salidroside decreases atherosclerotic plaque formation in low-density lipoprotein receptor-deficient mice," *Evidence-Based Complementary and Alternative Medicine : eCAM*, vol. 2012, article 607508, 2012.

[47] W. Liu and C. Jiang, "Rhodiola crenulate capsule on unstable thrombus formation in patients with angina pectoris effect," *Drugs and Clinical*, vol. 9, no. 9, 2015.

[48] G. Wei, X. Xu, H. Tong et al., "Salidroside inhibits platelet function and thrombus formation through AKT/GSK3β signaling pathway," *Aging*, vol. 12, no. 9, pp. 8151–8166, 2020.

[49] S. Liu, Y. Hsiao, E. Chong et al., "Rhodiola inhibits atrial arrhythmogenesis in a heart failure model," *Journal of Cardiovascular Electrophysiology*, vol. 27, no. 9, pp. 1093–1101, 2016.

[50] W. Lee, H. Chung, Y. Cheng, H. Lin, and J. Cheng, "Rhodiola-water extract induces β-endorphin secretion to lower blood

pressure in spontaneously hypertensive rats," *Phytotherapy Research : PTR*, vol. 27, no. 10, pp. 1543–1547, 2013.

[51] X. Wang, X. Wang, L. Xiong et al., "Salidroside improves doxorubicin-induced cardiac dysfunction by suppression of excessive oxidative stress and cardiomyocyte apoptosis," *Journal of Cardiovascular Pharmacology*, vol. 62, no. 6, pp. 512–523, 2013.

[52] H. Zhang, W. Shen, C. Gao, L. Deng, and D. Shen, "Protective effects of salidroside on epirubicin-induced early left ventricular regional systolic dysfunction in patients with breast cancer," *Drugs in R&D*, vol. 12, no. 2, pp. 101–106, 2012.

[53] R. Yang, K. Liu, and X. P. Chen, "Effect of Rhodiola sacra on left ventricular remodeling and its mechanism in spontaneously hypertensive rats," *Sichuan Da Xue Xue Bao. Yi Xue Ban*, vol. 44, no. 2, pp. 201–204, 2013.

[54] A. Alameddine, Z. Fajloun, J. Bourreau et al., "The cardiovascular effects of salidroside in the Goto-Kakizaki diabetic rat model," *Journal of Physiology and Pharmacology*, vol. 66, no. 2, pp. 249–257, 2015.

[55] Y. Ma, J. Wang, Y. Bai, M. Liu, M. Xie, and Z. Dai, "Salidroside contributes to reducing blood pressure and alleviating cerebrovascular contractile activity in diabetic Goto-Kakizaki rats by inhibition of L-type calcium channel in smooth muscle cells," *BMC Pharmacology and Toxicology*, vol. 18, no. 1, p. 30, 2017.

[56] X. Wang, W. Bao, J. Liu et al., "Inflammatory markers and risk of type 2 diabetes," *Diabetes Care*, vol. 36, no. 1, pp. 166–175, 2013.

[57] M. Donath, "Multiple benefits of targeting inflammation in the treatment of type 2 diabetes," *Diabetologia*, vol. 59, no. 4, pp. 679–682, 2016.

[58] M. Wang, L. Luo, L. Yao et al., "Salidroside improves glucose homeostasis in obese mice by repressing inflammation in white adipose tissues and improving leptin sensitivity in hypothalamus," *Scientific Reports*, vol. 6, no. 1, article 25399, 2016.

[59] T. Zheng, X. Yang, D. Wu et al., "Salidroside ameliorates insulin resistance through activation of a mitochondria-associated AMPK/PI3K/Akt/GSK3β pathway," *British Journal of Pharmacology*, vol. 172, no. 13, pp. 3284–3301, 2015.

[60] C. Niu, L. Chen, and H. Niu, "Antihyperglycemic action of Rhodiola-aqeous extract in type1-like diabetic rats," *BMC Complementary and Alternative Medicine*, vol. 14, no. 1, p. 20, 2014.

[61] S. Wang and J. Lu, "Protective effect of Rhodiola polysaccharide on pancreas in alloxan-induced hyperglycemic rats," *Chinese Archives of Traditional Chinese Medicine*, vol. 5, p. 218, 2018.

[62] J. Song, Y. Wu, G. Jiang et al., "Sulfated polysaccharides from Rhodiola sachalinensis reduce D-gal-induced oxidative stress in NIH 3T3 cells," *International Journal of Biological Macromolecules*, vol. 140, pp. 288–293, 2019.

[63] Y. Xu, H. Jiang, C. Sun et al., "Antioxidant and hepatoprotective effects of purified Rhodiola rosea polysaccharides," *International Journal of Biological Macromolecules*, vol. 117, pp. 167–178, 2018.

[64] H. Shakeri, K. Lemmens, A. Gevaert, G. De Meyer, and V. Segers, "Cellular senescence links aging and diabetes in cardiovascular disease," *American Journal of Physiology-Heart and Circulatory Physiology*, vol. 315, no. 3, pp. H448–H462, 2018.

[65] Y. Chen, S. Yuan, Y. Cao et al., "Gasotransmitters: potential therapeutic molecules of fibrotic diseases," *Oxidative Medicine and Cellular Longevity*, vol. 2021, Article ID 3206982, 18 pages, 2021.

[66] Q. Wang, X. Shao, E. Leung, Y. Chen, and X. Yao, "Selectively targeting individual bromodomain: drug discovery and molecular mechanisms," *Pharmacological Research*, vol. 172, article 105804, 2021.

[67] Y. Chen, X. Shao, X. Zhao et al., "Targeting protein arginine methyltransferase 5 in cancers: roles, inhibitors and mechanisms," *Biomedicine & Pharmacotherapy*, vol. 144, article 112252, 2021.

[68] Q. Wang, Q. Zhang, E. Leung, Y. Chen, and X. Yao, "Exploring the thermodynamic, kinetic and inhibitory mechanisms of 5-iTU targeting mitotic kinase haspin by integrated molecular dynamics," *Physical Chemistry Chemical Physics : PCCP*, vol. 23, no. 34, pp. 18404–18413, 2021.

[69] M. Jafari, J. Felgner, I. Bussel et al., "Rhodiola: a promising anti-aging Chinese herb," *Rejuvenation Research*, vol. 10, no. 4, pp. 587–602, 2007.

[70] C. Chen, J. Song, M. Chen et al., "Rhodiola rosea extends lifespan and improves stress tolerance in silkworm, Bombyx mori," *Biogerontology*, vol. 17, no. 2, pp. 373–381, 2016.

[71] M. Bayliak and V. Lushchak, "The golden root, Rhodiola rosea, prolongs lifespan but decreases oxidative stress resistance in yeast Saccharomyces cerevisiae," *Phytomedicine : international journal of phytotherapy and phytopharmacology*, vol. 18, no. 14, pp. 1262–1268, 2011.

[72] L. Sun, F. Dou, J. Chen et al., "Salidroside slows the progression of EA.hy926 cell senescence by regulating the cell cycle in an atherosclerosis model," *Molecular Medicine Reports*, vol. 17, no. 1, pp. 257–263, 2018.

[73] S. Xing, J. Li, L. Chen et al., "Salidroside attenuates endothelial cellular senescence via decreasing the expression of inflammatory cytokines and increasing the expression of SIRT3," *Mechanisms of Ageing and Development*, vol. 175, pp. 1–6, 2018.

[74] S. Steven, K. Frenis, M. Oelze et al., "Vascular inflammation and oxidative stress: major triggers for cardiovascular disease," *Oxidative Medicine and Cellular Longevity*, vol. 2019, Article ID 7092151, 26 pages, 2019.

[75] S. Kaptoge, S. Seshasai, P. Gao et al., "Inflammatory cytokines and risk of coronary heart disease: new prospective study and updated meta-analysis," *European Heart Journal*, vol. 35, no. 9, pp. 578–589, 2014.

Hindawi
Oxidative Medicine and Cellular Longevity
Volume 2022, Article ID 7547269, 9 pages
https://doi.org/10.1155/2022/7547269

Research Article

Vascular Endothelial Dysfunction in the Thoracic Aorta of Rats with Ischemic Acute Kidney Injury: Contribution of Indoxyl Sulfate

Keisuke Nakagawa,[1] Ryosuke Tanaka,[1] Masahide Donouchi,[1] Masaya Kanda,[1] Saaya Kamada,[1] Shuhei Kobuchi,[2] Masashi Tawa,[1] Yasuo Matsumura,[1] and Mamoru Ohkita[1]

[1]*Department of Pathological and Molecular Pharmacology, Faculty of Pharmacy, Osaka Medical and Pharmaceutical University, 4-20-1 Nasahara, Takatsuki, Osaka 569-1094, Japan*
[2]*Division of Pharmacology, Department of Pharmacy, School of Pharmacy, Hyogo University of Health Sciences, 1-3-6 Minatojima, Chuo-ku, Kobe, Hyogo 650-8530, Japan*

Correspondence should be addressed to Mamoru Ohkita; mamoru.ohkita@ompu.ac.jp

Received 14 December 2021; Revised 21 January 2022; Accepted 9 February 2022; Published 25 February 2022

Academic Editor: Abdur Rauf

Chronic kidney disease (CKD) and cardiovascular disease are known to be linked, and the involvement of indoxyl sulfate (IS), a type of uremic toxin, has been suggested as one of the causes. It is known that IS induces vascular dysfunction through overproduction of reactive oxygen species (ROS). On the other hand, the involvement of IS in the vascular dysfunction associated with acute kidney injury (AKI) is not fully understood. Therefore, we investigated this issue using the thoracic aorta of rats with ischemic AKI. Ischemic AKI was induced by occlusion of the left renal artery and vein for 45 min, followed by reperfusion 2 weeks after contralateral nephrectomy. One day after reperfusion, there was marked deterioration in renal function evidenced by an increase in plasma creatinine. Furthermore, blood IS levels increased markedly due to worsening renal function. Seven days and 28 days after reperfusion, blood IS levels decreased with the improvement in renal function. Of note, acetylcholine-induced vasorelaxation deteriorated over time after reperfusion, contradicting the recovery of renal function. In addition, 28 days after reperfusion, we observed a significant increase in ROS production in the vascular tissue. Next, we administered AST-120, a spherical adsorbent charcoal, after reperfusion to assess whether the vascular endothelial dysfunction associated with the ischemic AKI was due to a temporary increase in blood IS levels. AST-120 reduced the temporary increase in blood IS levels after reperfusion without influencing renal function, but did not restore the impaired vascular reactivity. Thus, in ischemic AKI, we confirmed that the vascular endothelial function of the thoracic aorta is impaired even after the recovery of kidney injury, probably with excessive ROS production. IS, which increases from ischemia to early after reperfusion, may not be a major contributor to the vascular dysfunction associated with ischemic AKI.

1. Introduction

Ischemia/reperfusion (I/R) is one of the leading causes of acute kidney injury (AKI), with a high morbidity and mortality in hospitalized patients [1]. In addition to there being no established treatment for AKI, a major medical problem is that after AKI develops, it progresses to chronic kidney disease (CKD) and end-stage renal disease. Although many studies have been conducted on the mechanism of transition to CKD after the onset of AKI, it is not fully understood [2, 3].

Decreased vascular endothelial function leads to the development of not only renal damage but also cardiovascular disease [4]. In this regard, vascular endothelial dysfunction is known to be caused by AKI [5, 6]. AKI is accompanied by reactive oxygen species (ROS)

overproduction [7], and increased ROS production is considered to lead to the inactivation and/or reduction of endothelium-derived relaxing factors, such as nitric oxide (NO) and endothelium-derived hyperpolarizing factor, resulting in vascular endothelial dysfunction [8]. Of note, vascular endothelial dysfunction associated with AKI is caused not only in the primary lesion [5] but also in distant sites [6], which is thought to create a vicious cycle of multiple organ injury. It is also possible that vascular endothelial dysfunction after the onset of AKI plays a role in the subsequent progression to CKD.

We reported that indoxyl sulfate (IS), a uremic toxin that accumulates during the progression of renal failure, promotes the generation of excess ROS in the thoracic aorta of normal rats and inactivates NO, leading to vascular dysfunction [9]. Of note, the administration of spherical adsorbent charcoal AST-120 to CKD model rats reduced blood IS levels and improved vascular endothelial function [10]. Thus, there is strong evidence and support for the involvement of IS in endothelial dysfunction in renal injury. In AKI, the blood IS concentration increases with a decline in renal function [11]. However, it is unclear whether IS is involved in the vascular endothelial dysfunction associated with AKI. In this study, we evaluated changes in vascular endothelial dysfunction and IS levels over time in ischemic AKI. Furthermore, AST-120 was administered from the onset of AKI to evaluate the contribution of IS on vascular endothelial dysfunction.

2. Materials and Methods

2.1. Animals. Male Sprague-Dawley rats (10 weeks of age, Japan SLC, Shizuoka, Japan) were used. Rats were housed in a light-controlled room with a 12 hr light/dark cycle and allowed ad libitum access to food and water. This study involving animals was approved by the Experimental Animal Committee at the Faculty of Pharmacy, Osaka Medical and Pharmaceutical University (permission code: 5, permission date: 31 March 2018).

2.2. Experimental Procedure. Experimental protocols are shown in Figure 1. At 8 weeks of age, the right kidney was resected through a small flank incision under anesthesia. In an experiment to examine vascular endothelial function after ischemic AKI, these animals were divided into two groups: (1) sham-operated control without ischemia and (2) ischemic AKI by renal I/R. In order to induce ischemic AKI, the left kidney was exposed through a small flank incision. The left renal artery and vein were occluded with a Schwartz microserrefine. After 45 min, the microserrefine was removed, and reperfusion was visually confirmed. In sham-operated control rats, the left kidneys were treated in the same manner as those in the ischemic AKI group except for the ischemia treatment. All rats were placed in metabolic cages 1, 7, and 28 days after reperfusion, and urine was collected for 5 hr. After collection of urine, rats were injected with heparin (1000 U/kg, i.v.), and blood samples were drawn from the abdominal aorta. The collected blood and urine were used to measure renal function parameters and IS concentrations. The thoracic aorta was then removed and used for measurements of vascular function and superoxide anion (O_2^-) production. Rats with vascular function measurements at 7 and 28 days after reperfusion were confirmed to have developed AKI by collecting blood samples from the jugular vein 1 day after reperfusion and checking the deterioration of renal function. The same procedure was performed in the sham group.

In separate experiments, to clarify the relationship between IS and vascular endothelial function in AKI, AST-120 (Kremezin, Kureha Corporation, Japan, 2.5 g/kg, p.o.) was administered 3, 6, and 24 hr after reperfusion. The steps for creating ischemic AKI are described above and Figure 1. Blood and urine samples were collected 1, 7, and 28 days after reperfusion, and on day 28, the thoracic aorta was removed, and vascular function was measured. The collected blood and urine were used to measure renal function parameters and IS concentrations.

2.3. Analytical Procedure. The plasma used for measurement was collected by centrifugation of the collected blood. Plasma and urinary creatinine were measured by the Jaffe method, and creatinine clearance was calculated.

IS concentrations in plasma and urine were measured by high-performance liquid chromatography (HPLC)-fluorescence, as previously reported [12]. Briefly, a 125 μL aliquot of diluted plasma and urine was added directly to 450 μL of acetonitrile. After centrifugation at 10,000 rpm for 15 min, the supernatant was assayed by HPLC. The HPLC system consisted of a pump L-2130 (Hitachi, Tokyo, Japan) and FL detector L-2485 (Hitachi, Tokyo, Japan). A COSMOSIL PBr Packed Column 4.6 mml.D.*250 mm (Nacalai Tesque Inc., Ltd., Kyoto, Japan) was used for the stationary phase. The mobile phase consisted of acetate buffer (0.02 M, pH 4.5)/acetonitrile. The flow rate was 1 mL/min. IS was detected using a fluorescence monitor. The excitation/emission wavelengths were 280/375 nm.

2.4. Vascular Function Study. Macrovascular dysfunction is well known to be coupled with cardiovascular diseases [13, 14]; therefore, we focused on the aorta in this study. The thoracic aortas of sham and ischemic AKI rats were isolated, and the connective and adipose tissues were carefully removed to make approximately 2 mm aortic ring segments. Each ring was suspended in an organ bath (10 mL) containing Krebs Ringer bicarbonate solution with the following composition (mM): NaCl 118.5, KCl 4.7, $MgSO_4$ 1.2, $CaCl_2$ 2.5, $NaHCO_3$ 25, glucose 10, and KH_2PO_4 1.2. The solution was bubbled with 5% CO_2 and 95% O_2 (37°C). The changes in vascular tone tension in response to vasoactive substances were continuously recorded by a polygraph system (RM 6000, Nihon Kohden, Tokyo, Japan) via an isometric force transducer (TB-612 T, Nihon Kohden). All aortic rings were precontracted with phenylephrine (Phe, 10^{-6} M). After reaching a plateau, each vasodilator (ACh [10^{-9} M -10^{-5} M)], sodium nitroprusside (SNP) [10^{-9} M -10^{-5} M]), was applied in cumulative concentrations. The vasorelaxation responses to vasodilators were presented as a percent relaxation of Phe-induced precontraction.

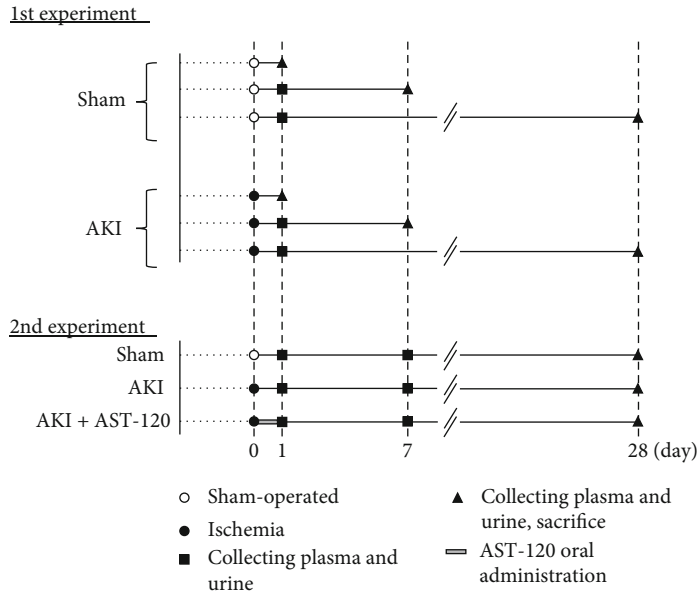

Figure 1: Schematic diagram depicting the experimental protocols. AKI: acute kidney injury.

2.5. Measurement of O_2^- Production in Vascular Tissues. The method for producing the aortic ring was the same as described above. Levels of $O_2\cdot^-$ in the aortic ring were measured by measuring lucigenin-enhanced chemiluminescence using a luminometer (Lumat 3, Belthold Technologies, Schwarzwald, Germany). The aortic ring was placed in a test tube containing Krebs-HEPES buffer (99.01 mM NaCl, 4.69 mM KCl, 1.87 mM $CaCl_2$, 1.2 mM $MgSO_4$, 1.03 mM K_2HPO_4, 25 mM Na-HEPES and 11.1 mM glucose, pH 7.4, 37°C), which were bubbled with a 5% CO_2 and 95% O_2 gas mixture. Thereafter, lucigenin (5 μM) was added to the test tube in a luminometer. The $O_2\cdot^-$ production level was expressed in relative light units (RLU)/min/mg dry tissue weight. The luminescence in the absence of an aortic ring was used as the background and subtracted from the measured value.

2.6. Histological Examination of the Thoracic Aorta. The thoracic aorta was immersed in phosphate-buffered 10% formalin and embedded in paraffin. The sample was cut at 3 μm and stained with hematoxylin-eosin.

2.7. Drugs. ACh and SNP were purchased from Sigma-Aldrich (St. Louis, MO, USA). Formaldehyde, lucigenin, and phenylephrine were purchased from Nacalai Tesque Inc., Ltd., (Kyoto, Japan). Heparin was purchased from the NIPRO Corporation (Osaka, Japan).

2.8. Statistical Analysis. All data represent the mean ± SEM. The unpaired Student's t-test was used for two-group comparisons, and a one-way analysis of variance (ANOVA) followed by Dunnett's tests was used for multiple comparisons (three groups). The least squares regression analysis was used to evaluate the relationships between variables. Differences were considered significant at $P < 0.05$.

3. Results

3.1. Renal Function after I/R. Renal I/R treatment caused a significant increase in plasma creatinine (Figure 2(a)) and decrease in creatinine clearance (Figure 2(b)) at 1 day after reperfusion. Thereafter, these parameters improved over time, and at 28 days after reperfusion, renal function was similar to that of the sham-operated rats.

3.2. Vascular Reactivity to ACh in the Thoracic Aorta 1, 7, and 28 Days after Reperfusion. The results after 1 day of reperfusion are shown in Figure 3(a). There was no influence of I/R treatment on the vasorelaxant response to ACh. However, as shown in Figures 3(b) and 3(c), there was a significant decrease in vascular reactivity to ACh with I/R treatment compared with the sham group at 7 and 28 days after reperfusion. In particular, the decrease was more marked 28 days after reperfusion. Throughout the period, the sham group had slightly augmented reactivity to ACh over time after surgery, but the AKI group had attenuated reactivity.

3.3. Vascular Reactivity to SNP in the Thoracic Aorta 28 Days after Reperfusion. Next, we assessed endothelium-independent vascular function 28 days after reperfusion using SNP, an NO donor. As shown in Figure 4, I/R treatment reduced the vascular reactivity to SNP.

3.4. O_2^- Production in the Thoracic Aorta 28 Days after Reperfusion. Next, we used the thoracic aorta 28 days after reperfusion to examine O_2^- production in the vascular tissue. As shown in Figure 5, there was a marked increase in O_2^- production in the thoracic aorta of rats with ischemic AKI.

3.5. Effects of AST-120 Administration on Renal Function after I/R. Similar to the results above, the renal I/R treatment caused the marked deterioration of renal function 1 day after

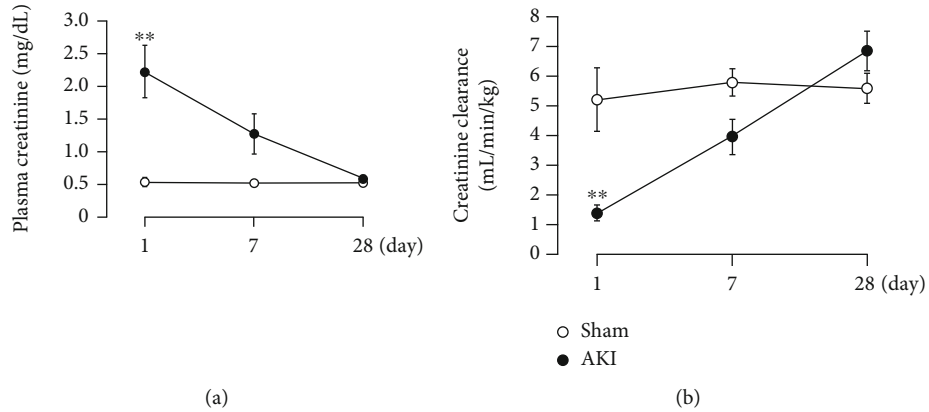

Figure 2: Changes in renal function ((a) plasma creatinine, (b) creatinine clearance) after renal I/R. Each point and bar represent the mean ± S.E.M. Sham-1 day, $n = 5$; sham-7 days, $n = 5$; sham-28 days, $n = 6$; AKI-1 day, $n = 8$; AKI-7 days, $n = 10$; AKI-28 days, $n = 8$. $^{**}P < 0.01$, compared with sham. AKI: acute kidney injury.

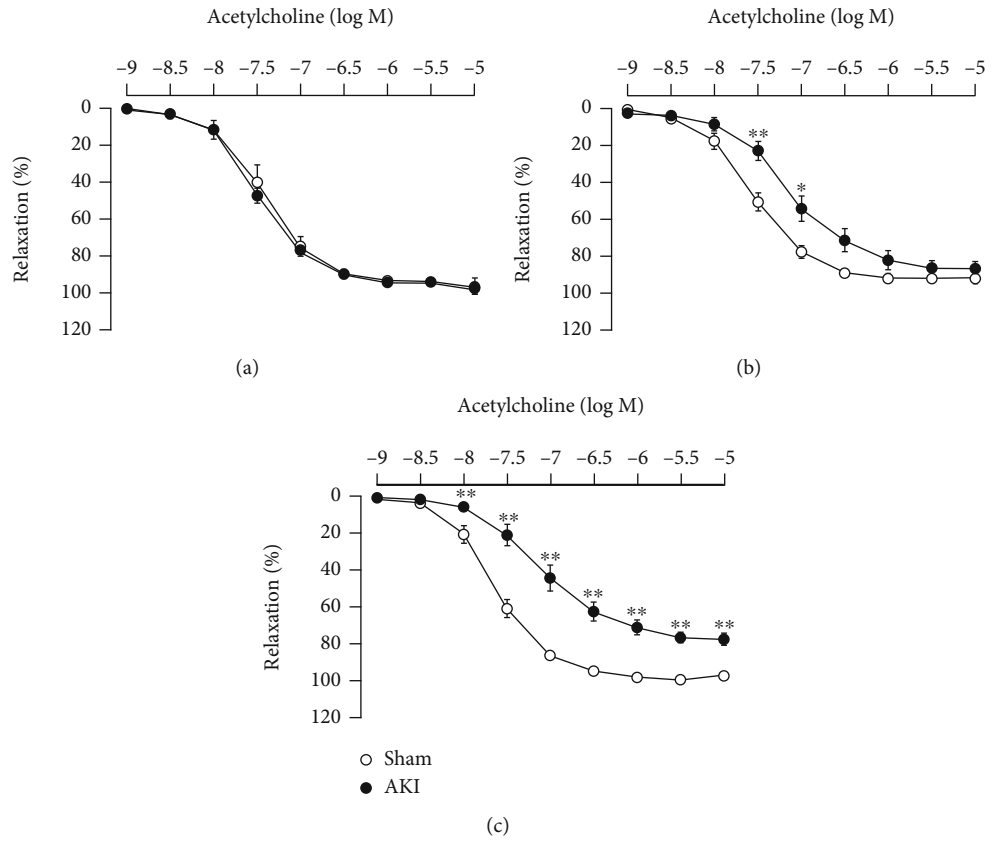

Figure 3: Vascular reactivity to ACh in the thoracic aorta (a) 1 day, (b) 7 days, and (c) 28 days after reperfusion. Each point and bar represent the mean ± S.E.M. Sham-1 day, $n = 5$; sham-7 days, $n = 5$; sham-28 days, $n = 6$; AKI-1 day, $n = 8$; AKI-7 days, $n = 10$; AKI-28 days, $n = 8$. $^{*}P < 0.05$ and $^{**}P < 0.01$, compared with sham. AKI: acute kidney injury.

reperfusion, followed by recovery over time. In addition, AST-120 administration did not cause significant changes in plasma creatinine (Figure 6(a)) and creatinine clearance (Figure 6(b)) at any time point after reperfusion.

3.6. Effects of AST-120 Administration on IS Concentration in Plasma and Urine after I/R. In the ischemic AKI group, the blood IS concentration markedly increased (Figure 7(a)), whereas the urinary IS concentration decreased (Figure 7(b)) compared with the sham group at 1 day after reperfusion; IS excretion into urine was likely suppressed by the marked deterioration of renal function. Seven and 28 days after reperfusion, the blood IS concentration decreased along with the recovery of renal function, and

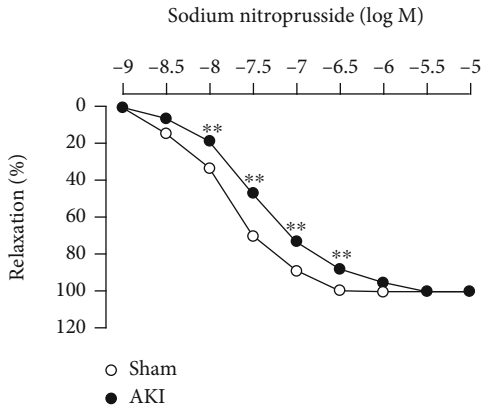

Figure 4: Vascular reactivity to SNP in the thoracic aorta 28 days after reperfusion. Each point and bar represent the mean ± S.E.M. Sham, $n = 6$; AKI, $n = 8$. $^{**}P < 0.01$, compared with sham. AKI: acute kidney injury.

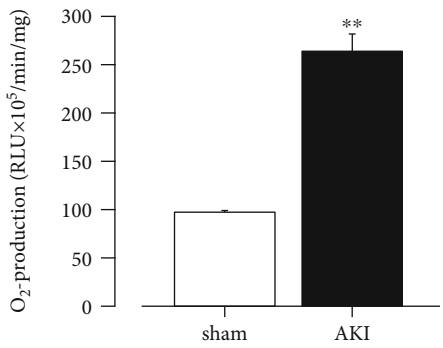

Figure 5: O_2^- production in the thoracic aorta 28 days after reperfusion. Each column and bar represent the mean ± S.E.M. Sham, $n = 6$; AKI, $n = 8$. $^{**}P < 0.01$, compared with sham. AKI: acute kidney injury; RLU: relative light units; O_2^-: superoxide anion.

the urinary IS concentration slightly increased. On the other hand, AST-120 reduced IS concentrations in blood and urine at 1 and 7 days after reperfusion; although, the plasma levels 28 days after reperfusion were comparable regardless of AST-120 administration.

3.7. Effects of AST-120 Administration on Decreased Vascular Reactivity to ACh in the Thoracic Aorta Associated with AKI. A significant decrease in the ACh-induced vasorelaxation response was observed in the thoracic aorta 28 days after reperfusion compared with the sham group. In addition, AST-120 administration did not improve vascular endothelial dysfunction after the onset of AKI (Figure 8).

3.8. Effects of AST-120 Administration on Increased O_2^- Production in the Thoracic Aorta Associated with AKI. The thoracic aorta 28 days after reperfusion exhibited significant O_2^- production compared with the sham group. In addition, AST-120 administration did not reduce the O_2^- overproduction associated with I/R (Figure 9).

3.9. Association between Plasma IS Levels and Vascular Reactivity to ACh and O_2^- Production in the Thoracic Aorta. We examined the association between blood IS levels 1 day after reperfusion and vascular endothelial function and O_2^- production 28 days after reperfusion. Regression analyses considering the presence of I/R revealed that the plasma concentration of IS is not associated with the vasorelaxing efficacy of ACh at 10^{-7} M, a concentration close to the half maximal effective concentration. Similarly, there was no association between the IS levels and O_2^- production (Table 1).

3.10. Histological Changes in the Thoracic Aorta 28 Days after Reperfusion. Since vascular reactivity to ACh in the thoracic aorta 28 days after reperfusion was markedly attenuated, we examined whether histological changes were present in the thoracic aorta. However, no histological differences in the vascular endothelium or smooth muscle were observed among all groups (Figure 10).

4. Discussion

AKI causes remote organ damage due to abnormal interorgan communication between the kidneys and other organs (brain, lungs, heart, liver, intestines, etc.) caused by the temporary or long-term accumulation of uremic toxins, electrolyte imbalance, and excessive fluid retention [15, 16]. In particular, the crosstalk between the kidneys and the heart is known as cardiorenal syndrome and has been the subject of numerous studies. As an example of cardiorenal syndrome, epidemiological studies demonstrated that the incidence of cardiovascular disease, such as heart failure and myocardial infarction, increases after the onset of AKI [17]. It is known that vascular endothelial dysfunction associated with renal injury is not only involved in the development and progression of cardiovascular disease but is also a risk factor for albuminuria and the progression of renal disorder [18]. Therefore, we first evaluated the endothelial function of the thoracic aorta, a large vessel, over time after the onset of AKI.

An important finding in this study was that although the endothelial function of the thoracic aorta was normal at the time when renal function declined due to I/R, endothelial dysfunction progressed thereafter in contrast to the recovery of renal function. However, no histological changes in the thoracic aorta were observed at 28 day after reperfusion. Changes in renal function in the ischemic AKI model are known to be markedly worse immediately after reperfusion, followed by recovery over time [19]. The present ischemic AKI model exhibited a similar tendency in renal function. Both renal arteries and blood vessels distal from the kidney were previously assessed regarding the relationship between AKI and vascular function. Renal arteries after AKI were reported to induce excessive vasoconstriction by adenosine, endothelin, and prostaglandins, in addition to NO trapping by the overproduction of oxidative stress due to promotion of the renin-angiotensin-aldosterone system [20]. Furthermore, the renal arcuate artery of rats subjected to 60 min of bilateral renal ischemia had markedly reduced

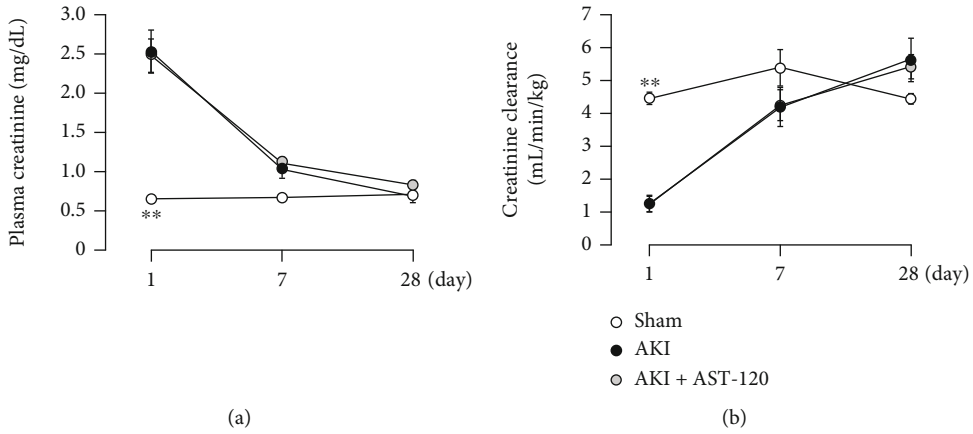

Figure 6: Effects of AST-120 on renal function ((a) plasma creatinine, (b) creatinine clearance) after renal I/R. Each point and bar represent the mean ± S.E.M. Sham, $n = 5$; AKI, $n = 7$; AKI + AST-120, $n = 8$. $^{**}P < 0.01$, compared with AKI each day. AKI: acute kidney injury.

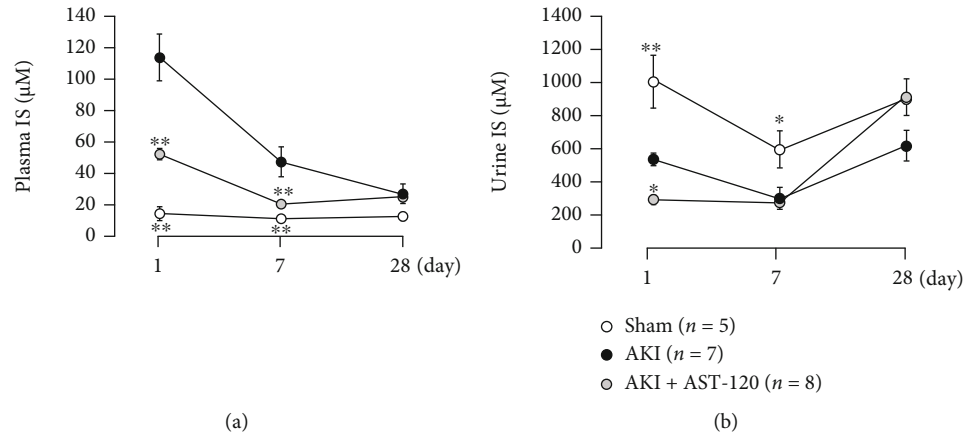

Figure 7: Effects of AST-120 on IS concentration in (a) plasma and (b) urine after renal I/R. Each point and bar represent the mean ± S.E.M. Sham, $n = 5$; AKI, $n = 7$; AKI + AST-120, $n = 8$. $^{*}P < 0.05$ and $^{**}P < 0.01$, compared with AKI each day. AKI: acute kidney injury; IS: indoxyl sulfate.

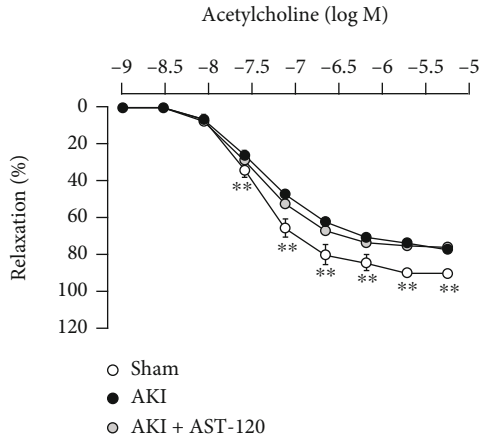

Figure 8: Effects of AST-120 on decreased vascular reactivity to ACh in the thoracic aorta associated with AKI. Each point and bar represent the mean ± S.E.M. Sham, $n = 5$; AKI, $n = 7$; AKI + AST-120, $n = 8$. $^{**}P < 0.01$, compared with AKI. AKI: acute kidney injury.

responsiveness to ACh at 1 hr after reperfusion [21]. Regarding the thoracic aorta, in the ischemic AKI model with 60 min of renal ischemia (45 min of ischemia in this experiment), there was a significant decrease in responsiveness to ACh and a slight decrease in responsiveness to SNP at 5 days after reperfusion [22]. Thus, in the kidney, which is the primary site of AKI, vascular endothelial dysfunction occurs early after reperfusion; on the other hand, in the remote vessels (i.e., thoracic aorta), endothelial dysfunction occurs in the same manner; although, the time of occurrence is later than in the primary site.

ROS, such as O_2^-, are highly involved in the development and progression of diseases [23]. In vascular tissues in particular, O_2^- reacts with NO, resulting in the inactivation of NO [24]. The overproduction of O_2^- after renal I/R has been reported to occur not only in renal tissue but also in remote vessels. As an example, excessive O_2^- production occurred in the gracilis artery 5 weeks after the onset of AKI, and O_2^- levels were normalized by administration of the NADPH oxidase inhibitor apocynin [25]. This supports this study, in which O_2^- production increased in vessels distal to the

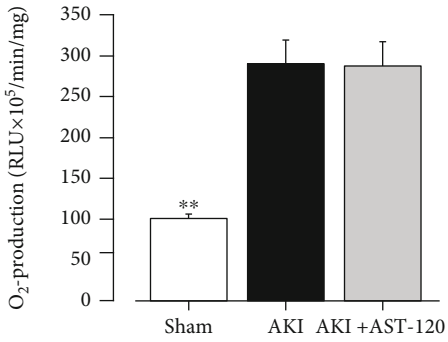

Figure 9: Effects of AST-120 on O_2^- production in the thoracic aorta associated with AKI. Each column and bar represent the mean ± S.E.M. Sham, $n = 5$; AKI, $n = 6$; AKI + AST-120, $n = 5$. ** $P < 0.01$, compared with AKI. AKI: acute kidney injury; RLU: relative light units; O_2^-: superoxide anion.

Table 1: Summary of the least squares regression analysis for significant relationships in vascular dysfunction and O_2^- overproduction.

Variable	Reactivity to ACh		O_2^- production	
	t value	P value	t value	P value
(Intercept)	22.38	<0.001	3.738	0.002
IS level	-1.068	0.301	0.581	0.571
I/R (+/-)	-2.959	0.009	3.929	0.002
R^2	0.578		0.744	
Adjusted R^2	0.528		0.705	

kidneys after the onset of AKI despite the recovery of renal function. Thus, excessive O_2^- production in vascular tissue may play a role in the loss of vascular endothelial function in a remote lesion that occurs after AKI.

The influence of IS on vascular tissue has been reported in many studies. For example, we previously reported that IS causes vascular endothelial dysfunction by trapping NO through O_2^- production induced by the activation of NADPH oxidase [9]. Furthermore, the responsiveness of the thoracic aorta to ACh was significantly attenuated in the 5/6 nephrectomized CKD model with a marked increase in the serum IS concentration. In addition, the administration of AST-120 significantly improved the responsiveness to ACh by suppressing the serum IS concentration [10]. In the ischemic AKI model we used in this study, blood IS levels increased markedly with the decline in renal function 1 day after reperfusion and then slightly decreased along with the recovery of renal function. Therefore, we hypothesized that a transient increase in IS after I/R is involved in the endothelial dysfunction associated with AKI and investigated the effects of AST-120. AST-120 can suppress blood IS levels by adsorbing indole, a precursor of IS, in the intestine [26]. IS is known to function in the progression of renal injury, and administration of AST-120 before ischemia was reported to prevent the development of ischemic AKI [11]; administration before ischemia is not suitable for assessing the impact of IS itself. In addition, in that study, AST-120 administration at 3, 6, and 24 hr after reperfusion resulted in a significant decrease in blood IS concentration without improvement in renal function. Referencing this study, we also administered AST-120 at 3, 6, and 24 hr after reperfusion. In this experiment, similar to the previous study, AST-120 administration markedly reduced the blood IS concentration. However, vascular endothelial function did not improve 28 days after reperfusion even though the increase in blood IS concentration early after reperfusion was suppressed by AST-120. Furthermore, there was no association between blood IS levels 1 day after reperfusion and responsiveness to ACh or O_2^- production 28 days after reperfusion. Taken together, the contribution of the temporarily increased IS to the decline in endothelial function of the thoracic aorta associated with ischemic AKI may not be great.

In this study, AST-120 administration after reperfusion significantly suppressed the increase in plasma IS level associated with I/R treatment, but it was not restored to the sham level. Importantly, even if AST-120 is administered prior to ischemia, the serum IS levels are different from those in the sham group [11, 27]. AST-120 is a spherical adsorbent and therefore cannot eliminate IS that is present in the blood before ischemia or at the onset of reperfusion. Thus, it is difficult to suppress the increase in plasma IS levels associated with AKI unless AST-120 is administered long before ischemia. On the other hand, AST-120 administration after reperfusion was reported to improve cardiac dysfunction associated with AKI without reversing the serum IS level to that in the sham group [28]. Therefore, we hypothesized that vascular endothelial dysfunction can be improved without completely normalizing the plasma IS level. In addition, as mentioned above, administration of AST-120 to CKD model rats markedly improved vascular endothelial dysfunction, but the serum IS level was reportedly only suppressed by approximately 56% and remained higher than that in sham rats [10]. In our studies, the plasma IS level 1 day after reperfusion was suppressed by approximately 62% by AST-120 administration, which is similar to the degree of suppression reported in [10], but vascular endothelial function was not improved. Taken together, the contribution of IS to vascular endothelial dysfunction may be considerably different between the early or temporary increase in IS in ischemic AKI and the chronic increase in CKD.

Excessive inflammatory response has been focused on as one of the causes of distant organ damage after AKI [29]. Abnormal promotion of the inflammatory cascade after the onset of AKI was reported to markedly increase plasma IL-6, leading to lung damage and other problems [30]. Of note, the administration of CNI-1493, which inhibits the release of macrophage-derived inflammatory cytokines, ameliorated the increased vascular permeability of pulmonary arteries that occurs after the onset of AKI without affecting renal function [31]. In addition, as activated neutrophils produce excessive amounts of ROS at the site of inflammation [30], it is possible that the excessive inflammatory response after AKI played a role in the vascular endothelial dysfunction accompanied by increased O_2^- production at the site distal from the kidney. The relationship between inflammatory

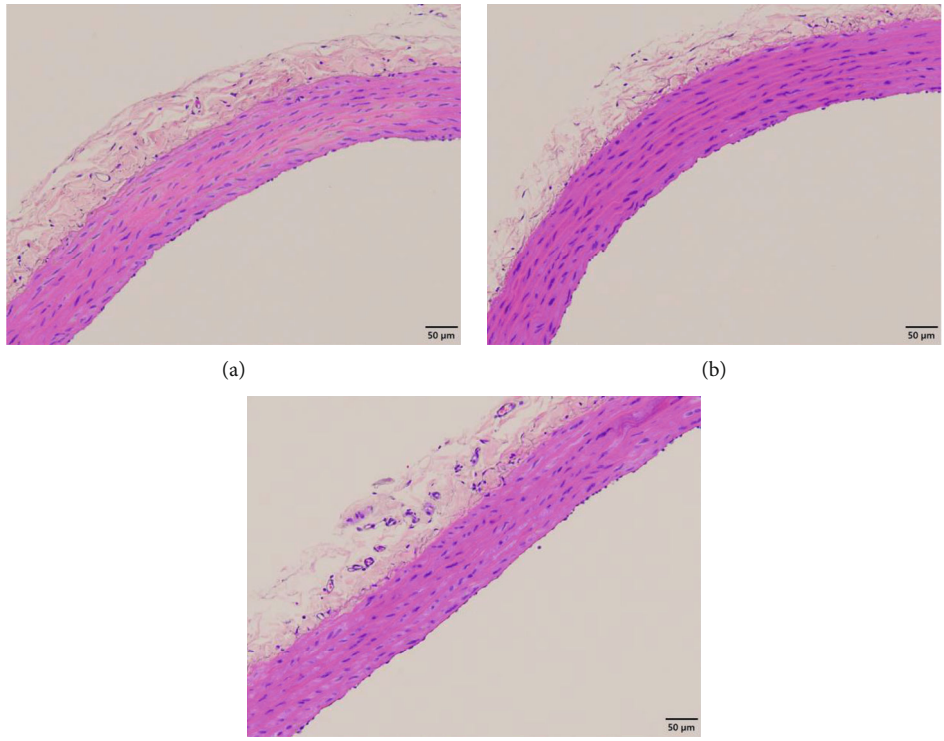

(a) (b) (c)

Figure 10: Representative images of the thoracic aorta 28 days after reperfusion stained with hematoxylin-eosin. (a) Sham, (b) AKI, and (c) AKI + AST-120. AKI: acute kidney injury.

response and vascular dysfunction after AKI should be investigated in the future.

There are three limitations in this study. The first is that we administered AST-120 only early phase after reperfusion. The second limitation is that we were unable to address whether there is a threshold level for IS to cause vascular endothelial dysfunction. The third limitation is that we have not evaluated the association of IS with vascular endothelial dysfunction in other ischemic AKI models, including the bilateral renal I/R model and unilateral renal I/R model with delayed contralateral nephrectomy. These issues need to be considered in the future.

5. Conclusions

In summary, impaired renal function due to AKI recovered over time; however, the endothelial function of the thoracic aorta deteriorated from the time when renal function shifted toward recovery. In addition, administration of the spherical adsorbent AST-120 early after reperfusion was ineffective against the vascular dysfunction associated with ischemic AKI, suggesting the possibility that the temporarily increased IS is not a major contributor. Moreover, it is important to examine whether the impaired vascular endothelial function in large vessels after ischemic AKI plays a role in the development of cardiovascular diseases and the transition to CKD.

Data Availability

All data used to support the findings of this study are included within the article.

Conflicts of Interest

The authors declare that there is no conflict of interest regarding the publication of this paper.

References

[1] S. Uchino, J. A. Kellum, R. Bellomo et al., "Acute renal failure in critically ill patients<SUBTITLE>a multinational, multicenter study</SUBTITLE>," *Journal of the American Medical Association*, vol. 294, no. 7, pp. 813–818, 2005.

[2] D. Aggarwal and G. Singh, "Effects of single and dual RAAS blockade therapy on progressive kidney disease transition to CKD in rats," *Naunyn-Schmiedeberg's Archives of Pharmacology*, vol. 393, no. 4, pp. 615–627, 2020.

[3] F. Guzzi, L. Cirilo, R. M. Roperto, P. Romagnani, and E. Lazzeri, "Molecular mechanisms of the acute kidney injury to chronic kidney disease transition: an updated view," *International Journal of Molecular Sciences*, vol. 20, no. 19, p. 4941, 2019.

[4] D. H. Endemann and E. L. Schiffrin, "Endothelial dysfunction," *Journal of the American Society of Nephrology*, vol. 15, no. 8, pp. 1983–1992, 2004.

[5] M. Kakoki, Y. Hirata, H. Hayakawa et al., "Effects of tetrahydrobiopterin on endothelial dysfunction in rats with ischemic acute renal failure," *Journal of the American Society of Nephrology*, vol. 11, no. 2, pp. 301–309, 2000.

[6] J. G. Kingma, J. C. Vincent, J. R. Rouleau, and I. Kingma, "Influence of acute renal failure on coronary vasoregulation in dogs," *Journal of the American Society of Nephrology*, vol. 17, no. 5, pp. 1316–1324, 2006.

[7] J. Kim, H. S. Jang, and K. M. Park, "Reactive oxygen species generated by renal ischemia and reperfusion trigger protection against subsequent renal ischemia and reperfusion injury in mice," *American Journal of Physiology. Renal Physiology*, vol. 298, no. 1, pp. F158–F166, 2010.

[8] G. A. Knock, "NADPH oxidase in the vasculature: expression, regulation and signalling pathways; role in normal cardiovascular physiology and its dysregulation in hypertension," *Free Radical Biology & Medicine*, vol. 145, pp. 385–427, 2019.

[9] K. Nakagawa, M. Itoya, N. Takemoto et al., "Indoxyl sulfate induces ROS production via the aryl hydrocarbon receptor-NADPH oxidase pathway and inactivates NO in vascular tissues," *Life Sciences*, vol. 265, article 118807, 2021.

[10] T. Namikoshi, N. Tomita, M. Satoh et al., "Oral adsorbent AST-120 ameliorates endothelial dysfunction independent of renal function in rats with subtotal nephrectomy," *Hypertension Research*, vol. 32, no. 3, pp. 194–200, 2009.

[11] H. Saito, M. Yoshimura, C. Saigo et al., "Hepatic sulfotransferase as a nephropreventing target by suppression of the uremic toxin indoxyl sulfate accumulation in ischemic acute kidney injury," *Toxicological Sciences*, vol. 141, no. 1, pp. 206–217, 2014.

[12] S. Ito, Y. Ohno, T. Tanaka et al., "Neutrophil/lymphocyte ratio elevation in renal dysfunction is caused by distortion of leukocyte hematopoiesis in bone marrow," *Renal Failure*, vol. 41, no. 1, pp. 284–293, 2019.

[13] Y. Matsuzawa, T. G. Kwon, R. J. Lennon, L. O. Lerman, and A. Lerman, "Prognostic value of flow-mediated vasodilation in brachial artery and fingertip artery for cardiovascular events: a systematic review and meta-analysis," *Journal of the American Heart Association*, vol. 4, no. 11, article e002270, 2015.

[14] Y. B. Shlomo, M. Spears, C. Boustred et al., "Aortic pulse wave velocity improves cardiovascular event prediction: an individual participant meta-analysis of prospective observational data form 17, 635 subjects," *Journal of the American College of Cardiology*, vol. 63, pp. 636–646, 2013.

[15] K. Doi and H. Rabb, "Impact of acute kidney injury on distant organ function: recent findings and potential therapeutic targets," *Kidney International*, vol. 89, no. 3, pp. 555–564, 2016.

[16] S. A. Lee, M. Cozzi, E. L. Bush, and H. Rabb, "Distant organ dysfunction in acute kidney injury: a review," *American Journal of Kidney Diseases*, vol. 72, no. 6, pp. 846–856, 2018.

[17] H. Gammelager, C. F. Christiansen, M. B. Johansen, E. Tonnesen, B. Jespersen, and H. T. Sorensen, "Three-year risk of cardiovascular disease among intensive care patients with acute kidney injury: a population-based cohort study," *Critical Care*, vol. 18, no. 5, p. 492, 2014.

[18] F. Persson, P. Rossing, P. Hovind et al., "Endothelial dysfunction and inflammation predict development of diabetic nephropathy in the irbesartan in patients with type 2 diabetes and microalbuminuria (IRMA-2) study," *Scandinavian Journal of Clinical and Laboratory Investigation*, vol. 68, no. 8, pp. 731–738, 2008.

[19] H. Chen, Y. Fang, J. Wu et al., "RIPK3-MLKL-mediated necroinflammation contributes to AKI progression to CKD," *Cell Death & Disease*, vol. 9, no. 9, p. 878, 2018.

[20] D. P. Basile and M. C. Yoder, "Renal endothelial dysfunction in acute kidney ischemia reperfusion injury," *Cardiovascular & Hematological Disorders Drug Targets*, vol. 14, no. 1, pp. 3–14, 2014.

[21] A. M. G. Versteilen, I. J. M. Korstjens, R. J. P. Musters, A. B. J. Groeneveld, and P. Sipkema, "Rho kinase regulates renal blood flow by modulating eNOS activity in ischemia-reperfusion of the rat kidney," *American Journal of Physiology. Renal Physiology*, vol. 291, no. 3, pp. F606–F611, 2006.

[22] Y. S. Bhalodia, N. R. Sheth, J. D. Vaghasiya, and N. P. Jivani, "Homocysteine-dependent endothelial dysfunction induced by renal ischemia/reperfusion injury," *Journal of Nephrology*, vol. 24, no. 5, pp. 631–635, 2011.

[23] S. Steven, K. Frenis, M. Oelze et al., "Vascular inflammation and oxidative stress: major triggers for cardiovascular disease," *Oxidative Medicine and Cellular Longevity*, vol. 2019, 26 pages, 2019.

[24] M. E. Assar, J. Angulo, and L. R. Manas, "Oxidative stress and vascular inflammation in aging," *Free Radical Biology & Medicine*, vol. 65, pp. 380–401, 2013.

[25] S. A. Phillips, K. R. Pechman, E. C. Leonard et al., "Increased ANG II sensitivity following recovery from acute kidney injury: role of oxidant stress in skeletal muscle resistance arteries," *American Journal of Physiology-Regulatory, Integrative and Comparative Physiology*, vol. 298, no. 6, pp. R1682–R1691, 2010.

[26] H. Hirakawa, M. Uchida, K. Kurabayashi, F. Nishijima, A. Takita, and H. Tomita, "In vitro activity of AST-120 that suppresses indole signaling in Escherichia coli, which attenuates drug tolerance and virulence," *PLoS One*, vol. 15, no. 4, article e0232461, 2020.

[27] N. Yabuuchi, M. Sagata, C. Saigo et al., "Indoxyl sulfate as a mediator involved in dysregulation of pulmonary aquaporin-5 in acute lung injury caused by acute kidney injury," *International Journal of Molecular Sciences*, vol. 18, no. 1, p. 11, 2017.

[28] W. C. Shen, Y. H. Chou, L. S. Shi et al., "AST-120 improves cardiac dysfunction in acute kidney injury mice via suppression of apoptosis and proinflammatory NF-κB/ICAM-1 signaling," *Journal of Inflammation Research*, vol. Volume 14, pp. 505–518, 2021.

[29] M. E. Grams and H. Rabb, "The distant organ effects of acute kidney injury," *Kidney International*, vol. 81, no. 10, pp. 942–948, 2012.

[30] S. C. Yap, H. T. Lee, and D. S. Warner, "Acute kidney injury and extrarenal organ dysfunction," *Anesthesiology*, vol. 116, no. 5, pp. 1139–1148, 2012.

[31] A. A. Kramer, G. Postler, K. F. Salhab, C. Mendez, L. C. Carey, and H. Rabb, "Renal ischemia/reperfusion leads to macrophage-mediated increase in pulmonary vascular permeability," *Kidney International*, vol. 55, no. 6, pp. 2362–2367, 1999.

Hindawi
Oxidative Medicine and Cellular Longevity
Volume 2022, Article ID 6227330, 25 pages
https://doi.org/10.1155/2022/6227330

Research Article

Hdac8 Inhibitor Alleviates Transverse Aortic Constriction-Induced Heart Failure in Mice by Downregulating Ace1

Tingwei Zhao,[1,2] Hae Jin Kee,[1,2] Seung-Jung Kee,[3] and Myung Ho Jeong[1,2,4]

[1]*Heart Research Center of Chonnam National University Hospital, Gwangju 61469, Republic of Korea*
[2]*Hypertension Heart Failure Research Center, Chonnam National University Hospital, Gwangju 61469, Republic of Korea*
[3]*Department of Laboratory Medicine, Chonnam National University, Medical School and Hospital, Gwangju 61469, Republic of Korea*
[4]*Department of Cardiology, Chonnam National University Medical School, Gwangju 61469, Republic of Korea*

Correspondence should be addressed to Hae Jin Kee; sshjkee@empas.com and Myung Ho Jeong; myungho@chollian.net

Received 8 November 2021; Revised 20 December 2021; Accepted 21 December 2021; Published 27 January 2022

Academic Editor: Yingqing Chen

Background. Heart failure is characterized by activation of the renin-angiotensin-aldosterone system, which is involved in the regulation of cardiac hypertrophy and hypertension. Recently, we reported that Hdac8 inhibition alleviates isoproterenol-induced and angiotensin II-induced cardiac hypertrophy or hypertension in mice. Here, the effect and regulatory mechanisms of the Hdac8 selective inhibitor PCI34051 on pressure overload-induced heart failure were examined. *Methods and Results*. At week 6 posttransverse aortic constriction (TAC), mice were administered with PCI34051 (3, 10, or 30 mg/kg bodyweight/day) for 2 weeks. The therapeutic effects of PCI34051 on TAC-induced cardiac and lung hypertrophy were determined by examining the heart weight-to-bodyweight and lung weight-to-bodyweight ratios and the cross-sectional cardiomyocyte area. Echocardiography analysis revealed that PCI34051 mitigated TAC-induced decreased ejection fraction and fractional shortening. Additionally, the expression of Hdac8 was upregulated in the cardiac and pulmonary tissues of TAC mice. The expression levels of Ace1 and Agtr1 were upregulated, whereas those of Ace2 and Agtr2 were downregulated in TAC mice. PCI34051 treatment or *Hdac8* knockdown alleviated inflammation as evidenced by Rela downregulation and Nfkbia upregulation in mice, as well as in cardiomyocytes, but not in cardiac fibroblasts. Hdac8 overexpression-induced Rela pathway activation was downregulated in *Ace1* knockdown cells. Picrosirius red staining, real-time polymerase chain reaction, and western blotting analyses revealed that PCI34051 alleviated fibrosis and downregulated fibrosis-related genes. Moreover, PCI34051 or *Hdac8* knockdown in rat cardiac fibroblasts alleviated cardiac fibrosis through the Tgfb1-Smad2/3 pathway. The results of overexpression and knockdown experiments revealed that Hdac8 and Ace1 promote inflammation and fibrosis. *Conclusions*. Treatment with PCI34051 enhanced cardiac and lung functions in the TAC-induced heart failure mouse model. These data suggest that HDAC8 is a potential novel therapeutic target for heart failure accompanied by pathological lung diseases.

1. Introduction

The prevalence, mortality, and morbidity rates of heart failure, a multifactorial disease accompanied by structural and functional damages to the tissues [1, 2], are increasing annually worldwide, including the United States of America (USA) [3–5]. Heart failure is often accompanied by fibrosis, which is the tissue response to inflammation. Previous studies have reported that the levels of inflammatory cytokines, such as tumor necrosis factor-alpha (TNFα), interleukin-1 beta (IL-1β), and interleukin-6 (IL-6) are upregulated in patients with heart failure [6, 7] and in the transverse aortic constriction- (TAC-) induced heart failure mouse model [8]. Heart failure promotes the neurohormonal activation of the sympathetic nervous system and the renin-angiotensin-aldosterone system (RAAS), which plays a critical role in the regulation of cardiovascular processes [9, 10]. Angiotensin II, a key molecule in the RAAS, regulates cardiac contractility and promotes adverse remodeling in heart failure [11]. ACE1 catalyzes the conversion of angiotensin I into angiotensin II,

while ACE2 catalyzes the conversion of angiotensin II into angiotensin (1–7) or angiotensin I to angiotensin (1–9), leading to cardioprotective effects on heart failure [12, 13]. ACE2 is also expressed in the lung vascular endothelial cells and consequently protects against acute lung failure [14, 15]. In mice, Ace2 deficiency leads to early cardiac hypertrophy [16], whereas Ace1 overexpression promotes atrial enlargement [17]. Therefore, the neurohormonal blockade using ACE inhibitors, angiotensin receptor blockers, and beta-blockers mitigates heart failure-induced cardiac remodeling [18, 19].

Recent studies have reported that histone deacetylases (HDACs) regulate gene expression. HDACs are classified into four classes. Class I HDACs comprise HDAC1, HDAC2, HDAC3, and HDAC8. Among class I HDACs, HDAC2 has been best characterized for its role in the modulation of cardiac hypertrophy [20, 21]. For example, the enzymatic activity but not the expression of HDAC2 promotes cardiac hypertrophy [22]. HDAC inhibitors, including trichostatin A and SK-7041, hypertrophy and heart failure [23–25]. HDAC3 increases postnatal cardiac myocyte proliferation but is not involved in cardiac hypertrophy [26]. Recently, we had reported that PCI34051, an HDAC8 selective inhibitor, mitigates angiotensin II-induced hypertension and isoproterenol-induced cardiac hypertrophy [27, 28]. Previous studies have demonstrated that HDAC8 regulates cardiac hypertrophy through the AKT/GSK3β pathway [29]. However, the role of HDAC8 in heart failure has not been elucidated. In contrast to class I HDACs, class II HDACs, such as HDAC5 and HDAC9, suppress cardiac hypertrophy [30].

This study demonstrated that pharmacological inhibition or downregulation of Hdac8 mitigates heart failure-related pathologies, including cardiac hypertrophy, pulmonary congestion, fibrosis, and inflammation in vivo (TAC-induced heart failure mouse model) and in vitro. The results of in vitro studies demonstrated that PCI34051 treatment or *Hdac8* or *Ace1* knockdown modulated inflammatory and fibrotic responses to transforming growth factor-beta 1 (TGF-β1) or TNFα stimulation. This is the first study to demonstrate the role of HDAC8 in the pathogenesis of heart failure.

2. Materials and Methods

2.1. Reagents. PCI34051 (10444) was purchased from Cayman Chemical Company (Ann Arbor, MI, USA). Anti-Actb (sc-47778), anti-Nppb (sc-271185), anti-Acta2 (sc-130617), anti-Ace1 (sc-20791), anti-Ace2 (sc-390851), and anti-Tgfb1 (sc-146) antibodies were obtained from Santa Cruz Biotechnology (Dallas, TX, USA). Anti-phospho-Smad2/3 (8828), anti-Smad2/3 (3102), anti-Rela (8242), and anti-Nfkbia (4812) antibodies were purchased from Cell Signaling Technology (Danvers, MA, USA). Anti-Nppa and anti-Hdac8 (ab187139) antibodies were purchased from GeneTex (GTX109255; Irvine, CA, USA) and Abcam (Cambridge, UK), respectively. Anti-Fn1 (MA5-11981) and anti-Ccl2 (PA5-34505) antibodies were purchased from Thermo Fisher Scientific Inc. (Waltham, MA, USA).

2.2. Establishment of the TAC-Induced Heart Failure Mouse Model. All animal experiments were approved by the Animal Experimental Committee of Chonnam National University Medical School (CNUH IACUC-18023) and conducted according to the Guide for the Care and Use of Laboratory Animals (US National Institutes of Health Publications, 8th edition, 2011). Male ICR mice (Orient, South Korea) aged 6 weeks were maintained in a 12 h light/dark cycle under specific pathogen-free conditions. The mouse skin was disinfected with ethyl alcohol, and the mice were anesthetized by intraperitoneally injecting a mixture of ketamine (120 mg/kg bodyweight) and xylazine (6.2 mg/kg body weight). The anesthetized mice were fixed on the transparent board in a supine position and connected to a small animal ventilator through laryngotracheal intubation. The lung characteristics of the mice were as follows: tidal volume, 0.1–0.3 mL and respiratory rate, 125–150 breaths/min. The aortic arch was exposed, and the thymus was removed. The transverse aortic arch was tied with a 7-0 silk suture between the brachiocephalic and left common carotid arteries using an overlaying 27G needle. The constriction needle was carefully removed, the chest and skin incision wounds were closed using a 4-0 silk suture, and the ventilator was disconnected. Mice were placed on warm pads until they woke up after surgery. The sham group underwent the same surgical procedure without aortic banding. The animals were randomized into the following six groups (5–6 mice per group): sham+vehicle, sham+PCI34051 (10 mg/kg bodyweight/day), TAC+vehicle, TAC+PCI34051 (3 mg/kg bodyweight/day), TAC +PCI34051 (10 mg/kg bodyweight/day), and TAC +PCI34051 (30 mg/kg bodyweight/day). PCI34051 was intraperitoneally administered daily for 2 weeks. All animals were sacrificed using CO_2.

2.3. Echocardiography. To evaluate the left ventricular functions, echocardiography was performed using a Vivid S5 echocardiography system (GE Healthcare, Chicago, IL, USA) equipped with a 13 MHz linear array transducer as described previously [28]. Before cardiac function measurements, mice were anesthetized by intraperitoneally administering tribromoethanol (Avertin; 114 mg/kg bodyweight). M-mode (2-D guided) images and parameters were acquired from the long-axis view of the left ventricle at the level of the papillary muscles.

2.4. Histological Analysis and Picrosirius Red Staining. Mouse cardiac tissues were fixed with 3.7% paraformaldehyde and embedded in paraffin. The paraffin-embedded tissues were cut into 4 μm thick sections. The sections were deparaffinized with xylene, rehydrated in a graded alcohol series, and subjected to hematoxylin and eosin (H&E) staining to measure the size of cardiomyocytes in the myocardial tissue [31]. Quantification of cell size was performed using the NIS Elements software (Nikon Eclipse 80*i* microscope, Tokyo, Japan).

Picrosirius red (Abcam) staining was performed to evaluate cardiac fibrosis. The rehydrated cardiac tissues were stained with Picrosirius red solution for 1 h. The samples were quickly washed twice with 0.5% acetic acid solution

and rinsed with absolute alcohol for 1 min. The sections were mounted with Canada balsam and imaged using a microscope (Nikon, Tokyo, Japan) at 400x magnification.

2.5. Isolation and Cell Culture of Primary Neonatal Cardiac Fibroblasts. Cardiac fibroblasts were isolated from rat neonatal hearts (15 pups) [32]. Briefly, the atrium was removed, finely chopped using scissors, and digested with 0.1% collagenase II in 1× ADS buffer (116 mM NaCl, 20 mM HEPES, 10 mM NaH_2PO_4, 5.5 mM glucose, 5 mM KCl, and 0.8 mM $MgSO_4$) at 37°C and 120 rpm on a shaker for 2 h. The cells were neutralized using fetal bovine serum (FBS, final concentration 10%) and centrifuged at 1200 rpm for 3 min. Fibroblasts were cultured in Dulbecco's modified Eagle's medium supplemented with 10% FBS and 1× antibiotic-antimycotic solution at 37°C in an incubator. Passage 2 fibroblasts were used for the experiments. Cardiac fibroblasts were pretreated with TGF-β1 (10 ng/mL) for 1 h and cultured in the presence of vehicle (0.1% dimethyl sulfoxide (DMSO)) or PCI34051 (10 μM) for 8 h. To investigate the roles of Hdac8 or Ace1 in fibrosis, fibroblasts were transfected with control short-interfering RNAs (si-RNAs) or siRNAs against *Hdac8* (si-Hdac8) or si-Ace1 and incubated with TGF-β1 (10 ng/mL) for 9 h.

2.6. Quantitative Real-Time Polymerase Chain Reaction (qRT-PCR). Total RNAs were isolated from the cardiac tissues using TRIzol reagent (Invitrogen/Life Technologies, Carlsbad, CA, USA). The RNA concentration was determined by measuring the absorbances of the sample at wavelengths of 260 and 280 nm. The isolated RNA (1 μg) was reverse-transcribed into complementary DNA using TOPscript RT DryMIX (Enzynomics, Daejeon, South Korea). qRT-PCR analysis was performed using the SYBR Green PCR kit and specific primers. The relative mRNA levels were determined using the $2^{-\Delta\Delta Ct}$ method. The sequence of primers used in qRT-PCR analysis is shown in Supplementary Table 1.

2.7. Western Blotting. Total proteins were isolated from the cardiac and pulmonary tissues using a radioimmunoprecipitation assay buffer as described previously [28]. The protein concentration was measured using the bicinchoninic protein assay kit. Equal amounts of proteins were subjected to sodium dodecyl sulfate-polyacrylamide gel electrophoresis. The resolved proteins were transferred to a polyvinylidene difluoride membrane (pore size: 0.45 μm; Merk Millipore, MA, USA). The membrane was blocked with 5% skim milk in Tris-buffered saline containing Tween-20 (TBST) (20 mM Tris, 200 mM NaCl, and 0.04% Tween 20) for 1 h at 25°C and probed with the primary antibodies (1 : 1000) overnight at 4°C. Next, the membrane was washed thrice with TBST for 5 min and incubated with the anti-rabbit or anti-mouse horseradish peroxidase-conjugated secondary antibodies (1 : 3000) for 1 h at 25°C. Immunoreactive signals were detected using Immobilon western blotting detection reagents (EMD Millipore, Billerica, MA, USA). The intensities of the protein bands were quantified using ImageJ software (https://imagej.net/).

2.8. Transfection. To overexpress Hdac8, H9c2 cells were transfected with 1.6 μg of *pCMV-HA-myc* or *pCMV-Hdac8-HA-myc* plasmids for 2 days using Lipofectamine and PLUS reagents, following the manufacturer's instructions. Additionally, the H9c2 cells were transfected with 1.6 μg of *pCMV6-SPORT6* or *pCMV6-SPORT6-Ace1* plasmids for 2 days to overexpress Ace1. The *pCMV6-SPORT6-Ace1* clone was obtained from the Korea Human Gene Bank, Medical Genomics Research Center, KRIBB, Korea.

To knockdown *Hdac8* or *Ace1*, H9c2 cells were transfected with 100 nM control siRNAs (cat no. SN-1003, Bioneer, Daejeon, South Korea), si-Hdac8 (cat no. L-096589-02-0005, Dharmacon, Lafayette, CO, USA), or si-Ace1 (product name 24310, Bioneer) using RNAiMAX reagent.

The siRNA sequences were as follows: control sense, 5′-CCU ACG CCA AUU UCG U-3′ and control antisense, 5′-ACG AAA UUG GUG GCG UAG G-3′; si-Ace1 #1, 5′-CUC AGU AAU GAA GCC UAC A-3′; si-Ace1 #2, 5′-CAU UUG ACG UGA GCA ACU U-3′; si-Ace1 #3, 5′-ACA AAC CCA ACC UCG AUG U-3′; si-Hdac8 #1: 5′-UAG AAU AUG GAC UAG GUU A-3′; si-Hdac8 #2, 5′-GAU CCA AUG UGC UCC UUU A-3′; si-Hdac8 #3, 5′-CAG CAU AUG GUC CUG AUU A-3′; and si-Hdac8 #4: 5′-CAG AAG GGA UAU UUG ACU A-3′.

2.9. Nuclear and Cytoplasmic Protein Extraction. H9c2 cells pretreated with TNFα (50 ng/mL) for 1 h were incubated with vehicle (0.1% DMSO) or PCI34051 (10 μM) for 5 h. The cytoplasmic extracts were prepared using the hypotonic lysis buffer (10 mM HEPES (pH 7.9), 10 mM KCl, 10 mM EDTA, 1 mM dithiothreitol (DTT), 0.4% IGEPAL, and 1× protease inhibitor). The extracts were incubated on ice for 10 min on a rocker and centrifuged at 13000 rpm and 4°C for 5 min. The supernatant was stored as cytoplasmic extracts. The nuclear pellets were resuspended in a high salt buffer (10 mM HEPES [pH 7.9], 400 mM NaCl, 1 mM EDTA, 1 mM DTT, and 1× protease inhibitor) and incubated on a rotating shaker on ice for 2 h. The samples were centrifuged at 13000 rpm and 4°C for 5 min to obtain the nuclear extracts.

2.10. Statistical Analysis. All data are represented as mean ± standard error. The means of two groups were compared using Student's t-test, whereas those of three or more groups were compared using one-way analysis of variance, followed by a Bonferroni multiple comparison test. Differences were considered significant at $P < 0.05$. All statistical analyses were performed using GraphPad Prism version 8.0.2 (GraphPad Software, La Jolla, CA, USA).

3. Results

3.1. PCI34051 Alleviates Cardiac Hypertrophy and Restores Cardiac Function in the TAC-Induced Heart Failure Mouse Model. Cardiac hypertrophy is often accompanied by hypertension and heart failure [33, 34]. We investigated the effects of different concentrations of PCI34051 (3, 10, and 30 mg/kg bodyweight/day), an HDAC8 selective inhibitor,

on concomitant cardiac hypertrophy using the TAC-induced heart failure mouse model. The timeline of the experiments is shown in Figure 1(a). The heart size in the TAC group was markedly higher than that in the sham group. Treatment with PCI34051 at a dose of 10 mg/kg bodyweight/day did not affect the heart weight-to-bodyweight (HW/BW) ratio in the sham group. In contrast, all three doses of PCI34051 significantly mitigated the TAC-induced enhanced HW/BW ratio. The HW/BW ratio in the group treated with PCI34051 at a dose of 30 mg/kg bodyweight/day was lower than that in the groups treated with PCI34051 at doses of 3 and 10 mg/kg bodyweight/day (Figure 1(b)).

Next, the size of cardiomyocytes in the H&E-stained cardiac tissues was examined. The cross-sectional area was not significantly different between the vehicle-treated sham and PCI34051-treated sham groups. However, PCI34051 dose dependently decreased the cross-sectional area of cardiomyocytes in the TAC-treated groups (Figures 1(c) and 1(d)). Furthermore, qRT-PCR (Figures 1(e) and 1(f)) and western blotting (Figures 1(g)–1(i)) analyses revealed that the mRNA and protein expression levels of the cardiac hypertrophic markers Nppa and Nppb in the TAC+PCI34051 (3, 10, or 30 mg/kg bodyweight/day) groups were downregulated when compared with those in the untreated TAC group.

Next, the effect of PCI34051 on cardiac function was evaluated using echocardiography. At week 6 post-TAC, the lumen of the left ventricle was enlarged, the left ventricle wall was thickened, and the cardiac function was significantly reduced (Supplementary Figure 1). Left ventricular internal dimension end-systolic (LVIDs) and left ventricular internal dimension end-diastolic (LVIDd) were not affected in the sham groups after 8 weeks (6 weeks of TAC+2 weeks of PCI34051 at a dose of 10 mg/kg/day). However, the administration of PCI34051 dose dependently mitigated TAC-induced enhanced LVIDs and LVIDd (Figures 1(j) – 1(l)). The effect of PCI34051 at a dose of 30 mg/kg bodyweight/day was higher than that of PCI34051 at doses of 3 and 10 mg/kg bodyweight/day. Fractional shortening (FS) and ejection fraction (EF) were significantly decreased in the TAC groups. However, PCI34051 dose dependently increased FS and EF (Figures 1(m) and 1(n)).

3.2. PCI34051 Regulates RAAS Genes in TAC Mice. Heart failure is characterized by neurohormonal activation [35, 36]. In this study, we investigated the effects of PCI34051 on the RAAS by evaluating the mRNA expression levels of *Ace1*, *Ace2*, *Agtr1*, and *Agtr2* in cardiac and pulmonary tissues. PCI34051 dose dependently mitigated the TAC-induced upregulation of *Ace1* mRNA levels (Figure 2(a)) and downregulation of *Ace2* mRNA levels in cardiac tissues (Figure 2(b)). Similar *Ace1* and *Ace2* expression patterns were observed in the pulmonary tissues (Figures 2(c) and 2(d)). The expression levels of Ace1 were downregulated in cardiac tissues in the sham group. However, TAC markedly upregulated the levels of Ace1, which was markedly mitigated upon PCI34051 treatment. PCI34051 mitigated the TAC-induced downregulation of Ace2 levels in cardiac tissues (Figures 2(e)–2(g)). Similar Ace1 and Ace2 expression patterns were observed in pulmonary tissues (Figures 2(h)–2(j)). qRT-PCR analysis revealed that PCI34051 mitigated the TAC-induced upregulation of *Agtr1* mRNA levels in cardiac and pulmonary tissues. In contrast, PCI34051 mitigated the TAC-induced downregulation of *Agtr2* mRNA levels (Figures 2(k)–2(n)).

3.3. PCI34051 Downregulates the Expression of Hdac8 and Inflammatory Markers in TAC Mice. Previous studies have reported that HDAC8 is involved in the induction of cardiac hypertrophy [28, 29]. We hypothesized that heart failure could also be alleviated through HDAC8 inhibition. To verify this hypothesis, mRNA levels of class I HDACs (*Hdac1*, *Hdac*2, *Hdac*3, and *Hdac*8) were determined in TAC mice. TAC did not affect the cardiac and pulmonary levels of *Hdac1*, *Hdac2*, and *Hdac3* (Supplementary Figure 2). However, TAC significantly upregulated the cardiac *Hdac8* mRNA levels. PCI34051 dose dependently mitigated the TAC-induced upregulation of cardiac *Hdac8* mRNA levels (Figure 3(a)). The upregulated levels of inflammatory biomarkers are reported to contribute to heart failure [37]. Therefore, the effect of PCI34051 on inflammatory marker expression was examined. PCI34051 dose dependently mitigated the TAC-induced upregulation of cardiac *Il1b*, *Ccl2*, and *Rela* mRNA levels (Figures 3(b)–3(d)). Additionally, PCI34051 mitigated the TAC-induced downregulation of cardiac *Nfkbia* mRNA levels (Figure 3(e)). The effects of TAC and PCI34051 on the expression patterns of *Hdac8* and inflammation-related genes in the cardiac tissues were similar to those in the pulmonary tissues (Figures 3(f)–3(j)). Western blotting analysis revealed that PCI34051 dose dependently mitigated the TAC-induced upregulation of Hdac8, Ccl2, and Rela in cardiac and pulmonary tissues, which was consistent with the qRT-PCR analysis results (Figures 3(k)–3(t)). PCI34051 mitigated the TAC-induced downregulation of Nfkbia (Figures 3(o) and 3(t)).

3.4. PCI34051 Suppresses Cardiac Fibrosis in TAC Mice. Previous studies have reported that interstitial cardiac fibrosis leads to the development of heart failure [38]. The therapeutic effect of PCI34051 on cardiac fibrosis was examined using Picrosirius red staining, qRT-PCR, and western blotting analyses. As shown in Figures 4(a) nad 4(b), TAC promoted collagen deposition in the perivascular and interstitial regions of the heart. PCI34051 dose dependently decreased TAC-induced collagen accumulation. The cardiac expression levels of the fibrosis-related genes *Col1a1*, *Fn1*, *Acta2*, and *Tgfb1* in the TAC group were upregulated compared with those in the sham group. Treatment with PCI34051 significantly downregulated the expression of these genes (Figures 4(c)–4(f)). The results of western blotting analysis were consistent with those of qRT-PCR analysis (Figures 4(g)–4(j)). TGF-β1/Smad2/3 signaling is reported to induce fibrotic gene expression [39]. Hence, the levels of phosphorylated Smad2/3 were examined. Treatment with PCI34051 mitigated the TAC-induced upregulation of cardiac p-Smad2/3 levels (Figures 4(g) and 4(k)).

3.5. PCI34051 Alleviates Pulmonary Congestion and Fibrosis in TAC Mice. Heart failure promotes pathological lung

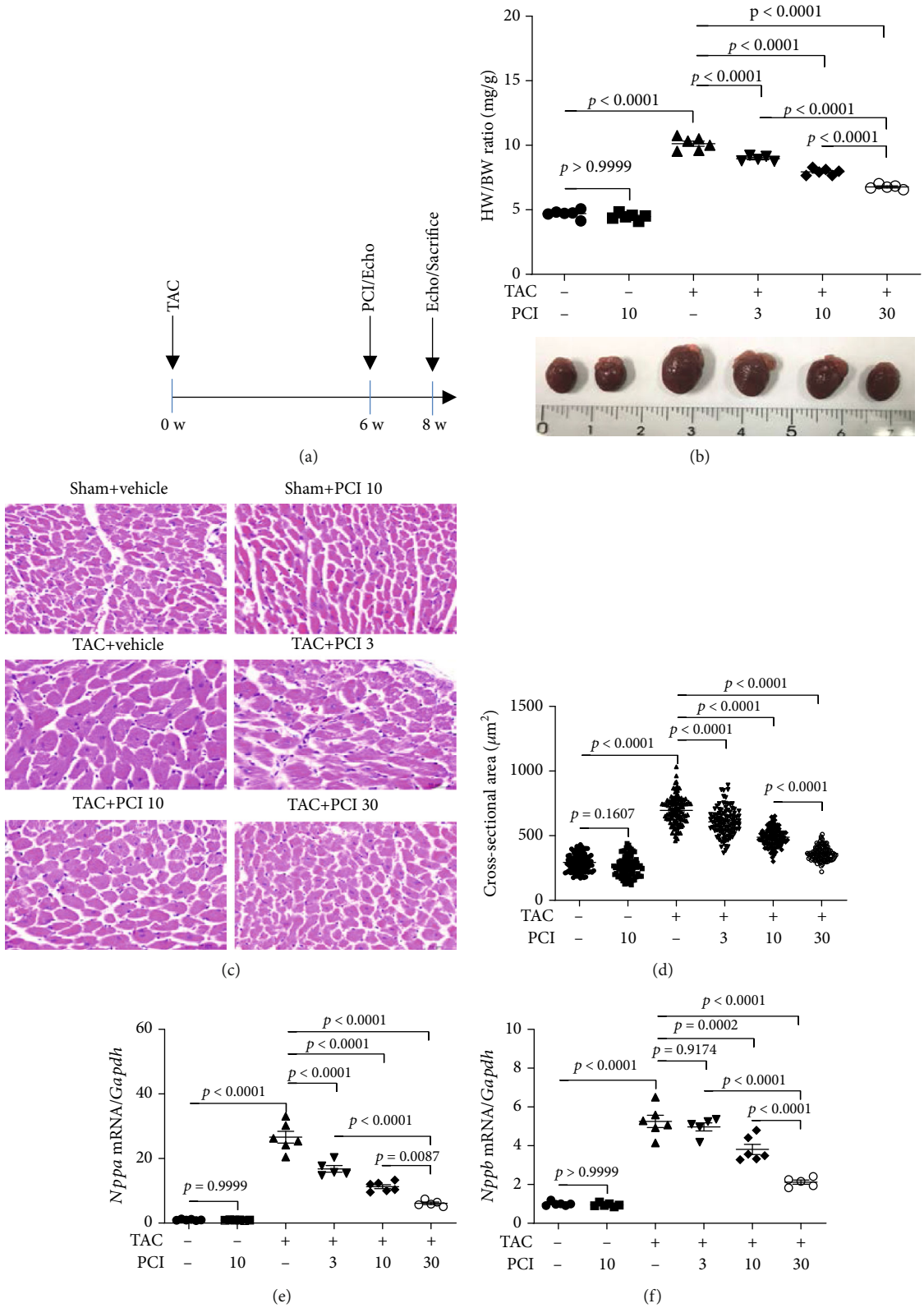

Figure 1: Continued.

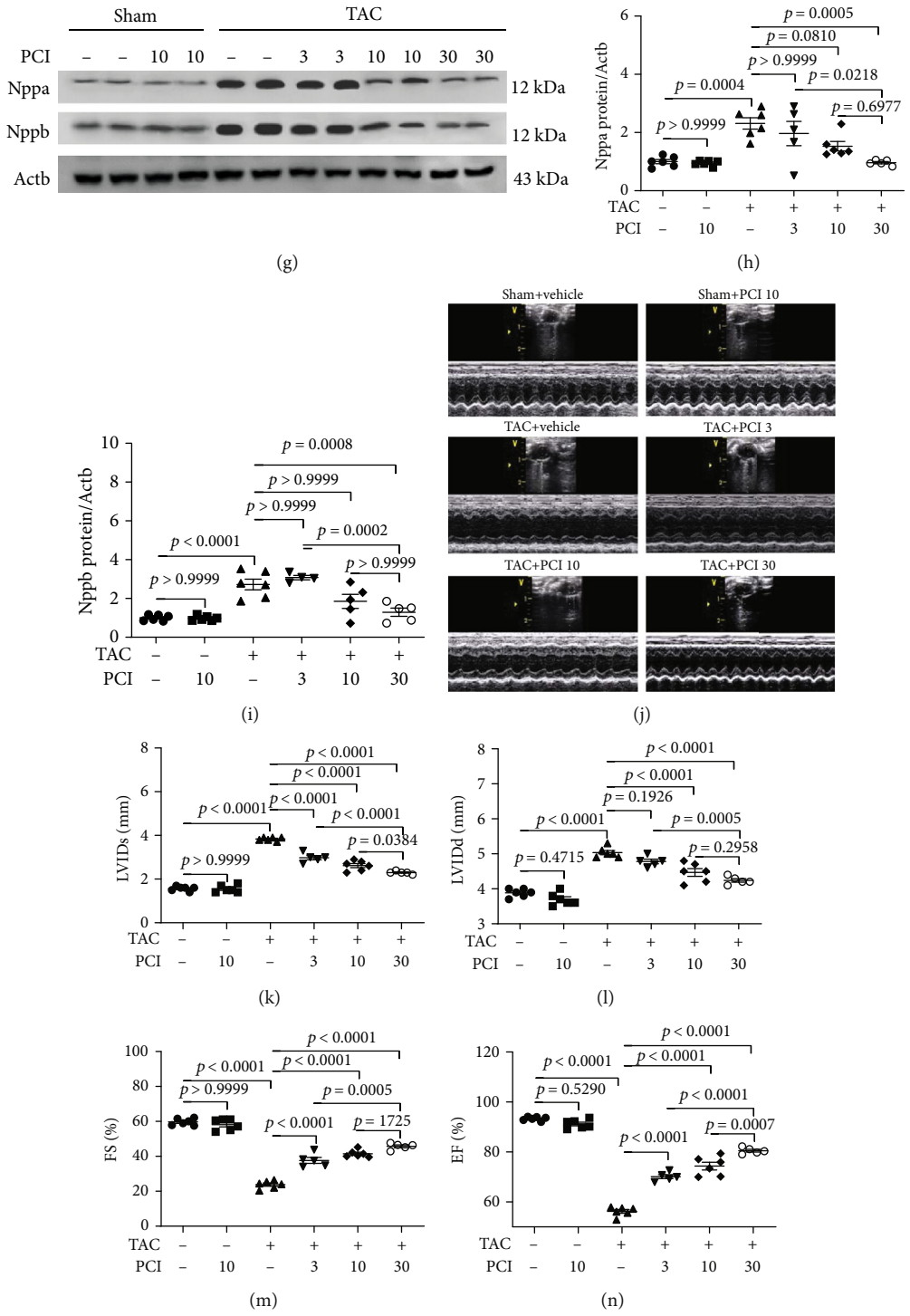

Figure 1: PCI34051 alleviates cardiac hypertrophy and left ventricular dysfunction in transverse aortic constriction- (TAC-) induced heart failure. (a) Schematic diagram of the TAC-induced heart failure mouse model and the PCI34051 treatment schedule. TAC promoted heart failure in mice. At week 6 post-TAC, mice were administered with vehicle or PCI34051 for 2 weeks as described in Materials and Methods. (b) Heart weight-to-bodyweight (HW/BW) ratio ($n = 5$–6 mice per group; A) and representative images (B) of heart from the sham+vehicle, sham+PCI34051 (10 mg/kg bodyweight/day), TAC+vehicle, and TAC+PCI34051 (3, 10, or 30 mg/kg bodyweight/day) groups. (c) Representative images of mouse cardiac tissues stained with hematoxylin and eosin ($n = 5$–6 mice per group). Scale bar = 50 μm. (d) Quantification of cardiomyocyte cross-sectional area of samples described in (b). (e, f) mRNA levels of *Nppa* and *Nppb* were determined using quantitative real-time polymerase chain reaction and normalized to those of *Gapdh*. (g) Nppa and Nppb levels in the cardiac tissues of mice described in (b). Representative western blot images. (h, i) Quantification of Nppa and Nppb levels. (j–n) Representative M-mode echocardiograms and parameters in mice. Quantification of left ventricular internal dimension end-systolic (LVIDs) and left ventricular internal dimension end-diastolic (LVIDd), fractional shortening (FS), and ejection fraction (EF) ($n = 5$–6 mice per group).

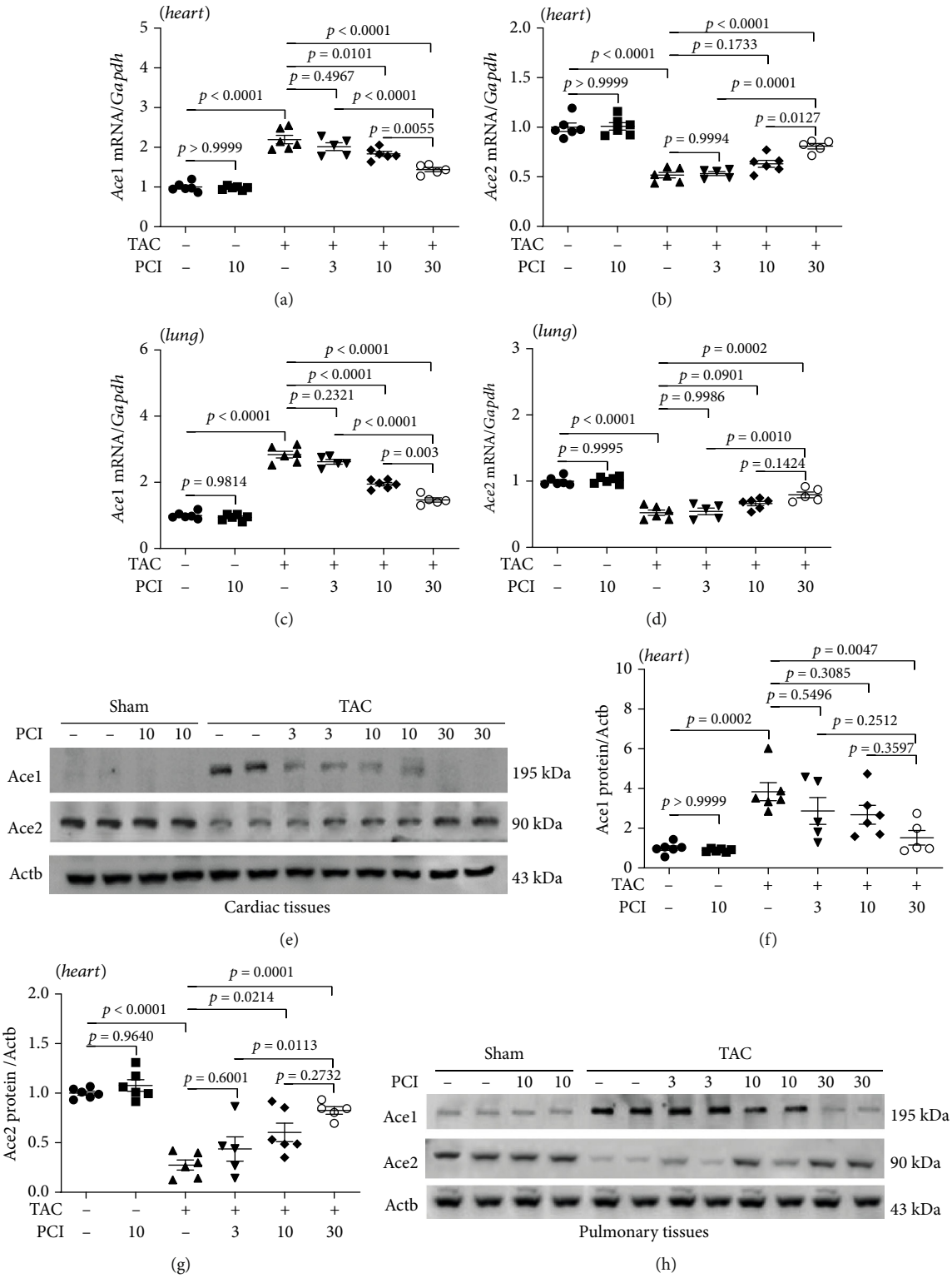

Figure 2: Continued.

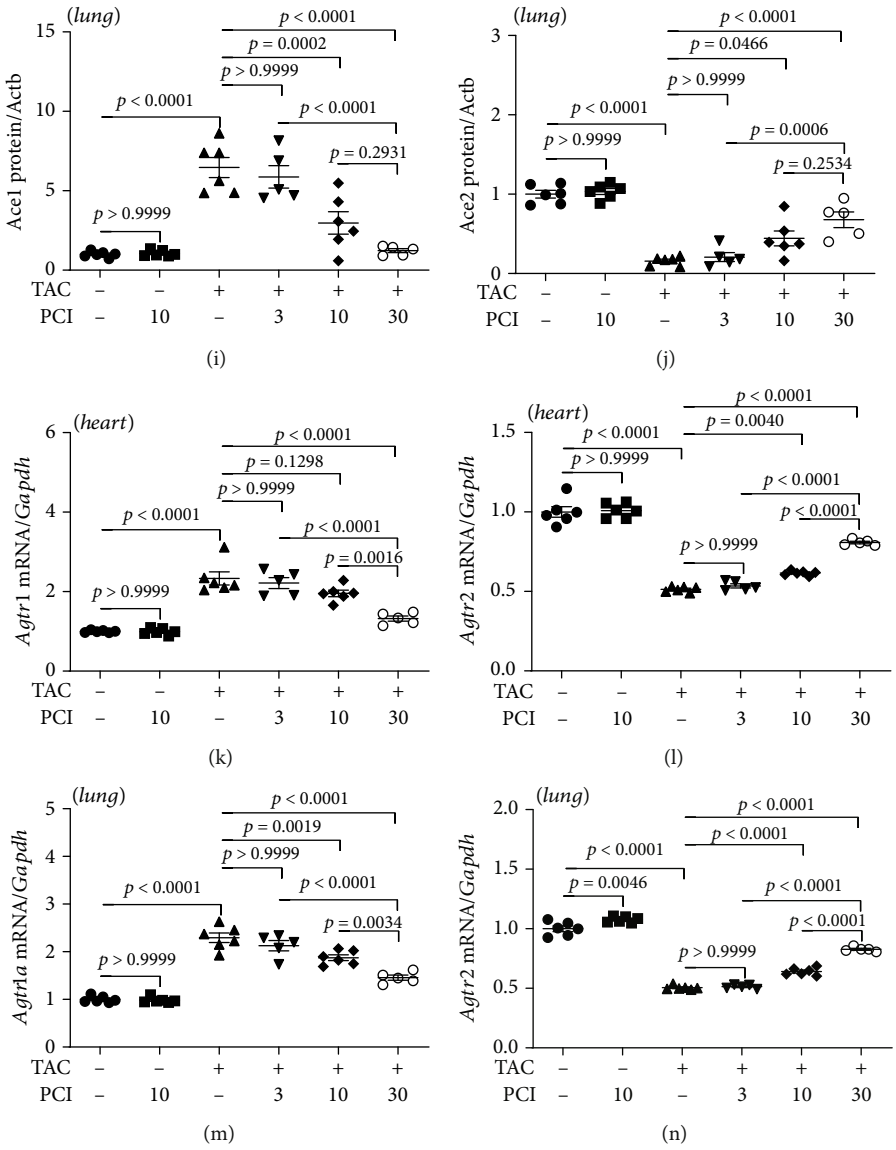

Figure 2: PCI34051 regulates renin-angiotensin system-related genes in the cardiac and pulmonary tissues of transverse aortic constriction (TAC) mice. (a–d) Cardiac and pulmonary mRNA levels of *Ace1* and *Ace2* in the sham+vehicle, sham+PCI34051 (10 mg/kg bodyweight/day), TAC+vehicle, and TAC+PCI34051 (3, 10, or 30 mg/kg bodyweight/day) groups ($n = 5$–6) were examined using quantitative real-time polymerase chain reaction (qRT-PCR). (e) Representative western blot images of Ace1 and Ace2 in cardiac tissues. (f, g) Quantification of Ace1 and Ace2 levels ($n = 5$–6). (h) Representative western blot images of Ace1 and Ace2 in the pulmonary tissues. (i, j) Quantification of Ace1 and Ace2 levels ($n = 5$–6). (k–n) Cardiac and pulmonary mRNA levels of *Agtr1* and *Agtr2* were determined using qRT-PCR and normalized to those of *Gapdh* ($n = 5$–6).

remodeling [40]. The effect of PCI34051 on TAC-induced lung remodeling was examined using histological, qRT-PCR, and western blotting analyses. The LW/BW ratio in the TAC group was higher than that in the sham group. PCI34051 significantly and dose dependently mitigated the TAC-induced enhanced LW/BW ratio (Figure 5(a)). H&E staining of pulmonary tissues revealed that the alveolar spaces were not significantly different between the vehicle-treated sham and PCI34051-treated sham groups. PCI34051 mitigated the TAC-induced decreased alveolar spaces (Figure 5(b)). Next, pulmonary fibrosis was evaluated using Picrosirius red staining. Treatment with PCI34051 dose dependently mitigated TAC-induced pulmonary fibrosis (Figurse 5(c) and 5(d)). To further characterize pulmonary fibrosis, the expression levels of fibrosis-related markers were examined using qRT-PCR and western blotting analyses. PCI34051 significantly mitigated the TAC-induced upregulation of *Col1a1*, *Fn1*, *Acta2*, and *Tgfb1* mRNA levels (Figures 5(e)–5(h)). The pulmonary levels of Fn1, Acta2, Tgfb1, and phosphorylated Smad2/3 in the TAC group were upregulated compared with those in the sham group. However, PCI34051 mitigated the TAC-induced upregulation of Fn1, Acta2, Tgfb1, and phosphorylated Smad2/3 in the pulmonary tissues (Figures 5(i)–5(m)).

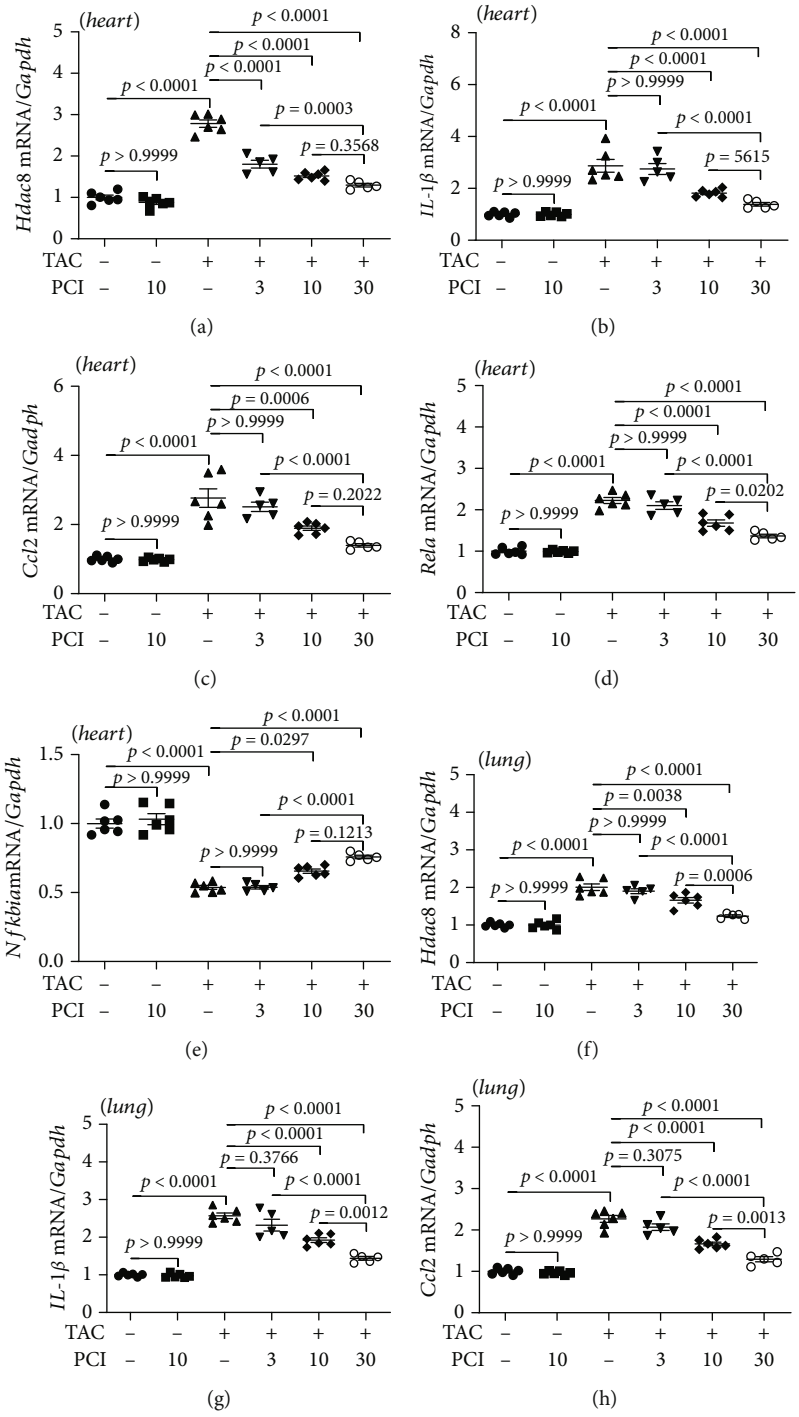

Figure 3: Continued.

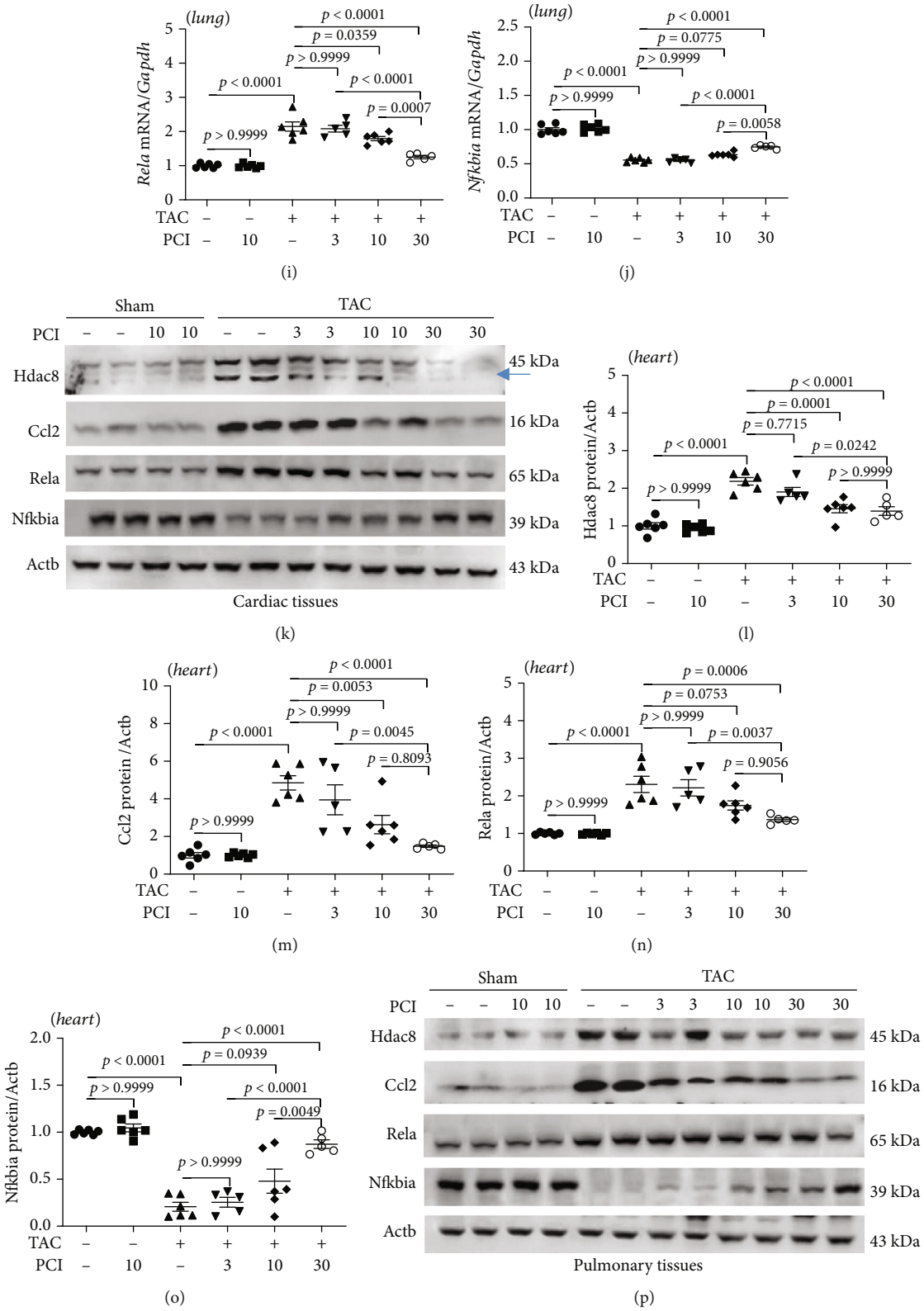

Figure 3: Continued.

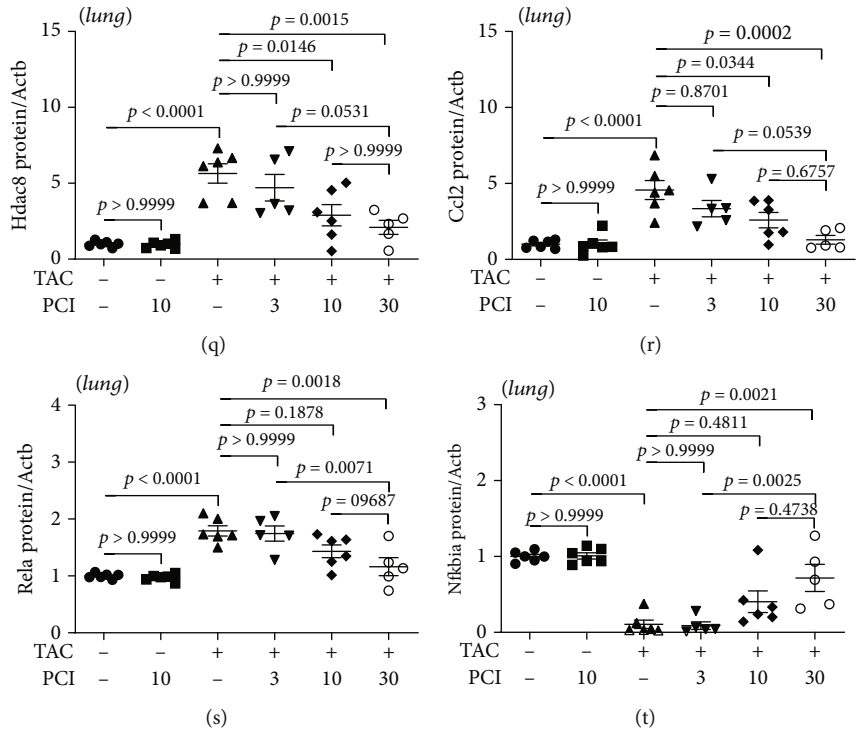

Figure 3: PCI34051 downregulates the expression of Hdac8 and inflammation-related genes in transverse aortic constriction (TAC) mice. (a–j) Cardiac and pulmonary mRNA levels of *Hdac8*, *Il1b*, *Ccl2*, *Rela*, and *Nfkbia* in the sham+vehicle, sham+PCI34051 (10 mg/kg bodyweight/day), TAC+vehicle, and TAC+PCI34051 (3, 10, or 30 mg/kg bodyweight/day) groups were determined using quantitative real-time polymerase chain reaction. (k) Cardiac expression levels of Hdac8, Ccl2, Rela, and Nfkbia; representative western blot images are shown. Actb was used as a loading control. (l–o) Quantification of Hdac8, Ccl2, Rela, and Nfkbia levels ($n = 5$–6 per group). (p) Pulmonary expression levels of Hdac8, Ccl2, Rela, and Nfkbia; representative western blot images. Actb was used as a loading control. (q–t) Quantification of Hdac8, Ccl2, Rela, and Nfkbia levels ($n = 5$–6 per group).

3.6. Knockdown of Hdac8 or Ace1 Suppresses TGF-β1-Mediated Fibrosis in Primary Rat Cardiac Fibroblasts. Heart failure is often accompanied by fibrosis, a process characterized by excess production of extracellular matrix in activated fibroblasts [41, 42]. To examine the role of HDAC8 in the regulation of fibrosis in vitro, primary rat cardiac fibroblasts were incubated with PCI34051 in the presence or absence of TGF-β1. PCI34051 significantly mitigated the TGF-β1-induced upregulation of *Hdac8* mRNA levels (Figure 6(a)). Additionally, PCI34051 mitigated the TGF-β1-induced upregulation of the fibrosis-related genes *Col1a1*, *Fn1*, and *Acta2* (Figures 6(b)–6(d)). TGF-β1 treatment upregulated the expression of *Tgfb1* (Figure 6(e)). The results of western blotting analysis were consistent with those of qRT-PCR analysis (Figure 6(f)–6(j)). Furthermore, PCI34051 mitigated the TGF-β1-induced upregulation of phosphorylated Smad2/3 levels (Figures 6(f) and 6(k)).

To determine whether TGF-β1-induced fibrosis was dependent on HDAC8, we transfected H9c2 cells with si-Hdac8. Transfection with si-Hdac8 markedly downregulated the endogenous *Hdac8* mRNA levels (Figure 6(l)) and mitigated the TGF-β1-induced upregulation of *Fn1*, *Acta2*, *Tgfb1* (Figures 6(m)–6(o)), and *Ace1* mRNA levels (Figure 6(p)). The results of the western blotting analysis were consistent with those of qRT-PCR analysis (Figures 6(q)–6(v)). Furthermore, transfection with si-Hdac8 mitigated the TGF-β1-induced upregulation of phosphorylated Smad2/3 levels (Figures 6(q) and 6(w)).

Next, the role of ACE1 in fibrosis was investigated by downregulating Ace1 expression using siRNAs. Transfection with si-Ace1 markedly downregulated the endogenous *Ace1* mRNA levels, whereas treatment with TGF-β1 upregulated the *Ace1* mRNA levels in rat cardiac fibroblasts (Supplementary Figure 3A). Additionally, transfection with si-Ace1 mitigated the TGF-β1-induced upregulation of *Hdac8*, *Fn1*, *Acta2*, and *Tgfb1* mRNA levels (Supplementary Figure 3B–E). The results of western blotting analysis were consistent with those of qRT-PCR analysis (Supplementary Figure 3F–K). Furthermore, transfection with si-Ace1 significantly downregulated the levels of phosphorylated Smad2/3 in TGF-β1-stimulated fibroblasts (Supplementary Figure 3F and L).

3.7. Cardiac Inflammation Is Regulated through the Hdac8-Ace1-Rela-Nfkbia Axis. To elucidate the regulatory mechanisms of PCI34051, the role of Hdac8 and Ace1 in inflammation was examined. H9c2 cardiomyocytes were transfected with *pCMV* or *pCMV-Hdac8* constructs. Hdac8 overexpression upregulated *Hdac8* and *Ace1* mRNA levels and downregulated *Ace2* mRNA levels. The NF-κB signaling pathway is reported to play a key role in various inflammatory diseases [43]. Hdac8 overexpression significantly

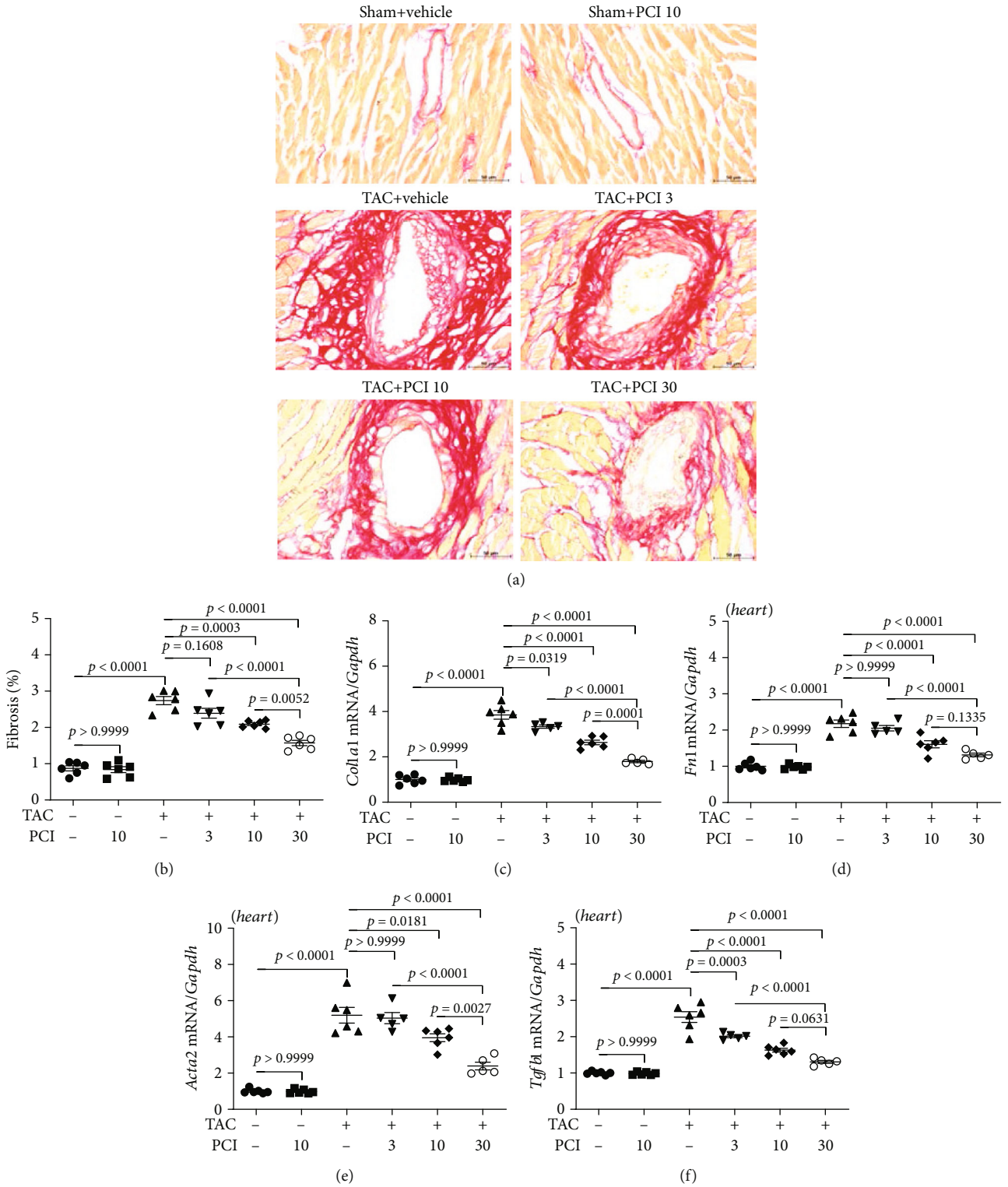

Figure 4: Continued.

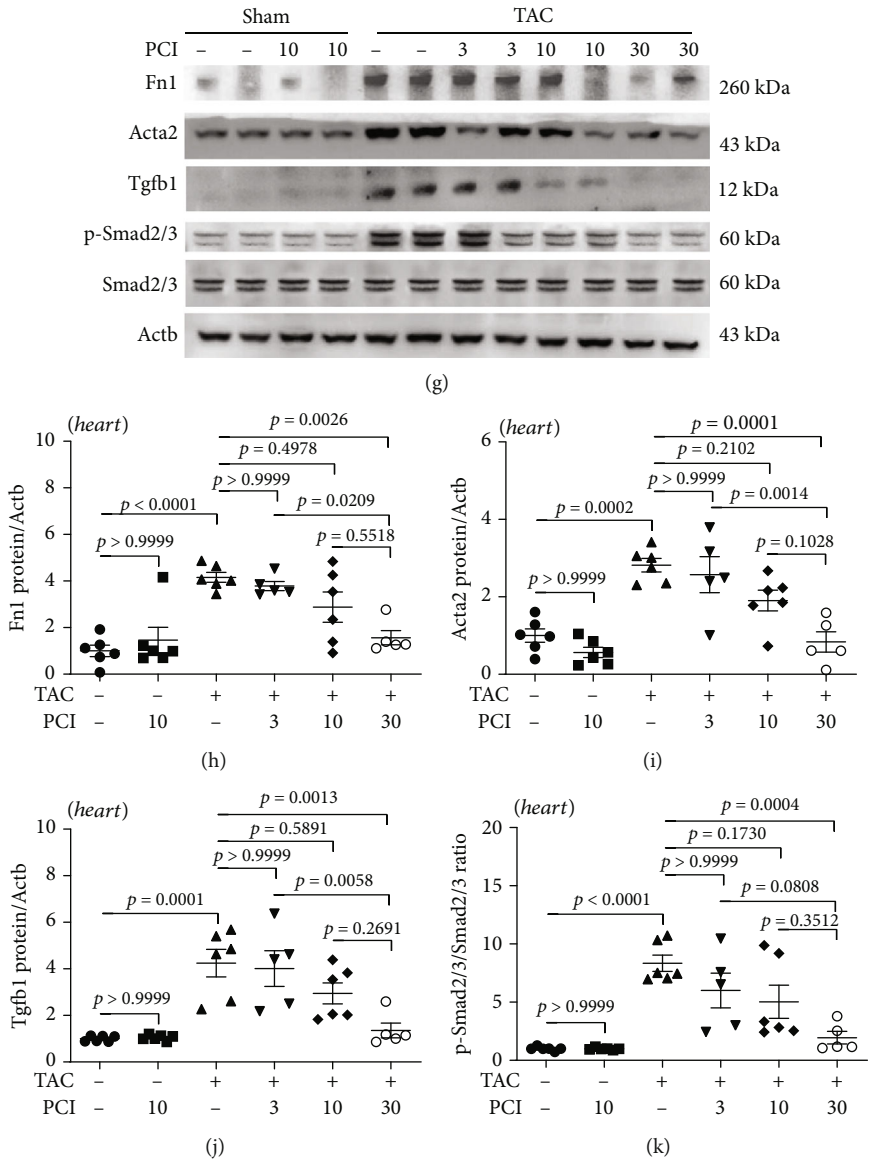

Figure 4: PCI34051 alleviates cardiac fibrosis in transverse aortic constriction (TAC) mice through the TGF-β1-Smad2/3 pathway. (a, b) Picrosirius red staining of mouse cardiac tissues; representative images and quantification are shown. Scale bar = 50 μm. The expression levels of the fibrosis marker genes *Col1a1* (c), *Fn1* (d), *Acta2* (e), and *Tgfb1* (f) were determined using quantitative real-time polymerase chain reaction (n = 5–6 per group). (g) The cardiac expression levels of Fn1, Acta2, Tgfb1, p-Smad2/3, and Smad2/3 were analyzed using western blotting. Actb was used as a loading control. Representative blots are shown. (h–k) Quantification of Fn1, Acta2, Tgfb1, and p-Smad2/3 to Smad2/3 (n = 5–6 per group).

upregulated *Rela* mRNA levels and downregulated *Nfkbia* mRNA levels (Figure 7(a)). Next, the expression of Hdac8 was knocked down using siRNA. Transfection with si-Hdac8 markedly decreased endogenous *Hdac8* mRNA levels but did not affect *Ace1* and *Ace2* mRNA levels. Additionally, transfection with si-Hdac8 downregulated *Rela* mRNA levels and upregulated *Nfkbia* mRNA levels (Figure 7(b)). To investigate the role of Ace1, the cells were transfected with *pCMV6* or *pCMV6-Ace1* constructs. Ace1 overexpression upregulated endogenous Ace1 levels and downregulated Ace2 levels. However, Ace1 overexpression did not affect Hdac8 levels. Additionally, Ace1 overexpression significantly upregulated Rela levels and downregulated Nfkbia levels (Figures 7(c) and 7(d)). Meanwhile, *Ace1* knockdown downregulated endogenous *Ace1* mRNA levels and upregulated *Ace2* mRNA levels. However, *Ace1* knockdown did not affect *Hdac8* mRNA levels but significantly upregulated *Nfkbia* mRNA levels (Figure 7(e)). To evaluate the effect of *Hdac8* knockdown on isoproterenol-induced inflammation, H9c2 cardiomyocytes were transfected with control siRNA or si-Hdac8 and treated with isoproterenol. Transfection with si-Hdac8 did not affect *Ace1* and *Ace2* mRNA levels. Additionally, si-Hdac8 mitigated the isoproterenol-induced upregulation of *Ace1* mRNA levels and downregulation of *Ace2* mRNA levels (Supplementary Figure 4A–B). Furthermore, si-Hdac8 mitigated the isoproterenol-induced upregulation of *Rela* mRNA levels and downregulation of *Nfkbia* mRNA levels (Figures 7(f) and 7(g)). Next, the role

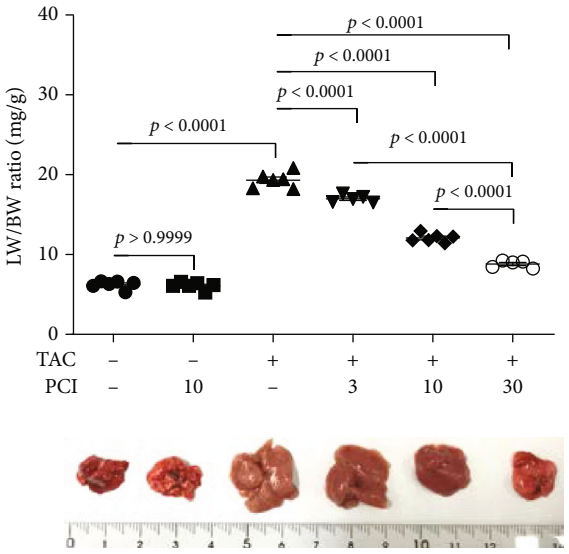

(a)

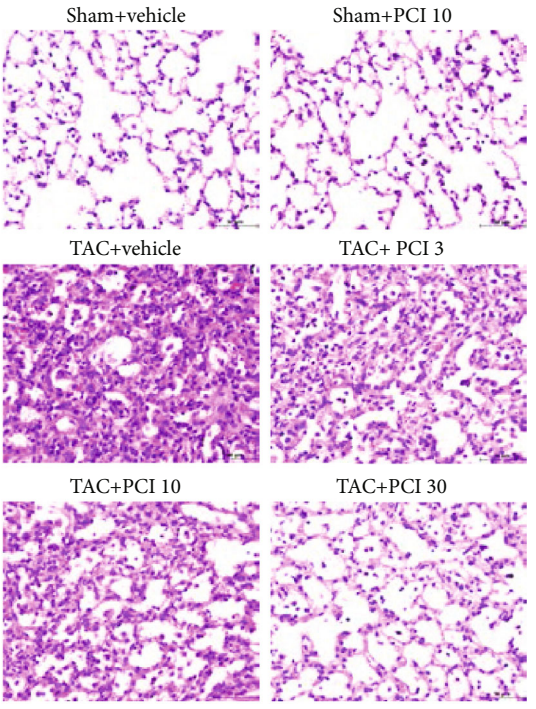

(b)

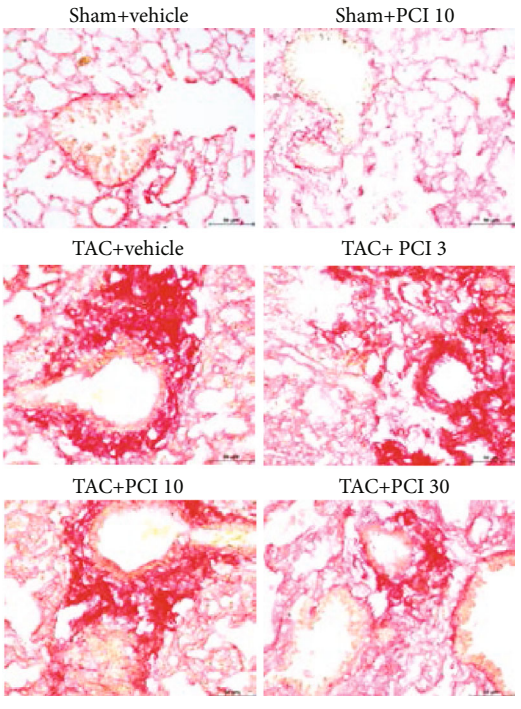

(c)

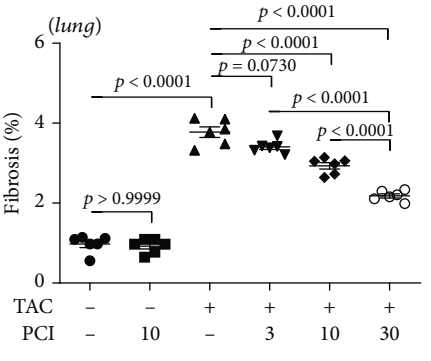

(d)

Figure 5: Continued.

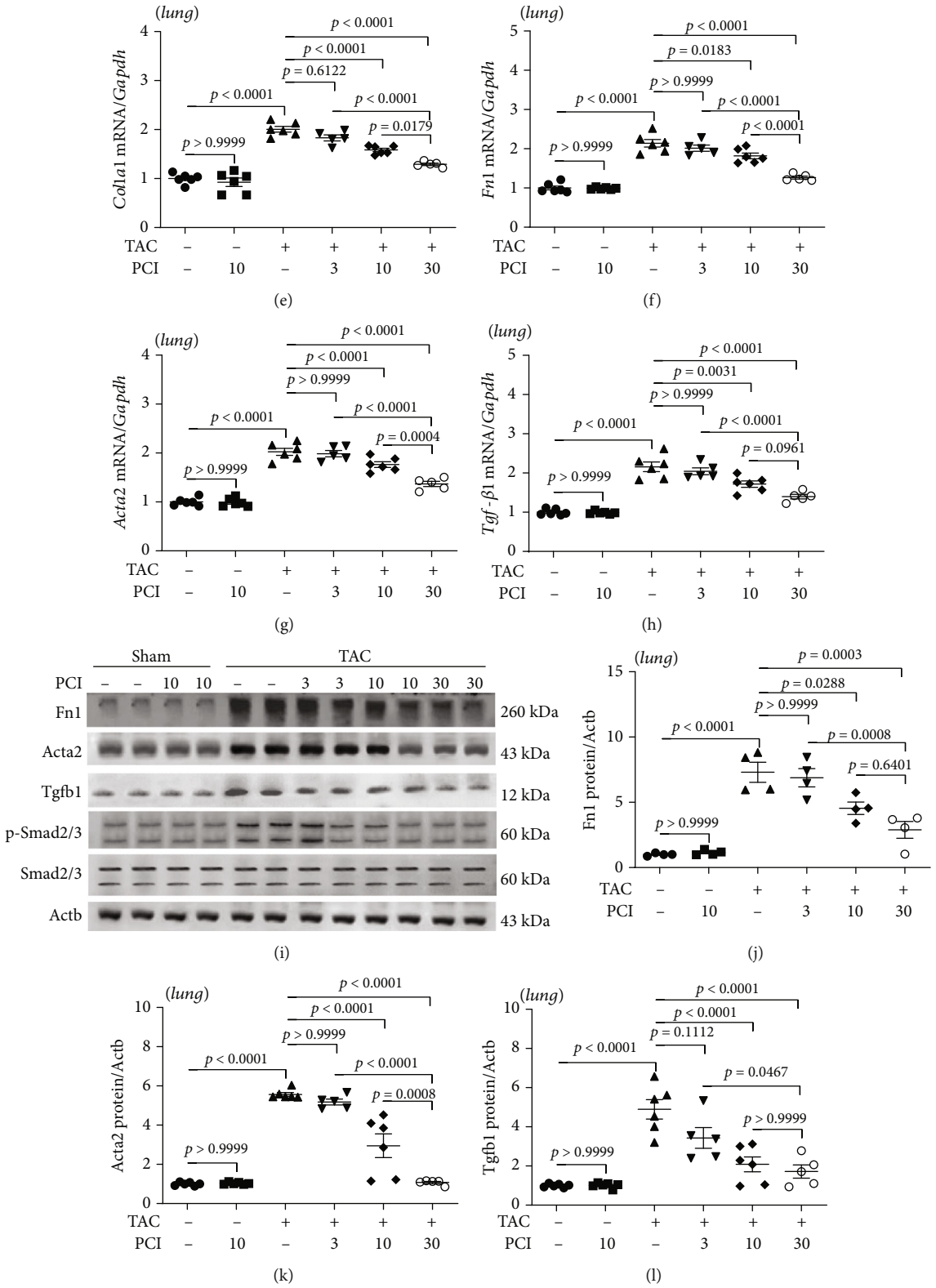

Figure 5: Continued.

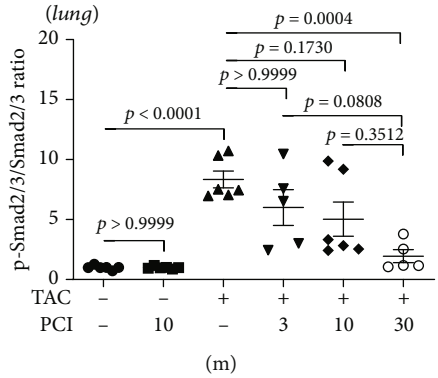

Figure 5: PCI34051 alleviates pulmonary congestion and fibrosis in transverse aortic constriction (TAC) mice. (a) The ratio of lung weight-to-bodyweight (LW/BW) in the sham+vehicle, sham+PCI34051 (10 mg/kg bodyweight/day), TAC+vehicle, and TAC+PCI34051 (3, 10, or 30 mg/kg bodyweight/day) groups ($n = 5$–6 per group) was determined. Representative images of mouse lungs (B). (b) Representative images of pulmonary tissues stained with hematoxylin and eosin. Scale bar = 50 μm. (c) Representative images of pulmonary tissues stained with Picrosirius red. Scale bar = 50 μm. (d) Pulmonary fibrosis was quantified using ImageJ software. (e–h) The mRNA levels of *Col1a1*, *Fn1*, *Acta2*, and *Tgfb1* were evaluated using quantitative real-time polymerase chain reaction ($n = 5$–6 per group). (i–m) Representative western blots and quantification of Fn1, Acta2, Tgfb1, p-Smad2/3, and Smad2/3 levels in the pulmonary tissues ($n = 5$–6 per group).

of ACE1 in HDAC8-mediated inflammation response was examined. H9c2 cells were transfected with *pCMV-Hdac8* construct and si-Ace1. Transfection with si-Ace1 did not affect Hdac8 levels, which suggested that *Ace1* is a downstream gene of Hdac8. Hdac8 overexpression mitigated si-Ace1-induced upregulation of Ace2. Furthermore, si-Ace1 mitigated Hdac8 overexpression-induced Rela upregulation and Nfkbia downregulation (Figures 7(h) and 7(i)). To analyze the association between HDAC8 and inflammation, H9c2 cells were incubated with PCI34051 in the presence or absence of TNFα. The localization of NF-κB (nuclear vs. cytoplasmic) was evaluated. Treatment with TNF-α did not affect the localization of Ace1 and Hdac8, which were localized in the nuclear fraction. PCI34051 mitigated the TNF-α-induced upregulation of nuclear Rela levels and downregulation of cytosolic Nfkbia levels (Figures 7(j) and 7(k)). These findings indicate that PCI34051 exerts cardioprotective effects through the downregulation of the NF-κB signaling pathway.

4. Discussion

In this study, we found that the selective HDAC8 inhibitor (PCI34051) alleviated pathological heart and lung conditions, mitigated cardiac dysfunction, and suppressed inflammation and fibrosis in TAC mice through the Hdac8-Ace1 axis (Figure 8).

The cardiac and pulmonary expression levels of Hdac8 but not those of other class I HDACs (HDAC1, HDAC2, and HDAC3) were upregulated in TAC mice. This suggested a distinct role of HDAC8 in the regulation of heart failure. The expression levels of Ace1 and Agtr1 were upregulated, whereas those of Ace2 and Agtr2 were downregulated in the cardiac and pulmonary tissues of TAC mice. Treatment with PCI34051 mitigated the TAC-induced changes in the expression levels of these genes, which suggested that HDAC8 promoted the activation of RAAS during heart failure. Hdac8 overexpression upregulated Ace1 and Agtr1 levels and downregulated Ace2 and Agtr2 levels in cardiomyocytes (Figure 7(a) and Supplementary Figure 5). Previous studies have reported that RAAS is activated in patients with heart failure [44]. However, the direct roles of RAAS components in the pathogenesis of heart failure are unclear. This study demonstrated that overexpression of Ace1 and Hdac8 upregulated the expression of inflammatory markers in cardiomyocytes, which was mitigated upon *Ace1* knockdown. ACE1 and ACE2 are reported to play an important role in inflammation [45, 46]. Therefore, the expression levels of Ace1 and Ace2 were examined in the TAC-induced mouse model. Overexpression of Hdac8 or Ace1 downregulated Ace2 levels, which suggested that Hdac8 is a novel negative regulator of Ace2 expression.

Recently, we reported that PCI34051 attenuates catecholamine-induced cardiac hypertrophy [28]. In this study, PCI34051 dose dependently alleviated cardiac hypertrophy and downregulated the expression of hypertrophy-specific genes (*Nppa* and *Nppb*) in the cardiac tissues of TAC mice. The TAC mouse model is characterized by decreased systolic function and development of heart failure with reduced EF [47]. PCI34051 regulated cardiac remodeling (increased the size of the left ventricular lumen) and consequently improved cardiac function. Heart failure is usually accompanied by cardiac hypertrophy. The role of HDAC2, which is the best characterized HDAC, in cardiac hypertrophy has been previously reported [20–22, 48, 49]. For example, SK-7041, a highly selective inhibitor of HDAC1 and HDAC2, alleviated cardiac hypertrophy in the rat TAC model [23]. Although HDAC2 and HDAC8 promote cardiac hypertrophy, the underlying mechanisms may vary. The enzymatic activity of HDAC2 was reported to be critical for the development of cardiac hypertrophy [21], whereas upregulation of HDAC8 expression was critical for promoting cardiac hypertrophy. Moreover, cardiac Hdac2 and Hdac8 expression levels are upregulated during

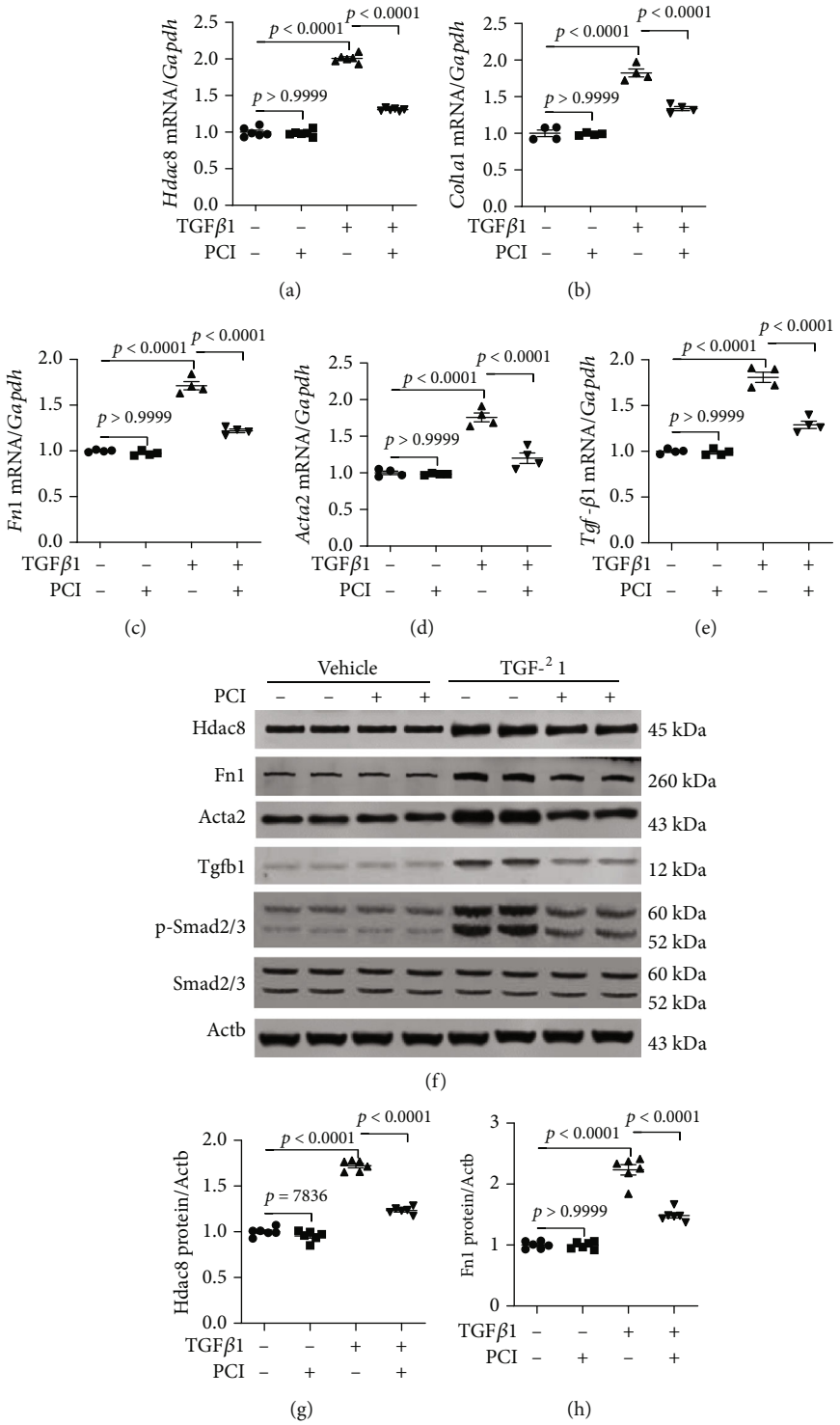

Figure 6: Continued.

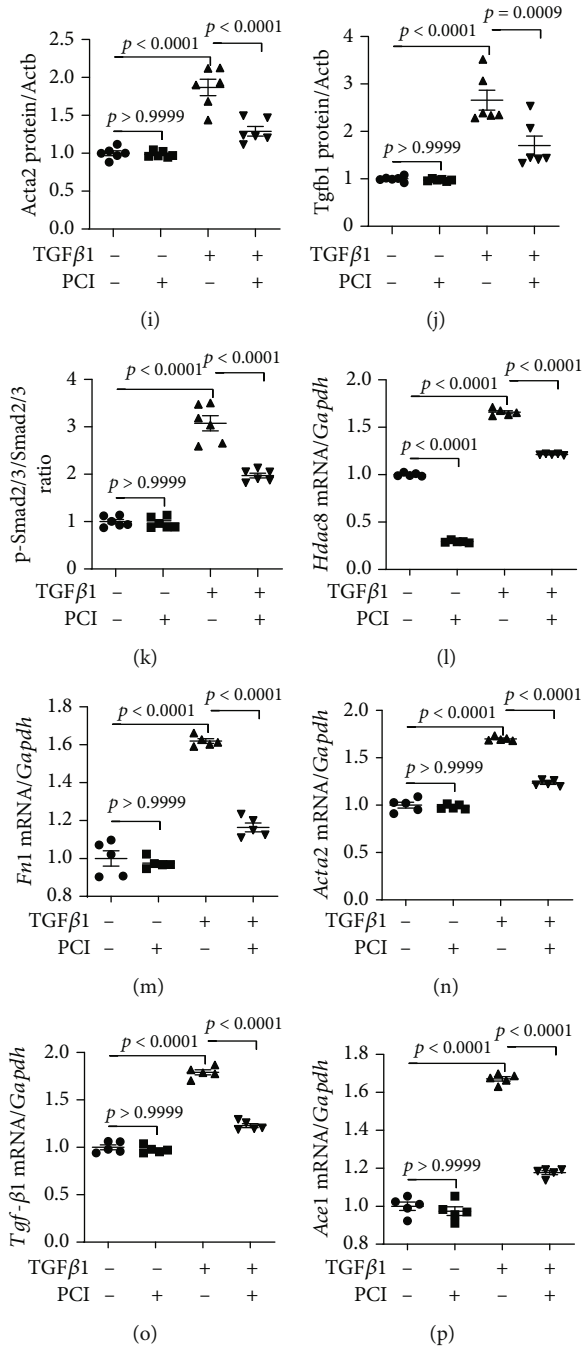

Figure 6: Continued.

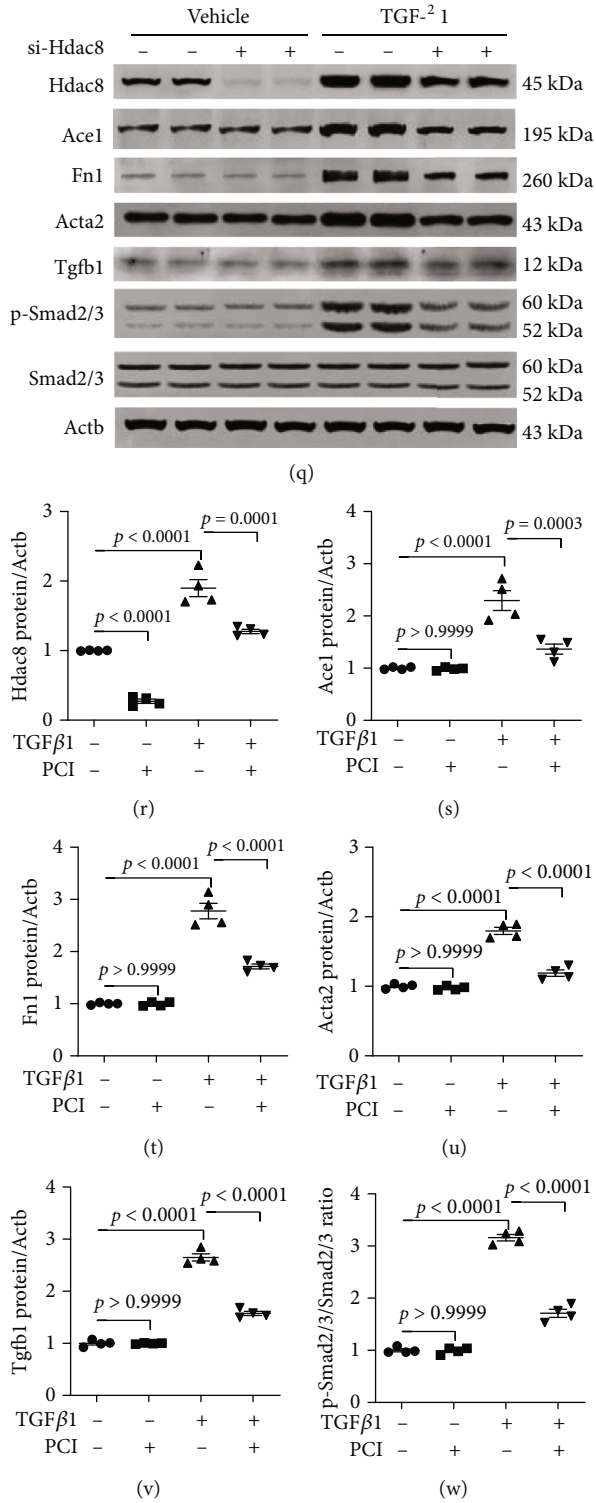

Figure 6: PCI34051 or *Hdac8* knockdown mitigates TGF-β1-induced fibrosis in rat cardiac fibroblasts. (a–e) Rat cardiac fibroblasts were pre-treated with TGF–β1 (10 ng/mL) for 1 h and cultured in the presence of vehicle or PCI34051 (10 μM) for 8 h. mRNA levels of *Hdac8*, *Col1a1*, *Fn1*, *Acta2*, and *Tgfb1* were evaluated using quantitative real-time polymerase chain reaction (qRT-PCR) ($n = 4$–6 per group). (f–k) Representative immunoblots and quantification of Hdac8, Fn1, Acta2, Tgfb1, p-Smad2/3, and Smad2/3 levels in rat cardiac fibroblasts ($n = 6$ per group). Actb was used as a loading control. (l–p) Rat cardiac fibroblasts were transfected with control or short-interfering RNA against *Hdac8* and treated with TGF-β1 (10 ng/mL) for 9 h. The mRNA levels of *Hdac8*, *Fn1*, *Acta2*, *Tgfb1*, and *Ace1* were determined using qRT-PCR ($n = 5$ per group). (q–w) Representative immunoblots and quantification of Hdac8, Ace1, Fn1, Acta2, Tgfb1, p-Smad2/3, and Smad2/3 levels in rat cardiac fibroblasts ($n = 4$ per group). Actb was used as a loading control.

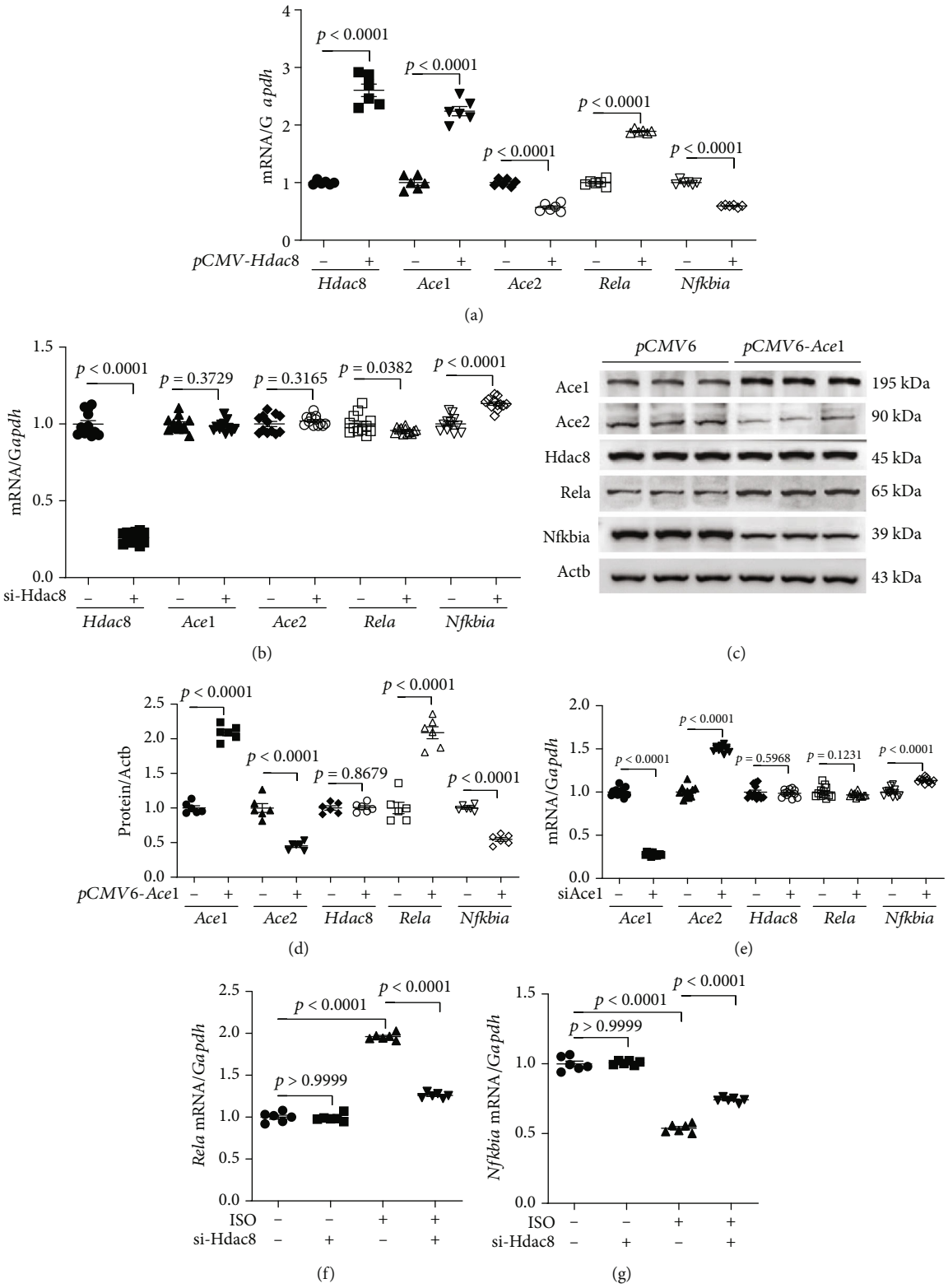

Figure 7: Continued.

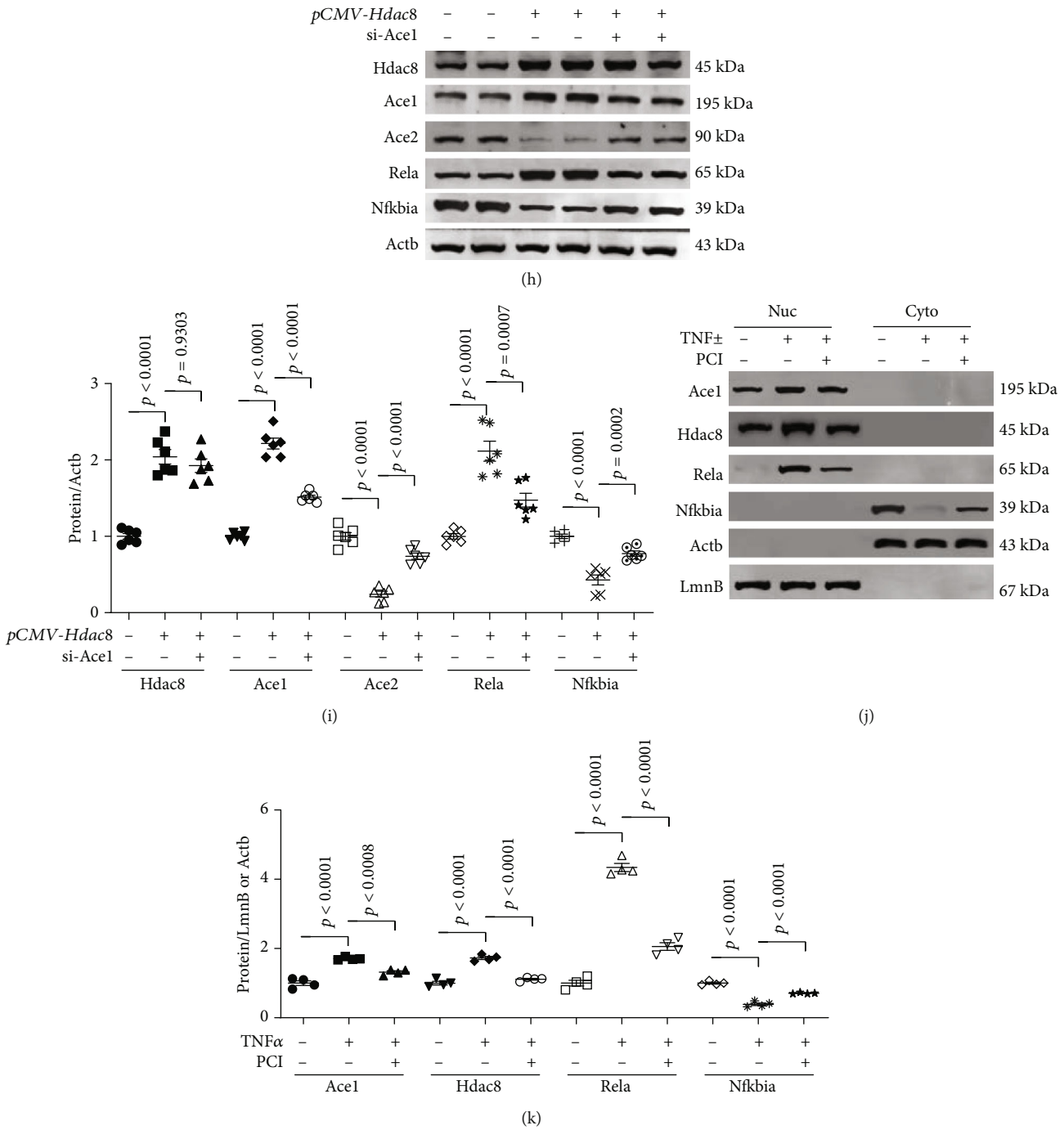

Figure 7: PCI34051 and *Hdac8* or *Ace1* knockdown regulate Rela and Nfkbia expression in cardiomyocytes. (a) mRNA levels of *Hdac8*, *Ace1*, *Ace2*, *Rela*, and *Nfkbia* in H9c2 cells transfected with *pCMV* vector or *pCMV-Hdac8* were evaluated using quantitative real-time polymerase chain reaction (qRT-PCR) ($n = 6$ per group). (b) mRNA levels of *Hdac8*, *Ace1*, *Ace2*, *Rela*, and *Nfkbia* in H9c2 cells transfected with control short-interfering RNA (siRNA) or siRNA against *Hdac8* (si-Hdac8) were evaluated using qRT-PCR ($n = 12$ per group). (c, d) Representative immunoblots and quantification of Ace1, Ace2, Hdac8, Rela, and Nfkbia levels in *pCMV6-Ace1*-transfected H9c2 cells ($n = 6$ per group). Actb was used as a loading control. (e) mRNA levels of *Ace1*, *Ace2*, *Hdac8*, *Rela*, and *Nfkbia* in H9c2 cells transfected with control siRNA or si-Ace1 were evaluated using qRT-PCR ($n = 12$ per group). (f, g) The mRNA levels of *Rela* and *Nfkbia* in H9c2 cells transfected with control siRNA or si-Hdac8 and treated with isoproterenol (10 μM) for 9 h were measured using qRT-PCR ($n = 6$ per group). (h, i) The expression levels of Hdac8, Ace1, Ace2, Rela, and Nfkbia in H9c2 cells transfected with *pCMV* or *pCMV-Hdac8* and control siRNA or si-Ace1; representative immunoblots and quantification of protein levels are shown ($n = 6$ per group). Actb was used as a loading control. (j, k) H9c2 cells were incubated with TNFα (50 ng/mL) for 1 h and cultured in the presence of vehicle or PCI34051 (10 μM) for 5 h. The nuclear and cytoplasmic fractions were obtained as described in Materials and Methods. Representative western blots and quantification of protein levels ($n = 4$ per group). Actb and LmnB were used as loading controls for the cytoplasmic and nuclear fractions, respectively.

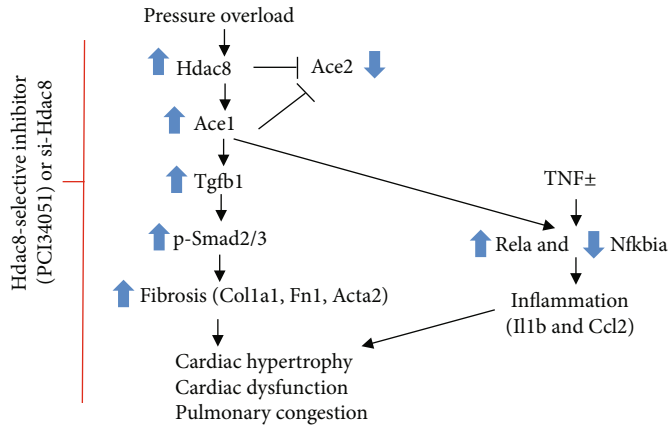

Figure 8: Suppression of HDAC8 attenuates fibrosis, inflammation, cardiac dysfunction, and pulmonary congestion in heart failure. Schematic diagram depicting the Hdac8 selective inhibitor- (PCI34051-) mediated or Hdac8 short-interfering RNA-mediated inhibition of transverse aortic constriction- (TAC-) induced heart failure. TAC-mediated pressure overload upregulates the expression of Hdac8 and Ace1 and downregulates the expression of Ace2 in the heart and lungs. In cardiomyocytes, overexpression of Hdac8 upregulates the expression of Ace1 and downregulates the expression of Ace2. PCI34051 treatment or *Hdac8* knockdown mitigates TGF-β1-induced upregulation of p-Smad2/3, Col1a1, Fn1, and Acta2 in vitro. PCI34051 regulates the TNFα-mediated or Ace1 overexpression-mediated expression of Rela and Nfkbia. PCI34051 alleviates cardiac hypertrophy and dysfunction, inflammation, fibrosis, and pulmonary congestion in heart failure.

cardiac remodeling in renovascular hypertensive rats [50]. One study reported that the expression levels of HDAC1, HDAC2, and HDAC8 were upregulated in patients with idiopathic pulmonary arterial hypertension [51]. Zhang et al. reported that calcium calmodulin kinase II promoted cardiac dysfunction by activating HDAC1 and HDAC3 [52]. However, these results are not consistent with some previous studies, which reported that HDAC3 is involved in postnatal cardiac myocyte proliferation and not cardiac hypertrophy [26]. The findings of this study suggested that sustained upregulation of Hdac8 mRNA and protein levels has a critical role in the transition from cardiac hypertrophy to heart failure.

Next, the expression levels of inflammation-related genes in the cardiac and pulmonary tissues of TAC mice were examined. TAC upregulated Rela levels and downregulated Nfkbia levels. Treatment with PCI34051 mitigated Rela upregulation and Nfkbia downregulation in vivo and in vitro. Additionally, PCI34051 mitigated the TNFα-induced nuclear localization of Rela, Ace1, and Hdac8 and downregulation of Nfkbia in the cytosol of cardiomyocytes. These findings indicate that PCI34051 exerts inhibitory effects on inflammatory signaling. Interestingly, the expression levels of *Rela* and *Nfkbia* were not affected in TGF-β1-stimulated cardiac fibroblasts (Supplementary Figure 6). Previously, we had demonstrated that PCI34051 downregulated the expression of inflammatory markers and adhesion molecules in hypertension [27]. WK2-16, an HDAC8 inhibitor, is reported to alleviate neuroinflammation both in vivo and in vitro [53]. CCL2, an inflammatory cytokine, plays an important role in the pathogenesis of heart failure [54]. In this study, PCI34051 mitigated the heart failure-induced upregulation of Ccl2.

Furthermore, the results of Picrosirius red staining revealed that PCI34051 dose dependently mitigated TAC-induced fibrosis in the mouse cardiac and pulmonary tissues. This indicated that HDAC8 is a potential novel therapeutic target for fibrosis. TGF-β1, a fibrogenic growth factor, upregulated the expression of *Hdac8* and fibrosis-related genes. The expression levels of Tgfb1 and phosphorylated Smad2/3 were upregulated in TAC mice and TGF-β1-treated cardiac fibroblasts. The antifibrotic effect of PCI34051 or *Hdac8* knockdown was potentially mediated through inhibition of the TGF-β1-Smad2/3 pathway. Interestingly, TGF-β1-induced fibrosis was dependent on Ace1. The expression levels of Fn1 and Acta2 were downregulated in TGF-β1-treated *Ace1* knockdown cardiac fibroblasts (Supplementary Figure 3). Moreover, the mRNA and protein levels of Ace1 were markedly upregulated in cardiac and pulmonary tissues of TAC mice. These observations suggest that the activation of RAAS contributed to pressure overload-induced fibrosis. The findings of this study are consistent with those in previous reports, which reported that ACE1 was upregulated and ACE2 was downregulated in bleomycin-induced lung fibrosis [55].

Cardiomyocytes were treated with actinomycin D, a transcription inhibitor, to elucidate the mechanisms underlying Hdac8 overexpression-mediated upregulation of Ace1 and Rela, downregulation of Ace2 and Nfkbia, and regulation of inflammation and fibrosis. Actinomycin D mitigated Hdac8 overexpression-induced upregulation of Ace1 and Rela. This indicated that Hdac8 upregulated the expression levels of Ace1 and Rela at the transcript level (Supplementary Figure 7).

5. Conclusions

This study demonstrated that the HDAC8 selective inhibitor PCI34051 alleviated cardiac hypertrophy, pulmonary congestion, inflammation, and fibrosis, which resulted in

improved cardiac functions in the pressure overload-induced heart failure mouse model. Among class I HDACs, only Hdac8 was upregulated in the cardiac and pulmonary tissues of the heart failure mouse model. Additionally, this study demonstrated that Hdac8 and Ace1 are involved in the proinflammatory Rela pathway and the fibrosis-related TGF-β1-Smad2/3 pathway. Thus, HDAC8 is a potential novel therapeutic target for heart failure.

6. Limitations of the Study

Here, we showed that the selective HDAC8 inhibitor PCI34051 alleviated heart failure. However, the inhibitory effects of PCI34051 on other types of HDACs cannot be ruled out. Therefore, future studies must confirm the therapeutic effects of PCI34051 on heart failure using the *Hdac8* knockout mouse model. Additionally, we used the cardiomyocyte cell line to determine the effects of Hdac8 or Ace1 overexpression on the expression of inflammation-related genes. HDAC8 regulates cardiac hypertrophy through the AKT/GSK3β pathway, which was not investigated in this study. Furthermore, this study used the H9c2 cell line to investigate the mechanisms of TGF-β1-induced fibrosis. In contrast to primary cardiomyocytes, the H9c2 cells are not beating cells. However, the hypertrophic responses of H9c2 cells are similar to those of primary cardiomyocytes.

Data Availability

The data used to support the findings of this study are included within the supplementary information file.

Conflicts of Interest

All authors declare no conflicts of interest.

Authors' Contributions

TZ performed the experiments, including TAC surgery, echocardiography, qRT-PCR, western blotting, and histological analysis. HJK conceived and designed the study and prepared the manuscript. SJK and MHJ supplied the reagents and proofread the manuscript. All authors have read and approved the final manuscript.

Acknowledgments

This study was supported by the Basic Science Research Program through the National Research Foundation of Korea (NRF) funded by the Ministry of Education (NRF-2021R1I1A3045431).

Supplementary Materials

Supplementary Figure 1: echocardiography parameters in mice at week 6 posttransverse aortic constriction (TAC). (A) Echocardiography parameters in mice belonging to the sham and TAC groups at week 6 post-TAC. Quantification of (A) left ventricular internal diameter end-systole (LVIDs, mm), (B) left ventricular internal diameter end-diastole (LVIDd, mm), (C) interventricular septum (IVSd, mm), (D) left ventricular posterior wall thickness (LVPWd, mm), (E) fractional shortening (FS, %), and (F) ejection fraction (EF, %), ($n = 5$–6). Data are presented as mean ± standard error and analyzed using one-way analysis of variance, followed by Bonferroni post hoc test. Supplementary Figure 2: cardiac and pulmonary mRNA expression levels of class I histone deacetylases (HDACs) in transverse aortic constriction (TAC) mice. The cardiac (A–C) and pulmonary (D–F) mRNA levels of *Hdac1*, *Hdac2*, and *Hdac3* in the sham, TAC, and TAC+PCI34051 (3, 10, or 30 mg/kg bodyweight/day) groups were examined using quantitative real-time polymerase chain reaction. The expression levels of target genes were normalized to those of *Gapdh*. Data are presented as mean ± standard error and analyzed using one-way analysis of variance, followed by Bonferroni post hoc test. Supplementary Figure 3: Ace1 knockdown downregulates the expression of fibrosis-related genes in primary rat cardiac fibroblasts. (A–E) Rat cardiac fibroblasts transfected with control or short-interfering RNAs against *Ace1* (si-Ace1) were incubated with TGF-β1. The mRNA levels of *Ace1*, *Hdac8*, *Fn1*, *Acta2*, and *Tgfb1* were determined using quantitative real-time polymerase chain reaction. (F–L) Representative blots and quantification of Ace1, Hdac8, Fn1, Acta2, Tgfb1, p-Smad2/3, and Smad2/3 levels in the cardiac tissues. Actb was used as a loading control. Data are presented as mean ± standard error and analyzed using one-way analysis of variance, followed by Bonferroni post hoc test. Supplementary Figure 4: Hdac8 knockdown regulates Ace1 and Ace2 mRNA levels in isoproterenol-treated H9c2 cells. (A, B) H9c2 cells transfected with control or short-interfering RNAs against *Hdac8* (si-Hdac8) were incubated with isoproterenol. The mRNA levels of *Ace1* and *Ace2* were determined using quantitative real-time polymerase chain reaction. The expression levels of target genes were normalized to those of *Gapdh*. Data are presented as mean ± standard error and analyzed using one-way analysis of variance, followed by Bonferroni *post hoc* test. Supplementary Figure 5: Hdac8 overexpression upregulates Agtr1 and downregulates Agtr2 in H9c2 cells. (A, B) H9c2 cells were transfected with an empty vector or a *pCMV-Hdac8* construct. The mRNA levels of *Agtr1* and *Agtr2* were determined using quantitative real-time polymerase chain reaction. Supplementary Figure 6: PCI34051 treatment or Hdac8 and Ace1 knockdown did not affect the expression of Rela and Nfkbia in rat cardiac fibroblasts. (A–B) Rat cardiac fibroblasts were treated with vehicle or PCI34051 in the presence or absence of TGF-β1. The mRNA levels of *Rela* and *Nfkbia* were determined using quantitative real-time polymerase chain reaction (qRT-PCR). (C–D) Rat cardiac fibroblasts transfected with control or short-interfering RNAs against *Hdac8* (si-Hdac8) were treated with TGF-β1. The mRNA levels of *Rela* and *Nfkbia* were determined using qRT-PCR. (E–F) Rat cardiac fibroblasts transfected with control or si-Ace1 were treated with TGF-β1. The mRNA levels of *Rela* and *Nfkbia* were determined using qRT-PCR. Data are presented as the mean ± standard error and analyzed using one-way analysis of variance, followed by Bonferroni *post hoc* test. Supplementary Figure 7: Hdac8 upregulated the expression of Ace1 and Rela at the transcript level. (A–E) H9c2 cells transfected with vector

or *pCMV-Hdac8* were treated with actinomycin D (2.5 μg/mL) for 6 h. The mRNA levels of *Hdac8*, *Ace1*, *Ace2*, *Rela*, and *Nfkbia* were determined using quantitative real-time polymerase chain reaction. Data are presented as mean ± standard error and analyzed using one-way analysis of variance, followed by Bonferroni *post hoc* test. Supplementary Table 1: primers for the RT-PCR. *(Supplementary Materials)*

References

[1] J. Schaper, S. Kostin, S. Hein, A. Elsässer, E. Arnon, and R. Zimmermann, "Structural remodelling in heart failure," *Experimental and Clinical Cardiology*, vol. 7, no. 2-3, pp. 64–68, 2002.

[2] R. A. Carels, "The association between disease severity, functional status, depression and daily quality of life in congestive heart failure patients," *Quality of Life Research*, vol. 13, no. 1, pp. 63–72, 2004.

[3] G. Savarese and L. H. Lund, "Global public health burden of heart failure," *Cardiac Failure Review*, vol. 3, no. 1, pp. 7–11, 2017.

[4] A. Groenewegen, F. H. Rutten, A. Mosterd, and A. W. Hoes, "Epidemiology of heart failure," *European Journal of Heart Failure*, vol. 22, no. 8, pp. 1342–1356, 2020.

[5] Y. Guo, G. Y. Lip, and A. Banerjee, "Heart failure in East Asia," *Current Cardiology Reviews*, vol. 9, no. 2, pp. 112–122, 2013.

[6] G. Torre-Amione, S. Kapadia, C. Benedict, H. Oral, J. B. Young, and D. L. Mann, "Proinflammatory cytokine levels in patients with depressed left ventricular ejection fraction: a report from the Studies of Left Ventricular Dysfunction (SOLVD)," *Journal of the American College of Cardiology*, vol. 27, no. 5, pp. 1201–1206, 1996.

[7] L. Gullestad, T. Ueland, L. E. Vinge, A. Finsen, A. Yndestad, and P. Aukrust, "Inflammatory cytokines in heart failure: mediators and markers," *Cardiology*, vol. 122, no. 1, pp. 23–35, 2012.

[8] M. Kallikourdis, E. Martini, P. Carullo et al., "T cell costimulation blockade blunts pressure overload-induced heart failure," *Nature Communications*, vol. 8, no. 1, article 14680, 2017.

[9] J. Hartupee and D. L. Mann, "Neurohormonal activation in heart failure with reduced ejection fraction," *Nature Reviews Cardiology*, vol. 14, no. 1, pp. 30–38, 2017.

[10] C. F. Notarius, P. J. Millar, and J. S. Floras, "Muscle sympathetic activity in resting and exercising humans with and without heart failure," *Applied Physiology, Nutrition, and Metabolism*, vol. 40, no. 11, pp. 1107–1115, 2015.

[11] W. C. de Mello and A. H. Danser, "Angiotensin II and the Heart," *Hypertension*, vol. 35, no. 6, pp. 1183–1188, 2000.

[12] S. Keidar, M. Kaplan, and A. Gamliellazarovich, "ACE2 of the heart: from angiotensin I to angiotensin (1-7)," *Cardiovascular Research*, vol. 73, no. 3, pp. 463–469, 2007.

[13] V. B. Patel, J. C. Zhong, M. B. Grant, and G. Y. Oudit, "Role of the ACE2/angiotensin 1-7 axis of the renin-angiotensin system in heart failure," *Circulation Research*, vol. 118, no. 8, pp. 1313–1326, 2016.

[14] K. Kuba, Y. Imai, and J. Penninger, "Angiotensin-converting enzyme 2 in lung diseases," *Current Opinion in Pharmacology*, vol. 6, no. 3, pp. 271–276, 2006.

[15] Y. Imai, K. Kuba, S. Rao et al., "Angiotensin-converting enzyme 2 protects from severe acute lung failure," *Nature*, vol. 436, no. 7047, pp. 112–116, 2005.

[16] G. Oudit, Z. Kassiri, M. Patel et al., "Angiotensin II-mediated oxidative stress and inflammation mediate the age-dependent cardiomyopathy in ACE2 null mice," *Cardiovascular Research*, vol. 75, no. 1, pp. 29–39, 2007.

[17] H. D. Xiao, S. Fuchs, D. J. Campbell et al., "Mice with cardiac-restricted angiotensin-converting enzyme (ACE) have atrial enlargement, cardiac arrhythmia, and sudden death," *The American Journal of Pathology*, vol. 165, no. 3, pp. 1019–1032, 2004.

[18] H. J. Kim, S. H. Jo, M. H. Lee, W. W. Seo, J. O. Choi, and K. H. Ryu, "Effect of prescribing patterns of renin-angiotensin system blockers and beta-blockers on prognosis of heart failure," *Advances in Therapy*, vol. 37, no. 9, pp. 3839–3849, 2020.

[19] H. Burnett, A. Earley, A. A. Voors et al., "Thirty years of evidence on the efficacy of drug treatments for chronic heart failure with reduced ejection fraction: a network meta-analysis," *Circulation: Heart Failure*, vol. 10, no. 1, 2017.

[20] C. M. Trivedi, Y. Luo, Z. Yin et al., "Hdac2 regulates the cardiac hypertrophic response by modulating Gsk3β activity," *Nature Medicine*, vol. 13, no. 3, pp. 324–331, 2007.

[21] H. J. Kee, G. H. Eom, H. Joung et al., "Activation of histone deacetylase 2 by inducible heat shock protein 70 in cardiac hypertrophy," *Circulation Research*, vol. 103, no. 11, pp. 1259–1269, 2008.

[22] G. H. Eom, Y. K. Cho, J. H. Ko et al., "Casein Kinase-2α1 induces hypertrophic response by phosphorylation of histone deacetylase 2 S394 and its activation in the heart," *Circulation*, vol. 123, no. 21, pp. 2392–2403, 2011.

[23] H. J. Kee, I. S. Sohn, K. I. Nam et al., "Inhibition of histone deacetylation blocks cardiac hypertrophy induced by angiotensin II infusion and aortic banding," *Circulation*, vol. 113, no. 1, pp. 51–59, 2006.

[24] D. J. Cao, Z. V. Wang, P. K. Battiprolu et al., "Histone deacetylase (HDAC) inhibitors attenuate cardiac hypertrophy by suppressing autophagy," *Proceedings of the National Academy of Sciences of the United States of America*, vol. 108, no. 10, pp. 4123–4128, 2011.

[25] Y. Kong, P. Tannous, G. Lu et al., "Suppression of class I and II histone deacetylases blunts pressure-overload cardiac hypertrophy," *Circulation*, vol. 113, no. 22, pp. 2579–2588, 2006.

[26] C. M. Trivedi, M. M. Lu, Q. Wang, and J. A. Epstein, "Transgenic Overexpression of Hdac3 in the Heart Produces Increased Postnatal Cardiac Myocyte Proliferation but Does Not Induce Hypertrophy∗," *The Journal of Biological Chemistry*, vol. 283, no. 39, pp. 26484–26489, 2008.

[27] H. J. Kee, Y. Ryu, Y. M. Seok et al., "Selective inhibition of histone deacetylase 8 improves vascular hypertrophy, relaxation, and inflammation in angiotensin II hypertensive mice," *Clinical Hypertension*, vol. 25, no. 1, p. 13, 2019.

[28] T. Zhao, H. J. Kee, L. Bai, M. K. Kim, S. J. Kee, and M. H. Jeong, "Selective HDAC8 inhibition attenuates isoproterenol-induced cardiac hypertrophy and fibrosis via p38 MAPK pathway," *Frontiers in Pharmacology*, vol. 12, article 677757, 2021.

[29] M. Yan, C. Chen, W. Gong et al., "miR-21-3p regulates cardiac hypertrophic response by targeting histone deacetylase-8," *Cardiovascular Research*, vol. 105, no. 3, pp. 340–352, 2015.

[30] S. Chang, T. A. McKinsey, C. L. Zhang, J. A. Richardson, J. A. Hill, and E. N. Olson, "Histone deacetylases 5 and 9 govern responsiveness of the heart to a subset of stress signals and play redundant roles in heart development," *Molecular and Cellular Biology*, vol. 24, no. 19, pp. 8467–8476, 2004.

[31] Y. Ryu, L. Jin, H. J. Kee et al., "Gallic acid prevents isoproterenol-induced cardiac hypertrophy and fibrosis through regulation of JNK2 signaling and Smad3 binding activity," *Scientific Reports*, vol. 6, no. 1, article 34790, 2016.

[32] L. Jin, S. Sun, Y. Ryu et al., "Gallic acid improves cardiac dysfunction and fibrosis in pressure overload- induced heart failure," *Scientific Reports*, vol. 8, no. 1, p. 9302, 2018.

[33] T. Kahan and L. Bergfeldt, "Left ventricular hypertrophy in hypertension: its arrhythmogenic potential," *Heart*, vol. 91, no. 2, pp. 250–256, 2005.

[34] N. Frey, H. A. Katus, E. N. Olson, and J. A. Hill, "Hypertrophy of the Heart," *Circulation*, vol. 109, no. 13, pp. 1580–1589, 2004.

[35] A. F. Lee, R. J. MacFadyen, and A. D. Struthers, "Neurohormonal reactivation in heart failure patients on chronic ACE inhibitor therapy: a longitudinal study," *European Journal of Heart Failure*, vol. 1, no. 4, pp. 401–406, 1999.

[36] A. P. Bolger, R. Sharma, W. Li et al., "Neurohormonal activation and the chronic heart failure syndrome in adults with congenital heart disease," *Circulation*, vol. 106, no. 1, pp. 92–99, 2002.

[37] S. A. Dick and S. Epelman, "Chronic heart failure and Inflammation," *Circulation Research*, vol. 119, no. 1, pp. 159–176, 2016.

[38] A. Gonzalez, E. B. Schelbert, J. Diez, and J. Butler, "Myocardial interstitial fibrosis in heart failure: biological and translational perspectives," *Journal of the American College of Cardiology*, vol. 71, no. 15, pp. 1696–1706, 2018.

[39] K. L. Walton, K. E. Johnson, and C. A. Harrison, "Targeting TGF-β mediated SMAD signaling for the prevention of fibrosis," *Frontiers in Pharmacology*, vol. 8, p. 461, 2017.

[40] Y. Chen, H. Guo, D. Xu et al., "Left ventricular failure produces profound lung remodeling and pulmonary hypertension in mice: heart failure causes severe lung disease," *Hypertension*, vol. 59, no. 6, pp. 1170–1178, 2012.

[41] D. Fan, A. Takawale, J. Lee, and Z. Kassiri, "Cardiac fibroblasts, fibrosis and extracellular matrix remodeling in heart disease," *Fibrogenesis & Tissue Repair*, vol. 5, no. 1, p. 15, 2012.

[42] C. Humeres and N. G. Frangogiannis, "Fibroblasts in the infarcted, remodeling, and failing heart," *JACC: Basic to Translational Science*, vol. 4, no. 3, pp. 449–467, 2019.

[43] T. Liu, L. Zhang, D. Joo, and S. C. Sun, "NF-κB signaling in inflammation," *Signal Transduction and Targeted Therapy*, vol. 2, no. 1, 2017.

[44] T. Unger and J. Li, "The role of the renin-angiotensin-aldosterone system in heart failure," *Journal of the Renin-Angiotensin-Aldosterone System*, vol. 5, no. 1, pp. S7–10, 2004.

[45] T. R. Rodrigues Prestes, N. P. Rocha, A. S. Miranda, A. L. Teixeira, and A. C. Simoes-E-Silva, "The anti-inflammatory potential of ACE2/angiotensin-(1-7)/mas receptor axis: evidence from basic and clinical research," *Current Drug Targets*, vol. 18, no. 11, pp. 1301–1313, 2017.

[46] R. R. Gaddam, S. Chambers, and M. Bhatia, "ACE and ACE2 in inflammation: a tale of two enzymes," *Inflammation & Allergy Drug Targets*, vol. 13, no. 4, pp. 224–234, 2014.

[47] C. Riehle and J. Bauersachs, "Small animal models of heart failure," *Cardiovascular Research*, vol. 115, no. 13, pp. 1838–1849, 2019.

[48] S. Yoon, M. Kim, H. K. Min et al., "Inhibition of heat shock protein 70 blocks the development of cardiac hypertrophy by modulating the phosphorylation of histone deacetylase 2," *Cardiovascular Research*, vol. 115, no. 13, pp. 1850–1860, 2019.

[49] S. Yoon, T. G. Lee, M. H. Choi et al., "Glucose-regulated protein 78 binds to and regulates the melanocortin-4 receptor," *Experimental & Molecular Medicine*, vol. 50, no. 9, pp. 1–14, 2018.

[50] R. F. Li, S. S. Cao, W. J. Fang et al., "Roles of HDAC2 and HDAC8 in cardiac remodeling in renovascular hypertensive rats and the effects of valproic acid sodium," *Pharmacology*, vol. 99, no. 1-2, pp. 27–39, 2017.

[51] P. Chelladurai, S. Dabral, S. R. Basineni et al., "Isoform-specific characterization of class I histone deacetylases and their therapeutic modulation in pulmonary hypertension," *Scientific Reports*, vol. 10, no. 1, p. 12864, 2020.

[52] M. Zhang, X. Yang, R. J. Zimmerman et al., "CaMKII exacerbates heart failure progression by activating class I HDACs," *Journal of Molecular and Cellular Cardiology*, vol. 149, pp. 73–81, 2020.

[53] F. L. Lin, J. L. Yen, Y. C. Kuo et al., "HADC8 inhibitor WK2-16 therapeutically targets lipopolysaccharide-induced mouse model of neuroinflammation and microglial activation," *International Journal of Molecular Sciences*, vol. 20, no. 2, 2019.

[54] J. Niu and P. E. Kolattukudy, "Role of MCP-1 in cardiovascular disease: molecular mechanisms and clinical implications," *Clinical Science*, vol. 117, no. 3, pp. 95–109, 2009.

[55] M. Shao, Z. B. Wen, H. H. Yang et al., "Exogenous angiotensin (1-7) directly inhibits epithelial-mesenchymal transformation induced by transforming growth factor-β1 in alveolar epithelial cells," *Biomedicine & Pharmacotherapy*, vol. 117, article 109193, 2019.

Hindawi
Oxidative Medicine and Cellular Longevity
Volume 2022, Article ID 7502632, 17 pages
https://doi.org/10.1155/2022/7502632

Research Article

miR-154-5p Affects the TGFβ1/Smad3 Pathway on the Fibrosis of Diabetic Kidney Disease via Binding E3 Ubiquitin Ligase Smurf1

Che Bian,[1] **Zhilin Luan**,[2] **Haibo Zhang**,[2] **Ruijing Zhang**,[2] **Jing Gao**,[3] **Yuxia Wang**,[1] **Jia Li**,[1] **and Huiwen Ren**[2]

[1]*Department of Endocrinology and Metabolism, The Fourth Affiliated Hospital of China Medical University, Shenyang, China*
[2]*Advanced Institute for Medical Sciences, Dalian Medical University, Dalian, Liaoning, China*
[3]*Department of Gerontology, Xin Hua Hospital, Shanghai Jiaotong University School of Medicine, Shanghai, China*

Correspondence should be addressed to Huiwen Ren; rhwcmu@163.com

Received 22 October 2021; Revised 20 December 2021; Accepted 3 January 2022; Published 27 January 2022

Academic Editor: Yingqing Chen

Aim. The study is aimed at verifying miR-154-5p and Smurf1 combination in glomerular mesangial cells regulating TGFβ1/Smad3 pathway-related protein ubiquitination in the model of diabetic rats renal tissues, primary mesangial cells, and cell lines. *Methods.* The diabetic SD rat model and high-glucose-cultured primary mesangial cells and cell lines were established. miR-154-5p mimic and inhibitor, Smurf1 siRNA, and TGF β 1/Smad3 inhibitor (SB431542) were pretreated to make the TGFβ1/Smad3 pathway and ubiquitin changes. Fluorescence in situ hybridization was used for the miR-154-5p renal localization; molecular biological detection was adopted for cell proliferation, renal function, urine protein, and pathway proteins. After bioinformatics predicted binding sites, luciferase and Co-IP were used to detect miRNA and protein binding. *Results.* miR-154-5p was significantly increased and mainly concentrated in the glomerular of renal cortex in well-established diabetic rat renal tissues. Rno-miR-154-5p combined Rno-Smurf1 3′ UTR, while Smurf1 combined Smad3 directly. Meanwhile, miR-154-5p regulates TGFβ1/Smad3-mediated cell proliferation via Smurf1 ubiquitination. *Conclusion.* miR-154-5p regulates the TGFβ1/Smads pathway through Smurf1 ubiquitination and promotes the fibrosis process of diabetic kidney disease.

1. Introduction

Diabetic kidney disease (DKD), formerly known as diabetic nephropathy (DN), is one of the most common chronic microvascular complications of diabetes mellitus, leading to end-stage renal disease (ESRD) [1], involving various renal sections mainly of glomerulus [2], and regarding urinary albumin to creatinine ratio (UACR) as one of the effective noninvasive detection methods [3–5]. The TGFβ1/Smads pathway is a classic DKD way to regulate the proliferation and fibrosis of mesangial cells [6, 7]. MicroRNA (miRNA) is a kind of noncoding RNA with the length of 18-25 highly conserved nucleic acids of which miR-154 is located in the miRNA-rich region of the 14q32 single-stranded chromosome in mammals [8], with one of the mature, miR-154-5p, indicating significant correlation with urine protein and fibrotic factors of diabetic patients in our previous studies [9, 10]. However, the specific mechanism of miR-154-5p regulating DKD has not been studied. Therefore, the purpose of this study is to detect the expression of miR-154-5p in various models *in vitro and in vivo* on the basis of the successful establishment of diabetic rat model in previous studies [11, 12], and to explore the specific molecular mechanism of miR-154-5p regulating DKD in glomerular mesangial cells through bioinformatics prediction and verification.

2. Materials and Methods

2.1. Reagents. All the reagents were listed in Table 1. The siRNAs targeting Smurf1, miR-154-5p mimics, inhibitors, and plasmid vectors using psiCHECK 2.0 Vector System for the construction of target gene 3′ UTR, as well as their corresponding negative controls, were designed and

Table 1: Information of reagents.

Names	Information
Treatment	
Rno-miR-154-5p mimic forward	5′ - UAG GUU AUC CGU GUU GCC UUC G -3′, GenePharma
Rno-miR-154-5p mimic reverse	5′ - AAG GCA ACA CGG AUA ACC UAU U -3′, GenePharma
Rno-miR-154-5p inhibitor	5′ - CGA AGG CAA CAC GGA UAA CCU A -3′, GenePharma
Rno-miR-negative control	5′ - CAG UAC UUU UGU GUA GUA CAA -3′, GenePharma
Smurf1 siRNA forward sequence	5′ - CAU AUC GCC AGA UCA UGA ATT -3′, GenePharma
Smurf1 siRNA reverse sequence	5′ - UUC AUG AUC UGG CGA UAU GTT -3′, GenePharma
Negative control siRNA forward	5′ - UUC UCC GAA CGU GUC ACG UTT -3′, GenePharma
Negative control siRNA reverse	5′ - ACG UGA CAC GUU CGG AGA ATT -3′, GenePharma
TGFβ1/Smad3 inhibitor, SB431542	#14775, 10 nM for 24 h, dissolved in DMSO, Cell Signaling Technology
Detection	
Rno-miR-154-5p probe	5′-FAM-CGA AGG CAA CAC GGA TAA CCT A-FAM-3′ for FISH, GenePharma
Rno-miR-154-5p primer forward	5′ - CTG CCG TAG GTT ATC CGT G -3′, GenePharma
Rno-miR-154-5p primer reverse	5′ - AGA GCA GGG TCC GAG GAT -3′, GenePharma
U6 primer forward	5′ - CTC GCT TCG GCA GCA CA -3′, GenePharma
U6 primer reverse	5′ - AAC GCT TCA CGA ATT TGC GT -3′, GenePharma
TGFβ1 primary antibody	Rabbit monoclonal antibody, ab215715, 44 kDa, 1 : 1000 for WB. Abcam
Smad3 primary antibody	Rabbit antibody, #9523, 52 kDa, 1 : 1000 for WB, 1 : 100 for IP, Cell Signaling Technology
pSmad3 primary antibody	Rabbit antibody, #9520, 52 kDa, 1 : 1000 for WB, Cell Signaling Technology
Smurf1 primary antibody	Mouse monoclonal antibody, sc-100616, 86 kDa, 1 : 200 for WB, 2 μg/100 μg total protein for IP, Santa Cruz Biotechnology
Ubiquitin primary antibody	Rabbit antibody, #3933, full bands, 1 : 1000 for WB, Cell Signaling Technology
β-Actin primary antibody	Rabbit antibody, #4970, 45 kDa, 1 : 1000 for WB, Cell Signaling Technology
IgG primary antibody	Rabbit antibody isotype control, #3900, for IP, Cell Signaling Technology
IgG primary antibody	Mouse antibody isotype control, #5415, for IP, Cell Signaling Technology
DAPI	For nucleus, #4083, for IF, Cell Signaling Technology
Anti-rabbit IgG	Anti-rabbit, #3678, for WB, Cell Signaling Technology
Anti-mouse IgG-HRP secondary antibody	Anti-mouse, #7076, for WB, Cell Signaling Technology
Anti-rabbit IgG-HRP secondary antibody	Anti-rabbit, #7074, for WB, Cell Signaling Technology

synthesized by GenePharma, Shanghai, China. These reagents were transfected into cells using Lipofectamine™ 2000 Transfection Reagent (Invitrogen, USA) according to the manufacturer's instructions. The TGF β 1/Smad3 pathway inhibitor, SB431542 (#14775, 10 nmol/l) was used to pretreat target cells as described in previous studies [13]. After the transfection and pretreatment, cells were collected and stored in liquid nitrogen for the follow-up experiments.

2.2. Animal Modeling. Sprague-Dawley (SD) rats (SPF grade, 7 weeks old, 180-220 g, purchased from Beijing Vital River Laboratory Animal Technology Co., Ltd.), were fed with free water and food at a constant temperature (23 ± 2°C) and humidity (50-60%), with a day/night cycle of 12/12 h. The experiments were conducted from 9:00 a.m. to 11:00 a.m. daily to prevent circadian rhythm from influencing the results. All experimental protocols for animals have been approved by the Institutional Animal Care and Use Committee (IACUC) of China Medical University (Approval No. 2021115).

Rats were randomly assigned after one week adaptive feeding as the diabetic nephropathy group (DN, $n = 10$ rats): fed with continuous high-fat diet (D12492, energy ratios of fat, carbohydrate, and protein as 60 : 20 : 20 kcal%, total energy of 5.24 kcal/gm, Research Diets, USA) and multiple injections with a low dose of streptozotocin (STZ, 35 mg/kg, cold 0.1 m sodium citrate buffer pH 4.5, S0130, Sigma-Aldrich, USA) after 8 weeks high-fat diet induction and the normal control group (NC, $n = 10$ rats): fed with control diet (D12450J, energy ratios of fat, carbohydrate, and protein as 10 : 20 : 20 kcal%, total energy of 3.85 kcal/gm, Research Diets, USA) and multiple injections with sodium citrate buffer as placebo. The specific modeling methods refer to our previous studies [11, 12].

2.3. Biochemical Detection. The intraperitoneal glucose tolerance test (IPGTT) and insulin release test (IRT) were performed for the detection of rat blood glucose and insulin levels. After 12-16 h starvation, rats were intraperitoneally injected with 2 g/kg glucose, and blood glucose testing strips

(OneTouch® Ultra, LIFESCAN, USA) were used for the detection of rat blood samples at 0, 5, 10, 30, 60, and 120 min, respectively. The enzyme-linked immunosorbent assay (ELISA) was used to measure rat insulin levels with the rat insulin ELISA kit (INS, CSB-E05070r, CUSABIO, USA). Homeostatic model of insulin resistance index (HOMA-IR) and insulin sensitivity index (ISI) were used to evaluate the insulin resistance and sensitivity, and GraphPad software was used to calculate the area under curve of glucose and insulin. When the metabolic cages were conducted, urine samples were collected and levels of urinary albumin with the rat microalbuminuria ELISA kit (MAU/ALB, CSB-E12991r, CUSABIO, USA) were detected. Chemiluminescence was used to detect creatinine (Cr) and blood urea nitrogen (BUN). Urinary albumin/creatine ratio (UACR, MAU/Cr ratio) is used for the detection of urinary protein.

2.4. Glomerular Isolation and Primary Mesangial Cell Culturing. Rat glomerulars were isolated from 2-3 rat renal tissues by dissecting renal cortex and medulla, digested with collagenase IV, subjected to serial sieving by cell strainer (70 and 100 μ m, BD Falcon), and rinsed with Hanks' balanced salt solution (Thermo Scientific™). Then, the glomerular was cultured with 10% FBS DMEM (Gibco™) supplemented with 100 U/ml penicillin-0.1 mg/ml streptomycin (Gibco™) or stored for subsequent experiments. Primary mesangial cells (PMCs) climbed out of the glomerular after 2-3 days of culturing and were first passaged after 5-7 days and then were cultured with the normal culturing process. Cells in their 3rd to 4th generation at a ratio of 2×10^5 viable cells/well in 6-well culture plates were used for subsequent experiments [14].

2.5. Primary Proximal Tubular Epithelial Cell Culturing. Mouse primary proximal tubular epithelial cells (PPTCs) were extracted from renal tissues of 4-6 mice by dissecting renal cortex as well as inner and outer medulla according to the previous literature [15]. Then, the cortex and outer medulla were digested with collagenase IV, subjected to serial sieving by cell strainer (40 μ m, BD Falcon), rinsed with Hanks' balanced salt solution (Thermo Scientific™), layered with Percoll® (Sigma-Aldrich), and cultured with 10% FBS DMEM/F12 (Gibco™) supplemented with insulin-transferrin-sodium selenite media supplement (Sigma-Aldrich), 1 mM hydrocortisone (MedChemExpress®), 50 mM vitamin C (MedChemExpress®), and 100 U/ml penicillin-0.1 mg/ml streptomycin (Gibco™). Cells at a ratio of 2×10^5 viable cells/well in 6-well culture plates were used for subsequent experiments.

2.6. Cell Line Culturing and Treatment. Rat mesangial cells (RMCs, CRL-2573™) and 293T cells (293T/17 or HEK 293T/17, CRL-1126™) were purchased from American Type Culture Collection (ATCC®) and cultured with Dulbecco's modified Eagle's medium (DMEM) containing 10% fetal bovine serum (FBS, North American Source, Gibco) at 37°C with saturated humidity in 5% CO_2 atmosphere. Cells in their 5th to 9th generation of logarithmic growth phase were inoculated into 25 cm^2 culture flasks at a ratio of 1×10^6/flask or 6-well tissue culture plates of 5×10^5/well. After synchronization via starvation in Opti-MEM (Gibco, USA) for 24 h and confluency reached 70-80%, cells were cultured with normal glucose (NG, 5.5 mmol/l D-glucose), high mannitol (HM, 5.5 mmol/l D-glucose and 24.5 mmol/l mannitol), and high glucose (HG, 30 mmol/l D-glucose), respectively, for 24 h and were collected and stored at -196°C for the follow-up experiments.

2.7. Luciferase Reporter Assay. After using 293T validation, RMCs were inoculated into 24-well plates of 5×10^5 cells/well beforehand and cotransfected with miR-154-5p mimic, inhibitor, pmirGLO-Smurf1-3′ UTR-WT or pmirGLO-Smurf1-3′ UTR-MUT reporter plasmids accordingly. After 24 h posttransfection, cells were lysed using passive lysis buffer (Promega) and the luciferase activity was measured with the Dual-Luciferase Reporter Assay System (Promega) and normalized to Renilla luciferase activity, respectively. Experiments were performed in triplicate.

2.8. Fluorescence In Situ Hybridization (FISH). FISH assays were performed using fluorescent in situ hybridization kit (Servicebio, China) according to the protocol. FAM-double-labeled miR-154-5p probe were designed and synthesized by Servicebio (China). Tissues were first fixed in 4% formaldehyde for 15 min, then permeabilized in PBS containing 0.5% Triton X-100 at 4°C for 30 min, and prehybridized at 37°C for 30 min in prehybridization solution. After that, probes were added in the hybridization solution and incubated with the tissue sections at 37°C overnight in the dark. The next day, the tissue sections were counterstained with DAPI for nuclear and imaged and then measured by a digital microscope application, CaseViewer (3DHISTECH Ltd.), for supporting histopathological diagnostic workflow and the microscope examination process in bioscience.

2.9. miRNA Real-Time PCR Assay. The miRcute miRNA Isolation Kit (DP501, Tiangen Biotech) was used for the isolation of miRNA and miRcute miRNA First-Strand cDNA Synthesis Kit (KR201, Tiangen Biotech) for the reverse transcription from miRNA into cDNA. The reverse transcriptional reaction process was 26°C for 20 min, 42°C for 40 min, and 85°C for 10 min holding. The miRcute miRNA qPCR Detection Kit (SYBR Green, FP401, Tiangen Biotech) was used to amplify the PCR reaction via Thermal Cycler Dice Real Time System (TaKaRa). The primer sequences of rno-miR-154-5p (designed and synthesized by GenePharma) were shown in Table 1. The PCR reaction system was 20 μl containing 2 μl cDNA with the response procedures: after initial degeneration at 95°C for 3 min, degeneration at 95°C for 12 s, annealing at 62°C for 40 s, and extension at 72°C for 30 s with 40 circles. The CT value was read for dissolution curve analysis with U6 snRNA (Tiangen Biotech) for internal standardization, while $2^{-\Delta\Delta CT}$ method was used to calculate the relative expression.

2.10. Co-immunoprecipitation. The EZ Magna RNA immunoprecipitation Kit (Millipore, USA) was used following the guidelines. Briefly, RMCs were lysed in RIP lysis buffer. Magnetic beads were preincubated with antibodies for 30 min at room temperature and the cell lysates were immunoprecipitated with beads for 6 h at 4°C. Then, protein was purified and detected by western blotting. Antibody information of Smurf1 and Smad3 is listed in Table 1.

2.11. Western Blotting. Protein samples were extracted with the lysis buffer containing the protease inhibitor, while total protein content was determined by the Pierce™ BCA Protein Assay Kit (Thermo Scientific™, USA). The SDS-PAGE electrophoresis was conducted after protein denaturation, and then, bands were transferred onto PVDF membranes according to a certain time. The membrane was blocked by 5% bovine serum albumin (BSA, Sigma Aldrich, USA) for 2 h and incubated with the corresponding concentration of primary antibodies (shown in Table 1) at 4°C overnight. After incubation of secondary antibodies at room temperature for 2 h, the Pierce™ ECL Western Blotting Substrate was used for membrane imaging via the imaging system (MicroChemi 4.2, Israel) with the detection of grey values by ImageJ 1.52i Java 1.8.0_172 (64-bit, National Institutes of Health, USA).

2.12. Cell Proliferation Assay. Cell samples were digested by trypsin and made into cell suspension. Appropriate cell density (5×10^3-2×10^4 cells/well) was inoculated on a 96-well plate for 24-72 h. Cell Counting Kit-8 (CCK-8, DOJINDO, Japan) Cell Proliferation and Cytotoxicity Assay Kit (Roche, USA) were used after cell adherence. CCK-8 detection solutions were added to 96-well plate for 2-4 h, while the absorbance of CCK-8 was read at 450 nm and 630 nm as reference by a full wavelength microarray (BioTek Power Wave XS).

2.13. Bioinformatics Analysis. Potential target mRNAs of miR-154-5p were predicted by the computer algorithm RNA22 V2 (https://cm.jefferson.edu/rna22/Interactive/). The mature miRNA sequences used by RNA22 V2 were downloaded from miRBase (http://www.mirbase.org/). Protein interaction analysis was performed using inBio_Map (v2016_09_12), IntAct Molecular Interaction Database, and STRING (version 11.0). All protein information was extracted from UniProtKB/Swiss-Prot database, and UbPred software was used to randomly predict the potential ubiquitination sites of proteins in the forest model. UbiBrowser and NetPath/NetSlim databases were used to verify ubiquitin ligase recognition characteristics and to locate known ubiquitin binding sites.

2.14. Statistical Analysis. The experiment was repeated more than three times under the same experimental conditions, and obtained data were statistically analyzed by SPSS 20.0 software. After testing each variable of normal distribution, normal distribution of measurement data was expressed with mean ± standard deviation ($\bar{x} \pm s$), while nonnormal distribution data with median (interquartile range). Students' t-test (between two groups) and one-way analysis of variance (ANOVA, among three or more groups) were used for the comparison followed by multiple comparison using the least square method t-test for homogeneity of variance and Tamhane's T2 test for heterogeneity of variance. $P < 0.05$ was considered of statistically significance with two tails.

3. Results

3.1. Changes of miR-154-5p and Pathway in Animal Models. We successfully established the diabetic rat model induced by high-fat diet and STZ based on previous studies. Physiological indexes indicated that the IPGTT overall level curve, HbA1c, area under curve of glucose, and HOMA-IR significantly increased, while the area under curve of insulin, area under curve of insulin/glucose ratio, and ISI significantly decreased, but the IRT curve does not appear to have an obvious peak in the DN group. In addition, DBP and SBP had no significant changes, excluding the influence of blood pressure. Renal function (BUN and Cr) and urinary protein (UACR) were significantly increased (Figure 1).

FISH results showed that the relative expression of miR-154-5p was significantly increased, and the localization of miR-154-5p was mainly concentrated in the renal cortex of well-established diabetic rat renal tissues. The enlarged graph showed that the expression of miR-154-5p was significantly enriched in the glomerular region (Figure 2(a)). To verify the results of the localization experiment, we performed fine anatomy of renal tissue. Real-time PCR results showed that the levels of the total renal tissues and cortex were significantly increased, while there were no significant changes in the inner and outer medulla (Figure 2(b)). The microdissection of the cortex and outer and inner medullary was seen in Figure 2(c). The results of the both experiments were consistent, indicating highly expression of miR-154-5p in the glomerulus. Moreover, pathway proteins (TGFβ1 and pSmad3/Smad3) were significantly increased in the diabetic renal tissues (Figure 2(d)).

3.2. Changes of miR-154-5p and Pathway in Primary Cell and Cell Lines. We successfully isolated rat glomerulus (Figure 3(a)), and on the basis of successful culturing PMCs and PPTCs (Figure 3(b)), it was found that the expression of miR-154-5p in PMCs was significantly increased under high-glucose culturing, while with no changes in PPTCs (Figure 3(c)). Further study on the expression of miR-154-5p showed that the relative expression of miR-154-5p in mesangial cell lines, RMCs, under high-glucose culturing also showed a time-dependent increase and tended to be stable after high-glucose culturing for 24 h (Figure 3(d)). Compared with the NG group, the area under curve of CCK-8 OD at 450 nm and the levels of fibrotic factors in the NG group were significantly increased (Figures 3(e) and 3(f)). In addition, there were no significant changes in the above results of the HM group, excluding the effect of osmotic pressure. TGFβ1 and pSmad3/Smad3 were both significantly increased in successfully established RMCs with a high-glucose culture (Figure 3(g)).

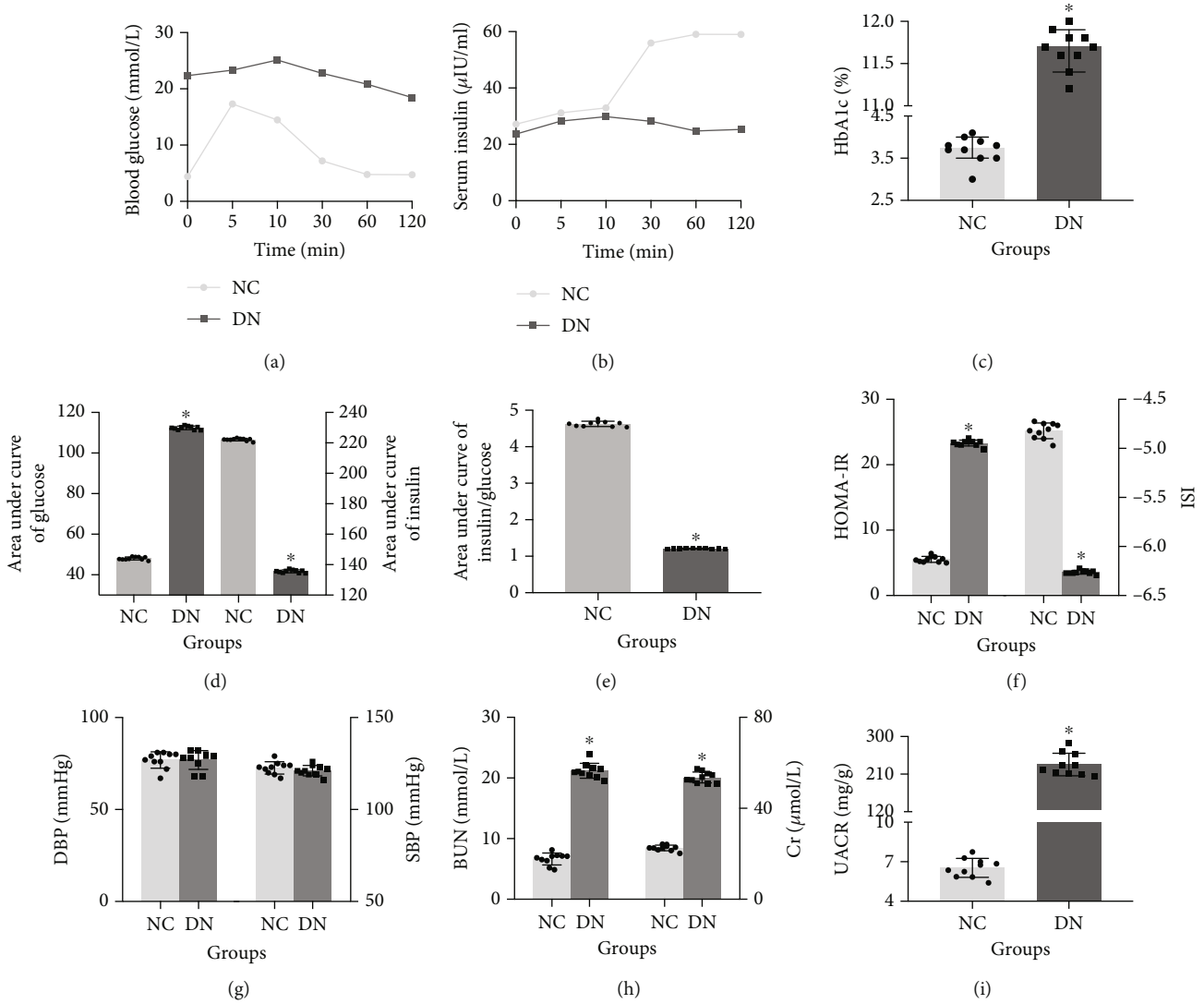

Figure 1: Physiological indexes in diabetic rats. Time-dependent curve in intraperitoneal glucose tolerance test (a) and insulin release test (b), HbA1c levels (c), area under curve of blood glucose (d left) and insulin (d right), area under curve ratio of insulin to blood glucose (e), HOMA-IR and ISI (f), DBP/SBP (g), renal function (h), and UACR (i). NC: normal control, DN: diabetic nephropathy. *vs. NC, $P < 0.05$. $n = 10$ rats/group.

3.3. The Role of miR-154-5p Regulating the TGFβ1/Smads Pathway. After the construction of the miR-154-5p mimic and inhibitor transfection, the expression of miR-154-5p proved that the transfection model was successfully constructed (Figure 4(a)). TGFβ1 and pSmad3/Smad3 were significantly increased, and CCK-8 showed abnormal proliferation in normal- and high-glucose-cultured RMCs with the miR-154-5p mimic treatment. On the contrary, TGFβ1 and pSmad3/Smad3 were significantly decreased in RMCs treated with the miR-154-5p inhibitor, and cell proliferation was decreased (Figures 4(b)–4(d)).

3.4. Verification of miR-154-5p Target Gene, Smurf1. To further investigate the function of miR-154-5p, we used the RNA22 V2 computer algorithm to predict the target genes of human and rat miR-154-5p, and the mature miRNA sequences were downloaded from miRBase. The results of bioinformatics analysis showed that there was a target gene, Smurf1, binding with miR-154-5p in humans and rats with multiple binding sites (Figure S1), suggesting that humans and rats had highly similar binding patterns. Changes of Smurf1 were observed in renal tissues of diabetic rats and in vitro models cultured with high glucose (Figures 5(a) and 5(b)). After that, miR-154-5p inhibitor, Smurf1 siRNA and TGFβ1/Smads pathway inhibitor were pretreated into RMCs cultured with high glucose, respectively. Levels of ubiquitin-related molecule, Smurf1, were significantly decreased in the Smurf1 siRNA group and significantly increased in the miR-154-5p inhibitor group. Smurf1 in the TGFβ1/Smads pathway inhibitor group was reduced compared with the miR-154-5p inhibitor group. The expression of TGFβ1 and pSmad3/Smad3 was significantly

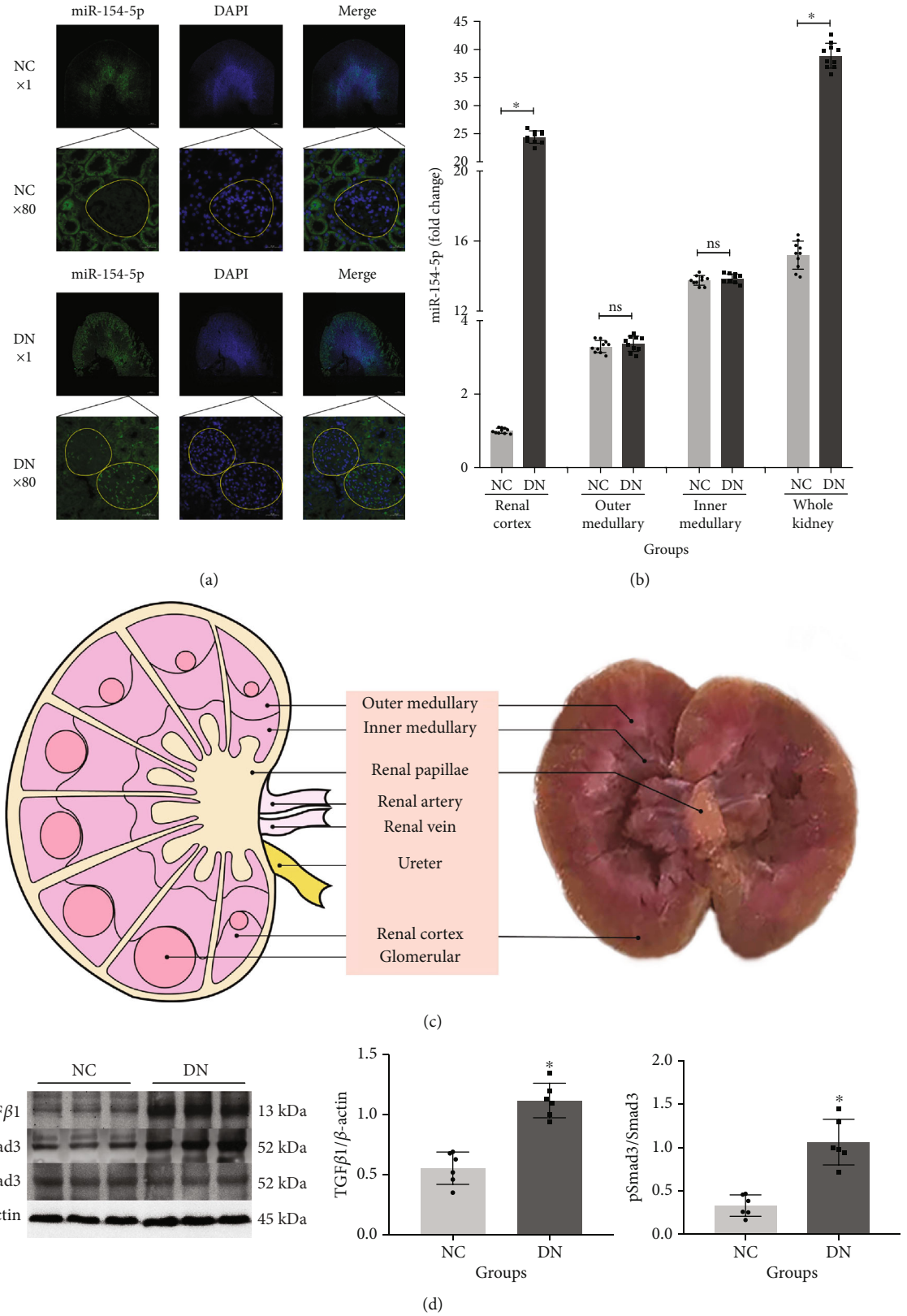

Figure 2: Expression of miR-154-5p in renal tissues. FISH detection for miR-154-5p localization in the kidney; significant enrichment of miR-154-5p in the cortical region of diabetic rats, in particular, glomerular (a). miR-154-5p in the cortex, outer medullary, inner medullary, and total kidney; homogenized semiquantified according to the NC group in the renal cortex (b). Microanatomy of the kidney (c). Protein levels in the whole kidney (d). NC: normal control; DN: diabetic nephropathy. Yellow circles indicate the glomerular. *vs. NC, $P < 0.05$; ns: vs. NC, $P > 0.05$. $n = 6$ samples/group.

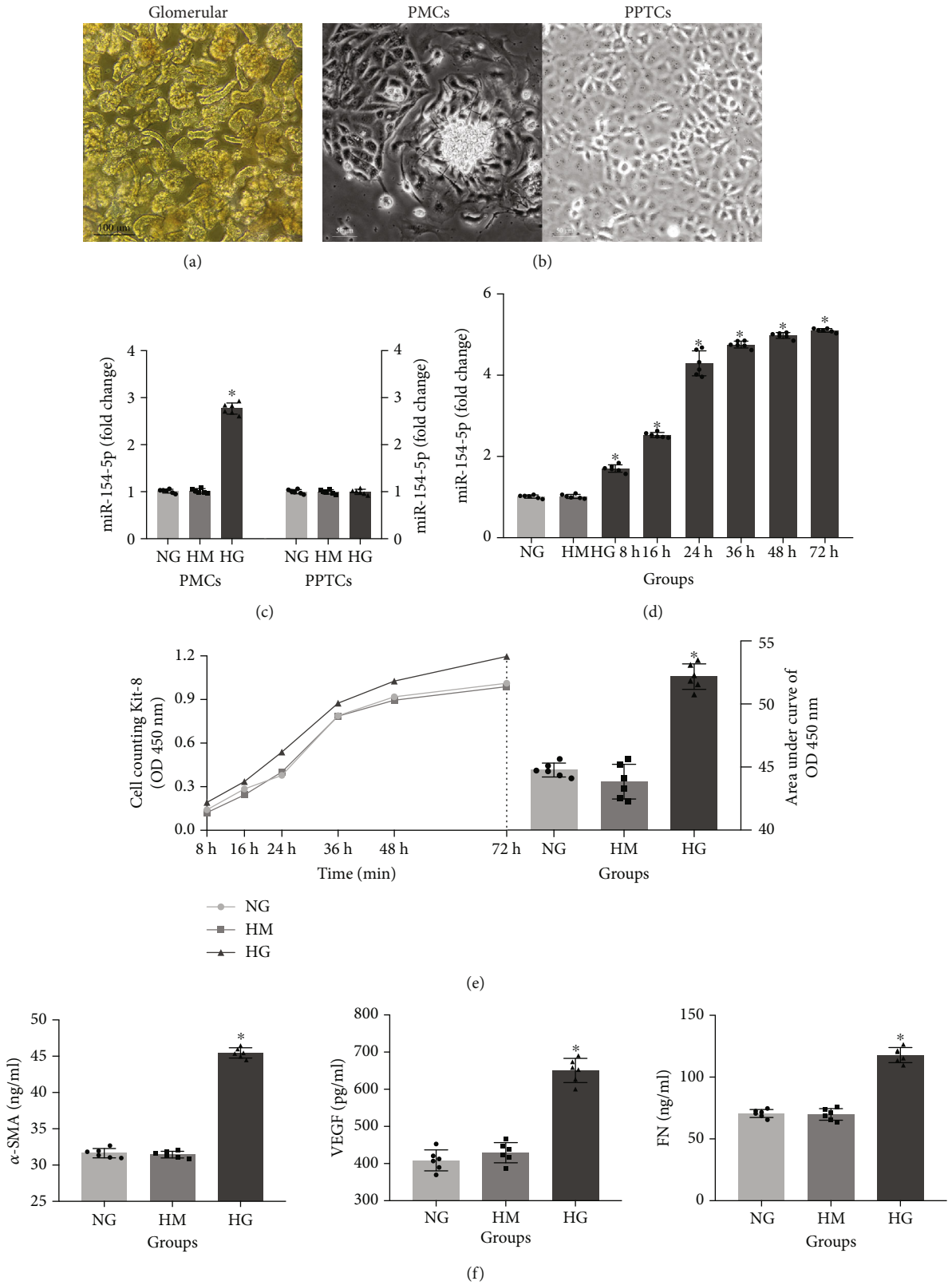

Figure 3: Continued.

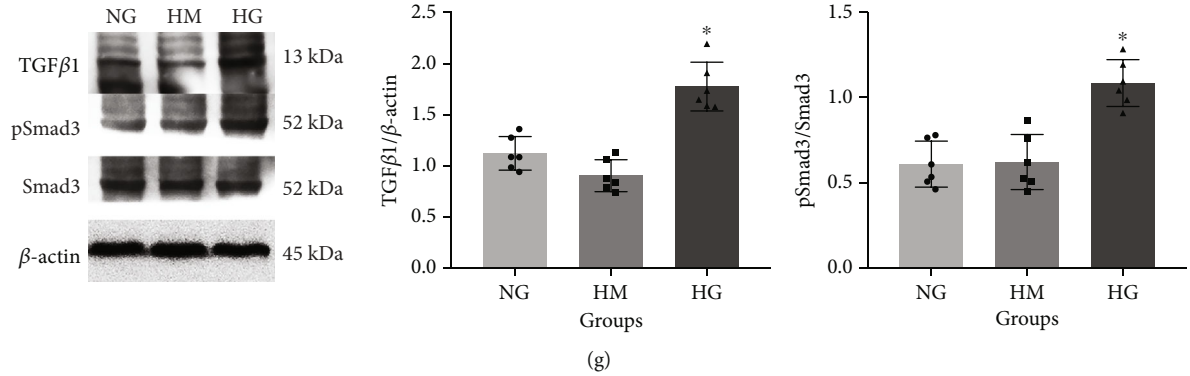

Figure 3: Expression of miR-154-5p in primary cells and cell lines. Rat glomerular isolation (a). Morphology extraction of primary mesangial cells (PMCs) and primary proximal tubular cells (PPTCs, b) with scale bar 50 μm. miR-154-5p in high-glucose-cultured PMCs and PPTCs (c) as well as RMCs at different time points (d). CCK-8 cell proliferation in RMCs at different time points (e). Levels of VEGF, α-SMA, and FN in RMC supernatant (f). Protein expression in high-glucose-cultured RMCs (g). NG: normal glucose; HM: high mannitol; HG: high glucose. *vs. NC, $P < 0.05$. $n = 6$ samples/group.

decreased in the miR-154-5p inhibitor and TGFβ1/Smads pathway inhibitor groups and significantly increased in the Smurf1 siRNA group (Figure 5(c)).

3.5. Smurf1 Regulates Ubiquitination through Smad3. As a member of HECT family with E3 ubiquitin ligases, Smurf1 is a key enzyme that determines substrate specificity in the ubiquitin-modifying pathway. It can recognize ubiquitinated protein substrates and selectively regulate the degradation process of effector molecules Smads ubiquitination. The mechanism was seen in Figure S2A. Based on the analysis of known ubiquitination binding sites in the NetPath/NetSlim database, it was found that the known ubiquitination binding sites for Smurf1 were RhoA, Smad7, and TRI (Figure S2B). Smurf1 interacts with TGFβ1 receptors, Smads, RhoA, Smurf2, and other Smurf1 proteins in inBio_Map (v2016_09_12) and IntAct Molecular Int analysis (Figure S3A). UbiBrowser database verified ubiquitin ligase recognition characteristics and found that Smurf1 had high ubiquitin binding ability to Smad2, Smad3, Smad4, and Smurf2, respectively (Figure S3B), and Smad3 had potential sites for binding to the C2 and HECT regions of Smurf1 (MH1: position 31-131, length 101; MH2: position 226-403, length 178), suggesting that Smurf1 and Smad3 may have a potential ubiquitination binding mode. Moreover, Smurf1 and Smad3 structures of humans and rats collected from the UniProtKB/Swiss-Prot database were compared. Sequence alignment results showed that the corresponding sequences in C2 and HECT regions of Smurf1 as well as the MH1 and MH2 regions of Smad3 were exactly the same in humans and rats (Figure S3C), indicating highly similar binding patterns in both humans and rats.

To verify the regulatory and binding effects of Smurf1 and Smad3, RMCs were treated with Smurf1 siRNA and TGFβ1/Smad3 inhibitor, SB431542. Smad3 was found to restore Smurf1-induced pSmad3/Smad3 and ubiquitin expression (Figure 6(b)) as well as the abnormal cell proliferation detected by CCK-8 (Figure 6(a)). In addition, Co-IP validation found direct binding sites between Smurf1 and Smad3 (Figure 6(c)).

3.6. miR-154-5p Influences Smurf1-Mediated Ubiquitination of Smad3. To further verify the regulation and binding of miR-154-5p and Smurf1, RMCs were pretreated with the miR-154-5p inhibitor and Smurf1 siRNA, and the detection found that Smurf1 can reverse the regulation of miR-154-5p on pSmad3/Smad3 and ubiquitin expressions (Figures 7(a) and 7(c)) as well as the abnormal cell proliferation detected by CCK-8 (Figure 7(b)). In addition, Rno-miR-154-5p and Rno-Smurf1 3′ UTR were able to bind directly in the predictive analysis, and luciferase validation showed that Rno-miR-154-5p and Rno-Smurf1 3′ UTR produced direct binding (Figure 7(d)).

4. Discussion

Type 2 diabetes mellitus (T2DM) is a long-term metabolic disorder characterized by hyperglycemia, insulin resistance, and relative deficiency of insulin [16]. Diabetic kidney disease (DKD) is one of the most common chronic microvascular complications of T2DM, which can lead to end-stage renal disease (ESRD) and even renal failure [1, 17, 18] and increased death caused by cardiovascular events [19], which bring heavy economic burden to the society and family. The characteristic clinical manifestation of DKD is continuous and has slow development of proteinuria. In clinical practice, in addition to invasive renal biopsy as the gold standard for diagnosis, noninvasive urinary albumin to creatinine ratio (UACR) and glomerular filter rate detection are also used as the basis for diagnosis and classification [3–5]. DKD lesions can involve all parts of the kidney, including abnormal proliferation of glomerular mesangial cells, thickening of basement membrane, glomerular sclerosis, and podocyte loss in early stage, while renal tubular basement membrane thickening, tubular atrophy, renal interstitial inflammatory infiltration, and renal interstitial fibrosis were observed in the later stage [2]. Among them, abnormal proliferation of mesangial cells, renal interstitial fibrosis, and podocyte injury are important pathological processes of fibrosis, which run through the whole process of DKD

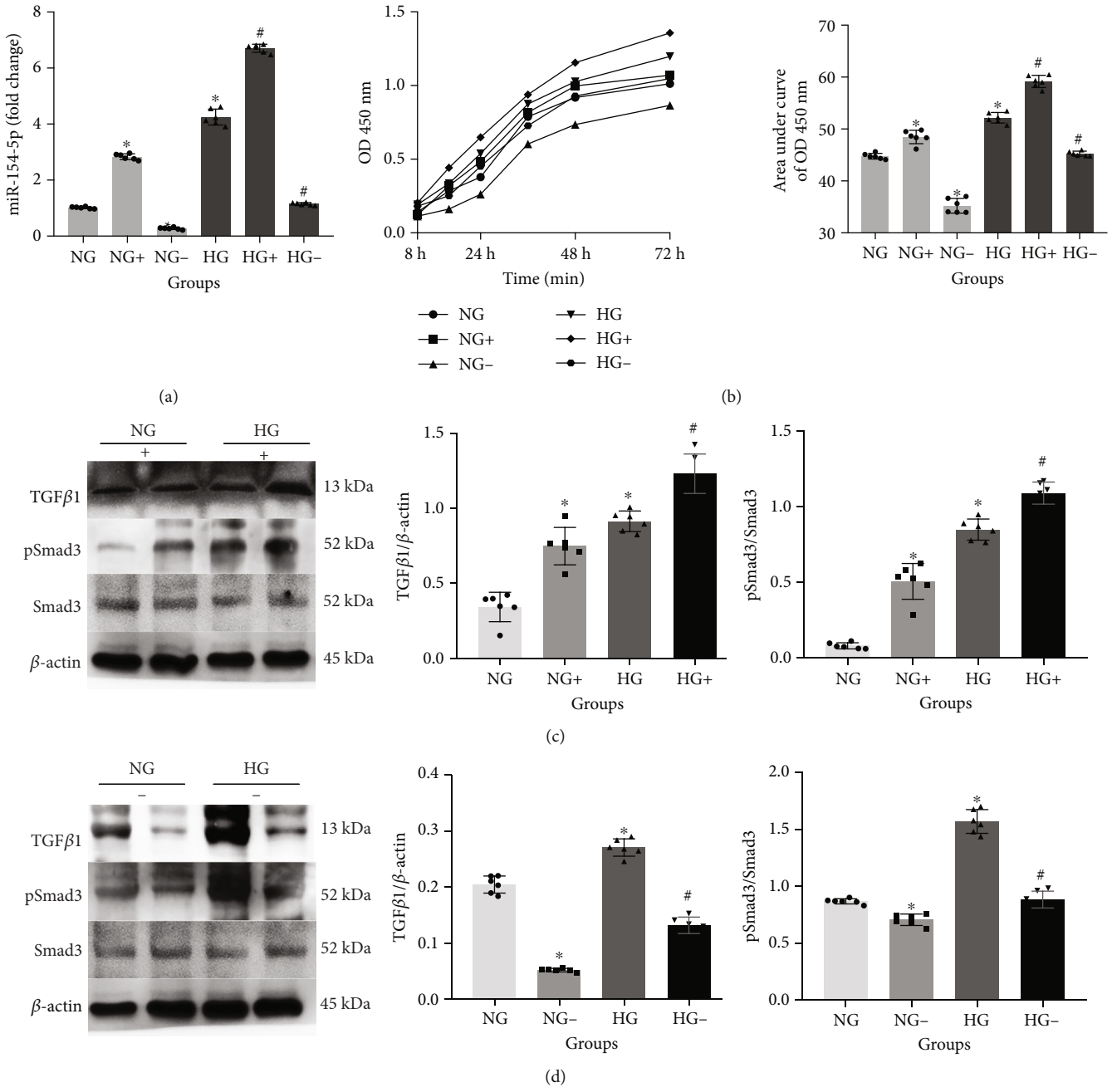

Figure 4: The role of miR-154-5p regulating the TGFβ1/Smads pathway. Levels of miR-154-5p (a), CCK-8 cell proliferation (b), and protein expression levels (c, d) in RMCs with miR-154-5p mimic and inhibitor. NG: normal glucose; NG+ or - : normal glucose with mimic or inhibitor; HG: high glucose, HG+ or - : high glucose with mimic or inhibitor. *vs NG, $P < 0.05$; #vs. HG, $P < 0.05$. $n = 6$ samples/group.

disease, and have become an important biomarker to evaluate the progress of DKD.

Fibrosis is the core of high morbidity and mortality associated with DKD, and its production is mainly the result of multiple factors such as high glomerular filtration, increased advanced glycation end products, and reactive oxygen species, as well as the activation of renin-angiotensin-aldosterone system. Abnormal proliferation of rat mesangial cells (RMCs) is an important pathological change in the early stage of DKD fibrosis, and RMCs cultured in high glucose are a classic model for the study of DKD [20, 21]. The intracellular molecular pathways are believed related to mesangial cell proliferation and fibrosis including the activation of renin-angiotensin system, transforming growth factor β1 (TGFβ1), monocyte chemotactic protein-1, connective tissue growth factor (CTGF), and fibronectin (FN), etc. [22–25], which can effectively assess the extent of renal injury and timely guide the clinical treatment of DKD [26–29].

MicroRNAs (miRNAs) are highly conserved noncoding RNAs with a length of 18-25 nucleic acids that regulate gene expression through incomplete complementary base sequences at the 3′ terminal untranslated region (UTR) of the target

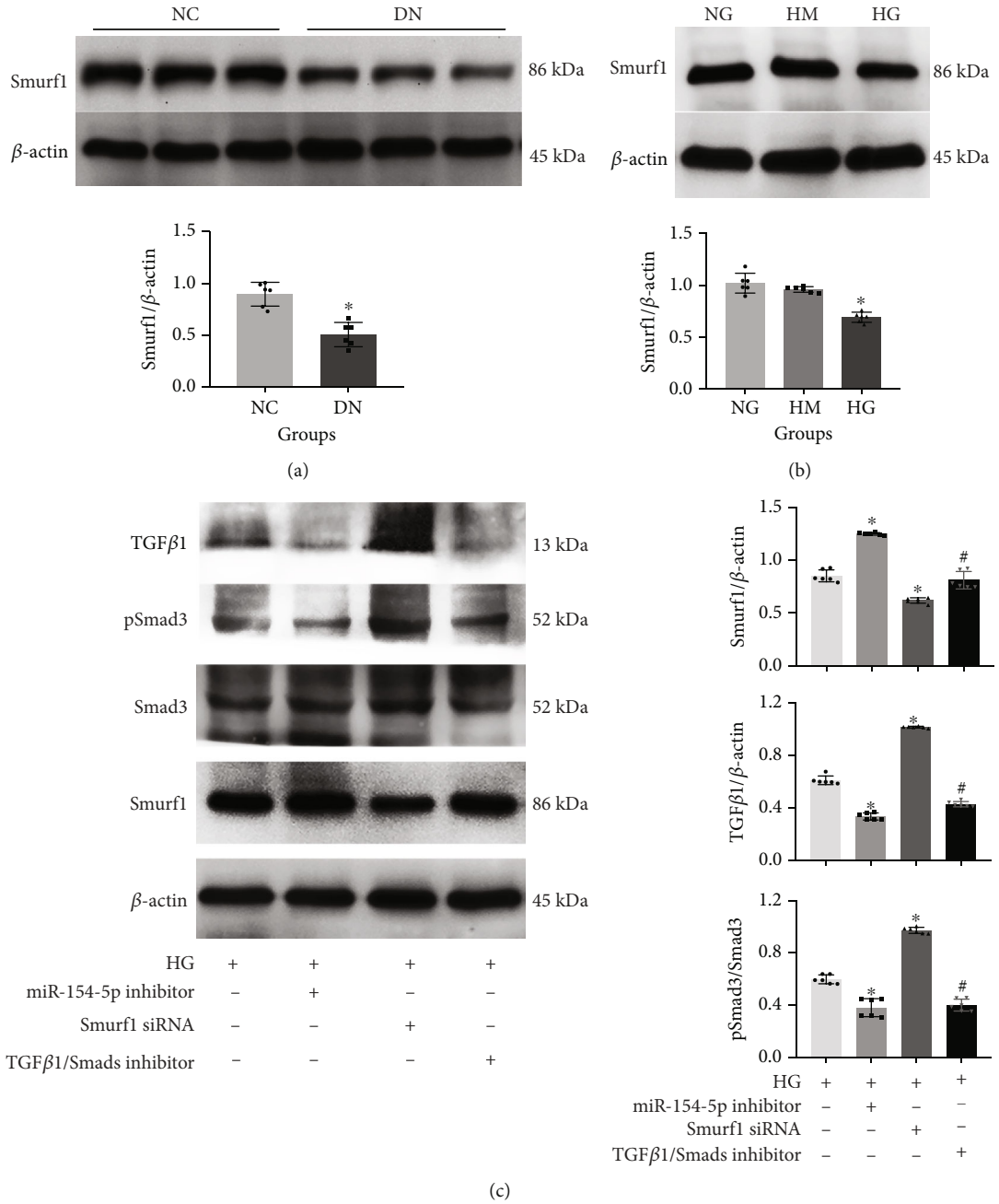

Figure 5: Indirect verification of the miR-154-5p target gene. Smurf1 in diabetic rats (a) and RMCs (b) cultured with high glucose. Smurf1 in RMCs with high glucose, miR-154-5p inhibitor, Smurf1 siRNA, and TGFβ1/Smads pathway inhibitor (c). NC: normal control; DN: diabetic nephropathy; NG: normal glucose; HM: high mannitol; HG: high glucose. *vs. NC or NG, $P < 0.05$; #vs HG, $P < 0.05$. $n = 6$ samples/group.

mRNA, thereby influencing multiple cellular processes ranging from growth and development to disease generation. Studies have shown that multiple families of miRNA clusters are involved in the pathogenesis of DKD, such as let-7 family, miR-21, and miR-377, which are involved in the proliferation and apoptosis of mesangial cells under the condition of high glucose, while miR-34a-5p, miR-184, and miR-1915-5p are associated with renal tubulointerstitial fibrosis [30, 31]. Our previous studies found that compared with the normal control group, serum miR-154-5p expression in type 2 diabetic patients was significantly increased and positively correlated with UACR, HbA1c, and fibrosis factors (CTGF, VEGF, FN and TGFβ1) [9, 10], indicating that human circulating miR-154-5p was closely related to renal fibrosis. This is the first time that miR-154-5p has been found to be associated with DKD fibrosis so far, suggesting that miR-154-5p in circulating blood may be potentially associated with blood glucose and proteinuria regulating the process of DKD glomerular fibrosis. In the high-fat diet and STZ-induced diabetic rats, FISH and PCR were used to detect the expression of miR-154-5p, and the results

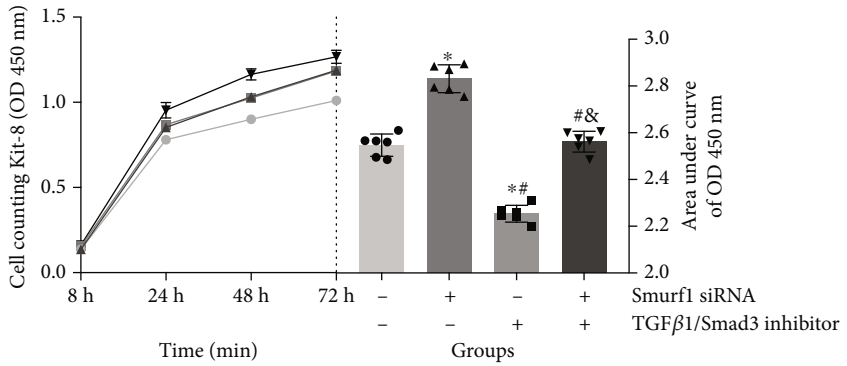

(a)

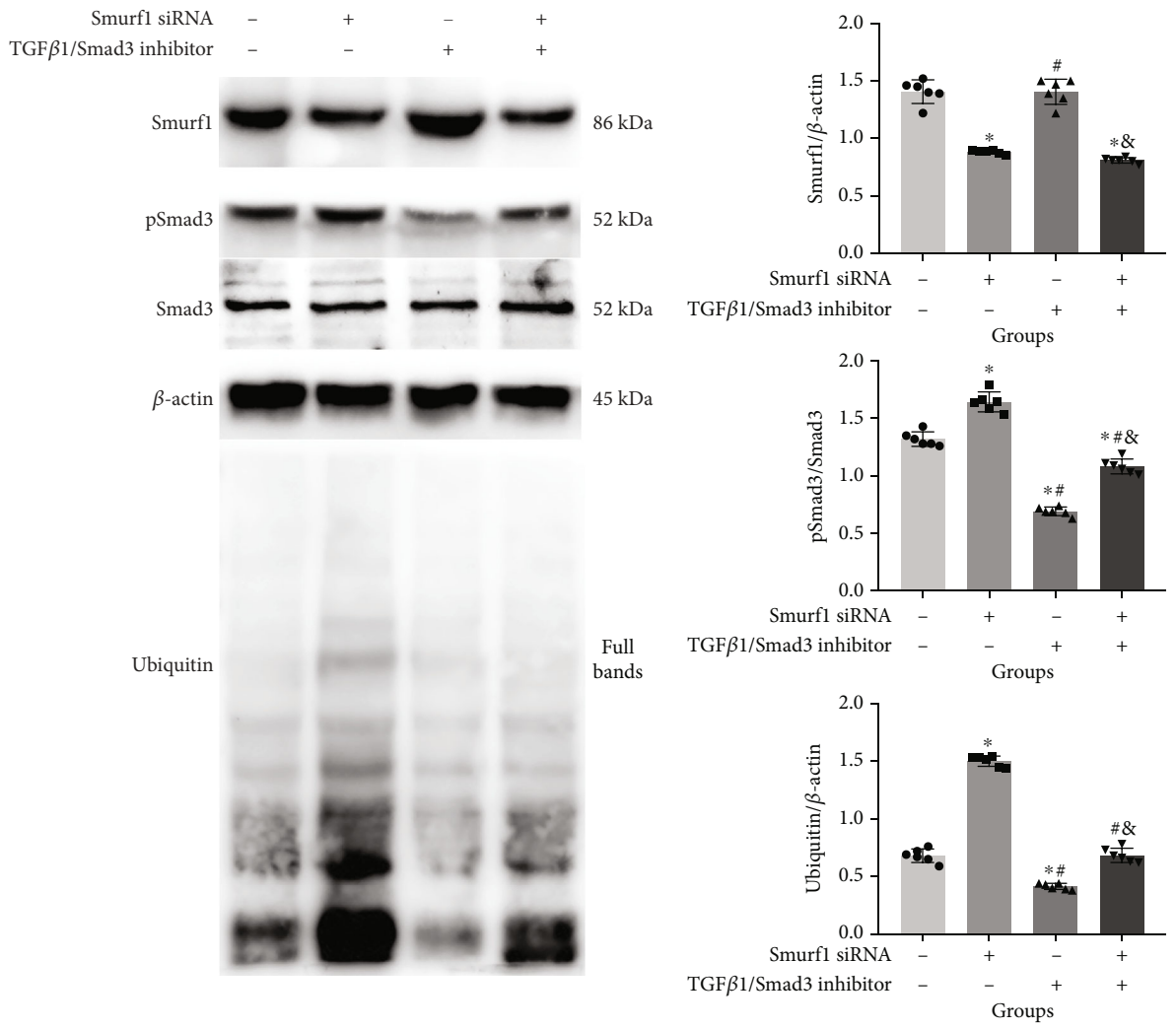

(b)

Figure 6: Continued.

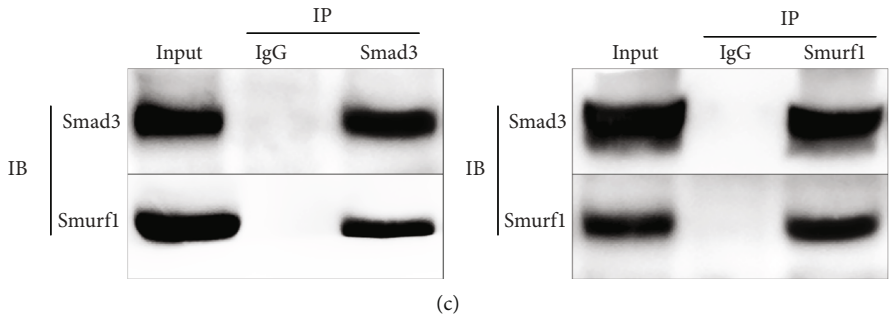

(c)

Figure 6: Smurf1 regulates ubiquitination through Smad3. CCK-8 cell proliferation (a) and related protein Smurf1, pSmad3/Smad3, and ubiquitin concentration (b). Co-IP verification for the combination of Smurf1 and Smad3 (c) after pretreatment with Smurf1 siRNA and TGFβ1/Smad3 inhibitor, SB431542. *vs. Group 1, $P < 0.05$; $^{\#}$vs. Group 2, $P < 0.05$; $^{\&}$vs. Group 3, $P < 0.05$. $n = 6$ samples/group.

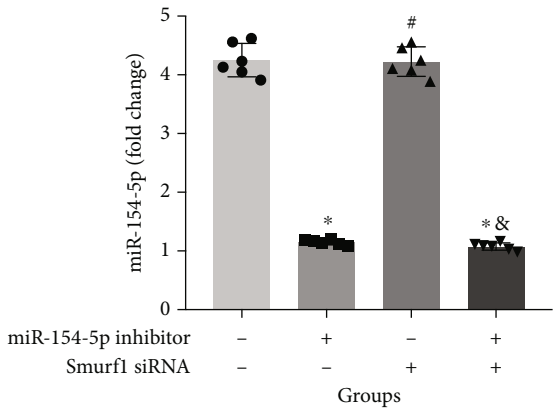

(a)

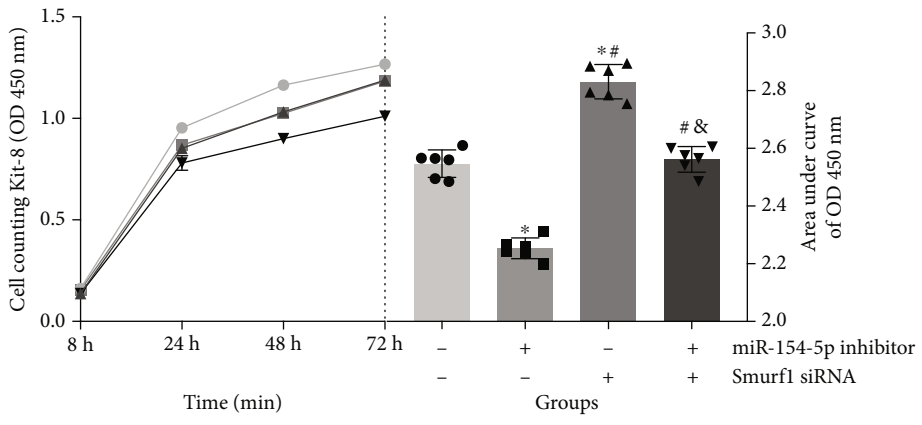

(b)

Figure 7: Continued.

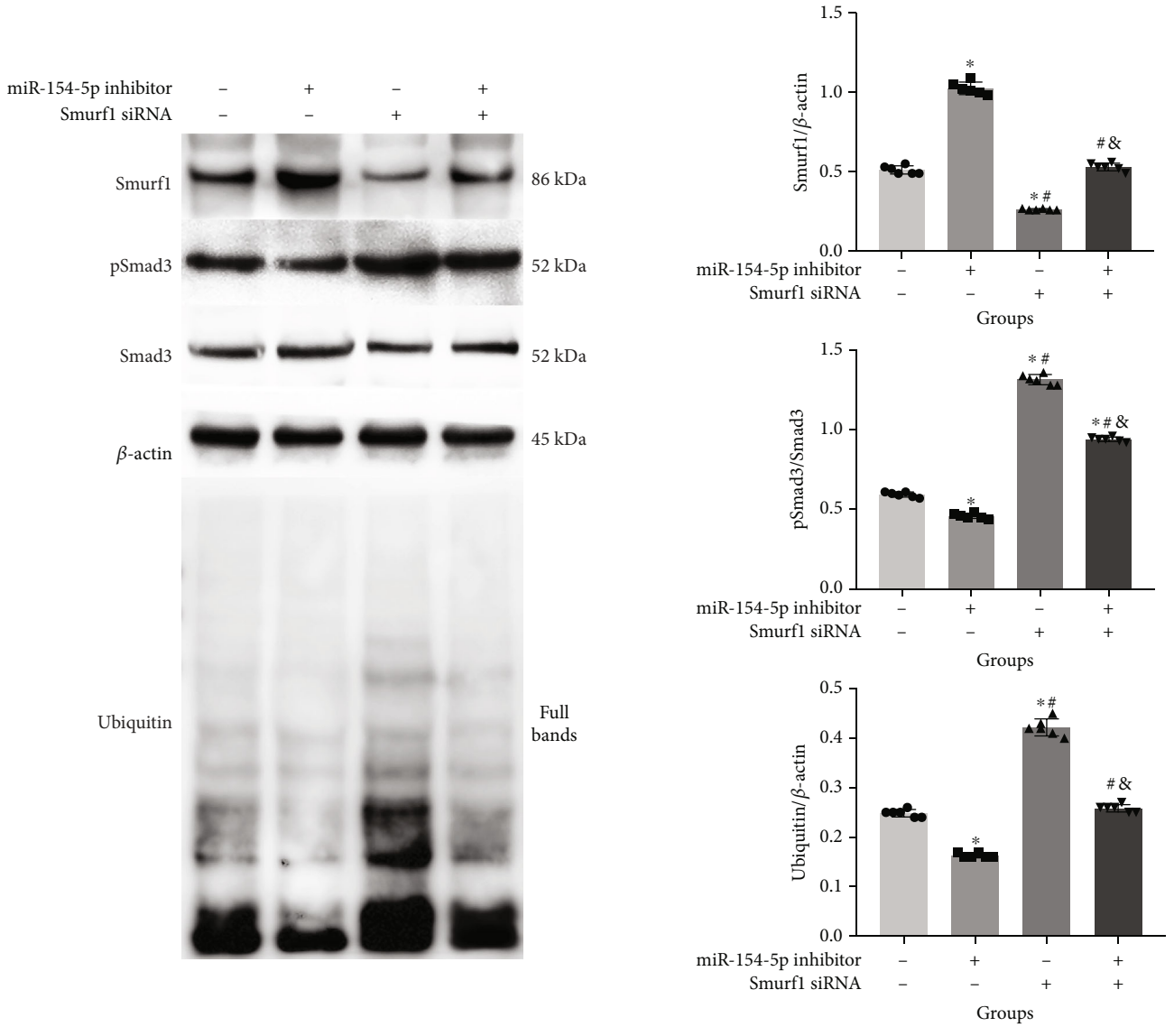

Figure 7: miR-154-5p influences Smurf1-mediated ubiquitination of Smad3. miRNA expression (a); CCK-8 cell proliferation (b); related protein Smurf1, pSmad3/Smad3, and ubiquitin concentration (c); luciferase verification for the binding of rno-miR-154-5p and rno-Smurf1 3′ UTR (d) after pretreatment with miR-154-5p inhibitor and Smurf1 siRNA. *vs. Group 1, $P < 0.05$; #vs. Group 2, $P < 0.05$; &vs. Group 3, $P < 0.05$. $n = 6$ samples/group.

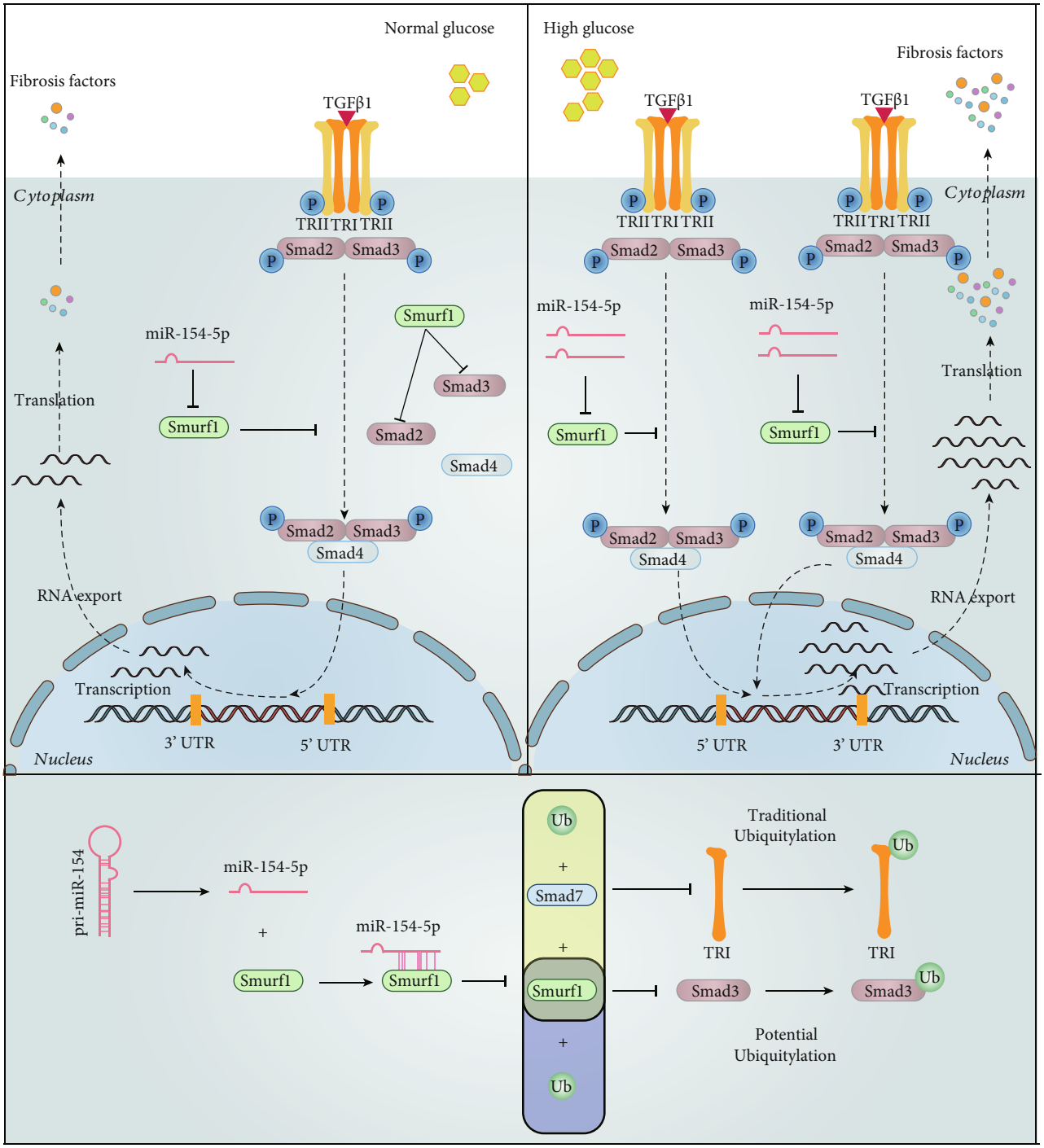

Figure 8: Possible mechanism. In the normal glucose state, TGFβ1 activates TRI and TRII in small amounts, causing phosphorylated Smad2 and Smad3 to bind Smad4 as polymers, which enter the nucleus and participate in transcriptional regulation of fibrosis. Smurf1 inhibits TGFβ1 signaling by regulating the classical pathway of Smad3 through TRI ubiquitination (Ub) via Smad7 or directly through the potential pathway of Smad3 ubiquitination. In the high glucose state, TGFβ1/Smads pathway increases activation, causing more miR-154-5p to inhibit Smurf1, thus indirectly promoting TGFβ1/Smads pathway activation and promoting the renal fibrosis process. The effect of lentivirus for the inhibitor of miR-154-5p can block this reaction thus indirectly alleviating diabetic kidney disease.

consistently showed that miR-154-5p was highly expressed in the glomerular rather than proximal tubules of the cortex region. The glomerulus is also an important structure involved in the filtration of urinary protein, which is consistent with the results of our clinical trials.

The specific mechanism of DKD producing urine protein is thought to be related to early pathological changes of the abnormal proliferation in glomerular mesangial cells. Thus, the classic model of RMCs under high-glucose cultivation is adopted to explore DKD [20]. On the basis of our previous

successful culturing RMCs [11, 12], we also successfully isolated the primary rat glomerular mesangial cells. Results by repeated detection of miR-154-5p showed that the expression of miR-154-5p was significantly decreased in both primary cells and cell lines pretreated by high-glucose culturing, and the cell proliferation activity was abnormally increased, which was consistent with the results *in vivo*, suggesting that miR-154-5p may be involved in the changes of glomerular mesangial cells in the early stage of DKD.

The important pathophysiological change of DKD is glomerular fibrosis, and the TGFβ1 pathway is one of the main pathways regulating the proliferation and fibrosis of mesangial cells. TGFβ1 binds to its membrane receptor, TGFβ receptor 1 (TRI), and activates another receptor, TRII. TRII phosphorylates Smad2 and Smad3 in cells to form heteropolymer with Smad4. After nucleation, this complex binds to transcriptional coactivators or coinhibitors, thereby regulating the transcription of downstream target genes. In contrast, Smad7 binds to TRI and TRII and inhibits phosphorylation of Smad2 and Smad3, which in turn inhibits the TGFβ1 pathway transmission. Smads are involved in the pathological process of the TGFβ1 pathway in mesangial cell proliferation and fibrosis through both positive and negative regulatory effects [6, 7]. TGFβ1 and pSmad3/Smad3 were significantly elevated in the diabetic animal model established in this study, which also suggested that the glomerular fibrosis of DKD was closely related to the TGFβ1/Smads pathway.

miR-154 is located on the miRNA-rich region in the single-stranded chromosome of mammalian 14q32 [8], and the 5′ arm of the precursor miR-154 (sequence: 5′-UAG GUU AUC CGU GUU GCC UUC G-3, mature to form miR-154-5p) has been demonstrated to be controlled by a 200 kb differential methylation region (DMR) in the Dlk1-Gtl2 (rodents)/Dlk-Dio3 (human) structural domain upstream of miRNA clusters [32–34]. Previous studies have confirmed that miR-154-5p is associated with the fibrosis mechanism of several diseases [35–38]. The transcription factor binding analysis showed that miR-154 is rich in Smad3 binding elements (SBEs) that mediate the TGFβ1 pathway during the growth and development stage [35, 39, 40], suggesting that miR-154 may be involved in the TGFβ1/Smad3 signaling pathway.

To investigate the relationship between miR-154-5p and the TGFβ1/Smads pathway, we treated RMCs with high glucose, miR-154-5p mimic, and inhibitor, respectively. The results showed that miR-154-5p could change the protein levels in the TGF β 1/Smads pathway and cell proliferation activity in RMCs. Moreover, in order to explore the regulatory mechanism of miR-154-5p involved renal fibrosis, we predicted the target genes of miR-154-5p indicating binding sites between human and rat miR-154-5p sequences and Smad ubiquitination regulatory factor 1 (Smurf1), suggesting that Smurf1 could bind with human and rat miR-154-5p. To verify the target genes of miR-154-5p, we detected the levels of ubiquitin-related molecule, Smurf1 in the successfully established models, and found that the expression was significantly decreased in diabetic rat renal tissues and high-glucose-cultured RMCs *in vivo and in vitro*.

As a member of HECT family, the E3 ubiquitin ligase, Smurf1, is a key enzyme that determines substrate specificity in the ubiquitin-modifying pathway. It can recognize ubiquitinated protein substrates and selectively regulate the ubiquitinated degradation process of effector molecules, Smads [41, 42]. The known ubiquitination binding sites were analyzed using the NetPath/NetSlim database, finding that RhoA, Smad7, and TRI were known ubiquitin binding sites of Smurf1. Protein interaction analysis showed that Smurf1 could interact with multiple Smads in the TGF β 1 pathway. By the comparison of Smurf1 and Smad3 structures in humans and rats, Smurf1 and Smad3 had high ubiquitination binding ability and similar binding mode with Smad3. The bioinformatics analysis provided the possibility for the binding research of both. It has been reported that Smurf1 participates in the fibrosis of DKD and obstructive nephropathy by inducing the apoptosis of glomerular mesangial cells [43] and regulating the epithelial-mesenchymal transition (EMT) induced by TGFβ [44–46]. These results suggest that Smurf1 may regulate the TGF β 1/Smads pathway and participate in mesangial cell fibrosis, suggesting that Smurf1 may directly regulate Smad3 ubiquitination in a new way.

Rescue and luciferase experiments were used to prove the regulatory effect of miR-154-5p and Smurf1 directly and indirectly. Results showed that regulating miR-154-5p could save the abnormal proliferation and fibrosis of RMCs caused by Smurf1 regulating Smad3 ubiquitination, and miR-154-5p could bind to the Smurf1 3′ UTR. Meanwhile, rescue and Co-IP experiments were used to verify the regulation of Smurf1 and Smad3 ubiquitination directly and indirectly, indicating that regulation of Smurf1 could also rescue the abnormal proliferation and fibrosis of RMCs caused by Smad3 ubiquitination and that Smurf1 and Smad3 could also be directly combined. All the above experiments proved that miR-154-5p could regulate the levels of Smad3 by combining with Smurf1, thereby regulating the abnormal proliferation and fibrosis of glomerular mesangial cells and affecting the generation of proteinuria in the early DKD stage.

In conclusion, miR-154-5p can affect proliferation in glomerular mesangial cells via E3 ubiquitin ligase, Smurf1, regulating TGFβ1/Smads pathway, thus affecting renal fibrosis of DKD. Hopefully, the inhibitor of miR-154-5p is expected to become a potential way for the DKD treatment. The possible mechanism is shown in Figure 8.

Data Availability

The data used to support the findings of this study are included within the article.

Ethical Approval

All animals were kept in a pathogen-free environment and fed ad lab. The procedures for care and use of animals were approved by the Institutional Animal Care and Use Committee (IACUC) of China Medical University (Approval No-2021115), and all experimental operations were complied with Guide for Laboratory Animal Care and Use and Animal Welfare Act. All applicable institutional and governmental regulations concerning the ethical use of animals were followed.

Conflicts of Interest

The authors declare that they have no conflicts of interest.

Authors' Contributions

Che Bian contributed to the conceptualization, methodology, software acquisition, validation, formal analysis, investigation, resources, data curation, writing—original draft, visualization, project administration, and funding acquisition. Zhilin Luan contributed to the methodology, validation, formal analysis, resources, data curation, and writing-review and editing. Haibo Zhang, Ruijing Zhang, Jing Gao, Yuxia Wang, and Jia Li contributed to the formal analysis, resources, and data curation. Huiwen Ren contributed to the conceptualization, methodology, software, validation, formal analysis, investigation, data curation, writing—original draft, writing—review and editing, visualization, supervision, and funding acquisition.

Acknowledgments

This study was supported by the Doctoral Research Initiation Fund Project of Liaoning Province (Grant No. 2021-BS-206) and Shenyang Young and Middle-aged Innovation Support Program (RC210460). Our team would like to thank the Department of Laboratory Animal Science of China Medical University, the Central Laboratory and the Laboratory of Endocrine and Metabolism of the First Hospital of China Medical University, Laboratory of Nuclear Receptor and Major Metabolic Disease of Dalian Medical University, the Kidney Disease Center of Dalian Medical University, and the Central Laboratory of Xinhua Hospital Affiliated to Shanghai Jiaotong University School of Medicine for technical assistance and equipment support.

Supplementary Materials

Supplementary 1. Figure S1: target gene prediction of miR-154-5p. Above, prediction results of RNA22 V2 on the target gene (hsa_SMURF1) of miR-154-5p (hsa_miR_154_5p) in human. Below, prediction results of RNA22 V2 on the target gene (rno_SMURF1) of miR-154-5p (rno_miR_154_5p) in rats.

Supplementary 2. Figure S2: schematic diagram of Smurf1 ubiquitination. Schematic diagram of Smurf1 as E3 ubiquitination ligase for substrate recognition (A). Ub: ubiquitin, E1-E3: ubiquitin ligase; analysis of known ubiquitination binding sites (B).

Supplementary 3. Figure S3: prediction of protein interactions and ubiquitinated binding sites. Protein interaction analysis (A), the UbiBrowser database for verification of the ubiquitin ligase recognition characteristics (B), Smurf1 with high ubiquitin binding ability with Smad2, Smad3, Smad4, and Smurf2 (marked in red); human and rat Smurf1 and Smad3 sequence alignment (C); light red for the anchored alignment area, and blue for the initiation and termination sites amino acid sequences.

References

[1] M. Afkarian, L. R. Zelnick, Y. N. Hall et al., "Clinical manifestations of kidney disease among US adults with diabetes, 1988-2014," *JAMA*, vol. 316, pp. 602–610, 2016.

[2] E. Espinel, I. Agraz, M. Ibernon, N. Ramos, J. Fort, and D. Seron, "Renal biopsy in type 2 diabetic patients," *Journal of Clinical Medicine*, vol. 4, pp. 998–1009, 2015.

[3] American Diabetes Association, "15. Diabetes Advocacy:Standards of medical care in diabetes-2018," *Diabetes Care*, vol. 41, Supplement_1, pp. S152–S153, 2018.

[4] UK NC, *Chronic Kidney Disease (Partial Update): Early Identification and Management of Chronic Kidney Disease in Adults in Primary and Secondary Care*, UK NC, London, 2014.

[5] American Diabetes Association, "16. Diabetes Advocacy:Standards of medical care in diabetes-2019," *Diabetes Care*, vol. 42, Supplement_1, pp. S182–S183, 2019.

[6] A. B. Roberts and R. Derynck, "Meeting report: signaling schemes for TGF-βA review of the meeting "The TGF-β Superfamily: Signaling and Development," FASEB Summer Research Conference, Tucson, Arizona, 7 to 12 July 2001," *Science's STKE*, vol. 2001, no. 113, p. pe43, 2001.

[7] J. Zhang, X. Zhang, F. Xie et al., "The regulation of TGF-β/SMAD signaling by protein deubiquitination," *Protein & Cell*, vol. 5, no. 7, pp. 503–517, 2014.

[8] A. Formosa, E. K. Markert, A. M. Lena et al., "MicroRNAs, miR-154, miR-299-5p, miR-376a, miR-376c, miR-377, miR-381, miR-487b, miR-485-3p, miR-495 and miR-654-3p, mapped to the 14q32.31 locus, regulate proliferation, apoptosis, migration and invasion in metastatic prostate cancer cells," *Oncogene*, vol. 33, no. 44, pp. 5173–5182, 2014.

[9] H. Ren, X. Ma, Y. Shao, J. Han, M. Yang, and Q. Wang, "Correlation between serum miR-154-5p and osteocalcin in males and postmenopausal females of type 2 diabetes with different urinary albumin creatinine ratios," *Frontiers in endocrinology*, vol. 10, p. 542, 2019.

[10] H. Ren, C. Wu, Y. Shao, S. Liu, Y. Zhou, and Q. Wang, "Correlation between serum miR-154-5p and urinary albumin excretion rates in patients with type 2 diabetes mellitus: a cross-sectional cohort study," *Frontiers in Medicine*, vol. 14, pp. 642–650, 2020.

[11] H. Ren, Y. Shao, C. Wu, X. Ma, C. Lv, and Q. Wang, "Metformin alleviates oxidative stress and enhances autophagy in diabetic kidney disease via AMPK/SIRT1-FoxO1 pathway," *Molecular and Cellular Endocrinology*, vol. 500, article 110628, 2020.

[12] H. Ren, Y. Shao, C. Wu, C. Lv, Y. Zhou, and Q. Wang, "VASH-1 regulates oxidative stress and fibrosis in diabetic kidney disease via SIRT1/HIF1α and TGFβ1/Smad3 signaling pathways," *Frontiers in Molecular Biosciences*, vol. 7, p. 137, 2020.

[13] H. Jiang, S. Zou, S. Chaudhari, and R. Ma, "Short-term high-glucose treatment decreased abundance of Orai1 protein through posttranslational mechanisms in rat mesangial cells," *American Journal of Physiology. Renal Physiology*, vol. 314, pp. F855–F863, 2018.

[14] H. Wang, J. Sheng, H. He et al., "A simple and highly purified method for isolation of glomeruli from the mouse kidney," *American Journal of Physiology. Renal Physiology*, vol. 317, pp. F1217–F1223, 2019.

[15] L. M. Wang, J. Chen, K. H. Chen, M. Y. Cai, X. Y. Wang, and Y. N. He, "Primary culture and identification of mouse renal

proximal tubular epithelial cells," *Sheng Li Xue Bao*, vol. 70, pp. 406–412, 2018.

[16] J. J. Chamberlain, A. S. Rhinehart, C. F. Shaefer Jr., and A. Neuman, "Diagnosis and management of diabetes: synopsis of the 2016 American Diabetes Association Standards of Medical Care in Diabetes," *Annals of Internal Medicine*, vol. 164, no. 8, pp. 542–552, 2016.

[17] L. Zhang, F. Wang, L. Wang et al., "Prevalence of chronic kidney disease in China: a cross-sectional survey," *Lancet*, vol. 379, no. 9818, pp. 815–822, 2012.

[18] World Health Organization, *WHO Global report on diabetes*, 2016.

[19] C. S. Fox, K. Matsushita, M. Woodward et al., "Associations of kidney disease measures with mortality and end-stage renal disease in individuals with and without diabetes: a meta-analysis," *Lancet*, vol. 380, no. 9854, pp. 1662–1673, 2012.

[20] Y. Lu, L. Tang, Y. Li, and Q. He, "High glucose-induced fibronectin upregulation in cultured mesangial cells involves caveolin-1-dependent RhoA-GTP activation via Src kinase," *Molecular Medicine Reports*, vol. 14, pp. 963–968, 2016.

[21] T. W. Tervaert, A. L. Mooyaart, K. Amann et al., "pathologic classification of diabetic nephropathy," *Journal of the American Society of Nephrology*, vol. 21, no. 4, pp. 556–563, 2010.

[22] M. K. Arora and U. K. Singh, "Molecular mechanisms in the pathogenesis of diabetic nephropathy: an update," *Vascular Pharmacology*, vol. 58, pp. 259–271, 2013.

[23] B. L. Riser, F. Najmabadi, B. Perbal et al., "CCN3/CCN2 regulation and the fibrosis of diabetic renal disease," *Journal of cell communication and signaling*, vol. 4, pp. 39–50, 2010.

[24] D. Macconi, G. Remuzzi, and A. Benigni, "Key fibrogenic mediators: old players. Renin-angiotensin system," *Kidney international supplements*, vol. 4, no. 1, pp. 58–64, 2014.

[25] C. Zoja, M. Locatelli, D. Corna et al., "Therapy with a selective cannabinoid receptor type 2 agonist limits albuminuria and renal injury in mice with type 2 diabetic nephropathy," *Nephron*, vol. 132, pp. 59–69, 2016.

[26] O. Ellina, A. Chatzigeorgiou, S. Kouyanou et al., "Extracellular matrix-associated (GAGs, CTGF), angiogenic (VEGF) and inflammatory factors (MCP-1, CD40, IFN-gamma) in type 1 diabetes mellitus nephropathy," *Clinical Chemistry and Laboratory Medicine*, vol. 50, pp. 167–174, 2012.

[27] X. Li, T. T. Wu, J. Chen, and W. Qiu, "Elevated expression levels of serum insulin-like growth factor-1, tumor necrosis factor-α and vascular endothelial growth factor 165 might exacerbate type 2 diabetic nephropathy," *Journal of diabetes investigation*, vol. 8, no. 1, pp. 108–114, 2017.

[28] S. Malik, K. Suchal, S. I. Khan et al., "Apigenin ameliorates streptozotocin-induced diabetic nephropathy in rats via MAPK-NF-κB-TNF-α and TGF-β1-MAPK-fibronectin pathways," *American Journal of Physiology. Renal Physiology*, vol. 313, no. 2, pp. F414–F422, 2017.

[29] A. S. Chang, C. K. Hathaway, O. Smithies, and M. Kakoki, "Transforming growth factor-β1 and diabetic nephropathy," *American Journal of Physiology. Renal Physiology*, vol. 310, no. 8, pp. F689–F696, 2016.

[30] P. Trionfini and A. Benigni, "MicroRNAs as master regulators of glomerular function in health and disease," *Journal of the American Society of Nephrology*, vol. 28, pp. 1686–1696, 2017.

[31] S. Bagga, J. Bracht, S. Hunter et al., "Regulation by let-7 and lin-4 miRNAs results in target mRNA degradation," *Cell*, vol. 122, pp. 553–563, 2005.

[32] H. Seitz, H. Royo, M. L. Bortolin, S. P. Lin, A. C. Ferguson-Smith, and J. Cavaille, "A large imprinted microRNA gene cluster at the mouse Dlk1-Gtl2 domain," *Genome Research*, vol. 14, pp. 1741–1748, 2004.

[33] A. Dixon-McIver, P. East, C. A. Mein et al., "Distinctive patterns of microRNA expression associated with karyotype in acute myeloid leukaemia," *PLoS One*, vol. 3, article e2141, 2008.

[34] Y. Altuvia, P. Landgraf, G. Lithwick et al., "Clustering and conservation patterns of human microRNAs," *Nucleic Acids Research*, vol. 33, pp. 2697–2706, 2005.

[35] J. Milosevic, K. Pandit, M. Magister et al., "Profibrotic role of miR-154 in pulmonary fibrosis," *American Journal of Respiratory Cell and Molecular Biology*, vol. 47, pp. 879–887, 2012.

[36] P. Dong, W. J. Liu, and Z. H. Wang, "MiR-154 promotes myocardial fibrosis through beta-catenin signaling pathway," *European Review for Medical and Pharmacological Sciences*, vol. 22, pp. 2052–2060, 2018.

[37] L. Y. Sun, Z. D. Bie, C. H. Zhang, H. Li, L. D. Li, and J. Yang, "MiR-154 directly suppresses DKK2 to activate Wnt signaling pathway and enhance activation of cardiac fibroblasts," *Cell Biology International*, vol. 40, pp. 1271–1279, 2016.

[38] B. C. Bernardo, S. S. Nguyen, X. M. Gao et al., "Inhibition of miR-154 protects against cardiac dysfunction and fibrosis in a mouse model of pressure overload," *Scientific Reports*, vol. 6, no. 1, p. 22442, 2016.

[39] H. Yang, L. Wang, J. Zhao et al., "TGF-β-activated SMAD3/4 complex transcriptionally upregulates _N_ -cadherin expression in non-small cell lung cancer," *Lung Cancer*, vol. 87, no. 3, pp. 249–257, 2015.

[40] K. V. Pandit, J. Milosevic, and N. Kaminski, "MicroRNAs in idiopathic pulmonary fibrosis," *Translational Research*, vol. 157, pp. 191–199, 2011.

[41] J. Wei, M. Ferron, C. J. Clarke et al., "Bone-specific insulin resistance disrupts whole-body glucose homeostasis via decreased osteocalcin activation," *The Journal of Clinical Investigation*, vol. 124, pp. 1–13, 2014.

[42] J. Shimazu, J. Wei, and G. Karsenty, "Smurf1 inhibits osteoblast differentiation, bone formation, and glucose homeostasis through serine 148," *Cell Reports*, vol. 15, pp. 27–35, 2016.

[43] S. Kume, M. Haneda, K. Kanasaki et al., "SIRT1 inhibits transforming growth factor beta-induced apoptosis in glomerular mesangial cells via Smad7 deacetylation," *The Journal of Biological Chemistry*, vol. 282, pp. 151–158, 2007.

[44] W. Gong, Z. Chen, Y. Zou et al., "CKIP-1 affects the polyubiquitination of Nrf2 and Keap1 via mediating Smurf1 to resist HG-induced renal fibrosis in GMCs and diabetic mice kidneys," *Free Radical Biology & Medicine*, vol. 115, pp. 338–350, 2018.

[45] H. Fukasawa, T. Yamamoto, A. Togawa et al., "Down-regulation of Smad7 expression by ubiquitin-dependent degradation contributes to renal fibrosis in obstructive nephropathy in mice," *Proceedings of the National Academy of Sciences of the United States of America*, vol. 101, pp. 8687–8692, 2004.

[46] Z. Chen, X. Sun, Q. Chen et al., "Connexin32 ameliorates renal fibrosis in diabetic mice by promoting K48-linked NADPH oxidase 4 polyubiquitination and degradation," *British Journal of Pharmacology*, vol. 177, pp. 145–160, 2020.

Hindawi
Oxidative Medicine and Cellular Longevity
Volume 2021, Article ID 1010496, 10 pages
https://doi.org/10.1155/2021/1010496

Research Article

Discoidin Domain-Containing Receptor 2 Is Present in Human Atherosclerotic Plaques and Involved in the Expression and Activity of MMP-2

Qi Yu,[1,2] **Ruihan Liu**,[3] **Ying Chen**,[4] **Ahmed Bilal Waqar**,[5] **Fuqiang Liu**,[6] **Juan Yang**,[1] **Ting Lian**,[1] **Guangwei Zhang**,[1] **Hua Guan**,[1] **Yuanyuan Cui**,[2] **and Cangbao Xu**[1]

[1]*Shaanxi Key Laboratory of Ischemic Cardiovascular Diseases & Shaanxi Key Laboratory of Brain Disorders, Institute of Basic and Translational Medicine, Xi'an Medical University, Xi'an 710021, China*
[2]*Department of Histology and Embryology, Xi'an Medical University, Xi'an 710021, China*
[3]*Department of Pathology, Zhengzhou Central Hospital, Zhengzhou 450007, China*
[4]*School of Computer Science and Technology, Xi'an University of Posts and Telecommunications, Xi'an 710121, China*
[5]*Faculty of Allied and Health Sciences, Imperial College of Business Studies, Lahore, Pakistan*
[6]*Cardiovascular Department, Shaanxi Provincial People's Hospital, Xi'an 710010, China*

Correspondence should be addressed to Qi Yu; qiyu6028@hotmail.com

Received 25 August 2021; Accepted 30 November 2021; Published 16 December 2021

Academic Editor: Xun Cui

Discoidin domain-containing receptor 2 (DDR2) has been suggested to be involved in atherosclerotic progression, but its pathological role remains unknown. Using immunochemical staining, we located and compared the expression of DDR2 in the atherosclerotic plaques of humans and various animal models. Then, siRNA was applied to knock down the expression of DDR2 in vascular smooth muscle cells (VSMCs), and the migration, proliferation, and collagen *I*-induced expression of matrix metalloproteinases (MMPs) were evaluated. We found that an abundance of DDR2 was present in the atherosclerotic plaques of humans and various animal models and was distributed around fatty and necrotic cores. After incubation of oxidized low-density lipoprotein (ox-LDL), DDR2 was upregulated in VSMCs in response to such a proatherosclerotic condition. Next, we found that decreased DDR2 expression in VSMCs inhibited the migration, proliferation, and collagen *I*-induced expression of matrix metalloproteinases (MMPs). Moreover, we found that DDR2 is strongly associated with the protein expression and activity of MMP-2, suggesting that DDR2 might play a role in the etiology of unstable plaques. Considering that DDR2 is present in the atherosclerotic plaques of humans and is associated with collagen *I*-induced secretion of MMP-2, the clinical role of DDR2 in cardiovascular disease should be elucidated in further experiments.

1. Introduction

Cardiovascular disease (CVD) is a major cause of death in the world. Atherosclerosis has been known as the common pathological basis for CVD [1]. Atherosclerotic plaque rupture primarily causes clinical events such as myocardial infarction, stroke, and thrombogenesis. Regarding previous studies, researchers suggest that the balance of macrophages and vascular smooth muscle cells (VSMCs) in the atherosclerotic plaque is a crucial factor for plaque stability. Briefly, as a result of macrophage proliferation in plaques, these inflammatory cells release many matrix metalloproteinases (MMPs) to effectively degrade extracellular matrix (ECM), such as collagens and elastin, resulting in plaque destabilization or rupture; conversely, VSMCs synthesize ECM to keep the plaque stable [2]. Despite the fact that VSMCs contribute to plaque stabilization, these cells may also promote plaque rupture by secreting MMPs during the phenotypic transition of VSMCs from the contractile to the synthetic state [3]. However, it is unknown what causes VSMCs to induce production of MMPs instead of synthesizing ECM. Notably, the major component of ECM is collagens, which account for

Table 1: Primers were used for real-time PCR.

Gene	Forward (5′-3′)	Reverse (5′–3′)
DDR2	GATCATGTTTGAATTTGACCGA	GCACTGGGGTTCACATC
MMP-2	TTGACCAGAACACCATCG	GGTCCAGGTCAGGTGTGT
MMP-3	GCTGTGTGCTCATCCTACC	TGACAACAGGGCTACTGTC
MMP-8	AGGAATGCCACTATGATTG	CAAGAAATCACCAGAGTCG
MMP-9	ACAGCGAGACACTAAAGGC	GGCAAGTCTTCGGTGTAGC
MMP-12	GCTGGTTCGGTTGTTAGG	GTAGTTACACCCTGAGCATAC
MMP-13	ACTCAAATGGTCCCAAAC	TATCAGCAGTGCCATCAT
MMP-14	GTACCCACACACAACGCT	TTATCTGGAACACCACAGC
GAPDH	TACCCACGGCAAGTTCAACG	CACCAGCATCACCCCATTTG

approximately 60% of the total protein in atherosclerotic plaques [4]. These collagens not only constitute atherosclerotic plaques but also affect cell proliferation, migration, and adhesion via collagen receptors [4]. Among these collagen receptors, Discoidin domain-containing receptor 2 (DDR2) is regarded as a subgroup of tyrosine-kinase receptors, which is activated by natural ligands including collagen of types I, II, III, and X and is responsible for the communication and link between collagens and the cells [5]. DDR2 is present in various tissues, including vascular tissue and is implicated in the regulation of cell metabolism, differentiation, and growth. Interestingly, activation of DDR2 can induce production of MMPs, and therefore, DDR2 is recognized as playing a very important role in fibrosis and cancer [6]. Considering that DDR2 is found in VSMCs, an interesting question arises as to whether DDR2 also affects plaque stability via mediating MMP expression in VSMCs [7, 8]. Consequently, we designed this study to elucidate the pathological role of DDR2 in atherosclerosis.

2. Materials and Methods

2.1. Atherosclerotic Specimens and Histological Staining. Japanese white rabbits were treated by a cholesterol-rich diet containing 0.3% cholesterol and 3% corn oil for 6 or 16 weeks to induce atherosclerosis ($n = 3$, respectively), and then, rabbits were euthanized by using pentobarbital sodium at each time point. The aortic arch of each rabbit was cut into 10 cross sections (4 μm) [9]. Male ApoE$^{-/-}$ mice were euthanized by cervical dislocation. Segments of heart tissue crossing the ascending aorta and aortic sinus from male ApoE$^{-/-}$ mice ($n = 4$) were embedded within OCT, and serial sections (8 μm thick) were made as previously described [10]. Hematoxylin and eosin (H&E), oil red O, and Masson's trichrome stains were performed according to the protocols as previously described [11, 12]. Moreover, sections were performed with immunohistochemical staining against DDR2 in mouse (1 : 200; Abcam, Cambridge, UK; CST, Beverly, MA, USA) human and rabbit (1 : 200; Santa Cruz Biotechnology, Inc, Dallas, TX, USA), RAM11 of macrophages (1 : 200; Dako, CA, USA), and α-actin of SMC (1 : 200; Thermo Fisher Scientific, CA, USA) as previously described [11].

Human carotid plaques were collected from patients who received endarterectomy at Zhengzhou Central Hospital. Informed consents were obtained from all patients enrolled in the study, and all experiments were implemented in accordance with the guidelines and regulations set by the Ethics Committee of Xi'an Medical University (Permit No. XYJZS-201609027-1). Japanese white rabbits, SD rats, and ApoE$^{-/-}$ mice were purchased from the laboratory animal center at Xi'an Jiaotong University (Xi'an, China). All animal experiments were performed in the animal facility of Institute of Basic and Translational Medicine at Xi'an Medical University. The animal experiments were strictly following the guidelines of animal experiment in Xi'an Medical University, which was adapted from the Guide for the Care and Use of Laboratory Animals (NIH; Bethesda, MD, USA; NIH Publication No. 85-23, revised 2011). The Laboratory Animal Administration Committee of Xi'an Medical University approved all animal experiments (Institutional Animal Care and Use Committee; Permit No. XYJZS-201608012-2).

2.2. VSMC Culture. VSMCs were obtained from the aortas of male SD rats (200-300 g) as previously described [13]. Cells were used in the experiments from passages 3 to 6. Before the initiation of each experiment, an additional incubation of serum-free DMEM for 24 h renders cells to be quiescent. Then, cells were exposed to oxidized low-density lipoprotein (ox-LDL) (0, 25, 50, and 100 mg/L; Yiyuan Biotechnologies, Guangzhou, China) for 24 h to simulate the proatherosclerotic condition. To activate DDR2, cells were incubated with collagen *I* (Sigma-Aldrich) for 48 h. To study the inhibition of signaling pathways, cells were treated with inhibitors for 30 min. SP600125 (20 μmol/L; Calbiochem) is an inhibitor for JNK (c-Jun N-terminal kinase), and SB203580 (10 μmol/L; Calbiochem) is an inhibitor for p38 MAPK (mitogen-activated protein kinase), and PD98059 (20 μmol/L; Calbiochem) is an inhibitor for MEK (MAPK/ERK (extracellular-signal-regulated kinase) kinase). The doses of the inhibitors were referenced by the previous studies [14, 15]. Then, cells were exposed to ox-LDL (100 mg/L).

2.3. siRNA Interference. Small interfering RNA (siRNA) was used to knock down DDR2 expression in VSMCs as previously described [16]. Referencing a previous study, siRNA

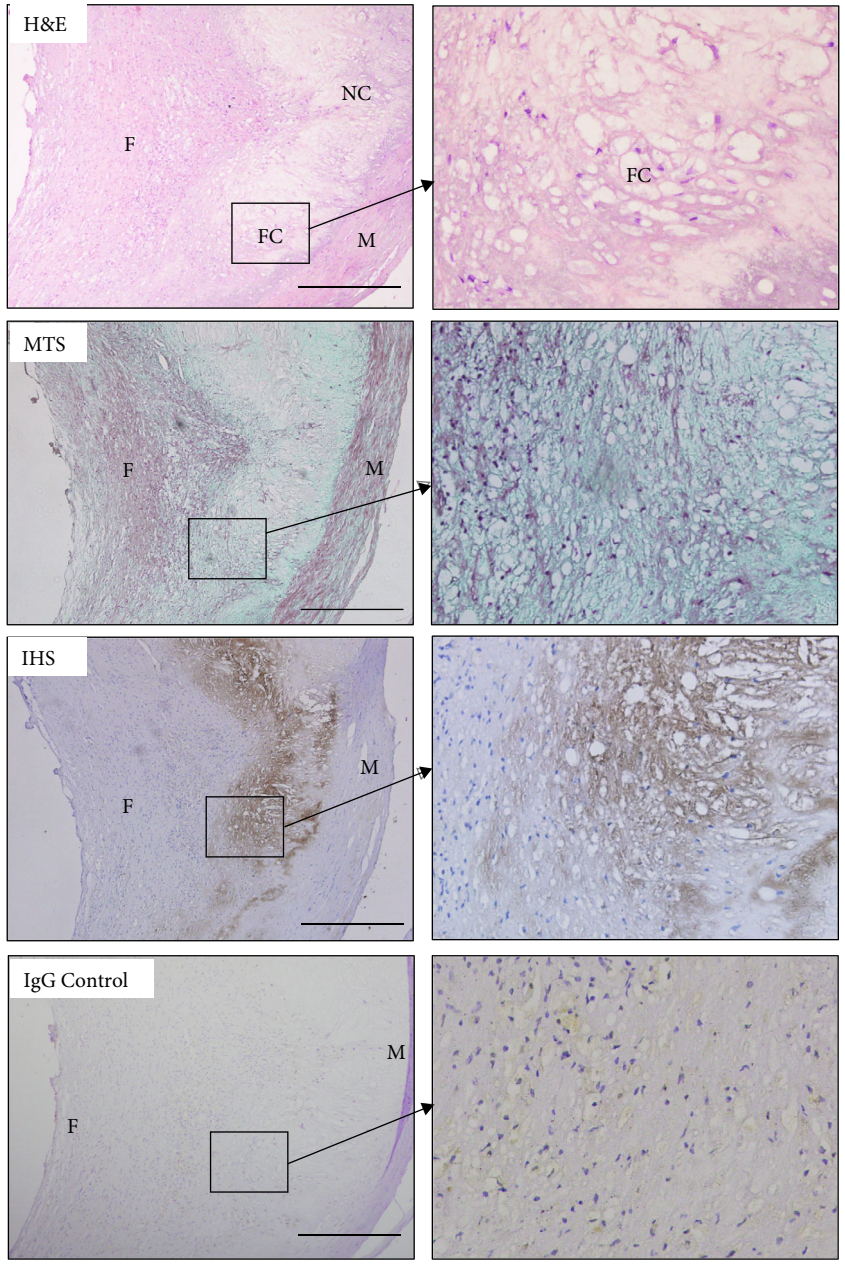

Figure 1: DDR2 in human carotid atherosclerotic plaque. Hematoxylin and eosin (H&E; 10x); Masson's trichrome stain (MTS; 10x); immunohistochemical staining against DDR2 (10x); rabbit IgG isotype control (10x). The area in the box is displayed as a high-power field in (b) (40x). NC: necrotic core; FC: fatty core; F: fibrous cap; M: middle membrane.

sequences were synthesized by a commercial company (sense strand, 5′- GAUGAUAGCAACACUCGGAUU-3′; antisense strand, 5′-UCCGAGUGUUGCUAUCAUCUU-3′; RiboBio, Guangzhou, China) [17]. siN05815122147 (RiboBio, Guangzhou, China) was used as a universal negative control. Transfection was performed with X-tremeGENE siRNA Transfection Reagent (Roche) and accorded to the manufacturer's instructions. Briefly, the cells were rinsed twice with phosphate-buffered saline (PBS) to reduce background interference. DDR2 siRNA with various doses (400 and 800 ng; approximately 40 and 80 pmol) were transfected into VSMCs for 6 h, and were then treated with ox-LDL (100 mg/L). The cells were collected to examine the DDR2 expression or to be performed by migration and proliferation assay.

2.4. Migration and Proliferation Assay. The migration of VSMCs was assessed by using the transwell permeable support insert (Corning, Lowell, MA, USA) as previously described [18]. After incubation of siRNA for 24 h without FBS, VSMCs were seeded on Matrigel (5 mg/mL; BD Biosciences, San Diego, CA, USA) of the upper compartment, and DMEM supplemented with 10% FBS was added into the lower compartment. Cells were cultured for another 24 h

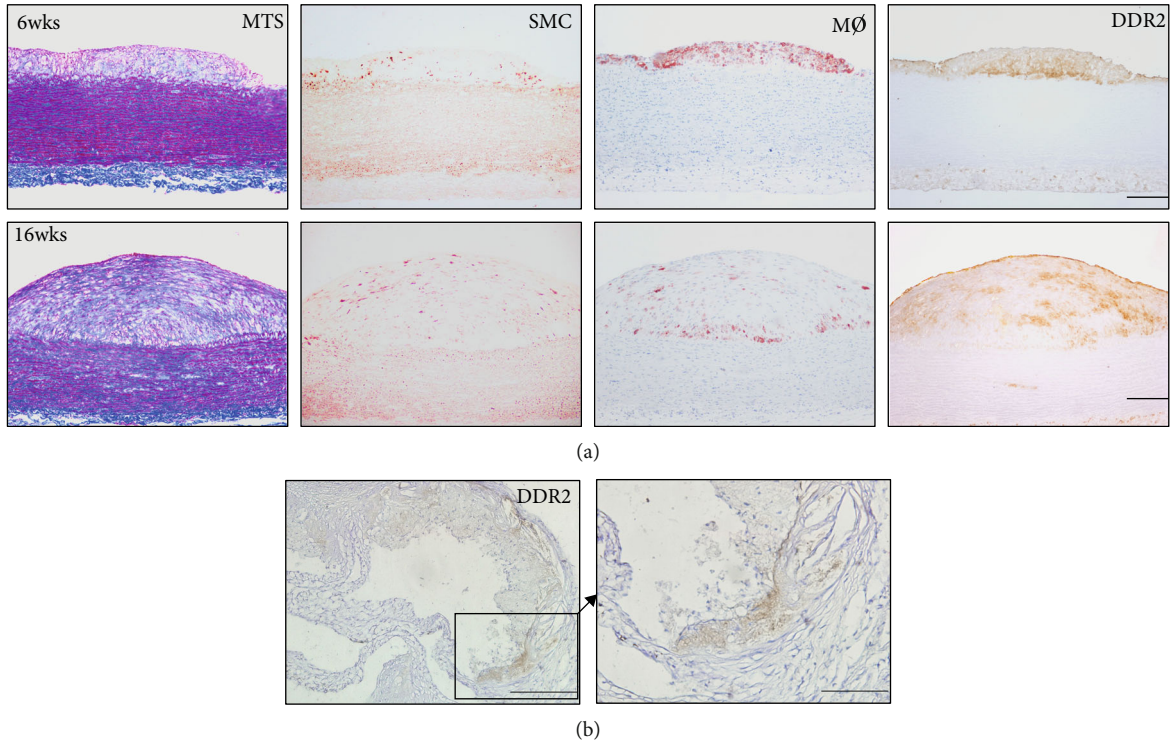

Figure 2: DDR2 in atherosclerotic plaques of animal models. Comparison of DDR2 expression and collagen distribution in atherosclerotic plaques of the HCD-induced rabbit model (a). Serial paraffin sections of aortic lesions were stained with Masson's trichrome stain (MTS) and immunohistochemical staining against α-smooth muscle actin (SMC), macrophages (Mϕ), and DDR2 (a) (bar = 200 μm). Atherosclerotic plaques of the apoE knockout mouse model and immunohistochemical staining against DDR2 (b) (bar = 100 μm). The area in the box is displayed as a high-power field on the right side (bar = 50 μm).

and then detected by crystal violet staining. Five different high-power fields per well were photographed. The positively stained VSMCs were counted by an observer blinded to the treatment protocol.

The proliferation of VSMCs was assessed by the wound-healing assay as previously described [19]. Briefly, after 24 h of siRNA treatment, a 10-l pipette tip was used to scrap an artificial wound in the monolayer across the bottom of the dish. After extensive washing, medium containing 10% FBS was removed, and cells started to migrate for the appropriate time in a 37°C incubation chamber with 5% CO_2. At various time points, images were obtained with a Nikon TE2000 Inverted Microscope. Meanwhile, some representative dishes were performed by immunofluorescence against α-actin of SMC (1 : 200; Thermo Fisher Scientific, CA, USA) with Alexa Fluor 488 (1 : 200; Thermo Fisher Scientific, CA, USA). The remaining open area of the wound was quantified by using ImageJ as previously described, with some modifications [20].

2.5. RNA Extraction and Real-Time PCR. Total RNA was extracted from the aorta and VSMCs. Real-time PCR was performed as previously described [21, 22]. The sequences of the primers are listed in Table 1.

2.6. Protein Extraction and Western Blotting Analysis. Total protein was extracted from the aorta of rabbits and VSMCs as previously described [22]. The primary antibodies were against rabbit's DDR2 (1 : 500; Santa Cruz Biotechnology, Santa Cruz, CA), rat's DDR2 (1 : 500; Santa Cruz Biotechnology, Santa Cruz, CA; CST, Beverly, MA, USA), MMP-2 (1 : 500; Abcam, Cambridge, MA), TIMP-1 (1 : 500; Abcam, Cambridge, MA), TIMP-2 (1 : 500; Abcam, Cambridge, MA), p-ERK1/2 (1 : 1000; CST, Beverly, MA, USA), and GAPDH (1 : 1000; Santa Cruz Biotechnology, Santa Cruz, CA). Western blotting analysis was applied as previously described, and relative protein expression was measured by ImageJ with gel analysis [22].

2.7. Zymography. The supernatants along with the total protein were extracted from cultured VSMCs. Under nonreducing conditions, the equal amounts of sample protein were analyzed by SDS-PAGE in gelatin-containing acrylamide gels (2 mg/mL gelatin and 7.5% polyacrylamide) as previously described [23].

2.8. Statistical Analysis. All data are expressed as the mean ± SE. Two groups of comparisons were used by Student's t-test. Multiple groups of comparisons were performed by using one-way ANOVA with the Bonferroni test. $P < 0.05$ was considered statistically significant. The statistical calculations were performed by using SPSS 19.0 software (IBM Corp., Armonk, NY, USA).

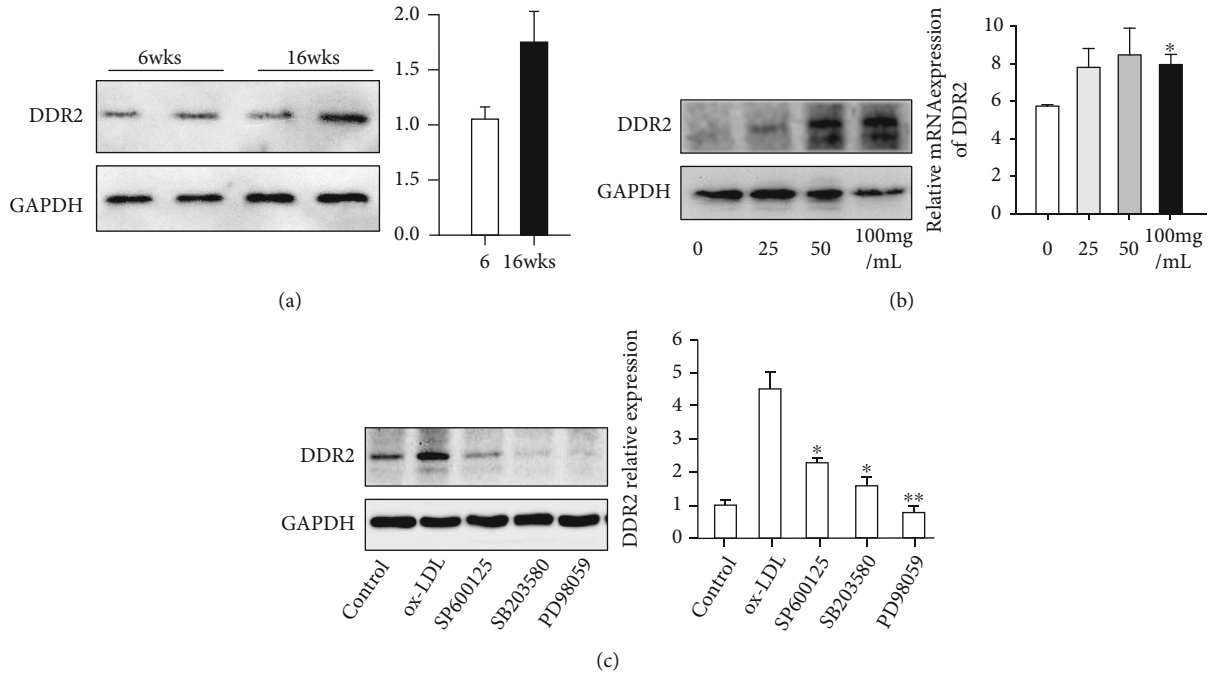

Figure 3: Protein expression of DDR2 in the aorta and VSMCs. Immunoblot analysis and quantification of DDR2 in aortas of HCD-induced atherosclerotic rabbits ((a); $n = 4$) and VSMCs that were incubated with various concentrations of 0, 25, 50, and 100 mg/L ox-LDL (b). Data are expressed as the mean ± standard error. $^{*}P < 0.05$ and $^{**}P < 0.01$ vs. the 0 mg group; $^{\#\#}P < 0.01$ 100 mg vs. the 25 mg group. Effect of MAPK inhibitors on ox-LDL-induced DDR2 expression (c). VSMCs were preincubated with inhibitors for 30 min and then treated with 100 ng/mL ox-LDL for 24 h in the presence of inhibitors (SP600125, SB203580, and PD98059 against JNK, MEK, and p38 MAPK, respectively). Data are expressed as the mean ± standard error. $^{*}P < 0.05$ and $^{**}P < 0.01$ vs. the ox-LDL group.

3. Results

3.1. DDRs Are Present in Atherosclerotic Lesions of Human Being. To examine whether DDR2 was present in atherosclerotic lesions, we used immunohistochemistry staining to identify DDR2 from human tissue to various animal species. Interestingly, we found expression of DDR2 in human carotid atherosclerotic plaques (Figure 1). Combined with the section with MST, we found that DDR2 distributes densely around the fatty cores of human carotid atherosclerotic plaques, and these positive stains were also adjacent to the fibrous cap and the middle membrane (Figure 1).

3.2. DDRs Are Present in Atherosclerotic Lesions of Animal Models. By using a rabbit model, we attempted to investigate the relationship between DDR2 expression and atherosclerotic progression. We found that DDR2 presented in the early and middle atherosclerotic lesions of rabbits, and this receptor was located in a similar position (Figure 2(a)). In the early-stage lesion, the majority of DDR2 was deposited along the lower edge of the lesion (Figure 2(a)). In the middle-stage lesion, DDR2 was diffusely distributed in the lesion and was deposited on the surface of the lesion (Figure 2(a)). DDR2 neither apparently overlapped with the cytoplasm of macrophages nor fully overlapped with VSMCs (Figure 2(a)). To compare MTS with DDR2 staining, indicating DDR2 expression and distribution might tend to localize around collagen fibers (Figure 2(a)). To further confirm the above results, we also used immunohistochemistry staining to identify DDR2 in atherosclerotic lesions of ApoE$^{-/-}$mice (Figure 2(b)). As Figure 2(b) shows, DDR2 was also found in atherosclerotic lesions of mice.

3.3. ox-LDL Upregulates DDR2 in VSMCs via the MAPK Pathway. Considering that DDR2 was abundant in atherosclerotic lesions, we questioned whether DDR2 expression was associated with atherosclerotic development. To compare the protein expression of DDR2, we found that there was no significant difference between the early and middle lesions (Figure 3(a)). Next, we also questioned what caused the upregulation of DDR2 in atherosclerotic lesions. Considering ox-LDL as a key atherogenic factor, we incubated the various concentrations of ox-LDL with VSMCs for 48 h. We found that 100 mg/mL of ox-LDL significantly increased DDR2 expression in VSMCs (Figure 3(b)).

Next, we also investigated which pathway may be involved in ox-LDL-induced DDR2 expression. By using inhibitors against the MAPK pathway, we found that blocking JNK, p48, and ERK1/2 in VSMCs could neutralize ox-LDL-induced DDR2 expression, suggesting that the MAPK pathway might be responsible for the ox-LDL-induced upregulation of DDR2 (Figure 3(c)).

3.4. DDR2 Affects the Migration of VSMCs. As reported in a previous study, a specific siRNA against DDR2 was applied to suppress DDR2 protein expression. First, we used various doses of siRNA to knock down DDR2 expression in VSMCs. We found that 800 ng of siRNA could efficiently inhibit ox-

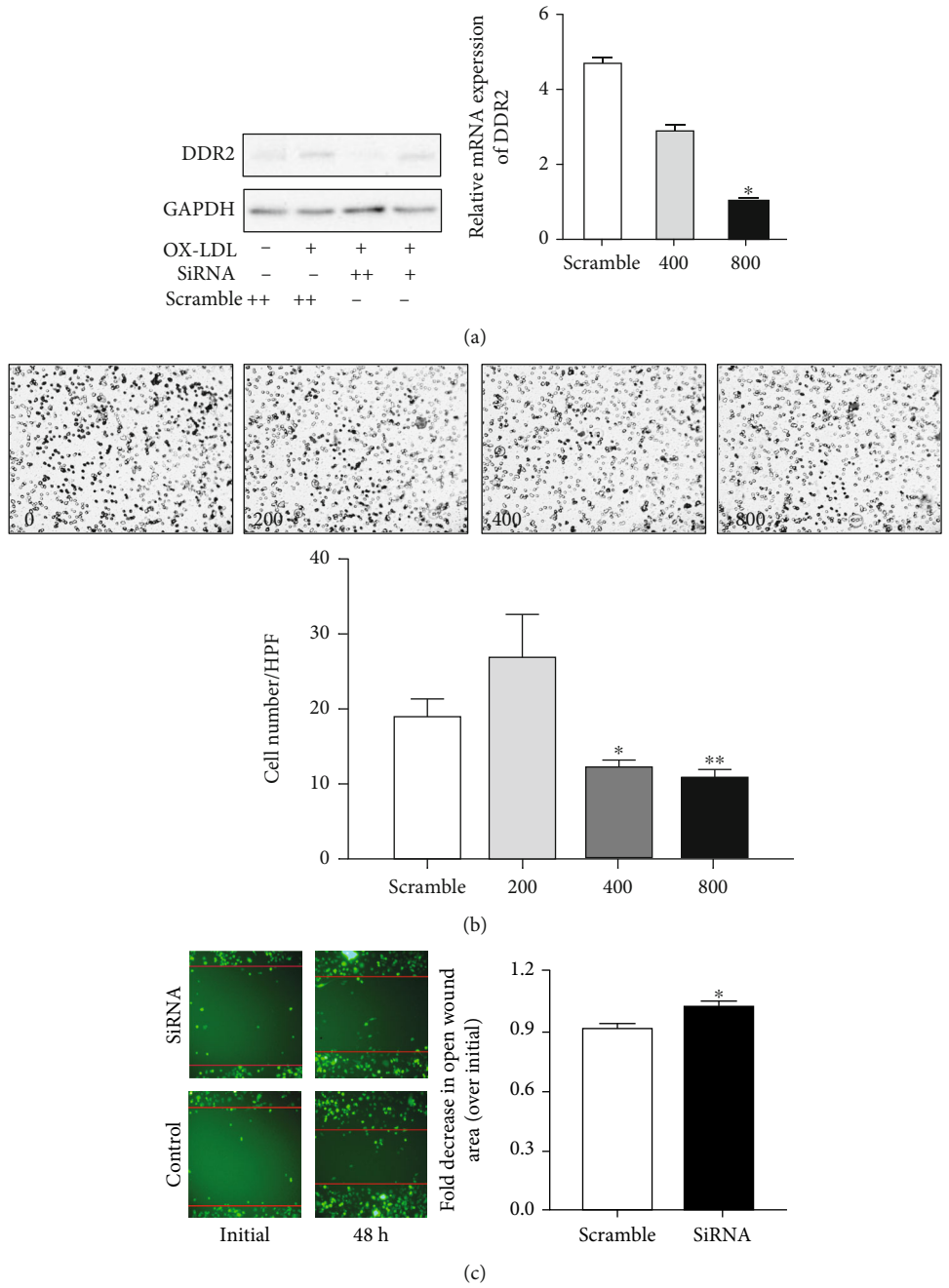

Figure 4: Effect of knockdown of DDR2 on the migration and proliferation of VSMCs. After 400 and 800 ng of siRNA treatments, DDR2 expression in VSMCs was analyzed and quantified by western blotting and real-time PCR (a). Migration and proliferation were assessed by transwell analysis (b) and wound healing assay (c). Data are expressed as the mean ± standard error. $^{*}P < 0.05$ and $^{**}P < 0.01$ vs. the scramble RNA-treated group.

LDL-induced DDR2 expression, which was quantified and confirmed with real-time PCR (Figure 4(a)). Next, to test whether inhibition of DDR2 in SMCs affected its migration, the transwell assay was performed after incubation of siRNA with VSMCs for 48 h (0, 200, 400, and 800 ng of siRNA, respectively). We found that 400 and 800 ng of siRNA reduced cell migration, indicating that the migration activity of VSMCs was inhibited by DDR2 reduction (Figure 4(b)). To confirm this result, we also used a wound healing assay to check the migration of VSMCs. As Figure 4(c) shows, we found that a decrease in DDR2 expression indeed inhibited the migration of VSMCs.

3.5. DDR2 Affects the mRNA Expression of MMPs in VSMCs. The invasion of VSMCs is determined by its collagenase secretion; thus, we examined whether MMP expression was reduced by DDR2 deficiency. First, we incubated collagen I with VSMCs for 48 h, and MMP (MMP-2, MMP-3, MMP-8, MMP-9, MMP-12, MMP-13, and MMP-14) expression was quantified by real-time PCR. Interestingly, we found

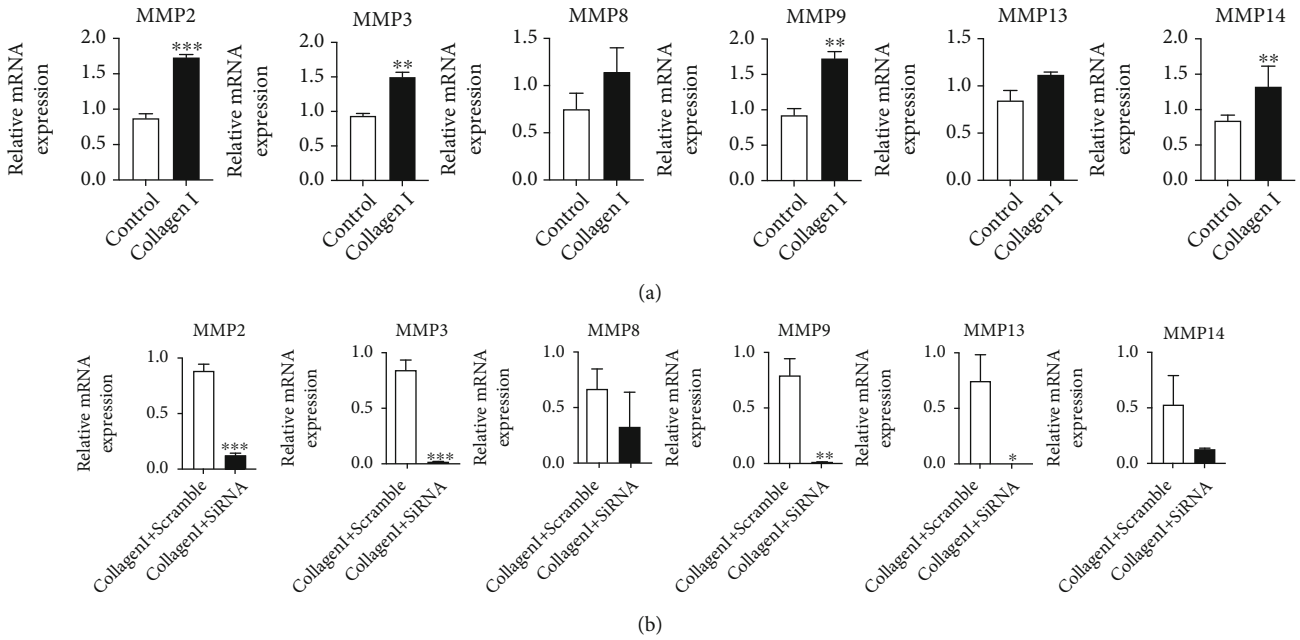

Figure 5: Effect of knockdown of DDR2 on mRNA expression of MMPs in VSMCs. Collagen I-induced MMP expression was assessed by real-time PCR (a). After siRNA treatment, collagen I-induced MMP expression was assessed by real-time PCR (b). Data are expressed as the mean ± standard error. $^{*}P < 0.05$, $^{**}P < 0.01$, and $^{***}P < 0.001$ vs. the collagen I-treated group or collagen I combined with siRNA-treated group.

that collagen I could upregulate MMP-2, MMP-3, MMP-9, and MMP-14 (Figure 5(a)). Next, we used 800 ng of siRNA to knock down DDR2 expression before collagen I incubation. As a result of mRNA quantification by real-time PCR, inhibition of DDR2 reversed the effect of collagen I on expression of MMPs and suppressed the mRNA expression of MMP-2, MMP-3, MMP-9, and MMP-13 (Figure 5(b)). In addition, we failed to find the mRNA expression of MMP-12 in VSMCS.

3.6. DDR2 Affects the Activity and Expression of MMP-2 in VSMCs. Considering that collagen I-induced mRNA expression of MMP-2 is dramatically suppressed after DDR2 deficiency, we next examined whether the inhibition of DDR2 affected the activity of MMP-2. As a result of zymography, MMP-2 activity was increased by collagen I incubation but was decreased by 800 ng of siRNA against DDR2 expression, and almost no MMP-2 activity was found without collagen I incubation before siRNA interference (Figure 6(a)). However, we did not find any bands of MMP-9 in the same zymography gel. To study whether deceased activity of MMP-2 was attributed to MMP-2 protein, we next examined MMP-2 protein expression via western blotting. Indeed, we found that MMP-2 production was decreased in the presence of siRNA against DDR2 expression (Figure 6(b)). Next, TIMP-1 and TIMP-2 were studied and quantified by western blotting, and the result showed that there was no significant difference between the two groups (Figure 6(c)). To further study the underlying mechanism, we also examined the ERK signaling according to previous report [6]. After inhibition of DDR2 by siRNA, phosphorylation of ERK1/2 was reduced (Figure 6(d)).

4. Discussion

Atherosclerotic plaque rupture is a serious problem for patients with cardiovascular disease, often causing unstable angina, myocardial infarction, and sudden coronary death [24]. However, how the atherosclerotic plaque becomes vulnerable remains unknown. The question remains as to why ECM tends to degrade in these unstable plaques. Notably, ECM not only constitutes atherosclerotic plaques but also activates collagen receptors to regulate the surrounding cells [25]. As a collagen receptor, DDR2 is involved with various diseases such as fibrotic diseases, arthritis, cancer, and atherosclerosis [5].

In the current study, we found that DDR2 was present in atherosclerotic plaques of various animal models, but DDR2 immunoreactivity did not totally overlap with macrophages and VSMCs. As previously described, DDR2 is highly expressed in VSMCs and also found in activated endothelial cells [26]. Based our observation, DDR2 expression is inclined to localize around collagens and fibrous caps. More importantly, for the first time, we have reported that DDR2 is highly expressed in carotid atherosclerotic plaques of human and is distributing around the fatty core of atherosclerosis and overlapping with collagen fibers. Combined to these findings, DDR2 expression in the specific regions of atherosclerotic plaque may be somehow upregulated by collagen or other proatherosclerotic factors, and the underlying mechanism needs to be addressed by the further studies. Given that ox-LDL is mainly a proatherosclerotic factor and abundant to the fat core, a question arises of whether ox-LDL can induce the expression of DDR2. Interestingly, the current research proves that ox-LDL can induce

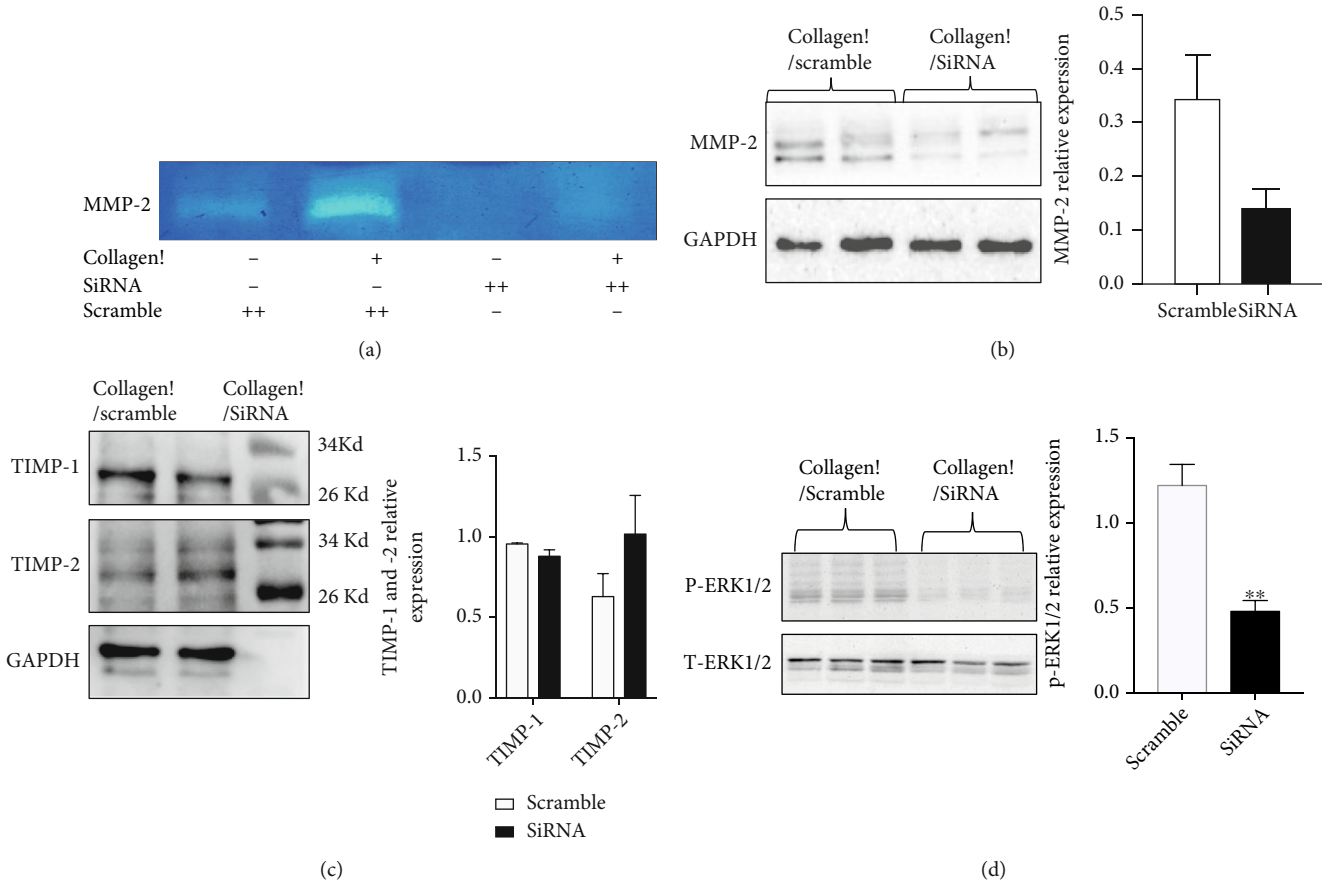

Figure 6: Effect of knockdown of DDR2 on the activity and expression of MMP-2 in VSMCs. The activity of MMP-2 was assessed by zymography (a). DDR2 protein expression was analyzed and quantified by western blotting (b). TIMP-1 and TIMP-2 were detected and quantified by western blotting (c). p-ERK1/2 protein expression was analyzed and quantified by western blotting (d). Data are expressed as the mean ± standard error. $^{*}P < 0.05$ vs. the scramble RNA-treated group.

upregulation of DDR2 in a dose-dependent manner, whereas such upregulation is neutralized by the inhibition of JNK, MAPK48, and ERK, showing that the MAPK pathway may be involved with ox-LDL-induced DDR2 expression. In the vasculature, SMCs not only are responsible for the secretion of collagen fibers but also express collagen receptors to interact with ECM, regulating their own proliferation, differentiation, and migration [27]. Accordingly, we speculate that DDR2 may affect the physiological functions of VSMCs, especially when these cells are stimulated by proatherosclerotic factors. As shown in our results, VSMCs with downregulation of DDR2 display reduced differentiation and migration. Considering that VSMC infiltration in intima is a vital process of atherogenesis, DDR2 could be a mediator to regulate atherosclerotic progression [3]. Notably, given that this depends on the secretion of MMPs, another question has been raised as to whether DDR2 also regulates MMPs [28]. Indeed, MMPs can almost determine the fate of atherosclerotic plaques because MMP-mediated breakdown of ECM is a typical feature of an unstable plaque [29]. In pathological conditions, excessive ECM also stimulates VSMCs to degrade ECM as a negative feedback regulation. As a natural ligand against DDRs, collagen I can activate DDR2 in VSMCs to produce MMPs for the degradation of ECM [30]. We observed that collagen I indeed promotes VSMCs to produce various types of MMPs, especially MMP-2 and MMP-3. However, collagen I-induced expression of MMPs can be completely neutralized by knockdown of DDR2, suggesting that DDR2 plays a pivotal role in the degradation of ECM. Of note, since MMP-2 expression is dramatically affected by the knockdown of DDR2, a causal relationship between DDR2 and MMP-2 is shown in the current study. Increased MMPs do not necessarily have enzymatic activity because MMPs are not only initially synthesized as inactive state of zymogens but are also inhibited by specific endogenous inhibitors such as metalloproteinases [31]. Thus, only if DDR2 mediates the activity of MMPs can this collagen receptor be made sure to be involved with vulnerable plaques. Interestingly, decreased DDR2 indeed also inhibits the protein expression and activity of MMP-2, indicating that the effect of MMP-2 in VSMCs may proceed via collagen I-activated DDR2. With regard to the previous studies, a mechanism is suggested that collagen I causes the expression and phosphorylation of DDR2 and finally upregulates MMP-2 expression via ERK1/2 signaling [6, 32]. Accordingly, we have confirmed that phosphorylation of ERK1/2 is suppressed by inhibition of DDR2 in VSMCs, indicating that ERK1/2

may be involved with expression and activity of MMP-2. Of note, this result needs to be proven by more experiments. Moreover, we did not find pro-MMP-2, pro-MMP-9, and MMP-9 in the zymography, which did not exclude the possible regulation of activated DDR2 to other MMPs.

In conclusion, we found high expression of DDR2 in atherosclerotic plaques of human and various animal models, and DDR2 in VSMCs was involved with collagen I-induced secretion of MMP-2, suggesting that the clinical role of DDR2 in cardiovascular disease should be elucidated in further experiments. Owing to the proatherosclerotic condition, an abundance of DDR2 is present in the atherosclerotic plaques of humans and various animal models; furthermore, excessive ECM such as collagen I may also activate DDR2 to produce MMP-2 for the degradation of ECM, which is ultimately involved in the ethology of unstable atherosclerotic plaques. Once this mechanism is clarified, DDR2 may become a novel target for developing new therapeutic strategy for the control of unstable atherosclerotic plaques.

Abbreviations

DDR2: Discoidin domain-containing receptor 2
VSMCs: Smooth muscle cells
MMPs: Metalloproteinases
CVD: Cardiovascular disease
ECM: Extracellular matrix
ApoE: Apolipoprotein E
siRNA: Small interfering RNA
MAPK: Mitogen-activated protein kinase
JNK: C-Jun N-terminal kinase
MEK: Extracellular-signal-regulated kinase.

Data Availability

The data used to support the findings of this study are available from the corresponding author upon request.

Disclosure

We have presented our data as a preprint [33].

Conflicts of Interest

The authors declare that they have no conflicts of interest.

Authors' Contributions

Qi Yu and Cangbao Xu designed this study. Qi Yu, Ruihai Liu, Ting Lian, and Hua Guan performed the cell experiment. Qi Yu, Juan Yang, Yuanyuan Cui, and Guangwei Zhang performed animal experiment and histological staining. Ruihai Liu and Fuqiang Liu collected the clinical specimen. Ahmed Bilal Waqar performed image analysis and interpretation. Qi Yu, Ahmed Bilal Waqar, and Ying Chen wrote this manuscript. All authors read and approved the final manuscript.

Acknowledgments

The present study was supported by the National Natural Science Foundation of China (81400328 and 81773795), Innovation Support Plan in Shaanxi Province of China (2020PT-003), and Research Foundation of Xi'an Medical University (2018XNRC02 and 2018PT23).

References

[1] N. Townsend, L. Wilson, P. Bhatnagar, K. Wickramasinghe, M. Rayner, and M. Nichols, "Cardiovascular disease in Europe: epidemiological update 2016," *European Heart Journal*, vol. 37, no. 42, pp. 3232–3245, 2016.

[2] P. Lacolley, V. Regnault, A. Nicoletti, Z. Li, and J. B. Michel, "The vascular smooth muscle cell in arterial pathology: a cell that can take on multiple roles," *Cardiovascular Research*, vol. 95, no. 2, pp. 194–204, 2012.

[3] D. A. Chistiakov, A. N. Orekhov, and Y. V. Bobryshev, "Vascular smooth muscle cell in atherosclerosis," *Acta Physiologica*, vol. 214, no. 1, pp. 33–50, 2015.

[4] E. Adiguzel, P. J. Ahmad, C. Franco, and M. P. Bendeck, "Collagens in the progression and complications of atherosclerosis," *Vascular Medicine*, vol. 14, no. 1, pp. 73–89, 2009.

[5] C. M. Borza and A. Pozzi, "Discoidin domain receptors in disease," *Matrix Biology*, vol. 34, pp. 185–192, 2014.

[6] B. Poudel, Y. M. Lee, and D. K. Kim, "DDR2 inhibition reduces migration and invasion of murine metastatic melanoma cells by suppressing MMP2/9 expression through ERK/NF- B pathway," *Acta Biochimica et Biophysica Sinica*, vol. 47, no. 4, pp. 292–298, 2015.

[7] N. Ferri, N. O. Carragher, and E. W. Raines, "Role of Discoidin Domain Receptors 1 and 2 in Human Smooth Muscle Cell-Mediated Collagen Remodeling: Potential Implications in Atherosclerosis and Lymphangioleiomyomatosis," *The American Journal of Pathology*, vol. 164, no. 5, pp. 1575–1585, 2004.

[8] E. Olaso, J. P. Labrador, L. Wang et al., "Discoidin Domain Receptor 2 Regulates Fibroblast Proliferation and Migration through the Extracellular Matrix in Association with Transcriptional Activation of Matrix Metalloproteinase-2∗," *The Journal of Biological Chemistry*, vol. 277, no. 5, pp. 3606–3613, 2002.

[9] Q. Yu, Y. Li, A. B. Waqar et al., "Temporal and quantitative analysis of atherosclerotic lesions in diet-induced hypercholesterolemic rabbits," *Journal of Biomedicine & Biotechnology*, vol. 2012, Article ID 506159, 7 pages, 2012.

[10] G. Zhang, C. Li, N. Zhu et al., "Sex differences in the formation of atherosclerosis lesion in apoE$^{-/-}$mice and the effect of 17β-estrodiol on protein S-nitrosylation," *Biomedicine & Pharmacotherapy*, vol. 99, pp. 1014–1021, 2018.

[11] Q. Yu, R. Liu, L. Han et al., "Dietary restriction slightly affects glucose homeostasis and delays plasma cholesterol removal in rabbits with dietary lipid lowering," *Applied Physiology, Nutrition, and Metabolism*, vol. 43, no. 10, pp. 996–1002, 2018.

[12] Y. Chen, Y. Qi, and X. Cang-Bao, "A convenient method for quantifying collagen fibers in atherosclerotic lesions by ImageJ software," *International Journal of Clinical and Experimental Medicine*, vol. 10, no. 10, pp. 14904–14910, 2017.

[13] L. Xu, J. T. Liu, K. Li, S. Y. Wang, and S. Xu, "Genistein inhibits Ang II-induced CRP and MMP-9 generations via the ER-p38/

ERK1/2-PPARγ-NF-κB signaling pathway in rat vascular smooth muscle cells," *Life Sciences*, vol. 216, pp. 140–146, 2019.

[14] S. Chen, Y. Ding, W. Tao, W. Zhang, T. Liang, and C. Liu, "Naringenin inhibits TNF-α induced VSMC proliferation and migration via induction of HO-1," *Food and Chemical Toxicology*, vol. 50, no. 9, pp. 3025–3031, 2012.

[15] B. Zheng, M. Bernier, X. H. Zhang et al., "miR-200c-SUMOylated KLF4 feedback loop acts as a switch in transcriptional programs that control VSMC proliferation," *Journal of Molecular and Cellular Cardiology*, vol. 82, pp. 201–212, 2015.

[16] C. Y. Wu, Z. H. Tang, L. Jiang, X. F. Li, Z. S. Jiang, and L. S. Liu, "PCSK9 siRNA inhibits HUVEC apoptosis induced by ox-LDL via Bcl/Bax-caspase9-caspase3 pathway," *Molecular and Cellular Biochemistry*, vol. 359, no. 1-2, pp. 347–358, 2012.

[17] K. G. Shyu, Y. M. Chao, B. W. Wang, and P. Kuan, "Regulation of discoidin domain receptor 2 by cyclic mechanical stretch in cultured rat vascular smooth muscle cells," *Hypertension*, vol. 46, no. 3, pp. 614–621, 2005.

[18] J. Marshall, "Transwell® Invasion Assays," in *Cell Migration*, pp. 97–110, Springer, 2011.

[19] M. Z. Mercure, R. Ginnan, and H. A. Singer, "CaM kinase II delta2-dependent regulation of vascular smooth muscle cell polarization and migration," *American Journal of Physiology Cell Physiology*, vol. 294, no. 6, pp. C1465–C1475, 2008.

[20] G. Zhang, Y. Chen, A. BilalWaqar et al., "Quantitative analysis of rabbit coronary atherosclerosis. Practical techniques utilizing open-source software," *Analytical and Quantitative Cytopathology and Histopathology*, vol. 37, no. 2, pp. 115–122, 2015.

[21] Q. Yu, Z. Liu, A. B. Waqar et al., "Effects of antisense oligonucleotides against C-reactive protein on the development of atherosclerosis in WHHL rabbits," *Mediators of Inflammation*, vol. 2014, Article ID 979132, 8 pages, 2014.

[22] Q. Yu, Y. Wang, Y. Yu et al., "Expression of TRPV1 in rabbits and consuming hot pepper affects its body weight," *Molecular Biology Reports*, vol. 39, no. 7, pp. 7583–7589, 2012.

[23] J. Liang, E. Liu, Y. Yu et al., "Macrophage metalloelastase accelerates the progression of atherosclerosis in transgenic rabbits," *Circulation*, vol. 113, no. 16, pp. 1993–2001, 2006.

[24] R. Virmani, A. P. Burke, A. Farb, and F. D. Kolodgie, "Pathology of the unstable plaque," *Progress in Cardiovascular Diseases*, vol. 44, no. 5, pp. 349–356, 2002.

[25] W. F. Vogel, R. Abdulhussein, and C. E. Ford, "Sensing extracellular matrix: an update on discoidin domain receptor function," *Cellular Signalling*, vol. 18, no. 8, pp. 1108–1116, 2006.

[26] K. Bibbins-Domingo, G. M. Chertow, P. G. Coxson et al., "Projected effect of dietary salt reductions on future cardiovascular disease," *The New England Journal of Medicine*, vol. 362, no. 7, pp. 590–599, 2010.

[27] B. Leitinger and E. Hohenester, "Mammalian collagen receptors," *Matrix Biology*, vol. 26, no. 3, pp. 146–155, 2007.

[28] V. A. Belo, D. A. Guimaraes, and M. M. Castro, "Matrix metalloproteinase 2 as a potential mediator of vascular smooth muscle cell migration and chronic vascular remodeling in hypertension," *Journal of Vascular Research*, vol. 52, no. 4, pp. 221–231, 2015.

[29] I. S. Murashov, A. M. Volkov, G. M. Kazanskaya et al., "Immunohistochemical features of different types of unstable atherosclerotic plaques of coronary arteries," *Bulletin of Experimental Biology and Medicine*, vol. 166, no. 1, pp. 102–106, 2018.

[30] S. Jia, M. Agarwal, J. Yang, J. C. Horowitz, E. S. White, and K. K. Kim, "Discoidin domain receptor 2 signaling regulates fibroblast apoptosis through PDK1/Akt," *American Journal of Respiratory Cell and Molecular Biology*, vol. 59, no. 3, pp. 295–305, 2018.

[31] V. A. Myasoedova, D. A. Chistiakov, A. V. Grechko, and A. N. Orekhov, "Matrix metalloproteinases in pro-atherosclerotic arterial remodeling," *Journal of Molecular and Cellular Cardiology*, vol. 123, pp. 159–167, 2018.

[32] B. Xie, W. Lin, J. Ye et al., "DDR2 facilitates hepatocellular carcinoma invasion and metastasis via activating ERK signaling and stabilizing SNAIL1," *Journal of Experimental & Clinical Cancer Research*, vol. 34, no. 1, p. 101, 2015.

[33] Q. Yu, L. Ruihan, C. Ying et al., *Research Square*, 2021.

Hindawi
Oxidative Medicine and Cellular Longevity
Volume 2021, Article ID 5945101, 22 pages
https://doi.org/10.1155/2021/5945101

Research Article

Intraperitoneal Lavage with *Crocus sativus* Prevents Postoperative-Induced Peritoneal Adhesion in a Rat Model: Evidence from Animal and Cellular Studies

Pouria Rahmanian-Devin,[1] Hassan Rakhshandeh,[2] Vafa Baradaran Rahimi,[2] Zahra Sanei-Far,[2] Maede Hasanpour,[3] Arghavan Memarzia,[4] Mehrdad Iranshahi,[3] and Vahid Reza Askari[5,6,7]

[1]*Department of Pharmaceutics, School of Pharmacy, Mashhad University of Medical Sciences, Mashhad, Iran*
[2]*Pharmacological Research Center of Medicinal Plants, Mashhad University of Medical Sciences, Mashhad, Iran*
[3]*Biotechnology Research Center, Pharmaceutical Technology Institute, Mashhad University of Medical Sciences, Mashhad, Iran*
[4]*Department of Physiology, Faculty of Medicine, Mashhad University of Medical Sciences, Mashhad, Iran*
[5]*Applied Biomedical Research Center, Mashhad University of Medical Sciences, Mashhad, Iran*
[6]*Department of Pharmaceutical Sciences in Persian Medicine, School of Persian and Complementary Medicine, Mashhad University of Medical Sciences, Mashhad, Iran*
[7]*Department of Persian Medicine, School of Persian and Complementary Medicine, Mashhad University of Medical Sciences, Mashhad, Iran*

Correspondence should be addressed to Vahid Reza Askari; askariv@mums.ac.ir

Received 31 August 2021; Revised 15 November 2021; Accepted 26 November 2021; Published 16 December 2021

Academic Editor: Xun Cui

Postoperative peritoneal adhesions are considered the major complication following abdominal surgeries. The primary clinical complications of peritoneal adhesion are intestinal obstruction, infertility, pelvic pain, and postoperative mortality. In this study, regarding the anti-inflammatory and antioxidant activities of *Crocus sativus,* we aimed to evaluate the effects of *Crocus sativus* on the prevention of postsurgical-induced peritoneal adhesion. Male Wistar-Albino rats were used to investigate the preventive effects of *C. sativus* extract (0.5%, 0.25% and 0.125% *w*/*v*) against postsurgical-induced peritoneal adhesion compared to pirfenidone (PFD, 7.5% *w*/*v*). We also investigated the protective effects of PFD (100 μg/ml) and *C. sativus* extract (100, 200, and 400 μg/ml) in TGF-β1-induced fibrotic macrophage polarization. The levels of cell proliferation and oxidative, antioxidative, inflammatory and anti-inflammatory, fibrosis, and angiogenesis biomarkers were evaluated both *in vivo* and *in vitro* models. *C. sativus* extract ameliorates postoperational-induced peritoneal adhesion development by attenuating oxidative stress [malondialdehyde (MDA)]; inflammatory mediators [interleukin- (IL-) 6, tumour necrosis factor- (TNF-) α, and prostaglandin E_2 (PGE_2)]; fibrosis [transforming growth factor- (TGF-) β1, IL-4, and plasminogen activator inhibitor (PAI)]; and angiogenesis [vascular endothelial growth factor (VEGF)] markers, while propagating antioxidant [glutathione (GSH)], anti-inflammatory (IL-10), and fibrinolytic [tissue plasminogen activator (tPA)] markers and tPA/PAI ratio. In a cellular model, we revealed that the extract, without any toxicity, regulated the levels of cell proliferation and inflammatory (TNF-α), angiogenesis (VEGF), anti-inflammatory (IL-10), M1 [inducible nitric oxide synthase (iNOS)] and M2 [arginase-1 (Arg 1)] biomarkers, and iNOS/Arg-1 ratio towards antifibrotic M1 phenotype of macrophage, in a concentration-dependent manner. Taken together, the current study indicated that *C. sativus* reduces peritoneal adhesion formation by modulating the macrophage polarization from M2 towards M1 cells.

1. Introduction

Postoperative peritoneal adhesions are considered the major complication after abdominal surgery. Peritoneal adhesion is an abnormal connective tissue that occurs between two tissues that have been damaged during the surgery [1, 2]. The peritoneum gets harmed and forms a temporary matrix during the surgery. After several hours, this provisional matrix becomes a clot, which can be destroyed by various factors such as macrophages and fibrinolysin enzymes.

Following the clot formation after 72 hours, the fibroblasts of the underlying tissues migrate into the clot and provide a field for forming sticky tissue [3, 4]. It has been emphasised that inflammation, free radicals, hypoxia, coagulation, and fibrinolysis are the main pathophysiological reasons responsible for forming peritoneal adhesion [2, 5].

Plasminogen activator (PA) is a protease that converts plasminogen into plasmin and prevents mesothelial cell adhesion [3]. Numerous inflammatory cytokines are released following the peritoneal injury, such as interferon-gamma (IFN-γ), interleukin-4 (IL-4), IL-10, IL-6, tumour necrosis factor-alpha (TNF-α), and prostaglandin E2 (PGE-2) [6–9]. These inflammatory cytokines play an essential role in the development of peritoneal adhesion. Transforming growth factor-beta (TGF-β) is expressed by adhesion fibroblasts and mesothelial cells, which lead to adhesion formation and fibrosis [7, 10]. Additionally, vascular endothelial growth factor (VEGF) is another important marker in angiogenesis, wound healing, and adhesion formation [2, 11].

The surgical technique is the first method for adhesion treatment; however, it is insufficient alone [12]. Other therapeutic approaches have been studied, such as barrier therapy [13, 14] and gene therapy [15]. However, there is still no approved method for the treatment or prevention of adhesion, although a high prevalence of postoperative adhesions.

Crocus sativus (*C. sativus*), popularly named *C. sativus*, is a small plant belonging to Iridaceae. Crocin, crocetin, and safranal are the major ingredients of *C. sativus* [16]. Several pharmacological properties of *C. sativus* have been reported, including the antioxidant [17, 18], anticancer, anti-inflammatory [19, 20], anti-ischemia, and cardioprotective [21, 22] effects.

To our knowledge, there is no study evaluating the protective effects of *C. sativus* extract on preventing postoperative intra-abdominal adhesions. Therefore, in the present study, we aimed to determine the anti-inflammatory and antioxidant effects of *Crocus sativus* on the formation and prevention of postoperative abdominal adhesions in a rat model of peritoneal adhesion.

2. Material and Methods

2.1. Drugs and Chemicals. Ethanol, methanol, acetonitrile, formic acid, dimethyl sulfoxide, ammonium chloride, HCl, and dexamethasone were purchased from Sigma®, USA. Ketamine and xylazine were obtained from ChemiDarou®, Iran. The injectable normal saline serum was also prepared from Samen®, Iran. Furthermore, enzyme-linked immunosorbent assay (ELISA) kits of IL-4, IL-10, IL-6, *TN*F-α, PGE_2, TGF-β, tissue plasminogen activator (tPA), and plasminogen activator inhibitor (PAI) and VEGF were purchased from Bender Med®, Germany. Dulbecco's modified Eagle's medium/F12 (DMEM/F12) culture media, fetal bovine serum (FBS), penicillin plus streptomycin (pen/strep), dimethyl sulfoxide (DMSO), and other chemicals used were of cell culture and analytical grade from Sigma-Aldrich (St. Louis, MO, USA). Recombinant mouse TGF-β1 (5231LC) was obtained from Cell Signaling Technology, Inc. The levels of malondialdehyde (MDA) as an oxidative marker and glutathione (GSH) as an antioxidative marker were measured using commercially available biochemistry kits (ZellBio®, Germany).

2.2. Preparation of C. sativus Extract. C. *sativus* was prepared from *C. sativus* farms of Qaen ($33^\circ 43' 33.02'' N\ 59^\circ 11' 21.65''$ E, South Khorasan, Iran) and identified by the herbarium of Ferdowsi University of Mashhad (herbarium No. 293-0303-1). The 70% *v*/*v* hydroethanolic extract of C. *sativus* was prepared using the maceration method as described previously [23]. Briefly, 10 g of its ground petal stigma was incubated with 400 ml of 70% *v*/*v* ethanol in a macerated extractor for 72 h. The prepared extract was dried in a rotatory evaporator and stored at -20°C until use.

2.3. High-Performance Liquid Chromatography- (HPLC-) Mass Spectrometry (MS) Apparatus and the Extracted Analysis. The LC-MS analysis was performed in an AB SCIEX QTRAP (Shimadzu) liquid chromatography coupled with a triple quadrupole Mass Spectrometer. Liquid chromatography separation was performed on a Supelco C18 (15 mm × 2.1 mm × 3 μm) column. MS analysis was carried out in both negative and positive modes of ionisation to monitor as many ions as possible and to ensure that the most significant number of metabolites extracted from the *C. sativus* sample was detected. The analysis was done at a flow rate of 0.2 ml/min. The gradient analysis started with 100% of 0.4% aqueous formic acid, isocratic conditions were maintained for 1 min, and then a 14 min linear gradient to 40% acetonitrile with 0.4% formic acid was applied. From 14 to 35 min, the acidified acetonitrile was increased to 100%, followed by 5 min of 100% acidified acetonitrile and 5 min at the start conditions to reequilibrate the column. The mass spectra were acquired in a range of 100 to 1500 within the 45 minutes scan time. Mass feature extraction of the acquired LC-MS data and maximum detection of peaks was done using the MZmine analysis software package, version 2.3.

2.4. In Vivo Study

2.4.1. Animals. Seventy male Wistar-Albino rats weighing 250 ± 15 g (six weeks old) were purchased from the animal laboratory unit of Faculty of Medicine, Mashhad University of Medical Sciences, Mashhad, Iran. Rats were housed in separated standard cages and ventilated room with a 12/12 h natural light-dark cycle, 60 ± 3% humidity, and temperature of 21 ± 2°C. They had free access to food and taped water before and during the experiments. More appropriate hygiene was provided with continuous cleaning and removal

Table 1: Adhesion score categories according to Nair et al. [32].

Grades	Description of adhesive bands
0	The complete absence of adhesions
1	A single band of adhesion, between viscera or from viscera to the abdominal wall
2	Two bands, either between viscera or from viscera to the abdominal wall
3	More than two bands, between viscera or viscera to the abdominal wall or whole intestines forming a mass without being adherent to the abdominal wall
4	Viscera directly adherent to the abdominal wall, irrespective of number and extent of adhesive bands

of faeces and spilt feeds from cages daily. All animals received human care in compliance with institutional guidelines.

2.4.2. Surgical Procedure. The ethical committee approved all animal-related procedures based on the guidelines of animal experiments in Mashhad University of Medical Sciences (ethical approved code http://IR.MUMS.fm.REC.1395.950309, Approval Date: 2017-03-01). The surgical method was accomplished as previously described [2, 24, 25]. In summary, animals received 100 mg/kg of ketamine and 10 mg/kg of xylazine intraperitoneally (i.p.) for anaesthesia. Following the skin's shaving and disinfection with alcohol and iodine solution, a three-centimeter incision was carefully done to reach the abdominal cavity. For intra-abdominal adhesion induction in rats, the peritoneal abrasion method was performed as one side of the middle abdominal incision was gently abraded using a soft sterilised paper polisher until the cecum provided an opaque presentation with fine petechiae. Afterwards, the peritoneum and the injured area were washed by 2 ml of the extract or vehicle. After the intervention, the cecum was returned to the abdomen and abdomen wall then closed with 4-0 poly-gelatine suture. The procedure lasted to a maximum of 10 minutes. After surgery, rats were kept in their cages in the recovery room for seven days. All treatments were done by lavage in the abraded and whole surgical zone with a 2 ml syringe. Furthermore, all rats received a single dose of antibiotic cefazolin (300 mg/kg intramuscularly; i.m.) immediately after ending the surgery to prevent possible wound infection [26–28].

2.4.3. Experimental Groups. Seventy male Wistar rats were randomly divided into seven groups containing ten animals and grouped as follows:

(1) Group 1: normal—rats received neither surgical nor intervention procedures.

(2) Group 2: control—rats received surgical and peritoneal adhesion procedures without treatment.

(3) Group 3: vehicle—rats received surgical and peritoneal adhesion procedures and were treated with 2 ml of the vehicle (the vehicle was sterilised distilled water containing 5% v/v of tween 80 [2]).

(4) Group 4: pirfenidone (PFD)—rats received surgical and peritoneal adhesion procedures and were treated with 2 ml of the 7.5% *w*/*v* of PFD (approximately 600 mg/kg or 150 mg/animal [29–31]), as positive control and the antifibrotic agent [29–31].

(5) Groups 5, 6, and 7: C. sativus extracts (S)—rats received surgical and peritoneal adhesion procedures and were treated with 2 ml of either 0.125% *w*/*v*, 0. 25% *w*/*v*, or 0.5% *w*/*v* of the extract (approximately 12.5, 25, and 50 mg/kg, respectively); the concentrations were chosen based on our preliminarily experiment.

2.4.4. Assessment of the Macroscopic Adhesion Grade. On the seventh day after the surgery, rats underwent a second laparotomy. Thereafter, two independent researchers blind to the protocol assessed the adhesion grading using the score published by Nair et al. [32] (Table 1). Additionally, cecum and peritoneal lavage fluid were collected for the measurement of inflammatory, fibrotic, and oxidative biomarkers.

2.4.5. Histological Assessment. In the current experiment, paraffin-embedded histological sections were stained by Masson's trichrome staining to assess the extent and distribution of fibrosis in rats' peritoneal tissue as described in previous studies [33–35]. In this regard, after removing formalin and washing with distilled water three times, the tissues were transferred to different alcohol concentrations (50-100%) for some minutes. Tissue sections were observed with magnifications of 4x, 20x, and 40x using a Nikon E-1000 microscope (Japan) under bright-field optics.

2.4.6. Evaluation of Oxidative Parameters. The levels of MDA, as an oxidative marker, and GSH, as an antioxidative marker, were measured in the peritoneal fluid using biochemistry kits (ZellBio®, Germany) according to the manufacturer's manuals [36, 37].

2.4.7. Assessment of Inflammatory and Anti-Inflammatory Biomarkers. The levels of TNF-α, IL-6, and PGE_2, as inflammatory markers, and IL-4 and IL-10, as anti-inflammatory markers, were evaluated in peritoneal lavage fluid by ELISA kits (Bender Med®, Germany) according to the manufacturer's instruction [38, 39].

2.4.8. Evaluation of Fibrosis and Angiogenesis Biomarkers and Tissue Plasminogen Activator (tPA) and Plasminogen Activator Inhibitor (PAI). According to the manufacturer's instruction, the concentrations of fibrosis biomarkers (TGF-β) and angiogenesis marker (VEGF) of peritoneal fluid specimens were assessed by the relevant ELISA kits.

Table 2: Peak assignment of metabolites in the hydroethanol extract of *C. sativus* (*Crocus sativus* L.) using LC-MS in the negative mode.

Peak no.	Compound identification	t_R (min)	[M-1] (m/z)	Ref.
1	4-(α-D-glucopyranosyl)-2,6,6-trimethyl-1-cyclohexene-1-carboxaldehyde (picrocrocin)	35.3	375.2	[76]
2	Crocetin di-(β-D-gentibiosyl) ester	37.0	975.3	[77]
3	Crocetin (β-D-glucosyl)-(β-D-neapolitanosyl) ester	40.4	975.0	[77]
4	Crocin E	40.4	489.4	[76]
5	Crocetin	37.2	327.3	[78]
6	Dimethyl crocetin	28.8	355.3	[78]
7	Quercetin 3-orutinosylrhamnoside	29.4	755.7	[77]
8	Quercetin 3-O-rutinoside	29.8	609.6	[77]
9	Isorhamnetin-3-orutinosylrhamnoside	35.8	769.5	[78]
10	Narcissin	42.1	623.8	[78]
11	Nepetalic acid	35.2	183.1	[79]
12	Geranic acid	30.6	167.0	[79]
13	Dihydrojasmonic acid, methyl ester	32.7	225.0	[79]
14	Kaempferol 3-glucoside	3.1	447.8	[77]
15	Angoluvarin	16.5	483.42	[79]
16	Isococculidine	5.1	284.6	[79]
17	4-Apiosyl-glucoside	1.1	593.3	[79]

Table 3: Peak assignment of metabolites in the hydroethanol extract of *C. sativus* (*Crocus sativus* L.) using LC-MS in the positive mode.

Peak no.	Compound identification	t_R (min)	[M+1] (m/z)	Ref.
1	Cinnamyl isovalerate	35.0	219.12	[79]
2	Crocin E	36.0	491.7	[78]
3	Crocetin	44.1	329.4	[78]
4	Isorhamnetin-3-O-β-D-glucopyranoside	38.0	479.7	[78]
5	Kaempferol 3-sophoroside-7-glucoside	42.8	772.2	[79]
6	Crocusatin	9.6	185.4	[80]
7	Taxifolin 7-O-hexoside	24.2	466.3	[80]
8	Kaempferol 3-O-hexoside-7-O-(acetyl)-hexoside	25.7	653.1	[80]
9	Sinapic acid	32.8	224.8	[80]
10	Adenosine	38.0	268.0	[80]
11	Tamarixetin 3-O-bihexoside	36.2	641.1	[80]
12	Rhamnetin	30.8	317.1	[79]
13	Naringenin	33.3	273.3	[79]
14	Tamarixetin O-kaempferol biflavonoid hexoside	23.1	747.1	[78, 80]
15	Karatavigenin B	24.3	569.3	[79]
16	Anhalonidine	28.0	224.1	[79]
17	Baicalein	30.9	271.2	[79]
18	4,6,8-Megastigmatriene	31.7	177.7	[79]

Additionally, according to the manufacturer's instruction, the levels of tPA, which digests fibrin substrates, and PAI were also evaluated in peritoneal lavage fluid by ELISA kits. Subsequently, the tPA/PAI ratio was calculated by dividing the level of tPA by PAI level. The levels of cytokines were reported as pg/mg protein.

2.5. In Vitro Study

2.5.1. Cell Culture Condition. Murine macrophage cell line, RAW 264.7, was purchased from Pasture Institute, Tehran, Iran. The cells were cultured in DMEM/F12 enriched with 10% v/v foetal bovine serum (FBS), 100 IU/ml penicillin, and 100 μg/ml streptomycin at 37°C in a humidified atmosphere with 5% v/v CO_2 [40].

2.5.2. Proliferation Assay. To investigate that *C. sativus* extract had no cytotoxicity and inhibitory effects on RAW 264.7 cells, the cells were cultured at a density of 3×10^3 cells/well in 96-flat well plates and incubated overnight [40]. Thereafter, the cells were incubated with different

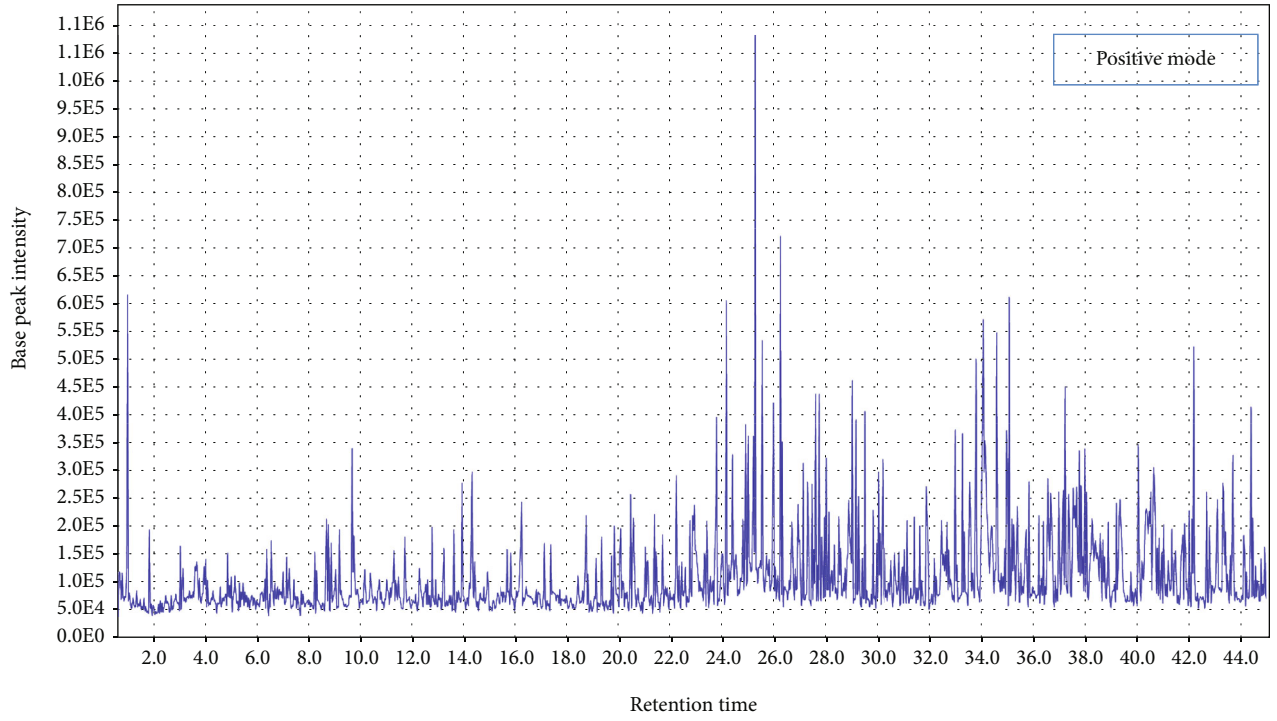

(a)

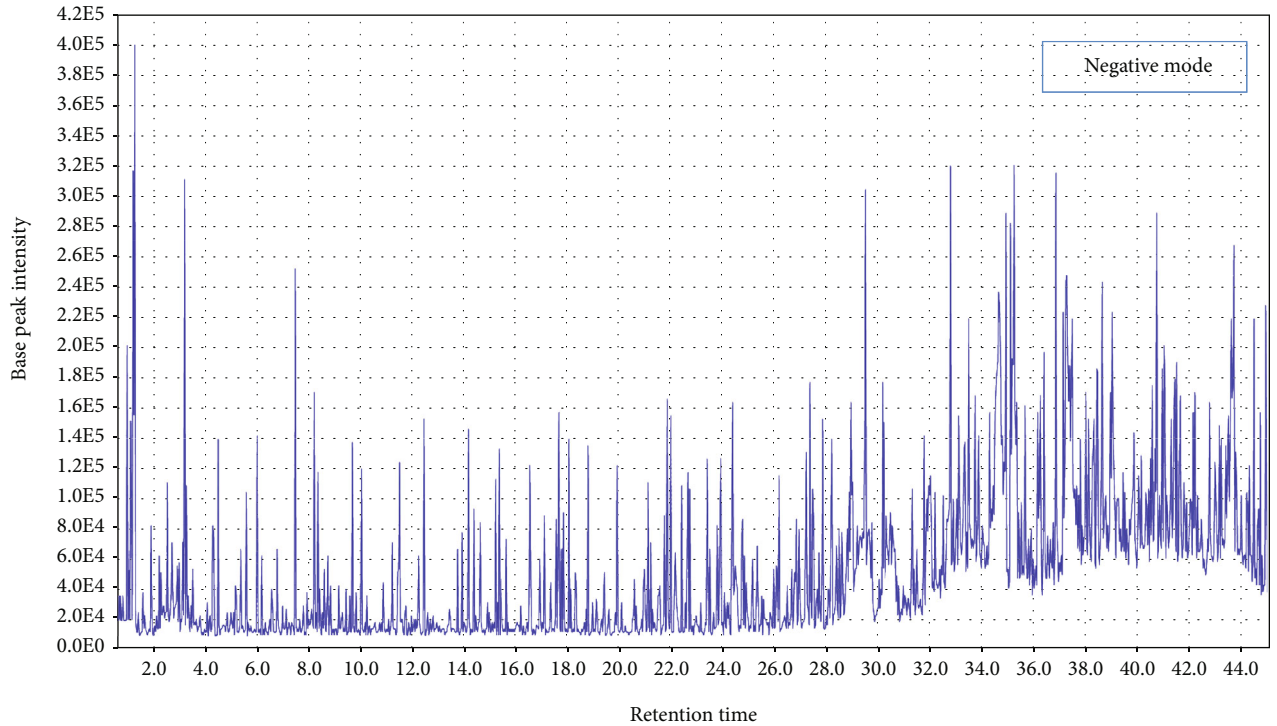

(b)

Figure 1: Continued.

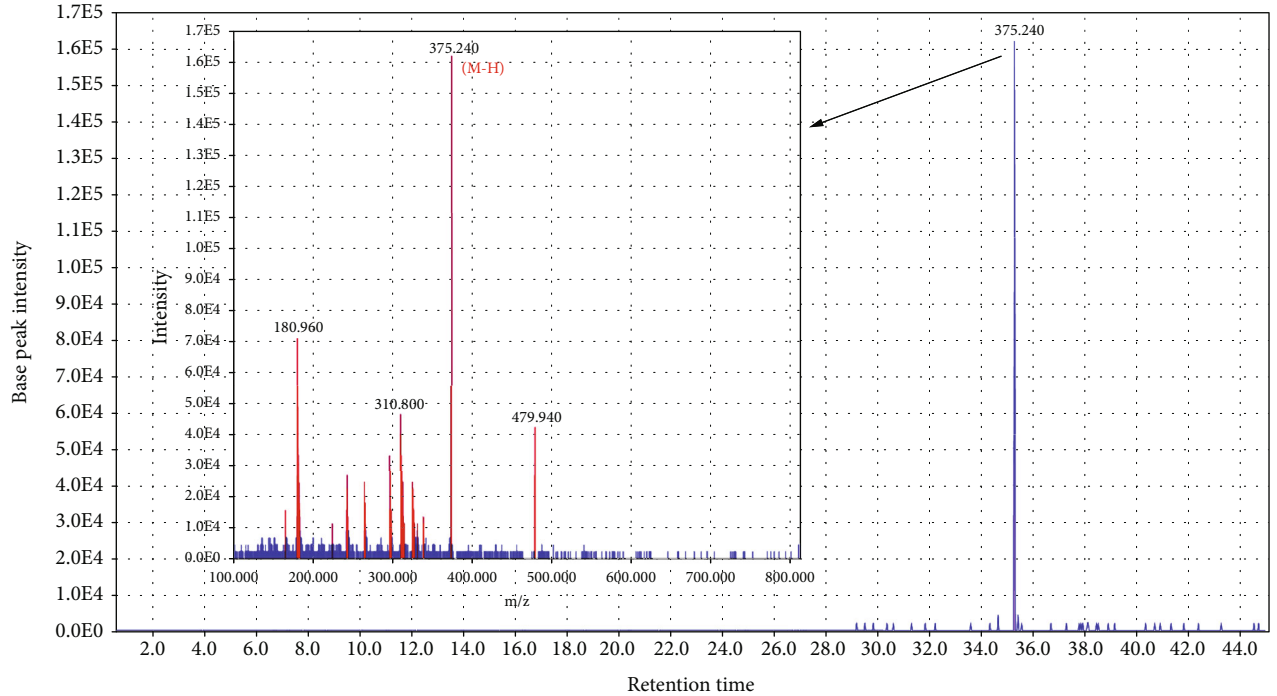

(c)

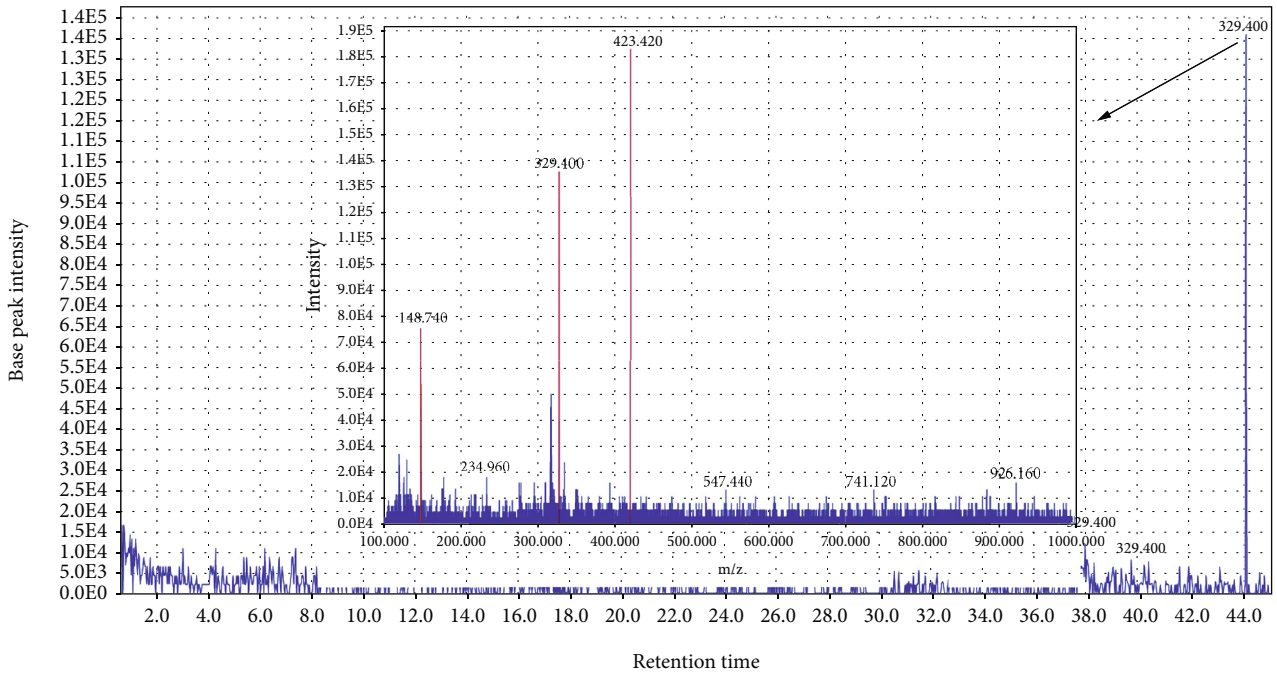

(d)

Figure 1: Continued.

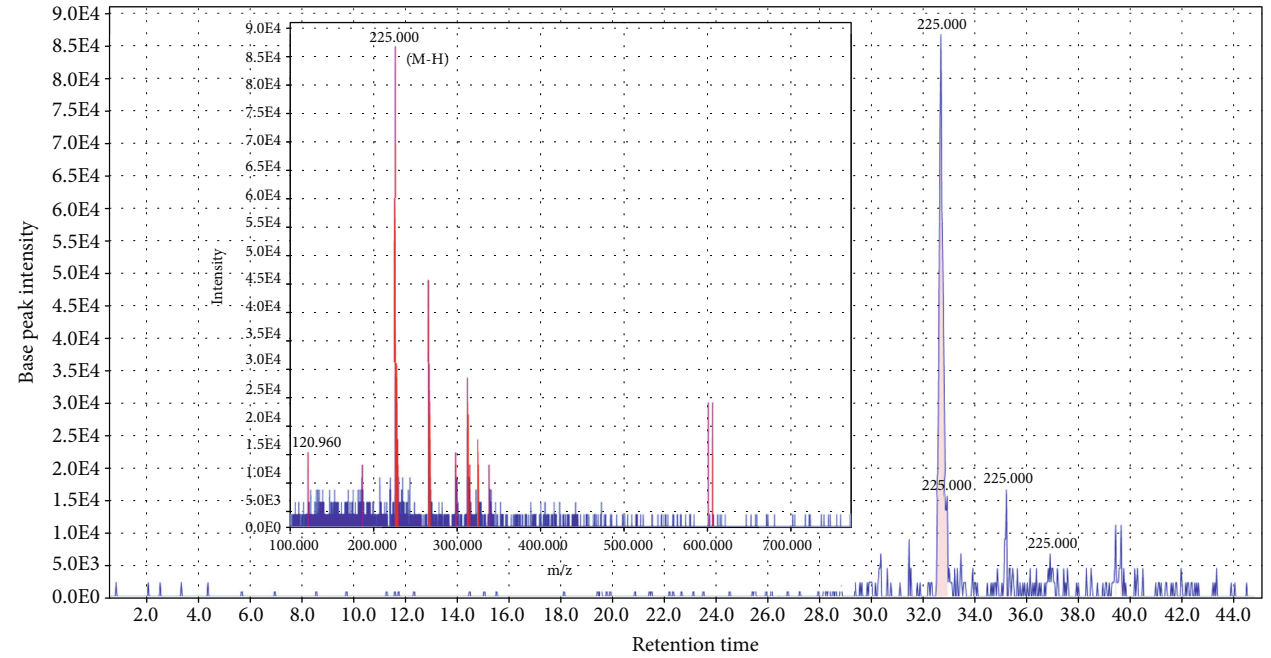

(e)

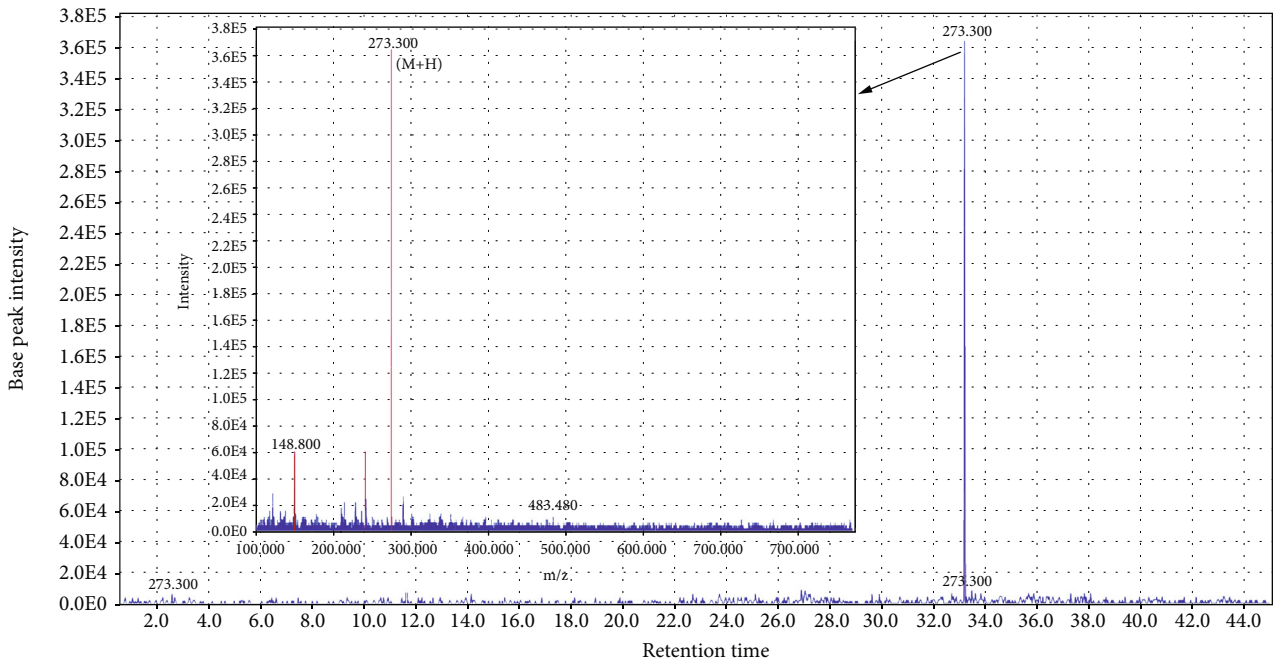

(f)

Figure 1: Continued.

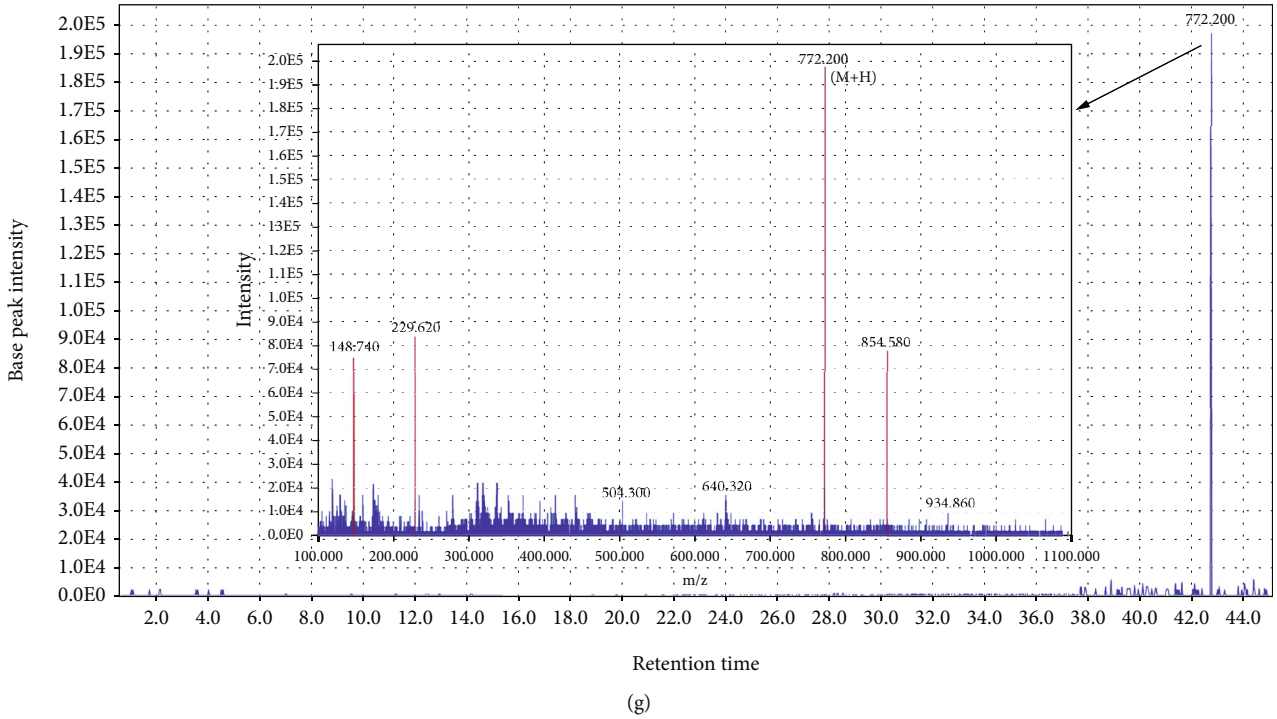

(g)

Figure 1: (a) The total ion chromatogram of *C. sativus* (*Crocus sativus* L.) using LC-MS in the positive mode. (b) The total ion chromatogram of *C. sativus* (*Crocus sativus* L.) using LC-MS in the negative mode. (c) Chromatogram of 4-(α-D-glucopyranosyl)-2, 6,6-trimethyl-1-cyclohexene-1-carboxaldehyde (picrocrocin), and corresponding mass adduct, [M-H], at *m*/*z* 375.2. (d) Chromatogram of dihydrojasmonic acid, methyl ester, and corresponding mass adduct, [M-H], at *m*/*z* 225.0. (e) Chromatogram of dihydrojasmonic acid, methyl ester and corresponding mass adduct, [M-H], at *m*/*z* 225.0. (f) Chromatogram of naringenin and corresponding mass adduct, [M +H], at *m*/*z* 273.3. (g) Chromatogram of Kaempferol 3-sophoroside-7-glucoside and corresponding mass adduct, [M+H], at *m*/*z* 772.2.

concentrations of *C. sativus* extract (100, 200, and 400 μg/ml, according to the preliminary evaluation), PFD (100 μg/ml, as a positive control group, [41]), or vehicle (contained 0.1% dimethyl sulfoxide, DMSO) for 48 h, at 37°C and 5% *v*/*v* CO_2.

In another set of experiments, we assessed the effects of different concentrations of *C. sativus* extract (100, 200, and 400 μg/ml, according to the preliminary evaluation), PFD (100 μg/ml, as a positive control group, [41]), or vehicle (contained 0.1% dimethyl sulfoxide, DMSO) in the presence of recombinant mouse TGF-β1 stimulation (20 ng/ml [42]) on cell proliferation. In this regard, the cells (3×10^3) were incubated with the extract, PFD, vehicle, or medium for 24 h and then coincubated with TGF-β1 (20 ng/ml [42]) for another 24 h, at 37°C and 5% *v*/*v* CO_2. Afterwards, cell proliferation was also assessed by the MTT method.

Finally, cell proliferation was assessed using the 3-(4,5-dimethylthiazol-2-yl)-2,5-diphenyl-2H-tetrazolium bromide (MTT) method. Briefly, 10 μl of MTT solution with a final concentration of 5 mg/ml was appended to each well to be incubated for 3 h. After discarding the medium culture (DMEM/F12), 100 μl of DMSO was used to dissolve the formed formazan crystals. The absorption of the 96-flat wells plate was recorded by ELISA reader (Awareness Inc., USA) at 570 nm and 620 nm [40, 43].

2.5.3. Assessment of Secretory Cytokines Levels and Intracellular Levels of iNOS and Arg-1. According to the manufacturer's instructions, the anti-inflammatory (IL-10) levels and inflammatory cytokine (TNF-α) and angiogenesis factor (VEGF) were measured by the ELISA-based method. The cells were cultured in 6-well plates (2×10^6 cells/each well) and incubated with different concentrations of *C. sativus* extract (100, 200, and 400 μg/ml, according to the preliminary evaluation), PFD (100 μg/ml, as a positive control group, [41]), or vehicle (contained 0.1% dimethyl sulfoxide, DMSO) in the presence of recombinant mouse TGF-β1 stimulation (20 ng/ml, providing M2 phenotype cells [42]) for 24 h and then coincubated with TGF-β1 (20 ng/ml [42]) for another 24 h, at 37°C in a 5% *v*/*v* CO_2 incubator. Finally, the supernatants were collected to measure the levels of cytokines. The levels of cytokines were reported as pg/mg protein. Moreover, the cells were collected and lysed using a lysis buffer and then homogenised (DIAX 100, Heidolph, Schwabach, Germany) on the cold water (0-4°C) for 2–3 min along with vortexing (every 30 sec). The samples were centrifuged at 12,000 g for 10 min at 4°C, and 50 μl of supernatants had then undergone an assessment. The levels of iNOS and Arg-1 were reported as ng/mg protein.

2.6. Statistical Analysis. Data were analysed using GraphPad Prism (version 6.01) software and presented according to the nature of parametric or nonparametric as the means ± SEM or median ± interquartile range, respectively. *P* values ≤ 0.001, 0.01, and 0.05 were statistically considered significant. For parametric data, one-way ANOVA was performed

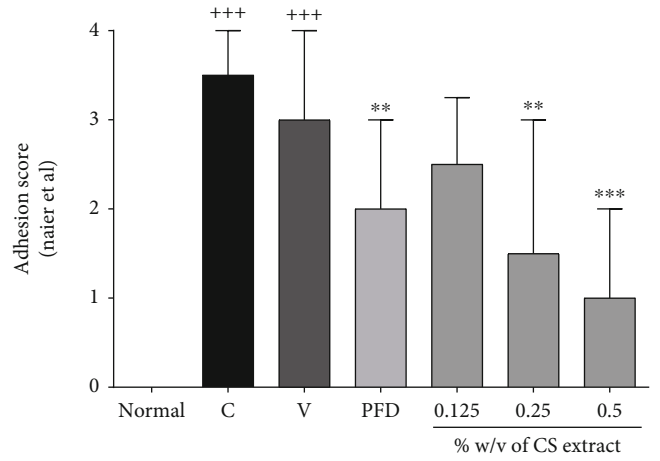

(a)

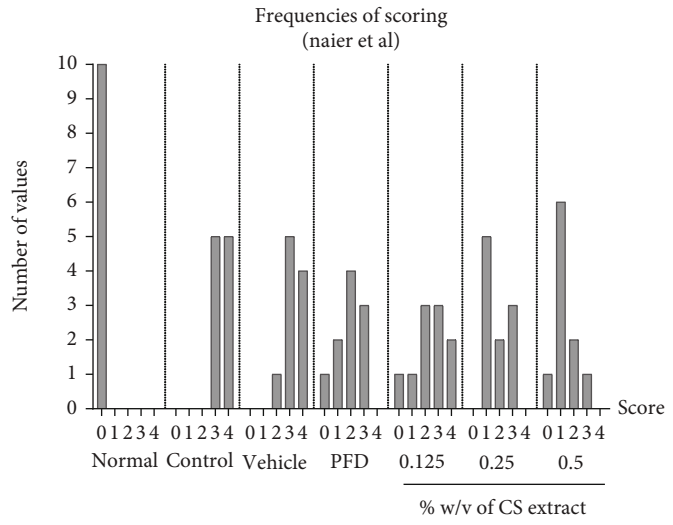

(b)

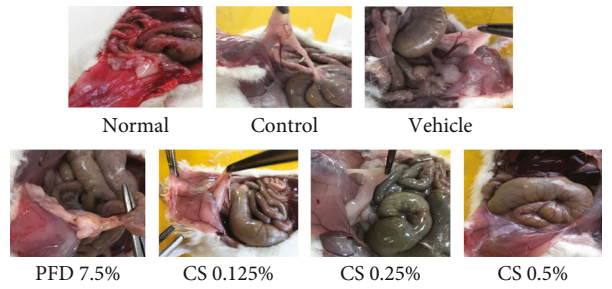

(c)

Figure 2: Continued.

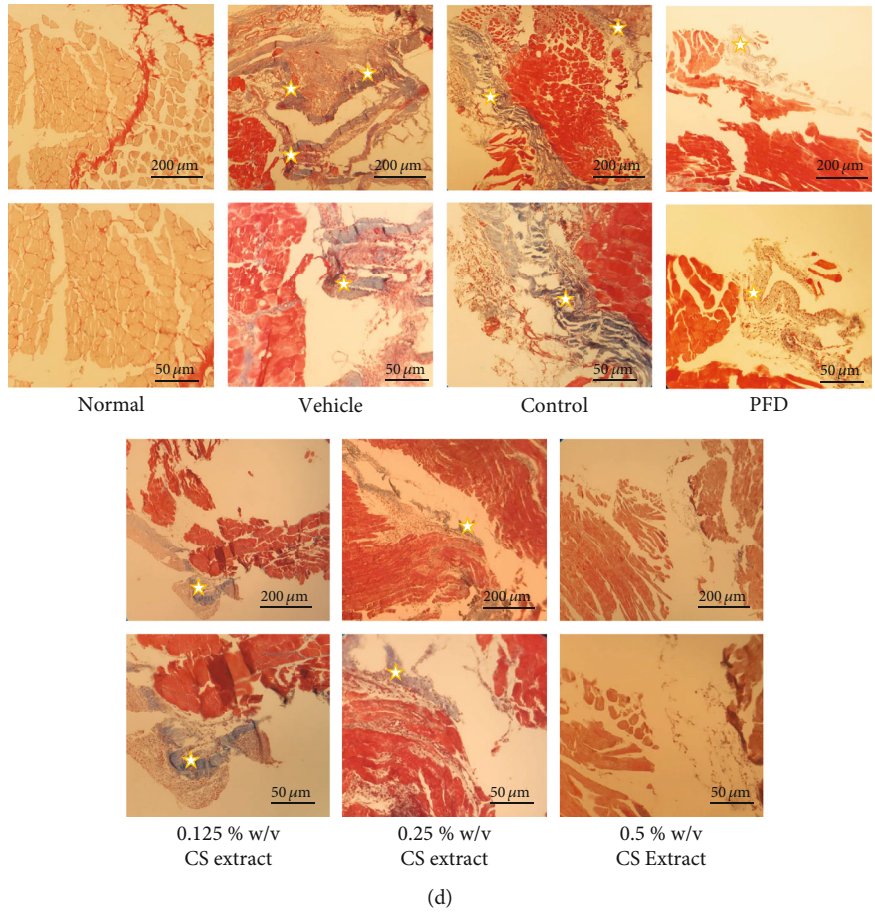

Figure 2: The effects of different concentrations of *C. sativus* (0.125, 0.25, and 0.5% *w*/*v*) and PFD (7.5% *w*/*v*) on adhesion score (a) and frequencies of scoring (b) following postoperational-induced peritoneal adhesion. (c) The images of adhesion bands in different groups. (d) The effects of different doses of *C. sativus* extract on adhesion formation and collagen deposition by histopathological evaluation using Masson's trichrome staining; blue colour intensities (marked with white stars) represent fibrosis and collagen deposition. Data were presented as the median ± interquartile range (IQR) ($n = 10$). $^{***}P < 0.001$ and $^{**}P < 0.01$ compared to the control group.

with the following Tukey's Kramer *post hoc* test. However, for nonparametric data (adhesion score), the Kruskal-Wallis test was done following Dunn's multiple comparisons posttest. The data and statistical analysis comply with the recommendations on experimental design, analysis [44], and data sharing and preclinical pharmacology presentation [45, 46].

3. Results

3.1. LC-MS Analysis and Characterisation of C. sativus L. Extract. Collectively, 35 compounds (in ESI+ and ESI−) were identified in the hydroethanolic extract of *C. sativus* L., including flavonoids and crocins (crocin and its derivatives). Data concerning the identification of the compounds are shown in Tables 2 and 3. The total ion chromatograms of *C. sativus* L. extract in both ESI+ and ESI− modes are shown in Figures 1(a) and 1(b), respectively. The MS spectral data were compared with the reported compounds in some previous literature. Figures 1(a)–1(f) are examples of extracted ion chromatograms from the total ion chromatogram and its related mass. Some flavonoids, including quercetin 3-orutinosylrhamnoside, quercetin 3-O-rutinoside, Kaempferol 3-glucoside, tamarixetin 3-O-bihexoside, rhamnetin, and naringenin, were detected in *C. sativus* L. extract. Apocarotenoids, including crocin, crocetin, and their derivatives, apart from imparting colours to *C. sativus*, also have antioxidant properties (40).

3.2. In Vivo Results

3.2.1. The Effect of C. sativus and PFD on Adhesion Score. The adhesion scores in both the control and vehicle groups were increased compared to those in the normal group ($P < 0.001$ for both cases, Figures 2(a)–2(c)). Treatment with PFD (7.5% *w*/*v*, $P < 0.01$) and *C. sativus* (0.25% *w*/*v*, $P < 0.01$, and 0.5% *w*/*v*, $P < 0.001$) significantly attenuated the levels of adhesion score compared to the control group (Figure 2(a)). The frequencies of adhesion score are indicated in Figure 2(b) according to the Nair et al. scoring system. Figure 2(c) shows the samples of the adhesion band in each group.

3.2.2. The Effects of PO Extract on Histopathological Alteration of Peritoneal Fibrosis. Our histopathological

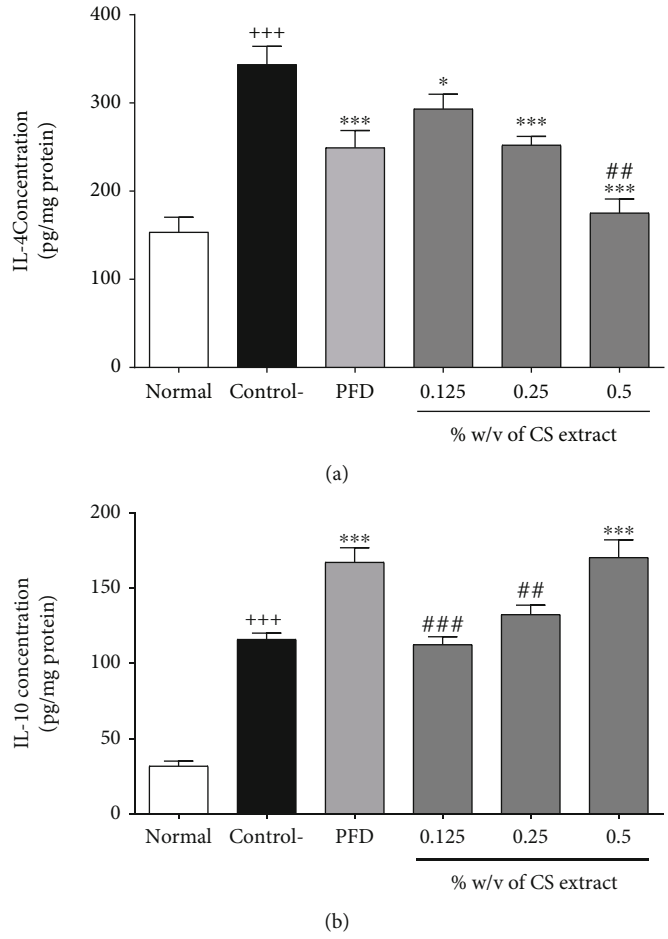

Figure 3: The effect of different concentrations of *C. sativus* (0.125, 0.25, and 0.5% *w*/*v*) and PFD (7.5% *w*/*v*) on IL-4 (a) and IL-10 (b) levels following the postoperational-induced peritoneal adhesion. Data were presented as the mean ± SEM ($n = 8$). $^{+++}P < 0.001$ compared to the normal group, $^{***}P < 0.001$ compared to the control group, and $^{\#\#\#}P < 0.001$ and $^{\#\#}P < 0.01$ compared to the PFD group. The lines represent a significant difference between the three *C. sativus* groups.

results showed the levels of tissue fibrosis and collagen deposition (blue colour) in both the vehicle and control groups (Figure 2(d)). On the contrary, the blue colour's intensities were notably lower in all doses of the extract groups and PFD as a positive control than the control group (Figure 2(d)).

3.2.3. The Effect of C. sativus and PFD on Anti-Inflammatory Biomarkers. Following the peritoneal adhesion induction, the levels of IL-4 and IL-10 were markedly increased in the control group compared to the normal group ($P < 0.001$ for both cases, Figures 3(a) and 3(b)). The level of IL-4 was notably diminished by treatment with either all concentrations of *C. sativus* (0.125% *w*/*v*, $P < 0.05$, 0.25% *w*/*v*, $P < 0.001$, and 0.5% *w*/*v*, $P < 0.001$, Figure 3(a)) or PFD (7.5% *w*/*v*, $P < 0.001$, Figure 3(a)) compared to the control group. The extract of *C. sativus* (0.5% *w*/*v*, $P < 0.01$, Figure 3(a)) significantly reduced IL-4 level in peritoneal lavage fluid than that in the PFD-treated group (7.5% *w*/*v*). Both PFD (7.5% *w*/*v*, $P < 0.001$, Figure 3(b)) and *C. sativus* (0.5% *w*/*v*, $P < 0.001$, Figure 3(b)) considerably increased the level of IL-10 in peritoneal lavage fluid.

3.2.4. The Effect of C. sativus and PFD on the Levels of tPA, PAI, and tPA/PAI Ratio. The levels of tPA ($P < 0.05$, Figure 4(b)) and tPA/PAI ratio ($P < 0.001$, Figure 4(c)) were diminished, but PAI level ($P < 0.001$, Figure 4(a)) was increased in the control group compared to the normal group. Treatment with *C. sativus* (0.125%*w*/*v*, $P < 0.05$, 0.5%*w*/*v*, $P < 0.001$, and 0.25%*w*/*v*, $P < 0.001$) and PFD (7.5%*w*/*v*, $P < 0.001$) significantly increased the tPA level in a concentration-dependent manner (Figure 4(b)). Treatment with a high concentration of *C. sativus* (0.5% *w*/*v*) and PFD (7.5% *w*/*v*) markedly decreased PAI level ($P < 0.01$ for both cases, Figure 4(a)) and significantly increased tPA/PAI ratio ($P < 0.001$ for both cases, Figure 4(c)) in the peritoneal lavage fluid compared to the control group.

3.2.5. The Effect of C. sativus and PFD on Fibrotic (TGF-β1) and Angiogenesis (VEGF) Parameters. The levels of TGF-β1 ($P < 0.001$, Figure 5(a)) and VEGF ($P < 0.001$, Figure 5(a)) were significantly increased in the control group compared to the normal group. Two higher concentrations of *C. sativus* (0.25% *w*/*v*, $P < 0.001$, and 0.5% *w*/*v*, $P < 0.001$)

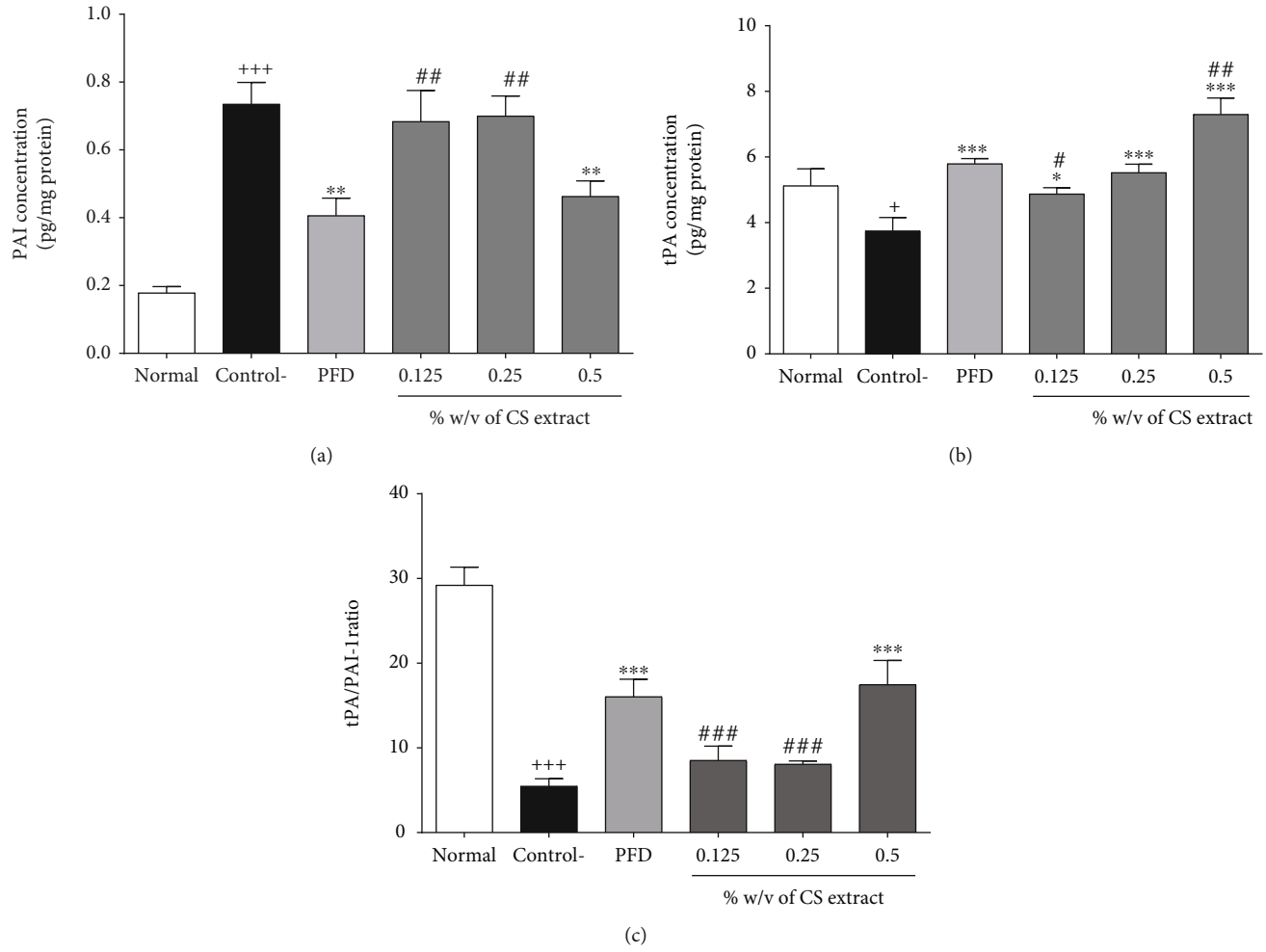

Figure 4: The effect of different concentrations of *C. sativus* (0.125, 0.25, and 0.5% *w*/*v*) and PFD (7.5% *w*/*v*) on PIA (a), tPA (b), and tPA/PAI ratio (c) levels following post-operational-induced peritoneal adhesion. Data were presented as the mean ± SEM ($n = 8$). $^{+++}P < 0.001$ and $P < 0.01$ compared to the normal group, $^{***}P < 0.001$ to $^{*}P < 0.05$ compared to the control group, and $^{\#\#\#}P < 0.001$ to $^{\#}P < 0.05$ compared to the PFD group. The lines represent a significant difference between the three *C. sativus* groups.

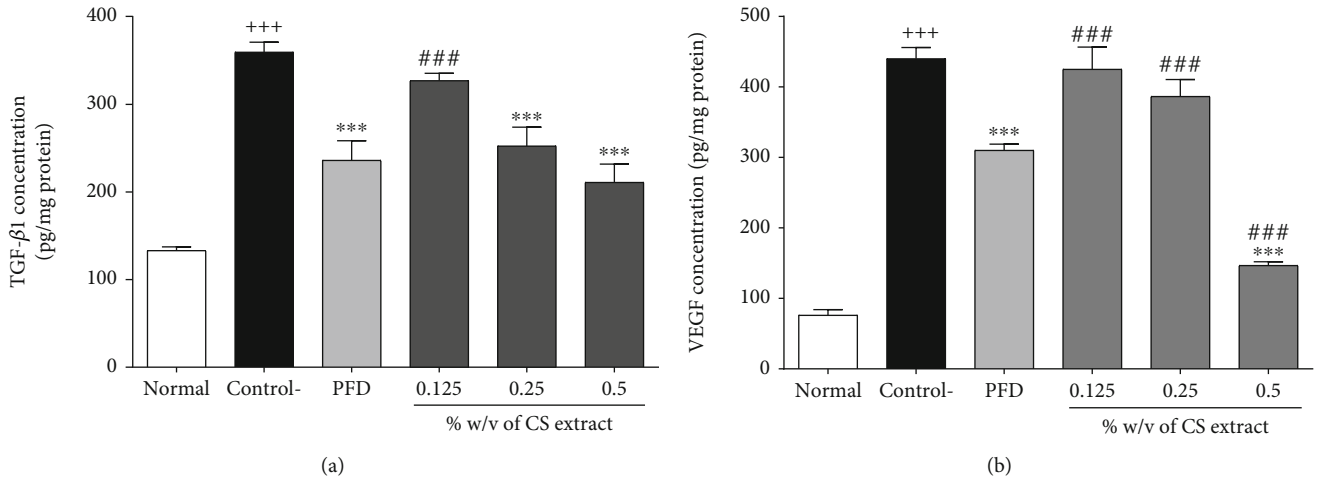

Figure 5: The effect of different concentrations of *C. sativus* (0.125, 0.25, and 0.5% *w*/*v*) and PFD (7.5% *w*/*v*) on TGF-β1 (a) and VEGF (b) levels following postoperational-induced peritoneal adhesion. Data were presented as the mean ± SEM ($n = 8$). $^{+++}P < 0.001$ compared to the normal group, $^{***}P < 0.001$ compared to the control group, and $^{\#\#\#}P < 0.001$ compared to the PFD group. The lines represent a significant difference between the three *C. sativus* groups.

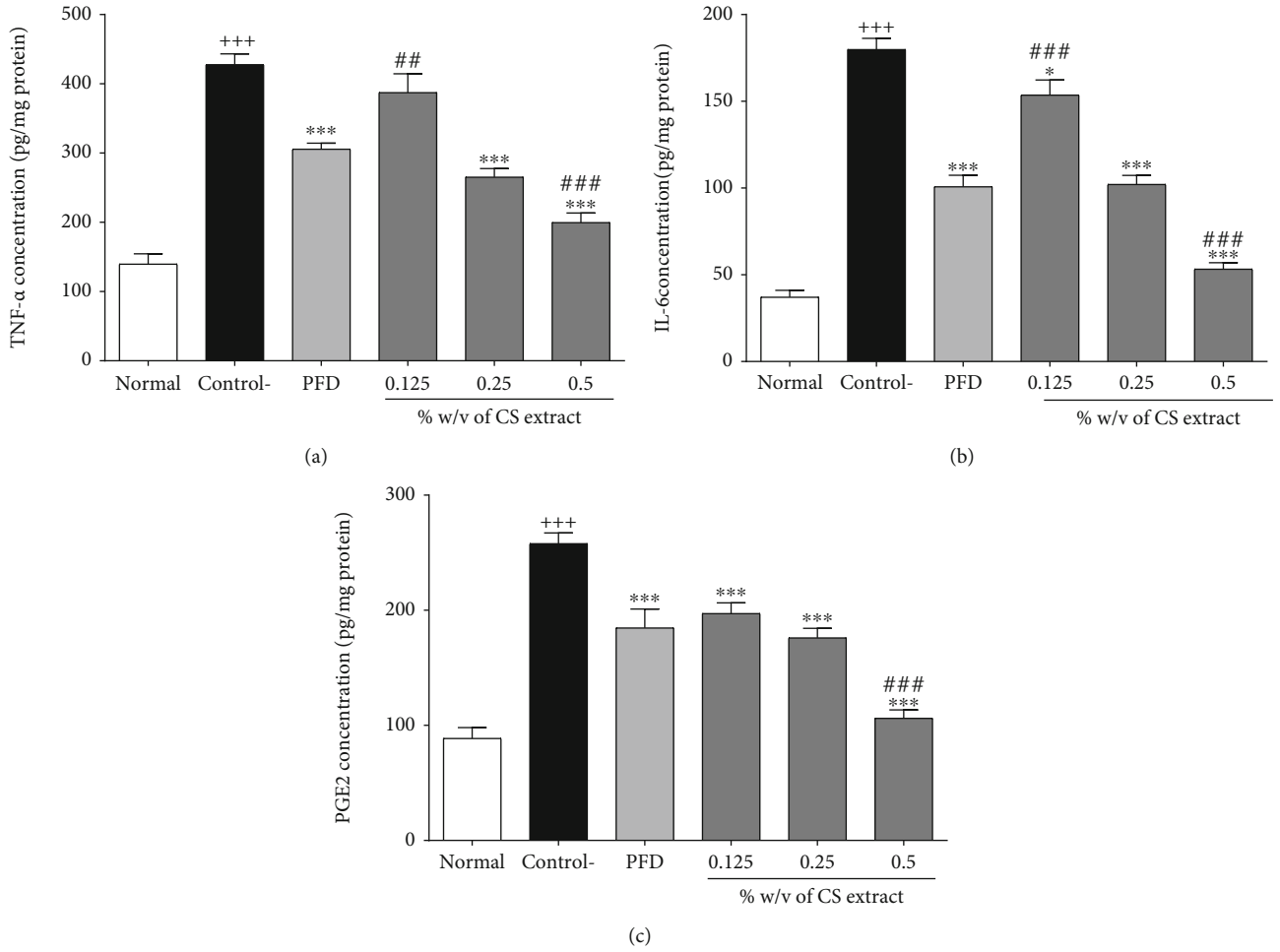

Figure 6: The effect of different concentrations of *C. sativus* (0.125, 0.25, and 0.5% *w*/*v*) and PFD (7.5% *w*/*v*) on TNF-*α* (a), IL-6 (b), and PGE_2 (c) levels following postoperational-induced peritoneal adhesion. Data were presented as the mean ± SEM ($n = 8$). $^{+++}P < 0.001$ compared to the normal group, $^{***}P < 0.001$ and $^{*}P < 0.05$ compared to the control group, and $^{###}P < 0.001$ and $^{##}P < 0.01$ compared to the PFD group.

and PFD (7.5% *w*/*v*, $P < 0.001$) significantly reduced the concentration of TGF-β1 compared to the control group (Figure 5(a)). However, the level of VEGF was significantly decreased by administration of either *C. sativus* (0.5% *w*/*v*, $P < 0.001$) or PFD (7.5% *w*/*v*, $P < 0.001$), compared to the control group (Figure 5(b)).

3.2.6. The Effect of C. sativus and PFD on Inflammatory Parameters (TNF-α, IL-6, and PGE_2). All inflammatory parameters (TNF-*α*, IL-6, and PGE_2) were increased in the control group compared to the normal group ($P < 0.001$ for all cases, Figures 6(a)–6(c)). All three concentrations of *C. sativus* (0.125, 0.25, and 0.5% *w*/*v*) and PFD (7.5% *w*/*v*) decreased IL-6 ($P < 0.001$-0.05 for all cases, Figure 6(b)) and PGE_2 ($P < 0.001$ for all cases, Figure 6(c)) levels. Moreover, *C. sativus* (0.25, 0.5% *w*/*v*) and PFD were diminished TNF-*α* concentration compared to the control group in peritoneal lavage fluid ($P < 0.001$ for all cases, Figure 6(c)).

3.2.7. The Effect of C. sativus and PFD on MDA and GSH. The concentrations of MDA ($P < 0.001$, Figure 7(a)) and GSH ($P < 0.001$, Figure 7(b)) were significantly increased and decreased in the control group compared to the normal group, respectively. The levels of MDA and GSH, respectively, diminished and increased following treatment with *C. sativus* (0.25, 0.5%*w*/*v*) and PFD (7.5%*w*/*v*) in comparison to the control group in peritoneal lavage fluid ($P < 0.001$ for all cases, Figures 7(a) and 7(b)).

3.3. In Vitro Results

3.3.1. The Effect of C. sativus Extract and PFD on Cell Proliferation. In the absence of TGF-β_1 stimulation, no significant changes were found in cell proliferation between the groups treated with vehicle, *C. sativus* extract (100, 200, and 400 μg/ml) and PFD (100 μg/ml) and the control group (Figure 8(a)). In the presence of TGF-β_1 stimulation (20 ng/ml), the levels of cell proliferation were significantly increased in both vehicle-treated and TGF-β_1 groups compared to the respected control group ($P < 0.001$ for both cases, Figure 8(b)). Pretreatment with *C. sativus* extract (200 and 400 μg/ml) and PFD (100 μg/ml) significantly

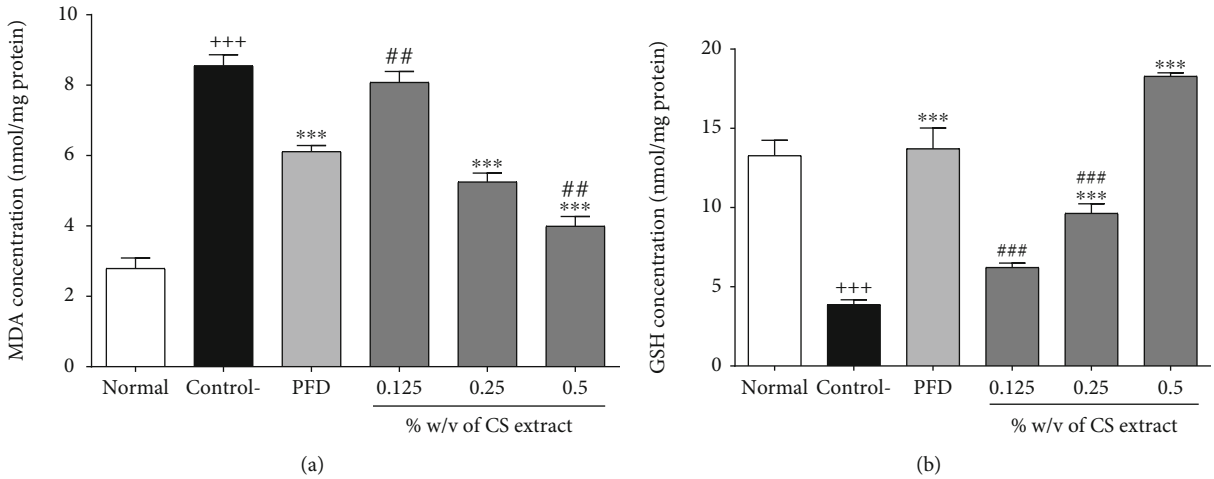

Figure 7: The effect of different concentrations of *C. sativus* (0.125, 0.25, and 0.5% *w*/*v*) and PFD (7.5% *w*/*v*) on MDA (a) and GSH (b) levels following postoperational-induced peritoneal adhesion. Data were presented as the mean ± SEM ($n = 8$). $^{+++}P < 0.001$ and $^{+}P < 0.05$ compared to the normal group, $^{***}P < 0.001$ compared to the control group, and $^{###}P < 0.001$ and $^{##}P < 0.01$ compared to the PFD group. The lines represent a significant difference between the three *C. sativus* groups. The lines represent a significant difference between the two groups shown.

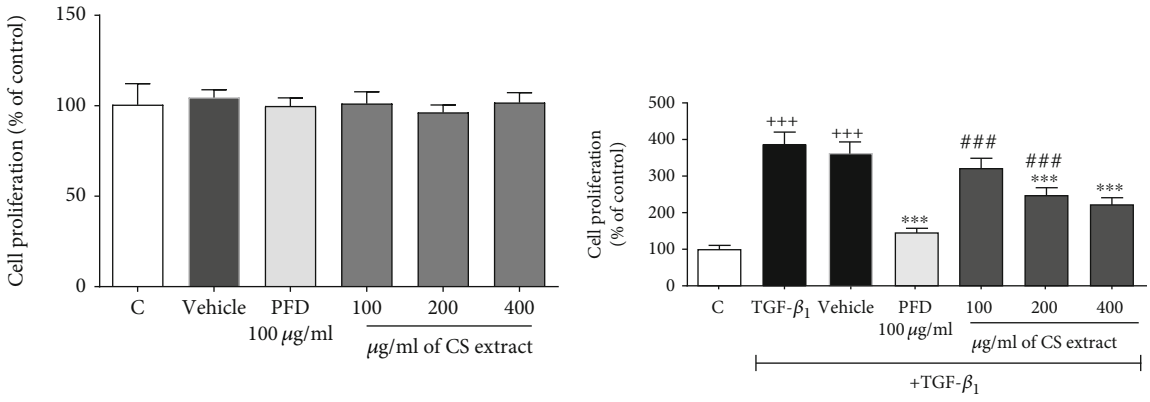

Figure 8: The effects of *C. sativus* extract (100, 200, and 400 μg/ml) and PFD (100 μg/ml) on proliferation level of RAW 264.7 macrophage cells. Cell proliferation without stimulation (a) and cell proliferation with TGF-β stimulation (20 ng/ml) (b). Data were presented as the mean ± SEM ($n = 6$). $^{+++}P < 0.001$, compared with the control group; $^{***}P < 0.001$, compared with the TGF-β_1 group; $^{###}P < 0.001$, compared with PFD group. The lines represent a significant difference between the two groups shown.

decreased the level of cell proliferation compared to the TGF-β1-treated alone group ($P < 0.001$ for all cases, Figure 8(b)). The potential protective effects of *C. sativus* extract (100 and 200 μg/ml) were lower than those of PFD (100 μg/ml) on decreasing the TGF-β_1-induced cell hyperproliferation ($P < 0.001$ for both case, Figure 8(b)).

3.3.2. The Effect of C. sativus Extract and PFD on TNF-α, IL-10, and VEGF. In the presence of TGF-β_1 stimulation (20 ng/ml), the TNF-α level had no considerable changes in both the TGF-β1 and vehicle groups compared to the control group (Figure 9(a)). In contrast, IL-10 ($P < 0.001$ for both cases, Figure 9(b)) and VEGF ($P < 0.001$ for both cases, Figure 9(c)) levels were significantly increased in TGF-β1 and vehicle groups compared to the control group. Premedication with PFD (100 μg/ml) enhanced the TNF-α level, but it had no statistically significant difference compared to the TGF-β1 group ($P = 0.0729$, Figure 9(b)). Pretreatment with *C. sativus* extract (200 and 400 μg/ml) significantly increased TNF-α ($P < 0.05$ and $P < 0.001$, respectively, Figure 9(a)) level and notably decreased VGEF ($P < 0.001$ for both cases, Figure 9(c)) level compared to the TGF-β1 group. However, pretreatment with a high concentration of *C. sativus* extract (400 μg/ml) significantly increased IL-10 level compared to the TGF-β1 group ($P < 0.001$, Figure 9(c)).

3.3.3. The Effect of C. sativus Extract and PFD on Protein Levels of iNOS and Arg-1 and iNOS/Arg-1 Ratio. In the presence of TGF-β_1 stimulation (20 ng/ml), iNOS level ($P < 0.001$, Figure 10(a)) and iNOS/Arg-1 ratio ($P < 0.001$, Figure 10(c)) were significantly diminished, but Arg-1 level

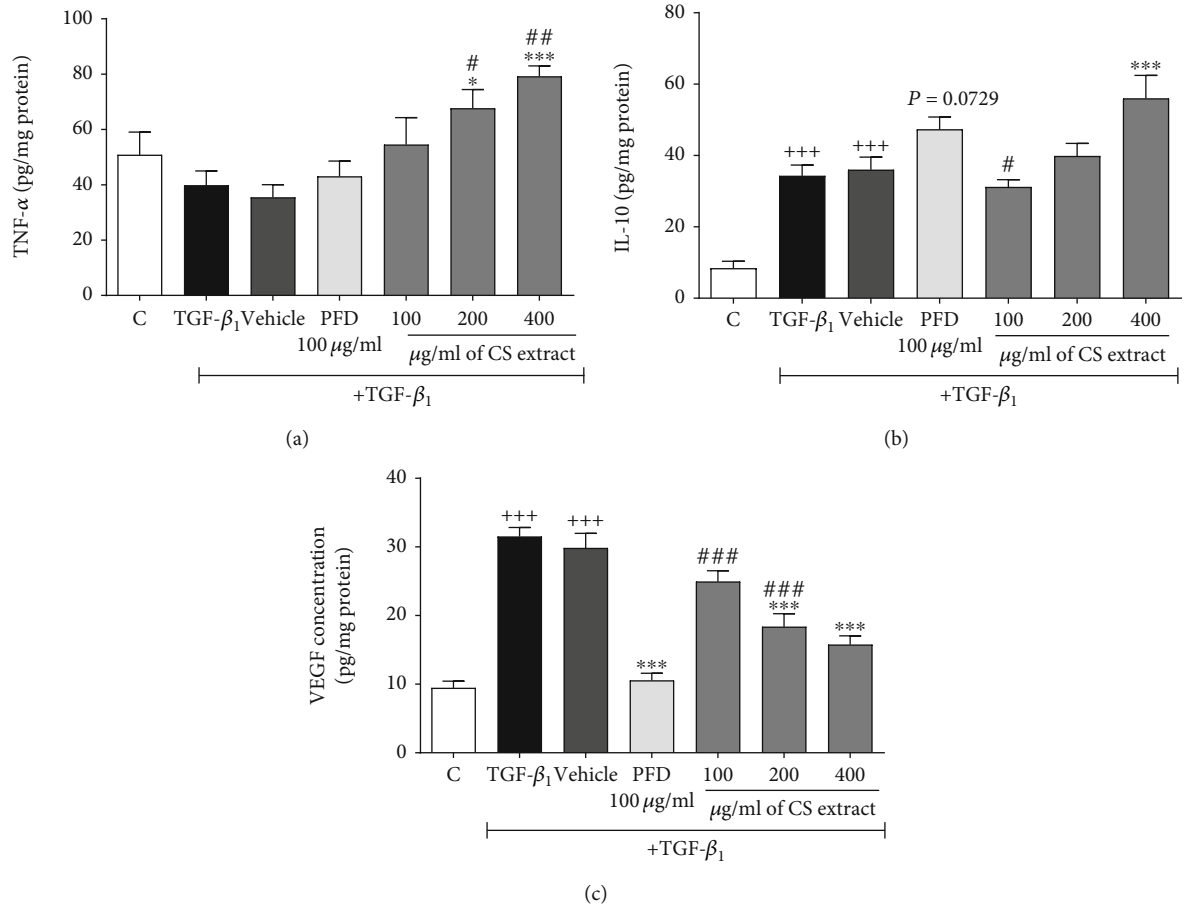

Figure 9: Effects of *C. sativus* extract (100, 200, and 400 μg/ml) and PFD (100 μg/ml) on the mRNA expression levels of proinflammatory factors of RAW 264.7 macrophage cells, including TNF-α (a), IL-10 (b), and VEGF (c) in the presence of TGF-β stimulation (20 ng/ml). Data were presented as the mean ± SEM ($n = 6$). $^{+++}P < 0.001$, compared with the control group; $^{***}P < 0.001$ and $^{*}P < 0.05$ compared with the TGF-β_1 group; $^{###}P < 0.001$ to $^{\#}P < 0.05$ compared with the PFD group. PFD was increased TNF-α level, but it had no significant difference compared to the TGF-β_1 group ($P = 0.0729$).

($P < 0.001$, Figure 10(b)) was meaningfully increased in the TGF-β1 and vehicle groups compared to the control group. Pretreatment with *C. sativus* extract (200 μg/ml, $P < 0.01$, and 400 μg/ml, $P < 0.001$) and PFD (100 μg/ml, $P < 0.001$) significantly increased iNOS level (Figure 10(a)) compared to the TGF-β1 group. On the contrary, *C. sativus* extract (200 μg/ml, $P < 0.05$, and 400 μg/ml, $P < 0.001$) and PFD (100 μg/ml, $P < 0.001$) significantly reduced Arg-1 level (Figure 10(b)) in comparison to the TGF-β1 group. Our results indicated that the highest concentration of *C. sativus* extract (400 μg/ml, $P < 0.05$) and PFD (100 μg/ml, $P < 0.001$) could increase the iNOS/Arg-1 ratio compared to the TGF-β1 group (Figure 10(c)).

4. Discussion

The present study evaluated the protective effects of hydroethanolic extract of *C. sativus* stigma against postoperational-induced peritoneal adhesion in a rat model. As a result, the current study demonstrated that *C. sativus* extract ameliorates postoperational-induced peritoneal adhesion development through attenuating oxidative stress (MDA), inflammatory mediators (IL-6, TNF-α, and PGE_2), and fibrosis (TGF-β1, IL-4, and PAI) and angiogenesis (VEGF) markers, while propagating antioxidant (GSH), anti-inflammatory (IL-10), and fibrinolytic (tPA) markers and tPA/PAI ratio. Moreover, we assessed the protective and antifibrotic effects of the extract against TGF-β1-induced fibrosis in RAW 264.7 murine macrophage cell line. Briefly, we revealed that the extract, without any toxicity, modulated the levels of cell proliferation and inflammatory (TNF-α), angiogenesis (VEGF), anti-inflammatory (IL-10), M1 (iNOS), and M2 (Arg-1) biomarkers and iNOS/Arg-1 ratio towards antifibrotic M1 phenotype of macrophage, in a concentration-dependent manner.

Numerous models have been suggested to evaluate postoperative peritoneal adhesion, including uterine horn damage, bacterial infection, and scarping model [47, 48]. In the current study, we used the scraping model due to the most similarity between the adhesion development by this model and abdominopelvic surgery [49, 50]. Furthermore, we scored the adhesions from zero to four using the Nair et al. and adhesion scheme scoring methods [25, 32, 50]. Our macroscopic data revealed that the adhesion score was

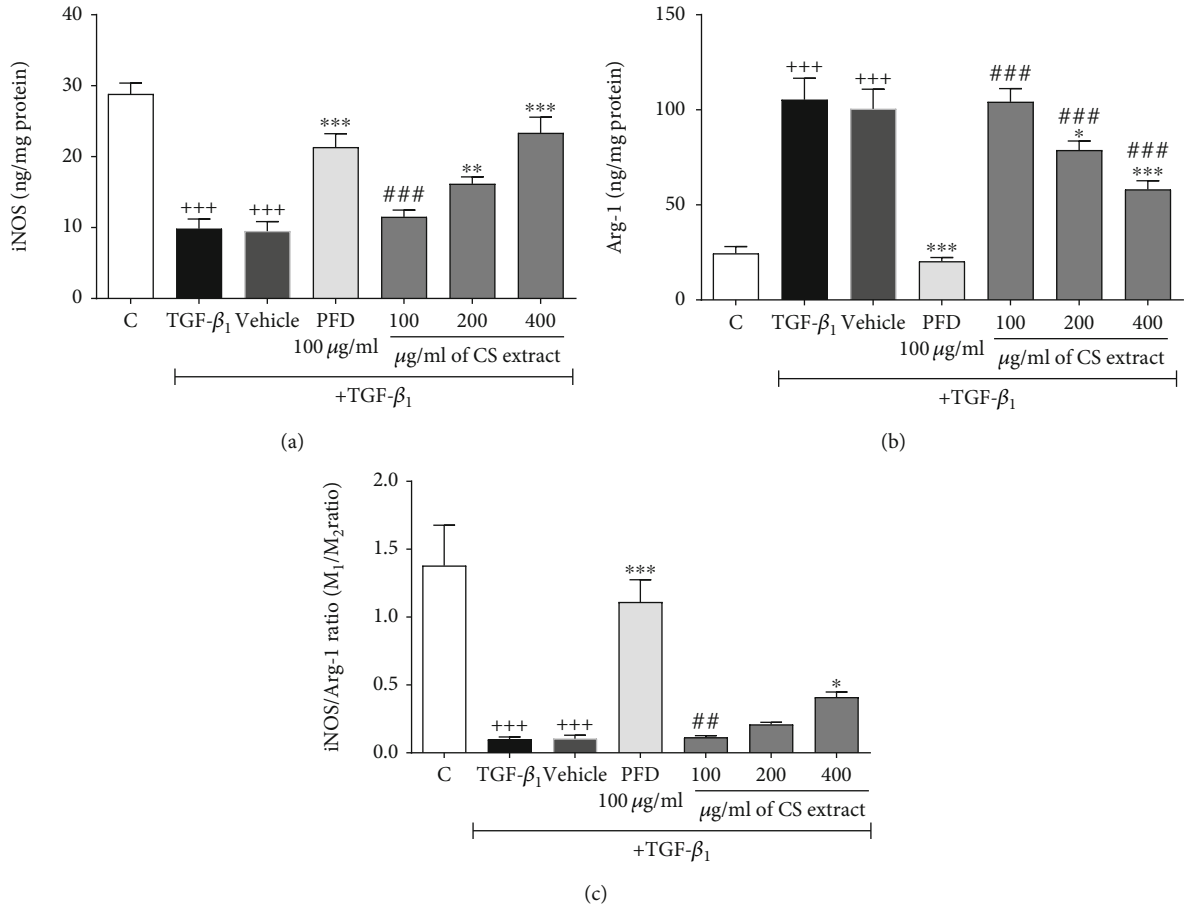

Figure 10: Effects of *C. sativus* extract (100, 200, and 400 μg/ml) and PFD (100 μg/ml) on the iNOS and Arg-1 levels iNOS/Arg-1 ratio of RAW 264.7 macrophage cells. (a) iNOS, (b) Arg-1, and (c) iNOS/Arg-1 ratio in the presence of TGF-β stimulation (20 ng/ml). Data were presented as the mean ± SEM ($n = 6$). $^{+++}P < 0.001$, compared with the control group; $^{***}P < 0.001$ and $^{*}P < 0.05$ compared with the TGF-β_1 group; $^{###}P < 0.001$ and $^{##}P < 0.01$ compared with the PFD group.

significantly increased in the control group, while *C. sativus* (0.25 and 0.5% *w*/*v*) concentration-dependently reduced the adhesion formation following postoperational-induced peritoneal adhesion in the rat. Our previous study also reported that the adhesion score is enhanced in the control group that received postoperative-induced peritoneal adhesion and decreased following the interventions, such as propolis, honey, and *Rosmarinus officinalis* treatments [2, 24, 25, 32].

In the present study, we used pirfenidone (PFD), a well-known antifibrotic medicine, as a positive control. We showed that PFD (7.5% *w*/*v*) provided a significant decrement in adhesion score, MDA, TNF-α, PGE_2, IL-6, IL-4, TGF-β, VEGF, and PAI levels, while making a significant increment in GSH, IL-10, and tPA levels as well as tPA/PAI ratio following postoperational-induced adhesion in the rat. Moreover, following the TGF-β1 stimulation, our cellular results also revealed that PFD (100 μg/ml) significantly reduced the levels of cell proliferation, VEGF, and Arg-1 but notably enhanced IL-10, iNOS, and iNOS/Arg-1 ratio (M1/M2 marker) and polarized the macrophage from fibrotic phenotype towards antifibrotic M1 cells. Following our results, Bayhan et al. indicated that oral administration of PFD (500 mg/kg po~6.25% *w*/*v*) for two weeks significantly reduced adhesions grade and the protein concentrations and mRNA expression levels of matrix metallopeptidase-9 (MMP-9), tissue inhibitor of metalloproteinase-1 (TIMP-1), tumour necrosis factor-alpha (TNF-α), and TGF-β1 [29]. Similarly, Ozbilgin and coworkers reported the protective effects of PFD (150 mg/animal~2 ml of 7.5% *w*/*v*) against peritoneal adhesion. In fact, they showed that PFD as the same concentration which used in our study (2 ml of 7.5% *w*/*v*) significantly diminished the peritoneal adhesion by decreasing the Th2 lymphocytes as fibrotic cells and increasing the Th1 lymphocytes as antifibrotic cells [31]. Moreover, in 2016, Hasdemir et al. also supported that intraperitoneal administration of PFD (150 mg/animal ip~2 ml of 7.5% *w*/*v*) significantly abolished adhesion scores, fibrosis, and vascular proliferation as well as the protein concentrations of IL-17 and TGF-β1 [30]. Intriguingly, in the cellular model of adhesion, PFD at 100 μg/ml reprogrammed the IL-4/IL-13-induced M2 fibrotic macrophages and polarized towards M1 cells by decreasing the levels of TGF-β1, collagen type one, and related markers, including YM-1 and CD206 and transferrin receptors [41]. Collectively, these studies can support the results of the positive control PFD used in the current study.

It has been demonstrated that oxidative stress is one of the major factors responsible for adhesion development. Activated oxygen and nitrogen species stimulate fibroblastic cells' growth in damaged areas and lead to fibrosis formation [51, 52]. Therefore, we investigated MDA levels as an oxidative agent and GSH as antioxidative factors. We found that *C. sativus* extract (0.25-0.5% *w*/*v*~25 and 50 mg/kg) meaningfully reduces MDA level and enhances GSH level following postoperational-induced peritoneal adhesion in a concentration-dependent manner. In line with our results, Ghadrdoost et al. determined that *C. sativus* extract (30 mg/kg) and crocin (15 and 30 mg/kg) diminish lipid peroxidation by reducing the MDA level. Simultaneously, the extract and its active constituent augmented total antioxidant activity, glutathione peroxidase, glutathione reductase, and superoxide dismutase activities following the oxidative stress and spatial learning and memory deficits induced by chronic stress in rats [53].

Additionally, it has been demonstrated that *C. sativus* aqueous extract (10, 20, and 40 mg/kg) mitigated MDA and nitric oxide levels, while it appended the levels of GSH and catalase and SOD activities following streptozotocin-induced diabetes in rats [54]. Akbari and coworkers figured out that *C. sativus* extract (40 mg/kg) attenuates MDA and IL-6 levels and propagates GSH level as well as glutathione peroxidase activity in exercised rats [55]. In one study, *C. sativus* stigmas and high-quality byproducts (petals +anthers-CTA) extracts (25 μg/ml) provided a significant decrement in ROS and lactate dehydrogenase levels in human colon cancer (HCT116) cell lines following hydrogen peroxide-induced oxidative stress. Moreover, CST and CTA alleviated MDA levels in rat colon specimens challenged with *E. coli* lipopolysaccharide [56]. Crocin, one of the major active constituents of *C. sativus*, decreased MDA and xanthine oxidase while it increased GSH levels in streptozotocin-induced diabetic rats [57]. These studies may endorse our results regarding the antioxidant effects of *C. sativus* extract.

Inflammation and inflammatory cytokines are considered one of the most critical factors responsible for postoperative adhesion formation. In damaged tissue, macrophages secret IL-6 and TNF-α, which cause coagulation and the formation of fibrin layers that extend adhesion [3]. By contrast, IL-10 as an anti-inflammatory cytokine inhibits the secretion of pro-inflammatory cytokines, such as IL-8, IL-6, and TNF-α, and plasminogen activator enzymes and prevents tissue damage [53]. Therefore, we measured the effects of *C. sativus* on the levels of TNF-α, IL-6, IFN-γ, and PGE_2 as inflammatory cytokines and IL-4 and IL-10 concentrations as anti-inflammatory cytokines. Our results revealed that *C. sativus* extract (0.25-0.5% *w*/*v*) concentration-dependently reduces the levels of TNF-α, IFN-γ, PGE_2, IL-6, and IL-4, while making a significant increment in IL-10 level following postoperational-induced adhesion in the rat. In line with our animal results, we observed that the level of IL-10 was increased following the TGF-β1 stimulation in the macrophage cell line. However, the level of TNF-α as an inflammatory cytokine was propagated at higher concentrations of the extract. In fact, this phenomenon was in contrast to the anti-inflammatory effects of the *C. sativus* extract observed in the animal section. It can be justified that TGF-β1 slightly reduces the TNF-α and leads to provide fibrotic macrophages (M2 cells), which produce higher levels of fibrotic and angiogenesis factors, as shown in our results of Figures 9 and 10. Indeed, by TGF-β1 stimulation, the macrophage phenotypes were polarized towards M2 cells by decreasing the level of increasing the level of Arg-1 as a marker of M2 cells and iNOS as a marker of M1 macrophage cells and iNOS/Arg-1 ratio (M1/M2 ratio). It justifies that the extract provides no inflammatory state but modulates the macrophage polarization towards nonfibrotic phenotypes that secrets higher TNF-α levels. Moreover, we assessed the level of IL-10 as supportive data, which endorse our vision on the direct effects of the extract on macrophage polarization and increasing the TNF-α level.

Christodoulou et al. demonstrated that *Crocus sativus* L. aqueous extract (30, 60, and 90 mg/kg/day) reduces IL-6, TNF-α, monocyte chemoattractant protein-1, matrix metalloproteinase- (MMP-) 2, MMP-3, and MMP-9 levels, and MMP/TIMP-2 ratio in diabetic atherosclerotic C57BL/6J wild-type mice [58]. In another study, *Crocus sativus* (20, 40, and 80 mg/kg) diminished IL-4 and NO levels, while it enhanced IFN-γ and IFN-γ/IL-4 ratio levels in ovalbumin-sensitised guinea pigs [59]. Faridi and coworkers suggested that hydroalcoholic extract of *C. sativus* (500 mg/kg) mitigates IFN-γ and IL-17 and augments IL-10 levels following streptozocin-induced autoimmune diabetes in C57BL/6 mice [60]. However, the levels of the extract were considerably higher than what we investigated in our study. Additionally, Hemshekhar et al. reported that crocin (10 and 20 mg/kg), one of the major active constituents of *C. sativus*, alleviates MMP-13, MMP-3, MMP-9, TNF-α, IL-1β, NF-κB, IL-6, COX-2, PGE_2, and ROS levels following Freund's complete adjuvant- (FCA-) induced arthritis in rats [61]. In another study, crocin (100 and 200 ppm~1 and 2% *w*/*v*) made a significant decrement in the levels of mRNA expression of TNF-α, IL-1β, IL-6, IFN-γ, NF-κB, COX-2, and iNOS and propagated Nrf2 mRNA expression in the colorectal mucosa following dextran sodium sulfate-induced colitis [62]. These studies may support our results regarding the anti-inflammatory properties of *C. sativus* extract.

The previous human and animal studies indicated that the levels of TGF-β are significantly increased in the peritoneal adhesions [2, 24, 50]. TGF-β is a suppressive and fibrotic cytokine that controls reproduction, differentiation, cell apoptosis, and wound healing. The active form of TGF-β increases the secretion of the extracellular matrix, leading to the formation of adhesion [3, 63]. Vascular endothelial growth factor (VEGF) is another growth factor and potent mitogen for endothelial cells and a vital angiogenesis factor, which is essential for wound healing and adhesion formation [2, 24, 50]. In fact, VEGF production is stimulated by lactate in macrophages, and lactate accumulation plays a critical role in adhesion development [2, 3, 24, 50]. It has been emphasised that the anti-VEGF monoclonal antibody decreases the postoperational peritoneal adhesion in mice [64]. The current study results figured out that *C. sativus* extract (0.25-0.5% *w*/*v* ~25 and 50 mg/kg) provided a

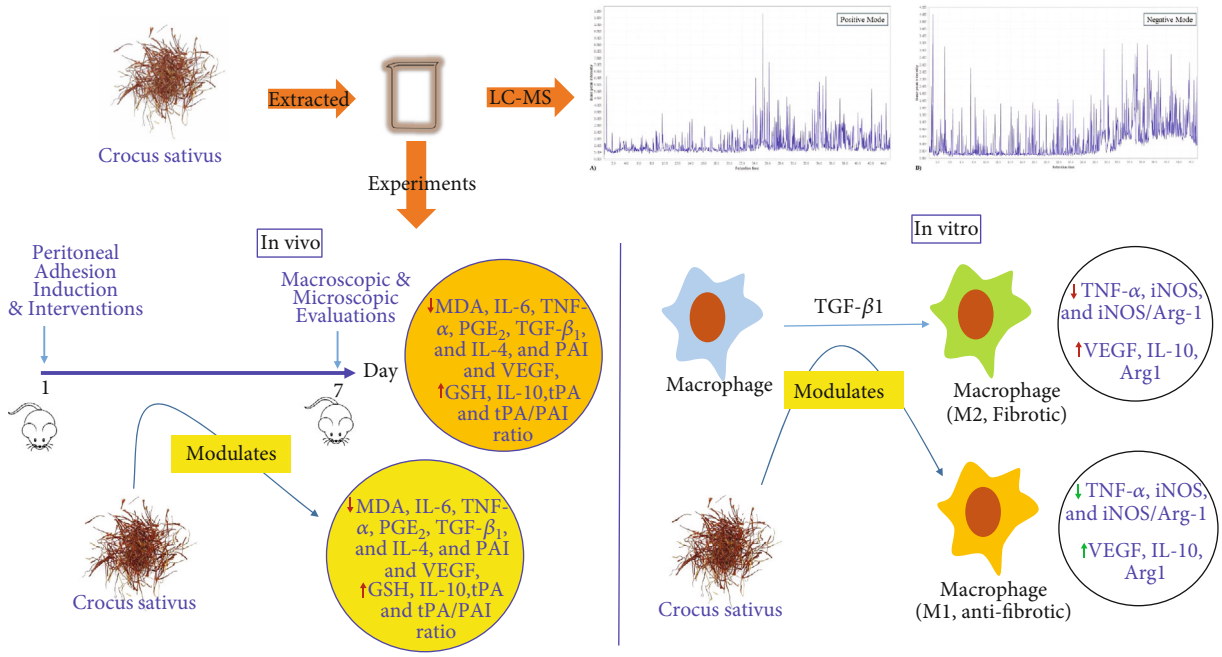

Figure 11: Preventive effects of *C. sativus* extract against postsurgical-induced peritoneal adhesion.

significant and concentration-dependent decrement in TGF-β and VEGF levels following the postoperational peritoneal adhesion. Interestingly, our in vitro study found that VEGF level was also meaningfully abrogated by *C. sativus* extract in a concentration-dependent manner.

In line with our results, Alemzadeh and Oryan investigated that *C. sativus* extract (20% *w*/*w*; topically) diminishes the expression of IL-1β and TGF-β1 and improves wound healing following the burn wounds in rats [65]. Additionally, crocin (20 mg/kg) mitigated TGF-β, NF-κB, and IL-6 expression levels following streptozocin-induced diabetic nephropathy in rats [66]. Algandaby also showed that crocin (25 and 100 mg/kg) attenuates the expression of TGF-β, alpha-smooth muscle actin (α-SMA) and collagen 1-α, NF-κB, COX-2, IL-1β, and TNF-α following thioacetamide-induced liver fibrosis in mice [67]. Kermani and coworkers demonstrated that *C. sativus* (100 mg/day) reduces VEGF, IL-2, and IL-1β while enhancing IL-10 levels compared to the placebo group in metabolic syndrome patients [68]. Furthermore, *C. sativus* aqueous extract (400 and 800 μg/ml) attenuated the expression levels of VEGF-A and VEGF-2 in the MCF-7 cell line and prevented angiogenesis [69]. Additionally, crocin (25 mg/kg) mitigated VEGF, IL-6, IFN-γ, and TNF-α levels in a mouse model of endometriosis [70]. In another study, crocin (250 and 500 μg/kg) attenuated VEGF, MMP-2, and MMP-9 expressions and TNF-α and IL-6 levels while it elevated IL-10 level in melanoma metastatic model in C57BL/6 mice [71]. These studies may endorse our animal and cellular results regarding the antifibrotic and antiangiogenesis effects of the extract.

Tissue plasminogen activator (tPA) is classified as a serine protease that prevents the progression of mesothelial cell adhesion by inhibiting plasminogen transformation to plasmin. In low tPA level condition, fibrin masses form a clot attacked by fibroblasts, collagens, and other proteins that lead to adhesion formation [72]. Plasminogen activator inhibitor (PAI), which is present in plasma, inhibits the tPA. Increasing the PAI level and decreasing the tPA level and tPA/PAI ratio are considered adhesion development causes [3, 73]. In one study, Atta and coworkers found lower TGF-β1 and PAI and higher tPA levels in the group with a lower rate of postoperative adhesion formation in rats [74]. Therefore, we determined the levels of TPA, PAI and the ratio of TPA/PAI. We found that *C. sativus* (0.25-0.5% *w*/*v* ~25 and 50 mg/kg) mitigates PAI level and propagates tPA and TPA/PAI ratio levels in a concentration-dependent manner following the postoperational induced peritoneal adhesion. Tsantarliotou and coworkers suggested that crocin at both low and high doses (10 and 100 mg/kg) could diminish PAI-1 levels in the liver and brain tissue following lipopolysaccharide-induced thrombosis in rats [75].

5. Conclusion

In summary, our results revealed that *C. sativus* could prevent postoperative peritoneal adhesion through attenuating adhesion score, oxidative stress, inflammatory cytokines, fibrosis, and angiogenesis markers, while propagating antioxidant and anti-inflammatory markers and tPA (Figure 11). Moreover, the current study indicated that *C. sativus* reduces peritoneal adhesion formation by modulating the macrophage polarization from M2 towards M1 cells (Figure 11). It could be concluded that *C. sativus* may be the right candidate for preventing postoperative peritoneal adhesion.

Abbreviations

COX2: Cyclooxygenase-2
GSH: Glutathione
IFN-γ: Interferon-gamma
IL-10: Interleukin-10
IL-4: Interleukin-4
IL-6: Interleukin-6
iNOS: Nitric oxide synthase
MDA: Malondialdehyde
MMP: Matrix metallopeptidase
NF-κB: Nuclear factor kappa-light-chain-enhancer of activated B cells
NO: Nitric oxide
PA: Plasminogen activator
PFD: Pirfenidone
PGE_2: Prostaglandin E2
SOD: Superoxide dismutase
TAP: Tissue plasminogen activator
TGF-β: Transforming growth factor-beta
TIMP-2: Tissue inhibitor of metalloproteinases-2
TIMPs: The tissue inhibitors of metalloproteinases
TNF-α: Tumour necrosis factor-alpha
VEGF: Vascular endothelial growth factor
α-SMA: Alpha-smooth muscle actin.

Data Availability

The data used to support the findings of this study are available from the corresponding author upon reasonable request.

Conflicts of Interest

The authors declare that they have no conflict of interest to disclose.

Authors' Contributions

Pouria Rahmanian Devin, Hassan Rakhshandeh, and Vafa Baradaran Rahimi had equal contributions as the first authors.

Acknowledgments

This study was supported by the research council of Mashhad University of Medical Sciences.

References

[1] K. M. Braun and M. P. Diamond, "The biology of adhesion formation in the peritoneal cavity," *Seminars in Pediatric Surgery*, vol. 23, no. 6, pp. 336–343, 2014.

[2] Y. Roohbakhsh, V. B. Rahimi, S. Silakhori et al., "Evaluation of the effects of peritoneal lavage with Rosmarinus officinalis extract against the prevention of postsurgical-induced peritoneal adhesion," *Planta Medica*, vol. 86, no. 6, pp. 405–414, 2020.

[3] M. W. Stommel, C. Strik, and H. van Goor, "Response to pathological processes in the peritoneal cavity–sepsis, tumours, adhesions, and ascites," *Seminars in Pediatric Surgery*, vol. 23, no. 6, pp. 331–335, 2014.

[4] Z. Alpay, G. M. Saed, and M. P. Diamond, "Postoperative adhesions: from formation to prevention," *Seminars in Reproductive Medicine*, vol. 26, no. 4, pp. 313–321, 2008.

[5] R. C. Lantz, G. J. Chen, A. M. Solyom, S. D. Jolad, and B. N. Timmermann, "The effect of turmeric extracts on inflammatory mediator production," *Phytomedicine*, vol. 12, no. 6-7, pp. 445–452, 2005.

[6] Y. Zhang, X. Li, Q. Zhang et al., "Berberine hydrochloride prevents postsurgery intestinal adhesion and inflammation in rats," *The Journal of Pharmacology and Experimental Therapeutics*, vol. 349, no. 3, pp. 417–426, 2014.

[7] V. B. Rahimi, A. Rajabian, H. Rajabi et al., "The effects of hydro-ethanolic extract of *Capparis spinosa* (*C. spinosa*) on lipopolysaccharide (LPS)-induced inflammation and cognitive impairment: Evidence from *in vivo* and *in vitro* studies," *Journal of Ethnopharmacology*, vol. 256, p. 112706, 2020.

[8] V. R. Askari, V. B. Rahimi, S. A. Tabatabaee, and R. Shafiee-Nick, "Combination of imipramine, a sphingomyelinase inhibitor, and β-caryophyllene improve their therapeutic effects on experimental autoimmune encephalomyelitis (EAE)," *International Immunopharmacology*, vol. 77, p. 105923, 2019.

[9] V. R. Askari, V. B. Rahimi, R. Zargarani, R. Ghodsi, M. Boskabady, and M. H. Boskabady, "Anti-oxidant and anti-inflammatory effects of auraptene on phytohemagglutinin (PHA)-induced inflammation in human lymphocytes," *Pharmacological Reports*, vol. 73, no. 1, pp. 154–162, 2021.

[10] N. Chegini, "TGF-β system: the principal profibrotic mediator of peritoneal adhesion formation," *Seminars in Reproductive Medicine*, vol. 26, no. 4, pp. 298–312, 2008.

[11] V. I. Shavell, G. M. Saed, and M. P. Diamond, "Review: cellular metabolism: contribution to postoperative adhesion development," *Reproductive Sciences*, vol. 16, no. 7, pp. 627–634, 2009.

[12] B. C. Ward and A. Panitch, "Abdominal adhesions: current and novel therapies," *The Journal of Surgical Research*, vol. 165, no. 1, pp. 91–111, 2011.

[13] D. Robertson, G. Lefebvre, N. Leyland et al., "Clinical practice gynaecology, adhesion prevention in gynaecological surgery," *Journal of Obstetrics and Gynaecology Canada*, vol. 32, no. 6, pp. 598–602, 2010.

[14] A. H. DeCherney and G. S. diZerega, "Clinical problem of intraperitoneal postsurgical adhesion formation following general surgery and the use of adhesion prevention barriers," *The Surgical Clinics of North America*, vol. 77, no. 3, pp. 671–688, 1997.

[15] W. Arung, M. Meurisse, and O. Detry, "Pathophysiology and prevention of postoperative peritoneal adhesions," *World Journal of Gastroenterology*, vol. 17, no. 41, pp. 4545–4553, 2011.

[16] F. I. Abdullaev, "Cancer chemopreventive and tumoricidal properties of saffron (Crocus sativus L.)," *Experimental Biology and Medicine (Maywood, N.J.)*, vol. 227, no. 1, pp. 20–25, 2002.

[17] S. Rahaiee, S. Moini, M. Hashemi, and S. A. Shojaosadati, "Evaluation of antioxidant activities of bioactive compounds and various extracts obtained from saffron (Crocus sativus L.): a review," *Journal of Food Science and Technology*, vol. 52, no. 4, pp. 1881–1888, 2015.

[18] S. I. Bukhari, M. Manzoor, and M. K. Dhar, "A comprehensive review of the pharmacological potential of *Crocus sativus* and

its bioactive apocarotenoids," *Biomedicine & Pharmacotherapy*, vol. 98, pp. 733–745, 2018.

[19] A. Milajerdi, V. Bitarafan, and M. Mahmoudi, "a review on the effects of saffron extract and its constituents on factors related to neurologic, cardiovascular and gastrointestinal diseases," *Journal of Medicinal Plants*, vol. 14, pp. 9–28, 2015.

[20] M. R. Khazdair, M. H. Boskabady, M. Hosseini, R. Rezaee, and A. M. Tsatsakis, "The effects of Crocus sativus (saffron) and its constituents on nervous system: a review," *Avicenna journal of phytomedicine*, vol. 5, no. 5, pp. 376–391, 2015.

[21] S. Kianbakht, "A systematic review on pharmacology of saffron and its active constituents," *Journal of Medicinal Plants*, vol. 28, pp. 1–27, 2008.

[22] A. R. Khorasany and H. Hosseinzadeh, "Therapeutic effects of saffron (Crocus sativus L.) in digestive disorders: a review," *Iranian journal of basic medical sciences*, vol. 19, no. 5, pp. 455–469, 2016.

[23] V. B. Rahimi, V. R. Askari, M. Hosseini, B. S. Yousefsani, and H. R. Sadeghnia, "Anticonvulsant activity of Viola tricolor against seizures induced by pentylenetetrazol and maximal electroshock in mice," *Iranian journal of medical sciences*, vol. 44, no. 3, pp. 220–226, 2019.

[24] V. R. Askari, V. B. Rahimi, P. Zamani et al., "Evaluation of the effects of Iranian propolis on the severity of post operational-induced peritoneal adhesion in rats," *Biomedicine & Pharmacotherapy*, vol. 99, pp. 346–353, 2018.

[25] V. B. Rahimi, R. Shirazinia, N. Fereydouni et al., "Comparison of honey and dextrose solution on post-operative peritoneal adhesion in rat model," *Biomedicine & Pharmacotherapy*, vol. 92, pp. 849–855, 2017.

[26] M. D. Sarap, K. S. Scher, and C. W. Jones, "Anaerobic coverage for wound prophylaxis: Comparison of cefazolin and cefoxitin," *American Journal of Surgery*, vol. 151, no. 2, pp. 213–215, 1986.

[27] D. L. Cavanaugh, J. Berry, S. R. Yarboro, and L. E. Dahners, "Better prophylaxis against surgical site infection with local as well as systemic antibiotics. An in vivo study," *The Journal of Bone and Joint Surgery. American Volume*, vol. 91, no. 8, pp. 1907–1912, 2009.

[28] P. Liang, W. Shan, and Z. Zuo, "Perioperative use of cefazolin ameliorates postoperative cognitive dysfunction but induces gut inflammation in mice," *Journal of neuroinflammation*, vol. 15, no. 1, p. 235, 2018.

[29] Z. Bayhan, S. Zeren, F. E. Kocak et al., "Antiadhesive and anti-inflammatory effects of pirfenidone in postoperative intra-abdominal adhesion in an experimental rat model," *The Journal of Surgical Research*, vol. 201, no. 2, pp. 348–355, 2016.

[30] P. S. Hasdemir, M. Ozkut, T. Guvenal et al., "Effect of pirfenidone on vascular proliferation, inflammation and fibrosis in an abdominal adhesion rat model," *Journal of Investigative Surgery*, vol. 30, no. 1, pp. 26–32, 2017.

[31] K. Ozbilgin, M. A. Üner, M. Ozkut, and P. S. Hasdemir, "The effects of pirfenidone on T helper cells in prevention of intraperitoneal adhesions," *The Kaohsiung Journal of Medical Sciences*, vol. 33, no. 6, pp. 271–276, 2017.

[32] S. K. Nair, I. K. Bhat, and A. L. Aurora, "Role of proteolytic enzyme in the prevention of postoperative intraperitoneal adhesions," *Archives of Surgery*, vol. 108, no. 6, pp. 849–853, 1974.

[33] C. Dees, A. Akhmetshina, P. Zerr et al., "Platelet-derived serotonin links vascular disease and tissue fibrosis," *Journal of Experimental Medicine*, vol. 208, no. 5, pp. 961–972, 2011.

[34] A. Jaafari, V. Baradaran Rahimi, N. Vahdati-Mashhadian et al., "Evaluation of the Therapeutic Effects of the Hydroethanolic Extract of Portulaca oleracea on Surgical-Induced Peritoneal Adhesion," *Mediators of Inflammation*, vol. 2021, Article ID 8437753, 18 pages, 2021.

[35] M. Hu, Y. Zhang, X. Guo et al., "Perturbed ovarian and uterine glucocorticoid receptor signaling accompanies the balanced regulation of mitochondrial function and NFκB-mediated inflammation under conditions of hyperandrogenism and insulin resistance," *Life Sciences*, vol. 232, p. 116681, 2019.

[36] V. B. Rahimi, V. R. Askari, and S. H. Mousavi, "Ellagic acid reveals promising anti-aging effects against d-galactose-induced aging on human neuroblastoma cell line, SH-SY5Y: a mechanistic study," *Biomedicine & Pharmacotherapy*, vol. 108, pp. 1712–1724, 2018.

[37] V. R. Askari, V. Baradaran Rahimi, A. Assaran, M. Iranshahi, and M. H. Boskabady, "Evaluation of the anti-oxidant and anti-inflammatory effects of the methanolic extract of *Ferula szowitsiana* root on PHA-induced inflammation in human lymphocytes," *Drug and Chemical Toxicology*, vol. 43, no. 4, pp. 353–360, 2020.

[38] V. B. Rahimi, V. R. Askari, R. Shirazinia et al., "Protective effects of hydro-ethanolic extract of *Terminalia chebula* on primary microglia cells and their polarization (M_1/M_2 balance)," *Multiple Sclerosis and Related Disorders*, vol. 25, pp. 5–13, 2018.

[39] V. Baradaran Rahimi, H. Rakhshandeh, F. Raucci et al., "Anti-inflammatory and anti-oxidant activity of Portulaca oleracea extract on LPS-induced rat lung injury," *Molecules*, vol. 24, no. 1, p. 139, 2019.

[40] F. Liu, H. Qiu, M. Xue et al., "MSC-secreted TGF-β regulates lipopolysaccharide-stimulated macrophage M2-like polarization via the Akt/FoxO1 pathway," *Stem Cell Research & Therapy*, vol. 10, no. 1, p. 345, 2019.

[41] M. Toda, S. Mizuguchi, Y. Minamiyama et al., "Pirfenidone suppresses polarization to M2 phenotype macrophages and the fibrogenic activity of rat lung fibroblasts," *Journal of Clinical Biochemistry and Nutrition*, vol. 63, no. 1, pp. 58–65, 2018.

[42] F. Zhang, H. Wang, X. Wang et al., "TGF-β induces M2-like macrophage polarization via SNAIL-mediated suppression of a pro-inflammatory phenotype," *Oncotarget*, vol. 7, no. 32, pp. 52294–52306, 2016.

[43] V. B. Rahim, M. T. Khammar, H. Rakhshandeh, A. Samzadeh-Kermani, A. Hosseini, and V. R. Askari, "Crocin protects cardiomyocytes against LPS-induced inflammation," *Pharmacological Reports*, vol. 71, no. 6, pp. 1228–1234, 2019.

[44] M. J. Curtis, R. A. Bond, D. Spina et al., "Experimental design and analysis and their reporting: new guidance for publication in BJP," *British Journal of Pharmacology*, vol. 172, no. 14, pp. 3461–3471, 2015.

[45] C. H. George, S. C. Stanford, S. Alexander et al., "Updating the guidelines for data transparency in the British Journal of Pharmacology – data sharing and the use of scatter plots instead of bar charts," *British Journal of Pharmacology*, vol. 174, no. 17, pp. 2801–2804, 2017.

[46] S. P. H. Alexander, R. E. Roberts, B. R. Broughton et al., "Goals and practicalities of immunoblotting and immunohistochemistry: a guide for submission to the British Journal of

Pharmacology," *British Journal of Pharmacology*, vol. 175, no. 3, pp. 407–411, 2018.

[47] H. A. Kayaoglu, N. Ozkan, E. Yenidogan, and R. D. Koseoglu, "Effect of antibiotic lavage in adhesion prevention in bacterial peritonitis," *Ulusal Travma ve Acil Cerrahi Dergisi*, vol. 19, no. 3, pp. 189–194, 2013.

[48] Y. Yue, S. Yan, H. Li, Y. Zong, J. Yue, and L. Zeng, "The role of oral fluvastatin on postoperative peritoneal adhesion formation in an experimental rat model," *Acta Chirurgica Belgica*, vol. 118, no. 6, pp. 372–379, 2018.

[49] L. Allegre, I. Le Teuff, S. Leprince et al., "A new bioabsorbable polymer film to prevent peritoneal adhesions validated in a post-surgical animal model," *PLoS One*, vol. 13, no. 11, 2018.

[50] M. Ghadiri, V. B. Rahimi, E. Moradi et al., "Standardised pomegranate peel extract lavage prevents postoperative peritoneal adhesion by regulating TGF-β and VEGF levels," *Inflammopharmacology*, vol. 29, no. 3, pp. 855–868, 2021.

[51] G. Wei, Y. Wu, Q. Gao et al., "Effect of emodin on preventing postoperative intra-abdominal adhesion formation," *Oxidative Medicine and Cellular Longevity*, vol. 2017, Article ID 1740317, 12 pages, 2017.

[52] C. Ara, A. B. Karabulut, H. Kirimlioglu, M. Yilmaz, V. Kirimliglu, and S. Yilmaz, "Protective effect of aminoguanidine against oxidative stress in an experimental peritoneal adhesion model in rats," *Cell Biochemistry and Function*, vol. 24, no. 5, pp. 443–448, 2006.

[53] B. Ghadrdoost, A. A. Vafaei, A. Rashidy-Pour et al., "Protective effects of saffron extract and its active constituent crocin against oxidative stress and spatial learning and memory deficits induced by chronic stress in rats," *European Journal of Pharmacology*, vol. 667, no. 1-3, pp. 222–229, 2011.

[54] S. Samarghandian, M. Azimi-Nezhad, and T. Farkhondeh, "Immunomodulatory and antioxidant effects of saffron aqueous extract (*Crocus sativus* L.) on streptozotocin-induced diabetes in rats," *Indian Heart Journal*, vol. 69, no. 2, pp. 151–159, 2017.

[55] M. Akbari-Fakhrabadi, M. Najafi, S. Mortazavian, M. Rasouli, A. H. Memari, and F. Shidfar, "Effect of saffron (Crocus sativus L.) and endurance training on mitochondrial biogenesis, endurance capacity, inflammation, antioxidant, and metabolic biomarkers in Wistar rats," *Journal of Food Biochemistry*, vol. 43, no. 8, 2019.

[56] L. Menghini, L. Leporini, G. Vecchiotti et al., "*Crocus sativus* L. stigmas and byproducts: Qualitative fingerprint, antioxidant potentials and enzyme inhibitory activities," *Food Research International*, vol. 109, pp. 91–98, 2018.

[57] E. Altinoz, Z. Oner, H. Elbe, Y. I. L. M. A. Z. Cigremis, and Y. Turkoz, "Protective effects of saffron (its active constituent, crocin) on nephropathy in streptozotocin-induced diabetic rats," *Human & Experimental Toxicology*, vol. 34, no. 2, pp. 127–134, 2015.

[58] E. Christodoulou, N. P. E. Kadoglou, M. Stasinopoulou et al., "*Crocus sativus* L. aqueous extract reduces atherogenesis, increases atherosclerotic plaque stability and improves glucose control in diabetic atherosclerotic animals," *Atherosclerosis*, vol. 268, pp. 207–214, 2018.

[59] G. Byrami, M. H. Boskabady, S. Jalali, and T. Farkhondeh, "The effect of the extract of *Crocus sativus* on tracheal responsiveness and plasma levels of IL-4, IFN- γ, total NO and nitrite in ovalbumin sensitized Guinea-pigs," *Journal of Ethnopharmacology*, vol. 147, no. 2, pp. 530–535, 2013.

[60] S. Faridi, N. Delirezh, and S. M. Abtahi Froushani, "Beneficial effects of hydroalcoholic extract of saffron in alleviating experimental autoimmune diabetes in C57bl/6 mice," *Iranian Journal of Allergy, Asthma, and Immunology*, vol. 18, no. 1, pp. 38–47, 2019.

[61] M. Hemshekhar, M. S. Santhosh, K. Sunitha et al., "A dietary colorant crocin mitigates arthritis and associated secondary complications by modulating cartilage deteriorating enzymes, inflammatory mediators and antioxidant status," *Biochimie*, vol. 94, no. 12, pp. 2723–2733, 2012.

[62] K. Kawabata, N. H. Tung, Y. Shoyama, S. Sugie, T. Mori, and T. Tanaka, "Dietary crocin inhibits colitis and colitis-associated colorectal carcinogenesis in male ICR mice," *Evidence-based Complementary and Alternative Medicine*, vol. 2012, Article ID 820415, 13 pages, 2012.

[63] M. Kianmehr, A. Rezaei, M. Hosseini et al., "Immunomodulatory effect of characterized extract of Zataria multiflora on Th1, Th2 and Th17 in normal and Th2 polarization state," *Food and Chemical Toxicology*, vol. 99, pp. 119–127, 2017.

[64] R. A. Cahill, J. H. Wang, S. Soohkai, and H. P. Redmond, "Mast cells facilitate local VEGF release as an early event in the pathogenesis of postoperative peritoneal adhesions," *Surgery*, vol. 140, no. 1, pp. 108–112, 2006.

[65] E. Alemzadeh and A. Oryan, "Effectiveness of a Crocus sativus extract on burn wounds in rats," *Planta Medica*, vol. 84, no. 16, pp. 1191–1200, 2018.

[66] H. O. Abou-Hany, H. Atef, E. Said, H. A. Elkashef, and H. A. Salem, "Crocin mediated amelioration of oxidative burden and inflammatory cascade suppresses diabetic nephropathy progression in diabetic rats," *Chemico-Biological Interactions*, vol. 284, pp. 90–100, 2018.

[67] M. M. Algandaby, "Antifibrotic effects of crocin on thioacetamide-induced liver fibrosis in mice," *Saudi journal of biological sciences*, vol. 25, no. 4, pp. 747–754, 2018.

[68] T. Kermani, M. Zebarjadi, H. Mehrad-Majd et al., "Anti-inflammatory effect of Crocus sativus on serum cytokine levels in subjects with metabolic syndrome: a randomized, double-blind, Placebo- Controlled Trial," *Current clinical pharmacology*, vol. 12, no. 2, pp. 122–126, 2017.

[69] M. Mousavi and J. Baharara, "Effect of Crocus sativus L. on expression of VEGF-A and VEGFR-2 genes (angiogenic biomarkers) in MCF-7 cell line," *Zahedan Journal of Research in Medical Sciences*, vol. 16, no. 12, pp. 8–14, 2013.

[70] Y. Liu, X. Qin, and X. Lu, "Crocin improves endometriosis by inhibiting cell proliferation and the release of inflammatory factors," *Biomedicine & Pharmacotherapy*, vol. 106, pp. 1678–1685, 2018.

[71] H. A. Bakshi, F. L. Hakkim, S. Sam, F. Javid, and L. Rashan, "Dietary crocin reverses melanoma metastasis," *Journal of Biomedical Research*, vol. 32, 2018.

[72] M. T. Lee, C. C. Lee, H. M. Wang et al., "Hypothermia increases tissue plasminogen activator expression and decreases post-operative intra-abdominal adhesion," *PLoS One*, vol. 11, no. 9, 2016.

[73] G. M. Saed and M. P. Diamond, "Modulation of the expression of tissue plasminogen activator and its inhibitor by hypoxia in human peritoneal and adhesion fibroblasts," *Fertility and Sterility*, vol. 79, no. 1, pp. 164–168, 2003.

[74] H. M. Atta, A. Al-Hendy, M. A. El-Rehany et al., "Adenovirus-mediated overexpression of human tissue plasminogen

activator prevents peritoneal adhesion formation/reformation in rats," *Surgery*, vol. 146, no. 1, pp. 12–17, 2009.

[75] M. P. Tsantarliotou, S. N. Lavrentiadou, D. A. Psalla et al., "Suppression of plasminogen activator inhibitor-1 (PAI-1) activity by crocin ameliorates lipopolysaccharide-induced thrombosis in rats," *Food and Chemical Toxicology*, vol. 125, pp. 190–197, 2019.

[76] A. Bolhassani, A. Khavari, and S. Z. Bathaie, "Saffron and natural carotenoids: biochemical activities and anti-tumor effects," *Biochimica et Biophysica Acta (Bba)-reviews on cancer*, vol. 1845, no. 1, pp. 20–30, 2014.

[77] L. Sabatino, M. Scordino, M. Gargano, A. Belligno, P. Traulo, and G. Gagliano, "HPLC/PDA/ESI-MS evaluation of saffron (Crocus sativusL.) adulteration," *Natural Product Communications*, vol. 6, no. 12, 2011.

[78] S. A. Baba, A. H. Malik, Z. A. Wani et al., "Phytochemical analysis and antioxidant activity of different tissue types of *Crocus sativus* and oxidative stress alleviating potential of saffron extract in plants, bacteria, and yeast," *South African Journal of Botany*, vol. 99, pp. 80–87, 2015.

[79] M. Guijarro-Díez, L. Nozal, M. L. Marina, and A. L. Crego, "Metabolomic fingerprinting of saffron by LC/MS: novel authenticity markers," *Analytical and Bioanalytical Chemistry*, vol. 407, no. 23, pp. 7197–7213, 2015.

[80] A. Termentzi and E. Kokkalou, "LC-DAD-MS (ESI+) analysis and antioxidant capacity of Crocus sativus petal extracts," *Planta Medica*, vol. 74, no. 5, pp. 573–581, 2008.